The Dissertation Committee for Christian Philip Armstrong Certifies that this is the approved version of the following dissertation:

Characterization of Expansive Clay Behavior using Centrifuge and Field Evaluations

Committee:

Jorge G. Zornberg, Supervisor

Chadi El Mohtar

Robert Gilbert

Amit Bhasin

Donggao Zhao

Characterization of Expansive Clay Behavior using Centrifuge and Field Evaluations

by

Christian Philip Armstrong

Dissertation

Presented to the Faculty of the Graduate School of

The University of Texas at Austin

in Partial Fulfillment

of the Requirements

for the Degree of

Doctor of Philosophy

The University of Texas at Austin

May 2018

Dedication

Ad majorem Dei gloriam.

"Where were you when I laid the foundation of the earth?

Tell me, if you have understanding.

Who determined its measurements – Surely you know!

On what were its bases sunk, or who laid its cornerstone,

when the morning stars sang together, and all the sons of God shouted for joy?"

Job 38:4-7

Acknowledgements

The research contained in this dissertation is the result of the help and support of friends and colleagues. I'd like to thank my adviser, Dr. Jorge Zornberg, for your mentorship and guidance, which propelled me to go to graduate school and pursue a doctorate degree. I'd also like to thank the faculty at the University of Texas, particularly Dr. Robert Gilbert and Dr. Desmond Lawler, who taught me as an undergraduate to look beyond equations and laboratory tests to the fundamental, intrinsic joy of research. Finally, I'd like to thank my committee members, including Dr. El Mohtar, Dr. Bhasin, and Dr. Zhao, who taught me the fundamentals and techniques in coursework and provided feedback and advice that made this dissertation possible.

I'd also like to thank my fellow colleagues and labmates for all the help with research, instrumentation, and their friendship. I've been very lucky to have such great friends and colleagues, particularly Julio Zambrano, Michael Plaisted, Marcelo Azevedo, Ryan Phillips, Jose Martinez, Hossein Roodi, Gaston Quaglia, Calvin Blake, Larson Snyder, Amr Morsy, Xin Peng, and Aaron Potkay, that really made the more difficult portions of research enjoyable. I'd also like to thank the countless undergraduate research assistants who were always a joy to work with.

I would also like to thank the Texas Department of Transportation for their financial funding of my project and Mike Arellano and Brett Haggerty for their valuable insight into practical applications and support for the research on expansive subgrades. The help I've been provided from TxDOT has been fantastic and allowed for me to examine a problem that affects the citizens of the great state of Texas.

My family has been such a blessing to me. Both of my parents have given me so many blessings, and I wouldn't be here without their support. Seeing my sister's family expand with three nieces has been fantastic to watch and helped mark the time I've spent here! I'd also like to thank my grandparents for their support when I was younger, always pushing me to learn about the joy of the pursuit of knowledge. I can only hope that I have made y'all proud.

For all my friends in Austin, I couldn't have done this without you. I particularly want to thank Holly Boerner, Tony Proskovec, Russell Marks, Erik Dumantay, Arturo Torres, Ruby McQuade, Lydia Villarreal, Eugene Martir, Albert Bedia, and the rest of my friends, who have been there for me during this process. We are only as strong as the support around us, and the group of friends here have given me a firm foundation to rest on. I am very much blessed by the amount of people who have helped with my research, and to each of you, I want to share a sincere thank you.

Finally, and most importantly, I want to thank God for guiding me through this wonderful journey. Understanding the complexities of the world around us has given me such an insight into how beautiful this world is, and I look forwards to discovering more of this beauty in my future work.

Characterization of Expansive Clay Behavior using Centrifuge and Field Evaluations

Christian Philip Armstrong, PhD

The University of Texas at Austin, 2018

Supervisor: Jorge G. Zornberg

Subsequent to the development of a centrifuge-based test methodology at the University of Texas at Austin, an extensive research program was conducted to quantify the parameters that govern the swelling behavior of expansive soils and to correlate field measurements of heave and moisture fluctuations with predictions from laboratory testing. The overall research was grouped into five self-contained research components. The first research component examined the effect of the initial conditions in centrifuge soil samples on the magnitude and time-history of swelling. The centrifugation of soil specimens was found to not affect the magnitude of swelling, further validating the centrifuge technique as practical and accurate. The second research component examined the effect of soil fabric on the swelling of laboratory-reconstituted and field-sampled clay specimens. Soil fabric was found to affect the time-history of swelling for laboratory-reconstituted specimens and to affect both the time-history and magnitude of swelling for field-sampled specimens. These results can be attributed to the field-sampled specimens containing a higher amount of peds and micro-void features, as revealed using scanning electron microscope micrographs. These micro-void features are removed during soil homogenization in the laboratory-reconstituted samples. The third research component examined the heterogeneity on a regional and local scale of two clay soils commonly

found in Central Texas. The results indicated that soil samples derived from geologically older parent material tended to swell more than soils derived from geologically younger parent material and that the method of soil sampling affected the magnitude of swelling. The fourth research component examined the field behavior at a site involving an expansive soil subgrade and was instrumented using moisture content and suction sensors. Moisture fluctuations were found to be significant regardless of the pavement surface, and soil-water retention curves were found not to vary significantly with depth. The heave measured at the site was less than that predicted by centrifuge test results due to volumetric strains and desiccation cracks. The final research component examined the large-scale swelling behavior of a column test, prepared to represent a field site. Results from the large column test were compared to the heave predicted using centrifuge test results and the previous field site. The large column was found to behave similarly to the predictions from centrifuge test results, but the infiltration occurred over a longer time frame than the field site. The difference in infiltration rates between the large column and field site was attributed to desiccation cracking at the field site. Overall, the five research components involving expansive soil behavior indicate that the field monitored swelling can be predicted using laboratory centrifuge tests when properly accounting for initial conditions, soil fabric, and spatial variability.

Table of Contents

List of Tables

List of Figures

Chapter 1: Introduction

1.1 Research Motivation

Expansive soils involve a comparatively high percentage of clay minerals that undergo significant volumetric changes upon seasonal moisture fluctuations. Specifically, these soils tend to shrink upon drying and expand upon wetting. These volumetric changes have a detrimental impact on infrastructure that imparts a comparatively low overburden pressure, causing problems such as environmental cracking that is not induced by structural loads. This low overburden infrastructure includes foundations for residential buildings, flexible pavement systems, pipelines, and railways. Expansive soils are prevalent in many regions throughout the United States, and damages due to their volumetric fluctuations have been estimated to exceed a billion dollars per year (Nelson and Miller, 1992). These financial damages are, on average, higher than those caused by other natural disasters such as earthquakes, hurricanes, and floods. The problem of expansive soils is particularly severe in Texas, with the distribution of expansive soils coinciding with the densely populated centers along the I-35 corridor from San Antonio to Dallas as shown in Figures 1.1 and 1.2. This distribution of expansive soils is problematic as it is compounded with the climate in the region, which classifies as a humid, subtropical climate (Cfa according to the Köppen climate types). This climate is characterized by frequent drought-like conditions that reduce the moisture content in soils, followed by intermittent, heavy and short duration rainfall events that significantly increase the moisture content in soils (Norwine et al., 2005).

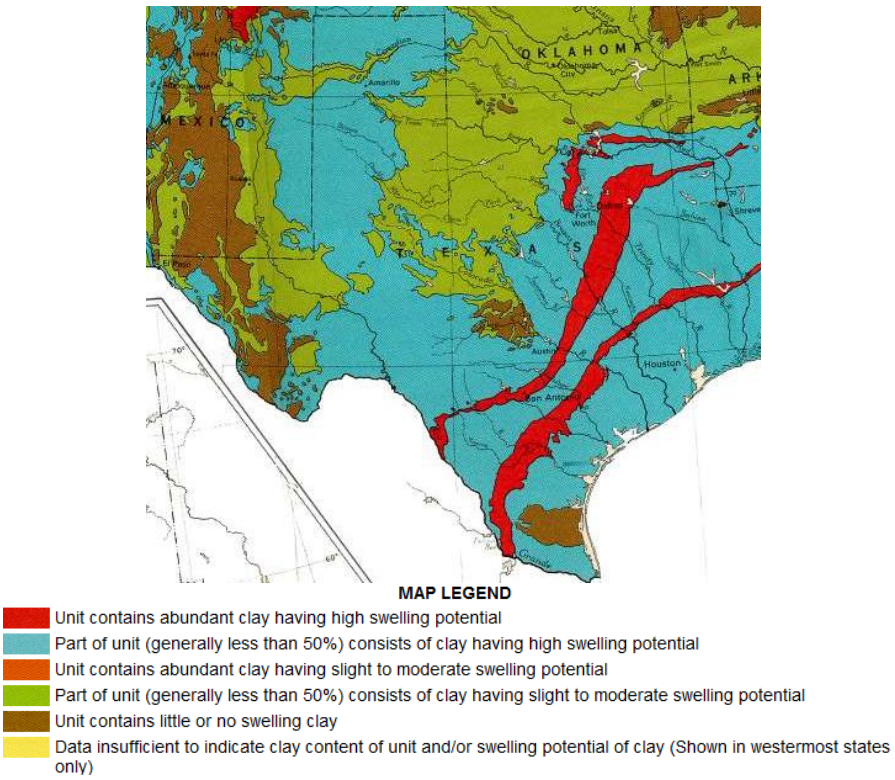

Figure 1.1: Distribution of expansive soils in Texas (Olive et al., 1998)

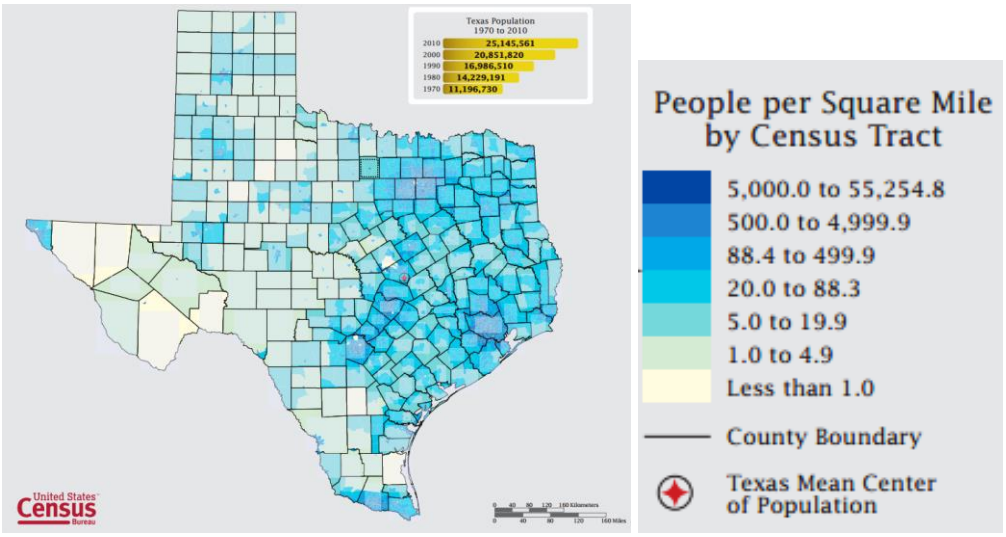

Figure 1.2: Population density of Texas (United States Department of Commerce, 2012)

Expansive soils have been studied extensively, not only because these soils are prevalent globally but also because specific clay minerals known to be expansive are used in various engineering projects (e.g. oil drilling, liner systems for waste disposal). Predictive methods have been developed that utilize soil index properties to estimate the expansive potential of soil deposits. However, these predictive methods tend to rely solely on index properties, disregarding differences in the genesis and geography of soil deposits and use numerous correlations to determine parameters such as the potential vertical rise. These predictive methods are especially prevalent in the design of transportation infrastructure in Texas. Consequently, a centrifuge-based testing methodology to obtain the swelling of soil deposits was developed at the University of Texas in order to more rapidly characterize soils to determine the actual swelling behavior of field soil deposits (Plaisted, 2008). This methodology was originally able to test only laboratory-reconstituted specimens but was further expanded to allow testing of field specimens from push-samplers (Armstrong, 2014). With this equipment, numerous tests have already been run on various soils sampled throughout the Central Texas region. This data was used to characterize individual deposits and the performance of the soils (Zornberg et al., 2017), but further understanding of the behavior of expansive soil deposits can be drawn from the data.

After the development of the centrifuge-based testing methodology, several questions remain about the behavior and characterization of expansive clays in Central Texas. The main question is whether the predictive methods or laboratory methods accurately predict the field behavior of expansive soil deposits, and, if they do not, whether there are methods to correct the data to more accurately predict the field behavior. Additional questions include whether the centrifugation of expansive soils and soil fabric affects the swelling characteristics and whether there is significant

heterogeneity between expansive soil deposits from the same soil series on a regional or local scale.

1.2 Research Objectives

Results for testing of expansive soils in Central Texas have typically been limited to specific sites. These results should be synthesized to link the results between sites, looking at the variability in properties and behavior, as well as differences between laboratory results and field behavior of expansive soils. In order to achieve this goal, the following objectives were pursued in the research conducted as part of this dissertation:

- Assess the potential effect that centrifugation of expansive soils may have on the trends observed in previous parametric evaluations involving the initial soil conditions and other relevant parameters.
- Evaluate the effect of internal soil structure, or soil fabric, on swelling characteristics of both laboratory-reconstituted and undisturbed expansive soil specimens.
- Quantify the spatial variability of soil properties and unsaturated behavior of clay soils on a regional scale.
- Assess the impact of heterogeneity in soil properties and swelling results on a more localized scale.
- Compare the volumetric moisture fluctuations from laboratory testing to those obtained from field expansive soil deposits.
- Validate the use of predictive tools (e.g. the potential vertical rise) by comparing vertical rise predictions obtained using field measurements with field monitoring results.

1.3 DISSERTATION ORGANIZATION

The dissertation is organized in five self-contained research components, with each being a research component that focuses on an aspect of the behavior of expansive soils. The first three research components focus primarily on the behavior of expansive soils in laboratory tests. The last two sections examine a field site and using a large column test, with results from these sections additionally compared against predictions using centrifuge-based swelling tests. A final chapter, included after the self-contained research components, incorporates results and conclusions from the self-contained research components for use in engineering practice.

Chapter 2 includes the results of a parametric evaluation of initial conditions on the swelling behavior of expansive soils in an accelerated gravitational environment. The motivation for this research component is to validate that the trends from centrifuge-based test results are consistent with those from previous research studies. The development of centrifuge technology and methodology for testing of expansive soils is detailed. The effects of initial conditions, such as the gravimetric moisture content, dry unit weight, gravitational level, and specimen height, are evaluated using three clays from different soil deposits.

Chapter 3 provides an examination of the effect of initial structure of the clay, or soil fabric, on the swelling characteristics of expansive soils. The motivation for this research component is to determine what effect fabric has on swelling characteristics and if laboratory-reconstituted specimens can be used to determine the swelling of expansive soil deposits. Results from centrifuge-based swelling tests conducted on both laboratory-reconstituted and field-sampled soil specimens are documented. Additionally, micrographs from electron microscopy that visualize the fabric of laboratory-reconstituted and field-sampled soils and examine differences in soil fabric are presented.

Chapter 4 studies the spatial variability of two well-known soils that comprise a significant portion of the Texas Blackland Prairies: the Houston Black and Branyon clays. Both soils are derived from the Taylor and Navarro groups, are located east of the Balcones fault zone, and serve as foundation soils for a significant number of structures. The motivation for this research component is to determine the variability between soil series in a similar geographic and geologic region. The variability of soil properties, soil-water retention curves, and stress-swell curves of both clays are examined in order to quantify the variability of soil series on a regional scale. A more localized field project, involving Shelby tube samples from 43 borings along an expansion of a roadway, is evaluated to determine the variability of Atterberg Limits and stress-swell curves of soils derived from the Taylor and Navarro groups on a local scale. Additionally, the variability of soil properties and swelling behavior is compared between the regional and local scales.

Chapter 5 examines the field behavior of an expansive soil deposit beneath a pavement structure. The motivation for this research component is to evaluate the differences between laboratory tests and the field behavior of an expansive soil deposit. The subgrade of a newly constructed roadway that contained an expansive soil deposit was instrumented to evaluate seasonal moisture content and suction fluctuations. The evaluations are grouped into two time periods; one where the sensors were beneath a flexible base with a prime coat surface and the other where the sensors were beneath a final asphalt surface. In addition to the monitoring of moisture fluctuations, the surficial pavement deflections were monitored with periodic site visits and a total station-based methodology. Results from the site are compared to laboratory test results, including the prediction of the maximum heave and measured soil-water retention curves.

Chapter 6 compares results from a large column test prepared to represent an expansive soil deposit with predictions from centrifuge swelling tests. The motivation for this research component is to compare the large-scale laboratory behavior of a soil column prepared to represent an expansive soil deposit with results from centrifuge-based swelling tests. The large column test was instrumented with moisture content and matric suction sensors to monitor moisture fluctuations. The heave during an infiltration test was monitored using image analysis techniques. Results from the large column test are compared to the predictions from centrifuge-based swelling tests conducted on laboratory-reconstituted soil specimens. Additionally, differences between two methodologies to measure suction, the filter paper and chilled mirror hygrometer tests, are compared to evaluate the consistency of the methodologies and the osmotic suction of laboratory-reconstituted specimens.

Chapter 7 contains a synthesis of the conclusions and research from this dissertation into application for practice. The method to correct laboratory test data using results from Chapters 2 and 3 is presented. Additionally, the results from Chapters 5 and 6 are used to incorporate the differences in the heave measured at the field site and the large column test with laboratory predictions.

Chapter 8 contains the conclusions from the preceding self-contained studies. Recommendations for future work and methods to further incorporate results from testing are also included.

The appendices contain information and results that are not included in the chapters. Appendix A contains complementary test results from the fabric testing regime in Chapter 2. Appendix B contains complementary test results from the IH-10 testing program at individual borings. Appendix C contains information complementing the hydraulic monitoring of the site from Chapter 5.

Chapter 2: Use of Centrifuge Techniques to Evaluate the Variables Governing Swelling of Expansive Soils

ABSTRACT

The results from a centrifuge-based experimental testing program were used to perform a parametric evaluation regarding the impact of initial and testing conditions on the swelling characteristics of three expansive soils from Central Texas. The variables evaluated in this study included the initial soil preparation conditions (i.e. gravimetric moisture content, dry unit weight, and degree of saturation), initial specimen height, and the gravitational level. The evaluated swelling characteristics included the vertical strains and void ratio at the end of primary swelling, the duration over which primary swelling occurred, and the porosity at the end of testing. The trends from the test results were compared against those reported in previous studies. The magnitude of vertical strains at the end of primary swelling was found to increase with increasing initial dry unit weight and decreasing initial gravimetric moisture content. The trends between the change of void ratio (from the initiation of inundation to the end of primary swelling) and both the initial gravimetric moisture content and dry unit weight were found to be linear for the three soils. However, the effect of the initial degree of saturation on the magnitude of verticals strains at the end of primary swelling was found to be non-linear. The vertical strains at the end of primary swelling were found to decrease with increasing gravitational level due to the corresponding increase in the vertical effective stress. The time periods to reach the end of primary and ultimate swelling were found to increase with increasing specimen height. The trends of variables evaluated in this research component were found to be consistent with those previously reported using results obtained from conventional tests, reaffirming that the use of a centrifuge-based experimental method as both a practical and accurate approach.

2.1 INTRODUCTION

Expansive soils typically involve highly plastic clays that undergo significant volumetric changes upon moisture fluctuations. These soils have been extensively studied in order to quantify the magnitude of the volumetric changes as a function of the soil initial conditions, their geotechnical index characteristics, and their mineralogy. Some of these studies have involved assessing the impact of the soil Atterberg limits (McDowell, 1959) and the impact of the soil initial conditions, including the initial dry density (Komine and Ogata, 1992) and gravimetric moisture content (Chen, 1988). However, the implementation of traditional testing methodologies to quantify volumetric changes has required particularly long testing durations. Consequently, the volume of data generated in previous studies has been comparatively scarce and from a limited number of soil deposits. A new methodology that involves the use of centrifugation to increase the hydraulic gradient in soils was developed to expeditiously characterize the swelling of expansive soils and evaluate this geotechnical problem with significant cost and maintenance implications (Zornberg et al., 2016).

After its development as part of a feasibility study, the centrifuge technology was further evaluated to assess whether centrifugation of soil specimens would adversely affect its swelling characteristics. Several studies, including those reported by Plaisted (2009), Zornberg et al. (2013), and Armstrong (2014), concluded that the magnitude of one-dimensional, vertical strains at the end of primary swelling obtained using the centrifuge-based methodology are consistent with those previously reported using traditional methodologies. However, additional evaluation is still needed to assess whether the trends inferred from previous studies (e.g. the effect of the initial gravimetric moisture content and initial dry unit weight) are adversely affected by the use of an increased gravitational environments. Additional variables that were evaluated as part of

this study to assess their effects on the swelling characteristics include the initial degree of saturation, gravitational level, and specimen height. The evaluated swelling characteristics include the vertical strains, void ratio, and change in void ratio at the end of primary swelling, the duration over which primary swelling occurs as well as the porosity at the end of testing. A parametric evaluation was conducted in this study using on three expansive soils from Central Texas. The evaluation aimed at assessing the trends and their consistency among expansive soils characterized by different levels of plasticity and percentages of fines.

2.2 BACKGROUND INFORMATION

The results of a literature review are reported herein, with focus on the variables that govern the swelling of expansive soils. Accordingly, the first section examines traditional concepts in unsaturated soil mechanics. The second section reviews conventional methodologies that have been used to characterize expansive soils. The third section presents centrifuge-based approaches that have been developed to characterize the swelling of expansive soils. Finally, the fourth section summarizes the results previous parametric evaluations conducted to evaluate the conditions affecting swelling characteristics.

2.2.1 Relevant Concepts in Unsaturated Soil Mechanics

Soil mechanics has traditionally focused on the behavior of soils under either dry or fully saturated conditions, presumably due to the complexities involved in considering a three-phase system involving both pore-water and pore-air pressures. While saturated soil conditions often corresponded to the worst-case scenario in terms of soil shear strength and volume changes induced by compressive loading, the assessment of soil under saturated conditions cannot address problems involving moisture flow and

volumetric changes, specifically swelling, for soils located in the unsaturated, or vadose, zone (Figure 2.1). The unsaturated zone is particularly important as it represents the surficial conditions for the majority of engineering projects.

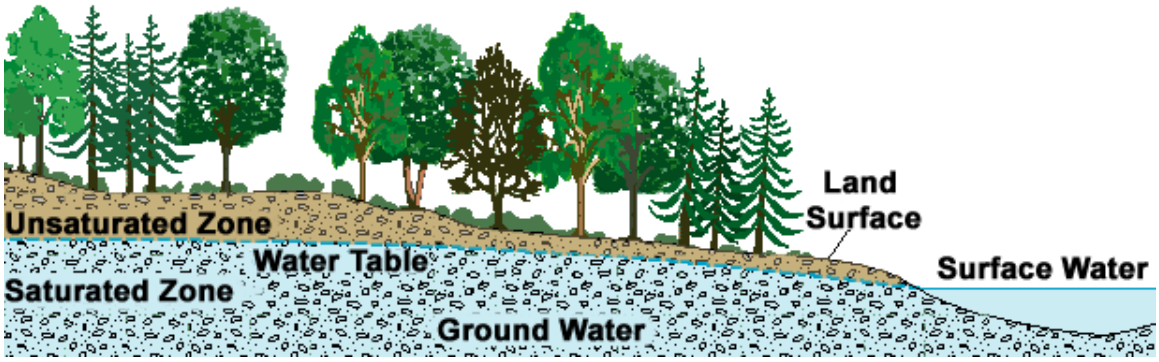

Figure 2.1: Delineation of saturated and unsaturated zones in natural systems (USGS, 2013)

In order to define the shear strength and hydraulic properties for soils in the unsaturated region, the difference between the pore-air and pore-water pressures acting on the soil, or matric suction, should be quantified. Flow in vadose zone can be modeled using Richard's Equation, which for the case of one-dimensional gravitational flow can be expressed as follows:

$$\frac{\partial \theta}{\partial t} = -\frac{\partial}{\partial z}\left[K(\theta)\left(\frac{\partial \psi}{\partial z} + 1\right)\right] \tag{2.1}$$

where θ is the volumetric moisture content, K(θ) is the unsaturated hydraulic conductivity function of the soil, and ψ is the soil matric suction. The relationship between the volumetric moisture content and suction is defined by a soil-water retention curve (SWRC). In order to measure the suction at a given volumetric moisture content, various testing methodologies can be used, including the hanging column, pressure plate, chilled

mirror hygrometer, and centrifuge methods (ASTM D6386). Results from these tests can be used to generate a soil-water retention curve as illustrated in Figure 2.2.

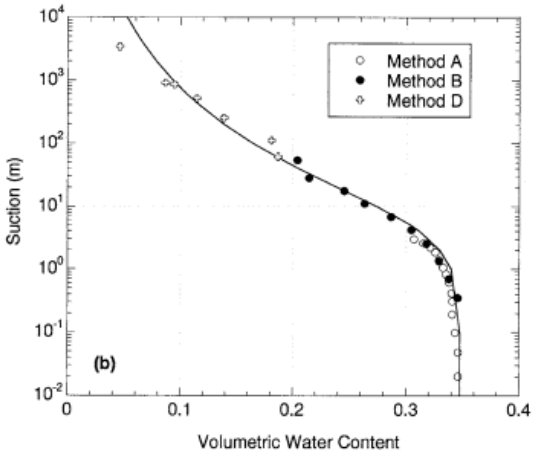

Figure 2.2: Typical soil-water retention curve (ASTM D6386)

2.2.2 Traditional Methodology for Swelling Tests

The traditional testing methodology used to determine the swelling characteristics of expansive soils is summarized in ASTM D4546. The test set-up involves placing a soil specimen in a consolidation cell, as illustrated in Figure 2.3.

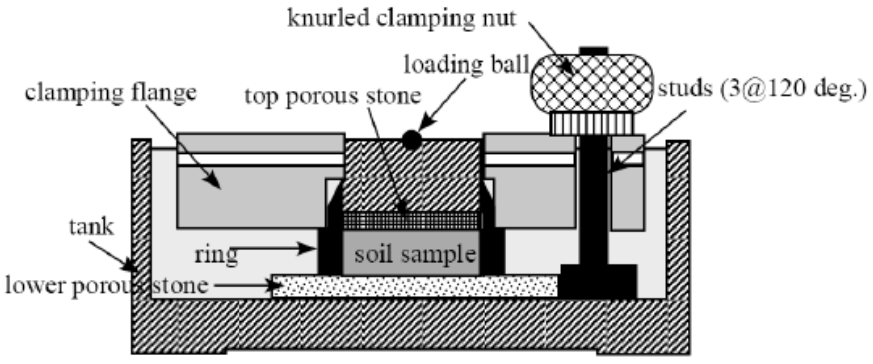

Figure 2.3: Fixed-ring consolidation cell for ASTM D4546 (Olson, 2007)

The consolidation cell is placed in a consolidation frame for testing. The testing procedures includes three methods. Method A, known as "wetting-after-loading tests on multiple specimens," involves measuring the swelling of identical soil samples, either remolded or undisturbed, using a minimum of four different overburden stresses. The soil specimens have a minimum initial height of 20 mm (0.8 in) and a minimum diameter of 50 mm (2.0 in). The soil specimens additionally have their initial water content and dry density measured. Remolded specimens use only the soil fraction passing the No. 10 sieve (2 mm mesh). The soil samples are first compressed under a target overburden stress, and they are then allowed to swell by allowing free access to water placed in the consolidation cells. The sample height is measured at time intervals of 0.5, 1, 2, 4, 8, 15, 30, 60, etc. minutes. Testing is typically conducted until the primary swelling has been clearly determined. The primary swelling is defined as the swelling at which lines tangent to the early, rapid swelling and subsequent, comparatively slower swelling portions of the swelling curve intersect. A typical swelling versus time curve, illustrating the determination of the end of primary swelling, is shown in Figure 2.4.

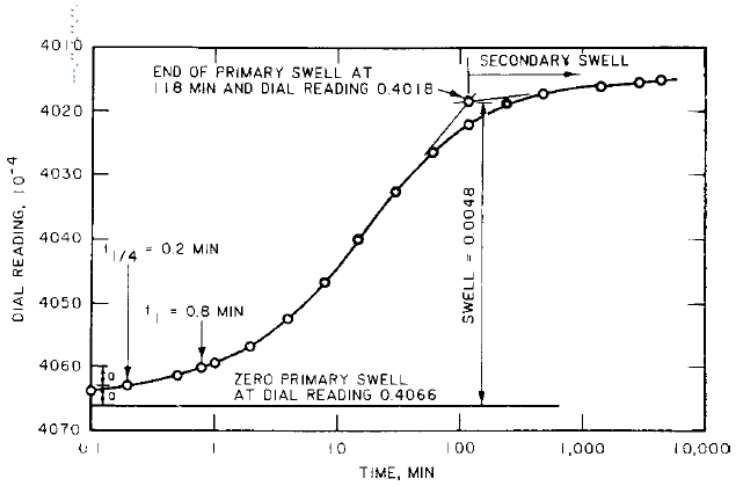

Figure 2.4: Typical swelling versus time curve (ASTM D4546)

Using the primary swelling results from a number of tests (typically four) at differing vertical stresses, a swelling versus stress curve can be generated. The swell pressure corresponds to the minimum pressure at which no swelling occurs. It is determined by fitting the magnitudes of the primary swelling against the corresponding vertical stresses. A typical swell-stress curve is shown in Figure 2.5.

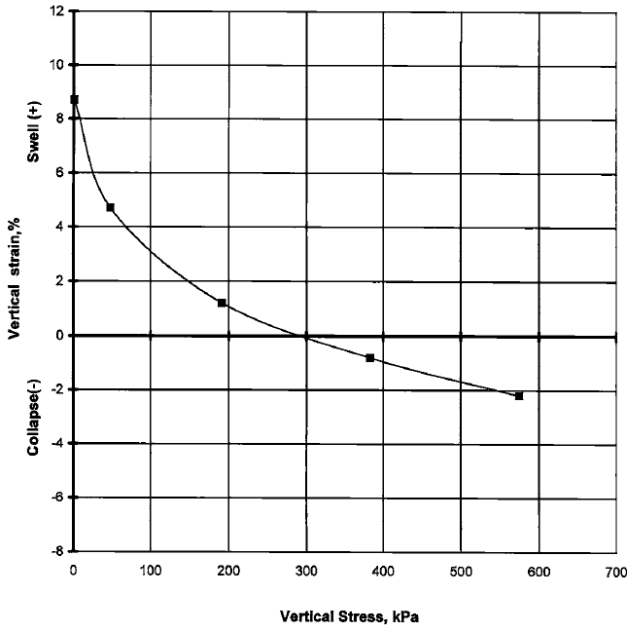

Figure 2.5: Deformation of soil specimens versus stress (ASTM D4546 - Method A)

Method B involves measuring the swelling of a single undisturbed soil specimen. The vertical testing stress is selected to be the in-situ or an overburden stress that is relevant for design. The method is commonly known as the "single point wetting-after-loading test on a single specimen." Method C involves measuring the deformation of a soil specimen that has previously been allowed to swell without having applied overburden stresses. After the soil specimen has undergone swelling (under no overburden stress), the specimen is loaded to the target overburden stress, and

measurements are taken during as changes in the specimen height occur. This method is commonly used to mimic the wetting of a soil deposit prior to construction activities.

The traditional methodology for soil swelling characterization has faced significant drawbacks that have limited their use to predict the field behavior of expansive soils, as follows: (1) The soil specimens are inundated, approaching full saturation during the test, a scenario that rarely occurs in practice. Therefore, the final degree of saturation of the soil specimen is typically higher than that encountered in the field. Consequently, the test provides an upper limit on the heave expected in the field. (2) Due to the rigid nature of the consolidation ring, lateral swelling is not captured in this methodology. However, under field conditions, lateral swelling is a relevant component of swelling and shrinkage (including the formation of desiccation cracks). (3) The soil specimens used in testing are typically remolded in the laboratory, which may minimize the influence of the in-situ soil fabric. (4) The testing procedures specify the removal of soil particles greater than the No. 10 sieve to prepare the remolded specimens. The removal of these particles may lead to an overestimation of the soil swelling based on the gradation in the field. Due to these issues, the swelling predicted using traditional methodologies may not match the actual response of expansive soils in the field.

Additionally, implementation of the traditional methodology has been severely limited in practice due to the significant time required for testing. The testing procedure requires a clear delineation of the regions corresponding to both primary swelling and secondary swelling, as shown in Figure 2.4. In the case of highly plastic clays, this delineation may require significantly long testing times.

2.2.3 Centrifuge-Based Approaches

In order to reduce the time of testing, centrifuges have been used in previous studies to characterize and model expansive soils. Frydman and Weisburg (1991) reported a test using a column of expansive soil placed in a centrifuge in order to reduce testing time. The soil column, with a diameter of 112 mm and a height of 300 mm, was compacted in 20 mm lifts while placing steel balls in the center of each layer. Gamma rays were subsequently used to measure displacements, moisture content, and the dry unit weight in the center of each compacted layers during testing. Additionally, a camera was used to capture the apparent swelling from the outside of the column. Water was ponded on top of the column and allowed to drain at its base through a sand layer. Results from the centrifuge testing were compared against those from column tests completed in a 1-G environment. Centrifuge test results were also compared against the stress-swell curve generated using the traditional methodology outlined in Section 2.2.2. The vertical strains measured in the 1-G columns were over-predicted by the centrifuge results at low stresses and under-predicted at high stresses, as illustrated in Figure 2.6. The difference between the vertical strains measured from centrifuge tests and those measured in the 1-G columns was attributed to side friction, with the frictional resistance of the centrifuge column increasing with depth. This explanation was validated by the differences in the photographs and gamma-ray measured strains with depth. The swelling results at the center of the column, as measured by the gamma ray method, were higher than those from the photographs, as illustrated in Figure 2.7.

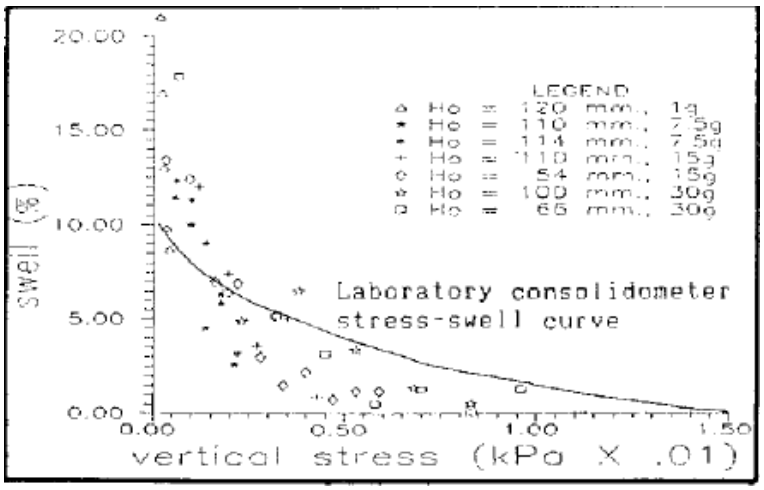

Figure 2.6: Comparison of stress-swell curves for the Mizra Clay between centrifuge and traditional swelling tests (Frydman and Weisburg, 1991)

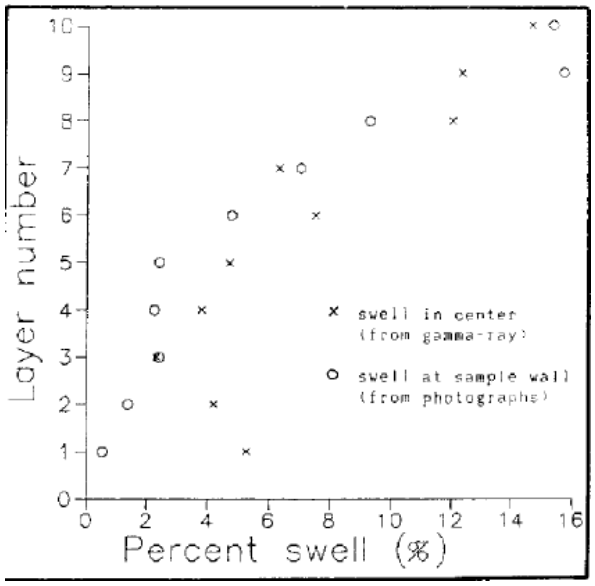

Figure 2.7: Strain in different soils layers for the centrifuge column tests (Frydman and Weisburg, 1991)

The centrifuge tests were also modeled numerically. Modeling of the column indicated that the hydraulic conductivity was independent of the gravitational level imposed due to the high suction within the expansive soil column. The suction gradients were found to dominate the influx of moisture into the soil column.

Gadre and Chandrasekaran (1994) used a geotechnical centrifuge to measure the magnitude of vertical strains of a highly plastic clay. Their set-up, shown in Figure 2.8, involved moisture flow through a porous disk at the base of the specimen. Vertical displacements were measured with an LVDT at the top of the specimen. Water was allowed to permeate into the soil specimen using a perforated disk placed at the top of the specimen.

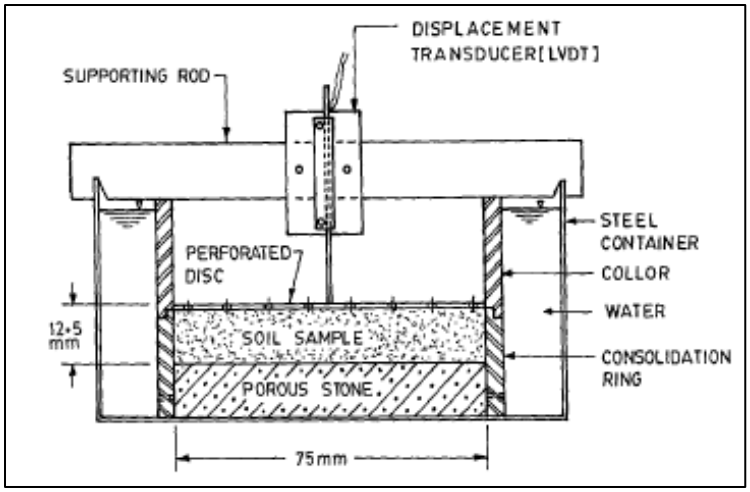

Figure 2.8: Experimental set-up for centrifuge testing of the Black Cotton clay (Gadre and Chandrasekaran, 1994)

Tests were conducted using specimens prepared with the Black Cotton clay, which had a liquid limit of 71 and a plasticity index of 39. The soil, sieved through the No. 40 sieve, was compacted in cutting rings with a 75 mm diameter to a 12.5 mm height. The soil samples were then tested under various gravitational levels. The results from centrifuge testing were compared to those from the traditional methodology. A swelling versus specimen height curve was generated using both the centrifuge-based and traditional methodology, as shown in Figure 2.9. Results from Gadre and Chandrasekaran (1994) using a centrifuge-based methodology showed good agreement with results from

traditional methodology, although using samples that are significantly smaller than those from Frydman and Weisburg (1991). The authors attribute this improvement to a reduction in the side friction due to the use of comparatively small specimen heights.

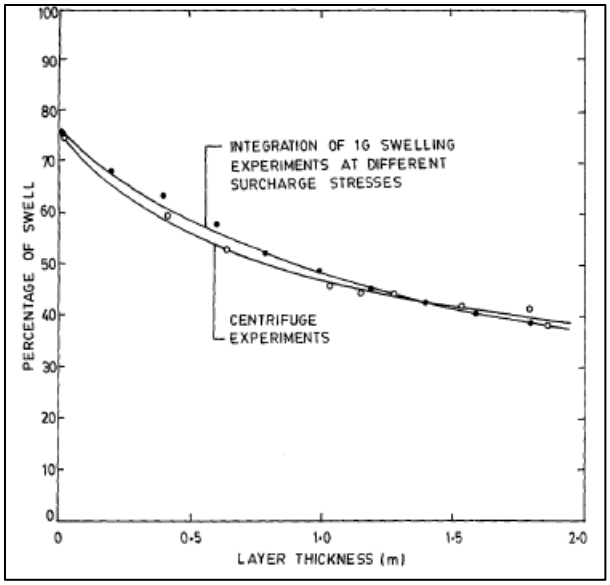

Figure 2.9: Comparison between centrifuge and oedometer tests for the Black Cotton clay (Gadre and Chandrasekaran, 1994)

A centrifuge-based approach to a test highly plastic clays was developed at the University of Texas at Austin, as documented by McCartney (2007), Plaisted (2009), Kuhn (2011), Zornberg et al. (2013), and Armstrong (2014). McCartney and Zornberg (2010) designed and constructed a new centrifuge, the Centrifuge Permeameter for Unsaturated Soils (CPUS) (Figure 2.10) to determine the unsaturated hydraulic characteristics of clays. The CPUS used a relatively high RPM to model flow processes in unsaturated soils in a comparatively smaller environment than traditional geotechnical centrifuges. Due to the relatively high RPMs, a high gravitational gradient could be imposed on the soil specimens. However, only two specimens could be tested during

each centrifuge test. While expeditious and suitable to measure variables such as the unsaturated hydraulic conductivity, the system would be impractical if the overall objective is to quantify the swelling of soils. For example, only two samples could be tested simultaneously.

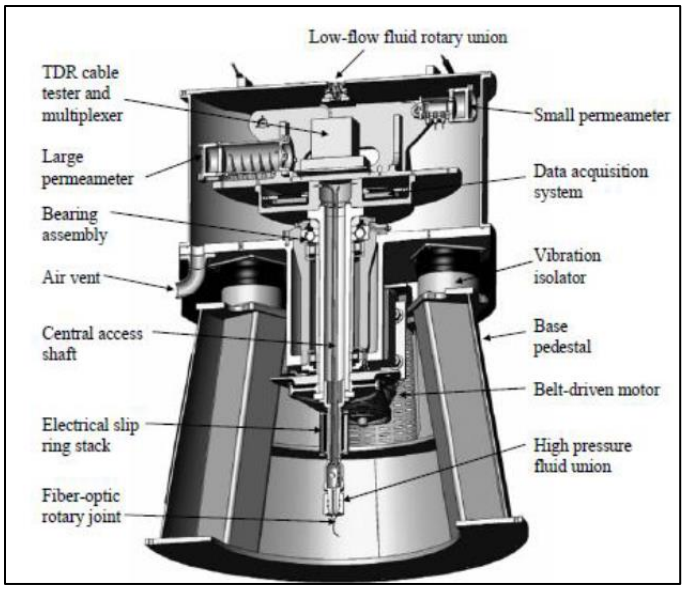

Figure 2.10: Large centrifuge set-up (McCartney, 2007)

With the explicit objective of characterizing the swelling in expansive soils, Plaisted (2008) developed a centrifuge-based testing methodology involving a comparatively small general-purpose centrifuge. The test involved one-dimensional infiltration of moisture from the top of soil specimens in order to match the boundary conditions that are typical in the field. Water was ponded on the specimen and allowed to infiltrate into the soil specimen and eventually to an outflow chamber while subjected to a specified gravitational level. A view of the centrifuge environment for testing is shown in Figure 2.11. Testing was conducted on laboratory reconstituted specimens of the Eagle Ford clay, a highly plastic clay with a Liquid Limit of 88 and a Plasticity Index of 49.

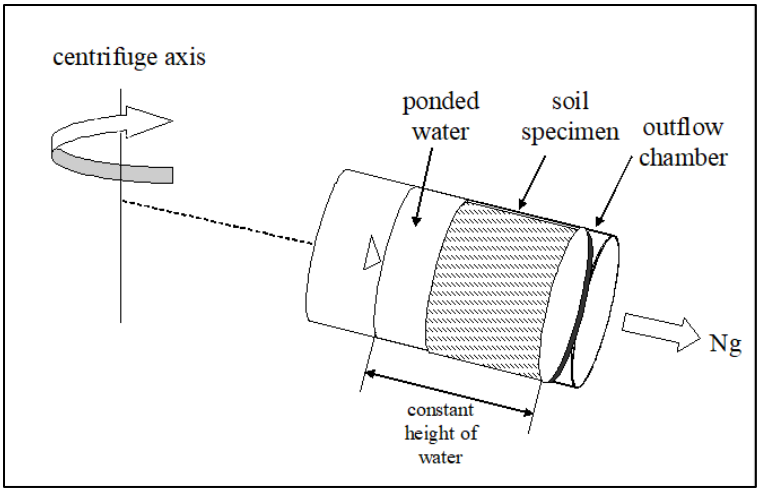

Figure 2.11: Centrifuge environment for the swelling of highly plastic clays (Plaisted, 2009)

The testing procedure involved an initial compression phase, in which specimens were loaded with an overburden stress similar to the one to be applied during the infiltration phase of testing. After the compression phase, the centrifuge was stopped, and the volume of water corresponding to a 2 cm head was ponded on the top of the soil specimen. The centrifuge was then re-started. Height measurements were made periodically by stopping the centrifuge and measuring the change in height using a caliper. Due to removal of the specimens from the centrifuge environment after the addition of water, swelling values measured using the centrifuge approach were found to be higher than those obtained using the traditional methodology, as shown in Figure 2.12. This discrepancy was attributed to the reduction of stresses in the soil specimens during the time period when measurements were made in the centrifuge specimens. The reduction in effective stresses was expected to have led to comparatively higher swelling.

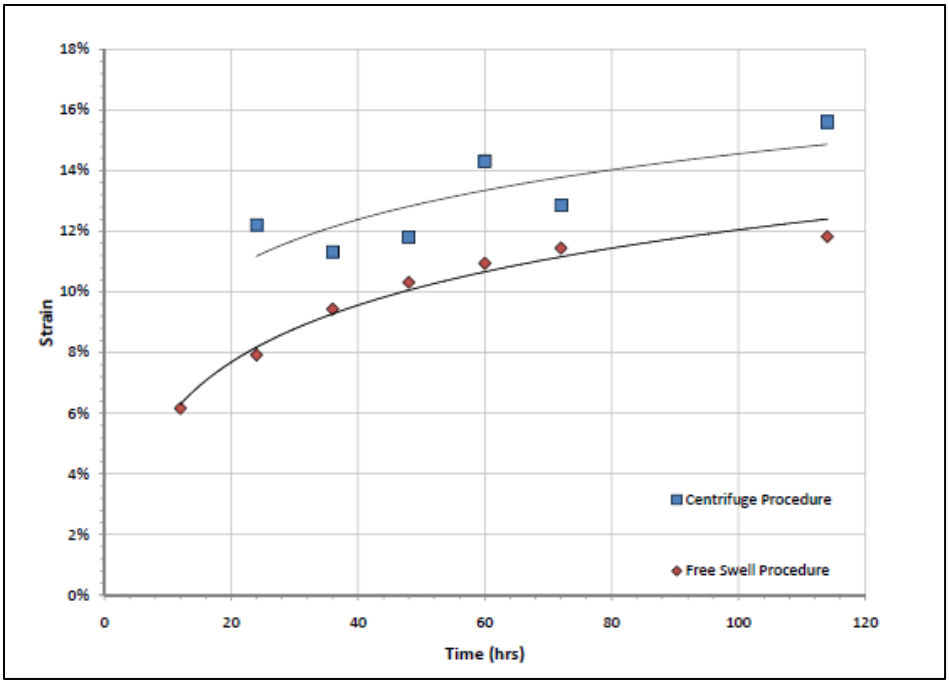

Figure 2.12: Swelling versus time between centrifuge and traditional tests (Plaisted, 2009)

The centrifuge procedure was found to lead to a comparatively large scatter and a higher swelling than the traditional methodology, labeled as the "free swell procedure" in Figure 2.12. Despite the higher swelling in the centrifuge-based approach those in the traditional approach, Plaisted showed the feasibility of using of small general-purpose centrifuge to evaluate a large number of expansive soil specimens.

Kuhn (2010) used the CPUS, which was equipped with a wireless data acquisition system, to examine the swelling behavior of the Eagle Ford clay. The data acquisition system allowed for in-flight measurement of changes in specimen height using a linear position sensor as well as the flow of moisture at the base of the specimen using an outflow tipping bucket. Water in the CPUS was applied on top of the specimen using a medical pump could impart a constant water flux during testing. By adding water using the pump, the level of ponded water was maintained constant, which led to uniform

overburden stress applied during testing under increased artificial gravitational level. The testing program involved testing specimens at 25, 50, and 100 g's for two testing series. Series (i) involved testing samples under a constant water height and surcharge mass but varying the artificial gravitational level. Series (ii) involved a testing program where the surcharge and artificial gravitational level were both varied to keep a constant water pressure (400 psf). These two testing series were used to verify that the water pressure under a gravitational level did not affect the swelling behavior of the expansive soils. Results from both testing series indicated that the void ratio at the end of testing followed a linear trend with total stresses, as illustrated in Figure 2.13.

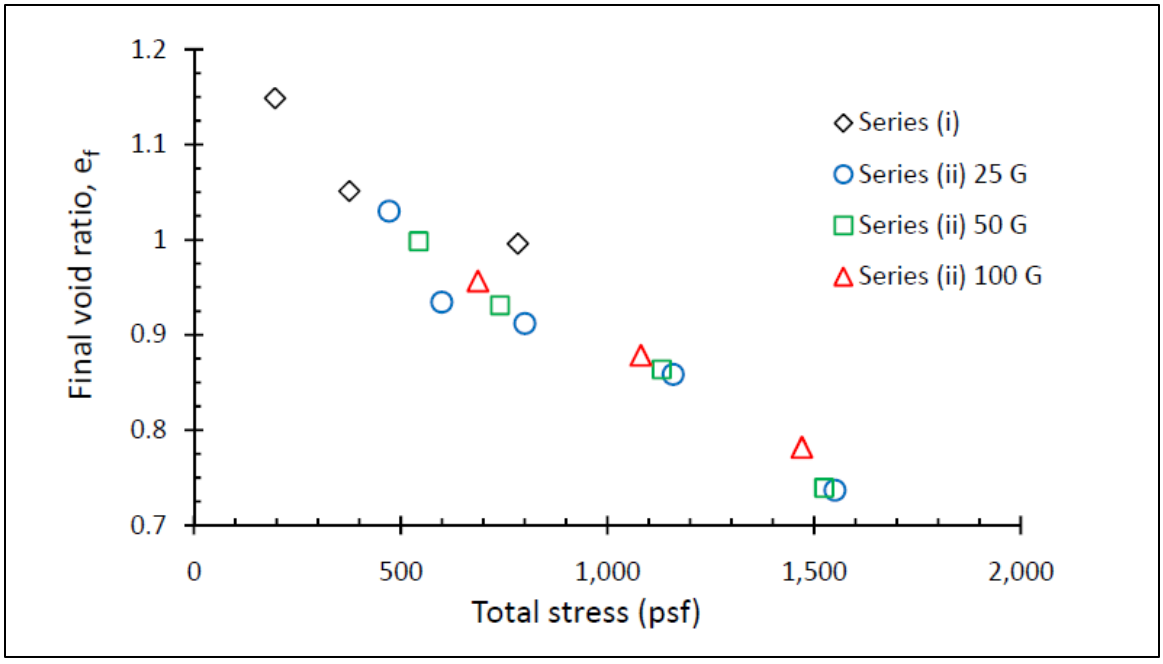

Figure 2.13: Final void ratio versus total stress for CPUS swelling tests (Kuhn, 2010)

Since both testing series followed the same trend, the water pressure was not found to affect the swelling behavior of expansive soils. Therefore, later centrifuge evaluations solely varied the gravitational level with a constant water level and surcharge. The

results from the centrifuge test series were also compared to results obtained from traditional methodology (referred in this study as "free-swell tests") and from 1-G infiltration tests conducted in a triaxial cell. The vertical strain at the end of testing versus the effective stress is shown in Figure 2.14 for these additional tests. The approached followed by Kuhn (2010) involved disregarding the strains from the upper third of specimens due to inconsistencies in testing results from this portion of the soil specimens and ponding of water on the surface of soil specimens at the end of testing. Comparison of results obtained using the three methodologies were found to show good consistency, indicating that the centrifuge technology may be useful to define a stress-swell curve.

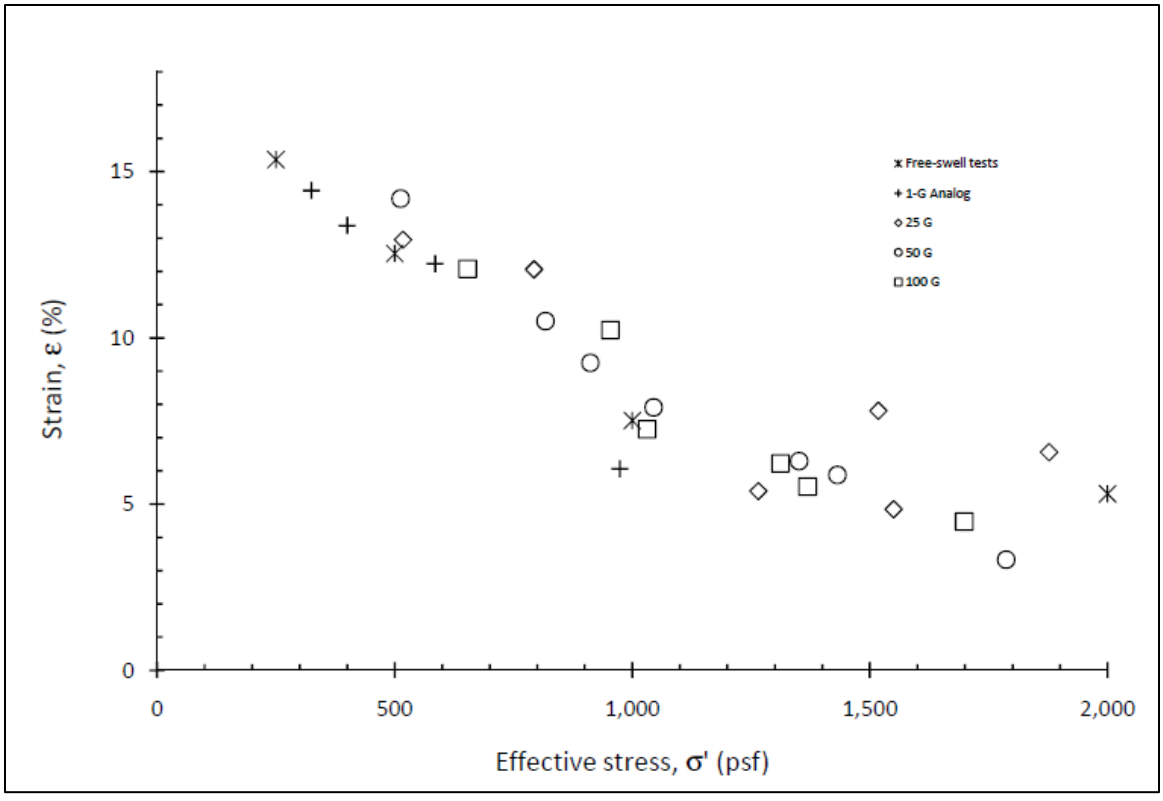

Figure 2.14: Vertical strain versus effective stress for CPUS swelling tests (Kuhn, 2010)

Additionally, Kuhn (2010) modeled the infiltration processes in the centrifuge and concluded that advancement of moisture into the specimen was primarily driven by high initial suction gradients rather than by an increased gravitational gradient. However, in order to reach a comparatively high degree of saturation (e.g. 95%), the time period was reduced from approximately 10 days required using the traditional methodology to less than 3 days when conducting centrifuge tests. This reduction in time was attributed to the increased gravitational gradient driving the infiltration of moisture after the initial suction gradient had been reduced. The availability of an in-flight data acquisition system facilitated understanding the multiple aspects governing the unsaturated flow during swelling. However, the use of the comparatively sophisticated CPUS system was deemed impractical for implementation of testing programs in practical applications.

Zornberg et al. (2013) reported the development of a wireless data acquisition system for the small general-purpose centrifuge. The instrumentation system involved the use of linear position sensors to measure the change in sample height and an accelerometer to measure the artificial gravitational level at a given radial distance. Data from these sensors were transmitted to an analog-to-digital converter to covert the sensor voltage into digital readings. The wireless data acquisition system transmitted the readings from the centrifuge to a nearby computer using two chip boards with an integrated radio system, the JeeNode kit with an Arduino boot loader. The external computer recorded the readings using a LabView program to store the digital readings into text files. The text files with digital readings could be processed to obtain changes in specimen heights at a given gravitational level using a script written using the Python programming language. Testing involved the one-dimensional infiltration set-up based on that reported in Plaisted (2009). The rotor in the centrifuge allowed for simultaneous testing of four soil specimens. Results from tests conducted using the centrifuge with the

data acquisition were compare to results from the traditional methodology, as shown in Figure 2.15. The vertical strains at the end of primary swelling obtained using the centrifuge approach were found to be consistent to those obtained at similar effective stresses using the traditional methodology. The good comparison indicated that the centrifuge technology could be used to define a stress-swell curve for expansive soils.

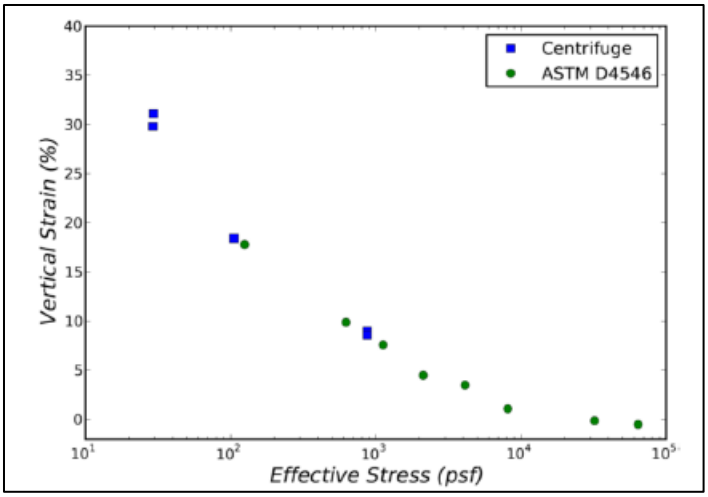

Figure 2.15: Vertical strain at the end of primary swelling versus effective stress between traditional methodology and centrifuge tests (Plaisted, 2009)

The original centrifuge testing set-up was found run into limitations associated with the use of a comparatively small volume of ponded water available for infiltration. Specifically, the height of ponded water could drop significantly when testing reconstituted specimens of comparatively high hydraulic conductivity. Additionally, the permeameter cups did not allow testing of undisturbed soil specimens. Accordingly, further development of the centrifuge-based methodology was conducted to address these limitations.

Armstrong (2014) further refined the centrifuge testing approach in order to minimize the rapid decrease in ponded water height and to allow for the testing of field-

collected, undisturbed soil specimens. The permeameter cup was modified by inserting a cutting ring at the base. The boundary condition was changed from a one-dimensional infiltration approach to an inundation approach that allowed for moisture to infiltrate from both top and bottom of the soil specimen (Figure 2.16). The inundation approach reduced the problems associated with the rapid drop in the height of ponded water and more closely matched the boundary conditions adopted in the traditional methodology.

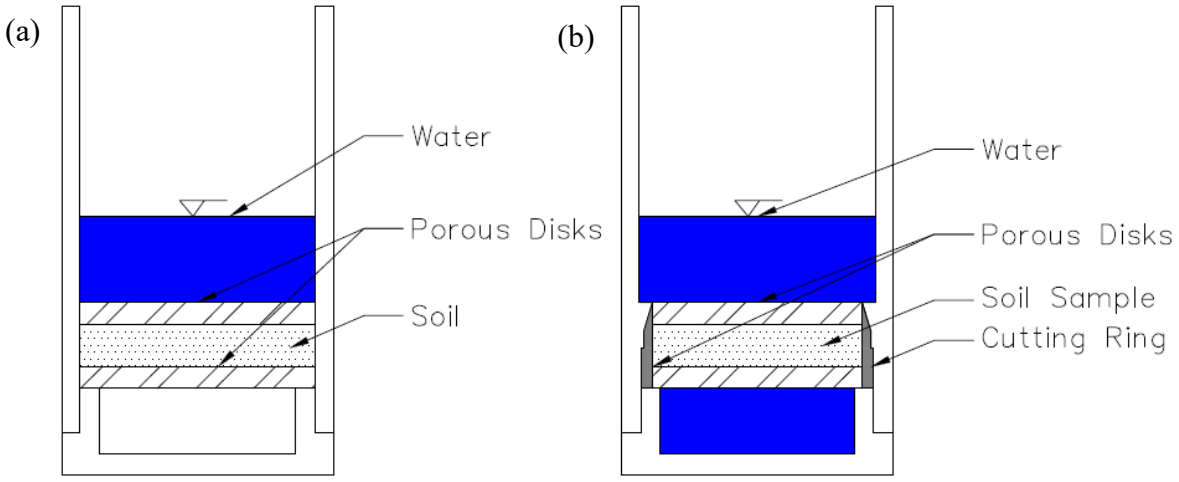

Figure 2.16: Change in boundary conditions between the infiltration (a) and inundation approach (b) (Armstrong, 2014)

The change in boundary conditions also resulted in improved repeatability of test results. The vertical strains at the end of primary swelling was found to be essentially independent on the selection of the boundary conditions used during centrifuge testing (i.e. inundation centrifuge methodology and one-dimensional infiltration centrifuge methodology).

2.2.4 Lessons Learned from Previous Parametric Evaluations

Several studies have been previously conducted using traditional testing methodologies to examine the relevance of index parameters and the impact of initial conditions on the magnitude of volumetric changes in expansive soils. McDowell (1959) reported that soil swelling can be correlated to the soil Atterberg limits and that volumetric change increase with increasing Plasticity Index. Later refinements of McDowell's research indicated that the fraction of soil passing the No. 40 sieve also affects the magnitude of swelling. Chen (1988) conducted a parametric evaluation on natural expansive soils using the methodology outlined in ASTM D4546 and found that the total swelling increased with decreasing initial water content and increasing dry density. Komine and Ogata (1992) conducted tests using the methodology outlined by ASTM D4546 using compacted bentonite specimens with varying initial dry densities and gravimetric moisture contents. They found a linear increase in the vertical strain with increasing initial dry density and decreasing initial gravimetric moisture content, as shown in Figure 2.17.

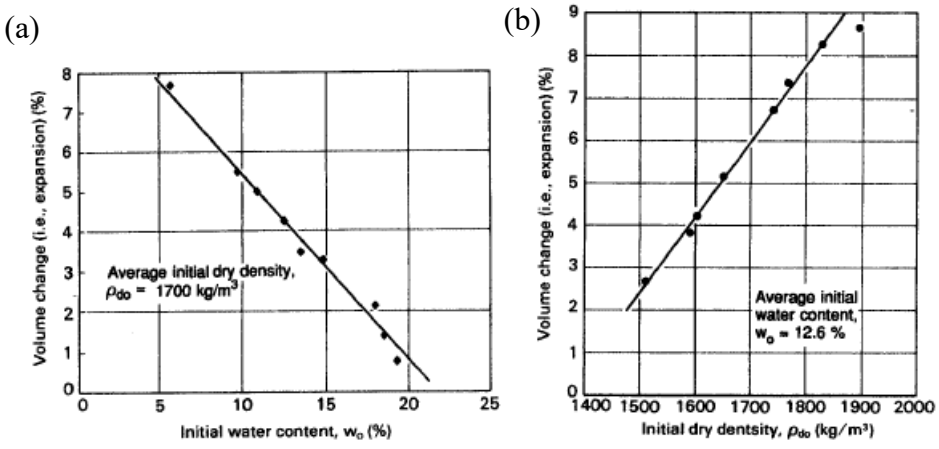

Figure 2.17: Effect of water content and dry density on the swelling of a compacted bentonite (Komine and Ogata, 1992)

Kong and Guo (2011) tested two soils, one of comparatively low swelling potential (having a Liquid Limit of 43) and a second one with medium swelling potential (having a Liquid Limit of 63). For both soils, the vertical strains increase with increasing initial dry density and decreasing initial gravimetric moisture content (Figure 2.18). Note that the trends were found to not to be linear, unlike the trends reported by Komine and Ogata (1992).

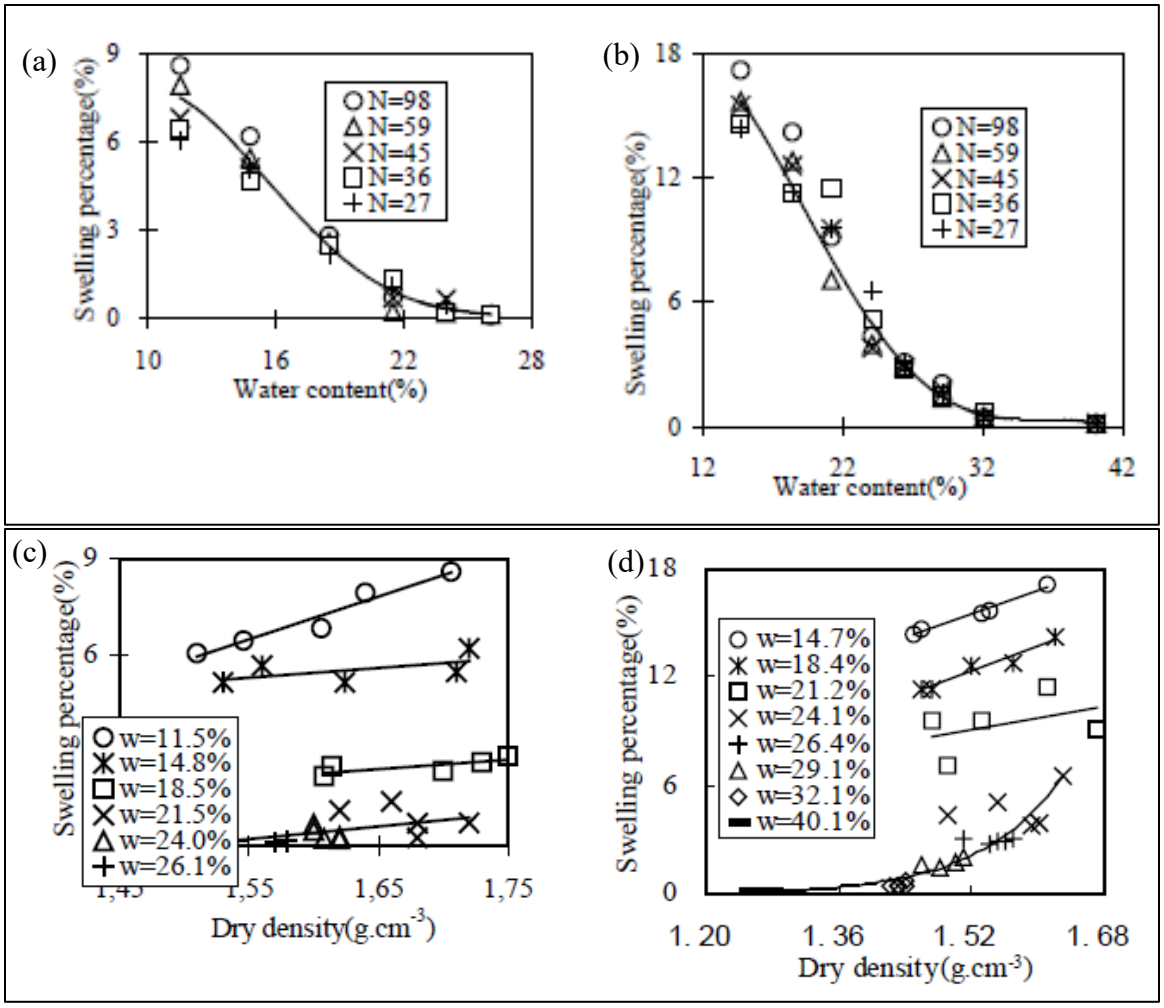

Figure 2.18: Primary swelling versus gravimetric moisture content (a,b) and dry density (c,d) for a low swelling potential soil (a,c) and a medium swelling potential soil (b,c) (Kong and Guo, 2011)

Using the one-dimensional infiltration centrifuge approach described by Zornberg et al. (2013), Walker (2012) performed a parametric evaluation using five expansive soils from Central Texas to quantify the effect of the initial gravimetric moisture content and compaction dry unit weight. Results from the parametric evaluation conducted using one of the soils, the Eagle Ford clay, are shown in Figure 2.19 for varying initial gravimetric moisture contents and in Figure 2.20 for varying initial (compaction) dry unit weights. Test results indicated a linear decrease in the vertical strains with increasing gravimetric moisture content and that there was not a clear trend between the strains and the compaction dry unit weights.

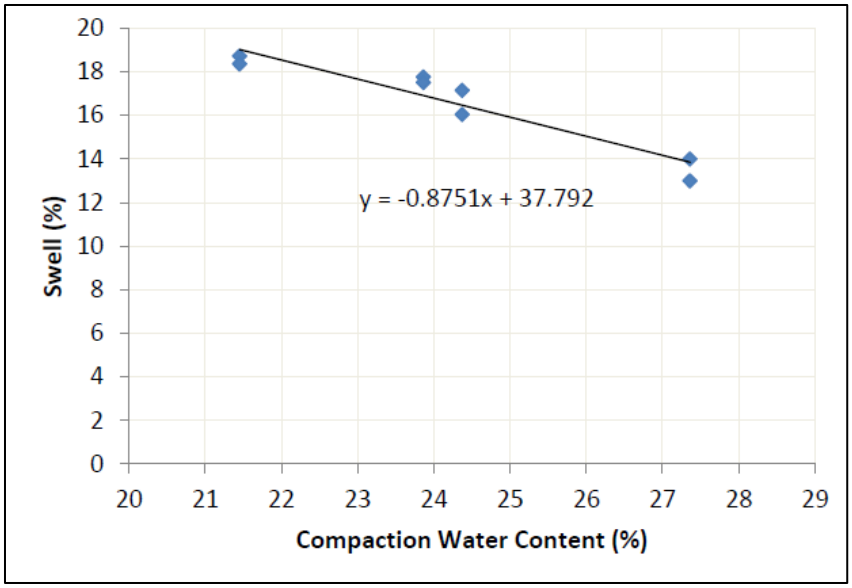

Figure 2.19: Swell versus compaction water content under constant gravitational acceleration for Eagle Ford clay (Walker, 2012)

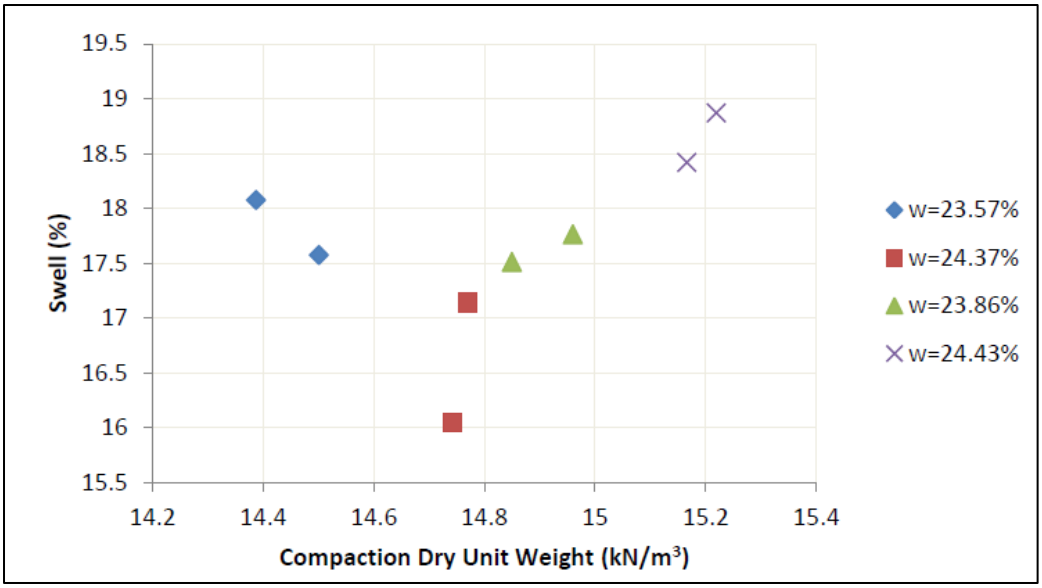

Figure 2.20: Swell versus compaction dry unit weight under constant gravitational acceleration for Eagle Ford clay (Walker, 2012)

The compaction dry unit weights considered in this study ranged from 14.4 kN/m^3 to the maximum dry unit weight according to Proctor tests compacted using standard effort, 15.25 kN/m^3. This range in dry unit weights was significantly smaller than Chen (1988), Komine and Ogata (1992), and Kong and Guo (2011).

Other studies have evaluated the influence of the environmental testing conditions on the magnitude of volumetric strain. Huang et al. (1995) conducted test using the traditional methodology outlined in ASTM D4546 on an expansive soil and then dried the tested specimen in an environmental chamber for two weeks. The dried soil specimens were then tested again using the traditional methodology. The influence of temperature was evaluated by varying the temperature of the infiltrating water, and the influence of the relative humidity was evaluated by varying the relative humidity used to dry the soil specimens after the initial test. Test results indicated that the water temperature has a negligible effect on the magnitude of vertical strain. However, the

relative humidity during drying was found to significantly affect the magnitude of vertical strains.

2.3 CENTRIFUGE TESTING PROGRAM

Three expansive soils were tested in the parametric evaluation conducted in this study. They include the Behring clay (sampled from SH-21 near Paige, TX), the Branyon clay (sampled from FM 685 near Hutto, TX), and the Eagle Ford clay (sampled from I-35 in Round Rock, TX). These three expansive soils were selected for the parametric evaluation as they had already been extensively evaluated as part of previous research projects (Zornberg et al., 2012, Armstrong, 2014, and Azevedo, 2016) and were located within a 10-mile radius in Central Texas. The three soils were collected in bulk from exposed soil deposits. The bulk samples of each soil were intermixed and air-dried at a temperature of approximately 23°C. The air-dried soil was processed using a rock crusher until the majority of the soil was finer than the No. 10 sieve. This soil was sieved in order to remove any remaining aggregates, particularly river stones from the Behring and Branyon clays. The three air-dried soils were then tested to obtain the Atterberg limits according to ASTM D4318. The three soils classify as highly expansive soils (CH) according to the United Soil Classification System (USCS) from ASTM D2487. The three soils were additionally tested for their maximum dry unit weight ($\gamma_{d,max}$) and optimum moisture content (ω_{opt}) considering Standard Proctor compaction energy (ASTM D698), fines content defined from wet sieving of the processed soil (ASTM D422), and clay content defined using hydrometer analysis of soil passing the No. 200 sieve (ASTM D422). A summary of the soils properties is shown in Table 2.1.

Table 2.1: Summary of characterization properties for clays used in parametric evaluation

Soil	Soil Classification (USCS)	Liquid Limit	Plastic Limit	Plasticity Index	Fines Content (%)	Clay Content (%)	ω_{OPT} (%)	$\gamma_{d,max}$ (kN/m^3)
Behring clay	CH	58	17	41	82	40	20	15.42
Branyon clay	CH	65	31	34	93	55	25.5	13.4
Eagle Ford clay	CH	88	39	49	97	76	24.3	15.25

While the three soils were found to be highly plastic clays, their grain-size distributions and Liquid Limits varied significantly. The Eagle Ford clay has a comparatively higher fines content, clay content, and Liquid Limit than the other two soils. The Behring clay has a lower fines content and clay content than the other two soils. However, its Liquid Limit is similar to that of the Branyon clay. Due to these differences in the soil index properties, trends from the parametric evaluation were evaluated for their consistency between expansive soils with differing percentages of fines and liquid limits.

To relate the swelling characteristics with other unsaturated soil properties, the soil-water retention curves for each soil were generated using procedures that measure total suction. Specifically, tests were conducted using a chilled mirror hygrometer, the WP4C from Decagon (ASTM D6836). Data from these tests were fitted to define soil-water retention curves. The van Genuchten model (1980) used to fit the soil-water retention curves can be represented by:

$$\theta = \theta_r + \frac{\theta_s - \theta_r}{[1 + (\alpha * \psi)^n]^m} \tag{2.2}$$

where θ is the soil volumetric moisture content, ψ is the soil suction, θ_s is the saturated volumetric moisture content, θ_r is the residual volumetric moisture content of the soil, α is the air entry pressure, and n and m are curve fitting parameters. Parameter m was estimated using the following assumption (van Genuchten, 1980):

$$m = 1 - \frac{1}{n} \tag{2.3}$$

The van Genuchten model can either involve the volumetric moisture content or degree of saturation as the dependent variable. For expansive soils, the degree of saturation depends on the soil saturated volumetric moisture content which varies based on factors such as hysteresis, soil fabric, and initial compaction conditions.

The curve fitting to define the soil-water retention was accomplished using the GRG Nonlinear Solver method from Microsoft Excel, which minimizes the root mean square error (RMSE). To verify the accuracy of the chilled mirror hygrometer test results, filter paper tests were also conducted according to ASTM D5298. The filter paper tests were performed using Behring clay specimens over a similar range of volumetric moisture contents. The matric suction was measured, as previous studies have shown the influence of the matric suction on the magnitude of swelling (Lin and Cerato, 2012).

Results from both methodologies and their fitted soil-water retention curves are shown in Figure 2.21 for the Behring clay. Note that the suction values are presented in terms of matric suction for the filter paper tests and in terms of total suction for the chilled mirror hygrometer tests.

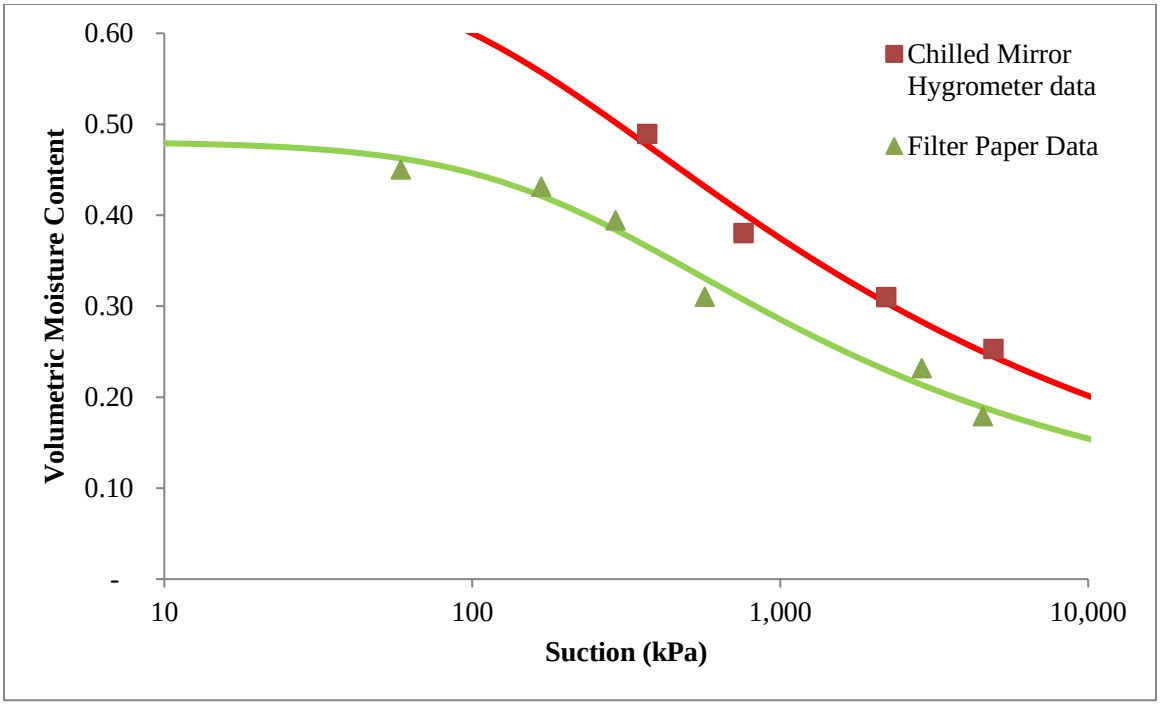

Figure 2.21: Comparison of soil-water retention curves defined using soil suction measurements from chilled mirror hygrometer tests and filter paper tests for the Behring clay

As expected, for a given volumetric moisture content, the total suction values obtained from chilled mirror hygrometer tests were found to be higher than the matric suction values from the filter paper tests. However, differences between the two soil-water retention curves at a given volumetric moisture content was found to be similar in the semi-log space below a volumetric moisture content of approximately 0.40. This trend is consistent with the assumption that the osmotic suction is relatively constant.

The total suction soil-water retention curves were used as a method to compare the initial conditions of the three soils. The total suction was used instead of the matric suction values due to the comparatively short time frame required to generate data using the chilled mirror hygrometer test. Assuming a constant osmotic suction, the difference in total suction between soil specimens can be used to estimate the difference in matric

suction between soil specimens. Total suction data from the chilled mirror hygrometer tests and the fitted soil-water retention curves are shown in Figure 2.22 for the three soils. The total suction for the Branyon clay was typically lower than the total suction for the Behring and Eagle Ford clays at a given volumetric moisture content.

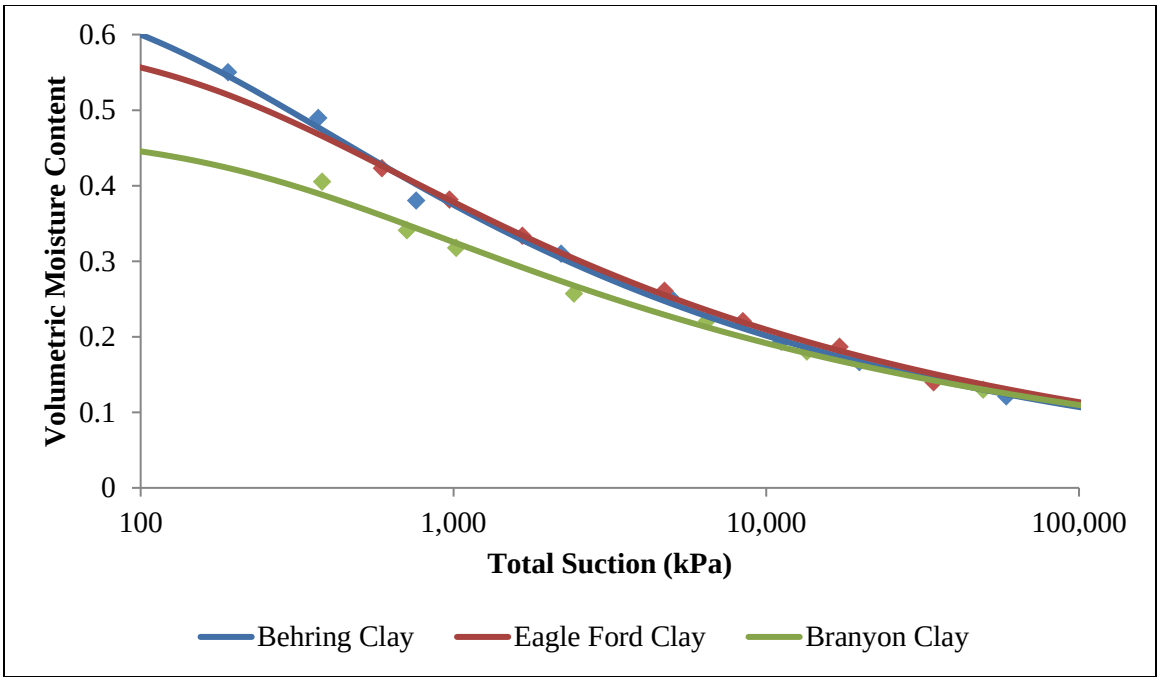

Figure 2.22: Soil-water retention curves defined using chilled mirror hygrometer measurements for the three tested soils

The experimental swelling testing program was performed using the testing methodology developed by Armstrong (2014), as outlined by Zornberg et al. (2017). Soil specimens are first compacted into cutting rings using kneading compaction. The compacted soil specimens and cutting rings are then inserted into a permeameter cup. Brass porous disks are used to allow free moisture access into the specimens. Naval brass was the selected material for the porous disk because of its high specific gravity (approximately 8.4), which facilitated their use to impart the overburden pressure, and its

high corrosion resistance. Filter papers are used to separate the brass porous disks and soil. The components of the swelling permeameter cup and an assembled cup are shown in Figure 2.23.

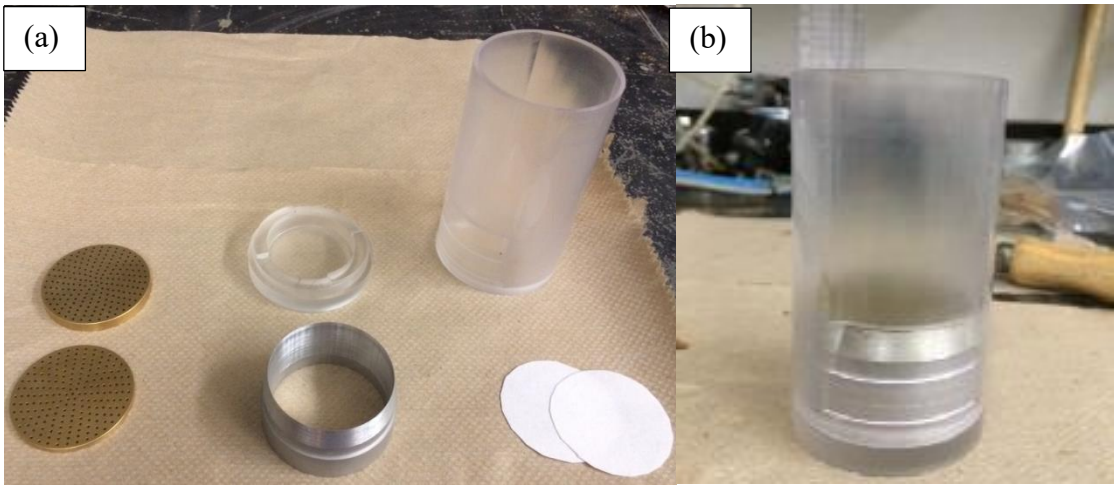

Figure 2.23: Centrifuge inundation permeameter cup: (a) individual components, (b) assembled cup

The permeameter cups are placed into swinging centrifuge buckets. The centrifuge buckets are placed into a general-purpose centrifuge fitted with an in-flight data acquisition system. The in-flight data acquisition system consists of linear position sensors that measure displacements of the soil specimen with time (Armstrong, 2014). Additionally, the centripetal acceleration is measured via an accelerometer. The relatively small specimen height allows for the log-linear interpolation of the gravitational gradient and calculation of the final vertical effective stress (Zornberg et al., 2013, and Armstrong, 2014). Testing involves an initial compression phase, where the soil specimens were loaded under a targeted gravitational level, for approximately an hour. A volume of water that results in a 2 cm head under a 1-G environment is added at the end of the compression phase. The centrifuge is restarted, and specimens are tested over periods

ranging from 24 to 72 hours, depending on the time required to reach the end of primary swelling. After testing, the soil specimens are removed from the centrifuge and placed in an oven for 24 hours at 110°C to obtain their initial and final gravimetric moisture content. Calculations used to define the void ratio, strain, and other relevant testing results from the centrifuge inundation test are outlined in Armstrong (2014).

2.3.1 Scope of Experimental Program

The parametric evaluation conducted in this research component was grouped into five test series. Each test series was conducted to assess the impact on swelling characteristics of variables that describe either the initial soil conditions or the testing conditions. The variables that describe the initial soil conditions include the gravimetric moisture content (Series I), dry unit weight (Series II), and degree of saturation (Series III). The variables that describe the testing conditions include the gravitational level (Series IV) and specimen height (Series V). The swelling characteristics examined in this study include the vertical strains and void ratio at the end of primary swelling, the final volumetric moisture content, and the time to the end of primary swelling. The end of primary swelling was selected as the basis for comparison between test results to be consistent with ASTM D4546. The vertical strains were calculated as follows:

$$\varepsilon_v = \frac{\Delta h}{h_i} \tag{2.4}$$

where ε_v is the vertical strain, Δh is the change in specimen height, and h_i is the initial specimen height.

The three soils presented in Table 2.1 were used in the parametric evaluation. However, each testing series did not necessary include all three soils. The three soils were tested to assess the effect of the initial gravimetric moisture content in Series I and dry unit weight in Series II. The Eagle Ford clay and Behring clay were tested to assess the

effect of sample height in Series III and the effect of the initial degree of saturation in Series V. The Branyon clay and Behring clay were tested to assess the effect of the gravitational level in Series IV. A summary of the experimental program is presented in Table 2.2.

Table 2.2: Scope of the experimental testing program

Series	Evaluated Variable	Variables Maintained Constant	Clays Type	Effective Stress (psf)	Number of Specimens
I	ω_i	γ_{dc}, σ', h_i, g	Eagle Ford	250	5
			Behring		5
			Branyon		12
II	γ_{dc}	ω_i, σ', h_i, g	Eagle Ford	250	5
			Behring		5
			Branyon	125	5
III	Degree of Saturation	σ', h_i, g	Eagle Ford	200 to 300	44
			Behring		36
IV	g-level	ω_i, γ_{dc}, h_i	Behring	10 to 1,000	6
			Branyon		11
V	h_i	ω_i, γ_{dc}, g	Eagle Ford	250	4
			Branyon		3

The variables in Table 2.2 include ω_i (initial gravimetric moisture content), γ_{dc} (dry unit weight at the end of the compression phase), σ' (average vertical effective stress in the soil specimen), g (gravitational level), and h_i (initial specimen height).

2.3.2 Effect of the Initial Moisture Content (Series I)

To assess the effect of the initial moisture content on the swelling characteristics of expansive soils, the soil specimens tested in Series I were prepared using a constant compaction dry unit weight with varying initial gravimetric moisture content. The soil specimens were compacted at a constant initial dry unit weight, which corresponded to the maximum dry unit weight according to Standard Proctor compaction energy (Table

2.1). Testing was performed using gravitational levels ranging from 28 to 30 g's, which correspond to a vertical effective stress of approximately 250 psf. The three soils listed in Table 2.1 were analyzed.

The gravimetric moisture content ranged from the air-dried residual moisture content to ten percentage points above the optimum moisture content, as defined according to Standard Proctor compaction tests. The range of the initial gravimetric moisture contents for the Branyon clay was varied to a wider range than the Eagle Ford and Behring clays to extend the validity of the trends. The vertical strains at the end of primary swelling are shown in Figure 2.24 versus a wide range of initial gravimetric moisture contents for the case of the Branyon clay.

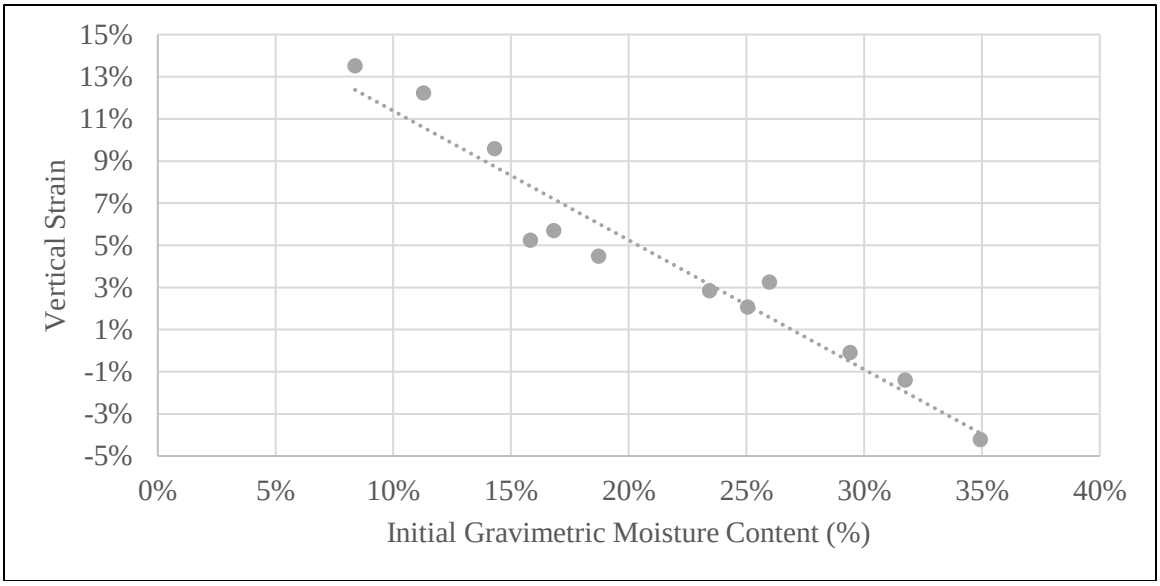

Figure 2.24: Effect of initial gravimetric moisture content on the vertical strains at the end of primary swelling for the Branyon clay, tested under an effective stress of 250 psf

The results obtained for the case of the Branyon clay indicate that increasing initial gravimetric moisture content results in decreasing vertical strains at the end of primary

swelling. This trend was found to be linear from the air-dried residual gravimetric moisture content (approximately 6%) to 10 percentage points wet of the optimum moisture content from Standard Proctor compaction curves (approximately 35%). The linear decrease in the vertical strains occurred both for specimens that swelled upon wetting and for specimens that compressed upon wetting. The soil specimens that had negative vertical strains (i.e. specimens that compressed upon wetting) have a higher gravimetric moisture content than the optimum gravimetric moisture content. This linear trend was determined to be approximately a 6% decrease in the vertical strains at the end of primary swelling for every 10% increase in the initial gravimetric moisture content.

To assess whether linear trends can be generalized for soils other than the Branyon clay, the vertical strains at the end of primary swelling versus initial gravimetric moisture content for the three soils are shown in Figure 2.24. Note that the range of gravimetric moisture contents that were tested for the Eagle Ford and Branyon clays ranged from the air-dried residual moisture content to the optimum moisture content from Standard Proctor compaction curves.

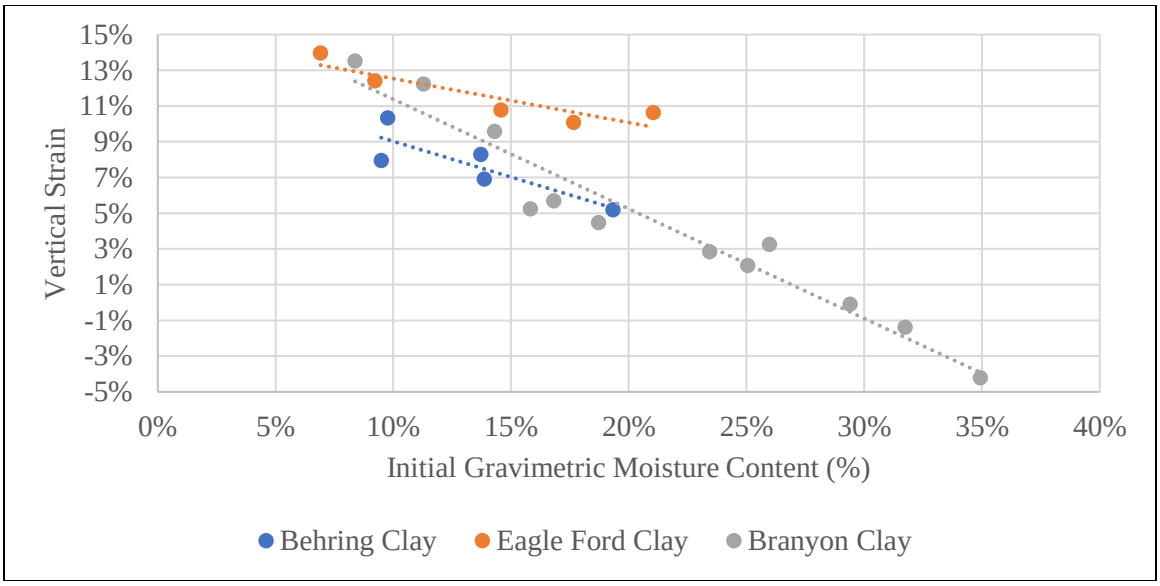

Figure 2.25: Effect of initial gravimetric moisture content on the vertical strains at the end of primary swelling for the three soils, tested under an effective stress of 250 psf

The vertical strains at the end of primary swelling was found to decrease linearly with increasing gravimetric moisture content for the three soils. This trend is consistent with trends reported in previous studies (Section 2.2.4). The slope of the linear relationship did not indicate a clear trend between the three soils as the slope of the Eagle Ford and Behring clays were similar despite the difference in plasticity and percentage of fines of the two soils. Additionally, the slope of the Behring and Branyon clays differed significantly despite the relatively similar Liquid Limits and percentages of fines of the two soils. Predictive approaches that rely on the Atterberg limits to determine the swelling of a soil would not capture this similar behavior between the Behring and Branyon clays. Therefore, the relationship between the vertical strains at the end of primary swelling and the initial gravimetric moisture content was found to vary for different expansive soils. However, a linear trend from each of the three soils can allow

for comparatively simple corrections in the swelling results from soil specimens tested using different initial gravimetric moisture contents. Use of this type of corrections will be reported later in Chapters 3 and 7 of this dissertation.

The increase in vertical strains at the end of primary swelling with decreasing initial moisture content can be attributed to the increase in initial suction with decreasing initial gravimetric moisture content. To explore the validity of considering suction as the main variable response for volume change, the volumetric moisture content was determined at the end of the compression phase, prior to the addition of water. This value of volumetric moisture content was used for each specimen to estimate the initial total suction using the soil-water retention curves for each soil (Figure 2.22). The total suction was used instead of the matric suction due to the comparatively short time frame for measurements and an assumed constant osmotic suction. The vertical strains at the end of primary swelling are shown in Figure 2.26 as a function of the estimated initial total suction for the three soils.

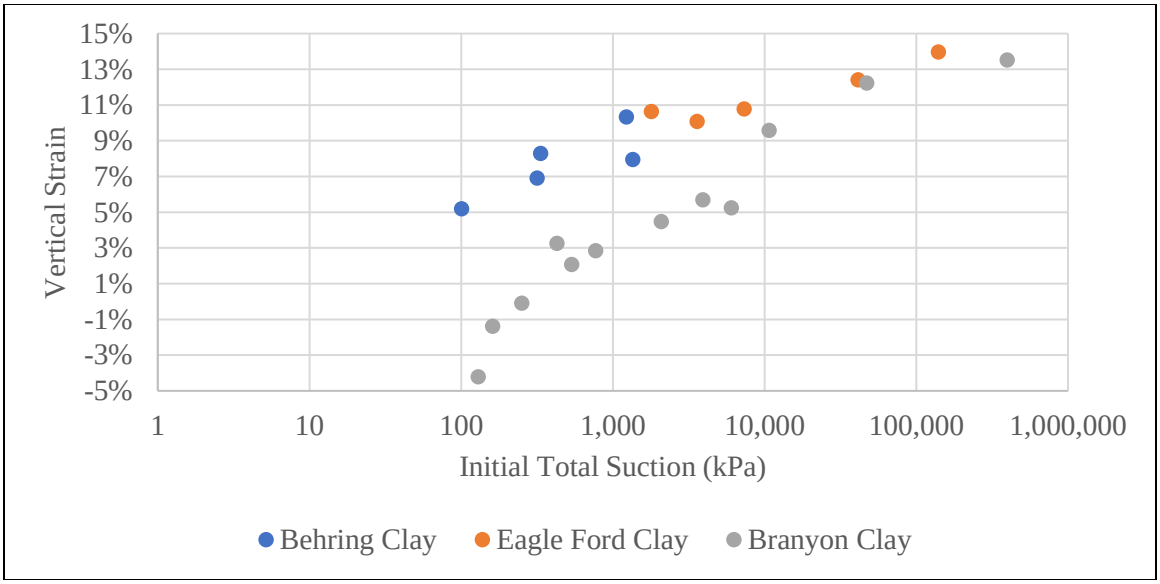

Figure 2.26: Effect of initial total suction on the vertical strains at the end of primary swelling for three soils, tested under an effective stress of 250 psf

The vertical strains at the end of primary swelling were found to increase non-linearly with increasing initial total suction. Using an assumed constant osmotic suction, the increase in the total suction can be correlated to an increase in the matric suction. Therefore, the vertical strains at the end of primary swelling was determined to increase with increasing matric suction. This trend is consistent with trends reported by previous studies (Lin and Cerato, 2012).

While Series I was performed using soil samples prepared at the same target compaction dry unit weight, some differences in dry unit weight in relation to the target occurred in the specimens occurred as part of the experimental approach. These differences were attributed to specimens with a higher initial gravimetric moisture content compressing differentially during the compression phase of the experimental method. The variability of the initial dry unit weight was approximately ±0.50 kN/m^3 for the three soils. In order to minimize the impact of the variability of the initial dry unit

weight in the interpretation of trends due to initial moisture content, the results are also presented in terms of void ratio. The void ratio at the end of primary swelling is shown in Figure 2.27 versus the initial gravimetric moisture content. The void ratio at the end of primary swelling was calculated as follows:

$$e_{ps} = \frac{\frac{SG * \rho_w}{m_s}}{A * (1 + \varepsilon_v) * h_i} - 1 \tag{2.5}$$

where e_{ps} is the void ratio at the end of primary swelling, SG is the specific gravity of the soil, ε_v is the vertical strain at the end of primary swelling, m_s is the mass of solids, and A is the inner area of the cutting ring. The specific gravity was measured to be 2.74 for the Eagle Ford clay and 2.84 for the Behring clay using the methodology from ASTM D854. The specific gravity was assumed to be 2.70 for the Branyon clay.

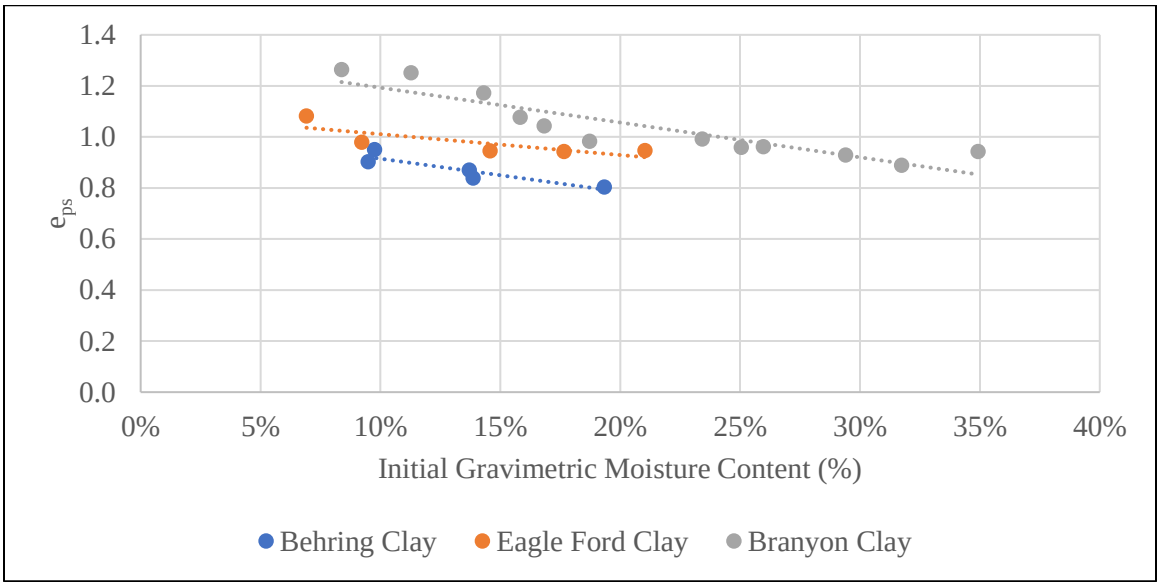

Figure 2.27: Void ratio at the end of primary swelling versus initial gravimetric moisture content for three soils, tested under an effective stress of 250 psf

The void ratio at the end of primary swelling was found to decrease with increasing gravimetric moisture content. This trend was consistent for the three soils. The slope of

this trend indicated a decrease of 0.14 in void ratio for every increase of 10 percentage points in the gravimetric moisture content. Additionally, the trend from Figure 2.27 is consistent with the trend observed in Figure 2.24 as the void ratio during testing can be related to the vertical strains during test as follows:

$$\varepsilon_v = \frac{e - e_i}{1 + e_i} \tag{2.5}$$

where e_i is the initial void ratio and e is the void ratio at a given time during testing. The initial dry unit weight affects the magnitude of the initial void ratio. The initial void ratio was calculated as follows:

$$e_i = \frac{\gamma_w * SG}{\gamma_{d,i}} - 1 \tag{2.6}$$

where γ_w is the unit weight of water, and $\gamma_{d,i}$ is the dry unit weight of the soil after the compression phase but prior to the addition of water. The dry unit weight at this stage during the testing process was used as it better represents the conditions of the soil prior to testing. Therefore, the linear decrease in the void ratio at the end of primary swelling with increasing gravimetric moisture content from Figure 2.27 indicated that the variability of the initial dry unit weight did not significantly affect the trends that were previously identified.

To assess the trends between testing series I and II, a single variable, the degree of saturation, which incorporates both the initial dry unit weight and initial gravimetric moisture, was also used to evaluate the data. The initial degree of saturation was calculated as follows:

$$S = \frac{\omega_i * SG}{e_i} \tag{2.7}$$

where S is the initial degree of saturation and ω_i is the initial gravimetric moisture content. The initial void ratio is calculated using the initial dry unit weight, as defined

using Equation 2.6. Thus, the initial degree of saturation combines both the initial gravimetric moisture content and initial dry unit weight. The void ratio at the end of primary swelling is shown in Figure 2.28 versus the initial degree of saturation of the soil.

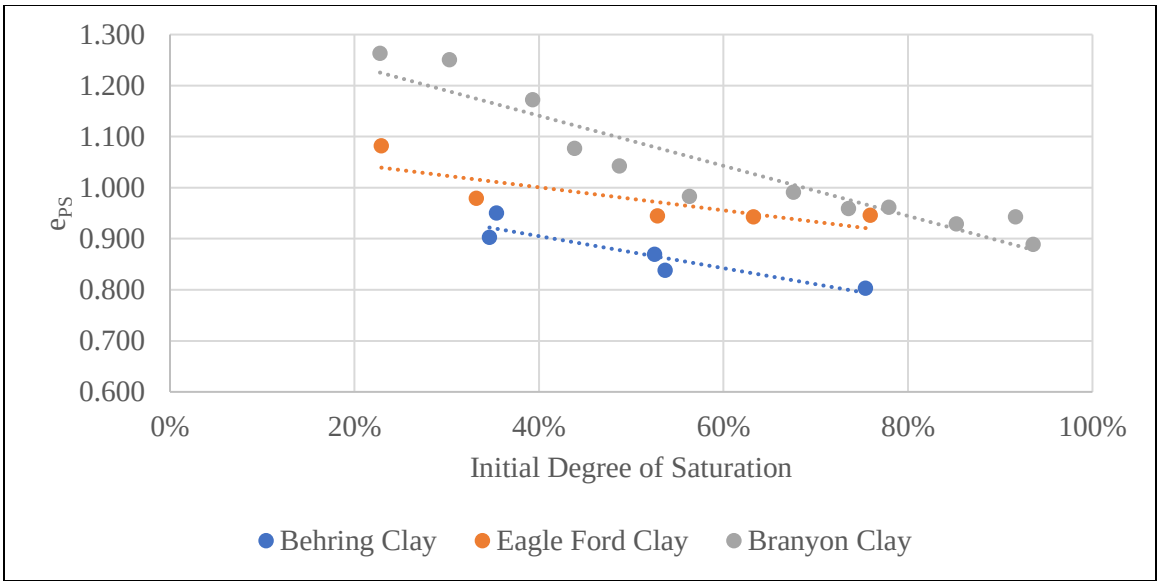

Figure 2.28: Void ratio at the end of primary swelling versus the initial degree of saturation for three soils, tested under a vertical effective stress of 250 psf

The results in Figure 2.28 indicate that the void ratio at the end of primary swelling decreases with increasing initial degree of saturation. The results are consistent with the results shown in Figure 2.27 as the variation in the initial dry unit weight did not significantly affect the initial void ratio. This linear trend between void ratio at the end of primary swelling and the initial degree of saturation will subsequently be analyzed as part of the evaluation of results from Series III.

An additional swelling characteristic is the period of time over which primary swelling develops. The time to the end of primary swelling is shown in Figure 2.29 versus the initial gravimetric moisture content.

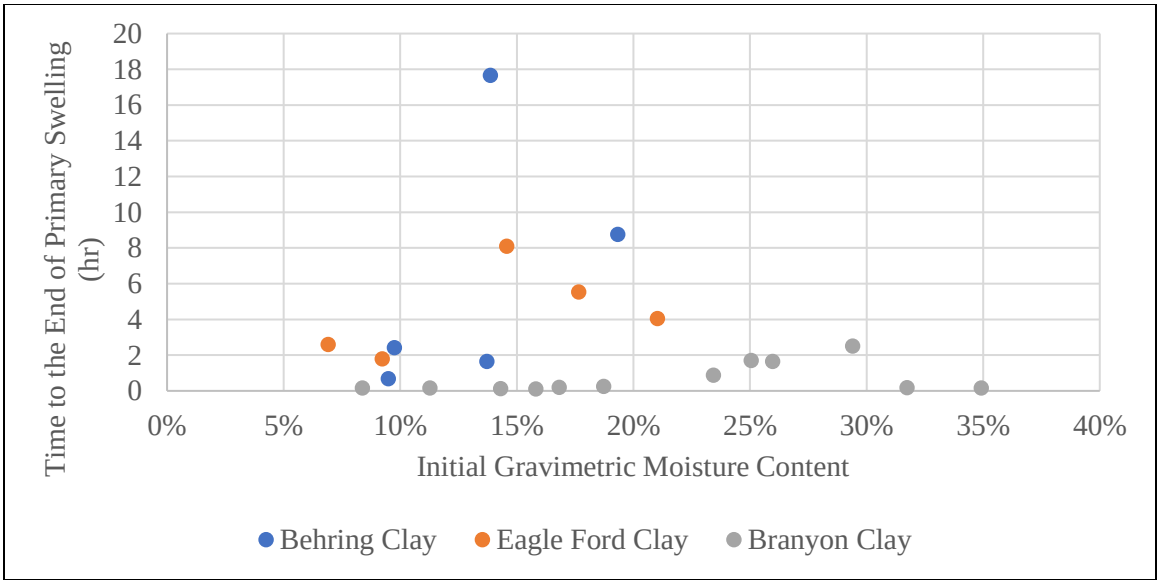

Figure 2.29: Time to the end of primary swelling versus initial gravimetric moisture content for three soils, tested under a vertical effective stress of 250 psf

In general, the time to the end of primary swelling was found to be smaller for specimens with the initial gravimetric moisture content that approaches the residual air-dried moisture content. This trend was attributed to the specimens with a lower initial gravimetric moisture content having a higher matric suction, as previously shown by Figure 2.26. The higher matric suction would increase the hydraulic gradient in the soil specimens. Modeling results reported by Kuhn (2010) indicated that the initial moisture infiltration into expansive soils is initially determined by a gradient in the matric suction. Thus, specimens with higher initial matric suction are expected to reach the end of

primary swelling in a shorter timeframe than specimens with lower initial matric suction due to the increased hydraulic gradient.

The porosity at the end of testing was calculated using the void ratio at the end of testing, as follows:

$$n_f = \frac{e_f}{1 + e_f} \tag{2.8}$$

where n_f is the final porosity, and e_f is the final void ratio. The final porosity can be used to estimate the saturated volumetric moisture content of the soil specimen by assuming that the soil specimen reaches full saturation at the end of testing. The relationship between final porosity and initial gravimetric moisture content is shown in Figure 2.30.

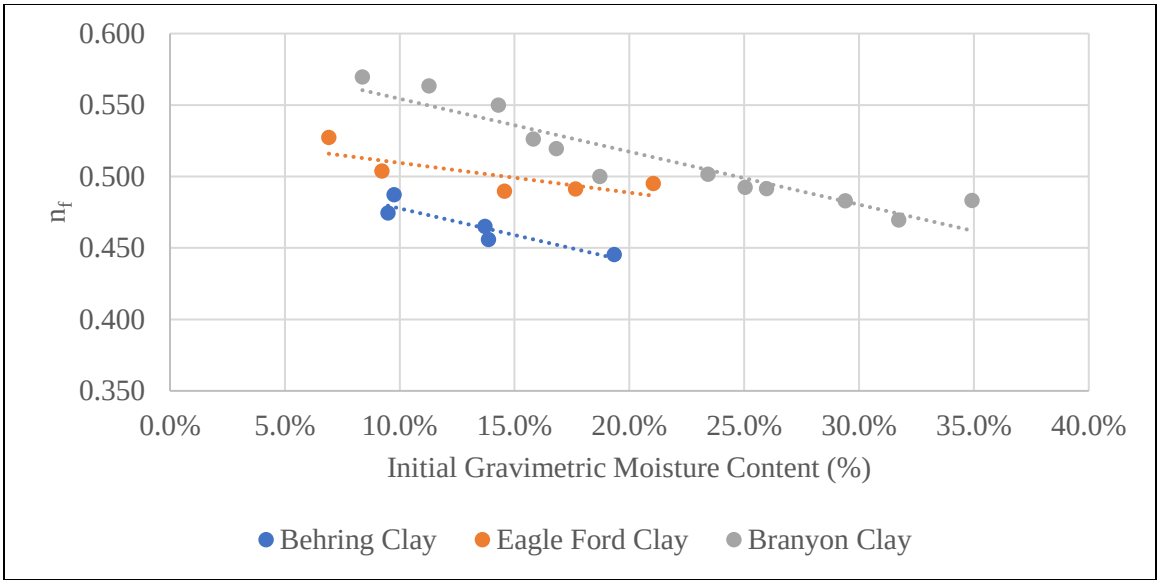

Figure 2.30: Final porosity versus initial gravimetric moisture content for three soils, tested under an effective stress of 250 psf

The final porosity was found to decrease with increasing initial gravimetric moisture contents for the three soils. This trend is consistent with the trends observed in Figure 2.24 for the initial gravimetric moisture content and vertical strain at the end of primary

swelling. Soils with higher vertical strains at the end of primary swelling will have a larger volume of voids and subsequently larger porosity. Using porosity as an estimate of the final volumetric moisture content, the final volumetric moisture content was found to increase with decreasing initial gravimetric moisture content. This trend will be analyzed further in Chapters 5 and 6 of this dissertation using instrumented field sites.

Overall, the results from Series I indicate that vertical strains increase with decreasing initial gravimetric moisture content for soil specimens prepared at the same initial dry unit weight. These trends are consistent with those from previous studies, confirming that the centrifugation of soil specimens does not adversely affect swelling behavior. Based on the estimated initial suction of soil specimens, the vertical strains at the end of primary swelling was found to increase with increasing initial suction. The void ratio at the end of primary swelling was found to decrease with increasing initial degree of saturation. The final porosity was used as a surrogate for the final volumetric moisture content by assuming that the soil specimens reach full saturation at the end of testing. The final porosity was found to decrease with increasing initial gravimetric moisture content.

2.3.3 Effect of the Initial Dry Unit Weight (Series II)

To assess the effect of the dry unit weight on the swelling of expansive soils, the soil specimens used in Series II were prepared using a constant initial gravimetric moisture content with varying compaction dry unit weight. The initial gravimetric moisture content was three percentage points dry of the optimum moisture content according to Standard Proctor compaction energy for Eagle Ford and the Branyon clays. This moisture content is identified as “dry condition” in this study. Samples were prepared at the optimum moisture content according to Standard Proctor compaction

energy for the Behring clay. The vertical effective stress was targeted at 250 psf for the Behring and Eagle Ford clays and at approximately 125 psf for the Branyon clay. Note that the dry unit weights and relative compaction were defined at the end of the compression phase in the centrifuge tests (i.e. not at the as-compacted conditions). The dry unit weights at the end of the compression phase were used to account for the decrease in volume prior to inundation. These dry unit weights are identified as the "initial dry unit weight" in this study.

The vertical strains at the end of primary swelling versus the initial dry unit weight are shown in Figure 2.31 for the Eagle Ford clay.

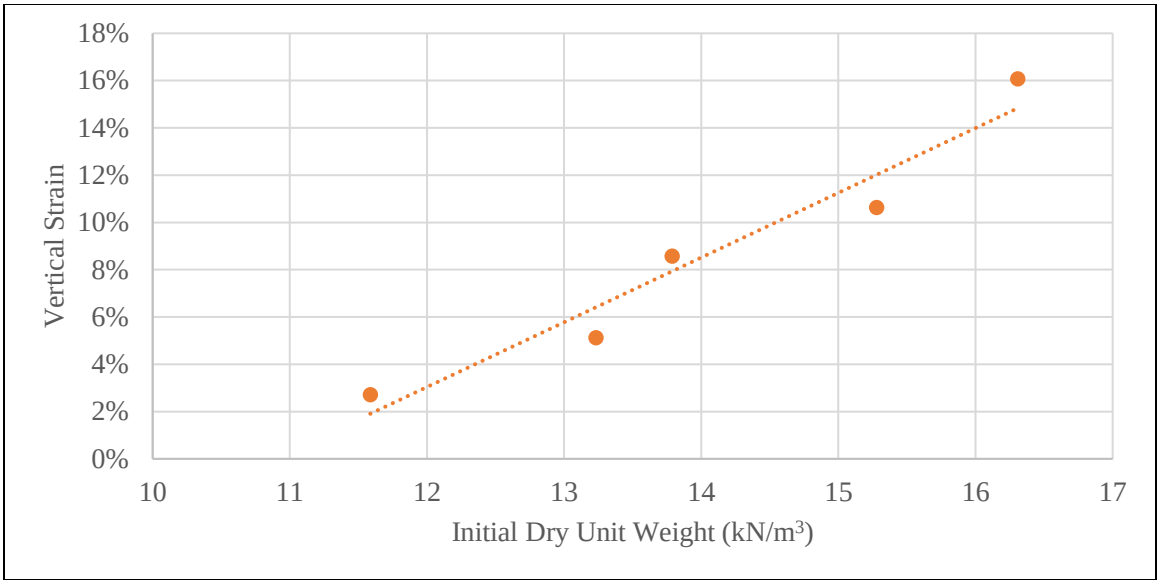

Figure 2.31: Effect of initial dry unit weight on the vertical strains at the end of primary swelling for the Eagle Ford clay

The vertical strains at the end of primary swelling were determined to increase linearly with increasing initial dry unit weight. This trend was found to be linear from dry unit weights both above and below the maximum dry unit weight according to Standard

Proctor compaction energy (15.25 kN/m^3). This trend was approximately a 3 percentage point increase in the vertical strains at the end of primary swelling for every 1 kN/m^3 increase in the dry unit weight.

To verify the trend from the Eagle Ford clay, the vertical strains at the end of primary swelling versus initial dry unit weight are shown in Figure 2.32 for the three soils. Note that the vertical effective stress differed for the Branyon clay, as the effective stress targeted was 125 psf instead of the 250 psf effective stress targeted for the Eagle Ford and Behring clays. Also note that the Behring clay specimens targeted the optimum gravimetric moisture content according to Standard Proctor compaction energy instead of the dry condition used for the Eagle Ford and Branyon clays. These differing initial conditions were used to evaluate the consistency of the effect of the initial dry unit weight.

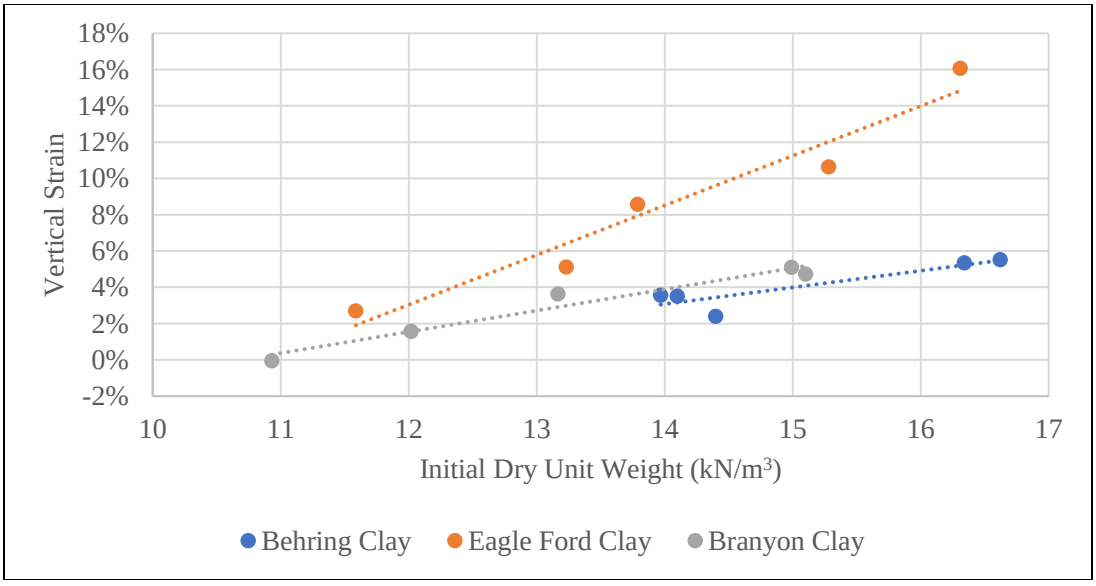

Figure 2.32: Effect of initial dry unit weight on the vertical strains at the end of primary swelling for three soils

The vertical strains at the end of primary swelling were found to increase linearly with increasing initial dry unit weight for all three soils. This result indicated that this trend is independent of the vertical effective stress (from the lower effective stress used for the testing of the Branyon clay), of the moisture condition (from the different moisture conditions between the Behring clay and the Eagle Ford and Branyon clays), and of the plasticity and percentages of fines of the soils (from the properties shown in Table 2.1 for the Eagle Ford clay and the Behring and Branyon clays). However, the linear trends from each of the three soils can be used for a comparatively simple correction of soil specimens with different initial dry unit weights. This correction will be analyzed further in Chapters 3 and 7 of this dissertation.

The range of the initial dry unit weights varied between the three soils. In order to normalize the initial dry unit weights, the relative compaction was calculated as follows:

$$RC = \frac{\gamma_{d,i}}{\gamma_{d,max}} \tag{2.7}$$

where RC is the relative compaction, $\gamma_{d,i}$ is the initial dry unit weight, and $\gamma_{d,max}$ is the maximum dry unit weight according to Standard Proctor compaction energy. The vertical strains at the end of primary swelling versus relative compaction are shown in Figure 2.33 for the three soils.

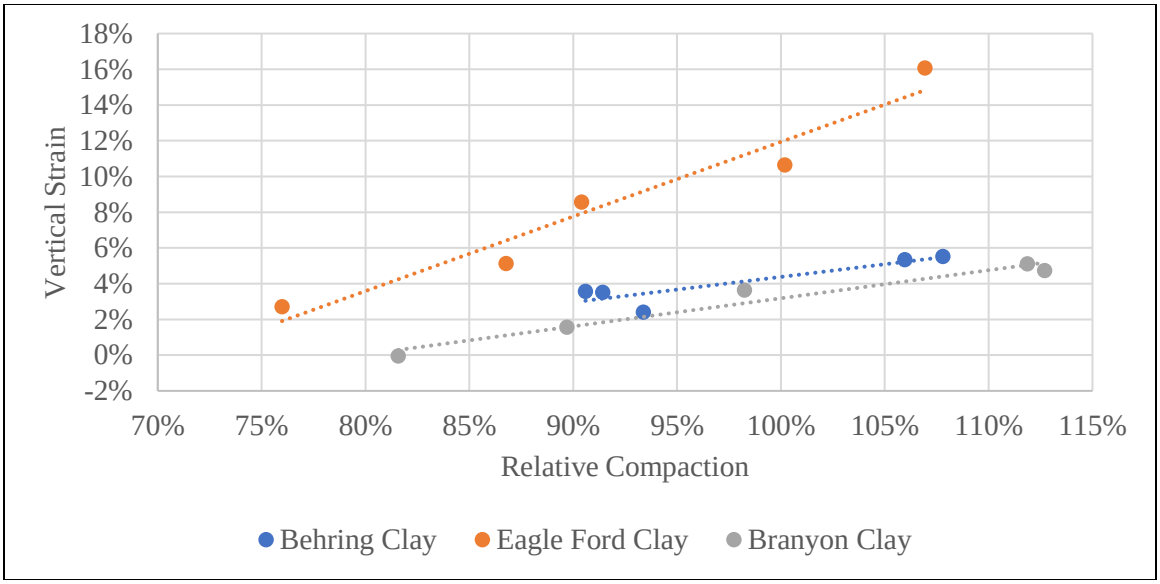

Figure 2.33: Effect of relative compaction on the vertical strains at the end of primary swelling for three soils

The vertical strains at the end of primary swelling were found to increase linearly with increasing relative compaction. This linear trend occurred both at low relative compactions and at relative compactions above the maximum dry unit weight from Standard Proctor compaction curves. This linear increase in the vertical strains also occurred for soils compacted at the optimum gravimetric moisture content according to Standard Proctor compaction energy (i.e. the Behring clay) and at a dry moisture content condition (i.e. the Eagle Ford and Behring clays). However, the linear increase in the vertical strains was not consistent for the three soils. This result indicates that the relationship between the vertical strains and relative compaction differs between soils.

From the results presented in Series I, the void ratio at the end of primary swelling can be used to analyze swelling results between specimens with different initial dry unit weights. The void ratios at the end of primary swelling versus the initial dry unit weight are shown in Figure 2.34.

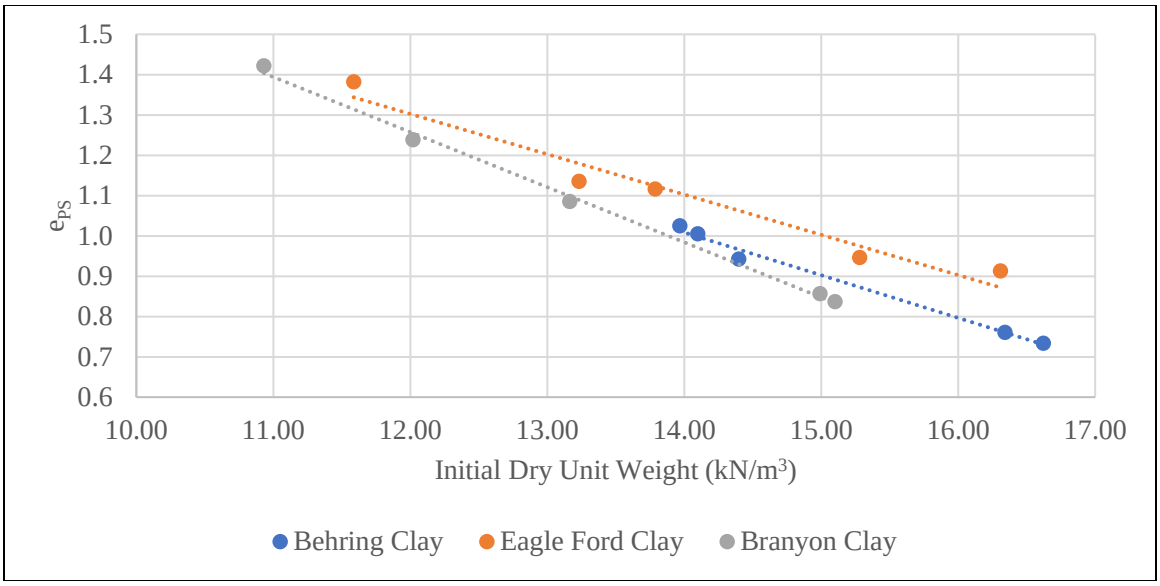

Figure 2.34: Effect of initial dry unit weight on the void ratio at the end of primary swelling for three soils

The void ratio at the end of primary swelling was determined to decrease linearly with increasing initial dry unit weight. For the three soils, the void ratio at the end of primary swelling was found to decrease approximately 0.1 for every 1 kN/m^3 increase in the initial dry unit weight. This linear decrease was similar between soils tested at the same effective stress (i.e. the Behring and Eagle Ford clays). The Branyon clay, which was tested at a lower effective stress, tended to have a slightly more steep decrease in the void ratio at the end of primary swelling with increasing dry unit weights. Therefore, this linear decrease may be dependent on the vertical effective stress.

The initial degree of saturation was calculated following the method previously outlined in Series I in order to combine the initial conditions into a single variable. Due to the differences in the initial moisture conditions between the three soils, the initial degree of saturation provides a normalization of the gravimetric moisture content and initial dry

unit weight of the three soils. Note that the dry unit weights used for the calculation of the initial degree of saturation were the dry unit weights at the end of the compression phase. The void ratios at the end of primary swelling versus the initial degree of saturation are shown in Figure 2.35.

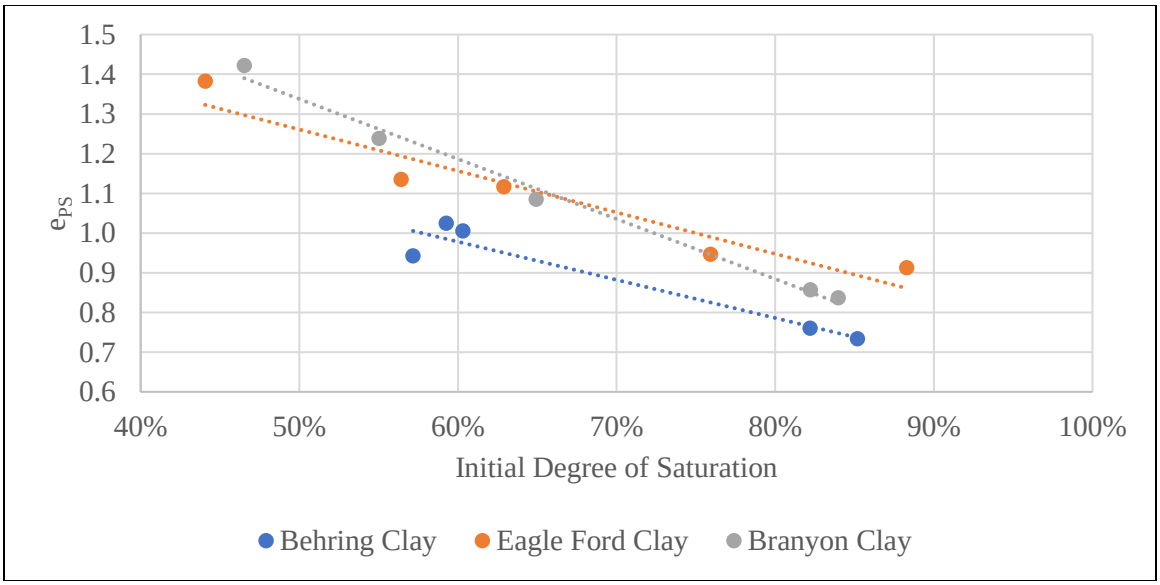

Figure 2.35: Effect of initial degree of saturation on the void ratio at the end of primary swelling for three soils

The void ratio at the end of primary swelling was found to decrease with increasing initial degree of saturation. This trend is consistent with the trend shown in Figure 2.28 from Series I. As with the results from Series I, the trend was similar for the Behring and Eagle Ford clays and differed for the Branyon clay. The difference in the behavior of the Branyon clay indicated that the linear trend may not be consistent among expansive soils or at differing effective stresses. The effect of the initial degree of saturation is further evaluated in Series III.

To explore the validity of considering suction as the main variable response for volume change, soil-water retention curves were generated based on measurements from the chilled mirror hygrometer. The Eagle Ford and Behring clay specimens were prepared using relative compaction values of 60%, 80% and 100% for the Eagle Ford clay and 80% and 100% for the Behring clay. The relative compaction was varied to analyze its effect on the soil-water retention curves. The results and fitted soil-water retention curves from the chilled mirror hygrometer data are shown in Figure 2.36 and Figure 2.37. For the Eagle Ford clay, the soil specimens were compacted to different relative compactions but using the same gravimetric moisture content for each set of data points (i.e. the first data point for each relative compaction was measured from soil prepared at the same initial gravimetric moisture content, the second data point for each relative compaction was measured from soil prepared at the same initial gravimetric moisture content that was lower than the gravimetric moisture content used for the first data point, etc.). The results indicated that the total suction at a given volumetric moisture content increases with decreasing relative compaction.

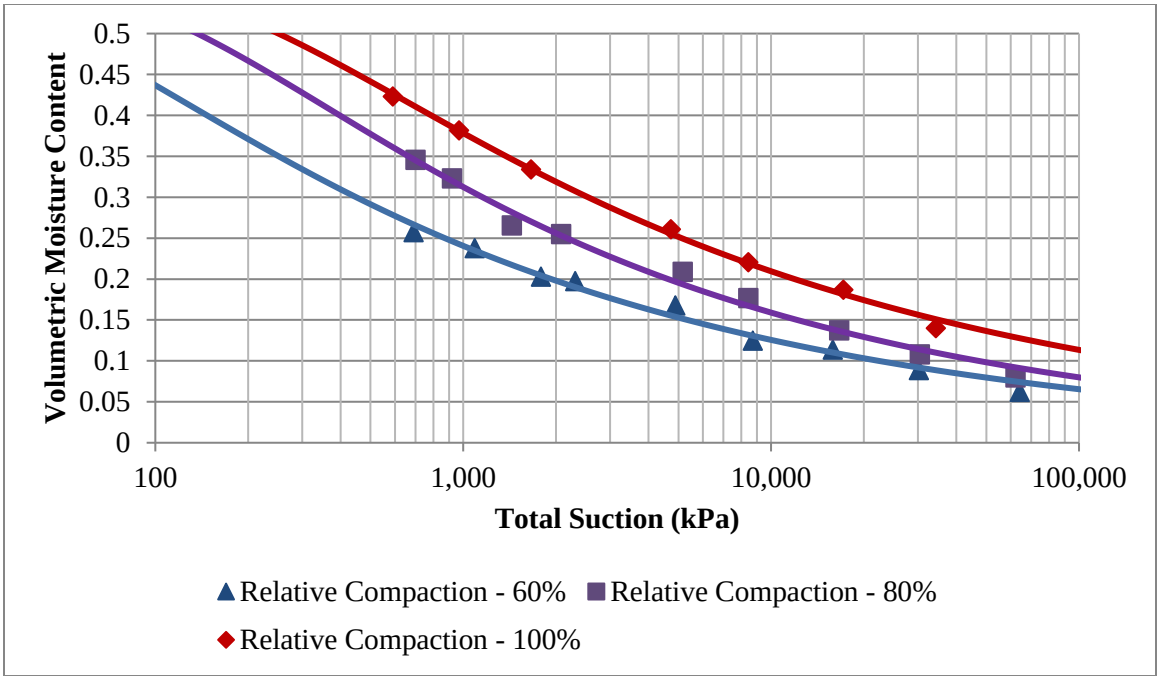

Figure 2.36: Effect of relative compaction on the soil-water retention curves for the Eagle Ford clay

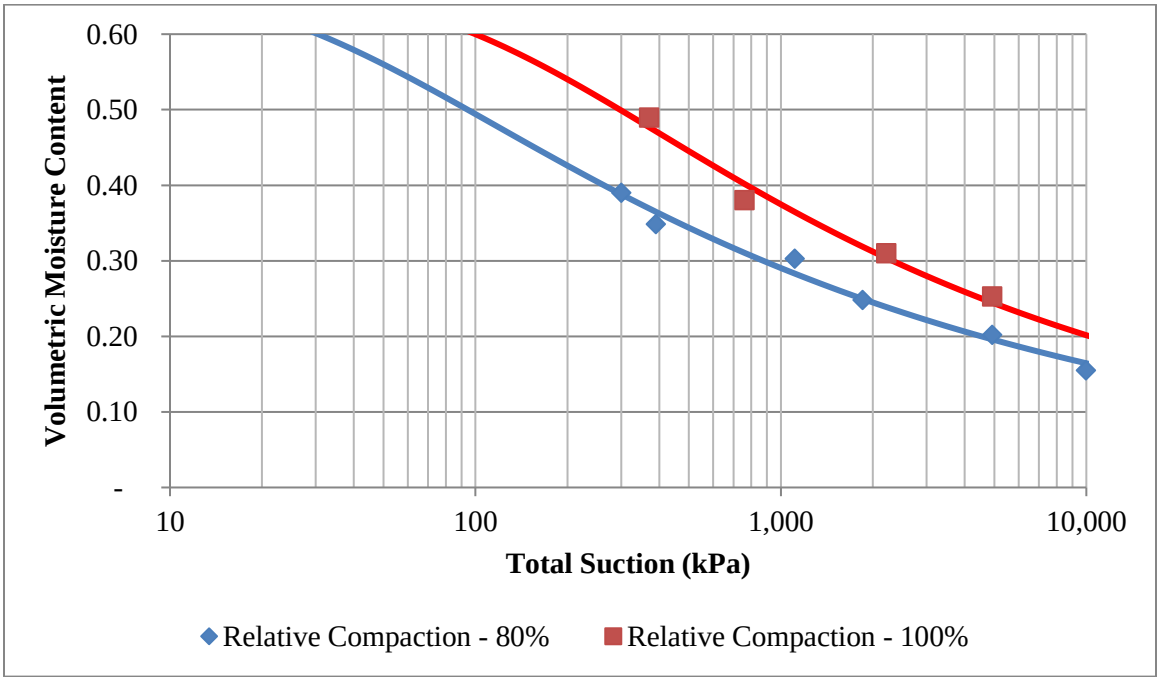

Figure 2.37: Effect of relative compaction on the soil-water retention curves for the Behring clay

The soil-water retention curves from the figures can be used to estimate the total suction for centrifuge soil specimens. Specifically, the total suction was estimated by assuming a semi-log-linear trend between the soil-water retention curves at different relative compactions. The vertical strains versus the estimated total suction are shown in Figure 2.38 for the Eagle Ford and Behring clays. Additionally, the vertical strains at the end of primary swelling is shown in Figure 2.39 versus the volumetric moisture content for the three soils. The volumetric moisture content was analyzed in order to include the Branyon clay, which did not have soil-water retention curves at different relative compactions defined. The initial volumetric moisture content was calculated as follows:

$$\theta_i = \frac{\omega_i * \gamma_{d,i}}{\gamma_w} \tag{2.8}$$

where θ_i is the initial volumetric moisture content, ω_i is the initial gravimetric moisture content, $\gamma_{d,i}$ is the initial dry unit weight, and γ_w is the unit weight of water. Since the specimens used in Series II were compacted at the same initial gravimetric moisture content, the volumetric moisture content increased with increasing dry unit weight. In general, the total suction is expected to decrease with increasing volumetric moisture content.

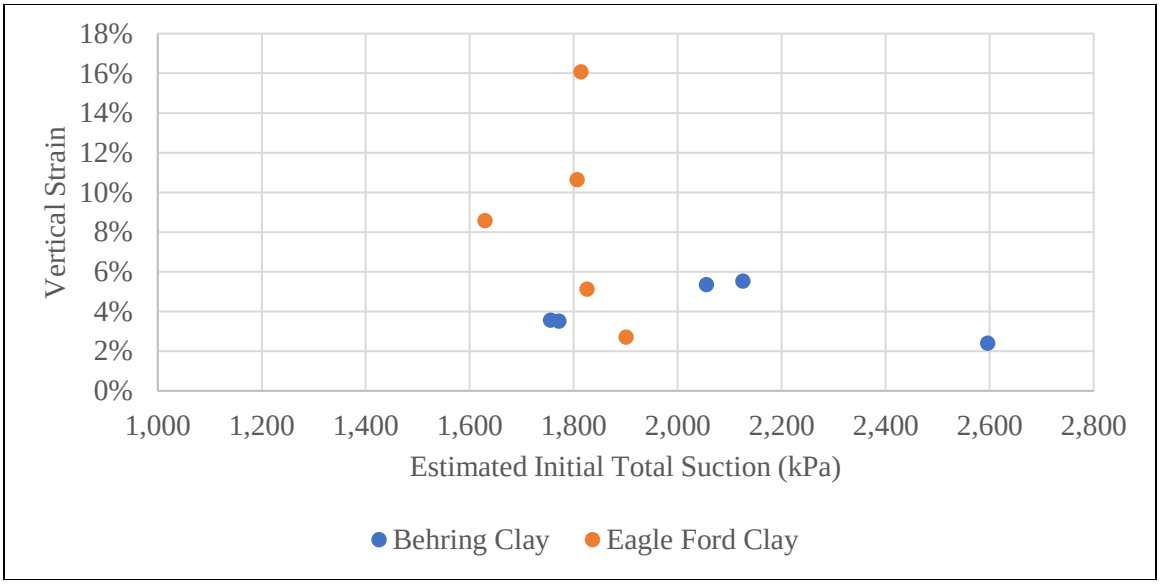

Figure 2.38: Vertical strains at the end of primary swelling versus estimated total suction for the Behring and Eagle Ford clay

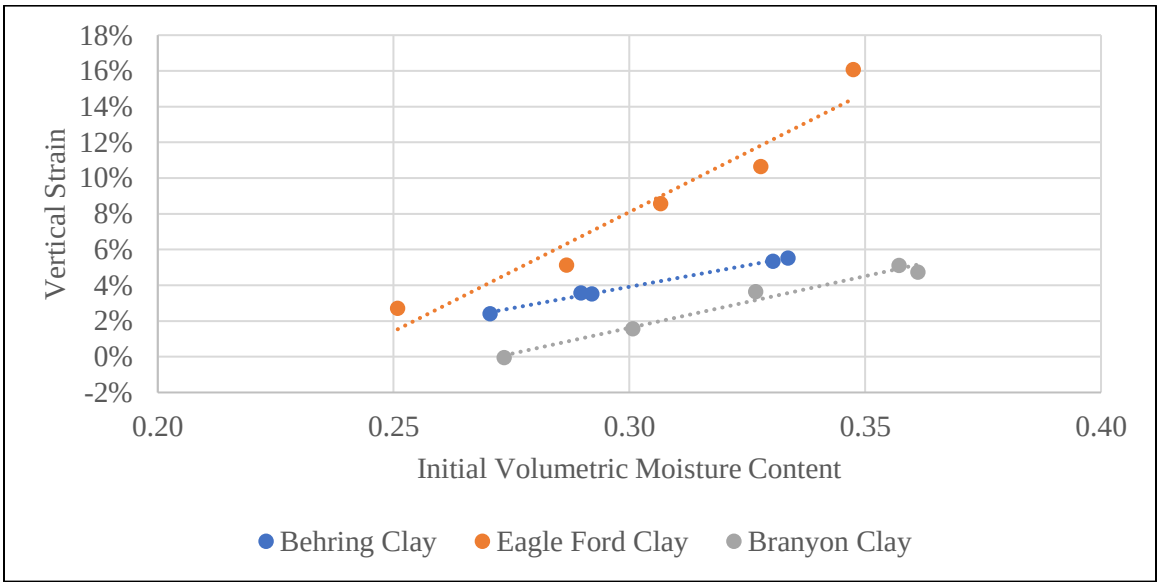

Figure 2.39: Vertical strains at the end of primary swelling versus initial volumetric moisture content for the three soils

There was not a clear trend between the initial total suction and vertical strains from Figure 2.38. However, the range in total suction was smaller than the range in the data

shown in Figure 2.26 from Series I. This trend differed from the trend in Series I and indicates that the increase in the vertical strains at the end of primary swelling for increasing dry unit weight is not related to the initial total suction. Additionally, the vertical strains at the end of primary swelling was found to increase with decreasing initial volumetric moisture content, as shown in Figure 2.39. The trend differs from the results presented in Series I. These results indicate that it is a combined effect between multiple variables and not solely the suction of soils that are responsible for volume change of expansive soils. A potential explanation for these trends is that, as that as the dry unit weight increases, the soil fabric changes as the macro-voids in the soil specimens decrease. This change in soil fabric could lead to more contact between clay peds which increases the swelling potential of the soil specimen.

The final porosity was calculated using Equation 2.4 in order to estimate the final volumetric moisture content. The final porosities versus the initial dry unit weight are shown in Figure 2.40.

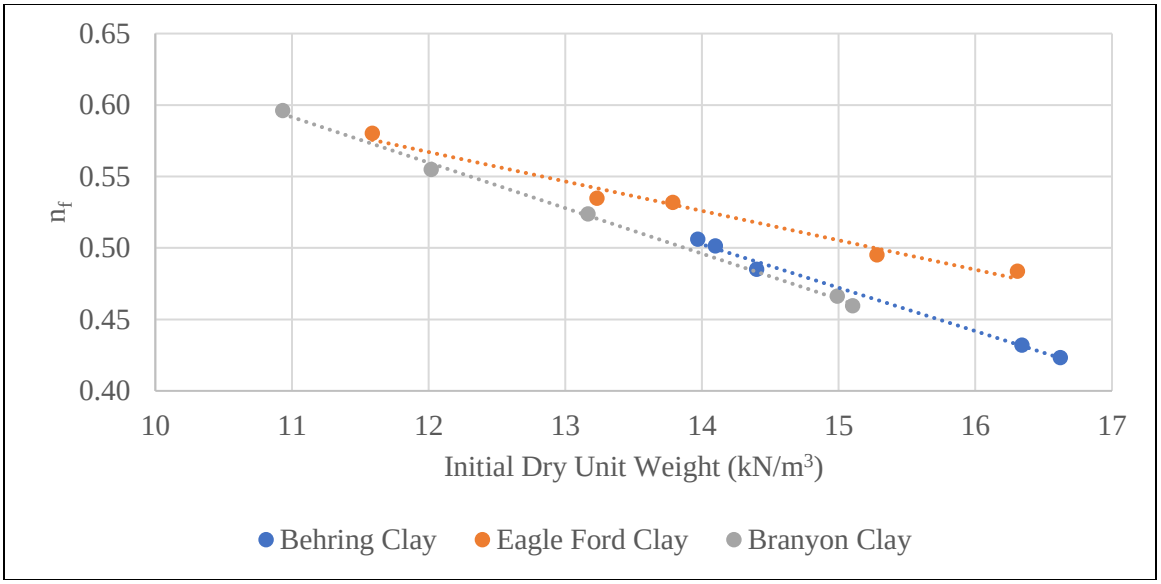

Figure 2.40: Effect of initial dry unit weight on the final porosity for the three soils

The final porosity was found to decrease with increasing dry unit weight. This decrease in the final porosity was attributed to a decrease in the volume of voids with increasing dry unit weight. This trend is examined further in Chapters 5 and 6 of this dissertation with the results from the field moisture monitoring of expansive soil deposits.

The time to the end of primary swelling is shown as a function of the initial dry unit weight in Figure 2.41.

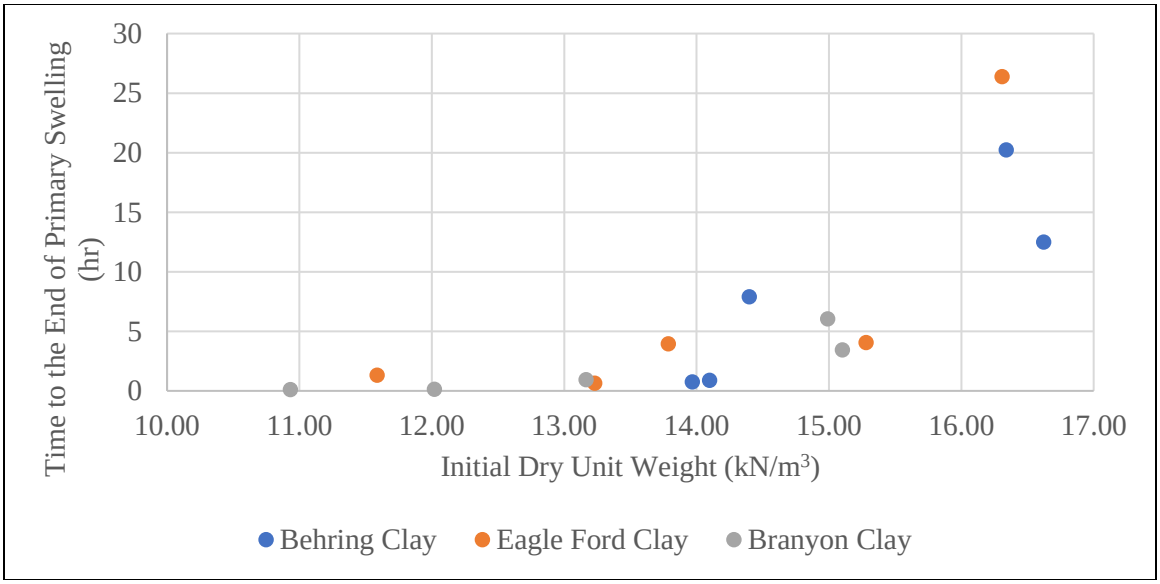

Figure 2.41: Effect of initial dry unit weight on the duration of primary swelling for three soils

The time to the end of primary swelling was determined to increase with increasing dry unit weight. This trend is more clear than that shown in Figure 2.29 for Series I. The time to the end of primary swelling tended to increase more significantly beyond the maximum dry unit weight from Standard Proctor compaction curves (Table 2.1). An explanation for this behavior is the difference in the hydraulic conductivity of soils compacted at different relative compactions. Previous studies have found that the hydraulic conductivity decreases with increasing initial dry unit weight (Mitchell et al., 1966). To evaluate the decrease in the hydraulic conductivity with increasing dry unit weight, conductivity tests using flexible wall permeameters were performed on the Eagle Ford and Behring clays using ASTM D5084. Tests were performed on only one specimen of each clay at different levels of confinement. Both the Eagle Ford clay and Behring clay were compacted dry of the optimum moisture content and at the maximum dry unit weight using Standard Proctor compaction energy. Based on these compaction

conditions, the soil fabric was expected to be more flocculated for both clays. As the soil confinement increased, the soils tended to consolidate. This consolidation led to a decrease in the void ratio and an increase in the dry unit weight. The saturated hydraulic conductivity versus effective stress is shown in Figure 2.42.

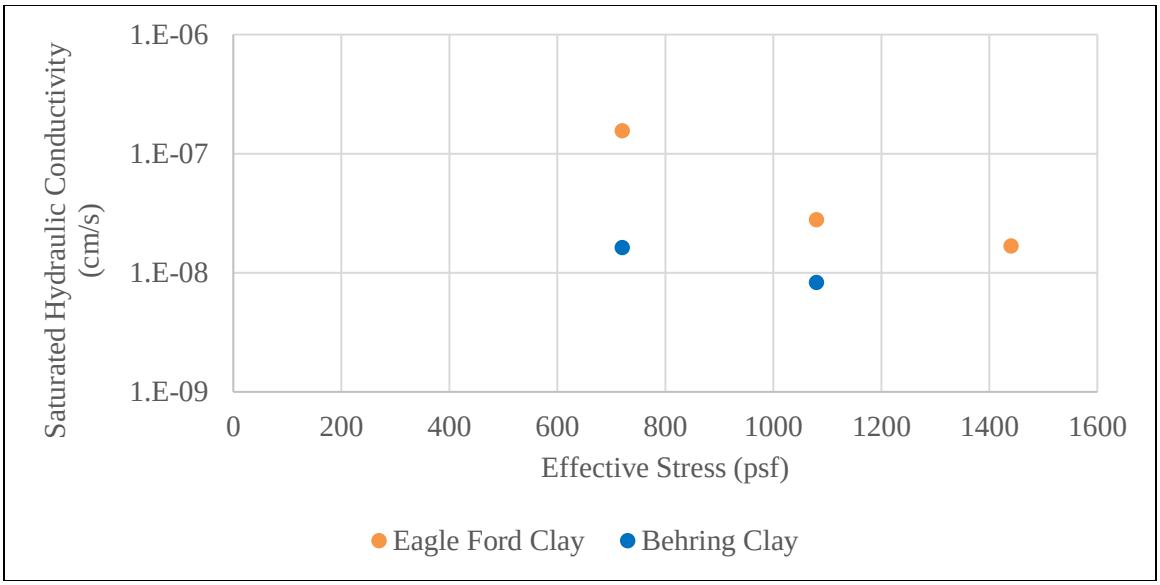

Figure 2.42: Saturated hydraulic conductivity versus effective stress for the Eagle Ford and Behring clays

Figure 2.42 indicated that the hydraulic conductivity of the soils decreases with increasing effective stress. This decrease was more significant for the Eagle Ford clay. However, the hydraulic conductivity was relatively low for the Behring clay based on the percentages of fines and Liquid Limit. From Figure 2.41, the Eagle Ford and Behring clays both had a significant increase in time to the end of primary swelling at dry unit weights above the maximum dry unit weight. Therefore, the decrease in hydraulic conductivity with increasing dry unit weight can be assumed to affect the time to the end of primary swelling.

Overall, the results from Series II indicated that soils prepared at the same initial gravimetric moisture content have increasing vertical strains with increasing dry unit weight. The increase in the vertical strains was found to be approximately linear for the three soils. These trends are consistent with those from previous studies, confirming that the centrifugation of soil specimens does not affect the trends in swelling. However, there was not a clear trend between the initial suction of the soil specimens and the vertical strains at the end of primary swelling. The increase in the vertical strains was instead attributed to the decrease in the macro-voids and space between clay peds. Additionally, the time to the end of primary swelling was found to increase with increasing initial dry unit weight. This trend was attributed to the decrease of the hydraulic conductivity of the specimens with an increase in the dry unit weight as determined from conductivity tests.

2.3.4 Effect of the Initial Degree of Saturation (Series III)

From Series I and II, the trends of the initial dry unit weight and initial gravimetric moisture contents on the vertical strains at the end of primary swelling were found to be consistent with previous studies. These consistent trends indicate that the use of an increased gravitational environment does not affect the behavior of expansive soils. With consistent trends and magnitude from primary swelling not being significantly affected as shown by Zornberg et al. (2013) and Zornberg et. al (2017), the centrifuge technology's benefit is the production of data in a shorter time frame that is consistent with the traditional testing methodologies.

Series III evaluated the effect of the initial degree of saturation on the swelling of expansive soils. From Table 2.2, Series III evaluated results from centrifuge tests conducted at a similar vertical effective stress. The initial degree of saturation varied between specimens. This variation of the initial degree of saturation was due to variations

in both the initial gravimetric moisture content and initial dry unit weight. If a clear trend between the degree of saturation and the magnitude of primary swelling could be observed, a single variable could be used to evaluate the variability in swelling of expansive soils.

A combined analysis of the test results from Series I and II are presented using the degree of saturation for the Eagle Ford clay. The results between Series I and II were compared as both series indicate that the void ratio at the end of primary swelling decreases with increasing degree of saturation. The void ratio at the end of primary swelling is shown in Figure 2.43 versus the initial degree of saturation for the Eagle Ford clay.

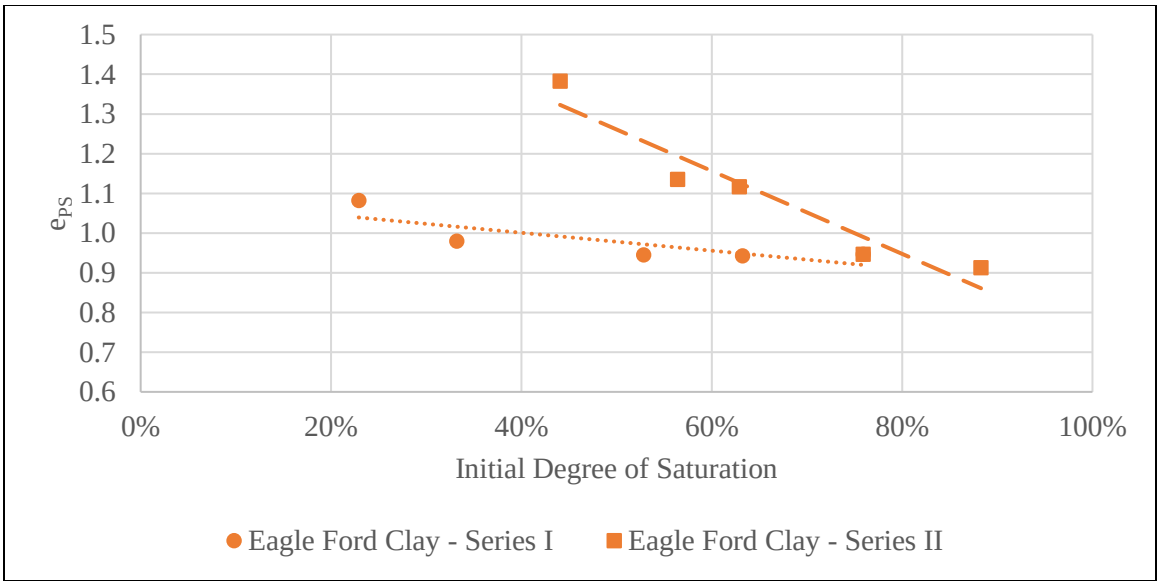

Figure 2.43: Effect of degree of saturation on the void ratio at the end of primary swelling for two soils

Figure 2.43 indicated that the void ratio at the end of primary swelling decreases with increasing initial degree of saturation. However, the decrease in the void ratio was not

consistent between the results from the two series. Specimens at the same initial degree of saturation did not reach the same void ratio at the end of primary swelling. The differing trends indicate that the effect of the initial degree of saturation is non-linear and dependent upon the compaction condition that was varied (i.e. either the gravimetric moisture content or dry unit weight).

The void ratio at the end of primary swelling is affected by the initial void ratio. However, initial void ratio is dependent upon the initial dry unit weight, as shown in Equation 2.6. In order to remove the influence of the initial dry unit weight, the change in void ratio at the end of primary swelling can be used instead. The change in the void ratio at the end of primary swelling was defined as follows:

$$\Delta e = e_{PS} - e_i \tag{2.9}$$

where Δe is the change in void ratio, e_{PS} is the void ratio at the end of primary swelling, and e_i is the initial void ratio. The change in void ratio at the end of primary swelling additionally acts as a surrogate for the vertical strains from Equation 2.5. The change in void ratio at the end of primary swelling is shown in Figure 2.44 versus the initial degree of saturation.

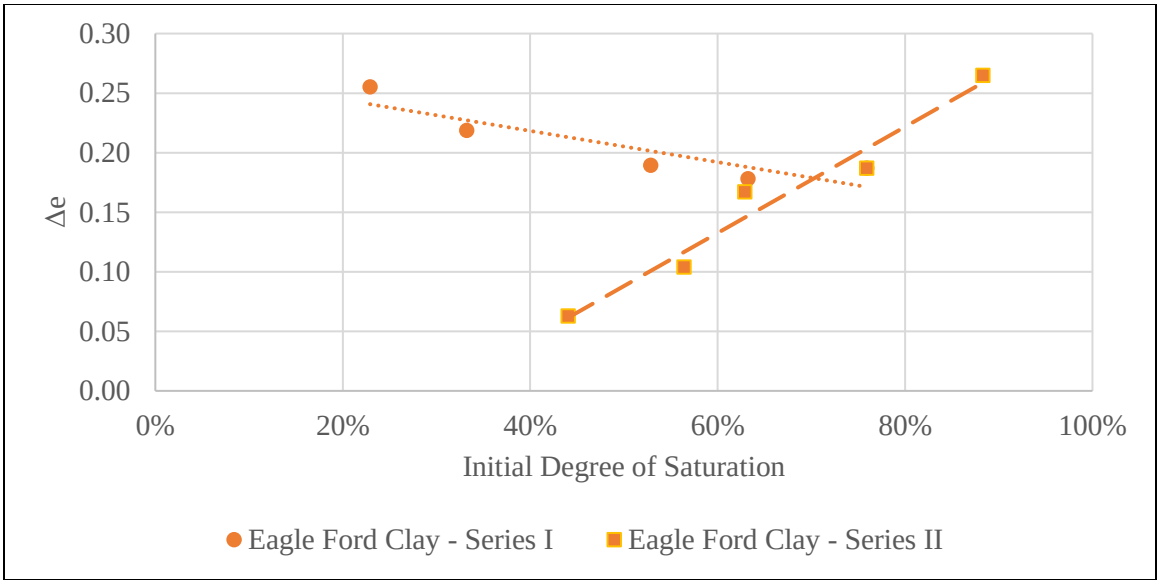

Figure 2.44: Effect of initial degree of saturation on change in void ratio at the end of primary swelling for two soils

The trends differed between the two testing series significantly. For Series I, an increase in the initial degree of saturation led to a decrease in the change in void ratio. For Series II, an increase in the degree of saturation led to an increase in the change in void ratio. These trends differed due to the effect of the initial conditions on the initial degree of saturation. For Series I, the initial degree of saturation increases with increasing initial gravimetric moisture content. Since the vertical strains at the end of primary swelling were determined to decrease with increasing gravimetric moisture content, an increase in initial degree of saturation would result in a decrease in the vertical strains. Additionally, the initial suction increases with decreasing initial degree of saturation. This increase in suction was attributed to the variable responsible for the swelling of soil specimens. For Series II, the initial degree of saturation increases with increasing initial dry unit weight. Since the vertical strains at the end of primary swelling were determined to decrease with increasing dry unit weight, an increase in initial degree of saturation would result in an

increase in the vertical strains. Additionally, the initial suction was not found to affect the swelling for soil specimens in Series II. This behavior was explained by the differences in the soil fabric and reduction in the spacing between clay peds with increasing dry unit weight.

In order to assess the validity of the trends from the Eagle Ford clay, the combined analysis of the test results from Series I and II are also presented using the degree of saturation for the Behring clays. Note that the results from the Branyon clay were not analyzed in this section as the results from Series I and II had differing vertical effective stresses. The void ratio at the end of primary swelling is shown in Figure 2.45 versus the initial degree of saturation. The change in void ratio at the end of primary swelling is shown in Figure 2.46 versus the initial degree of saturation.

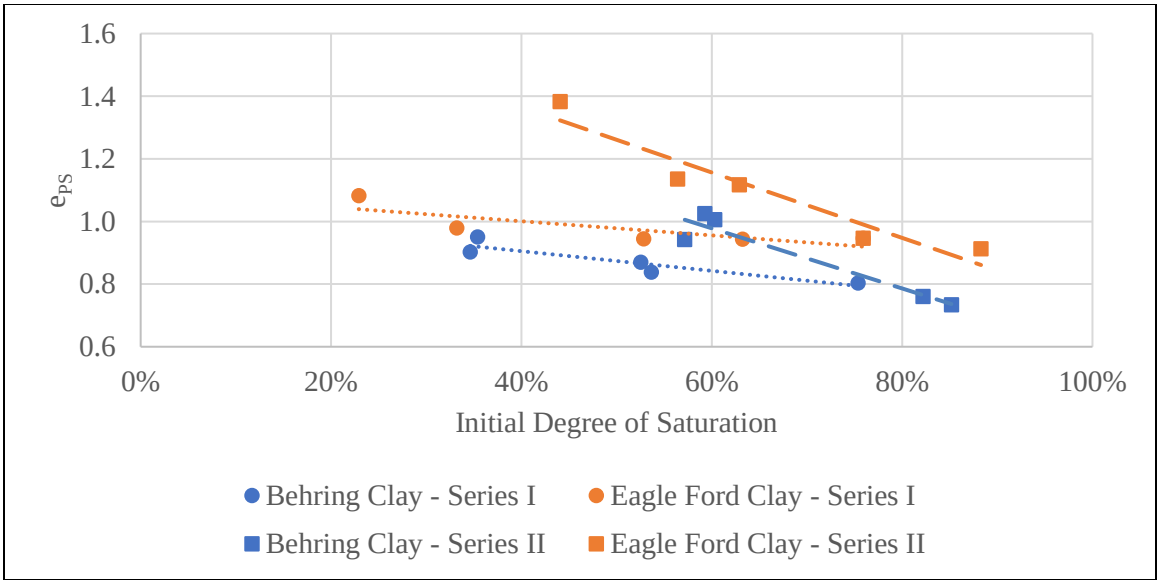

Figure 2.45: Effect of initial degree of saturation on the void ratio at the end of primary swelling for two soils

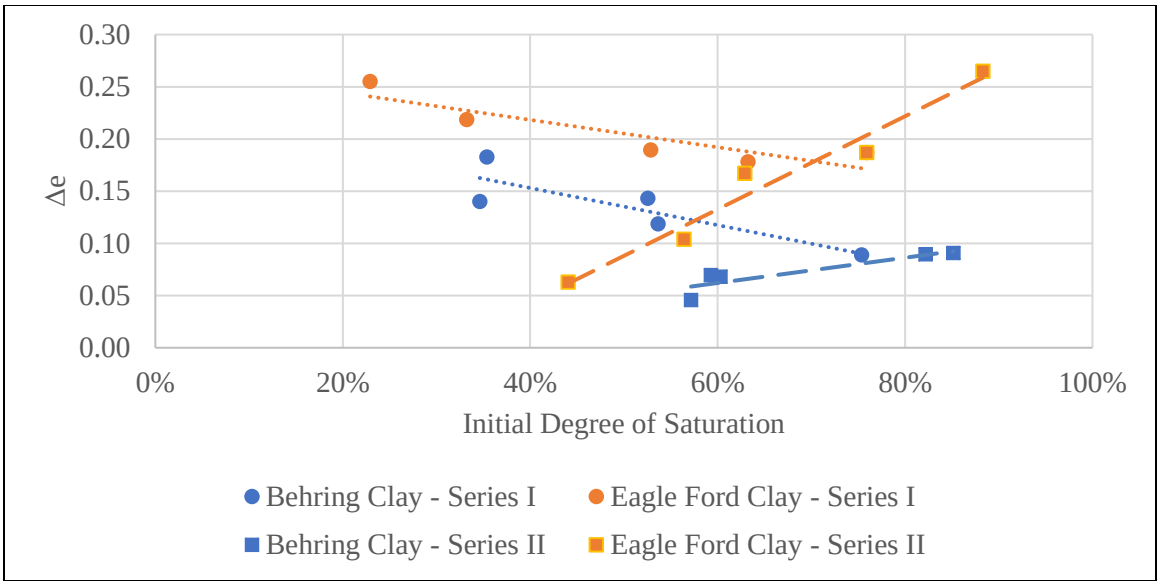

Figure 2.46: Effect of initial degree of saturation on the change in void ratio at the end of primary swelling for two soils

The trends from the Behring clay were consistent with the trends from the Eagle Ford clay. The void ratio at the end of primary swelling decreases with an increase in the initial degree of saturation. However, the change in the void ratio differs for both testing series with an increase in the initial degree of saturation. These results are consistent with the trends from Series II and indicate that the initial suction is not the primary variable responsible for swelling. Therefore, swelling of expansive soils varies based on multiple variables that include the soil suction, soil fabric and the spacing of clay peds.

In order to evaluate the effect of the initial degree of saturation and validate the trends from Series I and II, the results from additional centrifuge tests were evaluated. Additional centrifuge test results were taken from a database of test results. The results included data from previous centrifuge tests conducted on reconstituted samples of the Eagle Ford clay and Behring clay for an effective stress ranging from 200 to 300 psf.

This range of stresses contained a total of 36 tests for the Eagle Ford clay and 44 tests for the Behring clay for analysis. Results were evaluated in the initial dry unit weight versus gravimetric moisture content space. This initial dry unit weight versus gravimetric moisture content is defined as the "compaction space" for the study. Results from centrifuge tests are included on a third axis defined by a color bar. For this study, the Standard Proctor compaction curves and lines of constant degree of saturation for each were also included in the figures.

The first analysis in the compaction space plotted the vertical strains at the end of primary swelling on the third axis. The vertical strains at the end of primary swelling in the compaction space is shown in Figure 2.47. The vertical strains at the end of primary swelling were found to increase with increasing initial dry unit weight increases and decreasing initial gravimetric moisture content. These trends are consistent with the trends from Series I and II. The vertical strains tend to increase in the direction indicated by the direction of the arrow in Figure 2.49. However, the vertical strains were not consistent along lines of constant degree of saturation. This trend is consistent with the results from Figure 2.43. Therefore, soil specimens at the same initial degree of saturation can have differing vertical strains at the end of primary swelling.

The second analysis in the compaction space plotted the void ratio at the end of primary swelling on the third axis. The void ratio at the end of primary swelling in the compaction space is shown in Figure 2.47Figure 2.48. The void ratio at the end of primary swelling was found to decrease with increasing dry unit weight and increasing gravimetric moisture content. These trends are consistent with the trends from Series I and II. The increase in the void ratio at the end of primary swelling is indicated by the direction of the arrow in Figure 2.50. However, the void ratio at the end of primary swelling was not consistent along lines of constant degree of saturation. This trend is

consistent with that from Figure 2.43. In general, the void ratio at the end of primary swelling tended to be similar at initial degree of saturations above 90%.

Overall, the results from Series III indicated that the vertical strains and void ratio at the end of primary swelling decrease with increasing initial degree of saturation at the same vertical effective stress. However, unlike the results from Series I and II, there was not a linear trend between the swelling results and the initial degree of saturation. A database of test results was used to validate the trends from Series I, II, and III by including results from 60 additional soil specimens. The trends from the analysis of the database were consistent with the trends from Series I, II, and III. These trends and results indicate that the swelling of a soil is driven by a combination of multiple variables that include the initial soil suction, the soil fabric, and the spacing between clay peds.

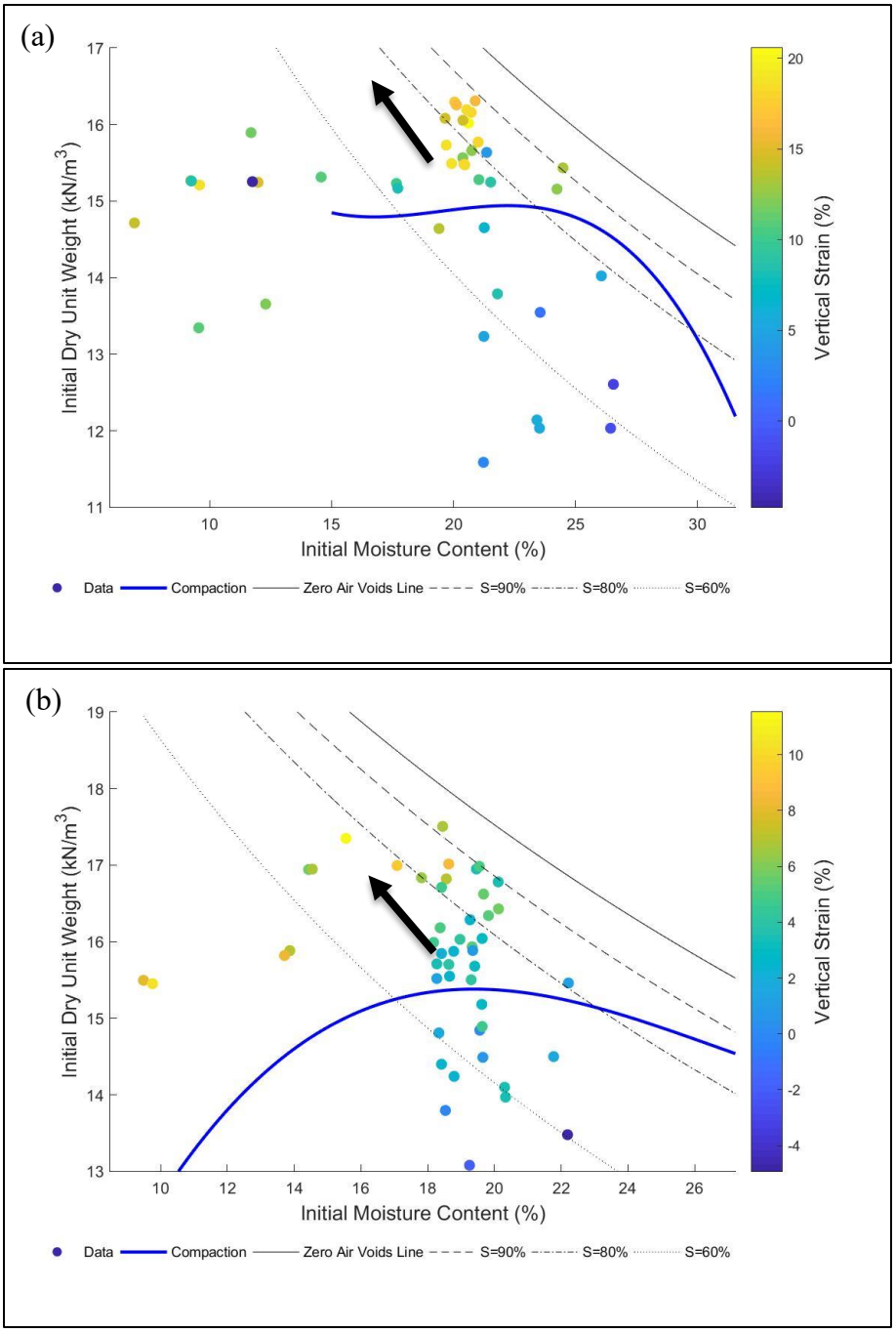

Figure 2.47: Variation in vertical strains at the end of primary swelling of the Eagle Ford (a) and Behring (b) clays in the compaction space

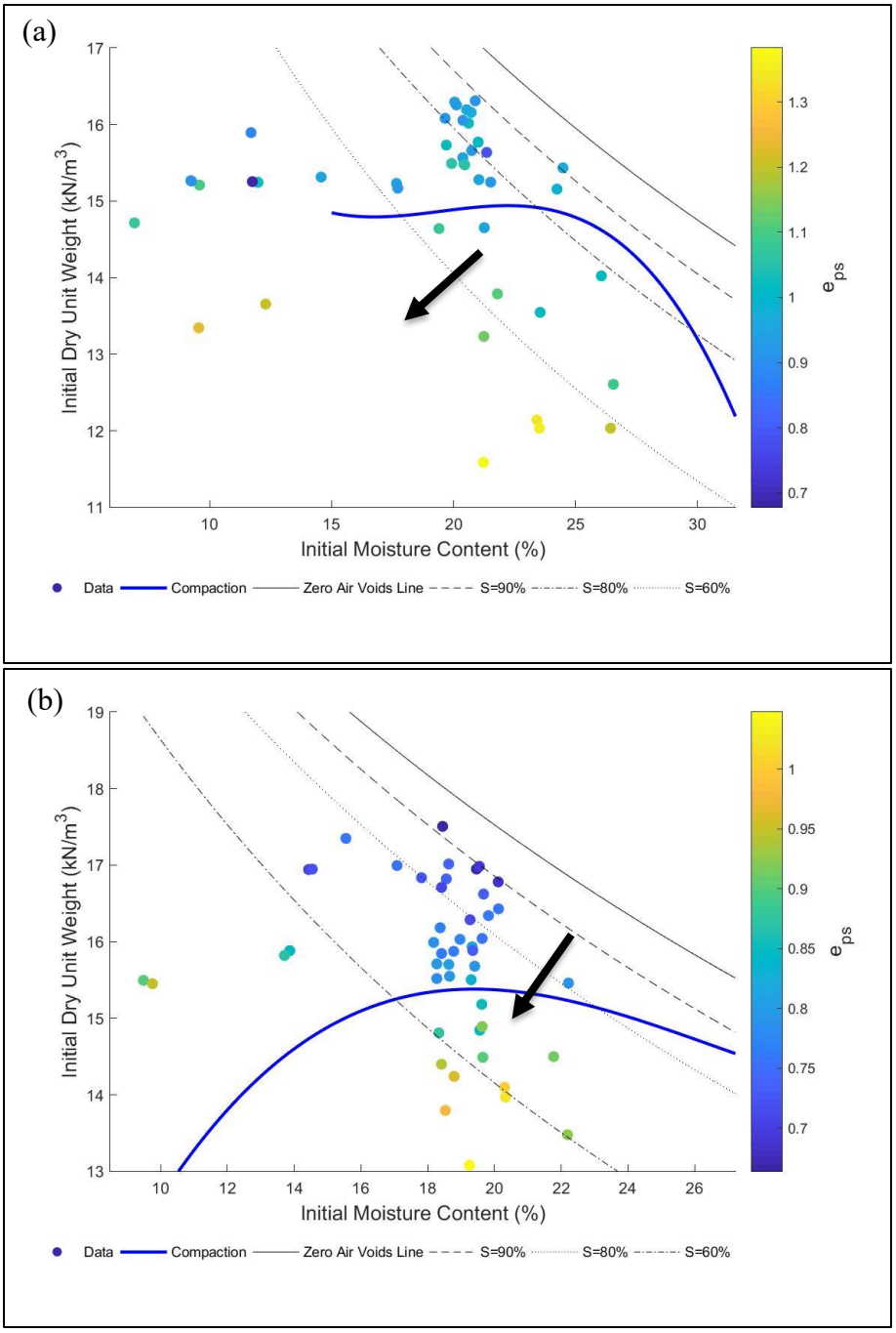

Figure 2.48: Variation in void ratio at the end of primary swelling of the Eagle Ford (a) and Behring (b) clays in the compaction space

2.3.5 Effect of the Gravitational Level (Series IV)

To evaluate the effect of the gravitational level on the primary swelling, the Behring clay and the Branyon clay were analyzed. Soil specimens were compacted at the optimum gravimetric moisture content and maximum dry unit weight from Standard Proctor compaction curves (Table 2.1). The gravitational level is varied by adjusting the angular velocity, or RPMs, and can be calculated as follows:

$$a_c = \omega^2 * r = N * g \tag{2.10}$$

where a_c is the centripetal acceleration, ω is the angular velocity, r is the radial distance from the central axis in the centrifuge, N is the ratio of the centripetal acceleration and the standard acceleration of gravity, and g is the standard acceleration of gravity. The variable N is commonly referred to as the g-level. The midpoint of the specimen was used to define the radial distance from the central axis of the centrifuge. The range of the g-level at the top and bottom of the soil specimens is narrow due to the small specimen height (Armstrong, 2014). The angular velocity was varied from 0 RPMs, at a natural 1-G environment, to approximately 1000 RPMs, at an artificial gravitational level of approximately 100 g's. The centrifugation of the soil specimens increases both the vertical confinement of soil specimens and the hydraulic head in specimens with the increased g-level. The hydraulic head in the specimens was increased by the increase in the gravitational gradient applied to specimens tested in the centrifuge (Kuhn, 2010).

The vertical strains at the end of primary swelling versus the g-level is shown in Figure 2.49.

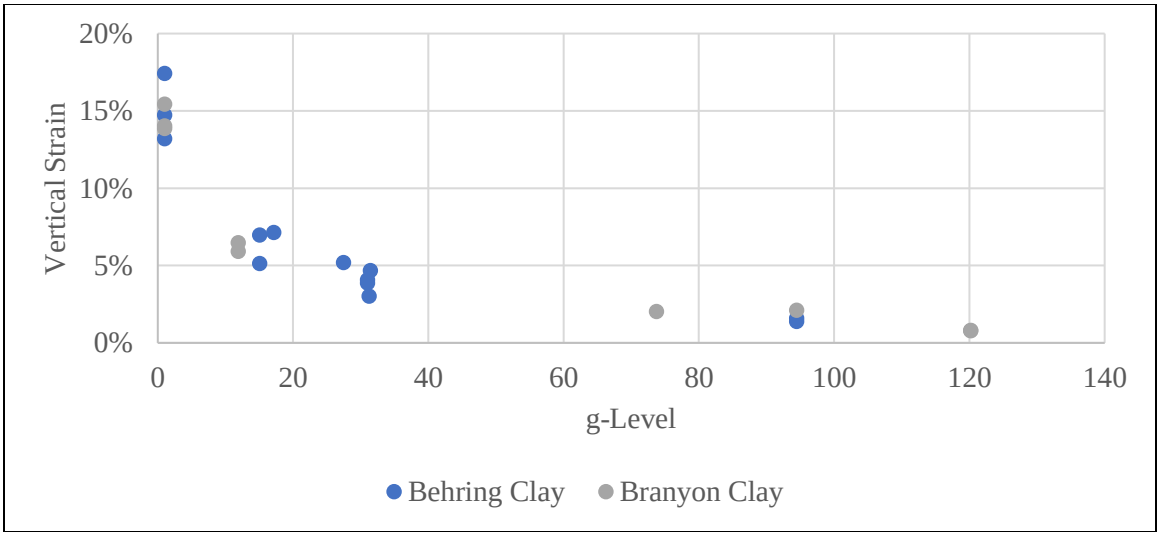

Figure 2.49: Effect of the g-level on the vertical strains at the end of primary swelling for two soils at optimum compaction conditions

The vertical strains were found to decrease with increasing g- level. This trend is due to an increase in the vertical effective stress with increasing imposed g-level. The vertical effective stress can be calculated from the g-level using the method outlined by Armstrong (2014). The vertical strains at the end of primary swelling is shown in Figure 2.50 versus the vertical effective stress.

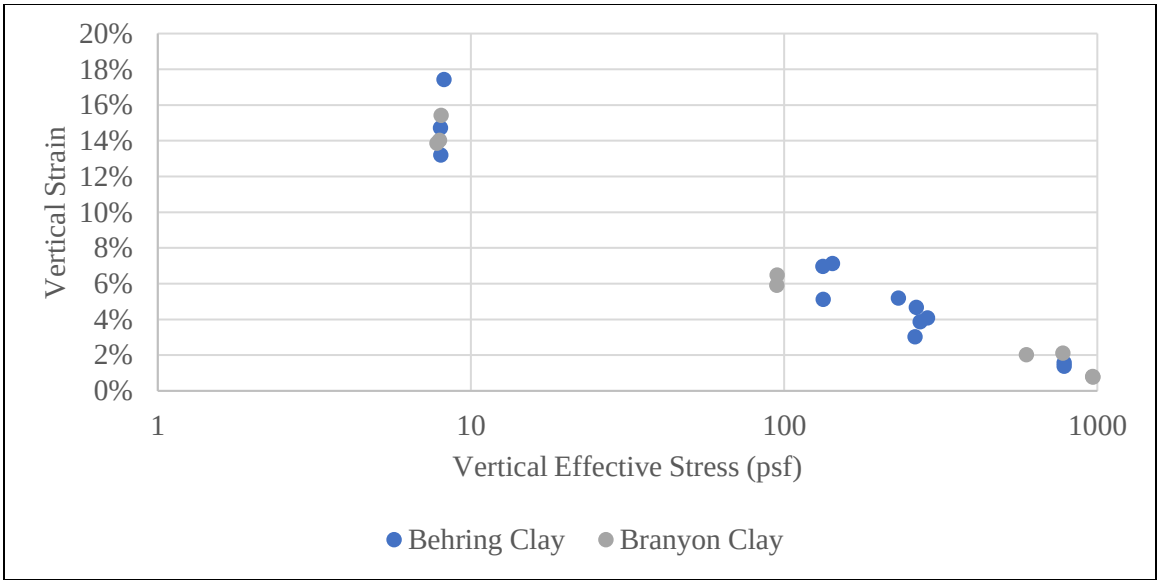

Figure 2.50: Vertical strains at the end of primary swelling versus vertical effective stress for two soils at optimum conditions

The magnitude in the vertical strains at the end of primary swelling decreased with increasing vertical effective stress. This trend is consistent with ASTM D4546 as the soil swelling potential is reduced with a higher confinement. Thus, the g-level affected the vertical strain at the end of primary swelling as it controls the vertical effective stress.

The effect of g-level on the time to the end of primary swelling was also evaluated. The time to the end of primary swelling is shown in Figure 2.51 versus the g-level for the Behring clay. Note that the specimens tested at 1 g were not included in this analysis as the gravitational gradient was not increased for these specimens.

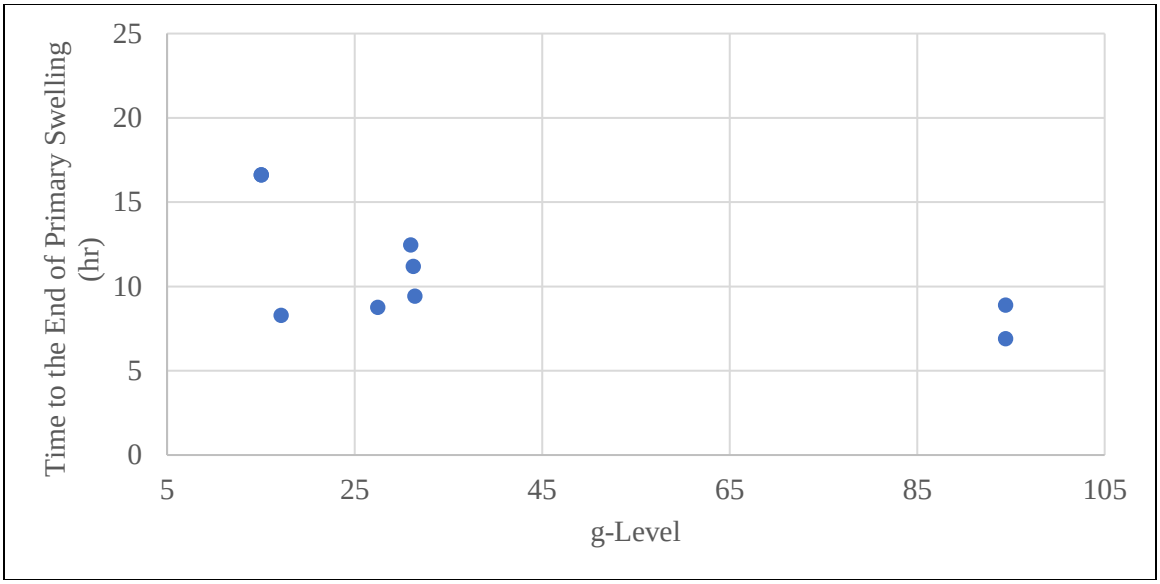

Figure 2.51: Effect of the g-level on the duration of primary swelling for the Behring clay

The time to the end of primary swelling was found to decrease with increasing g-levels. Additionally, the time to the end of primary swelling was affected by the increase in dry unit weight of the specimens during the compression phase and the increase in the gravitational gradient. For the effect of the increase in the dry unit weight, experimental testing procedures require a compression phase where the soil specimens are loaded to the expected effective stress during testing. During this compression phase, the dry unit weight of the soil specimens increased. To evaluate how significant the increase in the dry unit weight due to the compression phase was, the dry unit weight at the end of the compression phase is shown in Figure 2.52 versus the g-level. Note that the initial dry unit weight refers to the dry unit weight at the end of the compression phase.

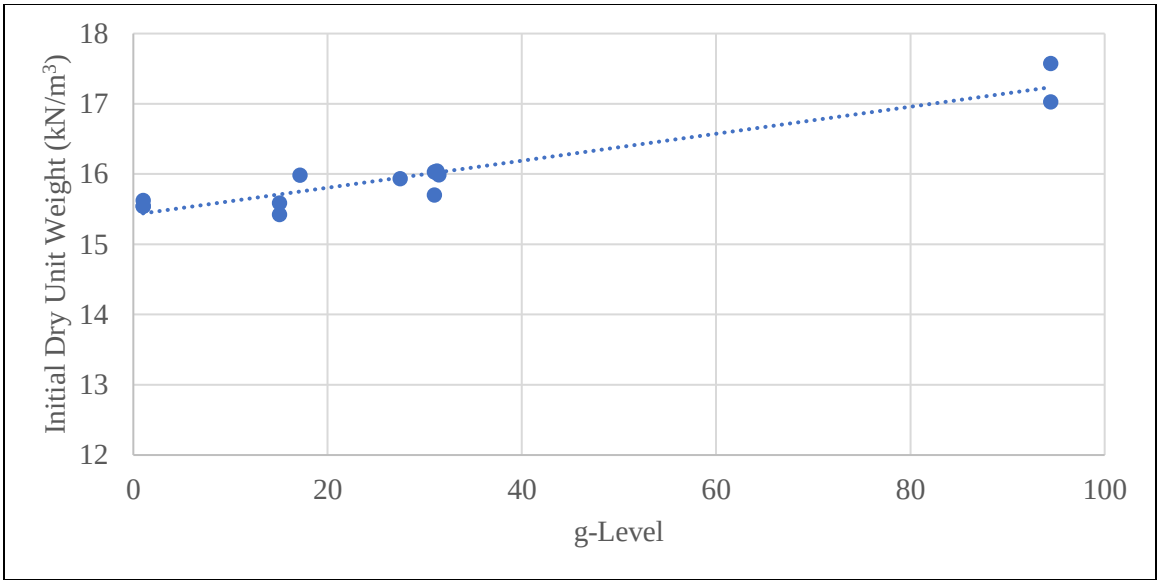

Figure 2.52: Effect of the g-level on the initial dry unit weight for the Behring clay

The initial dry unit weight was found to increase with increasing g-level for the Behring clay. An increase in the dry unit weight was previously shown to increase the time to the end of primary swelling in Figure 2.41. For the effect of the increase in the gravitational gradient, the gravitational gradient in the soil specimens increases with increasing g-level. Previous modeling by Kuhn (2010) indicated that an increase gravitational gradient increases the moisture infiltration into the soil specimens. In order to evaluate whether the time to the end of primary swelling was affected more by the increase in the g-level or the increase in the dry unit weight, the time to the end of primary swelling versus swollen dry unit weight is shown in Figure 2.53. The swollen dry unit weight is defined as the dry unit weight at the end of primary swelling. The time to the end of primary swelling is expected to decrease for specimens with a lower swollen dry unit weight due to the increase in the hydraulic conductivity for specimens with a lower dry unit weight.

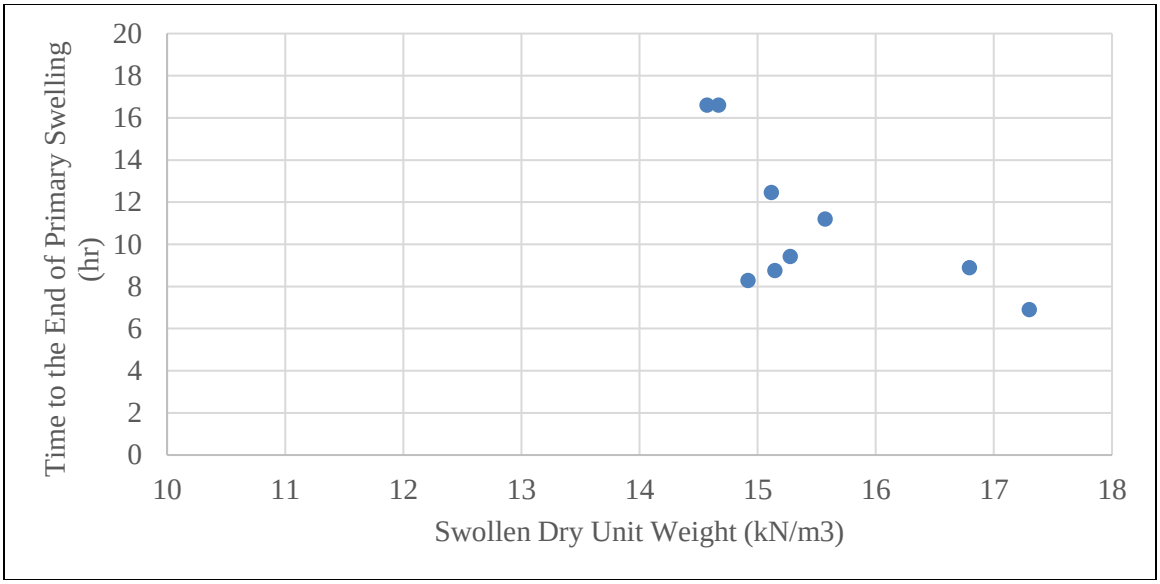

Figure 2.53: Effect of the swollen dry unit weight on the time to the end of primary swelling for the Behring clay

The trend differs from the expected behavior as the time to the end of primary swelling decreases with increasing swollen dry unit weight. This increase in the swollen dry unit weight corresponds with the increase in the initial dry unit weight and g-level from Figure 2.52. Since the time to the end of primary swelling was found to decrease with increasing g-level, the increased gravitational gradient significantly affected the time to the end of primary swelling more than the increased dry unit weight.

In order to assess the validity of the trends from the Behring clay, the results from the Branyon clay were compared to the test results from the Behring clay. The time to the end of primary swelling is shown in Figure 2.54 versus the g-level for the Behring and Branyon clays. The dry unit weight at the end of the compression phase is shown in Figure 2.55 versus the g-level for the Behring and Branyon clays.

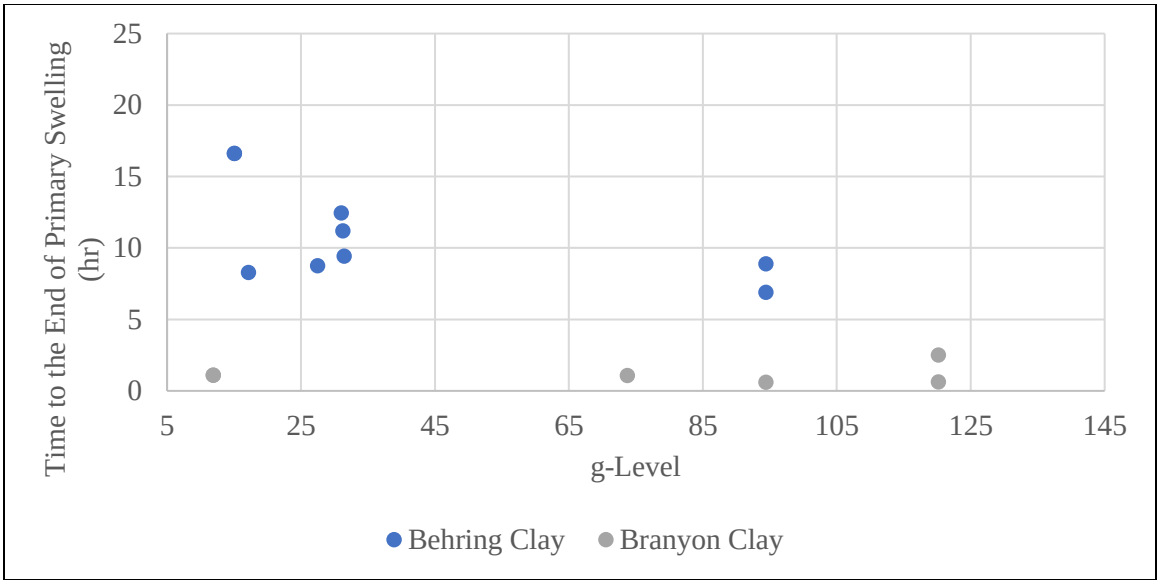

Figure 2.54: Effect of the g-level on the duration of primary swelling for the two soils

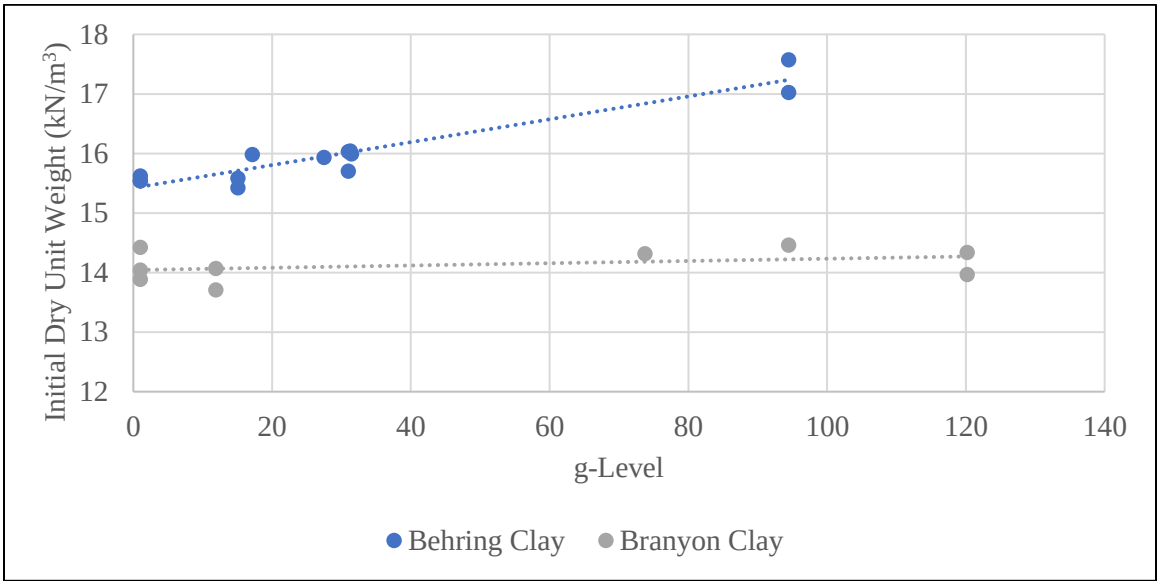

Figure 2.55: Effect of the g-level on the initial dry unit weight for two soils

The time to the end of primary swelling was not significantly affected by the increase in the g-level for the Branyon clay. Additionally, the increase in the initial dry unit weight with the g-level was not as significant for the Branyon clay. An explanation for these

differences is the initial dry unit weight of the specimens. The compaction curve according to Standard Proctor compaction energy was not defined for the Branyon clay (Table 2.1). The maximum dry unit weight according to Standard Proctor compaction energy and optimum moisture content was instead defined using NAVFAC correlations (1962) based on the Atterberg limits of the soil. Due to the reduction in the testing time and the relatively small change in the initial dry unit weight, the soil fabric for the Branyon clay can be assumed to be more flocculated. This structure is expected to have a higher hydraulic conductivity than soil fabric at optimum conditions or wet of optimum from the compaction curve according to Standard Proctor compaction energy (Mitchell et al., 1966).

The final porosity was used to estimate the final volumetric moisture content. The final porosity is shown in Figure 2.56 versus g-level.

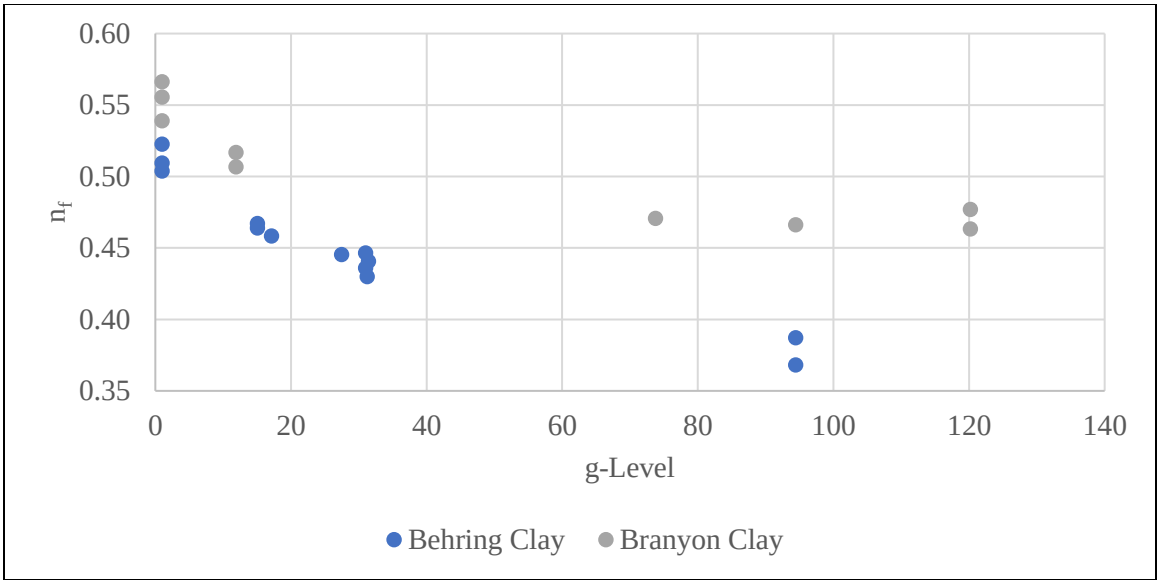

Figure 2.56: Effect of the g-level on the final porosity for two soils

The final porosity was found to decrease with increasing g-level. This trend is consistent with the decrease in vertical strains at the end of primary swelling with increasing vertical effective stress. A decrease in the vertical strains will lead to a decrease in the volume of voids, reducing the porosity of the soil specimen. Since the porosity is used as an estimation of the saturated volumetric moisture content, this trend also indicates that the saturated volumetric moisture content will decrease with increasing effective stress. This result is later evaluated in Chapter 5 for the maximum volumetric moisture content in an instrumented field site.

Overall, the parametric evaluation indicated that the vertical strains, time to the end of primary swelling, and saturated volumetric moisture content decrease with increasing g-level for soils at the same initial gravimetric moisture content and compaction dry unit weight. This decrease in vertical strains with increasing g-level was consistent with ASTM D4546 as the vertical effective stress increases with increasing g-level. The decrease in the time to the end of primary swelling with increasing g-level was attributed to the increase in the gravitational gradient. An increase in the gravitational gradient will increase the moisture infiltration into the specimens. The decrease in the saturated volumetric moisture content was attributed to the decrease in the vertical strains, which lead to a smaller volume of voids.

2.3.6 Effect of the Specimen Height (Series V)

To isolate the effect of the specimen height, the Eagle Ford and Behring clays were tested at various specimen heights. The Eagle Ford clay was tested at three heights of approximately 1 cm, 1.5 cm, and 2 cm, using approximately the same initial gravimetric moisture content of 24.4%, dry unit weight of 15.25 kN/m^3, and a g-level of 29. The Behring clay was tested at 4 different heights, 1 cm, 1.25 cm, 1.75 cm, and 2 cm,

again using approximately the same initial gravimetric moisture content of 20%, dry unit weight of 15.41 kN/m^3, and a g-level of 29. The g-levels targeted an effective stress of 250 psf for a 1 cm tall specimen. A g-level was targeted instead of an effective stress in order to impose the same gravitational gradient on the soil specimens. The 1 cm tall specimen was compacted in a single lift, while the other specimens were compacted in two lifts at half of their total target heights (e.g. the 2 cm tall specimen was compacted in 1 cm lifts).

The void ratio of the specimens is shown in Figure 2.57 versus time of testing for the Eagle Ford clay. Note that the heights of the specimens decreased during the compression phase of the centrifuge test. The heights at the end of the compression phase, prior to the addition of water, are labeled for each soil specimen.

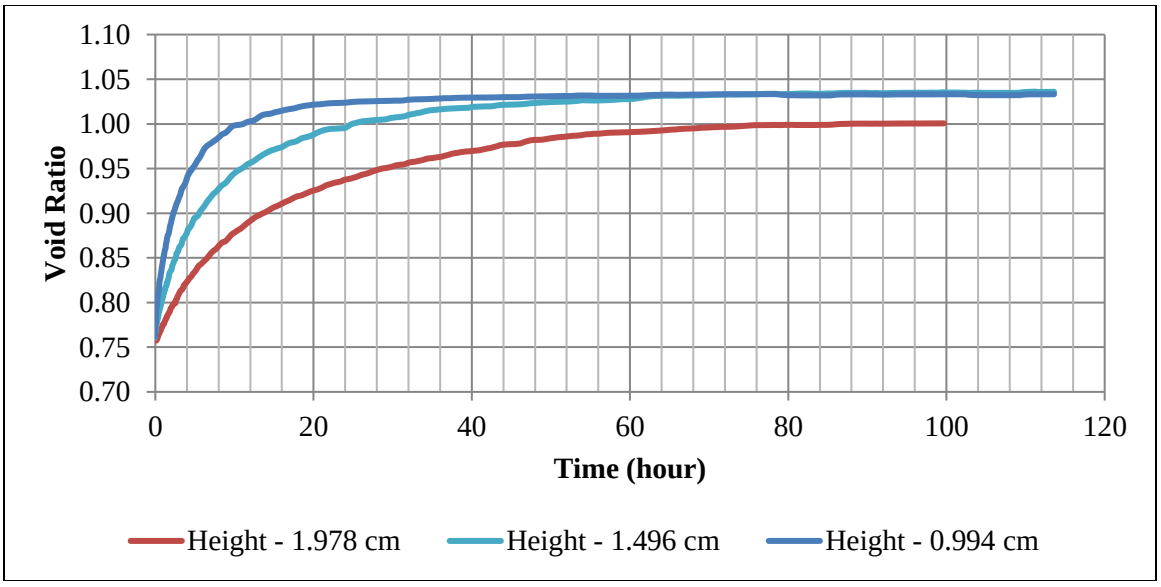

Figure 2.57: Void ratio versus time for various heights of the Eagle Ford clay during centrifuge swelling tests

The trends from Figure 2.57 indicate that the time to the end of primary and final swelling increases with increasing specimen height. However, the void ratio at the end of primary and ultimate swelling differed for specimens with differing specimen height from Figure 2.57. The discrepancies in the void ratio at the end of primary and ultimate swelling was attributed to the differences in the vertical effective stress. As the soil specimens were tested at the same g-level, the 2 cm tall specimen had an effective stress of 290 compared to the 250 psf effective stress for the 1 cm tall specimen.

The results are presented in terms of the ratio of the vertical strains to the ultimate vertical strain in order to normalize the swelling versus time curves. This normalization is used as based on the variability of the effective stresses in the soil specimens. Based on the results from Series IV, the variation in the effective stress would decrease the vertical strains at the primary and total swelling in the specimen. The ratio to the ultimate swelling is shown in Figure 2.58 versus time. Note that the end of testing swelling may not be the ultimate swelling for the 2 cm tall specimen. For the 2 cm tall specimen, the centrifuge test was stopped at 100 hours due to equipment limitations.

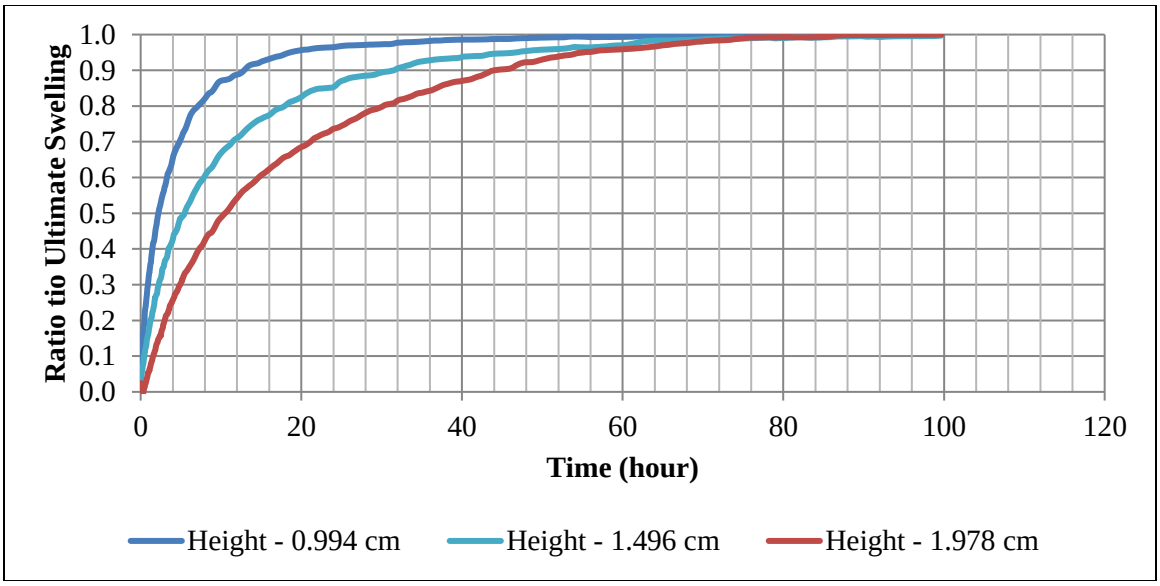

Figure 2.58: Ratio of swelling to ultimate swelling versus time for the Eagle Ford clay at various heights

The time to the end of primary swelling was approximately 16 hours for the 1 cm tall specimen, 35 hours for the 1.5 cm tall specimen, and 70 hours for the 2 cm tall specimen. The increase in the time to the end of primary swelling with increasing specimen height was found to be more than linear. The time to the ultimate swelling was approximately 50 hours for the 1 cm tall specimen, 80 hours for the 1.5 cm tall specimen, and 100 hours for the 2 cm tall specimen. This increase in the time to the ultimate swelling with the specimen height was found to be approximately linear. Thus, the time to the end of primary and ultimate swelling were found to increase with increasing specimen height.

To verify the trends from tests using the Eagle Ford clay, the Behring clay was additionally tested. The Behring clay was selected as it has a lower plasticity index and a lower percentage of fines than the Eagle Ford clay. The heights at the end of the

compression phase are labeled for each soil specimen. The ratio of the swelling to the ultimate swelling versus time are shown in Figure 2.59.

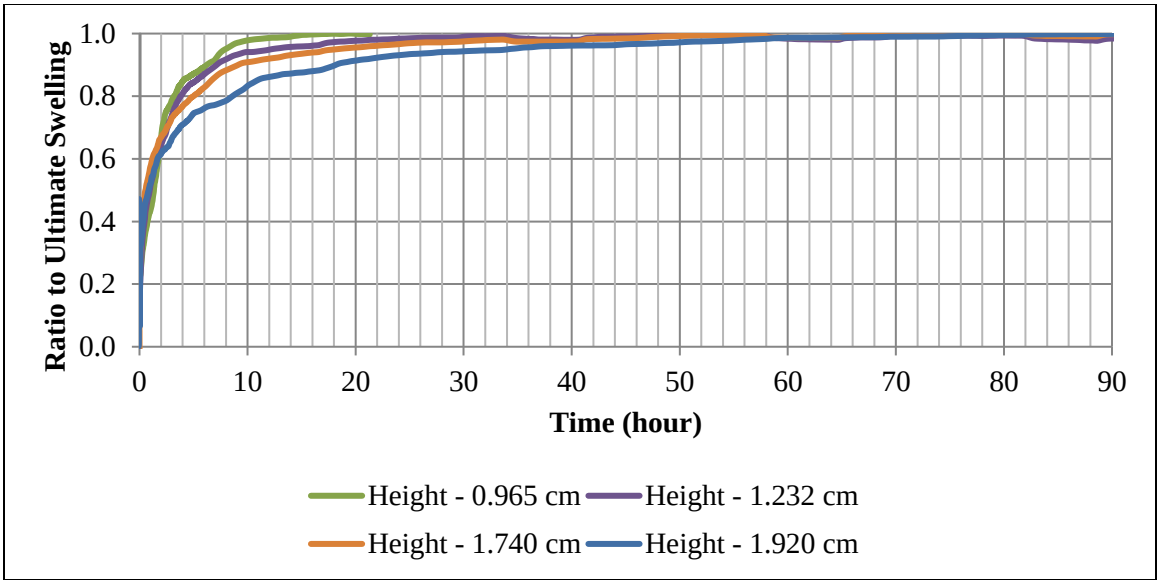

Figure 2.59: Ratio of swelling to ultimate swelling versus time for the Behring clay at various heights

The time to the end of primary and ultimate swelling was found to increase with increasing specimen height for the Behring clay. This trend is consistent between the Eagle Ford and Behring clay. The time to the end of primary swelling was approximately 10 hours for the 1 cm tall specimen, 10 hours for the 1.25 cm tall specimen, 11 hours for the 1.75 cm tall specimen, and 40 hours for the 2 cm tall specimen. Unlike the trends from the Eagle Ford clay, the time to the end of primary swelling was increased only for the 2 cm tall specimen. This increase in the time to the end of primary swelling was more than linear. The time to the ultimate swelling was approximately 20 hours for the 1 cm tall specimen, 30 hours for the 1.25 cm tall specimen, 50 hours for the 1.75 cm tall specimen, and 90 hours for the 2 cm tall specimen. The increase time to the end of

ultimate swelling with increasing specimen height was determined to be non-linear for the Behring clay. Therefore, the trend in the increase in the time to the end of final swelling differed between the Eagle Ford and Behring clays. This difference between the Eagle Ford and Behring clays can be explained by the differences in the magnitude of primary and ultimate swelling. The swelling for the Eagle Ford clay was higher than for the Behring clay. Due to the increase in the magnitude of swelling, the time to the end of primary and ultimate swelling was expected to increase.

In general, the time to the end of primary and ultimate swelling was found to increase with specimen height. The increase in the time to the end of primary swelling with increasing specimen height was determined to be more than linear for the Eagle Ford and Behring clays. However, the increase in the time to the end of ultimate swelling differed between the Eagle Ford and Behring clays. The time to ultimate swelling with specimen height was found to increase linearly for the Eagle Ford clay and non-linearly for the Behring clay. This difference was attributed to the difference in the magnitude of swelling for the two soils. Additionally, the vertical strains at the end of primary and ultimate swelling were found to decrease slightly with increasing specimen height. This trend was due to the increase in specimen height increasing the vertical effective stress at the same g-level.

2.4 CONCLUSIONS

The results from a centrifuge testing program were used to examine the impact of initial soil and testing conditions on the swelling characteristics of expansive soils. Three natural expansive soils with varying levels of plasticity and percentages of fines were tested using a centrifuge-based inundation approach. The evaluated variables included the

initial gravimetric moisture content, initial dry unit weight, initial degree of saturation, gravitational level, and initial specimen height.

From the evaluation of the effect of the initial gravimetric moisture content (Series I), the following conclusions can be made:

- The vertical strain at the end of primary swelling was found to increase linearly with decreasing gravimetric moisture content. This result is consistent with previous studies that involved traditional testing methodologies to characterize expansive soils.
- The vertical strains at the end of primary swelling were found to increase non-linearly with increasing total suction.
- The porosity at the end of testing, which was used to estimate the final volumetric moisture content, was found to decrease with increasing initial gravimetric moisture content.
- These trends were consistent in three soils with differing plasticity indices and percentage of fines. However, the magnitude of trends differed between the three soils, indicating that the effect of the initial gravimetric moisture content is specific to each soil.
- Results reveal the need of testing rather than relying on correlations with index properties.

From the evaluation of the effect of the initial dry unit weight (Series II), the following conclusions can be made:

- The vertical strains at the end of primary swelling was found to increase linearly with increasing initial dry unit weight.
- Soil suction was found to decrease with increasing relative compaction for soil specimens that are prepared at the same gravimetric moisture content.

- The time to the end of primary swelling was found to increase with increasing initial dry unit weight. This increase is consistent with the decrease in hydraulic conductivity with increasing dry unit weight.
- The final porosity was found to decrease with increasing initial dry unit weight.
- These trends were consistent for the three soils with differing plasticity indices and percentage of fines. However, the magnitude of trends differed between the three soils, indicating that the effect of the initial dry unit weight is specific to each soil.

A database of swelling results from centrifuge tests was additionally used to validate the trends from Series I and II and evaluate the effect of the initial degree of saturation. From this evaluation (Series III), the following conclusions can be made:

- The void ratio at the end of primary swelling was found to decrease with increasing degree of saturation. However, this trend was non-linear and with different trends for results from Series I and II.
- The trend of the change in void ratio (from the beginning of inundation to the end of primary swelling) with increasing degree of saturation differed between Series I and II. For Series I, the change in void ratio was found to decrease with increasing degree of saturation. For Series II, the change in void ratio was found to increase with increasing degree of saturation.
- These differing trends indicate that a single variable is not suitable to evaluate the effect of initial soil conditions on swelling characteristics.
- Additionally, the initial soil suction was found to not necessarily be the governing variable for swelling. Swelling is governed by the combination

of variables which include the initial soil suction, initial soil fabric, and spacing between clay peds.

- Trends using the database of centrifuge tests were consistent with the results from Series I and II. The vertical strains and void ratio at the end of primary swelling were found to increase with decreasing initial gravimetric moisture content and increasing initial dry unit weight.

From the evaluation of the effect of the gravitational level (Series IV), the following conclusions can be made:

- The vertical strains at the end of primary swelling were found to decrease with an increasing gravitational level. This decrease is consistent with the increase in the vertical effective stress with increasing gravitational level.
- The porosity at the end of testing was found to decrease with an increasing gravitational level. This trend was more prominent for the Behring clay, which were tested at the optimum compaction conditions according to Standard Proctor compaction energy.
- The time to the end of primary swelling was found to decrease with an increasing imposed artificial gravitational level. This decrease in time is consistent with the increase in the gravitational gradient.

From the evaluation of the effect of the specimen height (Series V), the following conclusions can be made:

- The time to the end of primary swelling was found to increase more than linearly with specimen height for both the Eagle Ford and Behring clays.
- The time to the end of ultimate swelling was found to increase with specimen height. This trend was linear for the Eagle Ford clay and non-linear for the Behring clay.

Overall, the impact of the initial gravimetric moisture content and dry unit weight on the magnitude of vertical strain at the end of primary swelling was found to be consistent with trends reported from previous studies. This consistency between studies validates the centrifuge methodology as being a practical and accurate methodology for analyzing the swelling behavior of expansive soils.

Chapter 3: Effect of Soil Fabric on the Swelling of Highly Plastic Clays

ABSTRACT

As discussed in Chapter 2, initial soil conditions are shown to play a key role in the swelling characteristics of expansive soil deposits. However, the effect of soil fabric, or internal clay structure, has not been thoroughly investigated so far. This research component focuses on the effect of soil fabric on the swelling characteristics of laboratory-reconstituted and field-sampled specimens. For the laboratory-reconstituted specimens, the soil fabric was found to primarily affect the duration of swelling. Specifically, the time to the end of primary swelling was higher for specimens prepared with a comparatively dispersed structure than specimens with a comparatively flocculated structure. The magnitude of primary and ultimate swelling were found to be negligibly affected by differing soil fabrics for laboratory-reconstituted specimens. For the case of field-sampled specimens, soil fabric was shown to affect both the magnitude and duration of swelling. Field-sampled soils tended to have a higher primary swelling in a shorter timeframe than the laboratory-reconstituted specimens. Additionally, for the laboratory-reconstituted specimens, the temperature used during drying was found to change the clay's properties. Specimens that were oven-dried at 110°C during preparation resulted in a lower primary swelling than specimens that were air-dried at 23°C. Electron microscopy was used to examine clay structure both at air-dried and wet states and found that the fabric differs significant between laboratory-reconstituted and field-sampled specimens. Via use of a Peltier cooling stage, the soil fabric of an unconfined, reconstituted expansive soil was shown to change significantly upon the first wetting and drying cycle.

3.1 INTRODUCTION

The original centrifuge test set-up required the use of laboratory-reconstituted specimens compacted in the permeameter cups due to the one-dimensional infiltration boundary conditions. However, literature has shown that there may be differences in swelling characteristics and behavior between specimens prepared using different compaction techniques (Attom et al., 2001). The changes in swelling behavior was attributed to the internal structure, or fabric, of the soil. Soil fabric of laboratory-reconstituted specimens is typically described as either a dispersed or a flocculated structure. The formation of these structures depends on the magnitude of the compactive effort and the initial soil conditions. Previous studies concluded that the soil fabric affects the engineering behavior of soils (Lambe, 1958). Thus, a study was conducted to evaluate the effect of soil fabric on swelling characteristics. If the effect of the soil fabric on swelling characteristics is found to only affect the duration of testing and not the magnitude of swelling, samples taken from the field can be replicated in terms of gravimetric moisture content and dry density, as opposed to attempting to re-create the in-situ soil fabric from seasonal moisture fluctuations. Therefore, this study is necessary to link the laboratory experiments to field results by demonstrating the effect, or lack of effect, of soil fabric on swelling characteristics.

The testing and analysis for the investigation into the effect of the soil fabric on the swelling of highly plastic clays is grouped into three sections. The first section focuses on the effect of the soil fabric on laboratory-reconstituted specimens. Specimens were prepared to achieve the same initial conditions before infiltration (i.e. gravimetric moisture content and dry density) but differing soil fabric. The second section examines the effect of the soil fabric on field-sampled specimens and corresponding laboratory-reconstituted specimens prepared and inundated at the same field conditions. Soils

sampled from two different deposits were selected to evaluated differences in swelling characteristics between laboratory-reconstituted and field-sampled specimens. Secondary analysis in this section included an evaluation of the swelling characteristics of laboratory-reconstituted specimens that were either air-dried or oven-dried. The final section includes a visualization of the soil fabric of both laboratory-reconstituted and field-sampled specimens using electron microscopy. A test that examined the change in the fabric of a soil undergoing cyclic wetting and drying was additionally performed and documented in this section.

3.2 BACKGROUND INFORMATION ON SOIL FABRIC

In order to understand the concepts previously evaluated for the effect of fabric on swelling characteristics, the results of a literature review are grouped into four sections. The first section examines the research that has previously focused on the difference in soil fabric of reconstituted specimens. The second section reviews research that evaluated the effect of cyclic-wetting and drying on reconstituted specimens. The third section examines previous experimental studies that attempted to quantify the effect of fabric on the swelling of expansive soils. The final section reviews the literature on electron microscopy and its use to visualize clays.

3.2.1 Soil Fabric and Compaction

Previous studies have evaluated the different soil fabric of clayey soils under varying compaction conditions and compactive effort. Lambe (1958) examined the structure of clayey soils compacted either wet or dry of the optimum gravimetric moisture content from compaction curves. The study found that soils compacted dry of the optimum moisture content tend to have more flocculated structures, or more random clay plate orientation, due to the inability of the diffuse double layer to fully develop. The

study also found that soils compacted wet of the optimum moisture content tend to have a more dispersed structure, or more uniform distribution of clay plate orientation, due an increase in repulsion from the diffuse double layer. A simplified representation of these soil fabrics is shown in Figure 3.1. Additionally, a more flocculated and more dispersed soil fabric are shown in Figure 3.2 from scanning electron micrographs.

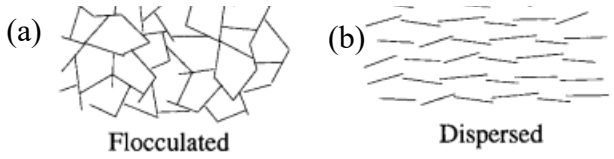

Figure 3.1: Generalized microstructure of compacted clays for (a) flocculated and (b) dispersed fabric (Prashant and Penumadu, 2007)

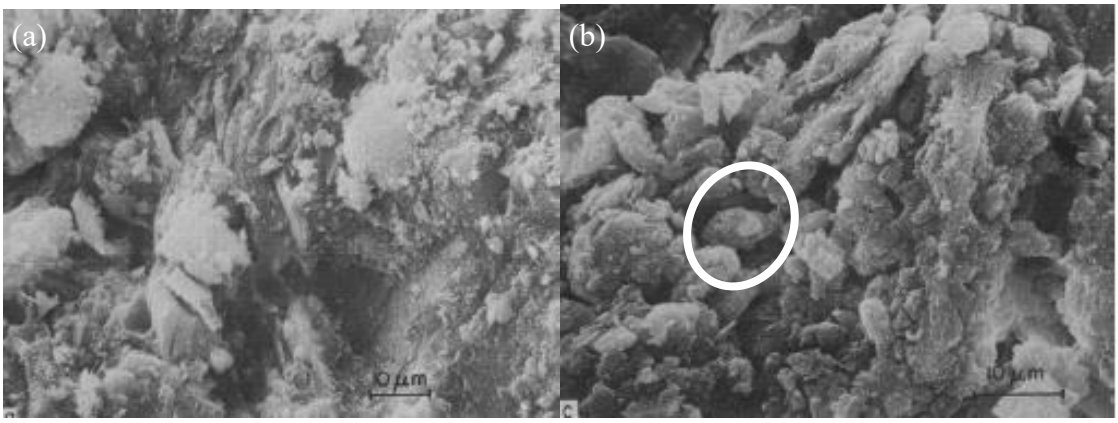

Figure 3.2: Micrographs of compacted clays with dispersed (a) and flocculated (b) fabric (Diamond, 1971)

In general, clay clusters, indicated by the white oval in the flocculated soil fabric in Figure 3.1, are more prevalent in the flocculated soil than the dispersed structure. The dispersed fabric tends to have clay particles oriented in a structure that appears visually smoother from scanning electron micrographs.

Previous research has indicated that the soil fabric affects the shear strength, stiffness, hydraulic conductivity, and swelling and shrinking properties. In terms of the shear strength, soils compacted dry of the optimum moisture content tend to have a higher shear strength due to the flocculated structure compared to soils compacted wet of the optimum moisture content (Seed and Chan, 1959). In terms of the stiffness, soils compacted dry of the optimum moisture content tend to be stiffer, but also more brittle, compared to those soils compacted wet of the optimum moisture content (Lambe, 1958). In terms of the hydraulic conductivity, soils compacted dry of the optimum moisture content tend to have a higher hydraulic conductivity as compared to those compacted wet of the optimum moisture content. This is because soils compacted dry of the optimum moisture content with a flocculated structure have large inter-particle voids that allow water to be transmitted more easily (Mitchell et al., 1966). Finally, soils compacted dry of the optimum moisture content tend to swell more upon wetting and shrink less upon drying as compared to those compacted wet of the optimum moisture content (Seed and Chan, 1959).

3.2.2 Cyclic Wetting and Drying of Expansive Soils

Expansive soils pose a significant risk to low-overburden infrastructure based on specific climatic conditions. These conditions are defined by time periods in which the soil is allowed to dry for a long time period followed by high intensity rainfall events. Laboratory studies have evaluated how these wetting and drying cycles affect the swelling potential and soil fabric of expansive soils. Allen and Gilbert (2006) developed an accelerated shrink-swell device that used forced ventilation of air to desaturate specimens after wetting. Testing was performed on undisturbed soil specimens in a consolidation cell set-up similar to that from the traditional swelling methodology,

ASTM D4546. A visualization of the macro changes in the soil specimens during the accelerated shrink-swell cycles is shown in Figure 3.3.

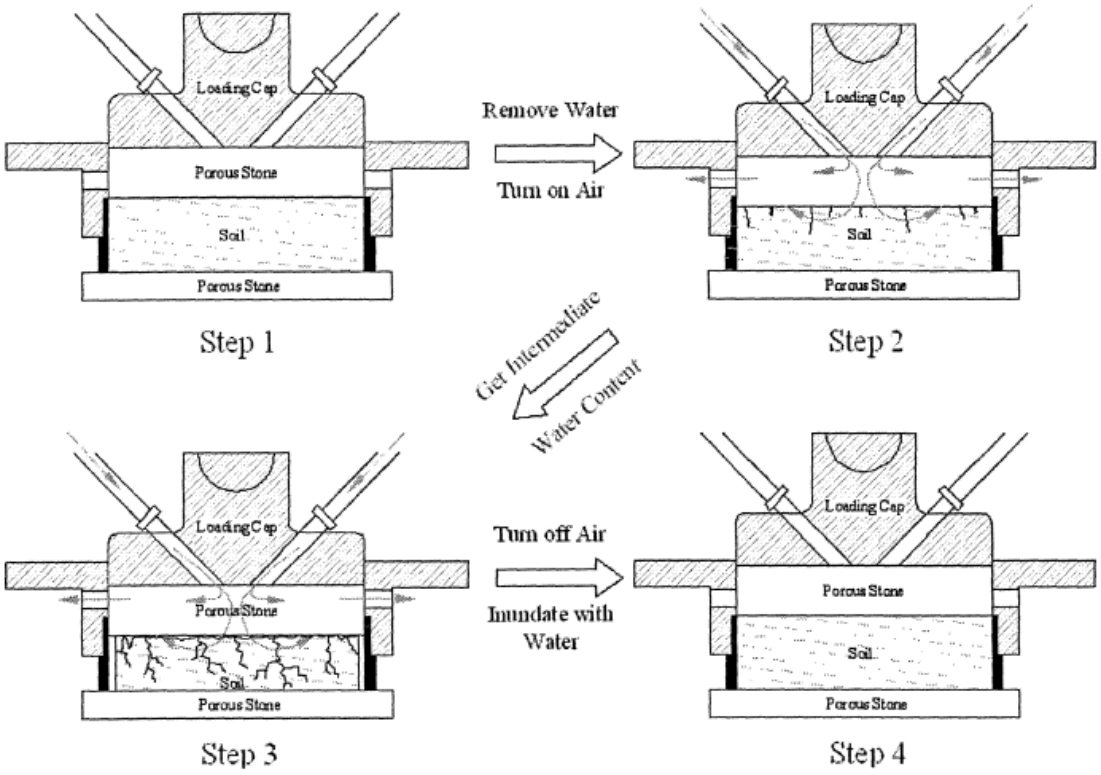

Figure 3.3: Change in soil specimen during accelerated shrink-swell test (Allen and Gilbert, 2006)

Results from the accelerated shrink-swell test were compared against those predicted by the methodology used by the Texas Department of Transportation to predict the potential vertical rise in expansive soils, Tex-124-E. Tex-124-E uses the method outlined from McDowell (1958), presented in Section 2.2, which correlates the potential vertical rise with the Atterberg limits of the soil. Allen and Gilbert found that Tex-124-E underpredicted the amount of vertical heave for specimens with low swelling potential and overpredicted the amount of vertical heave for specimens with high swelling potential. However, the accelerated shrink-swell test only tracks the vertical change in the

specimen and did not account for the formation of desiccation cracks that developed during drying cycles.

Tripathy and Rao (2009) utilized an oedometer set-up that controlled the air temperature to evaluate cyclic wetting and drying of expansive soils. Soils were inundated with water and allowed to saturate for three days. After three days, water was removed from the oedometer set-up, and the surrounding air temperature was increased in 40°C to dry the specimen. Soil specimens were found to reach an equilibrium value of vertical strain at the end of shrinkage and swelling after approximately 4 wetting and drying cycles. The researchers also reduced the imposed soil suction during the drying cycle. This decrease in suction led to an intermediate equilibrium of the change in vertical strain.

Lin and Cerato (2013) examined hysteresis on the soil-water retention curves and changes in the swell-shrink paths of expansive soils. The researchers used various methods to determine the soil-water retention curve of a compacted expansive soil, including filter paper, pressure plate, and chilled mirror hygrometer methods. The curves defined from these methods were used to determine the corresponding suction of specimens undergoing volumetric changes. Results indicated that there was a decrease in the swelling and an increase in the shrinkage with additional swell-shrink cycles. Further, the researchers encountered two forms of hysteresis in the specimens undergoing cyclic wetting and drying. The first form of hysteresis was between the primary drying and wetting loops that occurs due to the pore space between the clay peds. The second form of hysteresis was between the primary wetting and a secondary drying phase, which showed a decrease in the volumetric moisture content changes due to a presumed realignment of particles and stabilization of the macro-pores in the soil structure.

3.2.3 Effect of Soil Fabric on Swelling of Expansive Soils

Previous studies have evaluated the effect of the soil fabric on the swelling characteristics of expansive soils. Attom et al. (2001) examined the effect of sample preparation on the magnitude of primary swelling and swelling pressure. Specimens were compacted statically by applying a vertical static load, kneading with a pneumatic compactor, and dynamically via the standard proctor test. Test results from undisturbed field specimens were compared against the laboratory-reconstituted specimens. The magnitude of primary swelling for each of these compaction conditions using three highly plastic clays is shown in Figure 3.4. Note that the initial conditions (i.e. the initial gravimetric moisture content and dry unit weight) were similar for the multiple specimens.

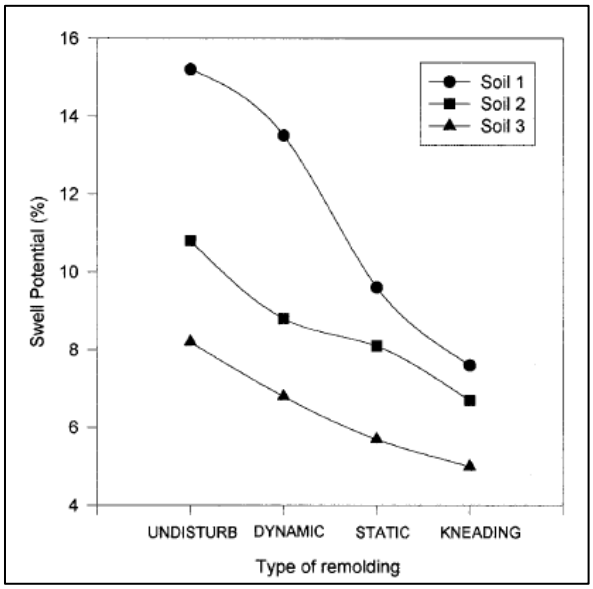

Figure 3.4: Swelling potential versus compaction methodology (Attom et al., 2001)

The undisturbed (field) specimen resulted in a higher amount of swelling than the laboratory-reconstituted specimens. Further, the type of compaction affected the magnitude of swelling. Since the densities were the same, the difference in the magnitude

of swelling was attributed to the different fabric and microstructure between the specimens. As the undisturbed sample underwent deposition over a long time period, thixotropy may have increased the volume of micropores, leading to an increased magnitude of swelling. Thus, reconstituted specimens may not accurately capture the magnitude of vertical strain of expansive soil deposits in the field.

Armstrong (2014) examined the effect of soil fabric on the swelling of laboratory-reconstituted specimens. Soils were compacted according to ASTM D698 with standard effort at three moisture conditions. The first condition was at a "dry" condition five percentage points dry of the optimum moisture content from the Standard Proctor compaction curve. The specimens at the dry condition were assumed to have a more flocculated structure. The second condition was at the optimum moisture content. The final condition was at a "wet" condition, five points wet of the optimum moisture content. The specimens at the wet condition were assumed to have a more dispersed structure. After preparation at differential initial moisture content values, soils underwent either drying or wetting to reach a targeted gravimetric moisture content. Soils were dried in an environmental chamber at a comparatively high and constant relative humidity. Soils were wetted by adding a specified amount of water to the surface of the compacted soil specimens, wrapping the specimens in aluminum foil, and allowing for moisture equilibrium to occur. After moisture adjusting, the soil specimens were tested with their results shown in Figure 3.5. Note that ω_c is the gravimetric moisture content at compaction, and ωi is the initial gravimetric moisture content.

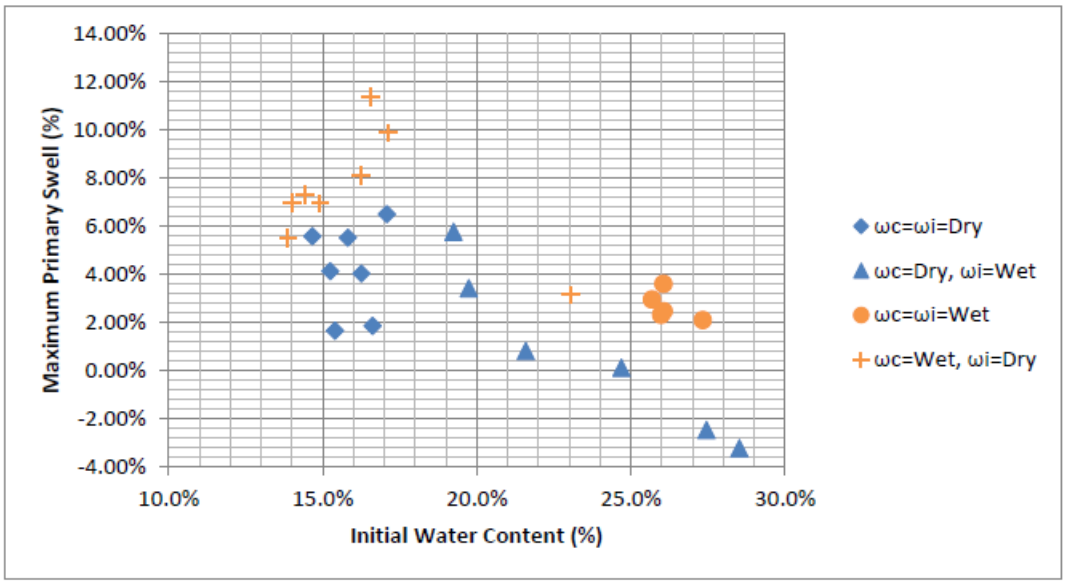

Figure 3.5: Effect of testing moisture content vs. compaction moisture content on the primary swelling (Armstrong, 2014)

Results indicated that specimens that were initially compacted at a wet condition and then dried resulted in a higher magnitude of primary swelling than specimens that were compacted at the dry condition. However, the specimens that were dried tended to have a significantly higher initial dry unit weight than those compacted at the dry condition. As shown in Chapter 2, the initial dry unit weight has a significant impact on the magnitude of vertical strain. Additionally, results indicated that the specimens that were compacted at the optimum and wet conditions resulted in a longer testing time to the end of primary swelling. This difference in the time to the end of primary swelling was attributed to differences in the soil fabric, with the more wet specimens having a more dispersed structure.

The soil fabric is additionally affected by the drying temperature of the soil. Note that the drying temperature is given as the temperature that reconstituted clay soils are dried at prior to rehydration and compaction of the soil specimens. Previous studies have

examined the effect of the drying temperature on the clay mineralogy and the removal of the attached water from clay particles. The removal of water attached to clay minerals has been shown to aggregate clay particles and reduce the cohesion (Lambe, 1964). Rao et al. (1989) compared air-dried and oven-dried at 110°C specimens of a marine clay as well as homogenized bentonites and montmorillonites with varying pore liquids. The marine clay showed a sharp decrease in the Atterberg limits and fines content when oven-dried. The homogenized soils showed a decrease in the Atterberg Limits that was more stark for the calcium, aluminum, and iron bentonite mixtures in comparison to the sodium bentonite mixture. Basma et al. (1994) examined the effect of the drying soils at 25 °C, 60°C, and 110°C on varying engineering properties. Results indicated that an increase in the drying temperature decreased the plasticity of the soil, reduced the swelling potential and pressure, increased the compression index and coefficient of compressibility, and decreased the unconfined compressive strength. However, these trends were not necessarily linear with an increase in the drying temperature. The effect of the drying temperature on the swell potential from Basma et al. (1994) is shown in Figure 3.6.

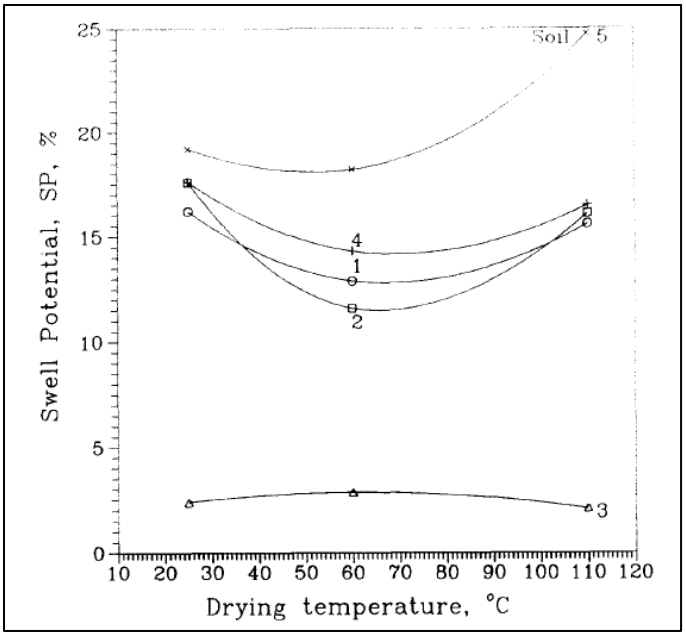

Figure 3.6: Swell potential with drying temperature (Basma et al., 1994)

The reduction in the swell potential typically was more significant at a drying temperature of 60 ºC than at 110 ºC. However, the authors recommended using only air-dried soils for characterization of highly plastic clays.

3.2.4 Electron Microscopy and Clays

Scanning electron microscopy has been used to visualize microscopic features of soil samples. The visualization of a sample's surface is accomplished by using an electron beam in a vacuum setting and collecting the signals produced from the sample using various detectors. An overview of the interaction of the electron beam with a sample surface is shown in Figure 3.7.

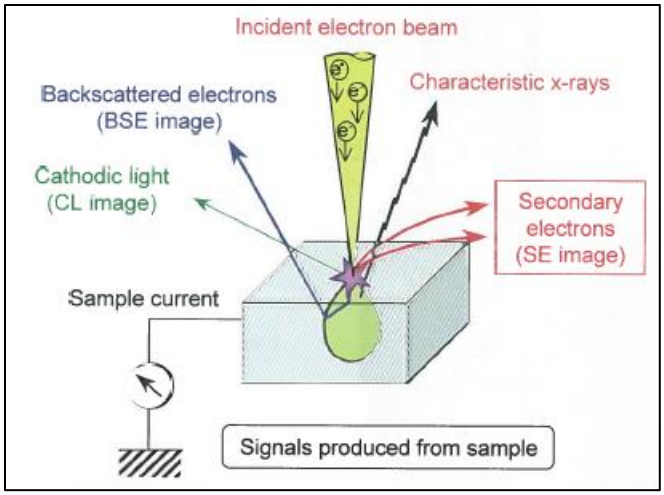

Figure 3.7: Basics of electron microscopy (Hitachi, 2008)

Based on the interaction of incident electron beam with the surface of the sample, various electrons or x-rays are released that can be collected to visualize or characterize the sample. Secondary and backscattered electrons allow for imaging of the topography of the sample. Additionally, the backscattered electrons also allow for identification of crystalline structure. A typical SEM uses vacuum to prevent noise and "skirting" in the beam to focus the electron beams on specific sections of the sample. Due to the applied vacuum, soil specimens are at the residual moisture content. In the SEM, the specimens must be non-conductive or coated to prevent charging of the specimen, which reduces the resolution of the topography.

Additionally, electron microscopy can be used with an environmental scanning electron microscope, which allows for the use of wet specimens, reduces the charging of specimens, and allows for the control of the water vapor pressure in the sample. The use of wet specimens is particularly important for the visualization of clays that have attached water molecules. The control of the water vapor pressure allows for wet specimens to be

placed in the ESEM. However, the ESEM has a comparatively low resolution from a skirting effect.

Additionally, a Peltier cooling stage can be used to more finely control the temperature and relative humidity of a sample. This stage is shown in Figure 3.8 and runs water through the stage to reduce the specimen temperature.

Figure 3.8: Peltier cooling stage for use in an ESEM

With control of the specimen temperature via the use of the cooling stage and the water vapor pressured via the use of the ESEM, the relative humidity near the specimen can be controlled. The isotherm of the relative humidity with temperature and water vapor pressure is shown in Figure 3.9.

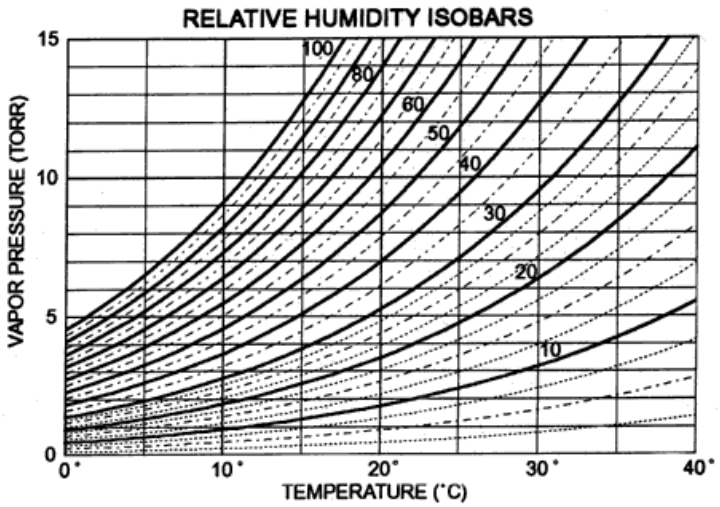

Figure 3.9: Relative humidity isobars for ESEM investigations (Messier and Vitale, 1993)

Via the use of the cooling stage, soil specimens can be covered with water at a given vapor pressure by lowering the temperature to increase the relative humidity to 100%. At this relative humidity, the soil specimen will be covered by water, allowing for moisture to infiltrate the soil specimen. Therefore, an ESEM with a Peltier cooling stage allows for visualization of a clay specimen undergoing cyclic wetting and drying.

Previous studies have examined highly plastic clays undergoing cyclic wetting and drying in either a SEM or an ESEM. Zemenu et al. (2009) used a SEM to visualize the soil structure of an expansive soil at the maximum swelling by removing the soil, cutting samples, freezing the samples immediately in liquid nitrogen and then using sublimation. The scanning electron microscope micrographs are shown in Figure 3.10 at the natural soil state (a), and after 1 (b), 3 (c), and 5 (d) cycles of swelling.

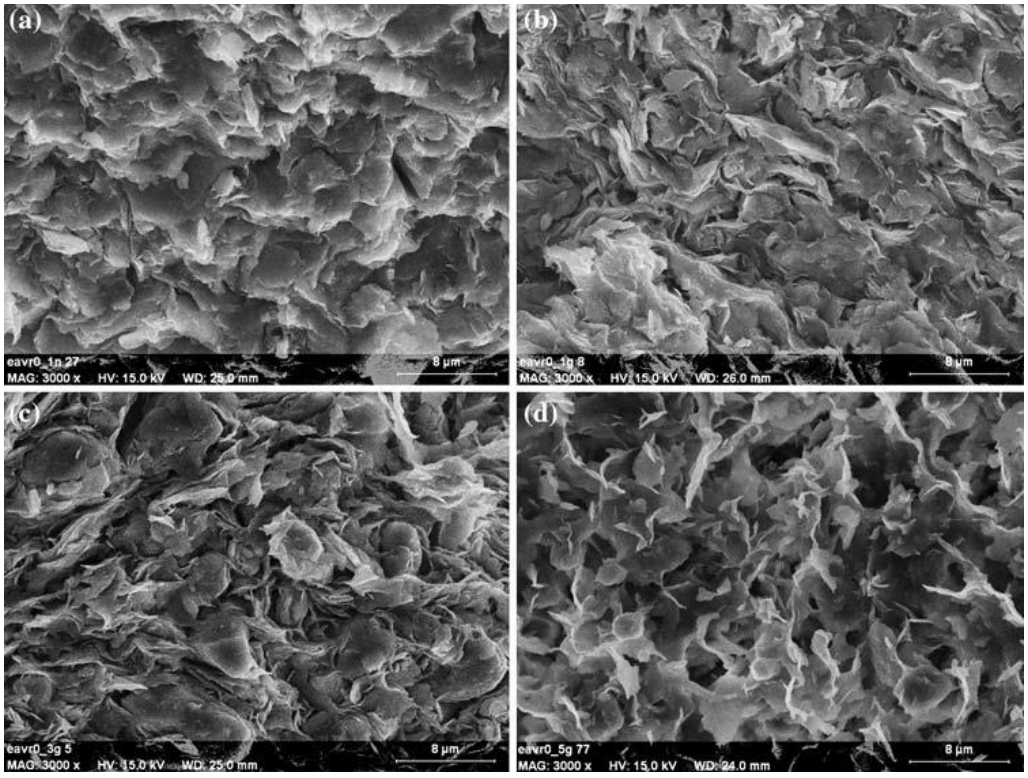

Figure 3.10: SEM micrographs of Argile verte de Romainville after 0 (a), 1(b), 3(c), and 5(D) cycles of swelling (Zemenu et al., 2009)

The micrographs indicate that the soil begins at a very layered structure with clay plates closely aligned. However, after undergoing wetting and drying cycles, the clay particles become more disrupted with a higher amount of voids between clay particles forming. Therefore, specimens with a more dispersed initial structure become more flocculated under cyclic wetting and drying. Lin and Cerato (2014) performed a study that additionally used an ESEM and cooling stage to evaluate the change in soil fabric with cyclic wetting and drying. Soil specimens underwent inundation in the ESEM, but there were issues with the relatively small amount of absorption/desportion of water in the soil specimens. Ito and Azam (2013) were able to identify fissures and the aggregation of clay

peds in in-situ and air-dried specimens. The authors additionally indicated that clay particles are randomly oriented in field deposits.

3.3 MATERIALS AND METHODOLOGY

For this research component, a centrifuge-based inundation swelling test, developed at the University of Texas at Austin and outlined in Zornberg et al. (2017), was used to evaluate the swelling characteristics of expansive soils. The experimental method involves a set-up similar to set-up from the odometer test outlined by ASTM D4546. Soil specimens were either compacted or trimmed into a cutting ring. The soil was confined by two brass porous disks. Filter paper was used as separation between the soil specimen and brass porous disks. The cutting ring was placed into an acrylic permeameter cup shown in Figure 3.11. The assembled permeameter cup with the cutting ring was then placed in a metal centrifuge bucket. The centrifuge buckets were put in a reconfigured general-purpose centrifuge with a wireless data acquisition system. The data acquisition system consists of linear position sensors to monitor changes in the soil specimen heights and an accelerometer to determine the gravitational level exerted on the soil specimen. Data was wirelessly transmitted to an external computer for real-time monitoring of testing results. The change in specimen height corresponds to the one-dimensional vertical strain of the expansive soil specimens based on Equation 2.4. An overview of the permeameter cup setup and of the centrifuge prior to testing is shown in Figure 3.11.

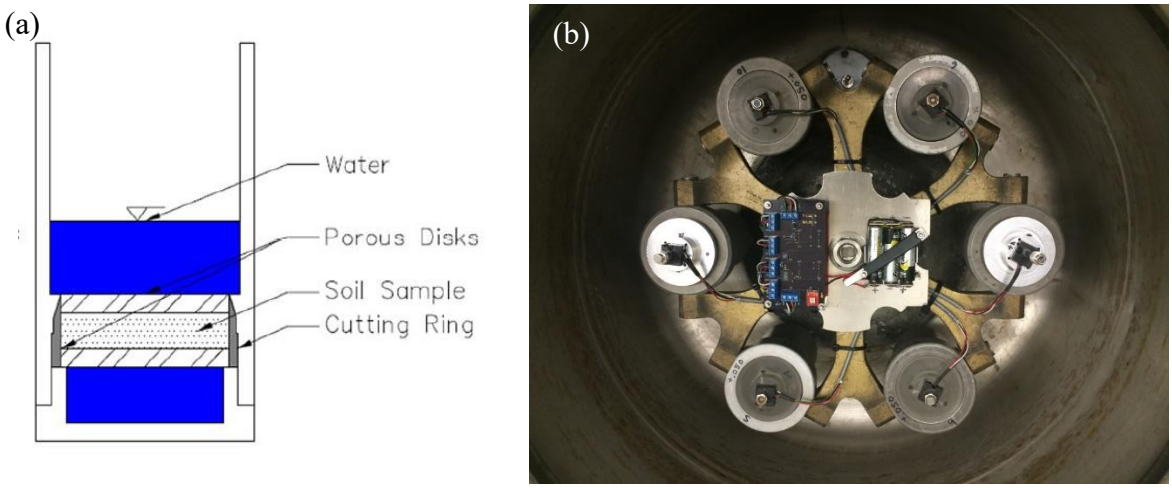

Figure 3.11: Side view of permeameter cup (a) and overview of centrifuge system (b) (Armstrong and Zornberg, 2017)

The increased gravitational environment from the centrifuge is used to reduce the time of testing due to the increased hydraulic head. Soil specimens undergo a compression cycle where the overburden stress is increased to testing conditions for approximately 1 to 2 hours. At the end of the compression cycle, the specimens are inundated with water and allowed to swell for approximately 48 to 72 hours. The specimens are then removed from the centrifuge and placed into an oven 110°C to determine the initial and final gravimetric moisture contents.

The initial gravimetric moisture content was controlled in order to evaluate the effect of the initial fabric. In order to reduce the initial gravimetric moisture content for specimens that were compacted wet of the optimum moisture content from Standard Proctor compaction curves, moisture adjusting was performed. This process involves the use of a glove box with a saturated salt solution and a scale. This set-up is referred to as the environmental chamber for drying and is shown in Figure 3.13. A saturated salt solution is used to control the rate of drying of the soil by increasing the relative humidity. A scale is used to monitor the mass of the soil specimens during drying. A

generic table salt is used for the solution as the table salt solution was able to keep the relative humidity relatively high (between a relative humidity of 80% and 95%). The relative humidity in the glove box is increased to reduce the rate of drying and prevent the formation of desiccation cracks. This reduction in the rate of drying is caused by the decrease in the total suction exerted by the environment on the soil specimen with increasing relative humidity. The theoretical relationship between the relative humidity and total suction is shown in Figure 3.12.

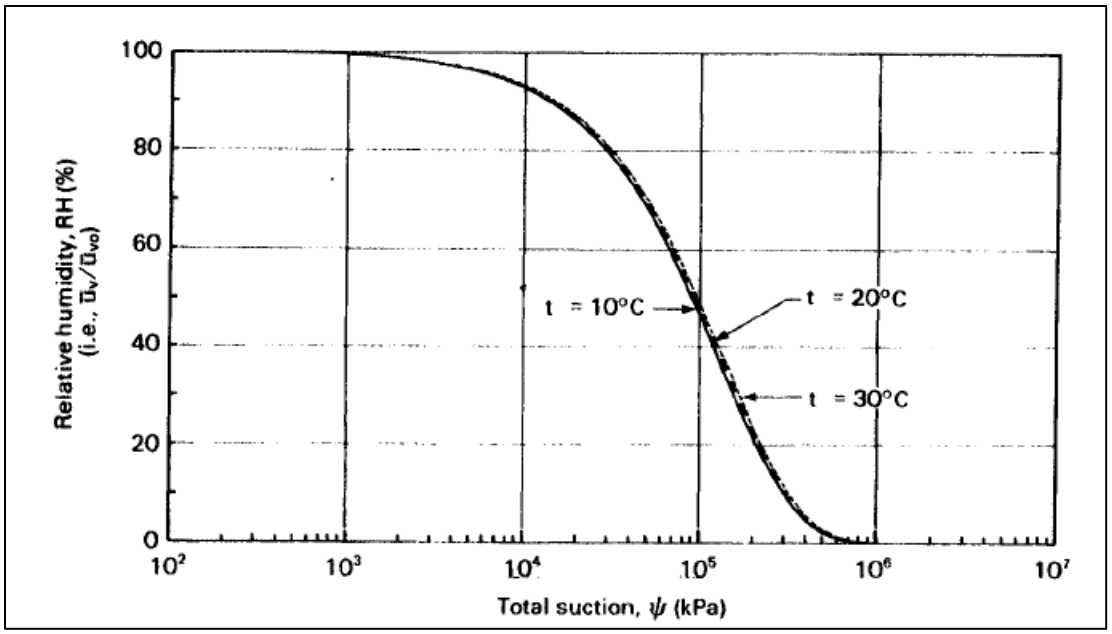

Figure 3.12: Relationship between relative humidity and total suction (Fredlund and Rahardjo, 1993)

The relative humidity in the laboratory typically varied between 30% and 50%. Based on Figure 3.12, the increase in the relative humidity to upwards of 80% led to a decrease in the total suction between one to two orders of magnitude. The reduction in the total suction decreases the drying rate by reducing the suction gradient in the soil specimen.

The initial mass and gravimetric moisture content of the soil specimens were measured prior to moisture adjusting, and a targeted mass was calculated based on a dry moisture condition. This dry condition is defined as 3 percentage points dry of the optimum gravimetric moisture content. For soils that did not have their optimum conditions defined from Standard Proctor compaction curves, a correlation from the Naval Facilities Engineering Command's Design Manual for Facilities (NAVFAC) (1962) was used to estimate the optimum compaction conditions. These correlations were previously found to reasonably estimate the optimum gravimetric moisture content of expansive soils sampled in Central Texas (Snyder, 2015). After reaching the mass corresponding to the dry condition, the soil specimens were wrapped in aluminum foil for 48 hours prior to testing in the centrifuge. This time period was used to allow moisture to come into an equilibrium across the soil specimen. A view of the environmental chamber used for moisture adjusting is shown in Figure 3.13.

Figure 3.13: Environmental chamber for moisture adjusting of specimens

For this study, four expansive soils were tested. The soils were grouped into either bulk sampled or undisturbed field-sampled soils. Two expansive soils were bulk sampled from exposed portions of the expansive soil deposit, and the other two soils were sampled using Shelby tube samplers to obtain undisturbed field specimens. The bulk sampled soils include the Behring clay (sampled from SH-21 near Paige, TX) and the Eagle Ford clay (sampled from I-35 and Hester's Crossing Boulevard in Round Rock, TX). These soils were selected for testing as they have been extensively studied in Wright et al. (2007), Armstrong (2014), and as part of the study reported in Chapter 2 of this dissertation. The undisturbed field-sampled soils include the Branyon clay (sampled from FM 487 near Weir, TX) and the Houston Black clay and underlaying parent material (sampled from IH-10 near San Antonio, TX).

The Eagle Ford, Behring, and Branyon clays were tested for the soil Atterberg limits according to ASTM D4318. The three clays were classified as highly plastic clays (CH) according to the United Soil Classification System (USCS) from ASTM D2487. The Eagle Ford and the Behring clays were additionally tested for soil specific gravity (G_s) according to ASTM D854, their maximum dry unit weight ($\gamma_{d,max}$) and optimum moisture content (ω_{opt}) from Standard Proctor compaction curves (ASTM D698), fines content from wet sieving of the crushed soil (ASTM D422), and clay content from hydrometer analysis of soil that passed through the No. 200 sieve (ASTM D422). A summary of the soil properties is shown in Table 3.1 for the Eagle Ford, Behring, and Branyon clays. Note that the soil properties for the soils sampled from IH-10 are presented in Section 3.4.3 as multiple locations and depths were tested for their characterization properties.

Table 3.1: Summary of characterization properties for Eagle Ford, Behring, and Branyon clays

Soil	Liquid Limit	Plasticity Index	Soil Classification (USCS)	Specific Gravity	ω_{opt} (%)	γ_{dmax} (kN/m^3)	Fines Content (%)	Clay Content (%)
Eagle Ford clay	88	49	CH	2.74	24.3	15.25	97	76
Behring clay	58	41	CH	2.78	20	15.42	82	40
Branyon clay	74	46	CH	-	-	-	-	-

Soil specimens that were laboratory-reconstituted differed in their preparation. The bulk-sampled soils (Eagle Ford and Behring clays) were air-dried at 23°C, passed through a rock crusher, and sieved through the No. 10 sieve to remove granular particles from the processed soil. The processed soils were then rehydrated prior to testing. For the Branyon clay, excess portions of the soil from the trimming of the Shelby tube samples were air-dried at 23°C and underwent a similar method to process and rehydrate the soil.

Laboratory-reconstituted specimens for the soils sampled from IH-10 were divided into either an "air-dried" or "oven-dried" condition. For the tests conducted on the soils sampled from IH-10, each boring was divided into 2 ft sections based on the recommendations from Texas Department of Transportation's potential vertical rise method, Tex-124-E. For "air-dried" condition, soil specimens from each 2 ft section were trimmed, air-dried at approximately 23°C, passed through a rock crusher, and re-hydrated. For the "oven-dried condition," a combination of soil trimmings of the 2 ft section and the remains of the field-sampled soil specimens was used. This combination of soils was oven-dried at 110°C, passed through a rock-crusher, and re-hydrated. The "air-dried" and "oven-dried" conditions were selected in order to evaluate the effect of the drying temperature on the swelling characteristics of expansive soils.

The initial soil fabric was determined by the initial moisture content and mass of soil at the time of compaction for the reconstituted specimens and the sampling method

for the Shelby tube samples. Based on Diamond (1971), soils compacted wet of optimum were expected to have a comparatively more dispersed clay structure and soils compacted dry of optimum were expected to have a comparatively more flocculated clay structure. Note that optimum refers to the optimum compaction conditions from Standard Proctor compaction energy. To create a dispersed structure, the Eagle Ford clay was compacted at 3 percentage points wet of the optimum moisture content at the maximum dry unit weight, and the Behring clay was compacted at 5 percentage points wet of the optimum moisture content at the maximum dry unit weight. Soil specimens were then moisture-adjusted to a dry condition to maintain the initial soil fabric but change the initial moisture content and dry unit weight. The clay structure of the field specimens is expected to be neither flocculated or dispersed due to cyclic wetting and drying from seasonal moisture fluctuations.

Non-moisture adjusted soils were compacted at the gravimetric moisture content and dry unit weight of the moisture adjusted soil. Note that the dry unit weight that was targeted corresponds to the dry unit weight of the moisture adjusted specimens prior to the compression phase in the centrifuge. Since these conditions were dry of the optimum moisture adjusted for the laboratory reconstituted specimens, the internal clay structure was assumed to be more flocculated.

A summary of the soil conditions for this research component is presented in Table 3.2. The testing program is grouped into the three soil specimen types that were tested in three testing series. Note that the ω_i and $\gamma_{d,i}$ refer to the moisture content and dry unit weight at the time of testing, while the ω_c and $\gamma_{d,c}$ refer to moisture content and dry unit weight at the time of compaction, and that the ω_f and $\gamma_{d,f}$ refer to moisture content and dry unit weight at the time of sampling in the field.

Table 3.2: Summary of soil conditions for fabric analysis

Soil Specimen	Testing Series	Soils Used	Compaction	Moisture Adjusted?	Testing ω	Testing γ_d
Laboratory-Reconstituted	I, II, III	All	Kneading	N	$\omega_i = \omega_c$	$\gamma_{d,i} = \gamma_{d,c}$
Laboratory-Reconstituted Moisture-Adjusted	I	Eagle Ford, Behring	Kneading	Y	$\omega_i < \omega_c$	$\gamma_{d,i} > \gamma_{d,c}$
Field-Sampled Moisture-Adjusted	II, III	Branyon, IH-10	Field	Y	$\omega_i < \omega_f$	$\gamma_{d,i} > \gamma_{d,f}$

3.4 Results from Centrifuge Testing and their Analysis

The testing program was grouped into three series. A summary of the testing series is presented in Table 3.3. Series I involved testing laboratory-reconstituted specimens of the Eagle Ford clay and the Behring clay at both moisture-adjusted and non-moisture-adjusted conditions. Series III involved the testing of both field-sampled and laboratory-reconstituted specimens of the Branyon clay from FM 487. Series III involved the testing of both field-sampled and laboratory-reconstituted specimens of the soils sampled from IH-10. The laboratory-reconstituted specimens from IH-10 were tested at an "air-dried" and "oven-dried" condition as outlined in Section 3.3.

Table 3.3: Summary of testing series for fabric analysis

Testing Series	Specimens Used	Soils Used
I	Laboratory-Reconstituted	Eagle Ford, Behring
	Laboratory-Reconstituted, Moisture-Adjusted	
II	Laboratory-Reconstituted	Branyon
	Field-Sampled, Moisture-Adjusted	
III	Laboratory-Reconstituted	IH-10
	Field-Sampled, Moisture-Adjusted	

Results for these tests are shown as swelling curves in the void ratio versus time space. Additionally, testing data is shown in a table containing experimental data at three conditions:

(1) initial conditions, including the gravimetric moisture content (ω_i), the dry unit weight ($\gamma_{d,c}$), void ratio (e_i), and volumetric moisture content at the end of the compression phase (θ_i);

(2) experimental results at the end of primary swelling, including the void ratio at the end of primary swelling (e_p) and the time to the end of primary swelling ($T_{E.O.P.}$)

(3) experimental results at the end of testing, including the void ratio at the end of testing (e_f), the final volumetric moisture content (θ_f), and the testing stress (σ')

Primary swelling was defined according to ASTM D4546 as the swelling at the intersection of lines tangents to the primary and secondary portion of the swelling curve. Strain was not used in this analysis as the initial void ratio differed slightly among tests.

3.4.1 Testing of Laboratory-Reconstituted Specimens (Series I)

The first testing series evaluated the effect of soil fabric on laboratory-reconstituted specimens. The soils used in this testing series were the Eagle Ford and the Behring clays. The characterization of these soils was presented in Section 3.3. Both soils were sampled in bulk from exposed portions of the expansive soil deposits. The sampled soils were processed and prepared to remove the field soil fabric. For this testing series, specimens that were moisture-adjusted were expected to have a dispersed fabric, and specimens that were non-moisture-adjusted were expected to have a flocculated fabric.

For testing on laboratory-reconstituted specimens of Behring clay, soil specimens were compacted at a 1 cm.-height prior to moisture adjusting of the soils. The dispersed soil specimens were initially compacted using kneading compaction at 5 percentage points wet of the optimum moisture content and at the maximum dry density shown in Table 3.1 prior to moisture conditioning. The results from a pair of tests is shown in Figure 3.14, with the testing conditions listed in Table 3.4.

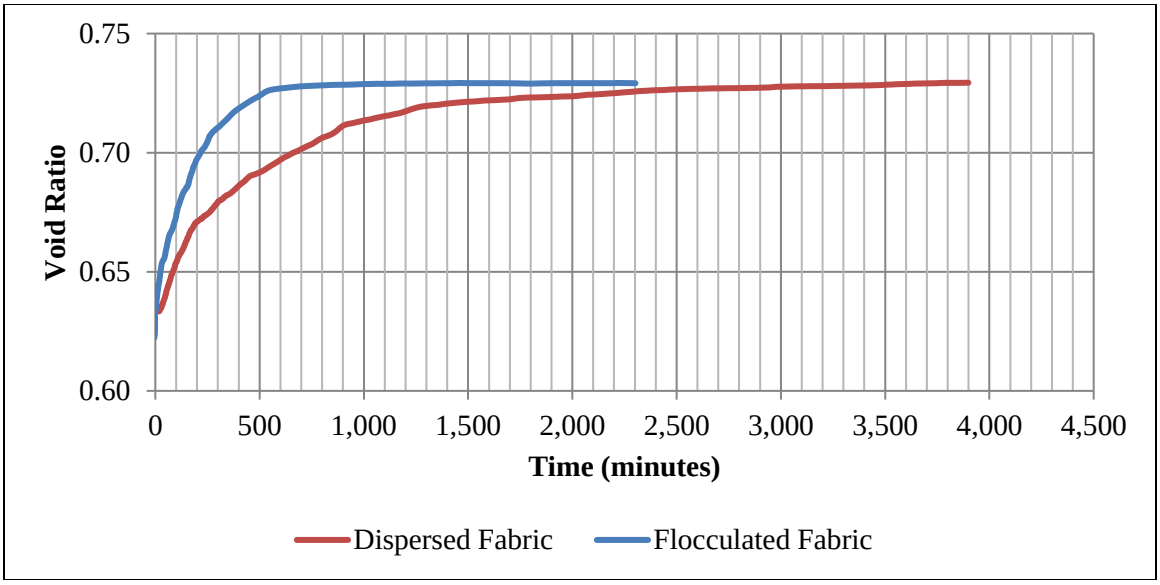

Figure 3.14: Swelling curves for tests on laboratory-reconstituted Behring clay specimens

Table 3.4: Experimental data tests on laboratory-reconstituted Behring clay specimens

Soil Fabric	ω_i (%)	$\gamma_{d,c}$ (kN/m^3)	e_i	e_p	e_f	θ_i	θ_f	σ' (kPa)	$T_{E.O.P.}$ (min)
Flocculated	17.8	16.8	0.622	0.727	0.729	0.3	0.422	11.3	604
Dispersed	17.5	16.8	0.627	0.72	0.73	0.307	0.422	11.7	1331

Test results indicated that void ratios at the end of testing were similar between specimens with different soil fabrics. The void ratio at the end of primary swelling was slightly higher for the flocculated specimen compared to the dispersed specimen. The void ratio at the end of primary swelling can be used to calculate the magnitude of primary swelling (Equation 2.5). Typically, a higher void ratio at the end of primary swelling indicates that the specimen had higher vertical strains at the end of primary swelling. Additionally, the duration of primary swelling differed among the specimens. The time to the end of primary swelling was approximately twice as long for the dispersed specimen compared to the flocculated specimen. Therefore, the soil fabric affected the duration and magnitude of primary swelling for laboratory-reconstituted specimens of the Behring clay.

The increased amount of time to reach the end of primary swelling can be attributed to the lower hydraulic conductivity of the dispersed soil specimen. Previous studies have found that saturated hydraulic conductivity is lower for soils with a more dispersed structure than for soils with a more flocculated structure for a given soil density (Mitchell et al., 1966). The higher amount of macro-voids in more flocculated soil fabric allow for moisture to more rapidly permeameter the soil specimen than in the more dispersed soils.

The difference in the hydraulic conductivity of the specimens can be assumed to affect the magnitude of secondary swelling. In more flocculated specimens, the increased volume of macro-voids is expected to lead to an increase the hydraulic conductivity of the specimen. Due to the higher hydraulic conductivity, a comparatively high number of voids are wetted during this primary swelling portion of the test. This hypothesis is consistent with test results as the flocculated specimen has a slightly higher amount of primary swelling than the dispersed specimen.

For testing of the reconstituted Eagle Ford clay, soil specimens were compacted at a 1 cm.-height prior to moisture adjusting of the soils. The dispersed soil specimens were initially compacted using kneading compaction at 3 percentage points wet of the optimum moisture content and at the maximum dry density from Table 3.1 prior to moisture conditioning. The results from a pair of tests are shown in Figure 3.15, with the testing conditions listed in Table 3.5.

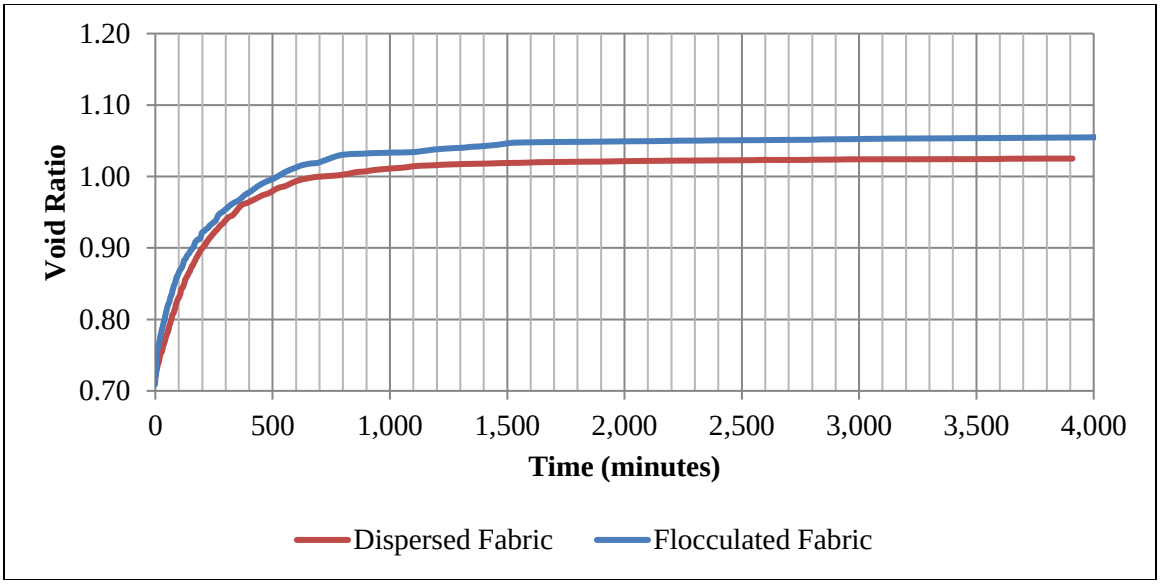

Figure 3.15: Swelling curves for tests on laboratory-reconstituted Eagle Ford clay specimens

Table 3.5: Experimental data for tests on laboratory-reconstituted Eagle Ford clay specimens

Soil Fabric	ω_i (%)	$\gamma_{d,c}$ (kN/m^3)	e_i	e_p	e_f	θ_i	θ_f	σ' (kPa)	$T_{E.O.P.}$ (min)
Flocculated	19.7	15.7	0.711	1.028	1.063	0.317	0.515	11.0	764
Dispersed	19.4	15.7	0.709	1.011	1.025	0.312	0.506	12.8	1009

The trends from the test results were similar to those from Behring clay. Both the dispersed and flocculated specimens reached similar void ratios at the end of testing. There was a small difference in these void ratios caused by a difference in the artificial gravitational level and overburden stress between the two specimens. Additionally, the time to the end of primary swelling was higher for the dispersed specimen compared to the flocculated specimen. However, this effect on the duration of primary swelling was not as significant for the Eagle Ford clay as for the Behring clay. The differences in the behavior of the two soils on the time to the end of primary swelling was attributed to the difference in the compaction moisture content for the dispersed specimens: 3 percentage points for the Eagle Ford clay as opposed to 5 percentage points for the Branyon clay. Furthermore, the higher amount of fines and clay content for the Eagle Ford clay compared to the Behring clay was expected to affect the time to the end of primary swelling. A higher fines content and clay content was expected to decrease in the volume of macro-voids in the soil specimen.

In order to assess the validity of the trends from Figure 3.14 and Figure 3.15, an additional set of testing results from a dispersed specimen and a flocculated specimen was compared. The evaluated soil specimens were both from the Eagle Ford clay, with the compaction conditions of the dispersed specimen similar to that from Table 3.5. Note that the results from the flocculated specimen were taken from a database of tests not directly tested for this evaluation. This comparison had initial soil conditions that were differed among the compared soil specimens (i.e. gravimetric moisture contents of the specimens differing by more than a percentage point). The results from a pair of tests are shown in Figure 3.16, with the testing conditions listed in Table 3.6.

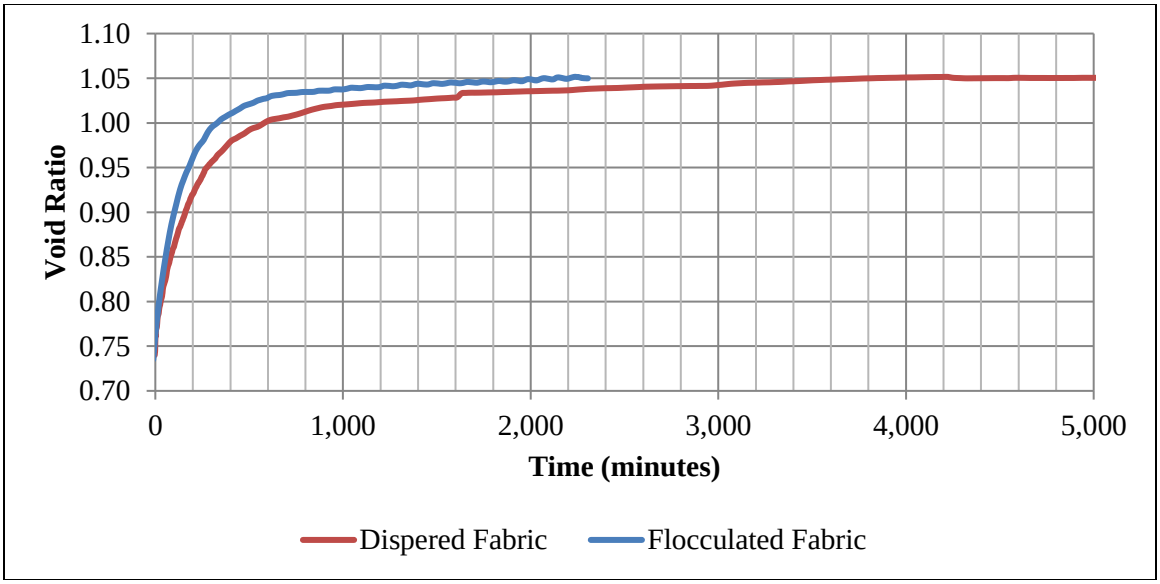

Figure 3.16: Swelling curves for additional fabric tests on laboratory-reconstituted Eagle Ford clay specimens

Table 3.6: Experimental data for additional tests on laboratory-reconstituted Eagle Ford clay specimens

Fabric	ω_i (%)	$\gamma_{d,c}$ (kN/m^3)	e_i	e_p	e_f	θ_i	θ_f	σ' (kPa)	$T_{E.O.P.}$ (min)
Flocculated	20.4	15.5	0.736	1.026	1.055	0.323	0.513	11.8	524
Dispersed	19.1	15.4	0.742	1.021	1.051	0.301	0.513	11.8	1007

While there were differences in the initial gravimetric moisture contents, the trends were similar to that from the previous tests conducted on the Behring and Eagle Ford clays. The time to the end of primary swelling was higher for the flocculated specimen. The void ratio at the end of primary swelling was slightly higher for the flocculated specimen. However, the end of testing void ratio was similar for both specimens. Based on these results, test results from the Eagle Ford clay indicated that the fabric affected the duration of primary swelling, slightly affected on the void ratio at the end of primary swelling, and negligibly affected on the void ratio at the end of testing.

Results from this testing series indicated that the soil fabric affected the duration of primary swelling. Specimens with a flocculated soil fabric reached the end of primary swelling in a shorter time frame than specimens with a dispersed soil fabric. Additionally, the soil fabric slightly affected the void ratio at the end of primary swelling. Specimens with a flocculated soil fabric had a slightly higher void ratio at the end of primary swelling than specimens with a dispersed soil fabric. Both of these trends were attributed to an increase in the hydraulic conductivity for specimens with a flocculated soil structure. However, the void ratio at the end of testing was similar between both soil fabrics. These trends were consistent between the two soils.

3.4.2 Testing of Specimens from FM 487 (Series II)

To validate the trends from the laboratory-reconstituted testing series, a testing series was conducted on soils sampled using Shelby tubes from an expansive soil deposit, the Branyon clay. Soil was sampled at various locations along the roadway to a depth of 5 ft. All of the sampling locations were located within a 400 ft.-section of the roadway that were determined to be in the same surficial soil deposit according to USDA soil surveys. The undisturbed samples were extruded in the field immediately after sampling and wrapped in aluminum foil to prevent moisture loss. The sampling of the undisturbed soil specimens and stratigraphy of the site from a nearby excavation pit are shown in Figure 3.17. The depth to the unweathered tan clay was approximately 5 to 6 ft in the excavation pit. Bulk samples of the Branyon clay from the excavation pit were additionally sampled and tested to determine their Atterberg limits and Standard Proctor compaction curves. The optimum condition according to Standard Proctor compaction energy of the Shelby tube sampled soils were estimated using the following NAVFAC (1962) correlations:

$$\omega_{OPT} = 6.77 + 0.43 * LL - 21 * PI \quad (3.1)$$

$$\gamma_{d,\max} = 20.48 - 0.13 * LL + 0.05*\text{PI} \quad (3.2)$$

Where ω_{OPT} is the optimum gravimetric moisture content in %, LL is the Liquid Limit, PI is the Plasticity Index, and $\gamma_{d,max}$ is the maximum dry unit weight in kN/m^3. Based on the Atterberg limits of the sampled soil and Equations 3.1 and 3.2, the optimum moisture content was estimated to be 28.9% and the maximum dry unit weight was estimated to be 13.11 kN/m^3. However, the field soil specimens were moisture conditioned to a gravimetric moisture content of 22% to match the optimum moisture content of the bulk samples taken from the borrow pit.

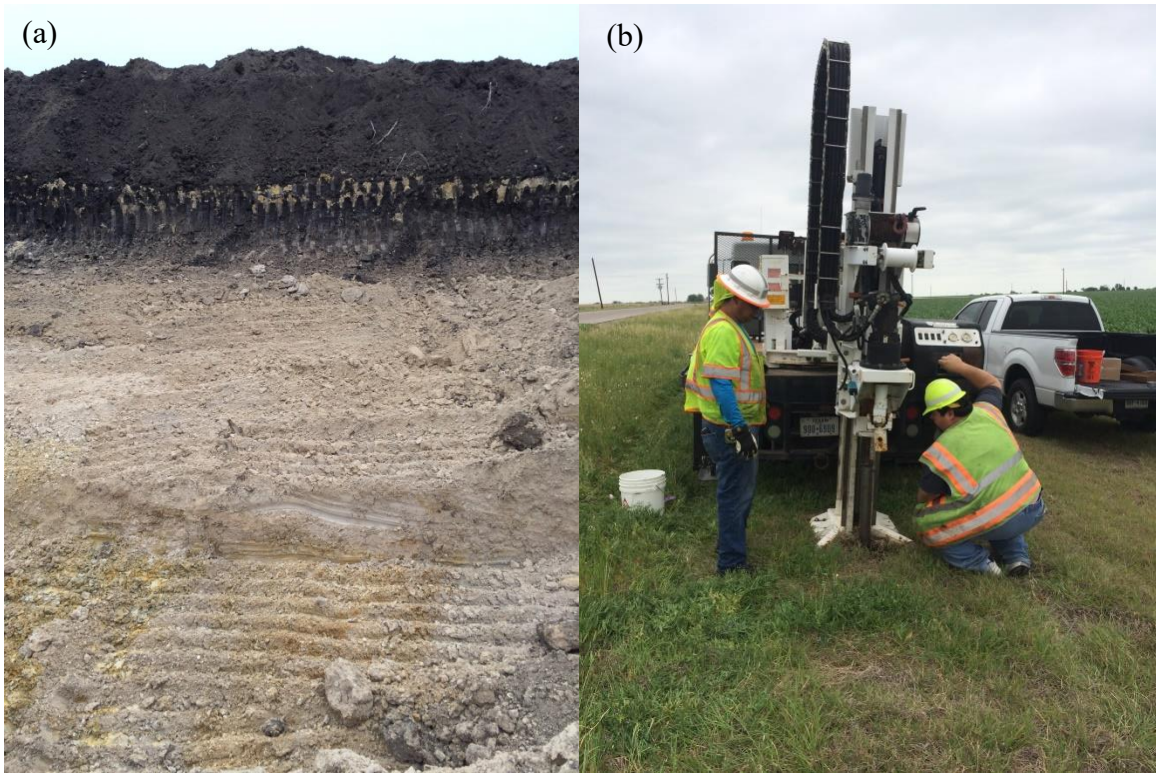

Figure 3.17*:* Soil stratigraphy of expansive soil deposit at the excavation pit (a) and undisturbed sampling of Branyon clay (b)

Soils specimens from a depth of approximately 4 ft beneath the top of the ground surface were tested for this soil series to reduce the effect of vegetation and stratigraphy of the soil horizons. Soil specimens were trimmed to a height of 2.5 cm. prior to moisture conditioning as outlined in Section 3.3. After moisture conditioning, the soils were trimmed into the cutting rings to a height of 2 cm and tested using the centrifuge-based inundation test. The excess soil from trimmings of the various borings were combined, air-dried at approximately 23°C, passed through a rock crusher, and rehydrated to create reconstituted specimens to compare against field-sampled, moisture-adjusted specimens. The laboratory-reconstituted, non-moisture-adjusted specimens were compacted to a height of 2 cm. in 1 cm. lifts. For this testing series, specimens that were moisture-adjusted were expected to have a field fabric, and specimens that were non-moisture-adjusted were expected to have a flocculated fabric.

In total, two pair of tests that compared specimens with field fabric and flocculated fabric were conducted. The results from the first pair of tests are shown in Figure 3.18, with the testing conditions listed in Table 3.7.

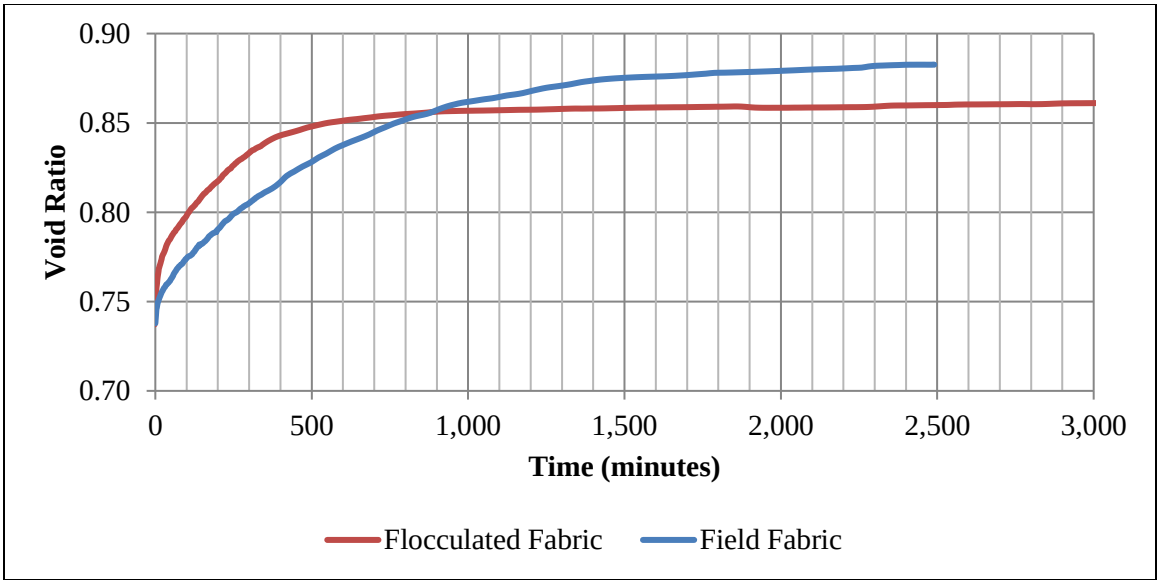

Figure 3.18*:* Swelling curves for first set of tests on the Shelby-tube sampled Branyon clay

Table 3.7*:* Experimental data for first set of tests on the Shelby-tube sampled Branyon clay

Fabric	**ω_i (%)**	**$\gamma_{d,c}$ (kN/m^3)**	**e_i**	**e_p**	**e_f**	**θ_i**	**θ_f**	**σ' (kPa)**	**$T_{E.O.P.}$ (min)**
Flocculated	21.3	15.3	0.737	0.85	0.862	0.333	0.463	14.8	553
Field	21.9	15.2	0.743	0.876	0.88	0.341	0.468	12.1	1302

The trends from the tests differed from the results from the laboratory-reconstituted testing series. The change in void ratio during testing differed significantly between the flocculated and field specimens. The difference in the void ratio at the end of primary swelling indicated that the vertical strains were higher for the field specimen. The difference in the overall magnitude of swelling was attributed to differences in the fabric of the specimens. Additionally, the laboratory-reconstituted specimen used soil that had been homogenized and processed from various horizons in the deposit. This preparation process may have removed variability between soil horizons in the soil deposit.

Additional evaluations that eliminated this potential homogenization of an expansive soil deposit and analyzed the effect of spatial heterogeneity of the expansive soil are later presented in the third testing series in Section 3.4.3 and in Chapter 4 of this dissertation. However, the effect on the time to the end of primary swelling was similar to that from the laboratory-reconstituted testing series. The time to the end of primary swelling was higher for the field specimen.

In order to assess the validity of the trends from the first pair of tests, the results from the second pair of tests are shown in Figure 3.19, with the testing conditions listed in Table 3.8.

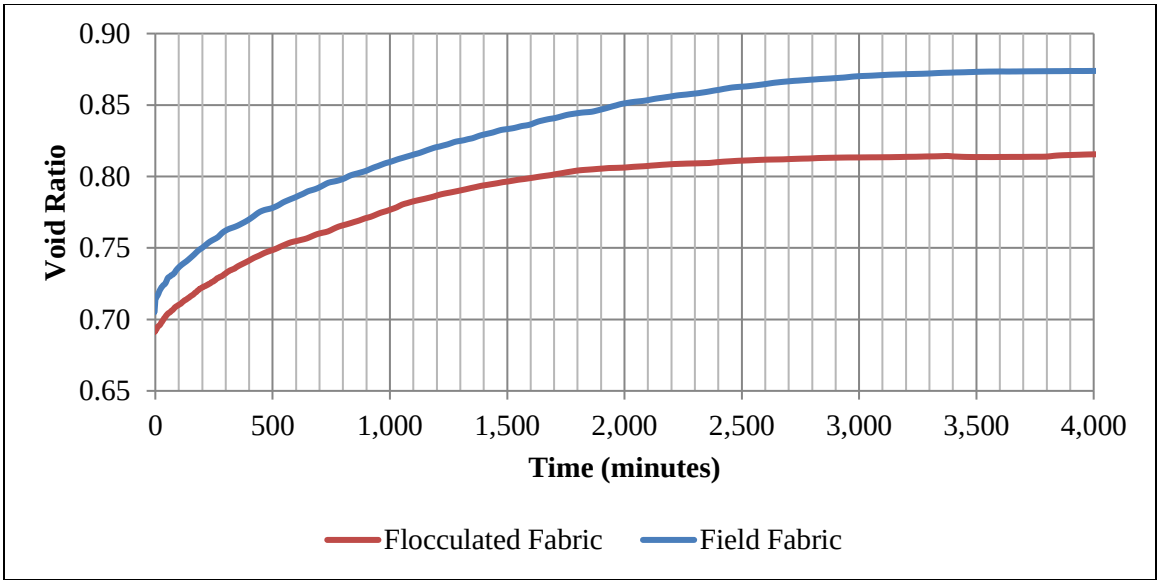

Figure 3.19: Swelling curves for second set of tests on the Shelby-tube sampled Branyon clay

Table 3.8*:* Experimental data for second set of tests on the Shelby-tube sampled Branyon clay

Fabric	**ω_i (%)**	**$\gamma_{d,c}$ (kN/m^3)**	**e_i**	**e_p**	**e_f**	**θ_i**	**θ_f**	**σ' (kPa)**	**$T_{E.O.P.}$ (min)**
Flocculated	21.4	15.7	0.692	0.81	0.816	0.342	0.449	13.3	1207
Field	22.4	15.5	0.709	0.873	0.879	0.355	0.468	13.4	2849

Note that there was some variability in the initial conditions, with the flocculated specimen having a lower initial gravimetric moisture content and higher dry unit weight than the field specimen. Based on the results from Chapter 2 of this dissertation, the decrease in the gravimetric moisture content and increase in the dry unit weight would result in an increase in the magnitude of primary swelling for the flocculated specimen. However, the void ratio at the end of primary swelling, and corresponding vertical strains at the end of primary swelling, was higher for the field specimen. This difference in the void ratio at the end of primary swelling was again attributed to difference in the fabric of the specimens. Additionally, the time to the end of primary swelling was higher for the field specimen.

Results from Series II, conducted on field-sampled and laboratory-reconstituted specimens of the Branyon clay, indicated that the soil fabric of field specimens may significantly affect both the void ratio at the end of primary swelling and the time to the end of primary swelling. The field specimens had a void ratio at the end of primary swelling with a longer time to the end of primary swelling than the flocculated specimens. However, these differences may be attributed to the homogenization of the laboratory-reconstituted specimens. Therefore, a more extensive evaluation to determine the effect of the field soil fabric is needed.

3.4.3 Testing of Specimens from IH-10 (Series III)

To verify the trends from Series II, additional soil specimens that were sampled using a Shelby tube sampler were evaluated. The objectives for this testing series were to verify the trends with a comparatively larger set of data and to remove issues with the homogenization of the soil for the laboratory-reconstituted specimens. The location sampled was a part of a geotechnical investigation along IH-10, east of San Antonio, shown in Figure 3.20.

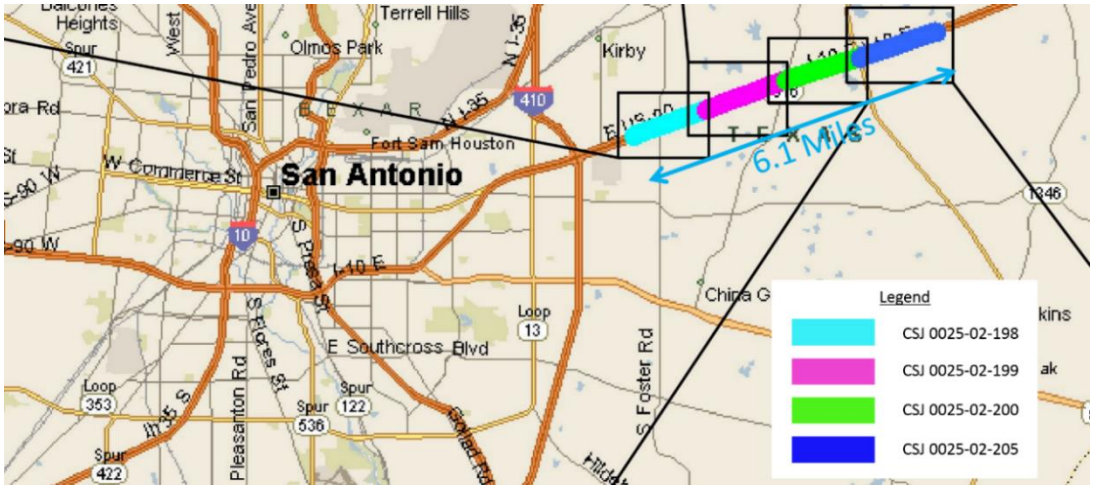

Figure 3.20: Location of IH-10 sampling project

The University of Texas was provided soil samples to determine the potential vertical rise of the subgrade along the proposed expansion. Centrifuge-based inundations tests were conducted on 46 borings along the proposed roadway alignment, each sampled to a depth of 8 ft. Each boring was subdivided into 2 ft sections per the Texas Department of Transportation's guidelines from their potential vertical rise method, Tex-124-E. Each section of the boring was tested at two different vertical stresses to generate a stress-swell curve. In total, four stress-swell curves were generated per boring to calculate the

potential vertical rise of the boring. The overall testing program is further detailed in Chapter 4.

For this testing series, five of the borings were selected for the analysis of the effect of soil fabric. The locations of these borings are shown in Figure 3.21.

Figure 3.21: Location of IH-10 borings used for soil fabric analysis (Google Earth, 2017)

Borings B-31 and B-32 were extensively evaluated for this testing series, with all 4 sections at two different stresses evaluated. Borings B-35, B-36, and B-38 were tested only at the surficial section, between 0 and 2 ft, and at the lowest stress. These conditions were selected based on the results from Borings B-31 and B-32 and with the assumption that the soil fabric is most significant closest to the ground surface due to more extensive wetting and drying cycles.

Laboratory-reconstituted specimens were grouped into air-dried and oven-dried specimens, as outlined in Section 3.3. The oven-dried reconstituted specimens were used to eliminate differences in clay mineralogy or distribution in the boring by testing the exact same soil during testing. There may be some spatial heterogeneity along the borings due to an ancient creek bed near boring B-35. Due to issues with the oven-drying of soil potentially removing attached water from clay minerals, air-dried reconstituted specimens were additionally tested. Descriptions of the soil from the boring logs, preliminary testing data, including the Atterberg limits and in-situ moisture content (ω_i), and the targeted gravimetric moisture content (ω_t), three percentage points dry of optimum moisture content based on the NAVFAC (1978) correlations, are shown in Table 3.9 for each of tested sections.

Table 3.9*:* Summary of preliminary investigation for IH-10 soils used in soil fabric analysis

Boring	Depth	Logger's Description	Liquid Limit (%)	Plasticity Index (%)	ω_i (%)	ω_t (%)
B-31	0-2	Brown CH with gravel at 8"	100	70	41.0%	32.0%
	2-4	Brown CH with some gypsum	111	74	58.4%	36.1%
	4-6	Brown-Dark Brown CH	65	44	25.5%	22.6%
	6-8	Brown-Dark Brown CH with gravel	112	78	47.5%	35.4%
B-32	0-2	Dark Brown CH	115	89	45.6%	34.4%
	2-4	Brown CH	42	26	36.8%	16.4%
	4-6	Brown CH with calcite	90	64	35.4%	29.1%
	6-8	Brown CH with calcite	69	49	39.7%	23.0%
B-35	0-2	Dark Brown CH	75	54	35.8%	24.5%
B-36	0-2	Dark brown CH	73	48	34.3%	25.2%
B-38	0-2	Dark brown CH	45	30	34.0%	17.1%

Soil survey mapping from the USDA indicated that borings B-31 and B-32 were sampled from the Houston Black clay and borings B-35, B-36, and B-38 were sampled from the Heiden clay. Based on the soil characteristics, the soils from borings B-35, B-36, and B-

38 had a Liquid Limit and Plasticity Index lower than the soils from borings B-31 and B-32. The differences in the Atterberg limits was attributed to differences between the Houston Black and Heiden clays and the proximity to the ancient creek bed.

Due to the compression phase during the centrifuge-based inundation test, the dry unit weight of the laboratory-reconstituted and in-situ soil specimens varied for Series III. Note that in Series III, the field-sampled specimens are referred to as "in-situ" specimens. The laboratory-reconstituted specimens were more dense than the in-situ specimens at the end of compression phase during testing. This difference exceeded 0.50 kN/m^3 for several specimens. Due to the increased dry unit weight, a correction of the swelling curves based on the initial dry unit weight was needed. Based on the results from Section 2.3.3, there is a linear decrease in the void ratio at the end of primary swelling with increasing initial dry unit weight. For the three soils tested, the linear relationship was approximately an 0.1 decrease in the void ratio with a corresponding 1 kN/m^3 increase in the initial dry unit weight. Using this relationship, the correction of the swelling curves in void ratio between the laboratory-reconstituted specimen and the in-situ specimen was calculated as follows:

$$\Delta e_{ps} = 0.1 * \left(\gamma_{d,is} - \gamma_{d,r}\right) \tag{3.3}$$

Where Δe_{ps} is the correction to the void ratio at the end of primary swelling, $\gamma_{d,is}$ is the dry unit weight of the in-situ specimen in kN/m^3, and $\gamma_{d,r}$ is the dry unit weight of the laboratory-reconstituted specimen in kN/m^3. Note that the constant, 0.1, has units of m^3/kN.

The change in the void ratio, calculated by Equation 3.2, could not directly be added to the void ratios along the swelling curve. The correction of the swelling curves required that the initial void ratio was additionally corrected as the initial void ratio is

dependent upon the initial dry unit weight, as shown by Equation 2.6. To account for both the change in the void ratio at the end of primary swelling and the initial void ratio, a scalar correction for the swelling curves, S, was applied as follows:

$$S = \frac{e_{ps,r} + \Delta e_{ps}}{e_{ps,r}} \tag{3.2}$$

Where $e_{ps,r}$ is the void ratio at the end of primary swelling for the laboratory-reconstituted specimens, and Δe_{ps} is the correction to the void ratio at the end of primary swelling calculated by Equation 3.1. The void ratios from the swelling curves were multiplied by this scalar factor in order to correct the data from testing. A comparison between the uncorrected and corrected swelling curves is shown in Figure 3.22.

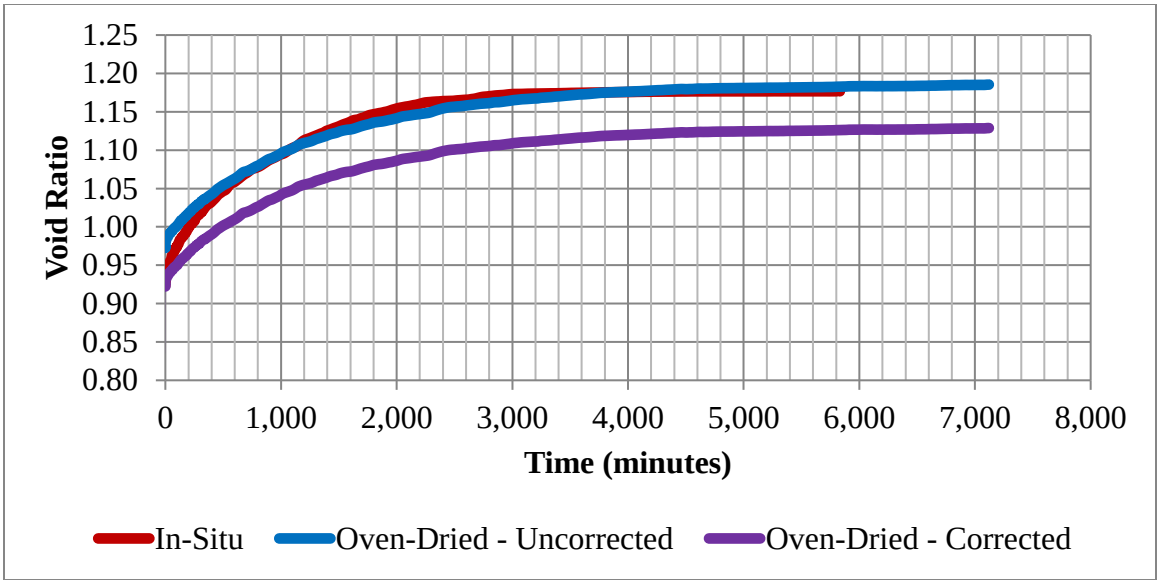

Figure 3.22: Example of scalar correction of data for the IH-10 soils

Based on the results from the figure, the scalar correction was able to both adjust the magnitude of the change in the void ratio at the end of primary swelling and shift the initial void ratio to the initial void ratio of the in-situ specimen.

Results from the IH-10 testing series are shown in the order that the specimens were tested. This chronological order was used to emphasize the refinement of the targeted dry unit weight for compaction. The compaction dry unit weight for the laboratory-reconstituted specimens originally targeted the dry unit weight at the end of the compression phase of the in-situ specimens. However, the laboratory-reconstituted specimens tended to compress beyond the initial dry unit weight of the in-situ specimens during the compression phase of testing. Due to this issue, the target dry unit weight for the laboratory-reconstituted specimens was changed to the dry unit weight prior to centrifugation of the in-situ specimens.

Specimens for this testing series were grouped into three conditions. The in-situ condition represented field-sampled specimens that were trimmed from the borings and moisture-adjusted prior to testing. The laboratory-reconstituted specimens were grouped into an air-dried and oven-dried condition. These conditions depended on the dry temperature of the soils prior to the soil preparation, as outlined in Section 3.3. The laboratory-reconstituted specimens were compacted at similar initial heights as the field specimens in order to minimize the effect of the sample height on the duration of primary swelling shown in Section 2.3.6.

Swelling curves are presented with the corrected curves in the void ratio versus time space. Testing conditions and test results are presented in an accompanying table and include the following:

- the initial (ω_i) and final (ω_f) gravimetric moisture contents
- the initial (θ_i) and final (θ_f) volumetric moisture contents
- the dry unit weight at the end of the compression phase ($\gamma_{d,i}$) in kN/m^3
- the total unit weight at the end of the test (γ_f) in kN/m^3
- the initial degree of saturation (Initial Sat.)

- the void ratio initially (e_i), at the end of primary swelling (e_{ps}), and at the end of testing (e_f)
- the change in the void ratio from the initial condition and at end of primary swelling (Δe)
- the vertical strain with at the end of primary swelling ($\varepsilon_{primary}$) and at the end of the testing (ε_{final})
- the time to the end of primary swelling (Time to ε_p) in minutes
- the vertical effective stress at the end of testing (σ') in psf

Note that the test results were calculated using both the corrected and uncorrected swelling curves. The vertical strains were assumed to be positive for swelling and negative for compression. The void ratios were calculated using Equation 2.5 and 2.6. The degree of saturation was calculated using Equation 2.7. Both of the void ratios and the degree of saturation were calculated assuming that the specific gravity of the soils was 2.70. The volumetric moisture contents were calculated as follows:

$$\theta = \frac{e}{1+e} * S \tag{3.3}$$

Where θ is the volumetric moisture content, e is the void ratio, and S is the degree of saturation. The degree of saturation was assumed to be 100% at the end of testing.

Soil specimens from borings B-31 and B-32, both from the Houston Black clay, were tested first. Results from tests conducted on the section of soil sampled a depth of 0 to 2 ft below the ground surface are shown in Figure 3.23 and Figure 3.24 for the corrected swelling curves and listed in Table 3.10 and Table 3.11 for the testing conditions and results.

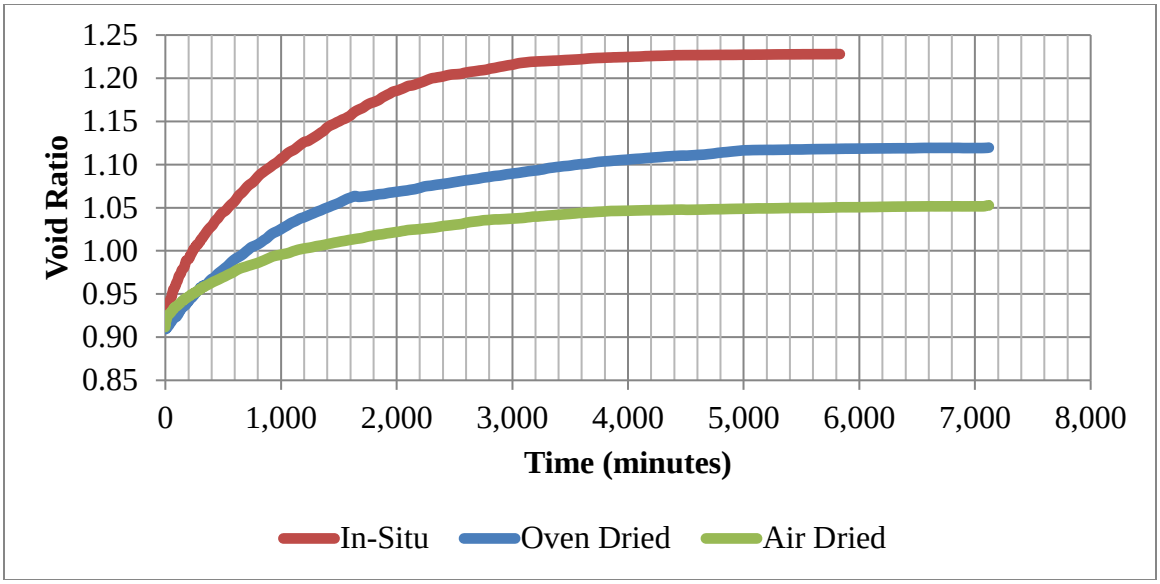

Figure 3.23*:* Corrected swelling curves for boring B-31 from 0 to 2 ft

Table 3.10*:* Testing conditions and results for specimens from boring B-31 from 0 to 2 ft

		Uncorrected		Corrected	
Condition	**In-Situ**	**Air-Dried**	**Oven-Dried**	**Air-Dried**	**Oven-Dried**
ω_i	32.7%	32.4%	31.8%	32.4%	31.8%
$y_{d,i}$ (kN/m^3)	13.86	14.12	14.13	13.86	13.86
Initial Sat.	0.97	1.00	0.98	0.96	0.94
e_i	0.912	0.876	0.874	0.912	0.912
e_f	1.220	0.997	1.073	1.036	1.117
e_{max}	1.228	1.013	1.076	1.050	1.118
Δe	0.308	0.121	0.200	0.124	0.205
$\varepsilon_{primary}$	16.1%	6.4%	10.7%	6.5%	10.7%
ε_{final}	16.5%	7.3%	10.8%	7.2%	10.8%
Time to ε_p	3260	2792	5050	2792	5050
ω_f	48.1%	43.0%	46.5%	43.0%	46.5%
y_f (kN/m^3)	17.68	18.97	18.71	18.47	18.32
θ_i	0.462	0.467	0.459	0.458	0.449
θ_f	0.551	0.503	0.518	0.512	0.528
σ' (psf)	202	217	216	217	216

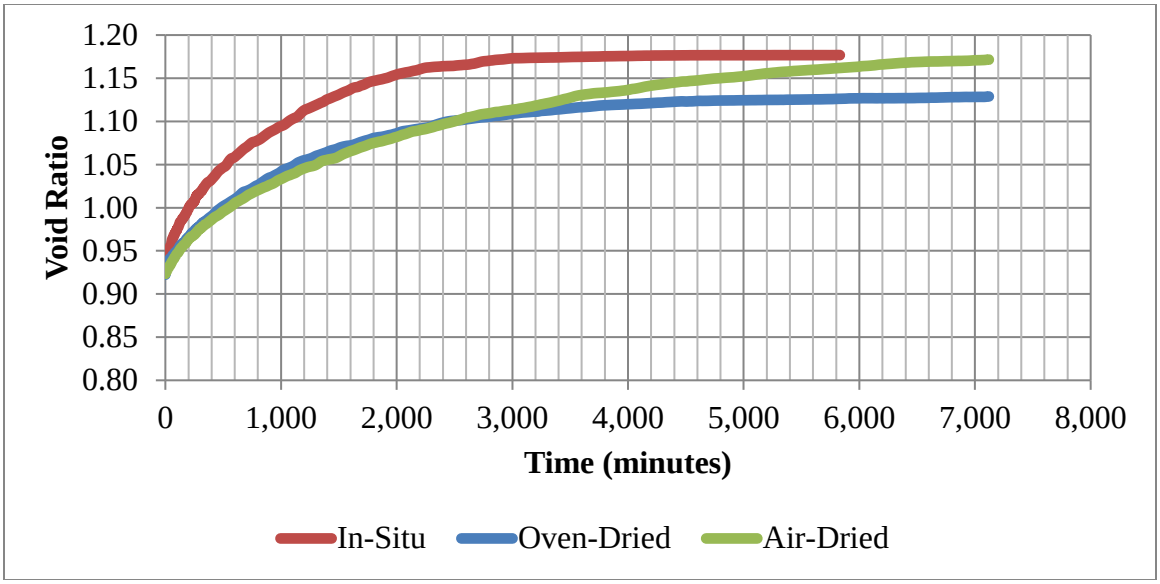

Figure 3.24*:* Corrected swelling curves for boring B-32 from 0 to 2 ft

Table 3.11*:* Testing conditions and results for specimens from boring B-32 from 0 to 2 ft

		Uncorrected		Corrected	
Condition	**In-Situ**	**Air-Dried**	**Oven-Dried**	**Air-Dried**	**Oven-Dried**
ω_i	32.1%	31.5%	30.5%	31.5%	30.5%
$y_{d,i}$ (kN/m^3)	13.77	14.07	13.42	13.77	13.77
Initial Sat.	0.94	0.96	0.85	0.92	0.89
e_i	0.924	0.883	0.974	0.924	0.924
e_f	1.173	1.121	1.166	1.169	1.110
e_{max}	1.177	1.124	1.185	1.161	1.126
Δe	0.250	0.239	0.193	0.245	0.187
$\varepsilon_{primary}$	13.0%	12.7%	9.8%	12.7%	9.7%
ε_{final}	13.2%	12.8%	10.7%	12.3%	10.5%
Time to ε_p	3033	6495	3086	6495	3086
ω_f	46.8%	45.9%	44.8%	45.9%	44.8%
y_f (kN/m^3)	17.90	18.21	17.70	17.88	18.04
θ_i	0.450	0.452	0.417	0.442	0.428
θ_f	0.541	0.529	0.542	0.537	0.530
σ' (psf)	205	217	217	217	217

Results from both borings indicate that there were significant differences between the initial dry unit weight at the end of the compression phase for the laboratory-reconstituted and in-situ specimens. After correcting the laboratory-reconstituted data, the general trend from both tests was that the primary swelling tends to be higher for in-situ, moisture-adjusted specimens than the laboratory-reconstituted specimens. However, the air-dried laboratory-reconstituted specimen from boring B-32 had a similar primary swelling as the in-situ, moisture-adjusted specimen. Additionally, unlike the results from Section 3.4.2, the time to the end of primary swelling for the laboratory-reconstituted specimens was similar or higher than the time for the in-situ, moisture-adjusted specimens. The final volumetric moisture content tended to be higher for the in-situ, moisture-adjusted specimen than for the laboratory-reconstituted specimens. These trends indicate that the soil fabric affected the swelling behavior of soil specimens.

Additional tests were performed on samples taken from a depth of 6 to 8 ft to verify the trends from the specimens sampled from a depth of 0 to 2 ft. As the specimens were sampled at a deeper depth, these specimens were not expected to have undergone as significant or frequent wetting and drying cycles as the specimens closer to the ground surface. Results from these tests are shown in Figure 3.25 and Figure 3.26 for the corrected swelling curves and listed in Table 3.12 and Table 3.13 for the testing conditions and test results.

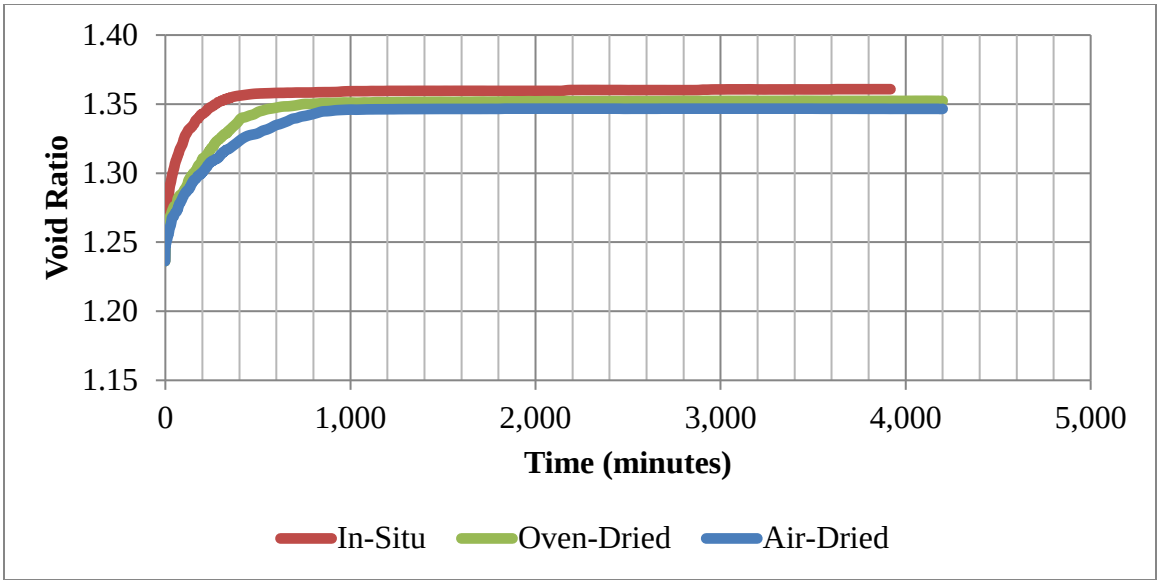

Figure 3.25*:* Corrected swelling curves for boring B-31 from 6 to 8 ft

Table 3.12*:* Testing conditions and results for specimens from boring B-31 from 6 to 8 ft

		Uncorrected		Corrected	
Condition	**In-Situ**	**Air-Dried**	**Oven-Dried**	**Air-Dried**	**Oven-Dried**
ω_i	33.0%	33.0%	32.2%	33.0%	32.2%
$y_{d,i}$ (kN/m^3)	11.85	12.16	11.87	11.85	11.85
Initial Sat.	0.72	0.76	0.70	0.72	0.70
e_i	1.236	1.177	1.231	1.236	1.236
e_f	1.354	1.283	1.342	1.345	1.347
e_{max}	1.361	1.285	1.347	1.347	1.352
Δe	0.117	0.106	0.111	0.109	0.111
$\varepsilon_{primary}$	5.2%	4.9%	5.0%	4.9%	5.0%
ε_{final}	5.6%	4.9%	5.2%	4.9%	5.2%
Time to ε_p	324	871	595	871	595
ω_f	52.5%	48.5%	50.6%	48.5%	50.6%
y_f (kN/m^3)	17.17	17.22	17.04	16.76	16.96
θ_i	0.399	0.409	0.389	0.398	0.388
θ_f	0.576	0.562	0.574	0.574	0.575
σ' (psf)	817	835	826	835	826

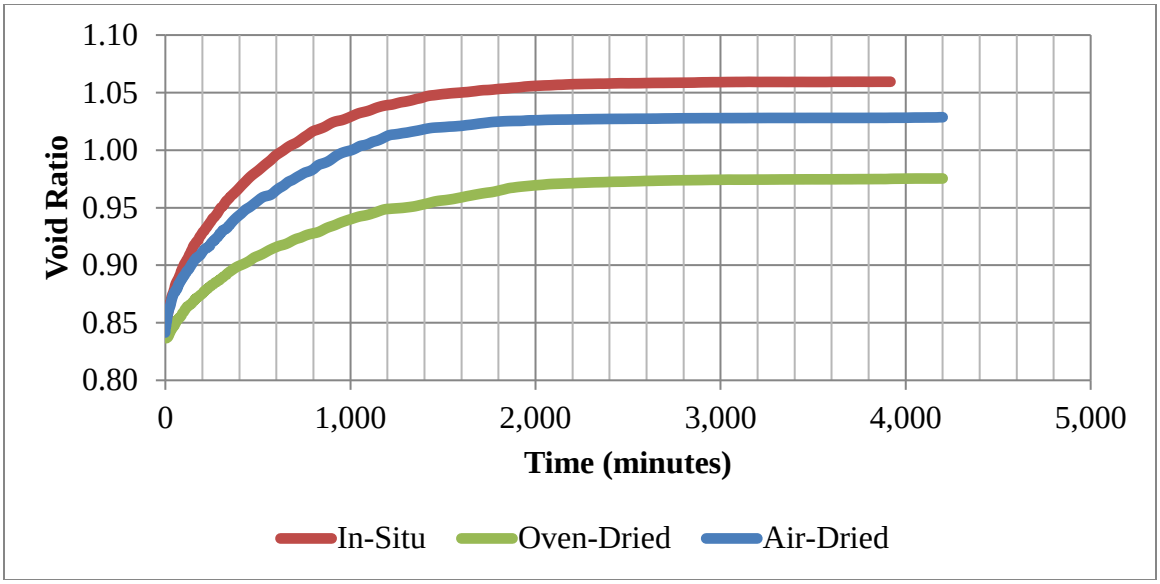

Figure 3.26*:* Corrected swelling curves for boring B-32 from 6 to 8 ft

Table 3.13*:* Testing conditions and results for specimens from boring B-32 from 6 to 8 ft

		Uncorrected		Corrected	
Condition	**In-Situ**	**Air-Dried**	**Oven-Dried**	**Air-Dried**	**Oven-Dried**
ω_i	22.5%	22.7%	22.1%	22.7%	22.1%
$y_{d,i}$ (kN/m^3)	14.39	14.25	14.25	14.39	14.39
Initial Sat.	0.72	0.71	0.69	0.73	0.71
e_i	0.841	0.859	0.859	0.841	0.841
e_f	1.049	1.039	0.991	1.020	0.971
e_{max}	1.059	1.048	0.995	1.029	0.975
Δe	0.207	0.181	0.131	0.178	0.129
$\varepsilon_{primary}$	11.3%	9.7%	7.1%	9.7%	7.0%
ε_{final}	11.8%	10.2%	7.3%	10.2%	7.3%
Time to ε_p	1518	1465	2133	1465	2133
ω_f	42.0%	40.7%	39.5%	40.7%	39.5%
y_f (kN/m^3)	18.36	18.27	18.56	18.37	18.70
θ_i	0.330	0.330	0.321	0.333	0.324
θ_f	0.514	0.512	0.499	0.507	0.494
σ' (psf)	827	852	862	852	862

The trends from the specimens from a deeper depth were consistent with the trends from the specimens near the ground surface. The primary swelling tends to be higher for the in-situ, moisture-adjusted specimens than the laboratory-reconstituted specimens. The time to the end of primary swelling for the laboratory-reconstituted specimens was similar or higher than the time from the in-situ, moisture-adjusted specimens. The final volumetric moisture content tended to be higher for the in-situ, moisture-adjusted specimen than the laboratory-reconstituted specimens. Therefore, the trends from testing were consistent with depth, indicating that the soil fabric in the field affected the swelling characteristics both at depths of significant moisture fluctuations and at depths where moisture fluctuations were not expected to be as significant. The moisture fluctuations near the surface may not affect the fabric as significantly as previously expected. The difference in the soil fabric may be attributed to the original deposition of the soil deposit as opposed to the cyclic wetting and drying.

To verify that the trends from borings B-31 and B-32 were consistent in different soils, the test results from borings B-31 and B-32 were compared to the results from a different expansive soil as identified from soil survey mapping. The soil from boring B-36 was sampled from the Heiden clay according to soil survey mapping, which differs from the Houston Black clay in borings B-31 and B-32. Results from testing on this soil are shown in Figure 3.27 for the corrected swelling curves and listed in Table 3.14 for the testing conditions and results.

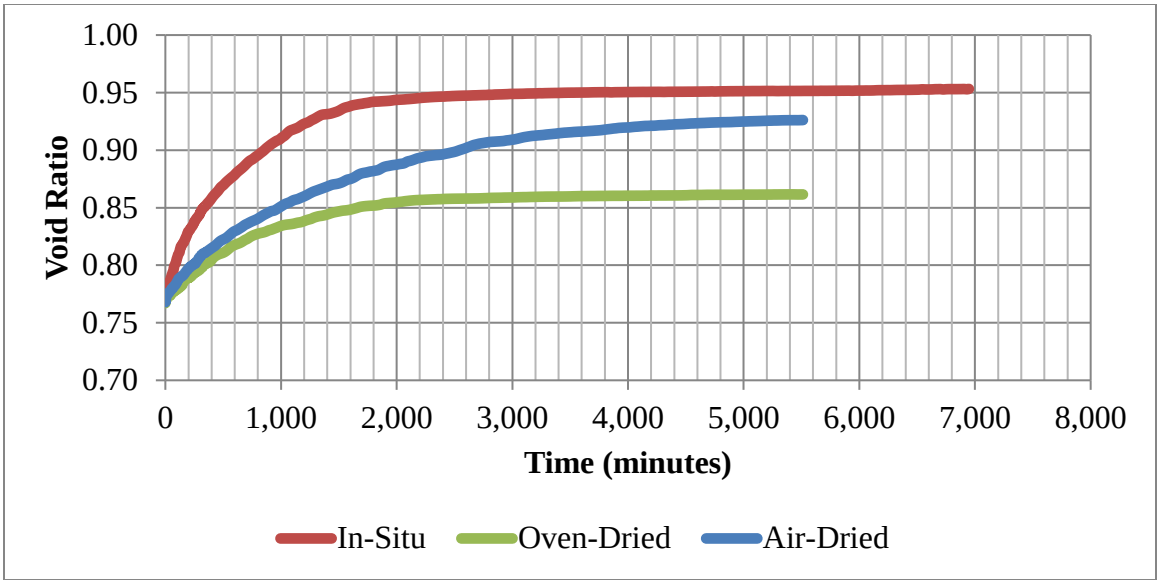

Figure 3.27*:* Corrected swelling curves for boring B-36 from 0 to 2 ft

Table 3.14*:* Testing conditions and results for specimens from boring B-36 from 0 to 2 ft

		Uncorrected		Corrected
Condition	**In-Situ**	**Air-Dried**	**Oven-Dried**	**Air-Dried**
ω_i	24.5%	23.5%	24.4%	23.5%
$\gamma_{d,i}$ (kN/m^3)	14.99	15.52	14.99	14.99
Initial Sat.	0.86	0.90	0.86	0.83
e_i	0.768	0.707	0.768	0.768
e_f	0.942	0.846	0.857	0.916
e_{max}	0.953	0.855	0.862	0.926
Δe	0.174	0.139	0.089	0.148
$\varepsilon_{primary}$	9.9%	8.1%	5.0%	8.4%
ε_{final}	10.5%	8.7%	5.3%	8.9%
Time to ε_p	1859	3510	2204	3510
ω_f	36.8%	34.6%	34.7%	34.6%
γ_f (kN/m^3)	18.66	19.33	19.22	18.51
θ_i	0.374	0.372	0.373	0.359
θ_f	0.488	0.461	0.463	0.481
σ' (psf)	201	198	196	198

Note that the oven-dried, laboratory-reconstituted specimens was not corrected due to refinement in the compaction procedure. The trends from boring B-36 were consistent

with those from borings B-31 and B-32. The primary swelling is higher for the in-situ, moisture-adjusted specimen than the laboratory-reconstituted specimens. The time to the end of primary swelling for the laboratory-reconstituted specimens was similar or higher than the time from the in-situ, moisture-adjusted specimens. The final volumetric moisture content was higher for the in-situ, moisture-adjusted specimen than the laboratory-reconstituted specimens. Therefore, the trends from Series III were consistent for soil samples collected from different soil series.

The trends from Series III differed from the trends in Series II. The laboratory-reconstituted specimens tended to have a similar or higher time to the end of primary swelling compared to the in-situ, moisture-adjusted specimens. This increase in the duration of primary swelling for the laboratory-reconstituted specimens was attributed to the compaction conditions. Specifically, the initial targeted dry unit weight was significantly higher than the estimated maximum dry unit weight from the NAVFAC correlations. In general, the maximum dry unit weight for a given soil increases with increasing compactive effort. Additionally, the optimum gravimetric moisture content tends to decrease with increasing compactive effort. Due to both of these effects, the optimum compaction conditions differ with increasing compactive effort. Due to the potential difference in the estimated versus actual optimal compaction conditions, the assumption that the soil fabric of the laboratory-reconstituted specimens was comparatively flocculated may not be valid.

Additional results from the IH-10 testing series are presented in Appendix A. While the majority of the testing series indicated that the trends were consistent with those presented previously, some testing results indicated that there was a different effect of soil fabric on the magnitude and duration of primary swelling. In order to examine the relative frequency of the effect of soil fabric on the swelling characteristics, the

probability of the trends was modeled as a series of events in a Bernoulli sequence. This model evaluates whether a condition, in this case a result from the laboratory-reconstituted specimens exceeding the in-situ, moisture-adjusted specimens, occurred in each trial. Thus, the probability that a test result from a laboratory-reconstituted specimen will exceed the test result from an in-situ, moisture adjusted specimen can be estimated as follows:

$$\hat{P} = \frac{1}{n}\sum_{i=1}^{n} X_i \tag{3.3}$$

Where X_i is the occurrence, n is the number of tests, and $\hat{P}$ is the probability that the variable exceeded the moisture adjusted, field specimen. This method can be used for either the air-dried or oven-dried testing condition. The probability of occurrence, or relative frequencies, was calculated for the following variables:

- the void ratio at the end of primary swelling (e_{ps}) and at the end of the test (e_{max})
- the strain at the end of primary swelling (ε_{ps}) and at the end of the test (ε_{max})
- the time to the end of primary swelling
- the final volumetric moisture content (θ_f)
- the change in the volumetric moisture content during testing ($d\theta$)

The frequencies are shown in Table 3.15. The frequencies are grouped between the corrected and uncorrected testing results. Additionally, the total number of tests used to calculate the probability of occurrence are shown.

Table 3.15*:* Probability of exceedance of variables between in-situ and laboratory-reconstituted specimens

Condition	Count	e_{ps}	e_{max}	ε_p	ε_f	Time to E.O.P.	θ_f	$d\theta$
Air-Dried	**11**	36%	36%	45%	45%	64%	36%	45%
Air-Dried- Corrected	**11**	45%	45%	45%	45%	64%	45%	36%
Oven-Dried	**19**	21%	21%	21%	16%	95%	21%	26%
Oven-Dried - Corrected	**15**	27%	27%	27%	27%	93%	27%	20%

The probability of occurrence that the results from both the air-dried and oven-dried tests exceeded the results from the in-situ tests were less than 50% for the test results that correspond to the magnitude of swelling (i.e. e_{ps}, e_{max}, ε_p, and ε_f) and the change in moisture (i.e. θ_f and $d\theta$). This trend indicates that the in-situ, moisture-adjusted specimens tend to have a larger primary swelling than the laboratory-reconstituted specimens. Additionally, the time to the end of the primary swelling tends to be higher for the laboratory-reconstituted specimens than for the in-situ, moisture-adjusted specimens. Finally, the final volumetric moisture content tended to be higher for the in-situ, moisture-adjusted specimen than the laboratory-reconstituted specimens. Therefore, the overall trends from Series III were consistent with the results presented in this section.

To further analyze the results from Series III, the difference between the test results from the in-situ, moisture-adjusted specimens and the air-dried and oven-dried laboratory-reconstituted specimens are presented in Table A.15 in Appendix A. The difference in the test results between the testing conditions was plotted using probability plots generated from MATLAB. The probability plots were used to evaluate how significant the difference in the magnitude and duration of primary swelling was between the specimens at different testing conditions. A normal distribution of the data was assumed for the theoretical distribution. Additionally, the difference in the test results were plotted for each probability plots. The probability plot for the difference in the

change in the void ratio to the end of primary swelling between the corrected air-dried and oven-dried laboratory-reconstituted specimens and the in-situ, moisture-adjusted field is shown in Figure 3.28. The probability plot for the difference in the change in the void ratio to the end of swelling between the corrected air-dried and oven-dried laboratory-reconstituted specimens and the in-situ, moisture-adjusted field is shown in Figure 3.29.

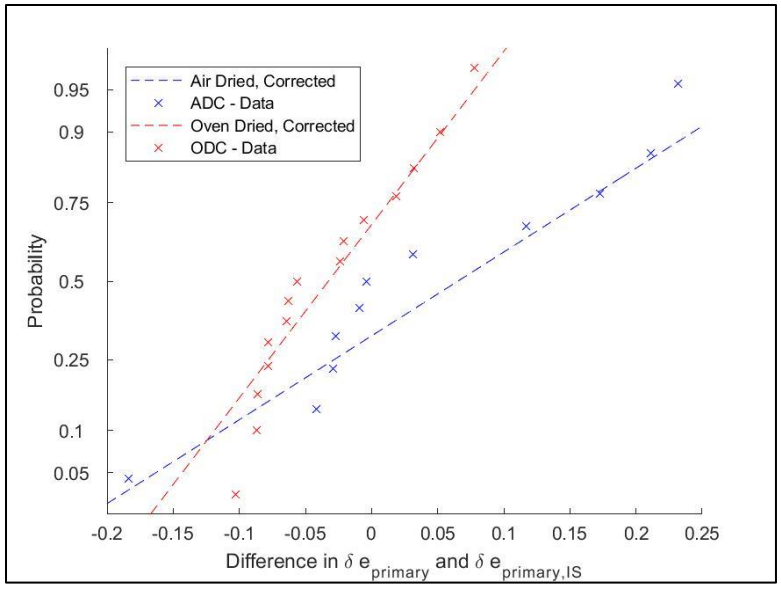

Figure 3.28: Probability plot for differences in change in void ratio at the end of primary swelling between corrected laboratory-reconstituted specimens and the in-situ specimens

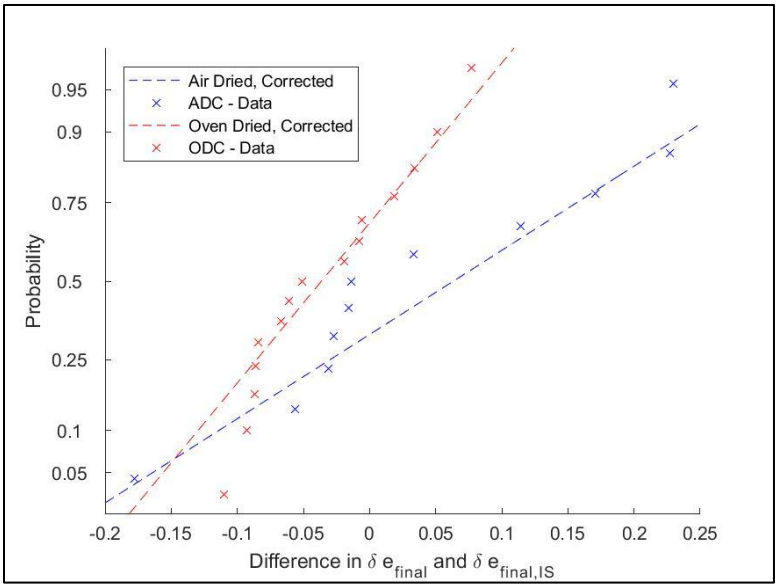

Figure 3.29: Probability plot for differences in change in void ratio at the end of the test between corrected laboratory-reconstituted specimens and the in-situ specimens

The probability plots are consistent with the results from the Bernoulli sequence analysis presented in Table 3.15. The laboratory-reconstituted specimens tend to have a lower magnitude of swelling than the in-situ, moisture-adjusted specimens. However, the variability in the difference in the test results was higher for the air-dried specimens than for the oven-dried specimens. The higher amount of variability for the air-dried specimens can be attributed to some heterogeneity in the soil with depth, preferential selection of specimens for testing that removed aggregate particles, and a higher volume of soil across the 2 ft section that was selected for air-drying. The test results from the oven-dried laboratory-reconstituted specimens tend to be significantly below the test results from the field specimens. The decrease in the swelling of the soil cab be attributed to the change in the soil fabric from the processing and preparation of reconstituted specimens and the difference in the clay mineralogy due to the higher drying temperature.

An additional objective for this testing series was to analyze the effect of the drying temperature on the swelling characteristics of laboratory-reconstituted specimens. The probability that the test results from air-dried specimens exceeded the test results from the corresponding oven-dried specimens are shown in Table 3.16. The probabilities were evaluated for both the original and corrected test results. The probabilities were calculated using the method outlined previously in Equation 3.3.

Table 3.16*:* Probability of exceedance of variables between air-dried and oven-dried specimens

Data	e_{ps}	e_{max}	ε_p	ε_f	Time to E.O.P.	θ_f	$d\theta$
Air-Dried	45%	73%	82%	82%	73%	73%	55%
Air-dried, Corrected	82%	82%	82%	82%	73%	73%	18%

Note that the initial dry unit weights differed significantly between the oven-dried and air-dried specimens. Due to the differences in the initial conditions, this analysis focuses on the trends from the corrected testing results. The air-dried specimens tend to have a higher magnitude of swelling at both the end of primary swelling and end of testing. Additionally, the air-dried specimens tend to have a higher duration of primary swelling than the oven-dried specimens. Finally, the air-dried specimens tend to have a higher final volumetric moisture content than the oven-dried specimens.

To examine the magnitude of these differences in primary and end of testing swelling, the difference in the magnitude of swelling, shown both in terms of the change in void ratio and strain between the beginning and end of the tests, are shown in Table 3.17. Note that the difference was defined as the magnitude in change for the air-dried specimen minus the magnitude in change for the oven-dried specimen.

Table 3.17*:* Difference in change in void ratio and strain between air-dried and oven-dried tests

		Uncorrected Data		Corrected Data	
Boring	**Depth**	**de_{max}**	**$d\varepsilon_{max}$**	**de_{max}**	**$d\varepsilon_{max}$**
B-31	0-2	-0.065	-3.5%	-0.068	-3.6%
B-31	2-4	0.322	17.3%	0.298	16.7%
B-31	4-6	0.048	2.4%	0.052	2.5%
B-31	6-8	-0.008	-0.4%	-0.006	-0.3%
B-32	0-2	0.030	1.6%	0.035	1.8%
B-32	2-4	0.271	15.2%	0.264	14.9%
B-32	4-6	0.159	8.5%	0.150	8.0%
B-32	6-8	0.054	2.9%	0.053	2.9%
B-35	0-2	0.078	4.4%	0.081	4.5%
B-36	0-2	0.055	3.2%	0.064	3.6%
B-38	0-2	-0.005	-0.3%	0.005	0.3%

The difference for both B-31 and B-32 at a depth of 2 to 4 ft were significantly higher than for the rest of the data. Since these two data points are between borings that are closely spaced and in the same soil deposit, a more expansive seam may be attributed for the heterogeneity in these outliers. Due to the possibility of an expansive seam, the results from these two borings and depths were not used in this analysis. After removing these outliers, the results from Table 3.17 were used to generate probability plots assuming a normal distribution. These probability plots are shown in Figure 3.30 for both the uncorrected and corrected data.

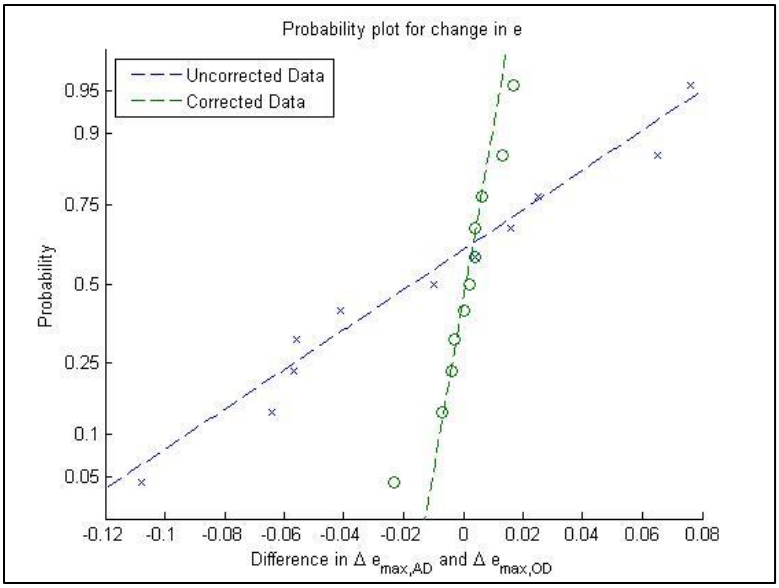

Figure 3.30: Probability plots for distribution of differences in change in void ratio for the air-dried and oven-dried specimens

The difference in the change in void ratio at the end of the test was more significant for the uncorrected data than for the corrected data. Additionally, both data sets indicate that a normal distribution is suitable for analysis. In order to further analyze these differences, the mean and standard deviation of the normal distributions from Figure 3.30 are shown for both the uncorrected and corrected data in Table 3.18.

Table 3.18*:* Statistical parameters for the differences in the change in void ratio and strain for the air-dried and oven-dried specimens

	Uncorrected Data		**Corrected Data**	
Parameter	**de_{max}**	**$d\varepsilon_{max}$**	**de_{max}**	**$d\varepsilon_{max}$**
Mean	0.085	4.7%	0.084	4.7%
Standard Deviation	0.119	6.5%	0.112	6.2%

These distributions indicated that the drying temperature of the laboratory-reconstituted specimens significantly affected the magnitude of swelling. The air-dried specimens tend to have a higher magnitude of swelling than the oven-dried specimens. A potential

explanation of this difference comes from the change in mineralogy of the soil with an increasing drying temperature. The drying temperature for the oven-dried soil exceeded the maximum threshold, 70 °C, at which the attached water starts to be removed from the surface of the clay particles. The removal of the attached water may significantly affect the increase in the diffuse double layer during the infiltration of moisture. Additionally, during the drying process, the removal of moisture from the oven-dried specimens occurs more rapidly than for the air-dried specimens. The oven-dried specimens were dried for 24 hours in comparison to the few weeks that the air-dried specimens were dried due to differences in the rate of drying. The slower rate of drying for the air-dried specimens may not significantly affect the removal of moisture from the clusters and micro-voids in the clay. Overall, specimens that are oven-dried tend to have a smaller magnitude of swelling than specimens that are air-dried. This result indicates that expansive soils taken from the field should be air-dried prior to testing in order to determine the swelling characteristics of an expansive soil deposit.

Results from testing of the soil sampled from IH-10 indicate that the soil fabric affects the swelling characteristics of expansive soils. The in-situ, moisture-adjusted specimens tend to have a higher magnitude of swelling than the laboratory-reconstituted specimens. This trend was consistent with previous sections and indicated that the soil fabric of field specimens affects the magnitude of swelling. However, unlike the results from previous sections, the in-situ, moisture-adjusted specimens tend to have a smaller time to the end of primary swelling. This trend was attributed to the laboratory-reconstituted specimens having a more dispersed soil fabric due to a higher compactive effort. Additionally, the temperature at which soil specimens were dried prior to being reconstituted was analyzed. Specimens that were air-dried at 23°C tend to have a higher magnitude of swelling and time to the end of primary swelling than specimens that were

oven-dried at 110°C. The difference in the air-dried and oven-dried laboratory-reconstituted specimens was attributed to the water attached to the clay minerals being removed at the higher drying temperature.

3.5 Results from Microscopy on Expansive Soils and their Analysis

In order to better visualize the internal structure of the clays, imaging using scanning electron microscopes (SEM) was conducted to examine the fabric of expansive soils. Two SEMs were used for three different soil conditions. For all the soil conditions, the size of the specimens was approximately 1 mm cubes. Specimens were placed onto their sample holders after which they were blown with compressed air to remove any contaminants from the surfaces.

The first condition involved high resolution imaging of air-dried and oven-dried clays to examine the fabric of compacted clays and bulk sampled clay. A Zeiss Supra 40VP SEM with a field emission gun at the Institute for Cellular and Molecular Biology was used for this study. The field emission gun allowed for higher resolution imaging. To reduce charging, specimens for this condition were placed on double-sided copper tape, had their edges painted with conductive carbon paint, and were coated with 10 nm of Platinum and Palladium. Imaging was done in a high-vacuum environment ($< 10^{-4}$ Torr). Due to the high vacuum, these soils were at their residual moisture contents.

The second condition involved imaging of in-situ and laboratory-reconstituted specimens to examine the differences their different fabrics. Specimens were trimmed from specimens tested using the centrifuge-based inundation tests from the IH-10 project, outlined in Chapter 4. The soils were air-dried at 23°C to their residual moisture contents. An environmental scanning electron microscope (ESEM), a Philips FEI XL30 with a thermionic tungsten gun at the Jackson School of Geology, was used for imaging. The

change from the field emission gun to the thermionic tungsten gun was expected to reduce the resolution at higher magnifications. To reduce charging, specimens were again placed on double-sided copper tape and had their edges painted with conductive carbon paint. However, the specimens were coated with 10 nm of gold coating due to differing equipment between the two laboratories. Imaging was again completed in a high-vacuum environment ($< 10^{-4}$ Torr).

The third condition involved imaging of "dirty" specimens, i.e. the specimens were not dried to a residual moisture content prior to imaging, via use of the ESEM at the Jackson School of Geology. A Peltier cooling stage was used in the ESEM to control the relative humidity around the specimens. Specimens for this condition were compacted Eagle Ford clay that were trimmed into the sample holder. Since the specimens were not at the residual moisture content, the ESEM mode, in which water vapor pressure exceeding 1 Torr. is introduced, was used for imaging. Due to the use of the ESEM mode, specimens were neither coated with a metal nor had its edges painted with carbon black paint. However, double-sided copper tape was used to attach the specimen to the cooling stage. Due to the use of the cooling stage, both the temperature and water vapor pressure at the specimen stage could be controlled, allowing for the control of the relative humidity. The relationship between the temperature and water vapor pressure is shown in Figure 3.9. For the wetting and drying cycles, a relative humidity of 100% and 10% was targeted.

3.5.1 Microscopy on Bulk-Sampled Soils

For the first condition, imaging was done on laboratory-reconstituted, air-dried specimens of the Eagle Ford and Behring clays. For the laboratory-reconstituted Eagle Ford clay, imaging was done at varying relative compactions (70% and 100% in relation

to the maximum dry unit weight from Standard Proctor compaction effort) to examine differences in the macro and micro-structure at different initial dry unit weights. The initial gravimetric moisture content prior to air-drying was at the optimum moisture content (Table 3.1). Due to this compaction moisture content, the specimens were expected to have areas in which the soil fabric was flocculated and areas in which the soil fabric was dispersed. All images were taken with a secondary electron detector and at a low accelerating voltage (5 kV) in order to prevent charging of the clay minerals.

Micrographs of the Eagle Ford clay are shown in Figure 3.31 for a relative compaction of 70% and in Figure 3.32 for a relative compaction of 100%.

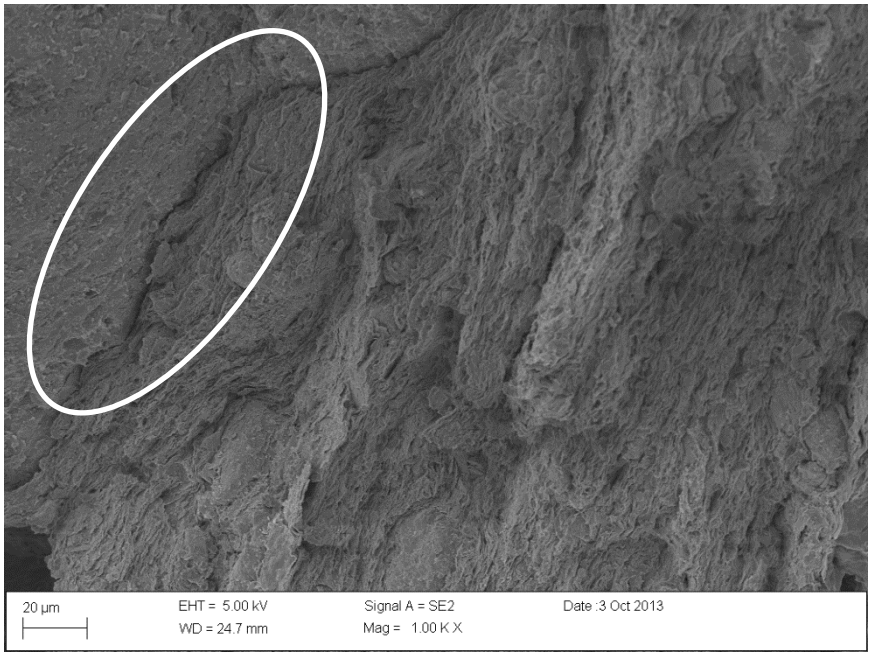

Figure 3.31: SE micrograph of laboratory-reconstituted Eagle Ford clay at a relative compaction of 70%

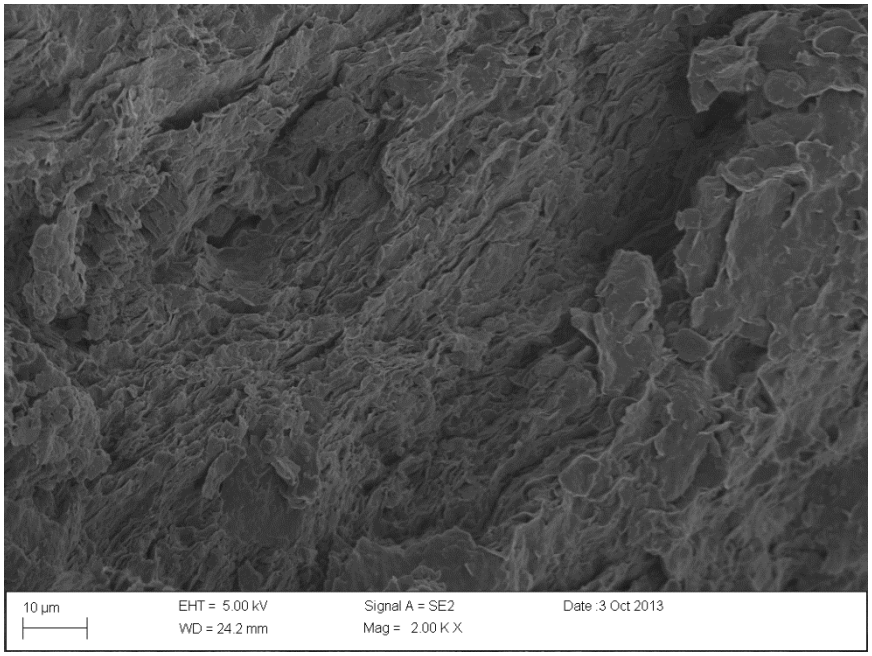

Figure 3.32*:* SE micrograph of laboratory-reconstituted Eagle Ford clay at a relative compaction of 100%

The micrographs indicate that the internal clay structure was laminar with plate to plate contact between individual clay minerals. In general, the orientation of the particles was relatively dispersed for both relative compactions. The main differences between the specimens was observed in the spacing between the peds of the clay, as indicated by the region outlined in a white oval in Figure 3.31 for the specimen at a lower relative compaction. This space at the contact between clay peds was not observed for the specimen at a higher relative compaction. Therefore, while the micro-structure of the individual clay minerals was similar between the two relative compactions, the macro-structure differed based on compactive effort. These macro-voids can be assumed to be primary cause for the reduction in the time to the end of primary swelling and increase in the saturated hydraulic conductivity seen in Section 2.3.3 of this dissertation. The voids in between peds allows for water to infiltrate more rapidly in specimens at lower relative

compactions. Additionally, these macro-voids can be assumed to reduce the one-dimensional vertical swelling in the specimens as the clay peds will swell laterally to fill these voids prior to swelling vertically.

Imaging of the Eagle Ford clay at a higher magnification was used to examine the layering of the laminar clay particles within the clay clusters. These laminar clay minerals were expected to be primarily smectite clay minerals. These micrographs are shown in Figure 3.33 for a relative compaction of 70% and in Figure 3.34 for a relative compaction of 100%.

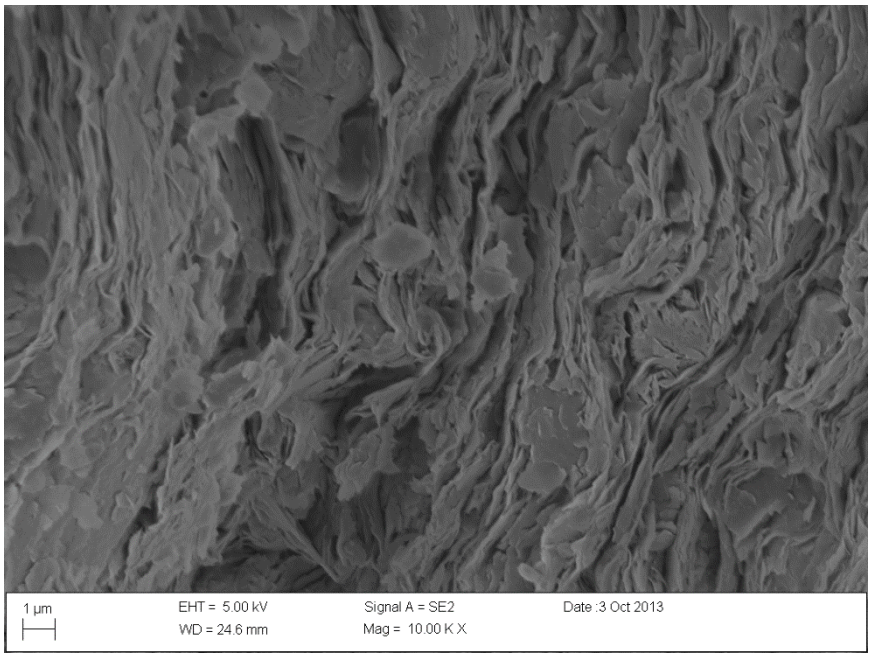

Figure 3.33: SE micrograph of laboratory-reconstituted Eagle Ford clay at a relative compaction of 70% at a higher magnification

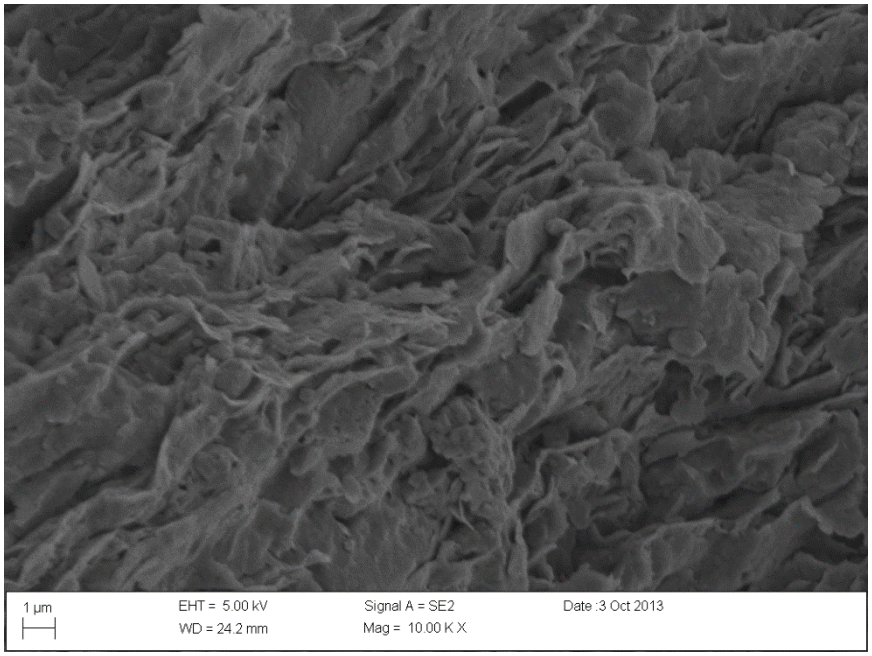

Figure 3.34*:* SE micrograph of laboratory-reconstituted Eagle Ford clay at a relative compaction of 100% at a higher magnification

The micrographs indicate that the clay particles were comparatively dispersed within individual clay peds and clusters. The laminar clay particles appeared to be composed primarily of smaller, plate-like clay minerals. This structure occurred both in specimens with a low and high relative compaction. This layering is consistent with a dispersed soil fabric and illustrates how closely spaced clay plates are within the micro-voids of an expansive soil deposit. Other clay minerals such as kaolinite were not observed in the Eagle Ford clay specimens. The close spacing between laminar clay particles (i.e. smectite) and the lack of less expansive clay minerals are consistent with the comparatively high magnitude of swelling for the Eagle Ford clay.

The process for reconstituting the clays involves passing the air-dried portions of the clay through a rock-crusher twice in order to create a fine soil prior to rehydration. This process can remove the original orientation of the clay particles and homogenizes

the clay. As such, the clay structure between the laboratory-reconstituted specimens may differ significantly from the field soil deposit. In order to assess differences in the laboratory-reconstituted and field-sampled specimens, imaging was also performed on an air-dried specimen of the original deposit. The clay was taken from a depth of approximately 10 ft below the ground surface and had a more apparent layering that was fissile and fine-grained (Wright et al., 2007). Due to this portion of the clay not being processed through a rock crusher, the original field fabric was expected to be more prominent despite the relaxation of stresses from sampling. The micrograph of the field-sampled specimen of the Eagle Ford clay is shown in Figure 3.35

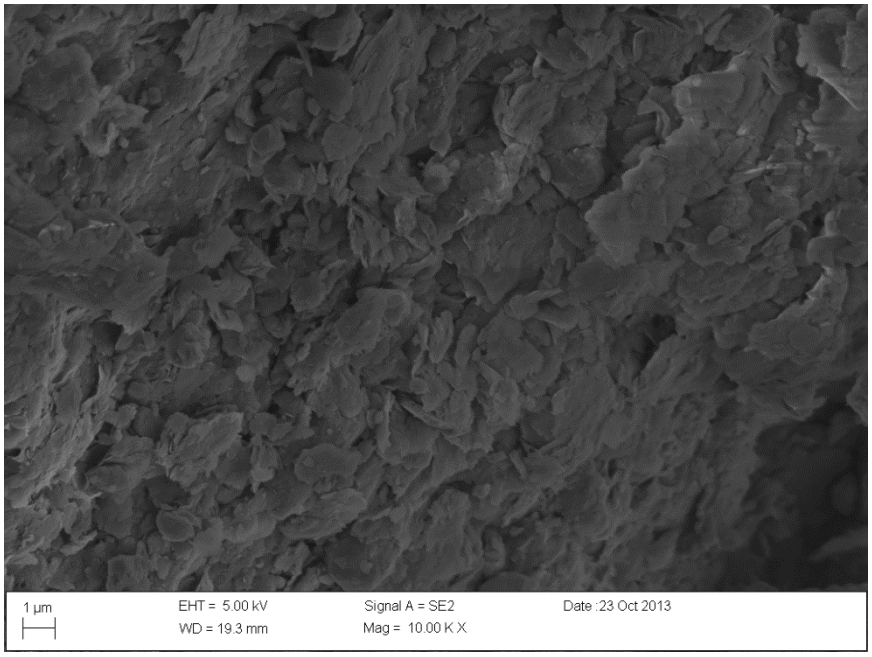

Figure 3.35*:* SE micrograph of air-dried, field-sampled Eagle Ford clay

Imaging of the shale indicates that the layering of the clay minerals seen in the laboratory-reconstituted specimen was not as significant in the field-sampled specimen. The soil fabric of the field-sampled specimen was more complex, as seen by distribution

of the clusters and inconsistent orientation of the clay particles. Additionally, the individual, plate-like clay minerals were found to be smaller for the field-sampled specimen than for the laboratory-reconstituted specimen and did not form laminar clay particles within the clay cluster. The smaller, plate-like clay minerals can be assumed to affect the magnitude of swelling due to an increase in the clay to clay contact. The higher clay to clay contact would increase the regions in which the diffuse double layer would swell the soil specimen. These differences indicate that the processing and rehydration of the soil significantly affect the soil fabric.

A specimen of an additional clay deposit, the Behring clay, were also examined in the SEM using the secondary electron detector. This clay was sampled from an exposed portion of the surficial soil deposit during construction of a roadway. The sample was approximately 1 mm by 1 mm in area. Unlike the specimens from the Eagle Ford clay, the specimen from the Behring clay was not trimmed at the imaging surface. Instead, a portion of the clay was removed from the surrounding clay mass on a presumed bedding plane. The specimen was allowed to air-dry to the residual moisture content from the in-situ gravimetric moisture content. Micrographs of the field-sampled clay at a low magnification is shown in Figure 3.36 and at a higher magnification in Figure 3.37.

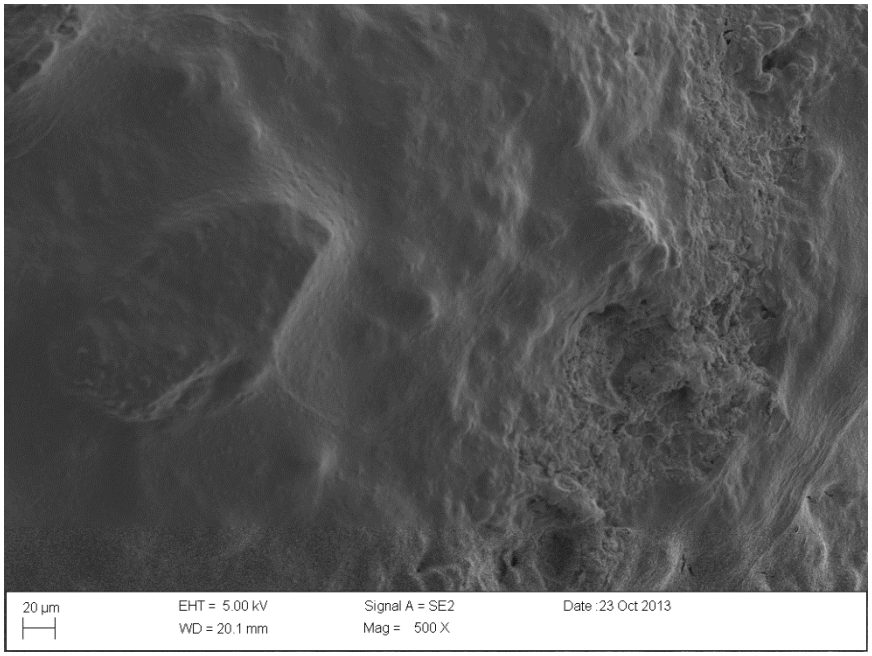

Figure 3.36*:* SE micrograph of air-dried, field-sampled Behring clay at a low magnification

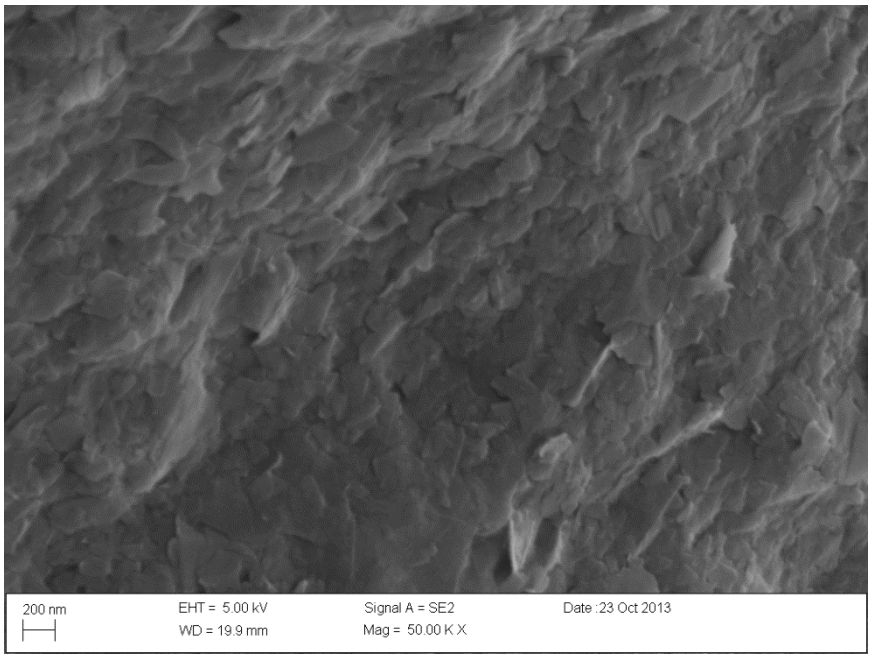

Figure 3.37*:* SE micrograph of air-dried, field-sampled Behring clay at a higher magnification

At the low magnification, the field-sampled Behring clay appears smooth, with a lack of bedding of laminar clay particles that was previously seen in the laboratory-reconstituted Eagle Ford clay. However, at higher magnifications, the clay surface is shown to be composed of multiple, smaller plate-like clay minerals as seen in Figure 3.37. This soil fabric is observed to be more dispersed and differs from the random orientation seen in Figure 3.35 for the Eagle Ford clay. However, this bedding of the field-sampled Behring clay indicates how expansive soils can be problematic as there is a high amount of clay to clay contact.

Other portions of the specimen of the Behring clay indicate a similar random orientation of clay minerals and clusters as the Eagle Ford clay. Micrographs of these locations are shown in Figure 3.38 and Figure 3.39. These sites were located away from the presumed bedding plane of the soil specimen.

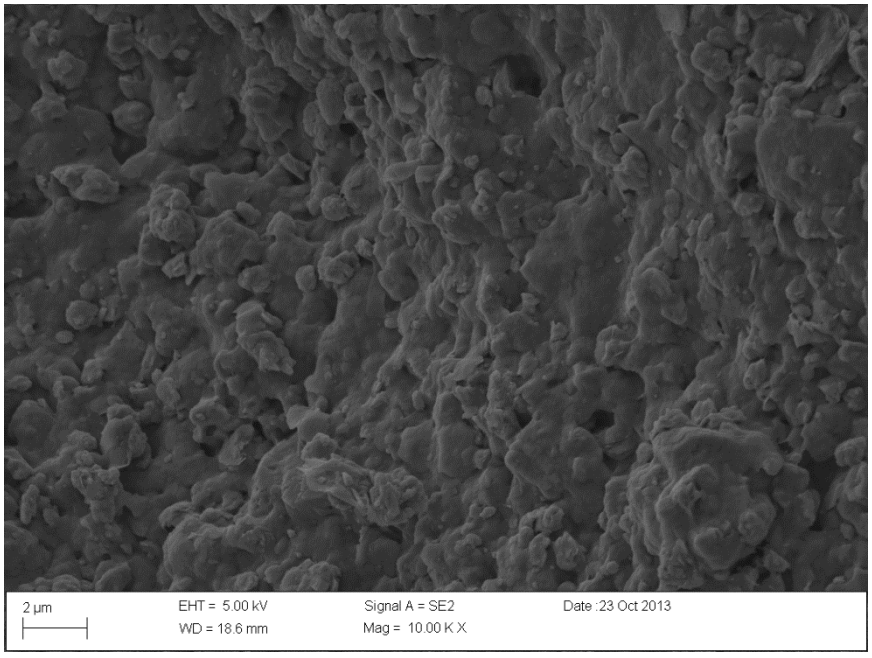

Figure 3.38*:* SE micrograph of air-dried, field-sampled Behring clay minerals and clusters

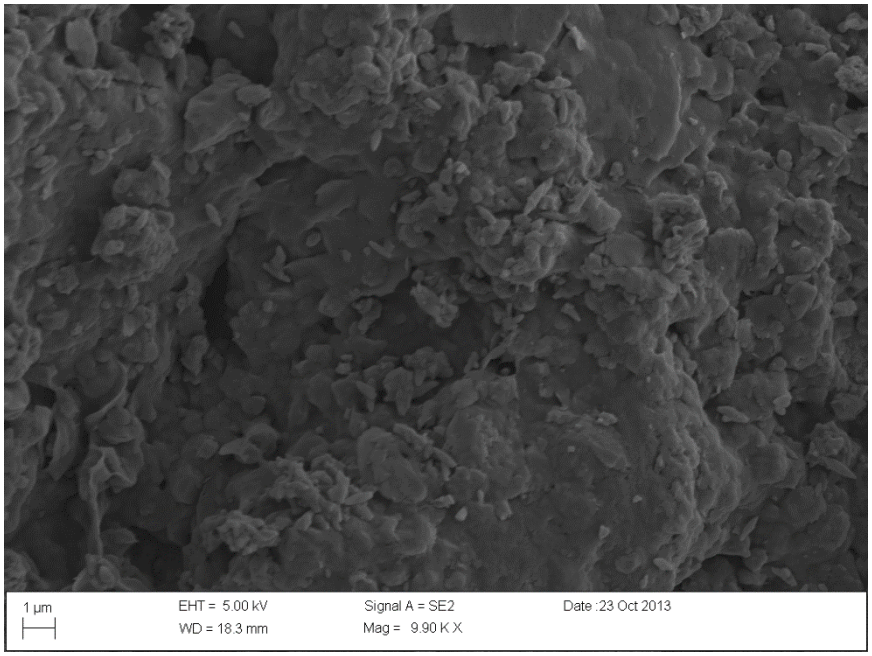

Figure 3.39*:* SE micrograph of air-dried, field-sampled Behring clay minerals and clusters at a secondary site

Both micrographs indicate that the soil fabric is more randomly oriented with a similar distribution of clay clusters and peds as the field-sampled Eagle Ford clay shown in Figure 3.35. The clay clusters and particles also were smaller than those from the laboratory-reconstituted Eagle Ford clay. The difference between the regions along the bedding plane (i.e. the dispersed fabric) and the regions away from the bedding planes (i.e. the reconstituted fabric) indicate that the soil fabric of field-sampled clays is neither dispersed or flocculated. This different soil fabric can be assumed to cause differences in swelling behavior between laboratory-reconstituted and field-sampled clay specimens tested using the centrifuge-based inundation test.

In addition to the orientation of the assumed smectite, other non-expansive clay minerals were present in the Behring clay that were not previously seen in the Eagle Ford clay. A micrograph of these additional clay minerals is shown in Figure 3.40.

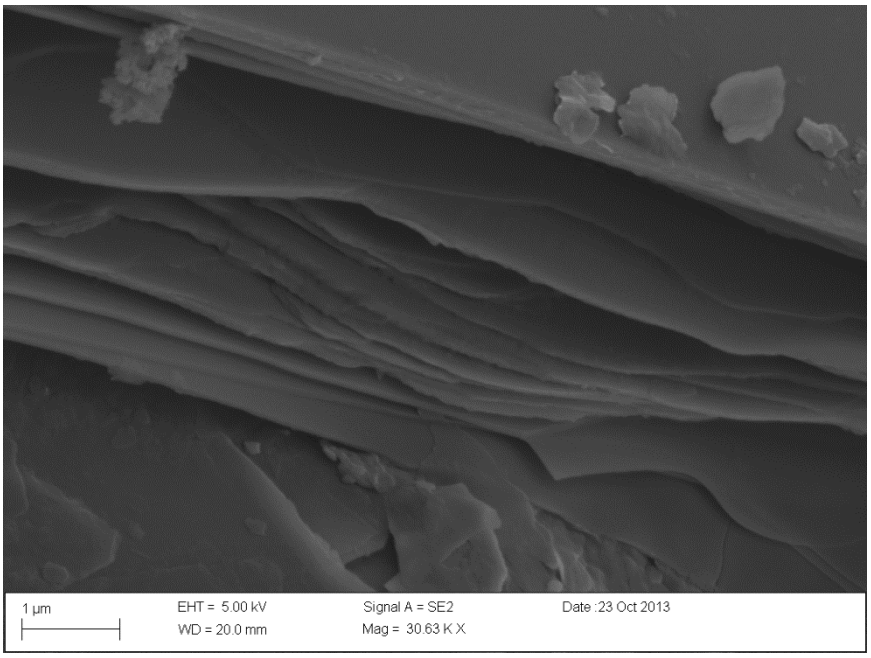

Figure 3.40*:* SE micrograph of kaolinite in air-dried, field-sampled Behring clay specimen

The clay mineral was assumed to be kaolinite based on the size of the mineral and the geologic history of the site. The thickness of this clay mineral is higher than other clay minerals typically found in expansive soils (i.e. illite and smectite). Differences between the thickness of clay minerals can be seen by the smaller clay particles in the upper right of the micrograph, which are assumed to be smectite, and the large, plate-like clay minerals in the center of the micrograph, which are assumed to be kaolinite. The presence of other minerals can be assumed to cause the reduced potential swelling for the Behring clay as compared to the Eagle Ford clay based on the results from Section 2.3 of this dissertation. Based on the geologic and depositional history of the site, the presence of kaolinite is expected as the soil layer was deposited in the Tertiary Age of the Cenozoic Era based on geologic map and NRCS soil surveys of the region. This time period

corresponds to the period in which marine deposits were formed close to the Gulf of Mexico (Eargle, 1968). Therefore, both geologic maps and NRCS soil surveys can provide valuable information about the depositional history of expansive soils deposits.

The layering and bedding of smectite minerals was found throughout the specimen. A micrograph of a significantly dispersed ped of smectite is shown in Figure 3.41.

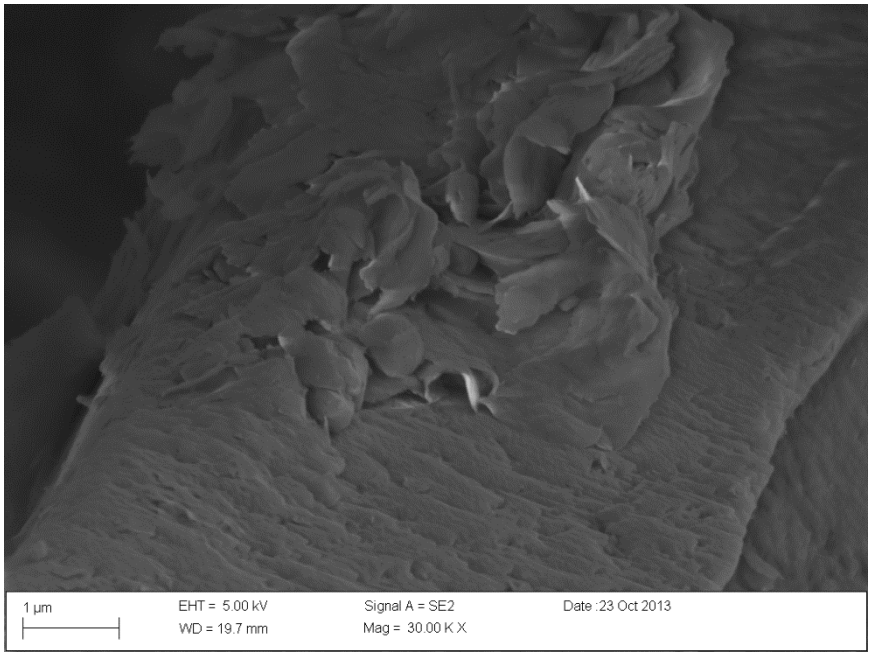

Figure 3.41*:* SE micrograph of smectite in air-dried, field-sampled Behring clay specimen

The smectite minerals are very closely spaced and arranged parallel to each other in a dispersed soil fabric. These areas in which smectite is presented and in plate to plate contact between minerals will increase the swelling potential of the soil significantly. As such, the Behring clay's expansive behavior can be attributed to the bedding of the smectite within the soil matrix.

Several conclusions from the imaging in this first section can be made for the soil fabric of laboratory-reconstituted and field-sampled expansive soils. Laboratory-reconstituted specimens with a lower relative compaction will have a higher amount of macro-voids than specimens at a higher relative compaction. The increase in the amount of macro-voids is assumed to decrease the magnitude and time to the end of primary swelling and increase the saturated hydraulic conductivity. Additionally, the structure of laboratory-reconstituted and field-sampled specimens differed significantly. Laboratory-reconstituted specimens had a more dispersed soil fabric with a significant arrangement of laminar clay particles and clusters. Field-sampled specimens had a more complex soil fabric, with regions of flocculated soil fabric and regions of dispersed soil fabric and had smaller clay particles and clusters. Additionally, the clay plates of the field-sampled clay were generally smaller than the plates from the laboratory-reconstituted clay. The different fabric between the field-sampled and laboratory-reconstituted specimens may be attributed for the differences in the swelling behavior from Section 3.4 as the clay plates may have more areas of contact between clay minerals. Finally, the additional clay minerals, including kaolinite, were present in the Behring clay. The presence of non-expansive clay minerals may be the cause for the smaller swelling observed for the Behring clay than for the Eagle Ford clay, where these minerals were not observed.

3.5.2 Microscopy on Shelby Tube-Sampled Specimens

For the second condition, imaging was performed on the in-situ boring specimens from the IH-10 expansion project that is outlined in Section 3.4.3 and Chapter 4 of this dissertation. Two borings in the Houston Black clay, derived from the Taylor-Navarro group, were selected for analysis. The two borings, B-31 and B-32, were previously evaluated for the effect of soil fabric on swelling characteristics in Section 3.4.3. Imaging

was performed on in-situ soil specimens as well as on oven-dried and air-dried laboratory-reconstituted specimens. Both the 2 ft section at the surface, at a depth of 0 to 2 ft below the ground surface, and lowest 2 ft section, at a depth of 6 to 8 ft below the ground surface, were evaluated. These locations were selected in order to evaluate an area where cyclic wetting and drying was more frequent and an area near the base of the active zone where cyclic wetting and drying was less frequent. Note that the laboratory-reconstituted specimens under through the same processing prior to rehydration as the Eagle Ford clay that is previously outlined in Section 3.3. The specimens used for imaging were trimmed directly from the borings for the in-situ specimens or either from laboratory-reconstituted specimens. Imaging was performed with a secondary electron detector and at a higher accelerating voltage (20 kV) in order to have a higher resolution with the thermionic tungsten gun. The objective for the second condition was to examine whether the soil fabric from undisturbed, in-situ specimens had similar trends as the field-sampled specimens from the first condition. Additionally, the second condition examined the effect of the drying temperature on the clay mineralogy for the laboratory-reconstituted specimens.

Micrographs of the first boring, B-31, taken perpendicular to the expected bedding and deposition in the field, is shown in Figure 3.42 for a depth of 0 to 2 ft.

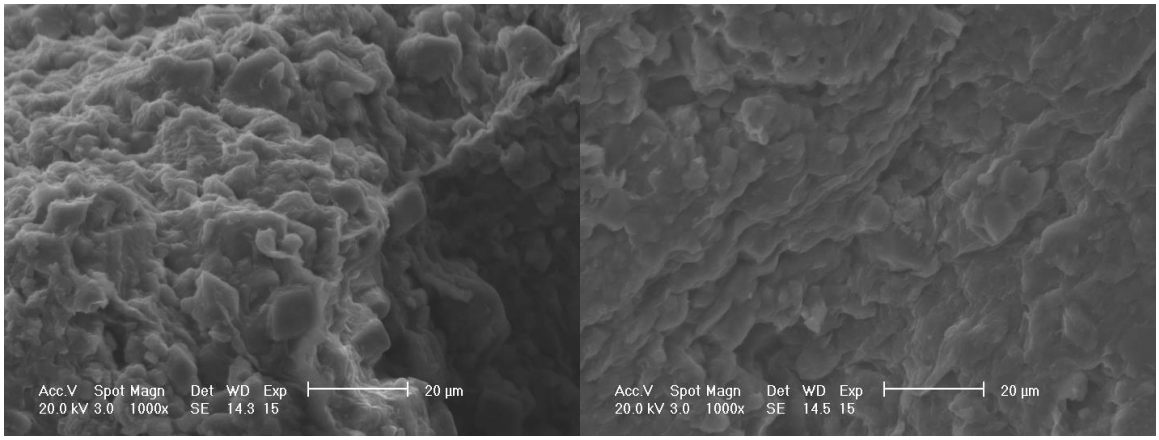

Figure 3.42: SE micrographs of B-31 from a depth of 0 to 2 ft from center of specimen

As with the imaging performed on the field-sampled portions of the Eagle Ford and Behring clays, a high amount of clay clusters and small, plate-like clay minerals is observed in the in-situ boring specimen. The amount of clay clusters was more significant for the in-situ specimens at low magnifications than the field-sampled portions of the Eagle Ford and Behring clays, indicating that the sampling technique can additionally affect the soil fabric. The orientation of the clay particles again indicates that the soil fabric of field soil deposits is neither flocculated or dispersed. To verify these trends, an additional region of the in-situ specimen, closer to the edges where the specimen was trimmed, was imaged as shown in Figure 3.43. The region closer to the edges was selected as it was expected to provide insight into the orientation of clay minerals parallel to the ground surface.

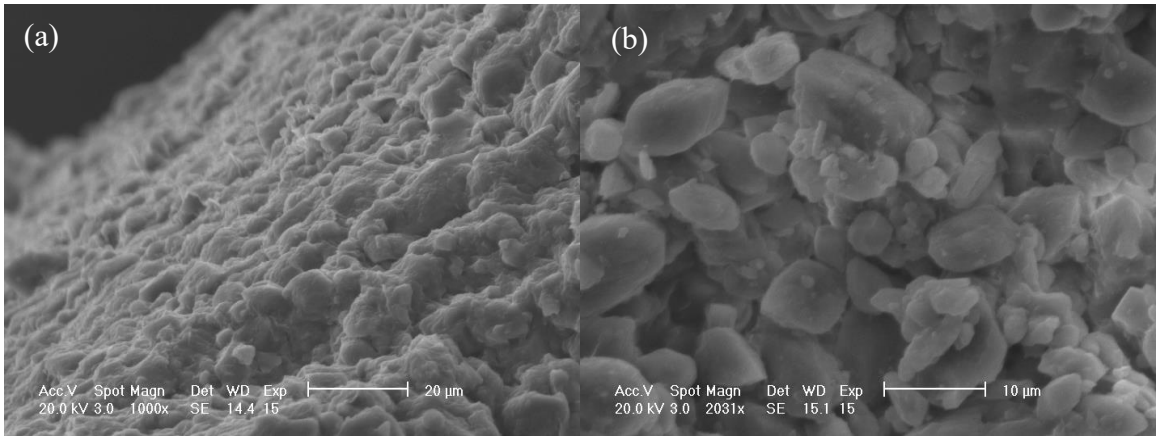

Figure 3.43: SE micrographs of B-31 from a depth of 0 to 2 ft from the edge of the specimen (a) and near the edge of the specimen (b)

Along the edge of the specimen (Figure 3.43a), the clay clusters and peds are in a relatively parallel orientation, indicating a dispersed soil fabric. However, at the trimmed surface near the edge (Figure 3.43b), a more random orientation and assortment of the clay clusters is observed. Both micrographs also indicate that the laminar clay minerals are not as prevalent as in the laboratory-reconstituted specimens of the Eagle Ford clay. Instead, there are a significant amount of clay clusters and smaller clay minerals that are visible. These results are consistent with imaging conducted on the top surface of the boring specimen in Figure 3.42. In general, the soil fabric of the in-situ specimen is neither dispersed or flocculated, and the soil fabric depends upon the orientation of clay clusters instead of clay minerals.

Laboratory-reconstituted specimens of boring B-31 from a depth of 0 to 2 ft were additionally evaluated. These specimens were grouped into either air-dried and oven-dried specimens in order to evaluate the effect of the drying temperature on clay mineralogy. Specimens were trimmed from laboratory-reconstituted specimens. Imaging was conducted perpendicular to the bedding (i.e. the SEM micrographs examined the

surface of compaction of the specimens). Micrographs of both laboratory-reconstituted specimens at a low magnification are shown in Figure 3.44.

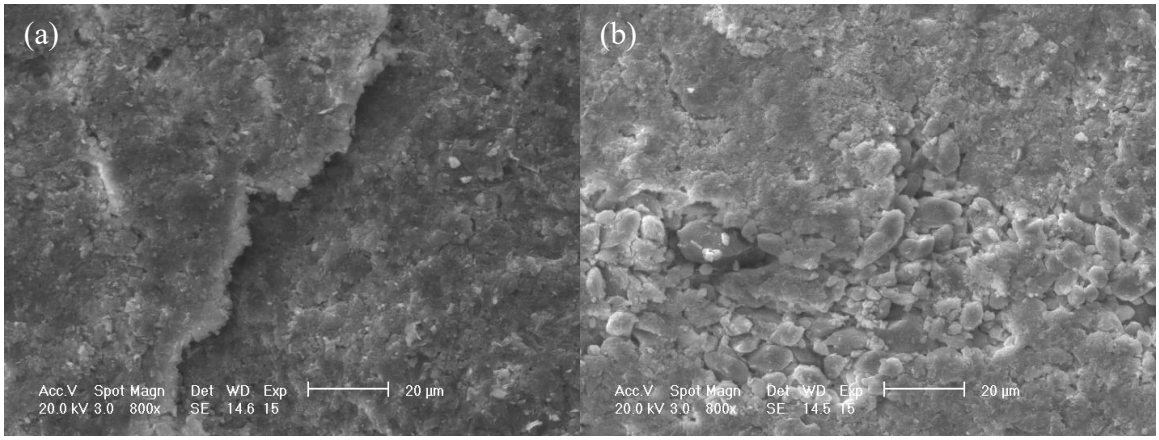

Figure 3.44: SE micrographs of laboratory-reconstituted oven-dried (a) and air-dried (b) specimens of B-31 from a depth of 0-2 ft

Despite the low magnification, both specimens indicate that the surface of the clay differed significantly from the in-situ specimens in Figure 3.42. The overall surface appears smooth and dispersed, presumably due to the compaction of the clay specimen and orientation of the surficial clay particles. As with the results from first condition, the laboratory-reconstituted specimens tend to have larger clay plates and particles than the in-situ specimens. There appears to be distinct macro-voids between clay peds in both the air-dried and oven-dried specimen. This macro-void indicates that clay peds may not come into complete contact during the compaction of laboratory-reconstituted specimens, which is expected to reduce the swelling. The difference in the size of the clay plates and particles can be assumed to affect the swelling characteristics of the soils. The in-situ soils will have a higher amount of clay to clay contact that will increase in the swelling, consistent with the results from Section 3.4.3. Additionally, the less uniform orientation of the clay peds and clusters for the in-situ specimens are assumed to increase the

hydraulic conductivity, resulting in a decreased time to the end of primary swelling. Again, this behavior is consistent with the results from Section 3.4.3. Between the two laboratory-reconstituted specimens, the air-dried specimen tends to have a higher amount of clays clusters, particularly in the middle of the micrograph. The oven-dried specimen tends to have more laminar clay minerals. The higher amount of laminar clay minerals and a reduction in the clay clusters for the oven-dried specimen was attributed to the water attached to the clay minerals being removed during the oven drying of the soil. Due to the increased drying temperature, clay clusters can be assumed to be less prevalent due to cracking of clusters and peds with the removal of water from clay minerals. The reduction in the smaller clay clusters would be expected to reduce the magnitude of swelling, consistent with the results from Section 3.4.3. Therefore, the drying temperature's effect on the mineralogy is shown to play a role in soil fabric of laboratory-reconstituted specimens.

Imaging on the laboratory-reconstituted specimens was also performed at a higher magnification. Imaging was taken near the edges of the compacted clay particles to again evaluate the orientation and structure of clay parallel to the direction of compaction. The micrographs for the higher magnification are shown in Figure 3.45.

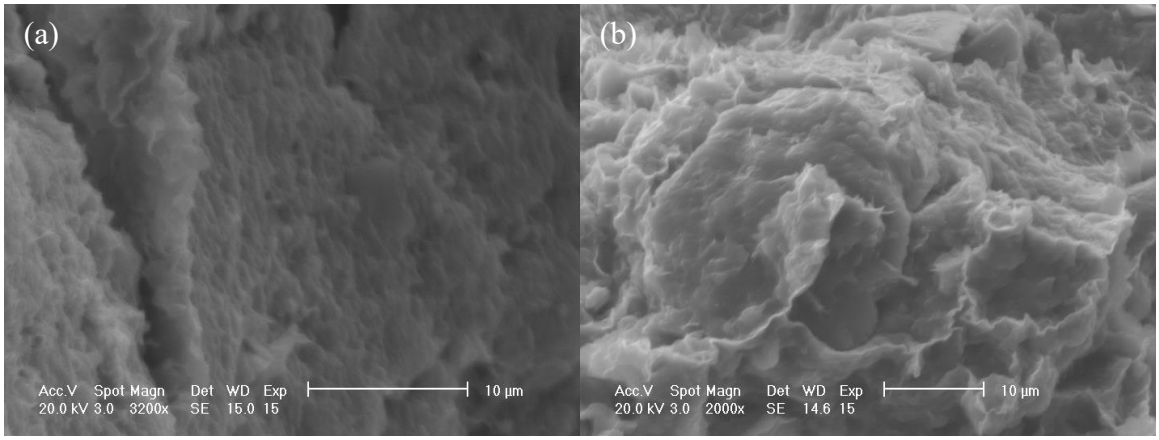

Figure 3.45: SE micrographs of laboratory-reconstituted oven-dried (a) and air-dried (b) specimens of B-31 from a depth of 0-2 ft at higher magnifications

Both laboratory-reconstituted specimens indicate that there is a high amount of plate to plate contact of clay minerals along the edges of the specimens. However, the amount of clay clusters is lower for both the oven-dried and air-dried specimens than for the in-situ specimen shown in Figure 3.43. Additionally, the clay plates are smaller for the in-situ specimen than the laboratory-reconstituted specimens. Due to these trends, the preparation of soils in the laboratory is assumed to affect the distribution of the clay particles and soil fabric at a micro-level. Differences in the micro-fabric are assumed to the cause for the differences in the swelling presented in Section 3.4.3. Based on the results from boring B-31, the laboratory-reconstituted specimens have significantly different soil fabric than in-situ specimens.

To evaluate the consistency of the trends from boring B-31, samples from boring B-32 were examined. Note that borings B-31 and B-32 are located close to each other and sit in a similar soil deposit of the Houston Black clay. In-situ specimens of boring B-32 were examined along with laboratory-reconstituted specimens at both an oven-dried and air-dried state. Unlike the boring B-31, imaging was performed parallel to the bedding (i.e. the specimens were rotated to see the bedding in the specimens as opposed to the

compaction surface). Micrographs of in-situ and air-dried, laboratory-reconstituted specimens of boring B-32 are shown in Figure 3.46.

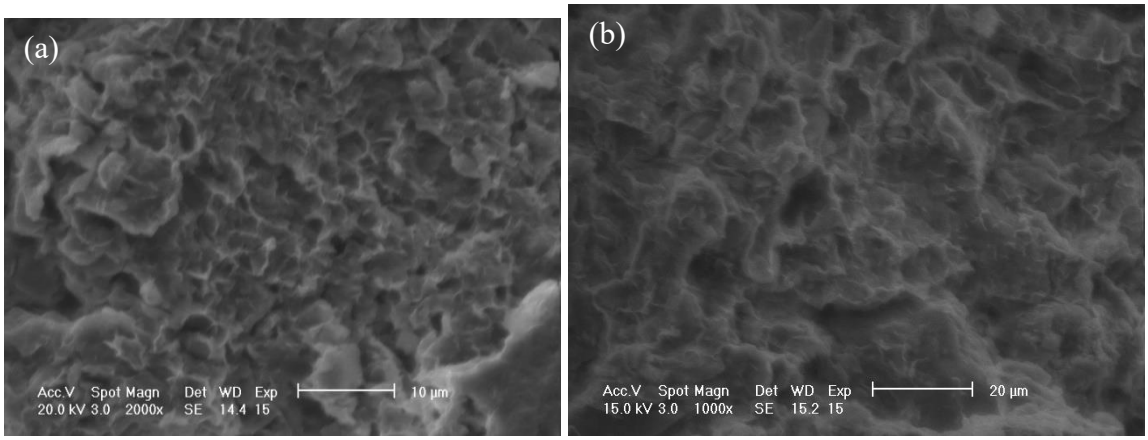

Figure 3.46: SE micrographs of in-situ (a) and laboratory-reconstituted air-dried (b) specimens of B-32 from a depth of 0-2 ft

Imaging indicates that in-situ specimen tends to have a more random orientation of clay plates than the laboratory-reconstituted specimen. Similar to the results from boring B-31, the laboratory-reconstituted specimens tend to have a high amount of laminar clay particles. The in-situ specimen tended to have a significant of laminar clay particles. However, the orientation of the clay minerals is not as layered as the laboratory-reconstituted specimens, and the size of the laminar clay particles is smaller than those from the laboratory-reconstituted specimens. Micro-voids are overserved to be more significant in the micrograph for the in-situ specimen due to smaller clay plates. Therefore, the soil fabric of in-situ specimens is neither dispersed or flocculated and differs significantly from the laboratory-reconstituted specimens.

To evaluate the effect of the drying temperature on clay mineralogy, additional laboratory-reconstituted specimens from boring B-32 that were either air-dried or oven-

dried were evaluated. Micrographs of oven-dried and air-dried specimens are shown in Figure 3.47.

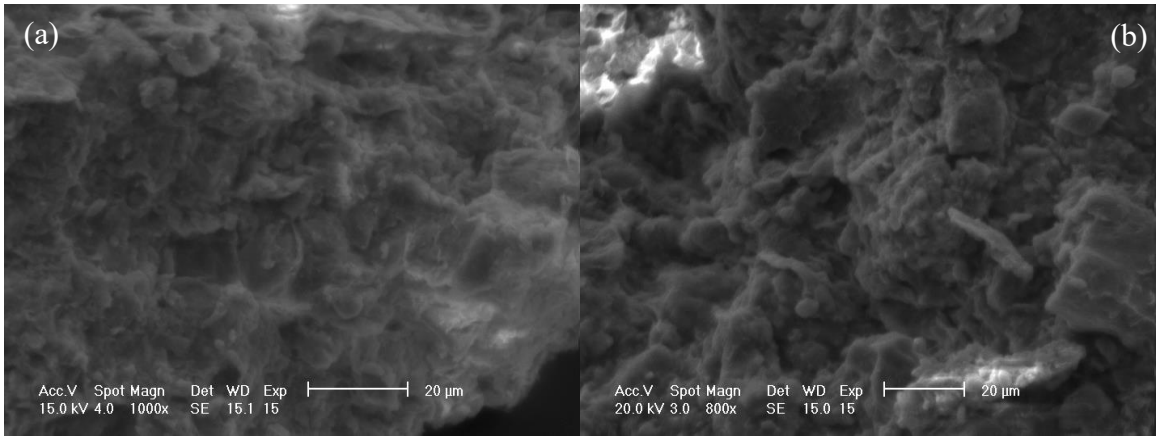

Figure 3.47: SE micrographs of laboratory-reconstituted oven-dried (a) and air-dried (b) specimens of B-32 from a depth of 0-2 ft

The micrographs indicate that there is a higher amount of clay clusters and particles in the air-dried specimen than the oven-dried specimen. This result is consistent with the trends from boring B-31. However, the laminar plate to plate contact of the clay minerals is not as dispersed as the results from boring B-31. Charging of the clay minerals for both laboratory-reconstituted specimens of boring B-32 limited imaging of the specimens.

To examine the change in soil fabric with depth in expansive soil deposits, specimens from the lowest 2 ft section of boring B-31, at a depth of 6 to 8 ft below the ground surface, were additionally examined in the ESEM. The soil fabric was expected to differ in this region due to the depth and a reduction in the amount of cyclic wetting and drying cycles. From the field logging of the specimens shown in Table 3.9, the soil tends to be more similar to the parent material, an underlying shale, at depth. Specimens from B-31 were oriented perpendicular to the bedding. Micrographs for the lowest section of boring B-31 are shown in Figure 3.48.

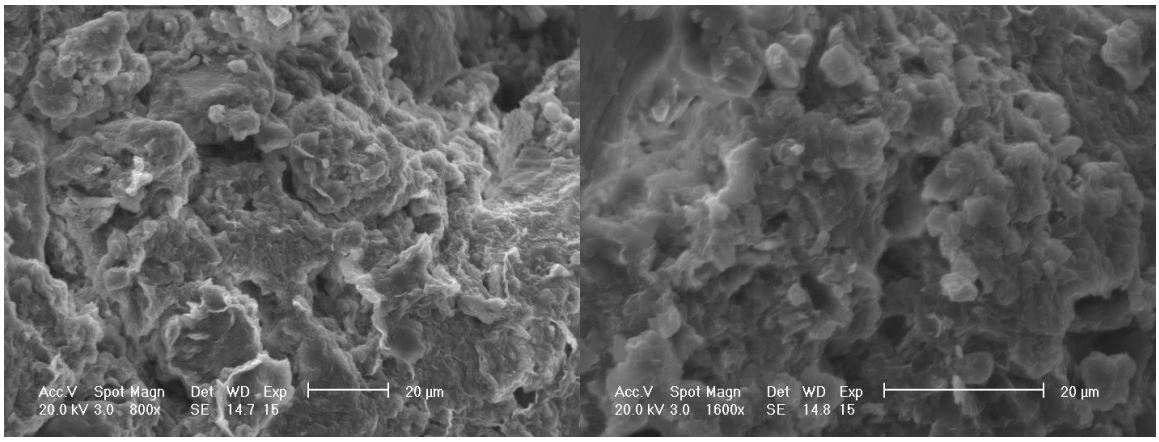

Figure 3.48*:* SE micrographs of in-situ specimens of B-31 from a depth of 6 to 8 ft

As with the specimens closer to the ground surface, clay clusters were significant for the specimens. However, size of the clay clusters did vary more significantly than the clay clusters closer to the surface shown in Figure 3.42. The clay clusters tend to be larger at depth than near the surface. This trend may indicate that cyclic wetting and drying is the primary cause for the smaller clay clusters and particles due to cracking of the internal clay structure. Macro-voids were present between clay clusters, but these voids were attributed to the sample preparation as opposed to the influence of the active zone.

Micrographs for laboratory-reconstituted specimens of soil taken from the lowest 2 ft section are shown in Figure 3.49 for both an oven-dried and air-dried state.

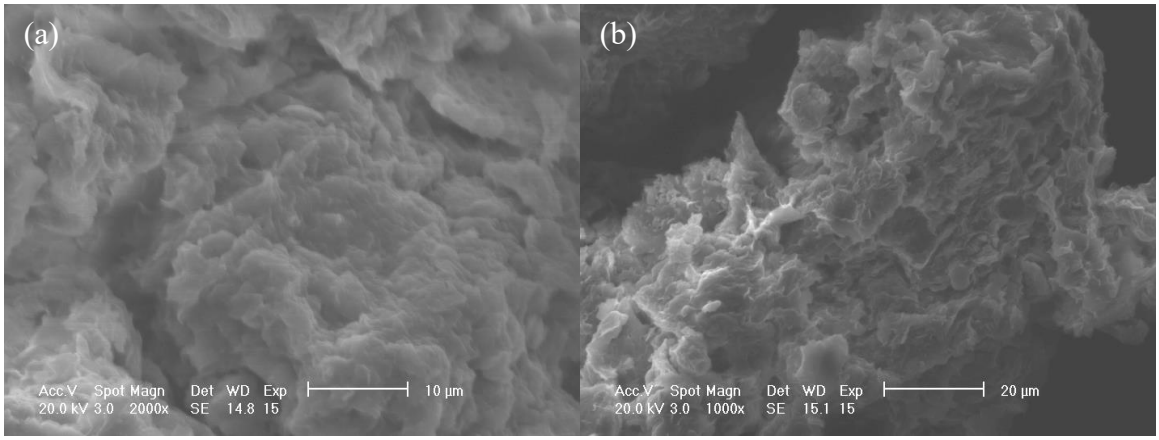

Figure 3.49: SE micrographs of laboratory-reconstituted oven-dried (a) and air-dried (b) specimens of B-31 from a depth of 6-8 ft

The amount of clay clusters was less for both specimens than the in-situ specimen. The sizes of the clay plates were also larger than the in-situ specimen. However, the soil fabric for the air-dried specimens did not differ significantly from the oven-dried specimen. The similarity of the soil fabric could indicate that the soil at depth may not be as affected by the drying temperature. The reduction in the effect of the drying temperature was attributed to the soil at depth being more similar to the underlying parent material and shale and the reduced amount of cyclic wetting and drying at depth.

To verify the results from the lowest 2 ft section of boring B-31, specimens from the lowest 2 ft section of B-32 were also evaluated in the ESEM. Micrographs from the in-situ and air-dried laboratory-reconstituted specimens are shown in Figure 3.50. Imaging was again performed parallel to the bedding (i.e. the specimens were rotated to see the bedding in the specimens as opposed to the compaction surface).

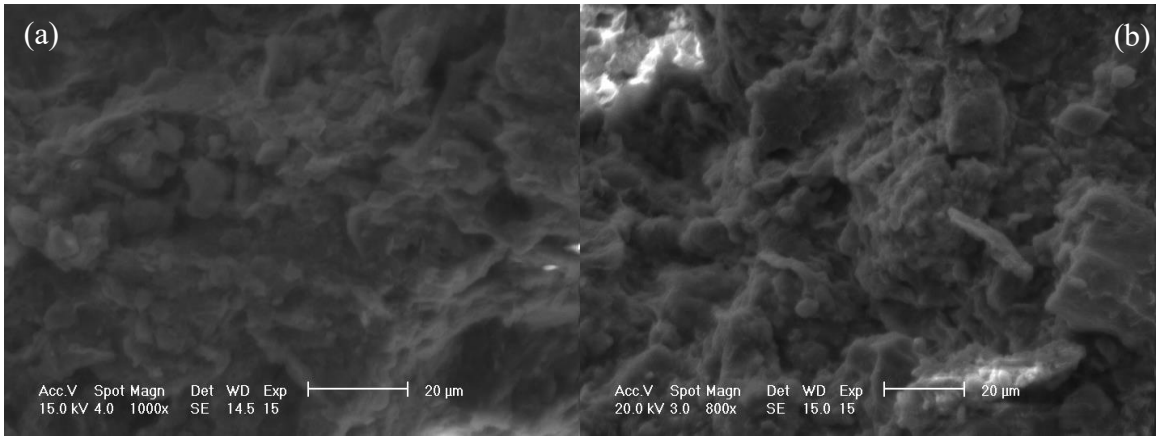

Figure 3.50: SE micrographs of in-situ (a) and laboratory-reconstituted air-dried (b) specimens of B-32 from a depth of 6-8 ft

The soil fabric of the in-situ specimen is more similar to the soil fabric of the laboratory-reconstituted specimen than the trends from imaging performed on specimens from near the surface. Due to the large clay clusters and particles in the in-situ specimen, the differences between the in-situ and laboratory-reconstituted specimens were not as significant. This trend differs from the results in Section 3.4.3 as the effect of the soil fabric between in-situ and laboratory-reconstituted specimens did not vary with depth.

In general, the soil-fabric of in-situ specimens differed significantly from laboratory-reconstituted specimens. The soil fabric of in-situ specimens tends to have a higher amount of clay clusters, which were not as prevalent for the laboratory-reconstituted specimens. Additionally, the clay plates tended to be smaller for the in-situ specimens than for the laboratory-reconstituted specimens. These differences attributed to the soil preparation methodology for the laboratory-reconstituted specimens and would increase the clay-to-clay contact for the in-situ specimen. This higher amount of clay-to-clay contact would increase the magnitude of swelling for the in-situ specimens, which is consistent with the results from Section 3.4.3. Additionally, in-situ specimens had a soil fabric that was neither more dispersed nor more flocculated but was a mix of both soil

fabrics. Between the laboratory-reconstituted specimens, the specimens that were air-dried tended to have a higher amount of clay clusters than the specimens that were oven-dried. This difference was attributed to the water attached to the clay minerals not being removed during drying for the specimens that were air-dried.

3.5.3 Microscopy on Cyclically Wetted and Dried Soils

To evaluate the changes in the soil fabric with wetting and drying cycles, a laboratory-reconstituted specimen of the Eagle Ford clay underwent cyclic wetting and drying in an ESEM with a Peltier cooling stage. Via the control of the temperature of the specimen with the Peltier cooling stage and the water vapor pressure with the ESEM, the relative humidity of the air around the specimen was varied to simulate wetting and drying cycles. The time for each wetting and drying cycle consisted of 20 to 30 minutes of wetting at a relative humidity of 100%, or inundation of the specimen, followed by an additional 20 to 30 minutes of drying at a relative humidity of approximately 10%. Imaging was performed using a gaseous secondary electron detector (GSE). Due to the presence of water vapor in the chamber, the resolution and magnification of the images were significantly affected. Additionally, the specimens were allowed to swell under no confinement.

The specimen used for testing was a compacted Eagle Ford clay specimen. The specimen was compacted using kneading compaction for a centrifuge-based inundation test, and a small portion, approximately a 1 mm cube, was trimmed and placed on a double- sided copper tape to reduce charging. The specimen was placed on the Peltier cooling stage that was set to a temperature of approximately 1°C. Imaging was performed at three separate sites on the specimen which had their relative locations marked in the software for the ESEM prior to the first inundation. However, due to issues with drifting

in the ESEM, the first site was unable to be used for imaging. Micrographs from this test for the second site are shown in Figure 3.51.

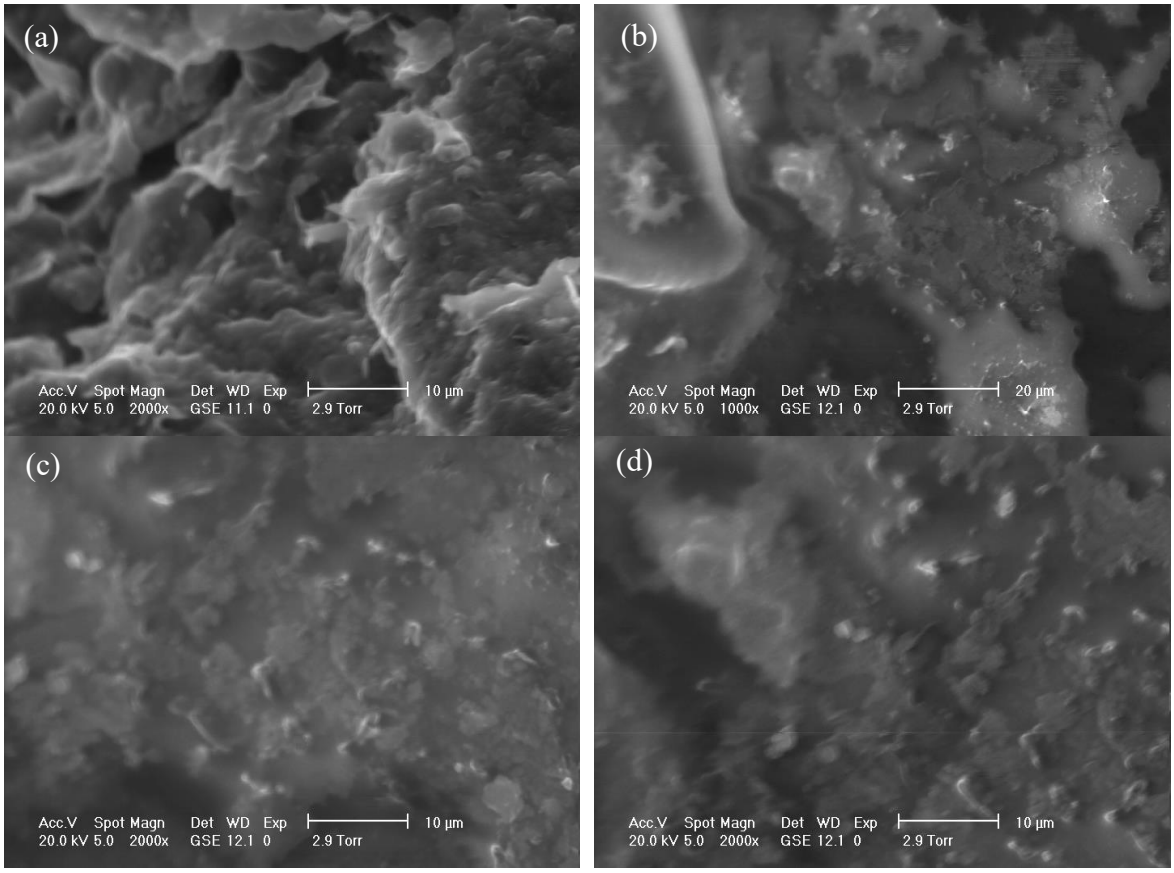

Figure 3.51*:* GSE micrographs of Eagle Ford clay at site 2 after 0 cycles (a), 1 cycle (b), 2 cycles (c) and 3 cycles (d) of inundation

The results indicate that a single cycle of the wetting-drying phase can significantly affect the internal soil fabric. The compacted clay initially tends to be at a more dispersed state, which is consistent with the results from the imaging in the first section. The clay tends to aggregate together after the first cycle, albeit the imaging becomes significantly less clear due to the change in the vapor pressure and slight movement of the particle during testing. The water from inside of the specimen does not appear to be removed during the

testing process, which may bias the results significantly. However, the outside portions of the aggregate became more smooth, similar to the micrographs from Figure 3.36 and Figure 3.37. This increase in the smoothness of the outer portion of the clay specimen indicates that the clay minerals were undergoing rearrangement during the wetting cycles. Therefore, wetting-drying cycles can significantly affect the internal clay structure. These cycles can be assumed to cause the smaller clay clusters and plates from Section 3.5.2. Micrographs of the third site during testing is shown in Figure 3.52.

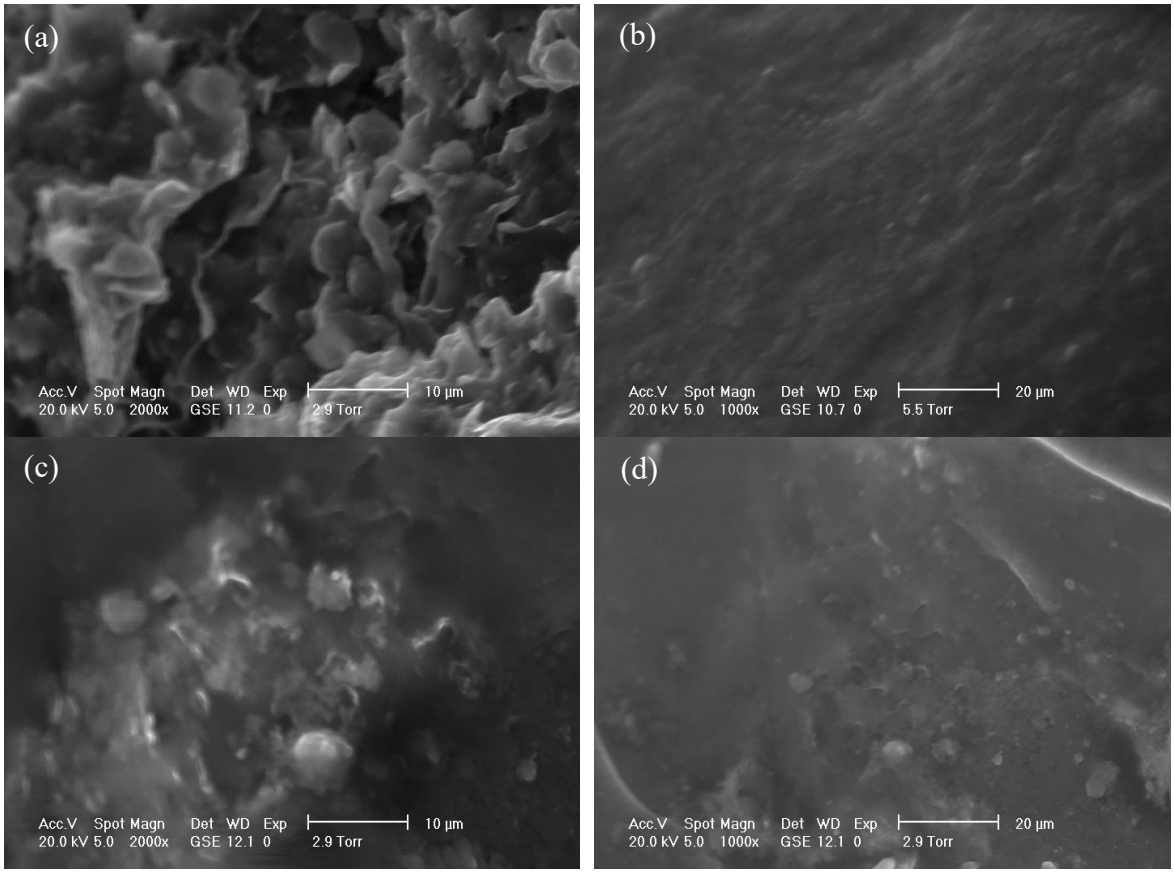

Figure 3.52: GSE micrographs of Eagle Ford clay at site 3 after 0 cycles (a), 1 cycle (b,c), and 2 cycles (d) of inundation

Imaging at Site 3 had similar trends to those from Site 2. After the first inundation cycle, significant changes occurred in the soil fabric in which the surface became "smoothed" with the re-arraignment of particles. When comparing the two micrographs at the site during the drying process, the removal of moisture from the site does allow for the particles to become slightly more flocculated, as seen in Figure 3.52c. However, by the second cycle, the increase in the flocculation of the clay minerals was not observed. Therefore, the methodology did show that rearrangement of particles occurs in expansive soils undergoing cyclic-wetting and drying. This rearrangement of particles was assumed to be the cause for the differing fabrics between laboratory-reconstituted and in-situ specimens.

Imaging done on an expansive soil specimen undergoing cyclic wetting and drying provided a visualization of the arraignment of particles. While this rearrangement of particles occurred under no confinement, the change in the fabric under a single wetting-drying cycle indicates that seasonal moisture fluctuations can significantly affect soil fabric. However, the low resolution of the micrographs due to the increase in the water vapor pressure prevented a more thorough visualization of the site.

3.6 CONCLUSIONS

An experimental testing program was performed in order to analyze the effect of soil fabric on the swelling characteristics of highly plastic clays. The overall testing program was grouped into three testing series using a centrifuge-based inundation method; Series I tested laboratory-reconstituted specimens, and Series II and III tested field-sampled specimens and laboratory-reconstituted specimens. An additional research component included the visualization of field-sampled and laboratory-reconstituted specimens using electron microscopy. Conclusions can be made based on the results from

testing using a centrifuge-based inundation method of laboratory-reconstituted and field-sampled specimens and the electron microscopy of expansive soil specimens.

From the centrifuge testing program to determine the effect of soil fabric on swelling characteristics of highly plastic clays, centrifuge-based tests were performed on laboratory-reconstituted specimens that were compacted to achieve either flocculated or dispersed soil fabric. Based on the results from testing, the following conclusions can be made:

- Soil fabric did not have a significant effect on the magnitude of swelling at the end of testing.
- Specimens with a comparatively flocculated fabric showed a slightly higher primary swelling than specimens with a comparatively dispersed fabric.
- Specimens with a comparatively flocculated fabric showed a shorter time to the end of primary swelling than specimens with a comparatively dispersed fabric.
- The trends on the magnitude of primary swelling and time to the end of primary swelling could be attributed to the higher hydraulic conductivity in the comparatively flocculated specimens.

Tests were also performed on undisturbed samples collected in-situ from expansive soil deposits. These field-sampled specimens were moisture conditioned and compared against laboratory-reconstituted specimens prepared at similar initial soil conditions in terms of γ and ω. Based on the results from this testing program, the following conclusions can be made:

- The in-situ soil fabric showed a significant effect on the magnitude of swelling. Moisture-adjusted, field-sampled specimens tended to have a higher primary and end of testing swelling than laboratory-reconstituted specimens.

- Laboratory-reconstituted specimens tended to swell over a longer time frame than moisture-adjusted, field sampled specimens.
- Laboratory-reconstituted specimens that were air-dried at 23°C tended to have a higher primary and final swelling than specimens that were oven-dried at 110°C.
- Specimens that were air-dried tended to swell over a longer time frame than oven-dried specimens.
- The trend observed on the magnitude of primary swelling and time to the end of primary swelling can be attributed to the effect of oven-drying of the soil which may have removed water from clay minerals.

For the microscopy analysis, both laboratory-reconstituted specimens and field-specimens, sampled either from Shelby tubes or in bulk, were examined in both a high-resolution SEM and an ESEM. Based on the use of microscopy, the following conclusions can be made:

- The laboratory-reconstituted specimens indicated that the macro-voids differ based on the compactive effort. Specimens at comparatively low relative compactions were observed to have a larger number of macro-voids at the clay ped interfaces than specimens at a comparatively high relative compaction.
- The laboratory-reconstituted specimens were not observed to have a significant difference with varying levels of relative compaction for the orientation of micro-voids and spacing of clay clusters.
- The field-sampled specimens were observed to have smaller clay clusters which were more randomly oriented than the laboratory-reconstituted specimens. This different microfabric indicates that the processing and

preparation of the soil significantly affects the soil fabric and was attributed for the differences in the magnitude of swelling between specimens.

- Results from a laboratory-reconstituted specimen that was imaged during wetting and drying cycles indicate that the soil fabric of laboratory-reconstituted specimens changes significantly after the first wetting and drying cycle. While these changes occurred under no confinement, cyclic wetting and drying is expected to cause the differences in clay fabric between field-sampled and laboratory-reconstituted specimens.

Chapter 4: Heterogeneity of Soils Derived from the Taylor-Navarro Groups in Central Texas

ABSTRACT

To understand the expected variability of parameters relevant to the swelling prediction of expansive soil deposits, this research component focused on quantifying differences between sampled soils on a regional and local scale. Specifically, this study focuses on soils derived from the Taylor-Navarro groups, which is typical in Central Texas. The first portion of the study examined differences in soil properties and unsaturated soil curves of bulk sampled portions of two important soils derived from the Taylor-Navarro groups, the Houston Black and Branyon clays. The Houston Black clay, whose parent material is a geologically older material, tends to more plastic and to have a higher percentage of fines than the Branyon clay. In terms of their unsaturated characteristics, the Houston Black clay tends to swell more than the Branyon clay, although the soil-water retention curves of the two soils were found to be similar. The second portion of the study involved comparison of the spatial variability of the Atterberg Limits and potential vertical rise along a 6 mile stretch of roadway under construction on the Taylor-Navarro groups. Results indicated that the distribution and variability of the Atterberg limits was similar between the more heavily sampled roadway project and from samples collected across the Central Texas region. However, the distribution of the potential vertical rise and primary swelling differed between the two scales, presumably due to the effect of the soil fabric from the undisturbed specimens used in the second study.

4.1 INTRODUCTION

As part of a research project with the Texas Department of Transportation, several expansive soil deposits were sampled in Central Texas and tested for their geotechnical

characteristics and swelling behavior (Zornberg et al., 2017). The expansive deposits were grouped into soil series based on National Resources Conservation Service (NRCS) soil survey maps. However, the expansive soil deposits in the same soil series differed in their soil properties and swelling behavior. Due to this variability, a research study was needed to evaluate the heterogeneity of expansive soil deposits in Central Texas and the variability of their soil properties and swelling behavior.

The research study to evaluate the heterogeneity of expansive soils in Central Texas was grouped into three sections. The first section focuses on the characterization of two soil series that are prevalent throughout Central Texas, the Houston Black and the Branyon clays. These two series derive from similar geologic parent material and are typically located close to one another geographically. Expansive soil deposits were sampled in bulk using an auger and subsequently homogenized for characterization and testing of their swelling behavior. The analysis evaluates the variability of soil properties, including the Atterberg Limits, optimum compaction conditions according to Standard Proctor compaction effort, and fines content, and the variability of the unsaturated soil behavior, including soil-water retention curves and stress-swell curves. The objective of this analysis is to examine the variability of expansive soil deposits from the same soil series.

The second section focuses on an evaluation of a heavily sampled portion of an expansive soil deposit along a highway in Central Texas. This location was selected in order to analyze the variability of the potential vertical rise determined from centrifuge test results and of the Atterberg Limits in a more localized region than the previous section. Additionally, the soils in this section were sampled using Shelby tubes to evaluate the variability of undisturbed, non-homogenized soil specimens. Geospatial estimators (i.e. kriging) are used to estimate the variability of the potential vertical rise in

this section. The potential vertical rise predicted from laboratory test results are compared to those from the predictive method used by the Texas Department of Transportation, Tex-124-E.

The third section compares the variability of soil properties and potential vertical rise between the regional and local scales, as evaluated in previous sections. The distribution of the Liquid Limit, Plasticity Index, potential vertical rise, and in-situ gravimetric moisture content are evaluated to determine their variability. The analysis focuses on the variability of these properties at a regional scale, using the results from the first section, and at a local scale, using the results from the second section.

4.2 BACKGROUND INFORMATION ON HETEROGENEITY OF EXPANSIVE CLAYS

In order to understand previous studies that have examined the heterogeneity of expansive soils and the geology of Central Texas, a literature review was performed. The literature review includes three sections. The first section examined the geology and the diagenesis of expansive soils in Central Texas. The second section evaluated research conducted to analyze the spatial variability of expansive soil deposits. The final section reviewed the concepts of the kriging method used for the geospatial estimation of variability.

4.2.1 Geology of Central Texas

The geology of Central Texas is foremost described the Balcones Escarpment, created from the Balcones Fault Zone, that creates two distinct regions. This escarpment in Central Texas is shown in Figure 4.1.

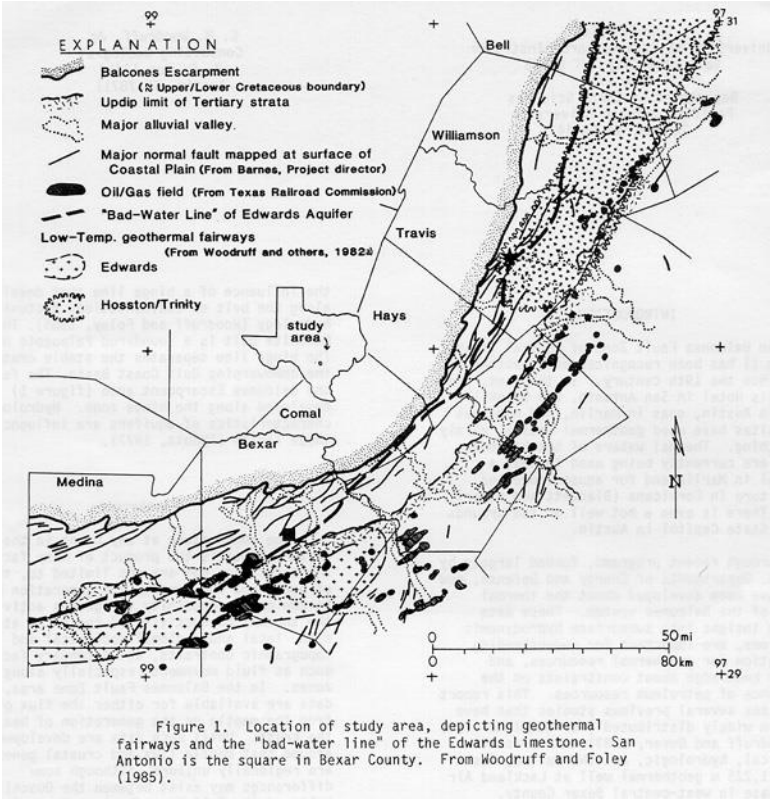

Figure 4.1: Location of the Balcones Escarpment (Foley and Woodruff, 1986)

The fault zone divides the Gulf Coast Basin to the east from the bedrock of the Texas Hill Country to the west. The area in the Texas Hill Country is predominately defined by cretaceous deposits of limestone, particularly, the Austin Chalk, Edwards Limestone, and Georgetown formation. East of the escarpment, soils consists of residuum of mudstones from the Cretaceous period and alluvial deposits from the Colorado River basin. These residuum and alluvial soil deposits form most of the expansive deposits in Central Texas.

The area immediately east of the Balcones Fault zone is commonly referred to as the Texas Blackland Prairies, shown in Figure 4.2 as Region 5 (dark gray).

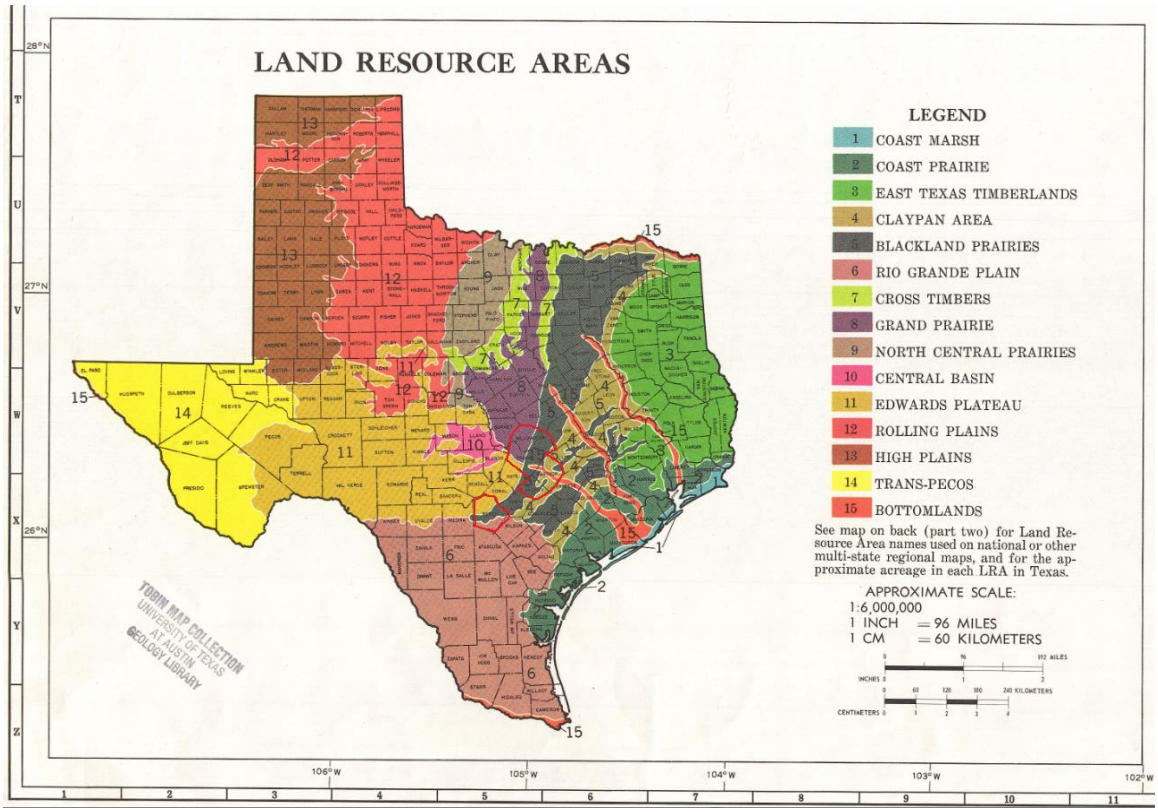

Figure 4.2: Land Resource Areas of Texas (Godfrey et al., 1968)

Two of the soils series that are prevalent throughout the Blackland Prairies are the Houston Black clay, the state soil of Texas, and the Branyon clay, which combine for approximately 27% of the soils in Williamson County and 21% of the soils in Travis County (USDA, 1974). These soils are typically found on gentle slopes and are well-known expansive soils. These soils generally derive from the underlying marl and residuum of the Taylor-Navarro groups, which leads to a calcareous, clayey soil deposits. The Houston Black clay specifically derives from residuum of the underlying marl of the Taylor-Navarro groups. The Branyon clay specifically derives from previous stream terraces whose parent material is clayey alluvium formed from Pleistocene mudstone.

Based on the parent material of the two soils, the Branyon clay is typically considered to be the younger soil deposit.

Several soil science studies have previously examined the Houston Black clay. Driese et al. (2000) evaluated the geochemical composition and mobility within gilgai topography. The microlows were shown to increase with the depth of the leaching in the deposit. The microhighs were found to draw moisture from evaporation, which precipitated metals and gypsum. Thus, differences between the microlows and microhighs increased the heterogeneity within the deposits. Driese et al. (2003) examined a Houston Black pedon for the variability of the minerals and element in the deposit. The study examined the differing amount of various elements, including sulfate, calcium, magnesium, phosphorous, and strontium, in the unsaturated portion of the soil deposit due to leaching. The researchers found that paleosols, such as the Houston Black series, may be composed of multiple parent materials. Due to the variability of the parent materials, the Houston Black series may have a significant variability between soil deposits.

Michel et al. (2013) compared the micromorphological and geochemical differences between the Houston Black and Heiden series in Texas. The Houston Black and Heiden series are typically found in close proximity in Central Texas. However, the Heiden series is typically less expansive than the Houston Black series (Zornberg et al., 2017 and Snyder, 2015). Michel et al. (2013) found that the Heiden series was observed to have parent material of marine origin (i.e. limestone) which was not present in the Houston Black series. The difference in the parent material was attributed to the Houston Black series forming on toe slopes, where chemical weathering of the parent material dominates the soil diagenesis, as opposed to the side slopes, where physical weathering

of the parent material dominates. This lack of the limestone parent material may affect the swelling behavior of the Houston Black series.

4.2.2 Spatial Variability in Expansive Soil Deposits

Previous studies have examined the variability of geotechnical characteristics of expansive soils at both a local and a regional scale. Williams (2008) used a GIS-based analysis to map the repairs to foundations with the geologic formation in the Dallas-Fort Worth area. The geologic formations and soil series were determined from geologic mapping of the area and NRCS soil survey maps. Properties of the soil series were estimated using the SSURGO database. Several properties were analyzed for the variability between the formations, including the clay content and clay mineralogy of the soil series. Results from the GIS mapping of the repairs indicated that the Bunt, Branyon, and Houston Black series were expansive soils that significantly affected the foundation of low-rise infrastructure. The Houston Black clay was especially problematic due to prevalence in the region. However, distribution of the repairs only showed general trends for the relationship between the soil properties and foundation repairs due to a high amount of scatter.

Dinka et al. (2013) examined the shrink-swell behavior across a vertisol in Central Texas. The region that was evaluated was smaller than that from Williams (2008). Seven hectares of a bermudagrass pasture was analyzed. The site contained portions of the Heiden and Houston Black series. Rods were installed at the site to measure vertical changes in the surface conditions. Moisture content sensors were installed to track changes in moisture content. Soil samples were collected at various locations to measure soil science properties. The site indicated that the runoff was negligible during seasons in which the soil was dry. After seasons in which the soil was

wet, run-off increased significantly. Using the results from the rods and moisture content sensors, the change in vertical heave with moisture storage was shown to differ based on the soil location, as shown in Figure 4.3.

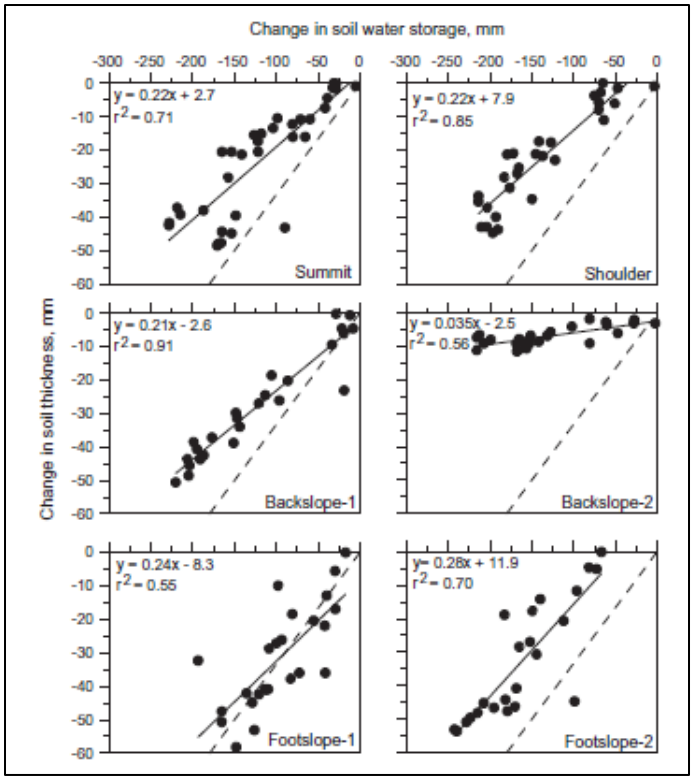

Figure 4.3: Changes in thickness with changes in water storage (Dinka et al., 2013)

Locations on the footslopes were found to see a higher amount of verticals changes with moisture fluctuations than locations on the blackslopes. The study also indicated that water loss during shrinkage was less than the commonly used 1:3 method depending on the location within the soil deposit. Combined with previous studies into the differing geochemistry and additional parent material, the geographic location of a vertisol additionally affects the properties and magnitude of heave of an expansive soil deposit.

4.2.3 Kriging and Geospatial Estimators

In order to estimate the changes in space, a geospatial interpolator is needed for analysis. The main method that was used in this study to estimate the data between data points is kriging, or Gaussian process regression. The secondary method was a linear interpolation between the data points. In order to understand these methods, a general outline of the kriging method and the interpretation of the semi-variogram is presented.

The kriging estimator involves weighing data from points closer to a given location more than data from points further away. The method utilizes an algorithm to assign weight to data points that decreases with increasing distance from the estimated location. For this research, the ordinary kriging method was used which assumes a constant mean throughout the evaluated space. The basic form of kriging, from Oliver and Webster (2014), is shown as follows:

$$Z(x) = \mu + \varepsilon(x) \tag{4.1}$$

Where μ is the mean of the properties, and ε(x) is a random quantity that has a mean of zero and a covariance that is dependent upon the special lag. Using the ordinary kriging method, the data from all the points and their distance from a given location is used to estimate ε(x).

The covariance function is determined from the semivariogram model that represents the residual of the variable. The semivariogram evaluates the difference between components that are separated by a specified lag. Previous studies, including Webster and Oliver (1993), have indicated that at least 150 points are needed to give a reliable estimation of the semivariogram. An example of a semivariogram is shown in Figure 4.4.

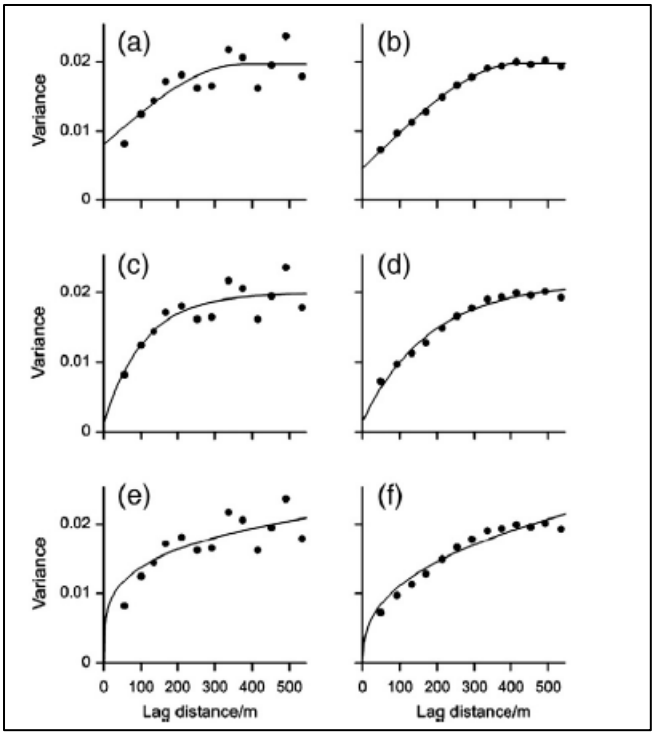

Figure 4.4: Example variogram and averaging of experimental data (Oliver and Webster, 2014)

The variogram typically involves three components. The first component is a nugget effect, which is the offset at a lag distance of 0. The second component is a sill, where the variogram appears to level out. The third component is a range, which is the distance to reach the sill. Figure 4.5 defines each of these three parameters in a typical semivariogram.

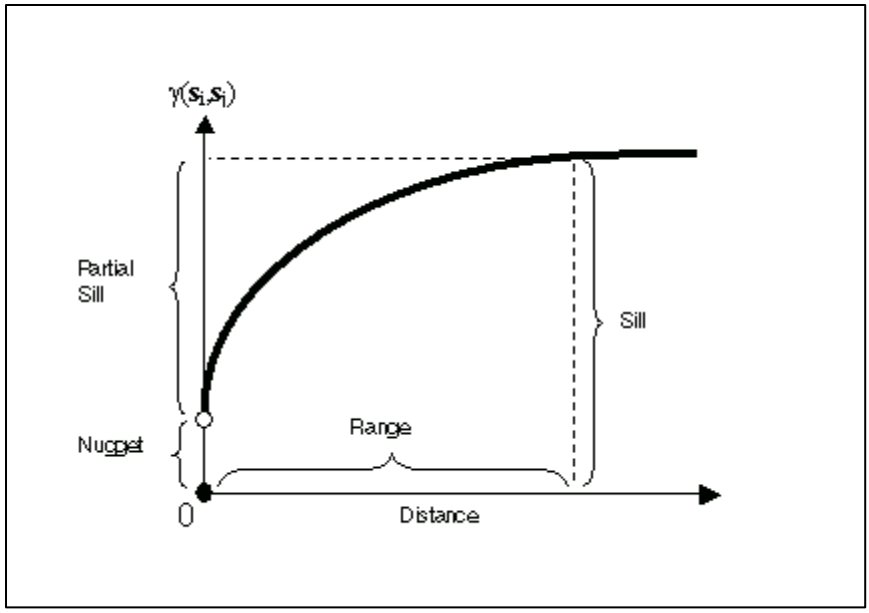

Figure 4.5: Various parameters in a variogram (ArcGIS, 2017)

An important aspect of the kriging method is the fitting of models to the semivariogram. Typically, an average of the data points in a given range is used for the fitting of the model. This averaging is done due to the amount of scatter with the variance. Figure 4.6 shows the method to average the models to fit a theoretical variogram to data sets of varying sizes. The amount of data points increases from the top left to the bottom right in Figure 4.6, and the circles are the mean values that are averaged from the surrounding values.

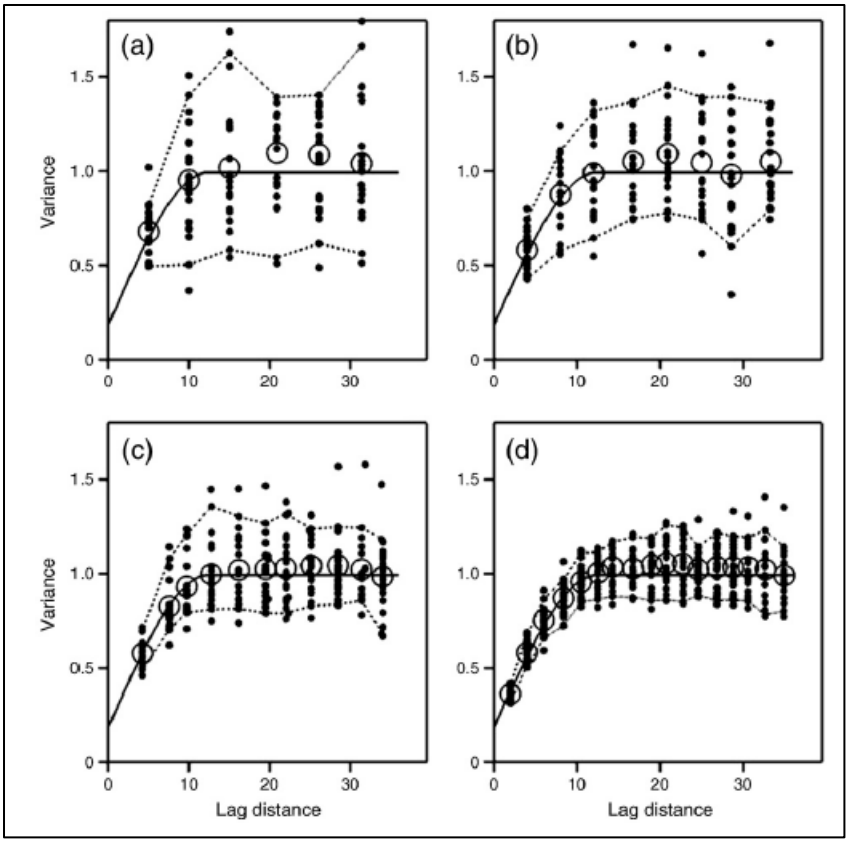

Figure 4.6: Averaging of experimental data to fit a semi-variogram. (Oliver and Webster, 2014)

The fitting of the variograms are highly dependent upon the sample size and anisotropy in the field. However, they are a key aspect of the kriging estimator as they allow for the kriging estimator to be solved with the influence of variance on the lag between points.

Research studies have previously used the kriging method to evaluate the variability of various properties versus spatial distance. Vaysse et al. (2017) used the method to evaluate the differences in the pH, organic carbon and clay content in various municipalities. Goovaerts (1999) utilized the technique and simulations to assess the uncertainty of whether critical values would be exceeded for specific soil properties.

Thus, the method is a well-used technique that can be applied to estimate the soil properties over a wide range of distances.

4.3 Results from Bulk Sampled Portions of the Taylor-Navarro Groups

Over the course of various research projects conducted for the Texas Department of Transportation, multiple locations of the Houston Black and Branyon clay in Central Texas were sampled in bulk and characterized for their soil properties, soil-water retention curves, and stress-swell curves. Soils deposits were sampled either by collecting augered soil up to a depth of 3 ft from the ground surface or by collecting hand samples from exposed portions of the deposit. In total, 13 locations of the Houston Black were sampled, and 6 locations of the Branyon clay were sampled. The sampling locations for the two soils in Central Texas are shown in Figure 4.7. The Houston Black clay sampling locations are shown in red, and the Branyon clay sampling locations are shown in blue. All of the sites are east of the Balcones fault zone on the Texas Blackland Prairie. A summary of the sampling locations and the soil horizons from USDA soil surveys are listed in

Table 4.1. The soil survey map unit is divided into the soil series (i.e. Br for the Branyon clay) and the soil horizon (i.e. A for the A soil horizon).

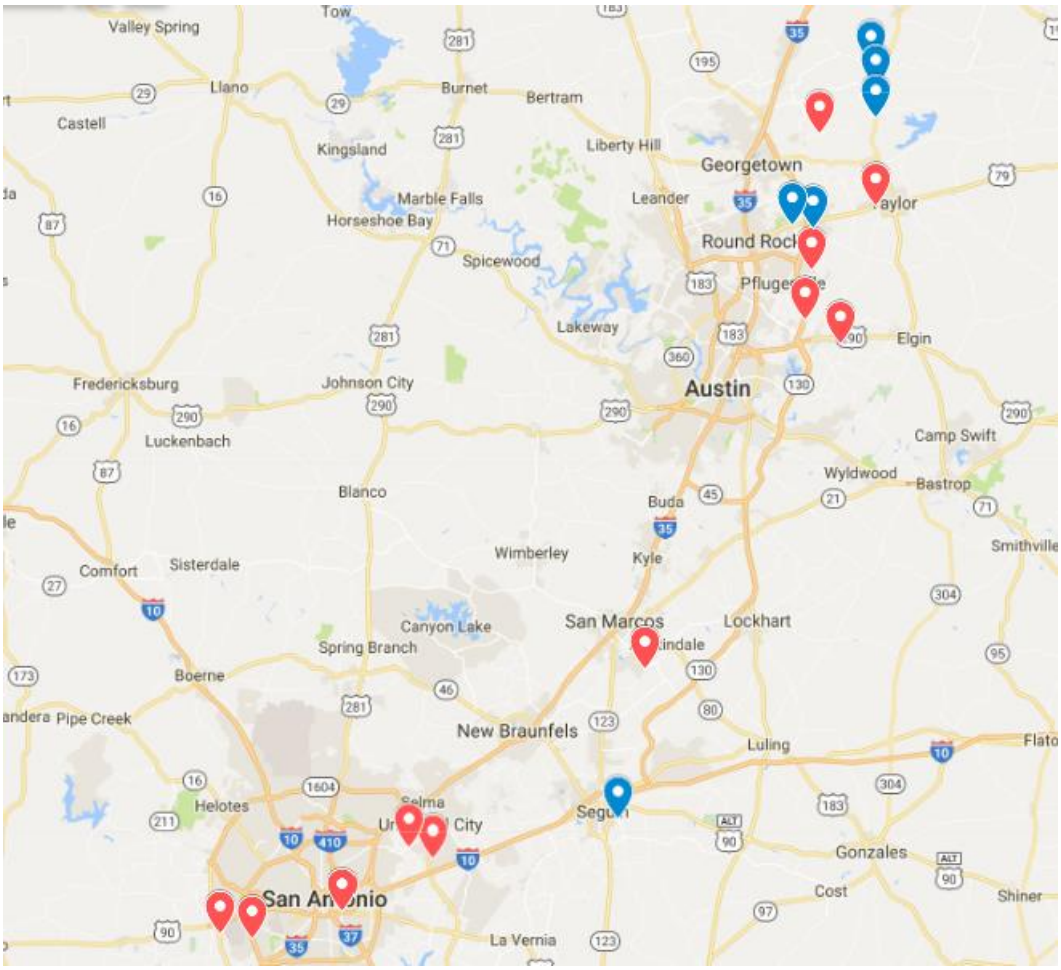

Figure 4.7: Sampling locations of the Houston Black and Branyon clays

Table 4.1: Sampling locations for the Taylor-Navarro heterogeneity analysis (USDA, 2014)

Soil Type	Soil Location	Soil Survey Map Unit	Soil Horizon
BR	FM 487	BrA	A
BR	SH-95	BrA	A
BR	FM466	BrA	A
BR	Hutto	BrB	B
BR	FM 972	BrB	B
BR	FM685	BrB	B
HB	Kelly Ln	HnA	A
HB	Manor -36	HnA	A
HB	Manor - 127	HnA	A
HB	Manor	HnA	A
HB	Gregory Manor	HnB	B
HB	FM 971	HuB	B
HB	FM1976	HoB	B
HB	Pue	HuB	B
HB	Graytown	HsB	B
HB	IH-10	HsB	B
HB	I-410	HuB	B
HB	FM1979	HsC	C
HB	Taylor TxDOT	HuC2	C

Soils were homogenized following the method outlined ASTM D421. The sampled soils were air-dried at approximately 23°C to the residual gravimetric moisture content. The air-dried soils were then passed through a rock-crusher to break up the clods and peds of the expansive soil. After the soils were processed and air-dried, the Atterberg limits, wet sieve, and hydrometer analysis were determined according to ASTM D4318 and ASTM D422. Portions of the sampled soils that were considered aggregates or river stones were removed by sieving the processed, air-dried soil through the No. 10 sieve prior to characterizing the soil-water retention and stress-swell curves. The larger soil

particles from the soil were removed to evaluate the swelling and suction measurements from clay portions of the expansive soil deposit.

The statistical analysis of the soil properties, soil-water retention curves, and stress-swell curves was grouped into two sections. The first section analyzed the variability of soil properties using histograms, probability density functions, and cumulative density functions. The second portion evaluated the variability of the soil-water retention and stress-swell curves by determining a mean curve and corresponding confidence intervals for the curves. For both sections, the variability of the properties and curves were compared between the two soil series.

4.3.1 Spatial Variability of Soil Properties derived from the Taylor-Navarro Groups

The variability of the soil properties of the sampled locations was evaluated in the first section. The soil properties that were evaluated include the Atterberg Limits as determined by ASTM D4318, the fines content as determined from wet sieve testing of the processed soil, the clay content as determined from hydrometer analyses of soil that passed the No. 200 sieve, the activity of the soil, and the optimum compaction conditions as determined by ASTM D698 using Standard Proctor compaction energy.

The Atterberg Limits (i.e. the Liquid Limit and Plasticity Index) were first analyzed as these properties are typically used in correlations for other mechanical and hydraulic properties for clayey soils. The analysis first determined the histograms for the soil properties. The bin sizes were estimated by the following equation (Izenman, 1991):

$$W = 2 * IQR * N^{-\frac{1}{3}} \quad (4.2)$$

Where W is the width of the bins, IQR is the interquartile range, and N is the number of values. The bin sizes were determined using the data from both the Houston Black and

Branyon clay. The optimal number of bins was assumed to be four or higher regardless of the calculated value from Equation 4.2. The variability of the Plastic Limit was not analyzed as the results were within a comparatively narrow range. The histograms for the Liquid Limit and Plasticity Index are shown in Figure 4.8.

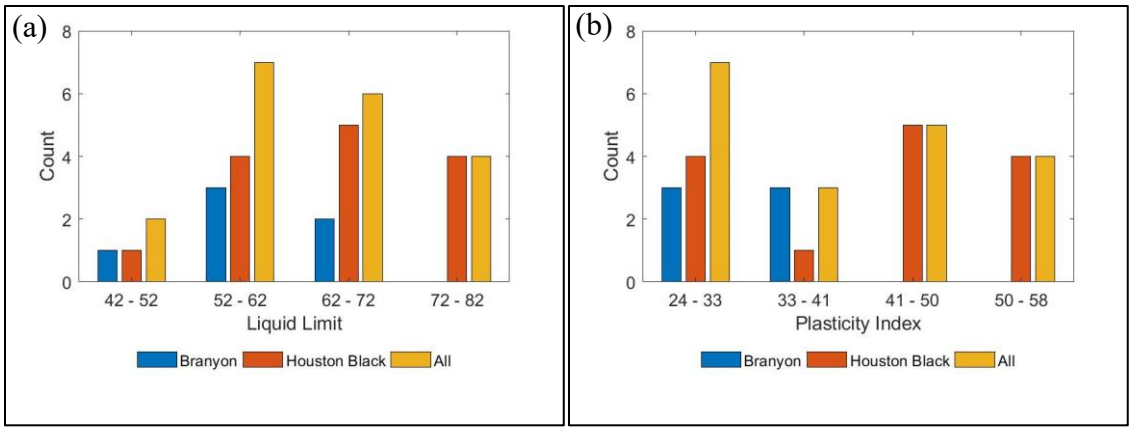

Figure 4.8: Histograms for Liquid Limit (a) and Plasticity Index (b) of sampled Houston Black and Branyon clays

The Liquid Limit and the Plasticity Index of the sampled soils were within the range of values measured in the Williamson County soil survey. The range of the Liquid Limit from the soil survey was 58-98 for the Houston Black clay and 25-80 for the Branyon clay. The range of the Plasticity Index from the soil survey was 34-72 for the Houston Black clay and 8-55 for the Branyon clay (USDA, 1983). The histograms indicate that the soil derived from older mudstone, i.e. the Houston Black clay, tend to have a higher Liquid Limit and Plasticity Index than the soil derived from more recent deposits, i.e. the Branyon clay. Based on previous research studies and predictive methods, the Houston Black clay, which tends to have a higher Liquid Limit and Plasticity Index, would be expected to have a higher potential for swelling than the Branyon clay.

In order to assess the distribution of the Atterberg Limits, an assumed normal and Weibull distributions were compared in Figure 4.9. The Weibull distribution was used as it is commonly used for grain-size distribution and failure analyses.

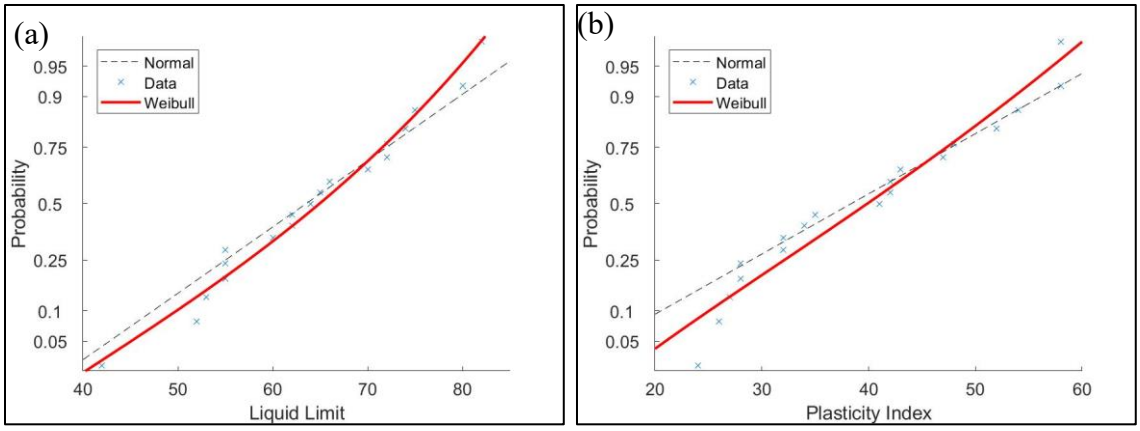

Figure 4.9: Probability plots for Liquid Limit (a) and Plasticity Index (b) of sampled Houston Black and Branyon clays

The Weibull distribution captured the distribution of the measured Atterberg Limits better than the Normal distribution, particularly at the extreme values of the datasets. Using an assumed Weibull distribution of values, the probability and cumulative density functions are shown in Figure 4.10 and Figure 4.11 for the Liquid Limit and Plasticity Index. A confidence interval of 90% was selected as the lower and upper bounds for the cumulative density function.

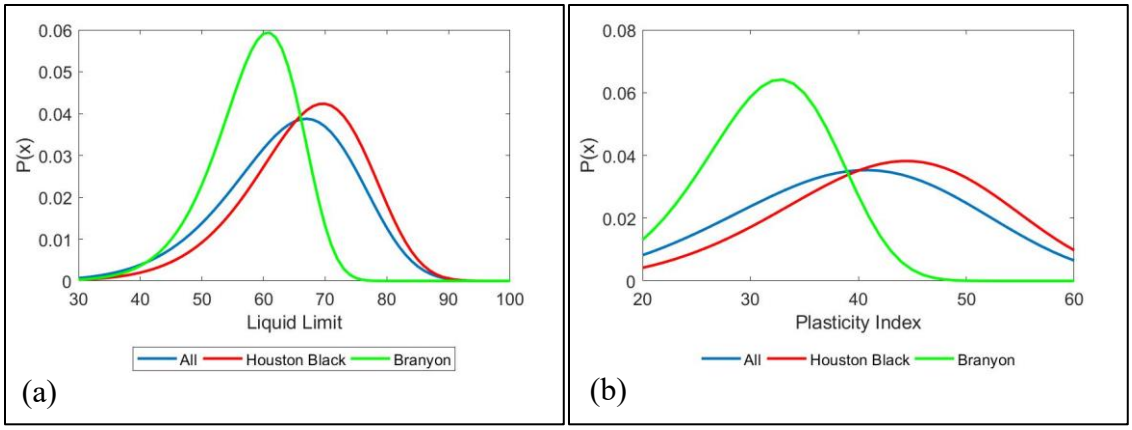

Figure 4.10: Probability density functions for the Liquid Limit (a) and Plasticity Index (b) of sampled Houston Black and Branyon clays

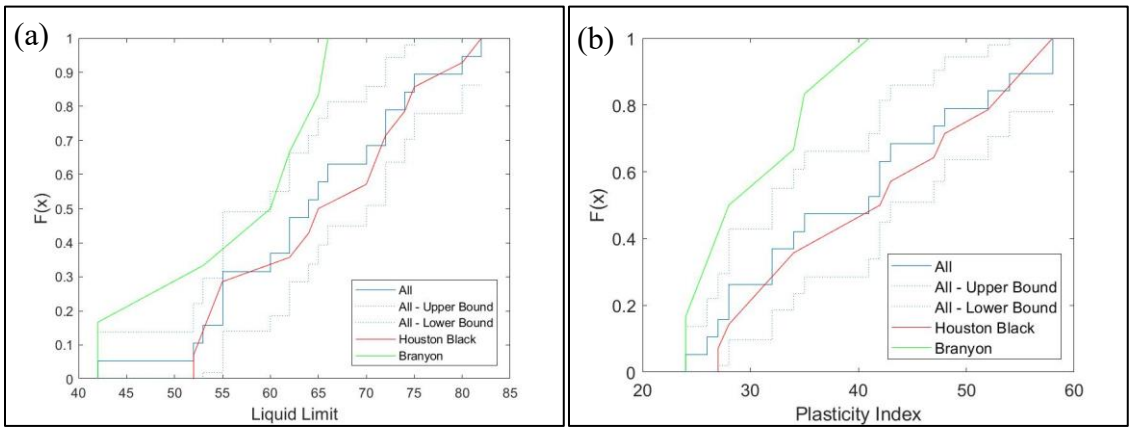

Figure 4.11: Cumulative density functions for the Liquid limit (a) and Plasticity Index (b) of sampled Houston Black and Branyon clays

Both the probability and cumulative distribution functions indicates that the Houston Black clay tends to have a higher Liquid Limit and Plasticity Index than the Branyon clay. These trends are consistent with those from the histograms. Additionally, the peaks in the probability density functions are higher for the Branyon clay due to smaller dataset.

The analysis of the histograms, probability density functions, and cumulative density function indicate that there is a significant difference between the Atterberg Limits of the Houston Black and Branyon clays. A potential explanation for these

differences is the differing depositional environment of the clays. As mentioned in Section 4.2, the Houston Black clay derives from the residuum of Cretaceous shale. The Branyon clay derives from the erosion and alluvial deposition of younger mudstone from the Pleistocene epoch. Therefore, the Houston Black clay can be deposited at the same location as its parent material, and the Branyon clay can be deposited at a different location as its parent material. These different depositional environmental can be assumed to affect the Atterberg Limits of the soil as the alluvial deposition of the Branyon clay is expected to result in a higher amount of non-clay particles and minerals.

Soil properties related to the grain-size distribution of the sampled soils were also analyzed. These properties include the fines content (i.e. the percentage of soil that passes the No. 200 sieve) and the clay content (i.e. the percentage of soil that is finer than 2 μm). Both of these properties are determined on a by-weight basis. Grain-size distributions were generated from the combined test results of air-dried, processed soils that were wet sieved and of portions of the processed of the soil that passed that No. 200 sieve that were analyzed using a hydrometer. These grain size distributions are shown for the Houston Black clay in Figure 4.12 and for the Branyon clay in Figure 4.13.

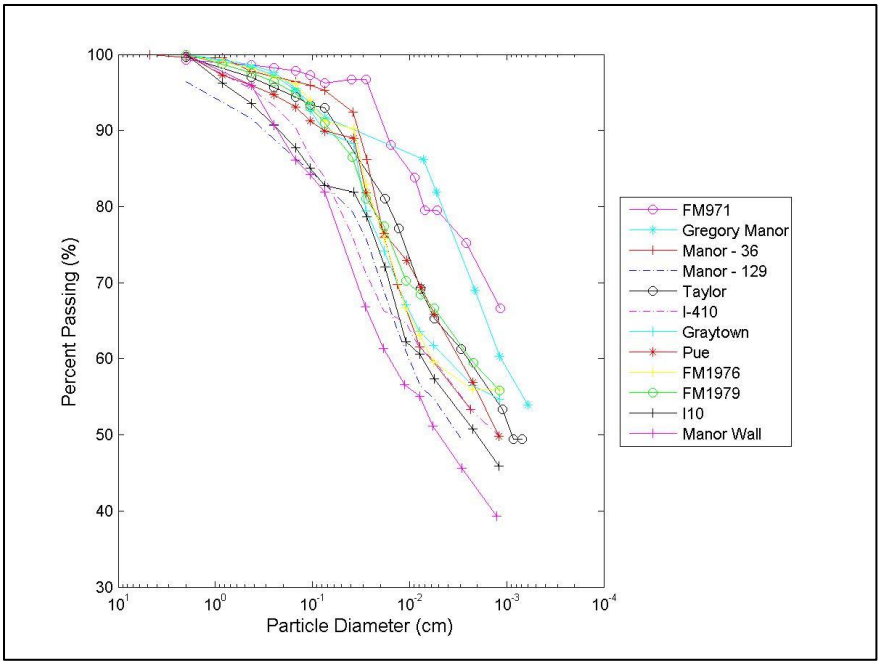

Figure 4.12: Grain-size distributions for the Houston Black clays generated using test results from wet sieving and hydrometer analyses

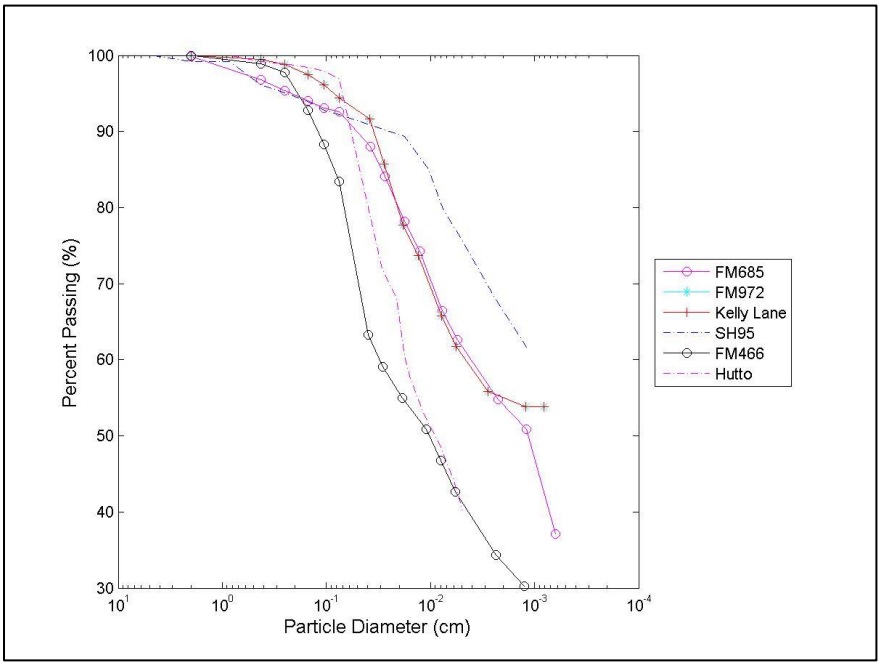

Figure 4.13: Grain-size distributions for the Branyon clays generated using test results from wet sieving and hydrometer analyses

The grain-size distributions varied between both the soil series and the sampling locations of the same soil series. To evaluate variability of the grain-size distributions of the Houston Black and Branyon clays, the fines content and the clay content were determined for each sampling location and analyzed. Histograms for both the fines content and clay content were generated using the method previously outlined for the histograms of the Atterberg Limits. The histograms for the fines content and clay content are shown in Figure 4.14.

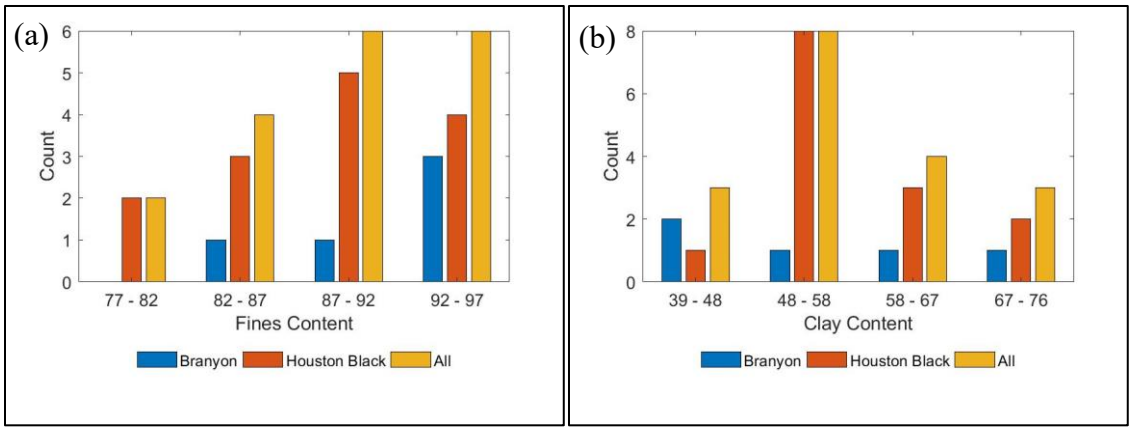

Figure 4.14: Histograms for fine content (a) and clay content (b) of sampled Houston Black and Branyon clays

The fines content and clay content tend to be higher for the Houston Black clay than for the Branyon clay. This trend is consistent with the results from the Atterberg Limits analysis as soils with higher Liquid Limits and Plasticity Indices tend to be have a higher percentage of clay minerals (Skempton, 1953). Also, the trend is consistent with the assumption that difference in the depositional environments and parent material of the clays affect the soil properties. Probability plots were generated for the distributions of the fines content and clay content using both a normal distribution and a Weibull distribution, as shown in Figure 4.15.

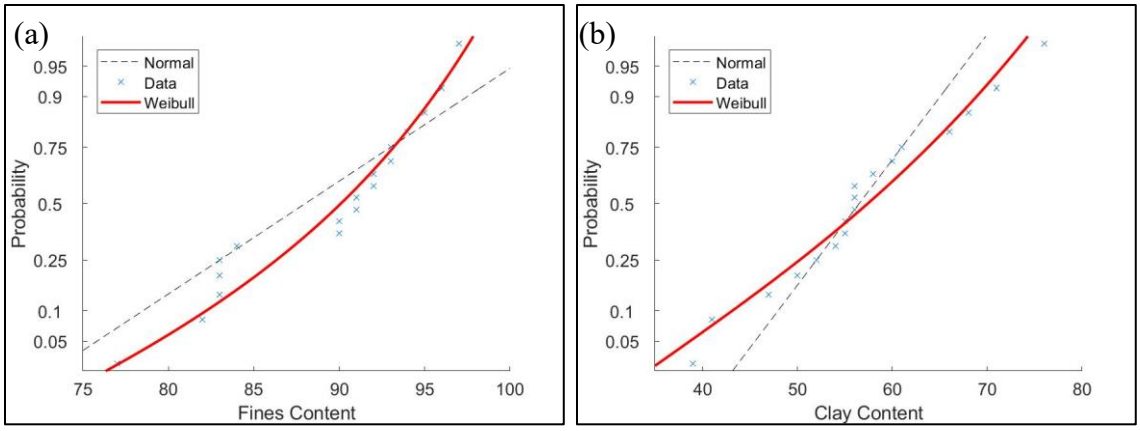

Figure 4.15: Probability Plot for fines content (a) and clay content (b) of sampled Houston Black and Branyon clays

The Weibull distribution again captured the distribution of the properties better than the normal distribution, particularly at the extremes of the dataset. Using an assumed Weibull distribution, the probability and cumulative density functions for both properties are shown in Figure 4.16 and Figure 4.17.

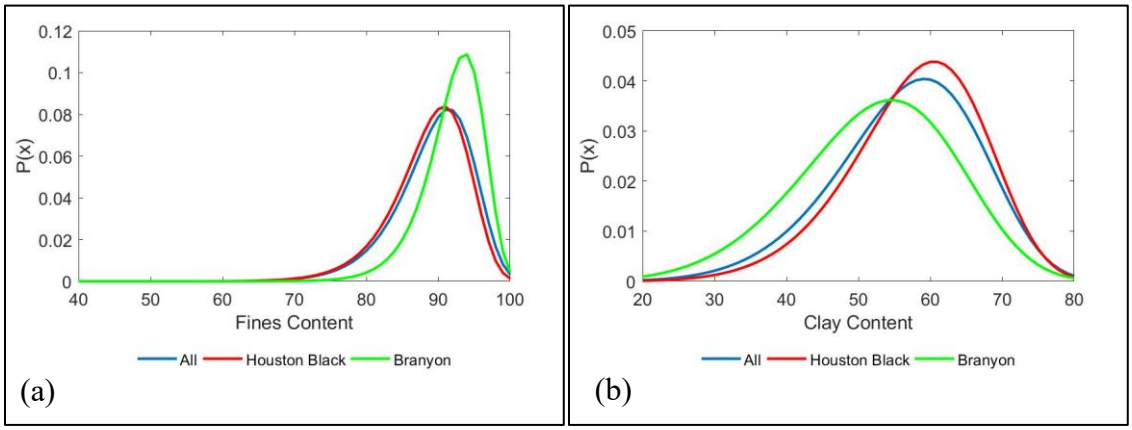

Figure 4.16: Probability density functions for fines content (a) and clay content (b) of sampled Houston Black and Branyon clays

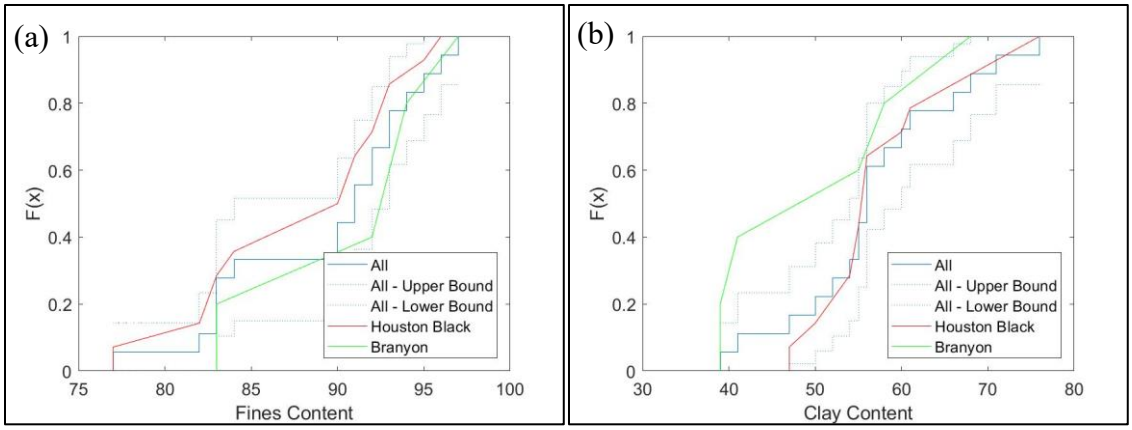

Figure 4.17: Cumulative density functions for fines content (a) and clay content (b) of sampled Houston Black and Branyon clays

The range of the liquid limit and the plasticity index were wider than the range reported by the Williamson County soil survey. The fines content ranges from the soil survey were 25-100 for the Branyon clay and 85-100 for the Houston Black clay. The clay content ranges from the soil survey were 30-60 for the Branyon clay and 40-60 for the Houston Black clay (USDA, 1983). The measured clay contents from this study exceeded than the upper bound of the range from the soil surveys. Despite these differences, the trends from the analysis were consistent with the results from the soil survey as the Houston Black clay tends to have a higher percentage of fines and clay minerals than the Branyon clay. The differences in these soil properties again can be assumed to result from the differences in the depositional environments and parent materials of the two clays.

The activity of the soil was additionally analyzed. The activity of the soil is defined as follows (Skempton,1953):

$$A = \frac{PI}{Clay\ Content} \tag{4.3}$$

Where A is the activity of the soil, and PI is the plasticity index of the soil. Previous studies indicate that soils with an activity greater 1.25 are typically considered to be an

expansive soil (Das, 2010). A histogram for the activity was determined using the method previously outlined. The histogram for the activity is shown Figure 4.18a. Additionally, the probability plot for the activity using both a normal distribution and a Weibull distribution is shown in Figure 4.18b.

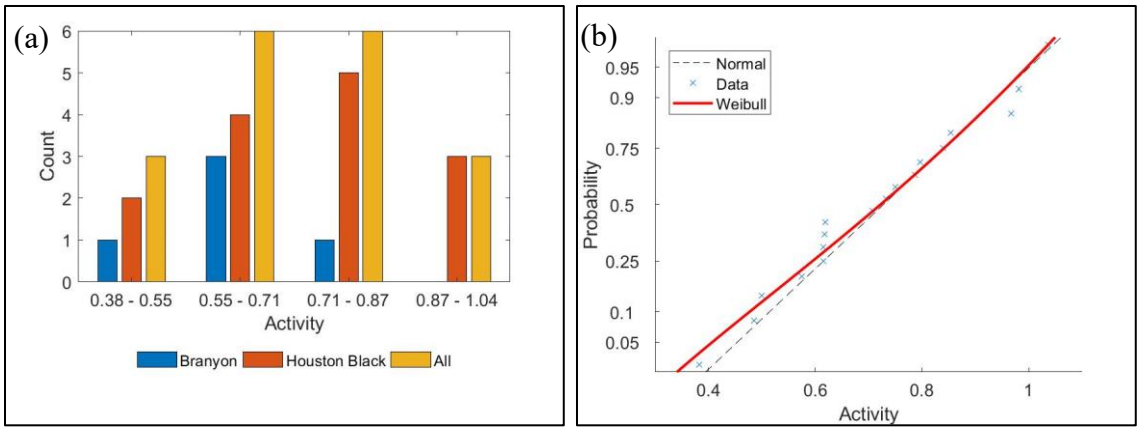

Figure 4.18: Histogram (a) and Probability Plot (b) for activity of sampled Houston Black and Branyon clays

The results indicate that the Houston Black clay tends to have a higher activity than the Branyon clay. This trend is consistent with the analyses on the distributions of the Plasticity Index and clay content. However, the activity for the sampled soils were less than an activity of 1. The smaller than expected activity values may be attributed to the clay content being determined from hydrometer analyses of soil that passed the No. 200 sieve. These hydrometer analyses may have biased the result, leading to a higher than expected clay content. Using an assumed Weibull distribution, the probability and cumulative density functions are shown in Figure 4.19.

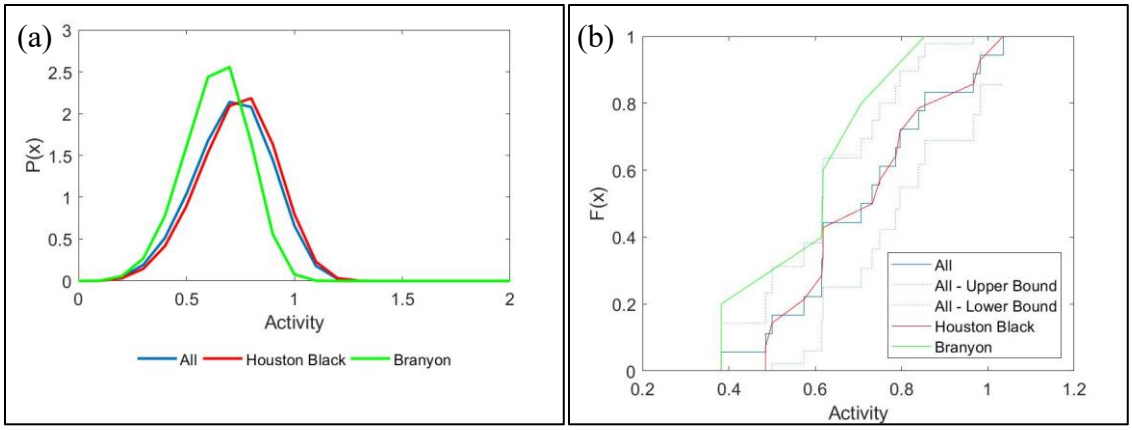

Figure 4.19: Probability (a) and Cumulative (b) density functions for activity of sampled Houston Black and Branyon clays

The results from the probability density function indicate that the activity of the Branyon clay was closer to the activity from the Houston Black clay than previous trends of the Plasticity Index and clay content would indicate. However, this result may be significantly affected by the method used to measure the clay content, as previously discussed.

Soil properties related to the optimum compaction conditions were additionally analyzed and include the optimum moisture content and maximum dry unit weight according to Standard Proctor compaction effort (ASTM D698). Histograms were again generated using the method outlined previously and are shown in Figure 4.20.

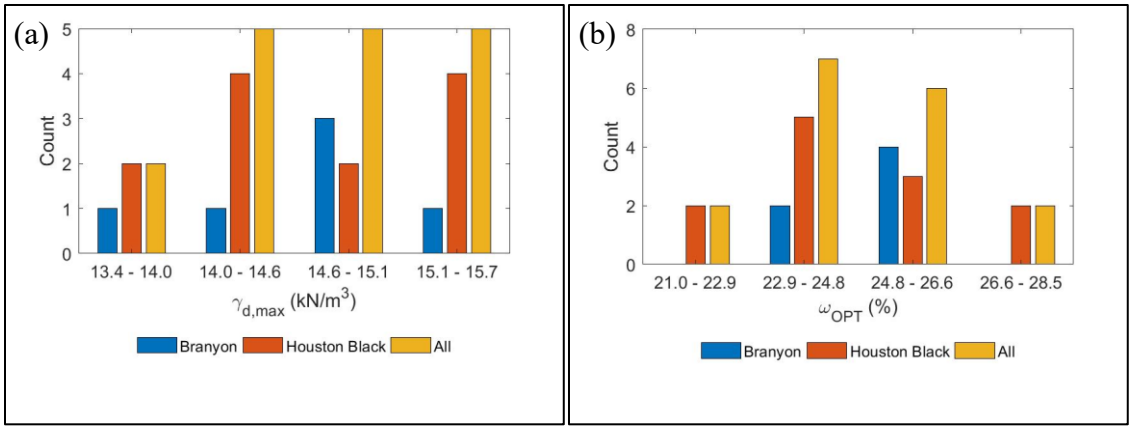

Figure 4.20: Histograms for maximum dry unit weight (a) and optimum moisture content (b) according to Standard Proctor compaction effort of sampled Houston Black and Branyon clays

Unlike previous analyses, there is not a clear trend for the optimum compaction conditions between the Houston Black and Branyon clays. To further evaluate the trends from the optimum compaction conditions, probability density functions were generated using an assumed Weibull distribution, as shown in Figure 4.21.

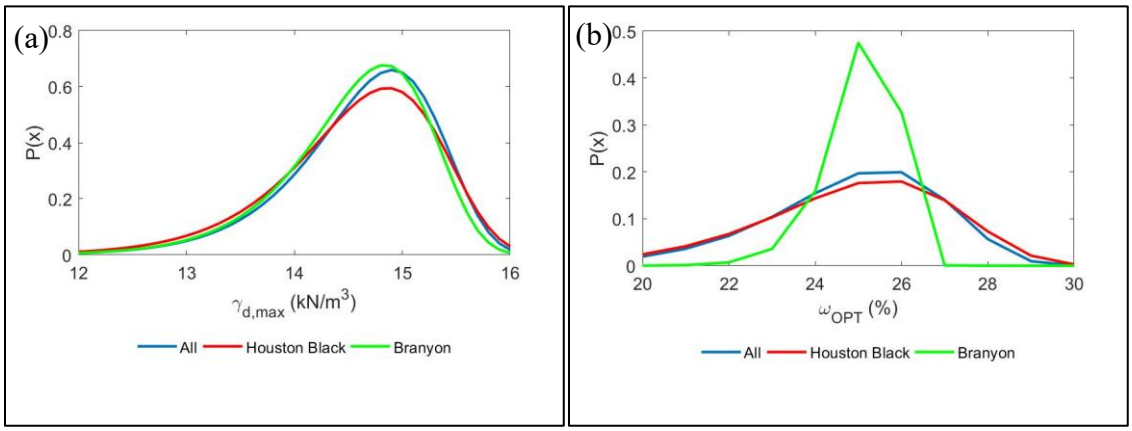

Figure 4.21: Probability density functions for maximum dry unit weight (a) and optimum moisture content (b) according to Standard Proctor compaction effort of sampled Houston Black and Branyon clays

Based on this analysis, the optimal compaction conditions did not vary significantly between the two soils. This result indicates that the use of correlations to estimate the optimum compaction conditions, such as the ones from NAVFAC (1962), are independent of soil series.

Several conclusions can be made based on the analysis of the variability of soil properties between the Houston Black and Branyon clays. The distribution of the Atterberg Limits, fines content, and clay content indicate that the Houston Black clay tends to be more plastic and with a higher percentage of fines and clay minerals than the Branyon clay. These differences were attributed to the difference in the depositional environment and parent material between the two soils. The soil that derives from older mudstone and is typically found at the site of the parent material, i.e. the Houston Black clay, tends to be more plastic and finer than the soil that derived from a younger parent material in alluvial deposits, i.e. the Branyon clay. Additionally, the method to measure the clay content may have affected the calculated activity of the soil deposits. Finally, the optimal compaction conditions according to Standard Proctor compaction effort did not vary significantly between the soil types, indicating that correlations used to estimate the optimal compaction conditions may be independent of soil series.

4.3.2 Spatial Variability in Soil-Water Retention and Stress-Swell curves from soils in the Taylor-Navarro Groups

The Houston Black and Branyon clays were also evaluated for the variability in unsaturated soil behavior, including their soil-water retention and stress-swell curves. The variability of the soil-water retention curves was analyzed as unsaturated soil mechanics significantly affects the hydromechanical behavior of the deposit. The variability of the stress-swell curves was analyzed as these curves are used for the prediction of the potential vertical rise. These predictions can indicate the potential for environmental

damages in low overburden infrastructure. Two statistical approaches were used to predict these curves. The first approach used step-wise linear regression to predict the curve-fitting parameters from measured soil properties (i.e. the Atterberg Limits, fines and clay content, activity, etc.). These predicted parameters were then used to generate curves based on a set of soil properties. The second approach calculated a probability density function using curves fitted from measurements on the sampled soils. These probability density functions were generated for the vertical strains at a given stress or the volumetric moisture content at a given total suction. These functions were then used to calculate a mean curve with confidence intervals. The step-wise linear regression method was found to be ineffective due to the relatively small data set. The models matched the curves from the sampled soils well but did not fit a hypothetical soil. Thus, the second approach that used the probability density functions was used to analyze the variability of the soil-water retention and stress-swell curves.

The total suction was measured on laboratory-reconstituted specimens from each of the sampled soil deposits. Soil specimens were compacted at a constant dry unit weight with varying initial gravimetric moisture contents. The targeted dry unit weight was the maximum dry unit weight according to Standard Proctor compaction energy, which was estimated using NAVFAC correlations (1962). The total suction was measured for each soil specimen using a chilled mirror hygrometer, the WP4C from Decagon (ASTM D6836). Total suction measurements were fitted to define a soil-water retention curve for each sampled soil. The model used for the fitting of the soil-water retention curves is shown as follows (van Genuchten, 1980:

$$\theta = \theta_r + \frac{\theta_s - \theta_r}{[1 + (\alpha * \psi)^n]^m} \tag{4.3}$$

Where θ is the volumetric moisture content of the soil, ψ is the suction of the soil, θ_s is the saturated volumetric moisture content, θ_r is the residual volumetric moisture content of the soil, α is the air entry pressure, and n and m are curve fitting parameters. The residual volumetric moisture content was assumed to be zero for curve fitting. Parameter m was estimated as follows (van Genuchten, 1980):

$$m = 1 - \frac{1}{n} \tag{4.4}$$

This model can use either the volumetric moisture content or degree of saturation. The curve fitting to define the soil-water retention was accomplished using the GRG Nonlinear Solver method from Microsoft Excel, which minimizes the root mean square error (RMSE). For the analysis of the soil-water retention curves, total suction values of 100 and 10,000 kPa were evaluated to determine the distribution model for the probability density functions. These total suction values were used as they represent the typical bounds of the total suction measured from the chilled mirror hygrometer.

For the stress-swell curves, soil specimens were tested using the centrifuge-based inundation method. Soil specimens were compacted at three percentage points dry of the optimum gravimetric moisture content and maximum dry unit weight according to Standard Proctor effort that was estimated from the NAVFAC correlations (1962). Soil specimens from each sampled location were tested at three stresses, approximately 100, 250, and 1,000 psf, to generate a stress-swell curve. The method to fit the stress-swell curve is outlined in Zornberg et al. (2017).

In order to evaluate the variability of the curves, a continuous probability distribution was assumed. Numerous continuous probability distributions were evaluated, including the normal, log-normal, exponential, chi-squared and Weibull distributions. Based on an analysis of the wellness of fits of these distributions, three distributions were

more rigorously evaluated: the normal, log-normal and Weibull distributions. Probability plots using these distribution for the volumetric moisture content at a given total suction are shown in Figure 4.22. These plots were generated at total suctions of 100 and 1,000 kPa.

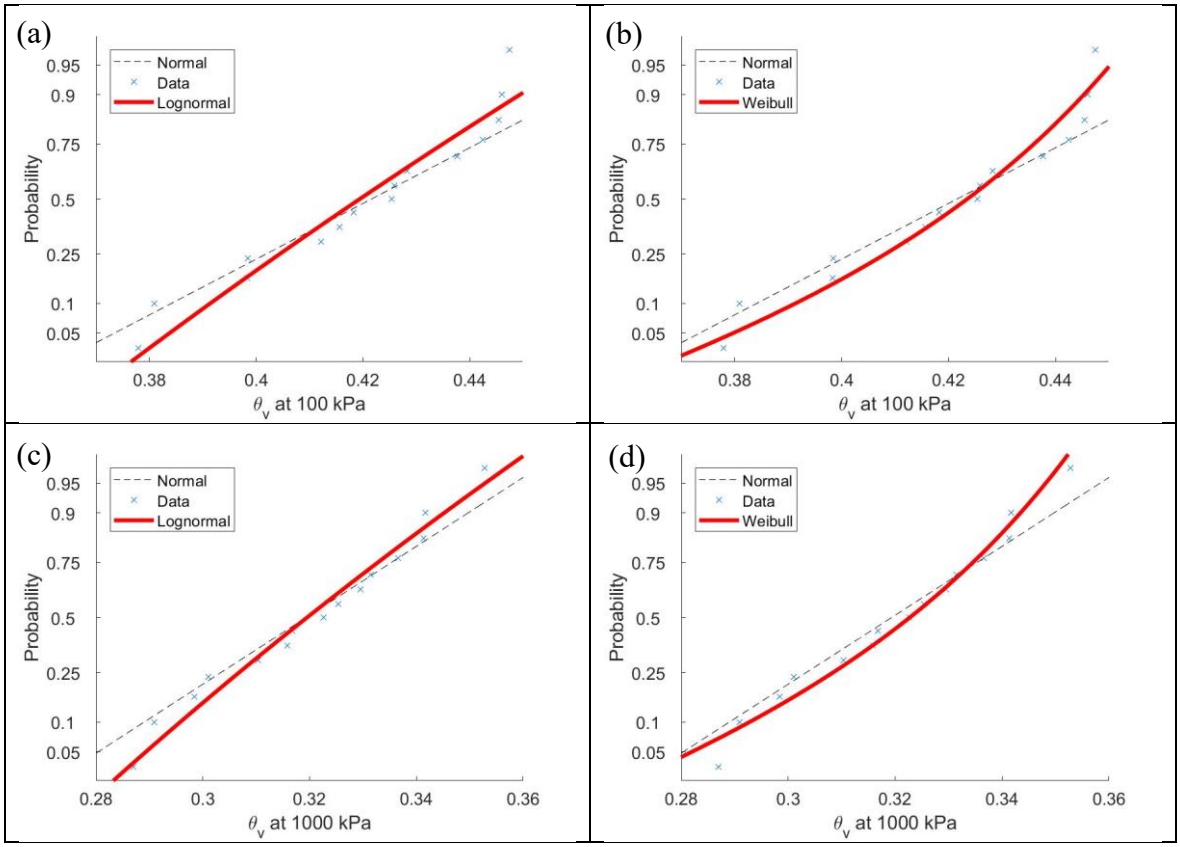

Figure 4.22: Lognormal (a,c) and Weibull (b,d) probability plots for soil-water retention curve distributions at 100 (a,b) and 1,000 kPa (c,d)

The plots indicate that the normal distribution is not suitable for this analysis due to the poor fit at the extremes. In general, both the Weibull and log-normal distributions are similar in terms of the wellness of fit. However, there are some differences in the distributions for a total suction of 100 kPa. At this suction, the Weibull distribution can fit the results at higher volumetric moisture contents better than the lognormal distribution. Due to these differences, the Weibull distribution was used for the analysis. However, confidence intervals of 90% were used in the analysis to eliminate the effect of the extreme portions of the data.

The distribution of the fitted soil-water retention curves using the volumetric moisture content are shown in Figure 4.23 for the Houston Black and Figure 4.24 for the Branyon clay. A Weibull distribution was used to evaluate the distribution of total suction for every 0.01 increase in the volumetric moisture content. Additionally, the Liquid Limit for each sampled location is shown by a corresponding color bar.

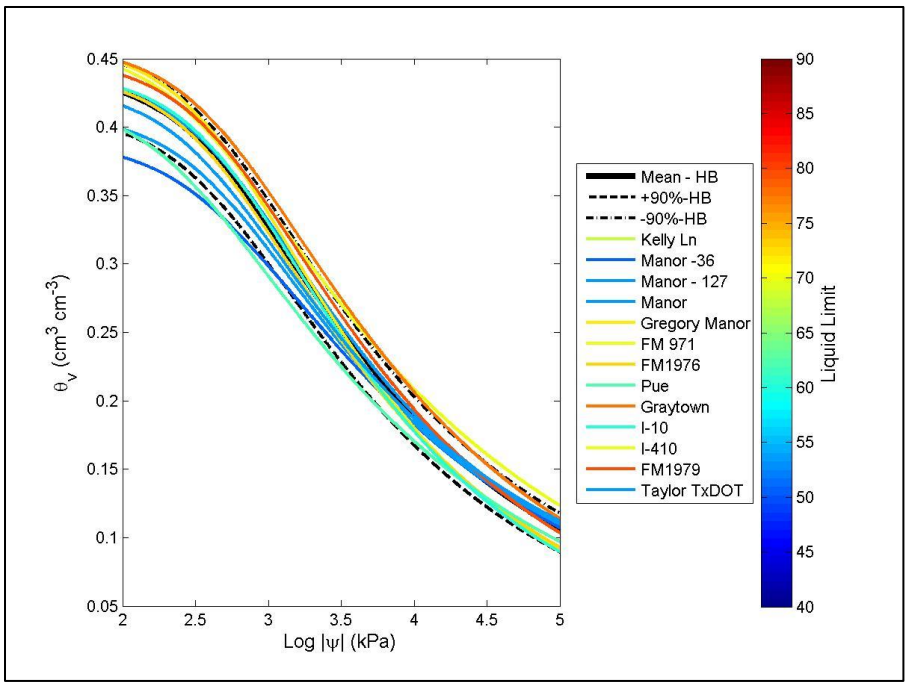

Figure 4.23: Individual and mean soil-water retention curves for sampled locations of the Houston Black clay

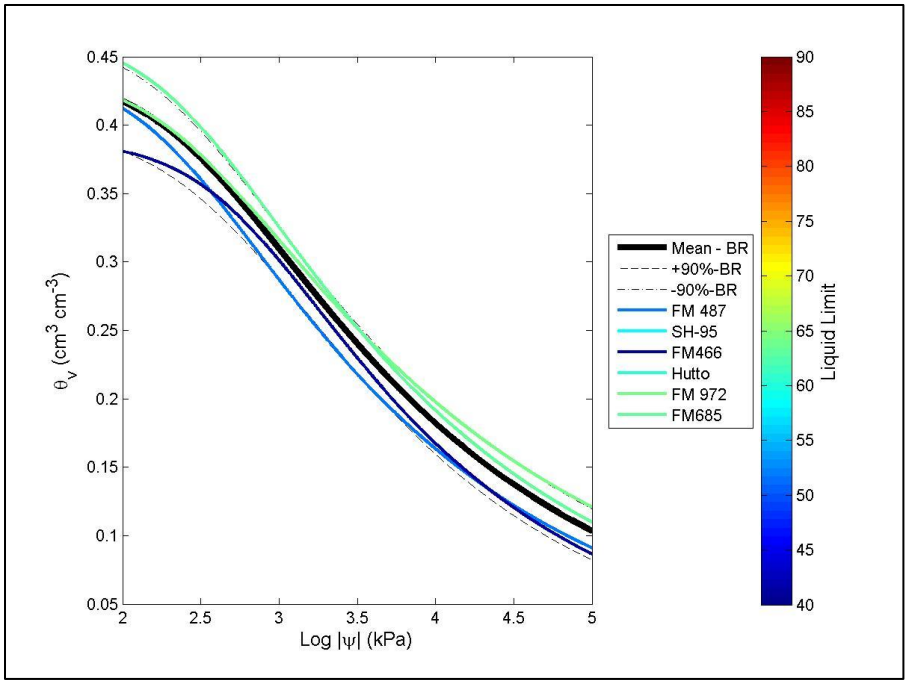

Figure 4.24: Individual and mean soil-water retention curves for sampled locations of the Branyon clay

In general, soils with a higher Liquid Limit tend to have a higher total suction at the same volumetric moisture content. This trend is consistent with previous studies and the results from Chapter 2 of this dissertation. However, the soil-water retention curves did not vary significantly between the sampling locations of the same soil series. In order to analyze the differences between the soil series, the mean distributions and confidence intervals of the soil-water retention curves are shown in Figure 4.25.

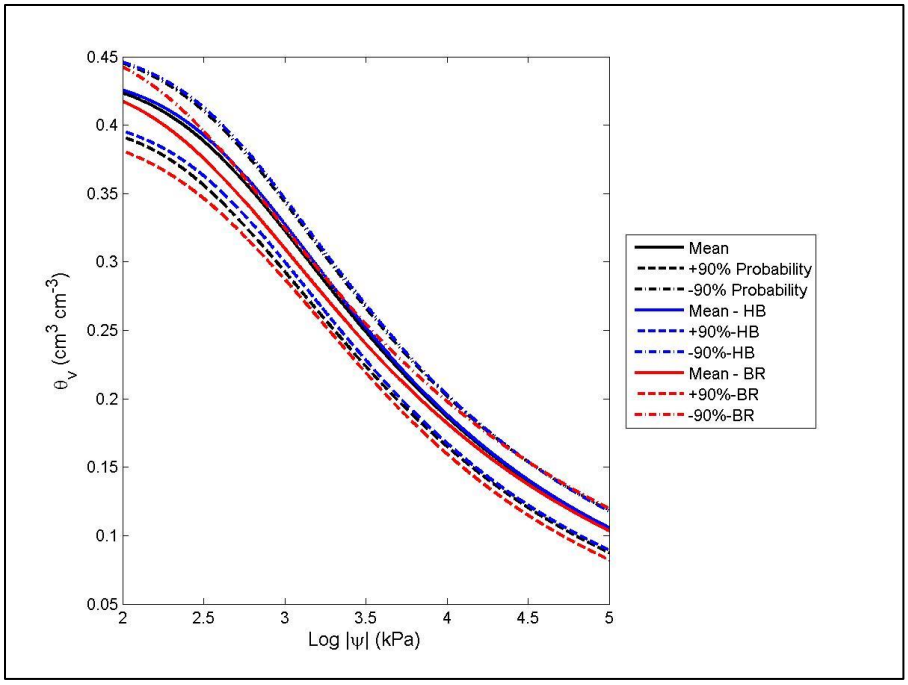

Figure 4.25: Mean and confidence intervals of the analyzed soil-water retention curves the Houston Black and Branyon clays

The mean soil-water retention curves were similar between the soil series. This result was not expected due to the differences in the soil properties and depositional environment of the soil series. However, the similarity between the soil series is consistent with the soil-water retention curves an expansive soil and non-expansive soil at the same location from Chapter 5 of this dissertation.

The soil-water retention curves were also generated using the degree of saturation. The degree of saturation can be calculated as follows:

$$S = \frac{\theta}{\theta_s} \tag{4.5}$$

Where S is the degree of saturation, θ is the volumetric moisture content reading, and θ_s is the saturated volumetric moisture content from curve fitting. The analysis of the soil-

water retention curves using the degree of saturation space are shown in Figure 4.26 for both the Houston Black and Branyon clay.

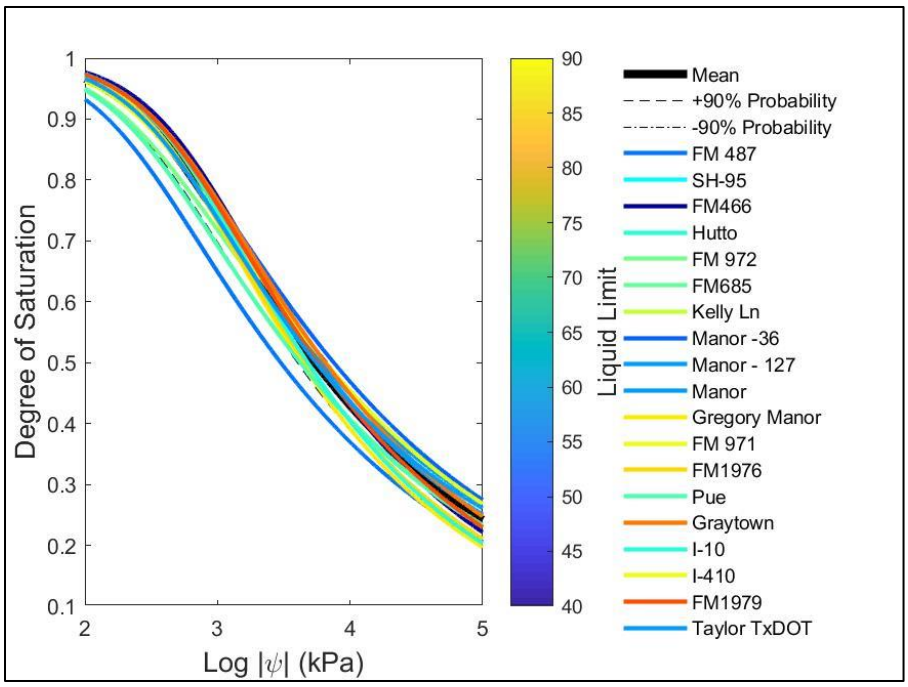

Figure 4.26: Individual and mean soil-water retention curves in the degree of saturation space for sampled locations of the Houston Black and Branyon clays

In general, the soil-water retention curves again were similar between the soil series. Soils with a lower Liquid Limit tend to have a lower total suction at the same degree of saturation. These results are consistent with the results using the volumetric moisture content. Therefore, the soil-water retention curves did not vary significantly between the soil series.

For the analysis of the stress-swell curves, a similar method was used to generate mean curves and confidence intervals for each soil series. Probability plots with the normal, log-normal and Weibull distributions are shown in Figure 4.27. The vertical

strains at a vertical effective stress of 100 and 1,000 psf were evaluated as these stresses typically encompass the range of stresses in the vadose zone.

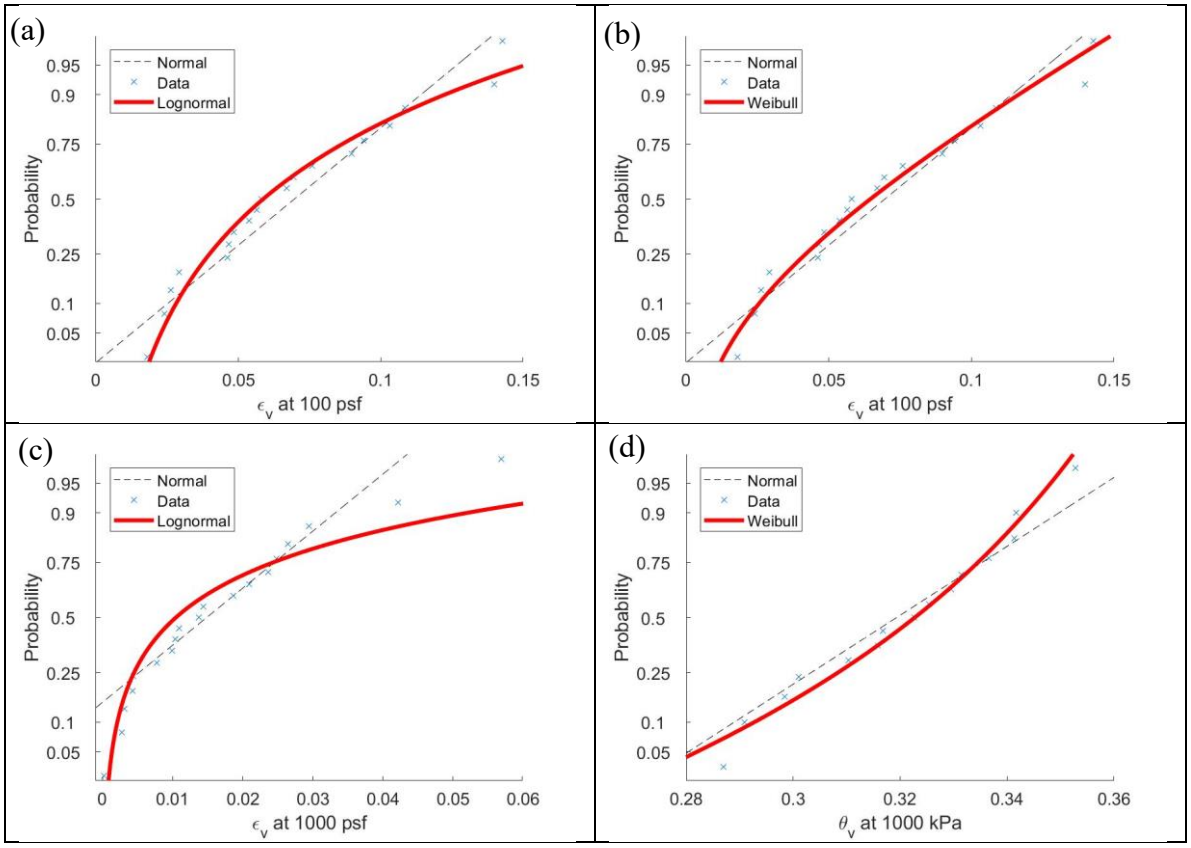

Figure 4.27: Log-normal (a,c) and Weibull (b,d) probability plots for stress-swell curve distributions at 100 (a,b) and 1,000 psf (c,d)

The log-normal distribution fits the data set at 100 psf better than the Weibull distribution for results near the mean and lower bound. However, the log-normal distribution did not fit the extremes of the vertical strains at 1,000 psf. Due to the better fit at the extremes of the data and for consistency with previous studies, the Weibull distribution was used for the analysis. The distributions of the stress-swell curves using a Weibull distribution are

shown for the Houston Black clay in Figure 4.28 and for the Branyon clay in Figure 4.29. The Liquid Limit for each sampled locations is shown by a corresponding color bar.

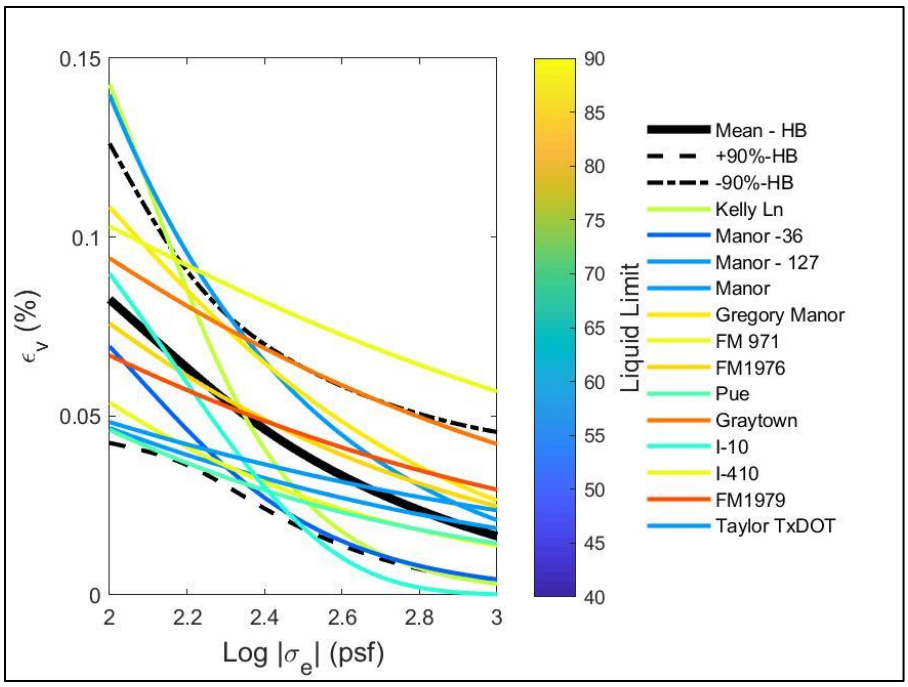

Figure 4.28: Individual and mean stress-swell curves for sampled locations of the Houston Black clay

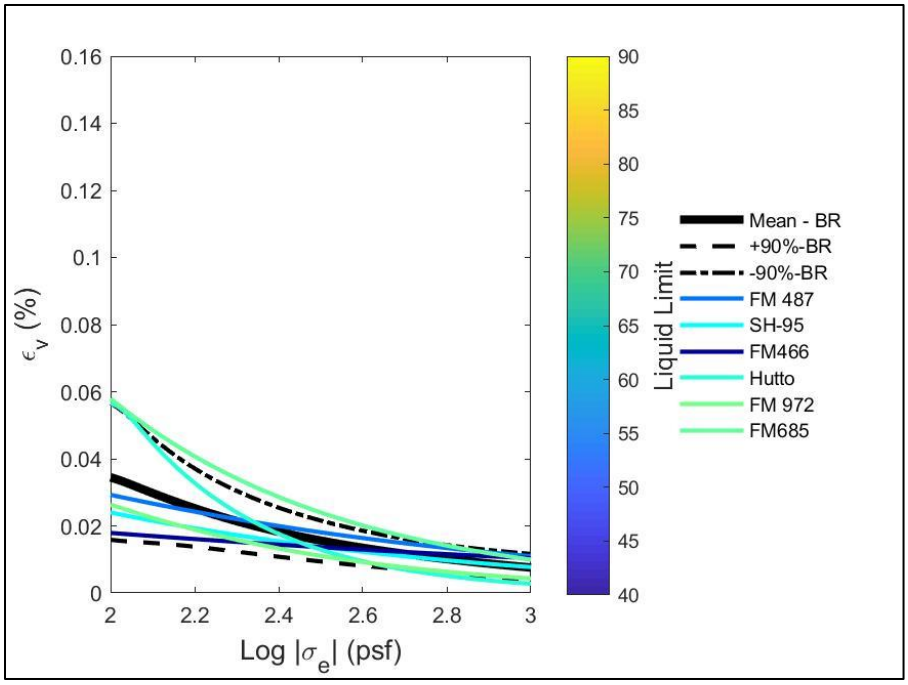

Figure 4.29: Individual and mean stress-swell curves for sampled locations of the Houston Black clay

The stress-swell curves are more heavily influenced by both the soil type and the Liquid Limit than the soil-water retention curves. Soils with a higher Liquid Limit tend to swell more at the same effective stress. Additionally, the Houston Black clay tends to have a swell more at the same effective stress than the Branyon clay. Both of these results are consistent with analysis of the soil properties. To further compare the two soil series, the mean stress-swell curves and confidence intervals for the Houston Black and Branyon clays are shown in Figure 4.30.

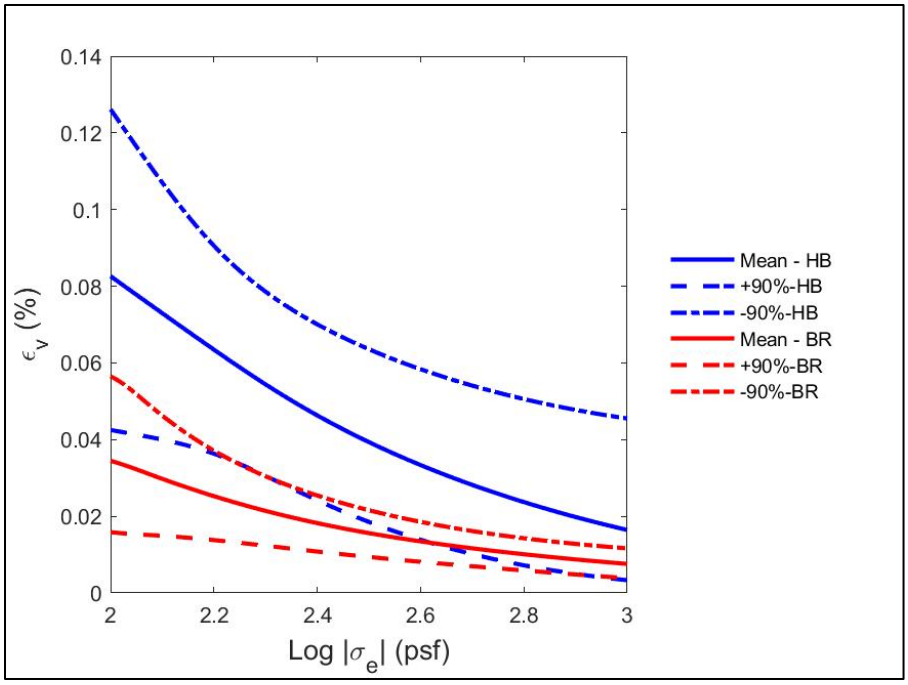

Figure 4.30: Mean and confidence intervals for stress-swell curves of Houston Black and Branyon clays

The trends indicate that the Houston Black clay tends to swell more than the Branyon clay, with the lower bound stress-swell curve for the Houston Black clay exceeding the mean stress-swell curve of the Branyon clay. The analysis of the stress-swell curves is consistent the assumption that the depositional environment and parent material affect the soil swelling behavior. The Houston Black clay derives from an older parent material and is found in residuum at the location of the parent material. The Branyon clay derives from younger parent material and is typically found in alluvial deposits. Due to these alluvial deposits, non-expansive soil particles, including sands, aggregates, and carbonates, that would reduce the swelling are expected for the Branyon clay. These non-expansive soil particles are expected to be not as prevalent for the Houston Black clay. Therefore, the soil swelling behavior is consistent with differences in both the soil properties and

depositional environment. Overall, the stress-swell curves were more dependent on the soil series than the soil-water retention curves.

The variability of the unsaturated soil behavior, namely the soil-water retention curves and stress-swell curves, were analyzed for the Houston Black and Branyon clays. For the analysis on the soil-water retention curves, both the Houston Black and Branyon clays have a similar distribution of the soil-water retention curves using both the volumetric moisture content and degree of saturation. Additionally, soils with a higher Liquid Limit tend to have a higher total suction at the same degree of saturation or volumetric moisture content. For the analysis on the stress-swell curves, the Houston Black clay have a higher vertical strain than the Branyon clay at the same effective stress. Additionally, soils with a higher Liquid Limit tend to have a higher vertical strain at the same effective stress. The difference in the soil swelling behavior was attributed to the difference in the soil properties, depositional environment, and parent material of the soils. These analyses indicate that a total suction-based predictive method may not adequately predict the potential vertical rise of a soil deposit.

4.4 Results from Undisturbed Samples from Taylor-Navarro Groups

In order to understand the variability of soil properties and swelling behavior on a localized scale, a research project which involved a significant amount of undisturbed borings was analyzed. The research project involved a portion of IH-10 that was extensively sampled and characterized for a planned roadway expansion. The location of the project was previously identified as an area of poor pavement performance and is located east of the IH-35 corridor and Balcones Fault zone. The location was evaluated based on geotechnical test results from a commercial geotechnical laboratory and the University of Texas at Austin and swelling test results from the centrifuge-based

inundation methodology. Additionally, geospatial estimators were used to evaluate the variability and heterogeneity of the Atterberg Limits and Potential Vertical Rise along the project.

4.4.1 Location and Overview of IH-10 Sampling Project

The research project was located along a six mile stretch of IH-10, east of San Antonio, as shown in Figure 4.31. The majority of the geotechnical investigation focused on the area between Foster Road and Graytown Road (i.e. the sections marked with the light blue, magenta, and green in Figure 4.31).

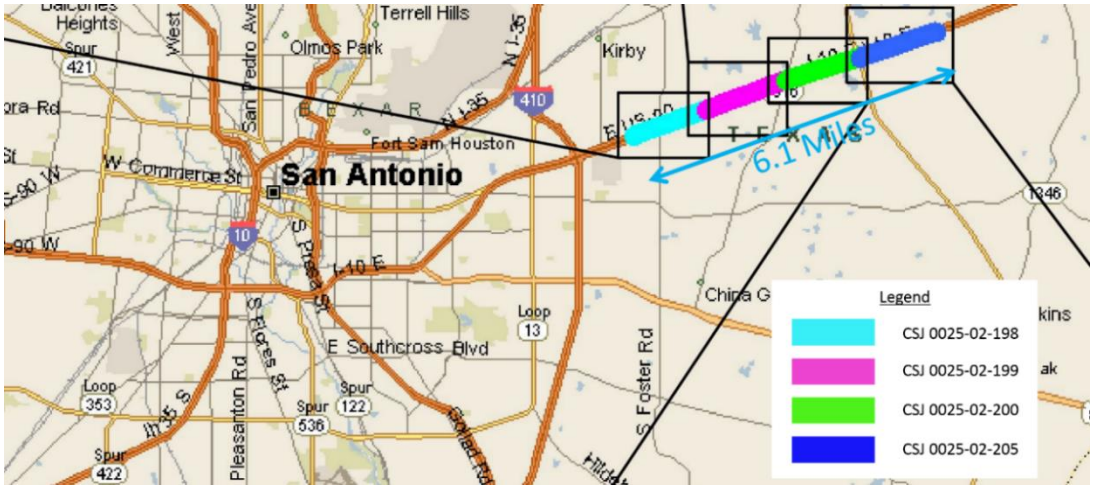

Figure 4.31: Research project location along IH-10 near San Antonio, Texas

The Texas Department of Transportation contracted a geotechnical consultant to characterize and design the pavement system for each of the four sections shown in Figure 4.31. The consultant sampled 44 locations at approximate equal spacing along the eastbound and westbound frontage roads using a Shelby tube sampler. Samples were characterized for their soil properties and potential vertical rise values were calculated for

each boring using Tex-124-E. The locations for these borings are shown in Figure 4.32. The classification and characterization of these borings are presented in Appendix B.

Figure 4.32: Locations of borings characterized by geotechnical consultants (Google, 2016)

The IH-10 expansion was also identified as a site for a future research project to study the reinforcement of pavement structures above expansive subgrades. Due to this research project, an additional geotechnical investigation was performed by researchers from the University of Texas at Austin to characterize the site. This geotechnical investigation identified an additional 46 boring locations to collect undisturbed samples as shown in Figure 4.33. Of these 46 boring locations, three boring locations were not sampled due to an extremely gravelly portion of the subgrade. Each boring location was sampled to a depth of 8 ft except where gravel or bedrock was encountered at depth.

Figure 4.33: Locations of borings characterized by the University of Texas at Austin (Google Earth, 2017)

The 46 boring locations were grouped into two major sets. The first set of borings included borings B-1 to B-30 and were sampled during the summer of 2016. The location for these borings included the same approximate locations as those sampled by the geotechnical consultant along eastbound frontage road of IH-10. Additionally, a smaller distance between borings was used between , borings B-4 to B-22, located between Foster Road and Woodlake Parkway, as shown in Figure 4.34. The borings were sampled approximately every 500 to 600 ft between B-4 to B-22 and sampled approximately 100 to 150 ft between B-8 and B-17. This portion of the roadway was more heavily sampled as it was identified as a potential location for the future research site based on NRCS soil survey maps and analysis of traffic studies.

Figure 4.34: Locations of borings between Foster Rd and Woodlake Parkway characterized by the University of Texas at Austin (Google Earth, 2017)

The second set of borings included borings B-31 to B-46 and were sampled during the spring of 2017. These borings were sampled from a portion of the eastbound frontage road that spanned approximately a mile east of Woodlake Parkway. Borings were sampled approximately 250 ft between borings B-31 to B-43 and approximately 500 ft between borings B-43 to B-46 as shown in Figure 4.35. This portion of the roadway was more heavily sampled as it was identified as an additional location for the future research project.

Figure 4.35: Location of second set of borings characterized by the University of Texas at Austin (Google Earth, 2017)

The IH-10 project was located east of the Balcones Fault zone and on the Texas Blackland prairie. The geology of the site is shown in Figure 4.36, using a geologic map overlay from the USGS in Google Earth. The majority of the borings were located within the extents of the Navarro Group and Marlbrook Marl (orange). Note that borings B-1 and B-2 were located on terrace deposits (Qt - tan) from the Quaternary period.

Figure 4.36: Location of soil borings for IH-10 Project with geologic formations in the area (USGS, 2016)

Additionally, NRCS soil surveys were used to identify the surficial soil series at each sampling location. The soil survey map for the extents of the IH-10 project is shown in Figure 4.37. The distribution of the surficial soil in the soil survey map is listed in Table 4.2.

Figure 4.37: Soil survey map of IH-10 project (USDA, 2016)

Table 4.2: Distribution of soils along IH-10 project (USDA, 2016)

Map Unit Symbol	Map Unit Name	Acres in AOI	Percent of AOI
HnB	Heiden clay, 1 to 3 percent slopes	0.8	0.0%
HnC2	Heiden clay, 3 to 5 percent slopes, eroded	217.9	7.7%
HnC3	Heiden-Ferris complex, 3 to 5 percent slopes, severely eroded	2.7	0.1%
HoD3	Heiden-Ferris complex, 5 to 10 percent slopes, severely eroded	195.0	6.9%
HsA	Houston Black clay, 0 to 1 percent slopes	198.9	7.1%
HsB	Houston Black clay, 1 to 3 percent slopes	479.9	17.0%
HsC	Houston Black clay, 3 to 5 percent slopes	90.2	3.2%
HtA	Branyon clay, 0 to 1 percent slopes	66.2	2.3%
HtB	Branyon clay, 1 to 3 percent slopes	68.5	2.4%
HuB	Houston Black gravelly clay, 1 to 3 percent slopes	509.1	18.1%
HuC	Houston Black gravelly clay, 3 to 5 percent slopes	661.5	23.5%
HuD	Houston Black gravelly clay, 5 to 8 percent slopes	88.3	3.1%
Pt	Pits and Quarries, 1 to 90 percent slopes	2.9	0.1%
Tc	Tinn clay, 0 to 1 percent slopes, occasionally flooded	11.3	0.4%
Tf	Tinn and Frio soils, 0 to 1 percent slopes, frequently flooded	215.3	7.6%
W	Water	12.1	0.4%
Totals for Area of Interest		**2,820.7**	**100.0%**

The predominant soil series along the IH-10 project is the Houston Black clay. Additionally, there are also significant portions of the Branyon and Heiden clays. The presence of several creeks, illustrated by the blue lines on the soil map in Figure 4.37, was consist with the predominance of gravelly Houston Black clay (i.e. HuB, HuC, and

HuD comprising 44.7% of surficial soil series). The gravel in the Houston Black clay was attributed to flooding events which would deposit river stones and gravel. In general, the soil survey of the IH-10 project was typical of an expansive soil deposit in the Taylor-Navarro groups. While borings B-1 and B-2 were located on terrace deposits from the geologic overlay, both of these borings were determined to have surficial deposits of the Houston Black series from the soil survey maps. For this analysis, borings were identified by their surficial soil series in order to group borings between sampling locations. However, soil series may vary with depth in the boring by the presence of additional soil horizons or parent material.

During sampling, soils were extruded from the Shelby tube in the field and logged by a geotechnical consultant. The Shelby tube sampler was typically run in approximately 2 ft sections. The samples for each run were extruded in the field, immediately wrapped in aluminum foil, and placed into sealed plastic bags after sampling to preserve the initial moisture content from the field. The extrusion in the field may affect the density of the specimens for testing.

4.4.2 Preliminary Testing of Soils Sampled from IH-10 Project

A preliminary geotechnical investigation was performed to characterize the Atterberg Limits and determine the in-situ gravimetric moisture content of the sampled soil. This investigation was conducted in order to define the initial soil conditions for the centrifuge-based inundation test. Each boring was divided into 2 ft. sections to match the method to calculate the potential vertical rise from Tex-124-E. Each boring subsection was tested for the in-situ gravimetric moisture content according to ASTM D42216. A summary of the measured in-situ gravimetric moisture content for each subsection is listed in Table 4.4. To measure the Atterberg Limits, portions of each boring suction,

approximately 2 to 3 in. tall, were trimmed and air-dried at approximately 23°C for approximately 7 days. An example of the trimmed boring subsections during the drying process is shown in Figure 4.38. The air-dried soil was then passed through a rock crusher twice to process the soil for the characterization of the Atterberg limits.

Figure 4.38: Example of air-drying of soil specimens

After the boring subsection was air-dried and processed, the Atterberg Limits of the soil were determined. Due to the limited amount of the soil, the Liquid Limit was measured according to ASTM D4318: Method B (i.e. the single-point Liquid Limit test). This method is used to estimate the Liquid Limit from a soil specimen with a number of blows to close the groove of between 20 and 30. Additionally, a second measured blow count between 10 and 40 was measured in order to assess the accuracy of the estimated single-point Liquid Limit. The Liquid Limit was estimated from this secondary measurement by

fitting a semi-log linear line between two measurements. If the estimated Liquid Limits using both methods differed by more than one percentage point, the Liquid Limit test was re-run with two additional points to determine the Liquid Limit. The Plastic Limit was estimated for boring subsections with a limit amount of soil by averaging the results from the geotechnical consultant. This average resulted in an estimated Plastic Limit of 18. If there was a suitable amount of soil, the Plastic Limit was measured according to ASTM D4318. A summary of the measured Liquid Limits and Plasticity Indices is listed in Table 4.3.

Due to the limited amount of sampled soil, the optimum moisture contents according to Standard Proctor compaction energy were estimated using the correlations from NAVFAC (1962). A dry moisture content, three percentage points dry of the estimated optimum moisture content, was targeted for the initial condition of the soil specimens used in the centrifuge-based inundation tests. Soil specimens with a higher in-situ gravimetric moisture content than the dry moisture content were dried using an environmental chamber, as shown in Figure 4.39. The environmental chamber used a saturated salt solution to maintain a high relative humidity. This higher relative humidity was targeted to slow the drying rate in order to prevent excessive desiccation or shrinkage cracks. After the specimens reaching to the targeted moisture content, soils specimens were wrapped in aluminum foil and placed in a temperature-controlled chest for at least 48 hours prior to centrifuge testing.

Figure 4.39: Environmental chamber for drying of soils

Specimens with a drier in-situ gravimetric moisture content than the dry moisture content were tested at their in-situ gravimetric moisture content. Some soil specimens were affected by a significant presence of gravel and river stone and were instead compacted to the maximum dry unit weight according to Standard Proctor compaction energy estimated using correlations from NAVFAC (1962). The in-situ and dry gravimetric moisture content are listed in Table 4.4. Soil specimens that required moisture conditioning in the environmental chamber are bolded.

Table 4.3: Summary of the Atterberg Limits of the IH-10 boring subsections

Boring	Depth (ft)	LL	PI	Boring	Depth (ft)	LL	PI	Boring	Depth (ft)	LL	PI	Boring	Depth (ft)	LL	PI
B-1	0-2	55%	35%	B-13	0-2	63%	47%	B-26	0-2	58%	39%	B-37	0-2	78%	56%
	2-4	62%	45%		2-4	73%	54%		2-4	38%	23%		2-4	79%	49%
	4-6	39%	21%		4-6	39%	11%		4-6	41%	24%		4-6	87%	64%
	6-8	32%	16%		6-8	87%	67%		6-8	-	-		6-8	68%	42%
B-2	0-2	62%	46%	B-14	0-2	95%	73%	B-27	0-2	57%	40%	B-38	0-2	45%	30%
	2-4	56%	39%		2-4	54%	36%		2-4	60%	35%		2-4	74%	56%
	4-6	33%	19%		4-6	55%	28%		4-6	-	-		4-6	69%	44%
	6-8	42%	31%		6-8	50%	25%		6-8	-	-		6-8	75%	48%
B-4	0-2	-	-	B-15	0-2	59%	35%	B-28	0-2	61%	39%	B-39	0-2	98%	76%
	2-4	65%	44%		2-4	109%	83%		2-4	41%	24%		2-4	88%	64%
	4-6	87%	60%		4-6	132%	98%		4-6	44%	28%		4-6	85%	64%
	6-8	80%	67%		6-8	127%	100%		6-8	52%	32%		6-8	77%	55%
B-5	0-2	58%	40%	B-16	0-2	51%	31%	B-29	0-2	54%	26%	B-40	0-2	-	-
	2-4	99%	81%		2-4	114%	86%		2-4	109%	85%		2-4	88%	61%
	4-6	88%	70%		4-6	148%	130%		4-6	93%	70%		4-6	80%	55%
	6-8	82%	65%		6-8	120%	84%		6-8	80%	55%		6-8	69%	46%
B-6	0-2	54%	39%	B-17	0-2	75%	56%	B-30	0-2	54%	32%	B-41	0-2	35%	18%
	2-4	65%	46%		2-4	77%	47%		2-4	49%	29%		2-4	82%	55%
	4-6	94%	69%		4-6	97%	71%		4-6	87%	62%		4-6	88%	60%
	6-8	53%	39%		6-8	93%	70%		6-8	84%	59%		6-8	84%	61%
B-7	0-2	54%	37%	B-20	0-2	53%	35%	B-31	0-2	100%	70%	B-42	0-2	71%	51%
	2-4	44%	24%		2-4	95%	77%		2-4	111%	74%		2-4	83%	54%
	4-6	53%	36%		4-6	83%	63%		4-6	65%	44%		4-6	82%	53%
	6-8	-	-		6-8	58%	34%		6-8	112%	78%		6-8	83%	56%
B-8	0-2	45%	24%	B-21	0-2	51%	31%	B-32	0-2	115%	89%	B-43	0-2	74%	53%
	2-4	80%	61%		2-4	71%	50%		2-4	42%	26%		2-4	72%	50%
	4-6	62%	44%		4-6	88%	62%		4-6	90%	64%		4-6	83%	59%
	6-8	72%	54%		6-8	97%	72%		6-8	69%	49%		6-8	73%	51%
B-9	0-2	64%	50%	B-22	0-2	65%	42%	B-33	0-2	84%	59%	B-44	0-2	41%	27%
	2-4	78%	52%		2-4	97%	62%		2-4	84%	63%		2-4	52%	33%
	4-6	65%	37%		4-6	83%	49%		4-6	83%	57%		4-6	56%	37%
	6-8	83%	65%		6-8	101%	69%		6-8	87%	61%		6-8	68%	48%
B-10	0-2	45%	30%	B-23	0-2	66%	44%	B-34	0-2	73%	53%	B-45	0-2	40%	25%
	2-4	88%	62%		2-4	50%	33%		2-4	55%	36%		2-4	57%	37%
	4-6	84%	66%		4-6	-	-		4-6	60%	44%		4-6	56%	33%
	6-8	80%	62%		6-8	-	-		6-8	77%	58%		6-8	62%	39%
B-11	0-2	76%	55%	B-24	0-2	62%	37%	B-35	0-2	75%	54%	B-46	0-2	52%	30%
	2-4	79%	54%		2-4	57%	37%		2-4	74%	56%		2-4	64%	42%
	4-6	84%	60%		4-6	51%	33%		4-6	80%	57%		4-6	37%	16%
	6-8	66%	39%		6-8	70%	52%		6-8	-	-		6-8	73%	47%
B-12	0-2	67%	49%	B-25	0-2	61%	41%	B-36	0-2	73%	48%	Note that some plastic limits were estimated from the average of the geotechnical consultant results at geographically and geologically similar locations			
	2-4	89%	61%		2-4	-	-		2-4	73%	44%				
	4-6	83%	57%		4-6	-	-		4-6	42%	27%				
	6-8	88%	62%		6-8	-	-		6-8	85%	54%				

Table 4.4: Summary of initial and dry gravimetric moisture contents for IH-10 boring subsections

Boring	Depth (ft)	ω_i	ω_{target}	Boring	Depth (ft)	ω_i	ω_{target}	Boring	Depth (ft)	ω_i	ω_{target}	Boring	Depth (ft)	ω_i	ω_{target}
B-1	0-2	22.4%	**20.1%**	B-13	0-2	29.3%	**21.1%**	B-26	0-2	21.4%	**20.7%**	B-37	0-2	34.0%	**25.6%**
	2-4	24.5%	**20.8%**		2-4	34.7%	**23.8%**		2-4	7.8%	15.4%		2-4	30.2%	**27.7%**
	4-6	12.6%	16.2%		4-6	29.2%	**18.2%**		4-6	5.1%	16.5%		4-6	28.2%	**27.9%**
	6-8	13.4%	14.1%		6-8	34.2%	**27.0%**		6-8	-	-		6-8	33.8%	**24.2%**
B-2	0-2	28.3%	**20.9%**	B-14	0-2	45.5%	**29.5%**	B-27	0-2	20.4%	**19.8%**	B-38	0-2	34.0%	**17.1%**
	2-4	26.7%	**19.6%**		2-4	27.6%	**19.5%**		2-4	20.2%	22.3%		2-4	36.2%	**23.7%**
	4-6	14.1%	**13.9%**		4-6	22.3%	**21.8%**		4-6	-	-		4-6	33.8%	**24.2%**
	6-8	19.5%	**15.2%**		6-8	61.6%	**19.9%**		6-8	-	-		6-8	36.5%	**26.1%**
B-4	0-2	-	-	B-15	0-2	17.1%	21.9%	B-28	0-2	18.3%	21.8%	B-39	0-2	39.9%	**30.0%**
	2-4	22.6%	22.4%		2-4	44.4%	**33.4%**		2-4	14.8%	**16.5%**		2-4	38.6%	**27.9%**
	4-6	25.2%	28.4%		4-6	52.8%	**39.8%**		4-6	18.2%	16.9%		4-6	33.4%	**27.0%**
	6-8	19.5%	24.0%		6-8	21.9%	37.4%		6-8	14.4%	19.4%		6-8	34.9%	**25.5%**
B-5	0-2	18.3%	20.2%	B-16	0-2	10.9%	19.2%	B-29	0-2	15.8%	21.7%	B-40	0-2	40.1%	-
	2-4	28.3%	29.3%		2-4	40.5%	**34.7%**		2-4	26.7%	32.7%		2-4	37.1%	**28.7%**
	4-6	25.5%	26.9%		4-6	51.7%	**40.2%**		4-6	26.3%	29.3%		4-6	28.7%	**26.7%**
	6-8	27.2%	**25.6%**		6-8	35.9%	37.9%		6-8	27.4%	**26.7%**		6-8	26.6%	**23.6%**
B-6	0-2	10.7%	18.7%	B-17	0-2	16.6%	**24.0%**	B-30	0-2	25.3%	**20.6%**	B-41	0-2	14.3%	15.0%
	2-4	31.7%	**22.2%**		2-4	28.8%	**27.3%**		2-4	13.5%	18.9%		2-4	34.5%	**27.4%**
	4-6	30.6%	**29.6%**		4-6	38.0%	**30.7%**		4-6	32.8%	**28.1%**		4-6	37.4%	**28.8%**
	6-8	20.2%	**18.5%**		6-8	36.8%	29.1%		6-8	34.5%	**27.3%**		6-8	35.9%	**27.3%**
B-7	0-2	27.8%	**19.3%**	B-20	0-2	14.4%	**19.2%**	B-31	0-2	41.0%	**32.0%**	B-42	0-2	13.6%	23.7%
	2-4	26.7%	**17.8%**		2-4	34.9%	**28.4%**		2-4	58.4%	**36.1%**		2-4	35.4%	**28.0%**
	4-6	21.9%	18.8%		4-6	37.8%	**26.3%**		4-6	25.5%	**22.6%**		4-6	38.6%	**27.8%**
	6-8	-	-		6-8	36.8%	**21.7%**		6-8	47.5%	**35.4%**		6-8	27.2%	27.6%
B-8	0-2	16.0%	18.2%	B-21	0-2	30.8%	**19.0%**	B-32	0-2	45.6%	**34.4%**	B-43	0-2	8.5%	24.5%
	2-4	26.4%	**25.5%**		2-4	31.7%	**23.7%**		2-4	36.8%	**16.4%**		2-4	31.6%	**24.3%**
	4-6	31.1%	**21.2%**		4-6	38.1%	**28.4%**		4-6	35.4%	**29.1%**		4-6	28.2%	**27.1%**
	6-8	32.0%	**23.3%**		6-8	37.5%	**30.6%**		6-8	39.7%	**23.0%**		6-8	19.3%	24.6%
B-9	0-2	12.0%	20.9%	B-22	0-2	21.4%	22.9%	B-33	0-2	36.3%	**27.4%**	B-44	0-2	10.1%	15.7%
	2-4	36.6%	**26.4%**		2-4	42.6%	**32.5%**		2-4	35.1%	**26.7%**		2-4	22.8%	**18.9%**
	4-6	38.0%	**23.9%**		4-6	59.4%	**29.3%**		4-6	35.1%	**27.4%**		4-6	21.3%	**19.9%**
	6-8	36.0%	**25.8%**		6-8	39.4%	**32.6%**		6-8	36.4%	**28.6%**		6-8	23.7%	**22.9%**
B-10	0-2	34.3%	**16.7%**	B-23	0-2	18.9%	22.9%	B-34	0-2	37.7%	**24.0%**	B-45	0-2	8.6%	15.9%
	2-4	37.4%	**28.4%**		2-4	10.1%	18.6%		2-4	40.5%	**20.0%**		2-4	28.9%	**20.6%**
	4-6	35.7%	**26.2%**		4-6	-	-		4-6	27.0%	**20.6%**		4-6	28.2%	**20.9%**
	6-8	35.6%	**25.1%**		6-8	-	-		6-8	31.3%	**24.6%**		6-8	28.1%	**22.4%**
B-11	0-2	39.2%	**25.0%**	B-24	0-2	14.9%	22.6%	B-35	0-2	35.8%	**24.5%**	B-46	0-2	24.6%	**20.0%**
	2-4	36.3%	**26.2%**		2-4	20.4%	20.7%		2-4	30.6%	**23.7%**		2-4	22.6%	**22.2%**
	4-6	35.2%	**27.4%**		4-6	12.3%	18.9%		4-6	43.8%	**26.0%**		4-6	36.1%	**16.2%**
	6-8	35.9%	**24.2%**		6-8	29.3%	**22.8%**		6-8	-	-		6-8	22.5%	25.2%
B-12	0-2	27.1%	**22.4%**	B-25	0-2	24.6%	**21.4%**	B-36	0-2	34.3%	25.2%	Note that the targeted moisture contents were taken three points dry of the NAVFAC estimated optimum moisture content			
	2-4	36.0%	**29.2%**		2-4	-	-		2-4	36.9%	**25.8%**				
	4-6	36.3%	**27.4%**		4-6	-	-		4-6	23.0%	**16.4%**				
	6-8	35.6%	**28.7%**		6-8	-	-		6-8	38.0%	**29.1%**				

The potential vertical rise of each boring subsection was determined using the centrifuge-based inundation test outlined in Zornberg et al. (2017). The targeted stresses for the centrifuge tests were based on the estimated maximum and minimum overburden stress in each boring subsection. These stresses assumed a 200 psf surcharge from the weight of the pavement structure and are listed for each depth in Table 4.5. For the first set of borings (i.e. borings B-1 to B-30), a minimum of two samples at each stress were tested. For the second set of borings (i.e. borings B-31 to B-46), a minimum of one sample at each prescribed stress was tested.

Table 4.5: Targeted stresses for swelling testing program

Sample Depth (ft)	Lower Target Stress (psf)	Upper Target Stress (psf)
0-2	200	400
2-4	400	600
4-6	600	800
6-8	800	1000

A log-linear stress-swell curve was assumed for each 2 ft subsection due to the comparatively small range of stresses. The curve, defined from ASTM D4546, used to fit the stress-swell curves in each subsection is shown as follows:

$$\varepsilon(\sigma') = A * \ln(\sigma') + B \tag{4.6}$$

Where A is the magnitude of the log-linear slope and B is the swelling at 1 psf. Both A and B were fitted by ordinary least-squares log-linear regression to minimize the root-mean square error. For some of the boring subsections, the primary swelling at the maximum stress was slightly higher than the primary swelling at the lower stress. In these subsections, the slope, A, was assumed to be 0, and an average magnitude of swelling from the testing results was used to fit the stress-swell curve for the 2 ft subsection. For boring subsections that compressed, A and B were set to 0 (i.e. no volume change was

assumed). In cases where gravel or bedrock was encountered, these materials were assumed to not undergo volumetric changes upon wetting. These assumptions were made in order to calculate the maximum potential vertical rise for a given initial moisture condition.

The potential vertical rise of each 2-ft subsection was calculated by numerically integrating the stress-swell curve between the upper and lower stresses in each subsection, as outlined in Zornberg et al. (2017). These stresses were calculated using the overburden stress from the overlaying layers and the average end of testing total unit weight in each subsection. The potential vertical rise of each boring was determined to be the sum of the potential vertical rise of each of the 2-ft. subsections. Additionally, this calculated potential vertical rise for each boring was compared to the potential vertical rise calculated using Tex-124-E.

4.4.3 Centrifuge Testing of Soils Sampled from IH-10 Project

In total, 460 soil specimens were tested using the centrifuge-based inundation test. Test results, including the vertical strain at the end of primary swelling, the effective overburden stress at the end of testing in psf, and the total unit weight at the end of testing in pcf, were analyzed using MATLAB. A script calculated and plotted the stress-swell curve and potential vertical rise for each subsection. The script also calculated the potential vertical rise from Tex-124-E method. The potential vertical rise from Tex-124-E was used to generate a synthetic stress-swell curve to compare against the results from the centrifuge swelling tests. Additionally, the potential vertical rise from each subsection was plotted individually and cumulatively from the bottom of the boring. Typical results, using those from boring B-12, are shown in Figure 4.40. These results include the primary swelling from centrifuge tests, the stress-swell curve for each subsection from

centrifuge test results, the results and stress-swell curve from Tex-124-E. Additionally, a typical profile of the individual and cumulative potential vertical rise, again determined from boring B-12, are shown in in Figure 4.41.

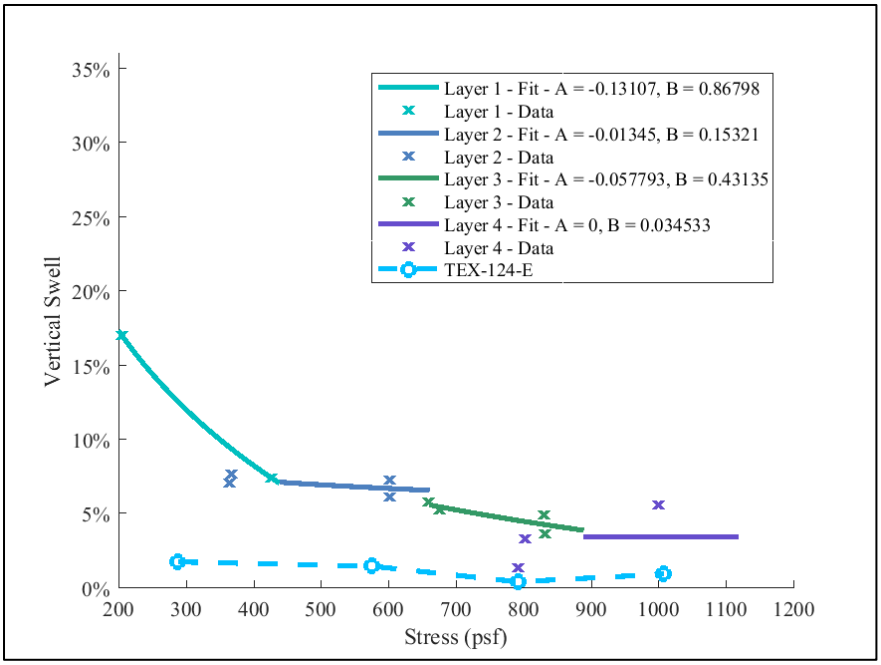

Figure 4.40: Measured stress-swell curves and comparison of curves from centrifuge data to Tex-124-E for boring B-12

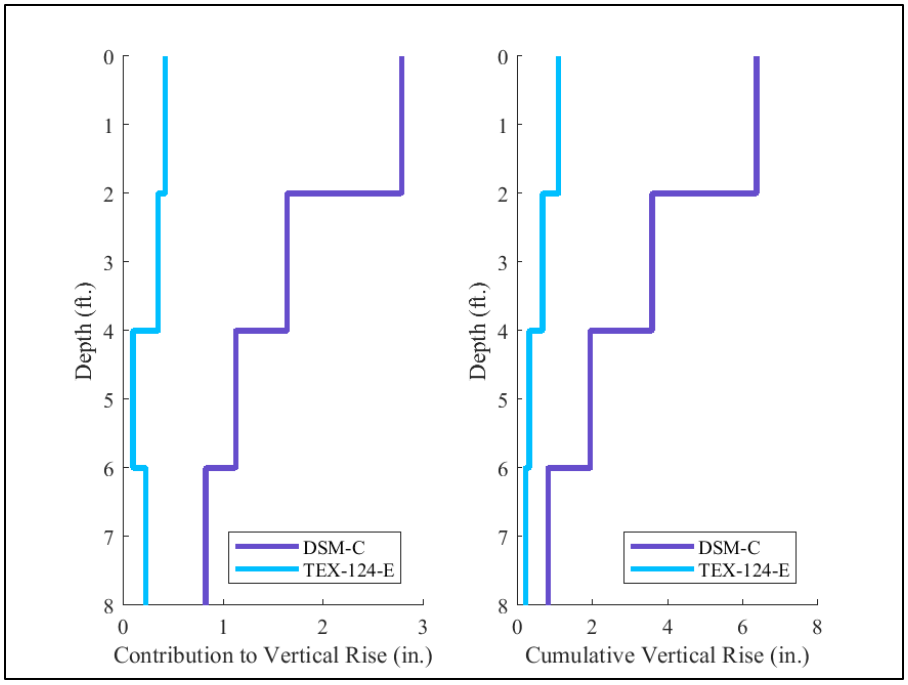

Figure 4.41: Calculated vertical rise for each 2-ft section (left) and cumulative vertical rise (right) for both Centrifuge and Tex-124-E methods for boring B-12

These results indicate that the potential vertical rise was higher using test results from field-sampled specimens that the potential vertical rise calculated using Tex-124-E. Additionally, the primary swelling tends to decrease in the subsections at depth, and the individual potential vertical rise from each subsection tends to decrease with depth. These general trends are relatively consistent in the tested borings with a few exceptions.

However, trends from several borings differed than the trends from typical results. Boring B-32 is an example of one of these borings. Results from boring B-32 are shown in Figure 4.42 in terms of the results from centrifuge tests and the fitted stress-swell curves and in Figure 4.43 for the individual and cumulative potential vertical rise.

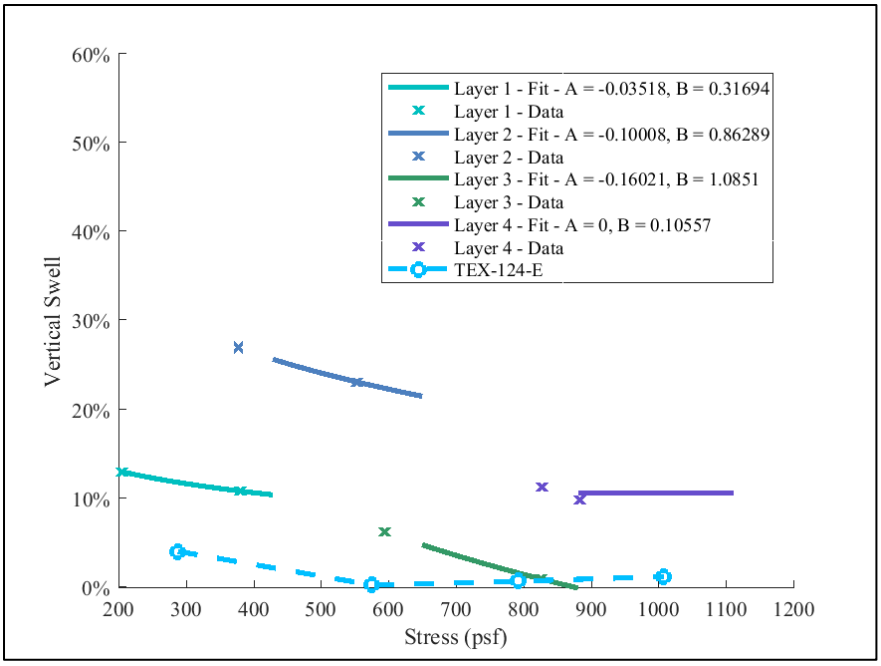

Figure 4.42: Measured stress-swell curves and comparison of curves from centrifuge data to Tex-124-E for boring B-32

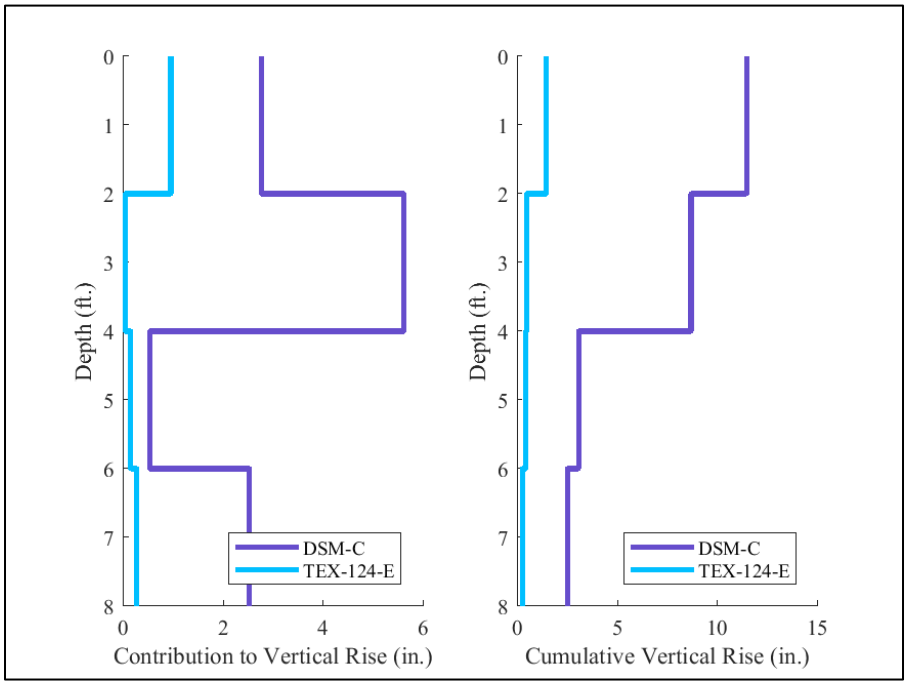

Figure 4.43: Calculated vertical rise for each 2-ft section (left) and cumulative vertical rise (right) for both Centrifuge and Tex-124-E methods for boring B-32

Results from boring B-32 indicate that the subsection from a depth of 2 to 4 ft tend to have a higher potential vertical rise than the subsections from a depth of 0 to 2 ft and 4 to 6 ft. Further, the layer from a depth of 6 – 8 ft tended to have a higher potential vertical rise than the subsection from a depth of 4 to 6 ft. These trends indicate that the deposition of soil, particularly the location of non-expansive materials and parent materials, can significantly affect the potential vertical rise of a boring. Field specimens should be sampled using undisturbed methods in order to identify locations of differing soil material in order to accurately assess the potential vertical rise.

An additional issue with the potential vertical rise calculated from the centrifuge tests was with the range of stresses used to generate the stress-swell curves for each boring subsection. Several boring subsections were tested at stresses that exceeded the stresses used to calculate the potential vertical rise. This increase in the testing stress was attributed to inconsistencies in the RPM of the centrifuge. Due to the limited amount of soil, these boring subsections were not re-tested.

The calculated potential vertical rise for each subsection and the total potential vertical rise of each boring are listed in Table 4.6. The stress-swell curves and potential vertical rise at depth for each of the remaining borings are shown in Appendix B.

Table 4.6: Summary of centrifuge testing results for IH-10 soils

Boring	Depth (ft)	PVR - 2 ft section (in)	PVR - 8 ft section (in)	Boring	Depth (ft)	PVR - 2 ft section (in)	PVR - 8 ft section (in)	Boring	Depth (ft)	PVR - 2 ft section (in)	PVR - 8 ft section (in)	Boring	Depth (ft)	PVR - 2 ft section (in)	PVR - 8 ft section (in)
B-1	0-2	0.43	1.39	B-13	0-2	2.14	6.05	B-26	0-2	0.70	0.70	B-37	0-2	1.42	3.52
	2-4	0.49			2-4	0.00			2-4	0.00			2-4	0.78	
	4-6	0.47			4-6	2.46			4-6	0.00			4-6	0.39	
	6-8	0.00			6-8	1.45			6-8	0.00			6-8	0.93	
B-2	0-2	1.80	3.23	B-14	0-2	4.20	13.84	B-27	0-2	0.51	0.85	B-38	0-2	3.39	6.18
	2-4	1.15			2-4	2.83			2-4	0.34			2-4	1.95	
	4-6	0.28			4-6	0.91			4-6	0.00			4-6	0.28	
	6-8	0.00			6-8	5.89			6-8	0.00			6-8	0.56	
B-4	0-2	0.00	1.78	B-15	0-2	0.56	6.90	B-28	0-2	0.13	0.32	B-39	0-2	1.68	4.53
	2-4	0.83			2-4	2.31			2-4	0.03			2-4	1.63	
	4-6	0.95			4-6	3.94			4-6	0.00			4-6	0.85	
	6-8	0.00			6-8	0.09			6-8	0.16			6-8	0.38	
B-5	0-2	0.92	3.42	B-16	0-2	0.85	6.25	B-29	0-2	0.29	2.31	B-40	0-2	1.60	4.41
	2-4	0.89			2-4	2.05			2-4	1.04			2-4	1.52	
	4-6	0.87			4-6	2.80			4-6	0.94			4-6	0.49	
	6-8	0.73			6-8	0.55			6-8	0.04			6-8	0.80	
B-6	0-2	0.18	2.72	B-17	0-2	0.47	6.80	B-30	0-2	2.40	6.53	B-41	0-2	0.11	1.74
	2-4	1.33			2-4	2.01			2-4	0.56			2-4	0.77	
	4-6	0.85			4-6	2.71			4-6	0.90			4-6	0.39	
	6-8	0.36			6-8	1.61			6-8	2.68			6-8	0.47	
B-7	0-2	1.62	3.06	B-20	0-2	0.40	8.02	B-31	0-2	3.07	9.75	B-42	0-2	0.10	1.50
	2-4	1.07			2-4	0.95			2-4	4.85			2-4	0.61	
	4-6	0.37			4-6	5.11			4-6	0.33			4-6	0.57	
	6-8	0.00			6-8	1.55			6-8	1.50			6-8	0.22	
B-8	0-2	0.09	4.76	B-21	0-2	2.34	7.32	B-32	0-2	2.77	11.47	B-43	0-2	0.53	2.92
	2-4	1.60			2-4	1.65			2-4	5.62			2-4	1.22	
	4-6	1.40			4-6	2.13			4-6	0.54			4-6	0.54	
	6-8	1.67			6-8	1.21			6-8	2.53			6-8	0.64	
B-9	0-2	0.25	4.54	B-22	0-2	0.19	5.00	B-33	0-2	1.31	3.72	B-44	0-2	-0.04	0.93
	2-4	1.67			2-4	1.74			2-4	1.27			2-4	0.18	
	4-6	1.50			4-6	2.28			4-6	0.53			4-6	0.39	
	6-8	1.12			6-8	0.79			6-8	0.61			6-8	0.39	
B-10	0-2	2.59	6.06	B-23	0-2	0.36	0.36	B-34	0-2	1.40	2.80	B-45	0-2	0.05	1.84
	2-4	1.46			2-4	0.00			2-4	0.24			2-4	1.15	
	4-6	0.95			4-6	0.00			4-6	0.58			4-6	0.56	
	6-8	1.06			6-8	0.00			6-8	0.58			6-8	0.09	
B-11	0-2	2.77	7.22	B-24	0-2	1.85	4.77	B-35	0-2	1.88	4.63	B-46	0-2	0.42	1.77
	2-4	1.24			2-4	1.12			2-4	0.73			2-4	-0.18	
	4-6	1.62			4-6	1.29			4-6	2.02			4-6	1.41	
	6-8	1.59			6-8	0.50			6-8	0.00			6-8	0.11	
B-12	0-2	2.79	6.39	B-25	0-2	0.85	0.85	B-36	0-2	1.93	3.50				
	2-4	1.64			2-4	0.00			2-4	0.92					
	4-6	1.13			4-6	0.00			4-6	0.64					
	6-8	0.83			6-8	0.00			6-8	0.00					

In order to assess the accuracy of current methods to determine the potential vertical rise, the swelling behavior of each boring was compared between the centrifuge test results and results from Tex-124-E. The potential vertical rise estimated using Tex-

124-E and those calculated from the centrifuge test results are listed in Table 4.7. The centrifuge calculated potential vertical rise is labeled as DMS-C and was calculated using each of the boring subsections to a depth of 8 ft. In order to compare the results between the two methods, a plot of the centrifuge calculated and Tex-124-E estimated potential vertical rise is shown in Figure 4.44 with a dashed 1:1 line.

Table 4.7: Comparison of centrifuge calculated and Tex-124-E predicted potential vertical rise

Boring	Vertical Rise (in)		Boring	Vertical Rise (in)	
	DMS-C	TEX-124-E		DMS-C	TEX-124-E
B-1	1.39	0.37	B-26	0.70	0.88
B-2	3.23	0.61	B-27	0.85	1.14
B-4	1.78	1.66	B-28	0.32	1.00
B-5	3.42	3.19	B-29	2.31	2.72
B-6	2.72	1.84	B-30	6.53	0.78
B-7	3.06	0.51	B-31	9.75	2.09
B-8	4.76	1.45	B-32	11.47	1.45
B-9	4.54	1.66	B-33	3.72	1.29
B-10	6.06	0.99	B-34	2.80	1.25
B-11	7.22	1.57	B-35	4.63	1.33
B-12	6.39	1.11	B-36	3.50	1.33
B-13	6.05	1.51	B-37	3.52	1.33
B-14	13.84	1.30	B-38	6.18	1.13
B-15	6.90	2.27	B-39	4.53	1.59
B-16	6.25	2.80	B-40	4.41	0.73
B-17	6.80	1.74	B-41	1.74	0.71
B-20	8.02	1.63	B-42	1.50	1.75
B-21	7.32	1.01	B-43	2.92	2.05
B-22	5.00	1.58	B-44	0.93	0.92
B-23	0.36	1.07	B-45	1.84	0.55
B-24	4.77	1.27	B-46	1.77	0.97
B-25	0.85	0.26			

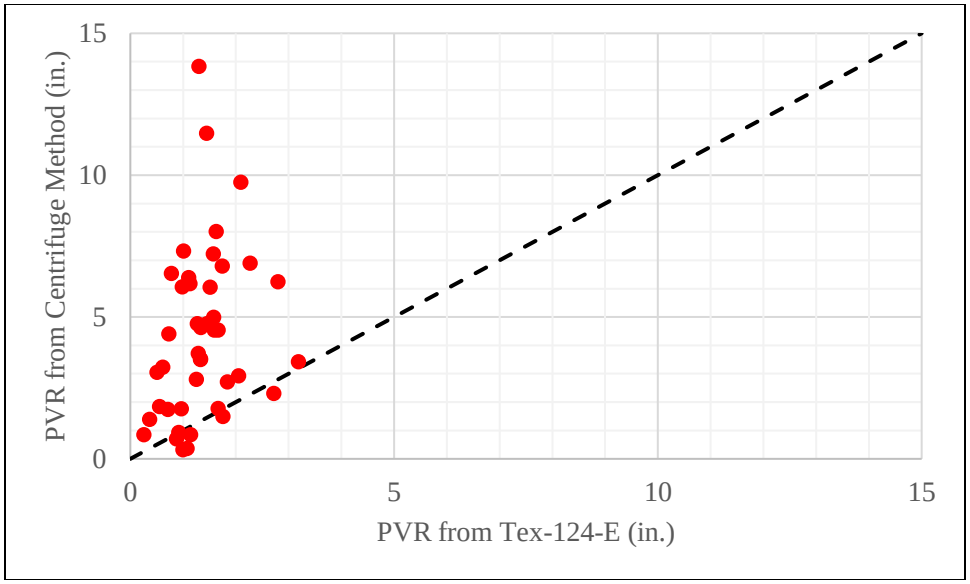

Figure 4.44: Comparison in potential vertical rise between the Tex-124-E and Centrifuge methods

In general, the calculated potential vertical rise from centrifuge tests tends to be higher than the potential vertical rise from Tex-124-E. This trend can be attributed to the centrifuge calculated potential vertical rise using results from sampled soil instead of correlations. Note that Tex-124-E is limited due to small number of soils originally sampled from a single county in Texas. Additionally, while the method accounts for differences in initial dry unit weight, the method does not account for minor differences in the gravimetric moisture content or the effect of soil fabric previously discussed in Chapter 2 and 3 of this dissertation.

The calculated potential vertical rise from centrifuge tests was significantly affected by the results from the deepest 2 ft boring subsection. This subsection was assumed to be affected by the presence the parent material or unweathered shale and tended to more highly expansive than the shallower portions of the boring. Theoretically, if the soil in these 2 ft subsections were the parent material, these subsections would not

be expected to undergo as significant of cyclic moisture fluctuations. An example of the influence of these subsections is shown in Figure 4.45 and Figure 4.46 from boring B-14. Additionally, an additional example of this influence of these subsections is shown for boring B-32 in Figure 4.43 and Figure 4.44.

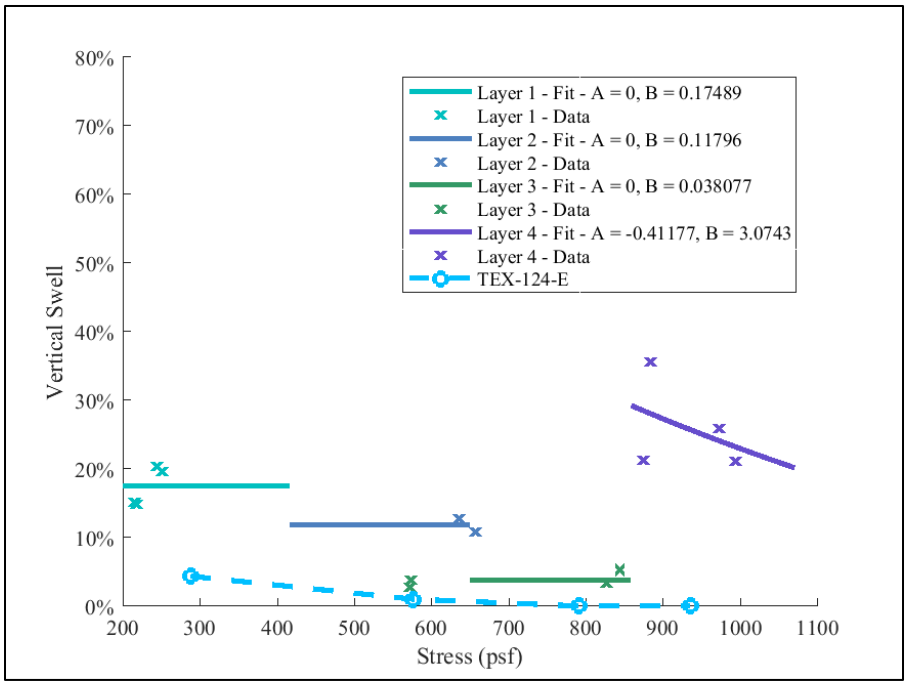

Figure 4.45: Measured stress-swell curves and comparison of curves from centrifuge data to Tex-124-E for boring B-14

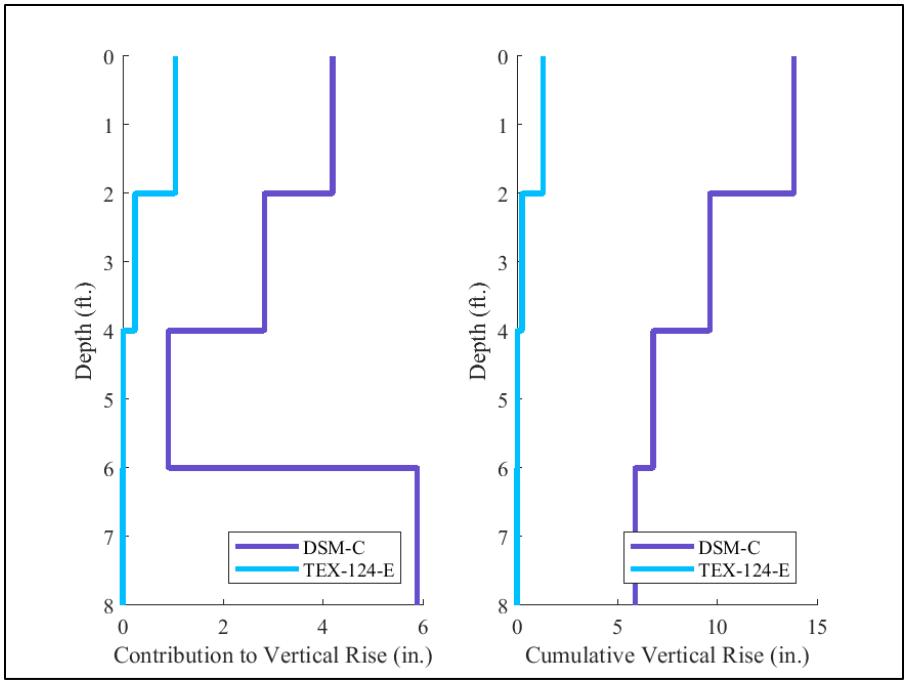

Figure 4.46: Calculated vertical rise for each 2-ft section (left) and cumulative vertical rise (right) for both Centrifuge and Tex-124-E methods for boring B-14

For boring B-14, the bottom 2 ft subsection significantly affected the calculated potential vertical rise. The swelling from this subsection accounted for approximately 50% of the cumulative potential vertical rise with strains that were significantly higher than the surficial soil. Due to these subsections with assumed parent material, several borings significantly affected the analysis of the heterogeneity and variability of the potential vertical rise in the subgrade. Section 4.4.4 and 4.4.5 further analyzes the influence of these subsections on the potential vertical rise by geospatially analyzing test results that either includes these subsections (i.e. assumes an 8 ft active zone) or excludes these subsections (i.e. assumes a 6 ft active zone).

4.4.4 Geospatial Estimation of Potential Vertical Rise

In order to estimate the potential vertical rise of the subgrade between borings, two geospatial estimators were used. The first geospatial estimator was a simple linear interpolation of the potential vertical rise between borings. The second geospatial estimator used the ordinary kriging method outlined in Section 4.2.3. This method a constant mean potential vertical rise in the subgrade. The theoretical semi-variogram was estimated by taking an average of a ten data point region. These averaged values were used to fit a theoretical gaussian variogram to the data. Due to the variability of the surficial soil series and horizons, an additional objective for this section was to assess whether grouping the data based on the surficial soil series improved the estimations.

The potential vertical rise along the IH-10 project was originally analyzed using the results from all borings and assuming an 8-ft. active zone. This analysis incorporated the deepest 2 ft boring subsections that were problematic in Section 4.4.3. The estimated potential vertical rise is indicated using a color bar to display the relative magnitude of the potential vertical rise. The analysis is presented using the surveyed location of each boring and the overall alignment of the roadway. The estimation of the potential vertical rise using a linear interpolation is shown in Figure 4.47, and the estimation of the potential vertical rise using kriging is shown in Figure 4.48.

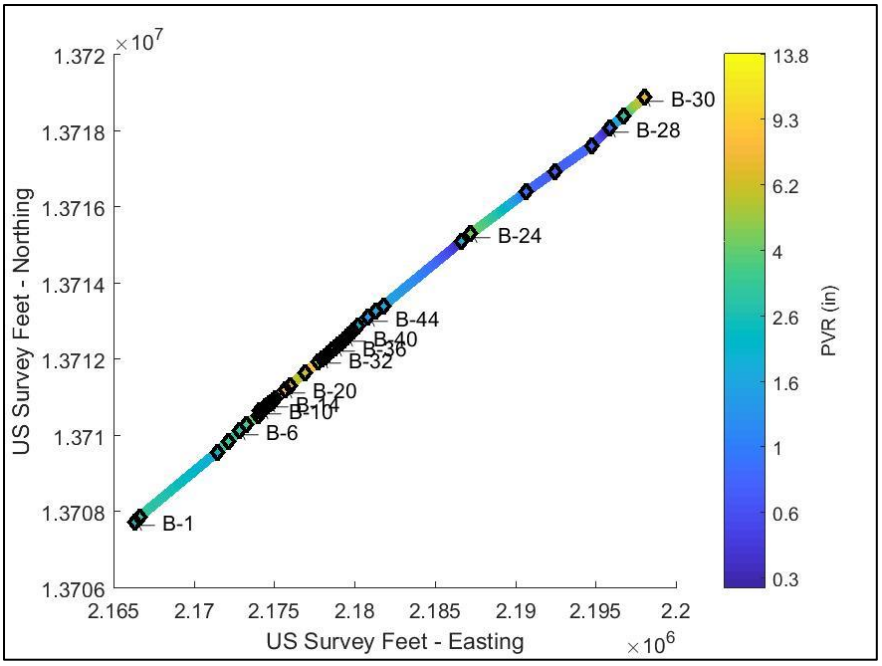

Figure 4.47: Estimation of potential vertical rise along IH-10 Project using all boring data and linear interpolation

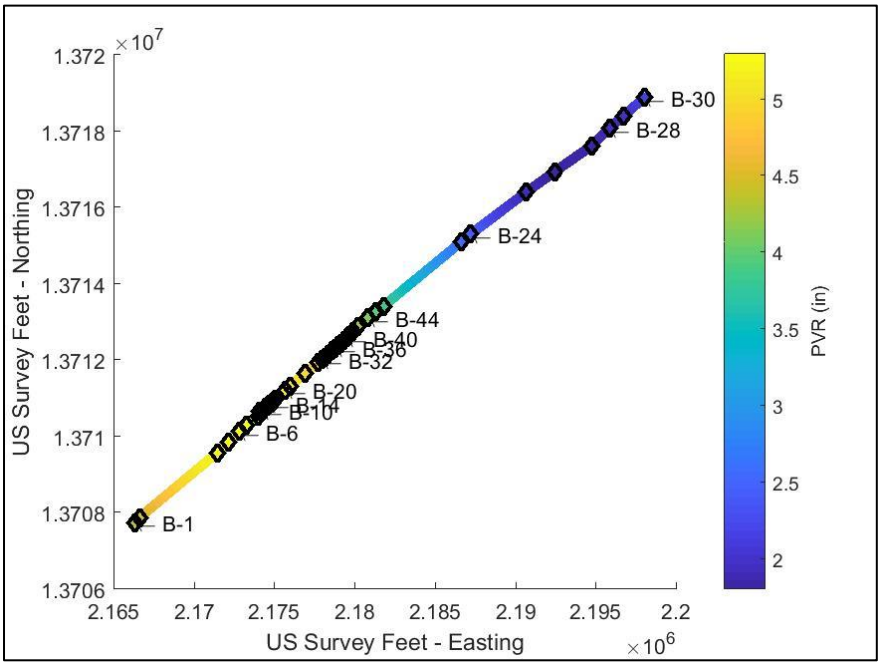

Figure 4.48: Estimation of potential vertical rise along IH-10 Project using all boring data and the ordinary kriging method

In general, potential vertical rise is higher for the estimations using linear interpolation than the estimations using kriging. This difference can be attributed to the kriging method tending to smooth the data between extreme values. Additionally, due to the spacing of the borings, the resolution of the potential vertical rise in the region between B-3 and B-46 was relatively poor. To better visualize the potential vertical rise in the subgrade, the distance of each boring location from the first boring location is shown in Figure 4.49 versus the estimated potential vertical rise using the linear interpolation and in Figure 4.50 versus the estimated potential vertical rise using kriging. The calculated potential vertical rise from each boring is shown via a black diamond. Additionally, the magnitude of the potential vertical rise along the roadway is indicated via a color bar to better visualize differences along the roadway.

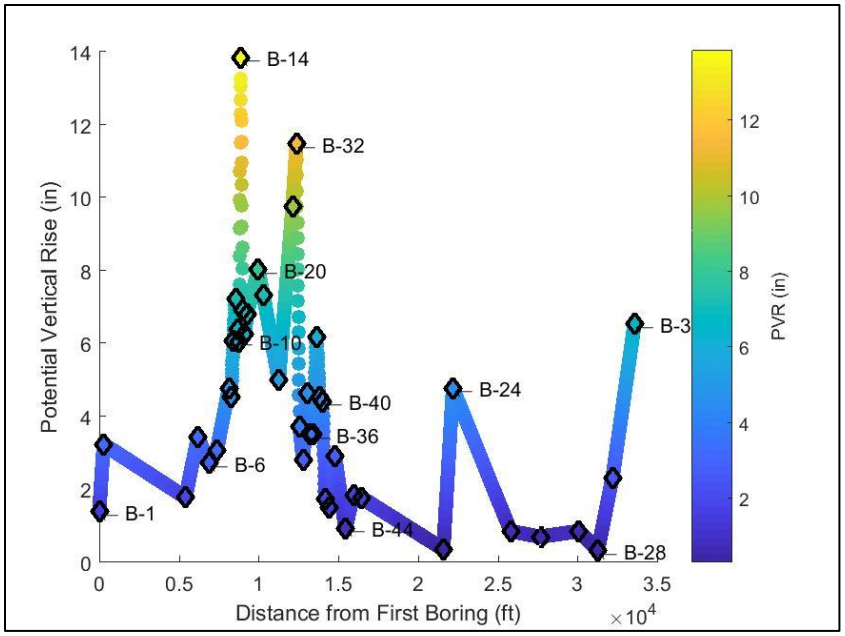

Figure 4.49: Estimated potential vertical rise along the IH-10 project using all boring data and linear interpolation

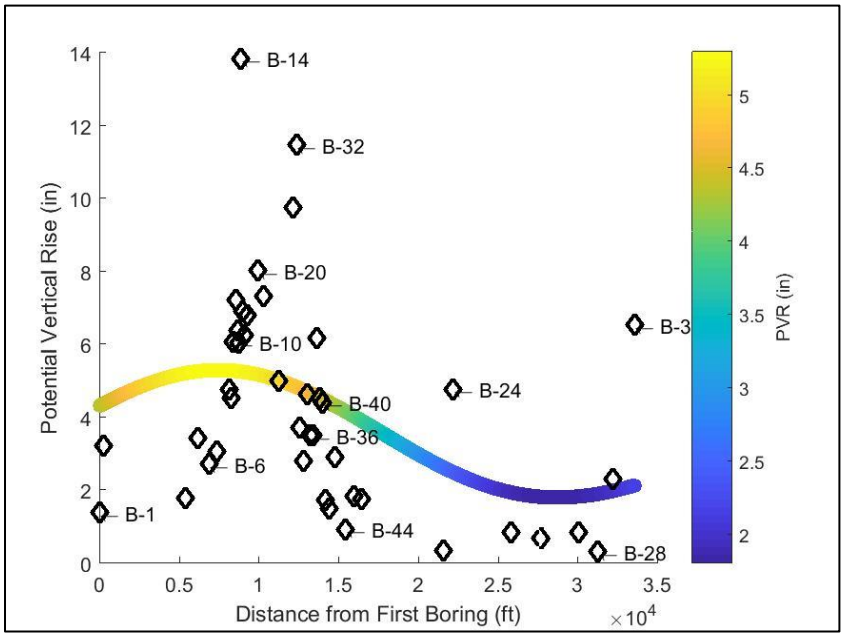

Figure 4.50: Estimated potential vertical rise along the IH-10 project using all boring data and the kriging method

The smoothing of the potential vertical rise using the kriging method is significant, particularly in the region between borings B-6 and B-36. This smoothing occurs as the method of ordinary kriging tends to estimate the potential vertical rise closer to the overall mean value of the data set. Due to this, the spike in the potential vertical rise is not estimated correctly. In order to improve accuracy of the kriging method, that data used must be refined. For the results using linear interpolation, a significant amount of variability was observed for using the results from estimator (e.g. the spike in potential vertical rise between borings B-6 and B-36).

As mentioned in Section 4.4.3, the potential vertical rise from several of the deepest 2 ft. subsections differed significantly from the potential vertical rise of the soil closer to the ground surface, affecting the calculated potential vertical rise of the boring. This difference can be attributed to the presence of parent material which may not be a part of the subgrade that experiences significant moisture fluctuations. To reduce the influence of these deepest subsections on the geospatial estimators, the potential vertical rise calculated using only the upper 6 ft of the boring was used with the geospatial estimators. The data from all of the boring locations were used for this analysis. The estimated potential vertical rise using linear interpolation is shown in Figure 4.51 versus the distance from the first boring. The estimated potential vertical rise using the kriging method is shown in Figure 4.52 versus the distance from the first boring.

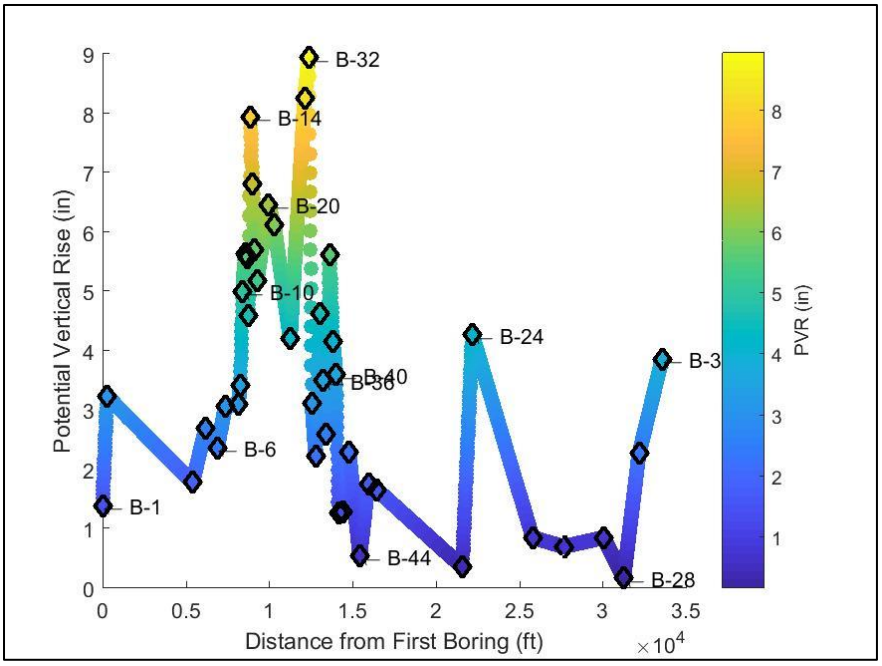

Figure 4.51: Estimated potential vertical rise along the IH-10 project using boring data to a depth of 6 ft and linear interpolation

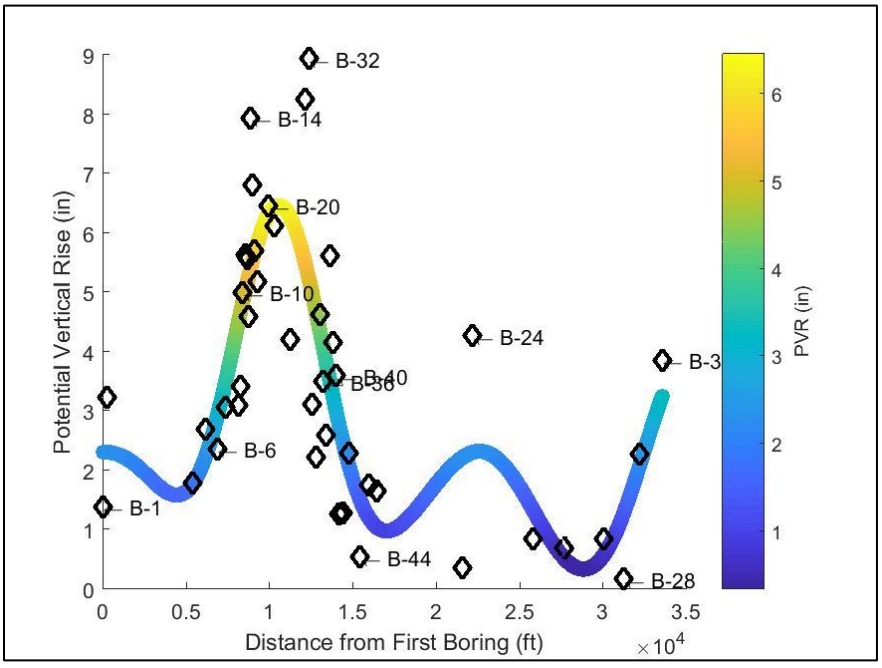

Figure 4.52: Estimated potential vertical rise along IH-10 Project using boring data to a depth of 6 ft and the kriging method

The removal of the results from the deepest 2 ft subsections significantly improved the estimation of the potential vertical rise using the kriging method by reducing the range of the potential vertical rise calculated from the borings. The maximum potential vertical rise was reduced from 14 in. to 6 in, which indicates that the deepest 2 ft subsections could significant affect the overall potential vertical rise. The estimations from the kriging method were more consistent with the calculated rise from centrifuge tests due to the reduction in the variance, improving the estimations for the region between boring B-6 to B-36. The peak in this region for the estimations was more sharp and distinct in Figure 4.52 than Figure 4.50. Therefore, the estimations using the kriging method were significantly improved by removing the results from the deepest 2 ft subsections. For the estimations using linear interpolation, there was not as significant of scatter in the region between borings B-6 to B-36 due to the reduction in the range of the potential vertical rise.

To further refine the data set used by the geospatial estimators, only borings from the Houston Black clay, as identified from NRCS soil survey maps, between borings B-8 and B-43 were used. These conditions were selected to remove any effect of the different soil series along the roadway and to focus on the test results located within the extents of the future research site. Based on the results from the previous analysis, only the results from the upper 6 ft of each boring were used. The estimation of the potential vertical rise using linear interpolation is shown in Figure 4.53 versus the distance from boring B-8. The estimation of the potential vertical rise using the kriging method is shown in Figure 4.54 versus the distance from boring B-8.

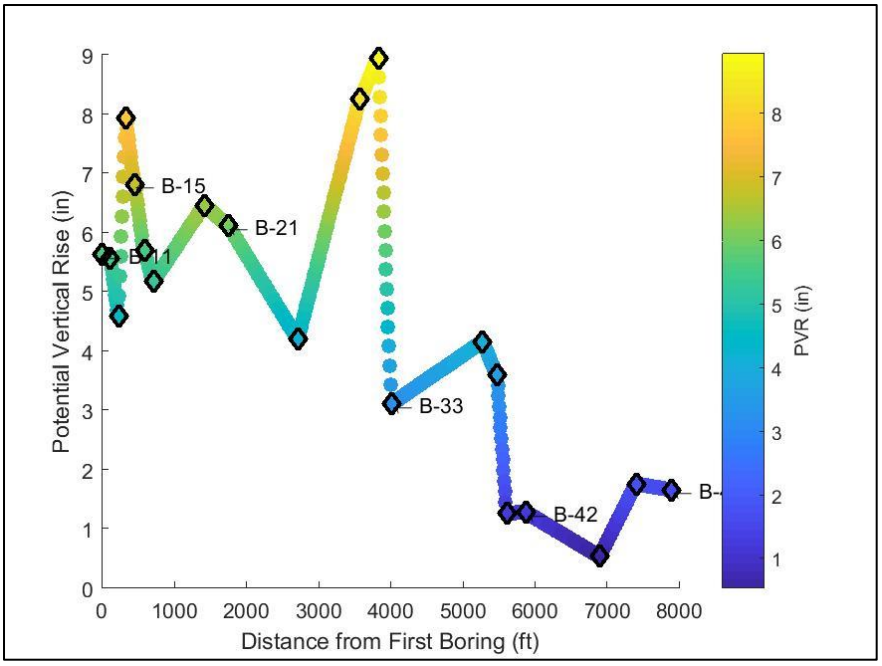

Figure 4.53: Estimated potential vertical rise along the IH-10 project using data from the Houston Black clay to a depth of 6 ft and linear interpolation

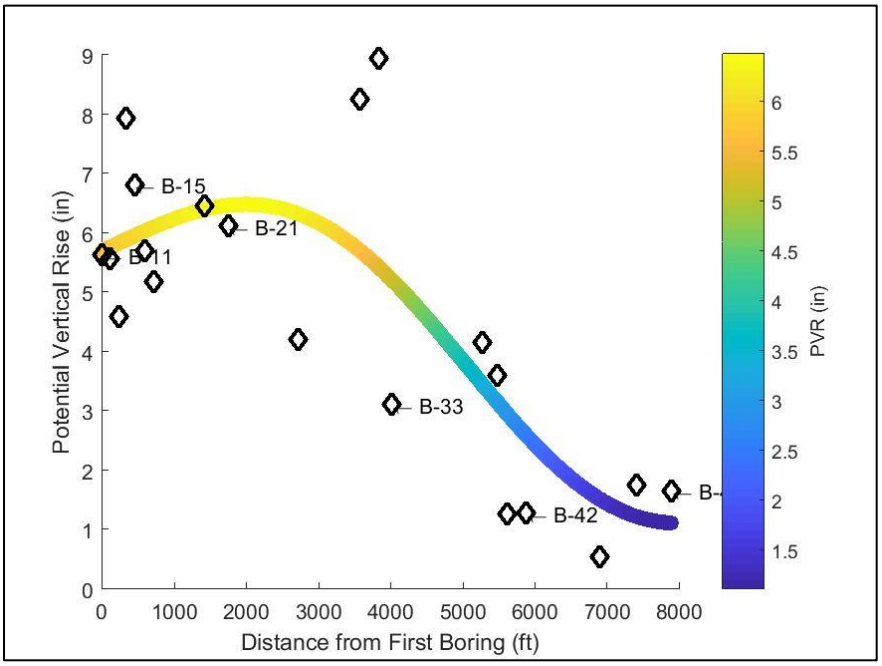

Figure 4.54: Estimated potential vertical rise along the IH-10 project using data from the Houston Black clay from B-8 to B-46 to a depth of 6 ft and kriging method

By using results from borings in the same soil series and in the same sampling location, the estimations of the potential vertical rise using the kriging method were similar to the calculated potential vertical rise from centrifuge test results. However, the estimations using these additional conditions were similar to estimations that only eliminated the results from the deepest 2 ft subsection, previously shown in Figure 4.52. Additionally, the removal of the non-Houston Black borings removed some borings with higher potential vertical rise. These results indicate that the variability of the potential vertical rise was not dependent upon the soil series in a similar sampling region. These results indicate that the subgrade may be affected by the geographic region more than the surficial soil deposit.

The use of the kriging method can additionally be used to evaluate the spacing between borings necessary to capture the variability of the potential vertical rise of the subgrade. This evaluation involves the analysis of the variograms from the kriging method in order to determine the range that the sill occurs. The variograms of the potential vertical rise from the kriging method were analyzed for various conditions Figure 4.55 uses the results from all borings to a depth of 6 ft, Figure 4.56 uses results from the borings in the Houston Black clay to a depth of 6 ft, and in Figure 4.57 uses results from the borings in the Houston Black clay to a depth of 6 ft that were located in the region between borings B-8 and B-46.

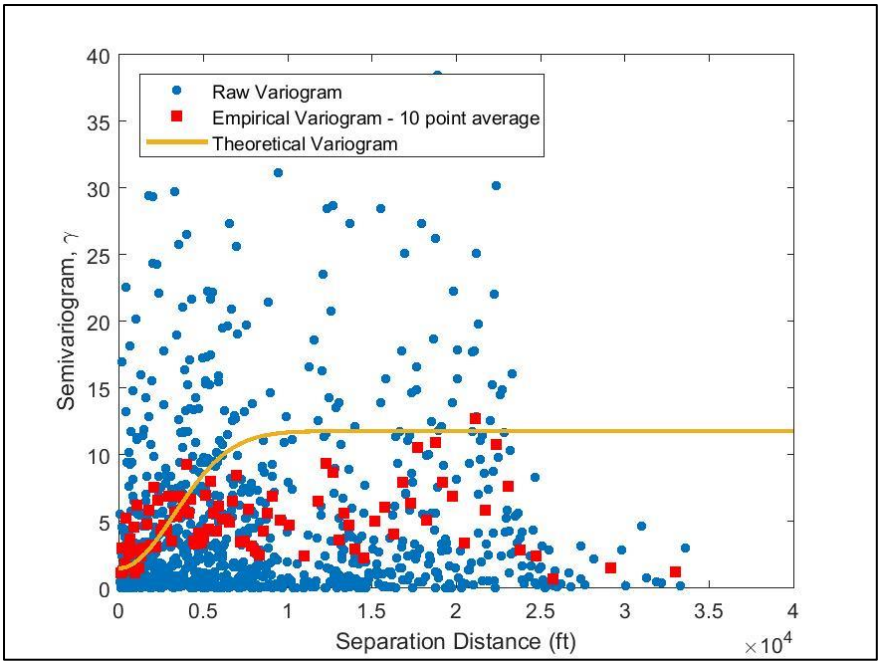

Figure 4.55: Variogram of potential vertical rise using data from the boring data to a depth of 6 ft

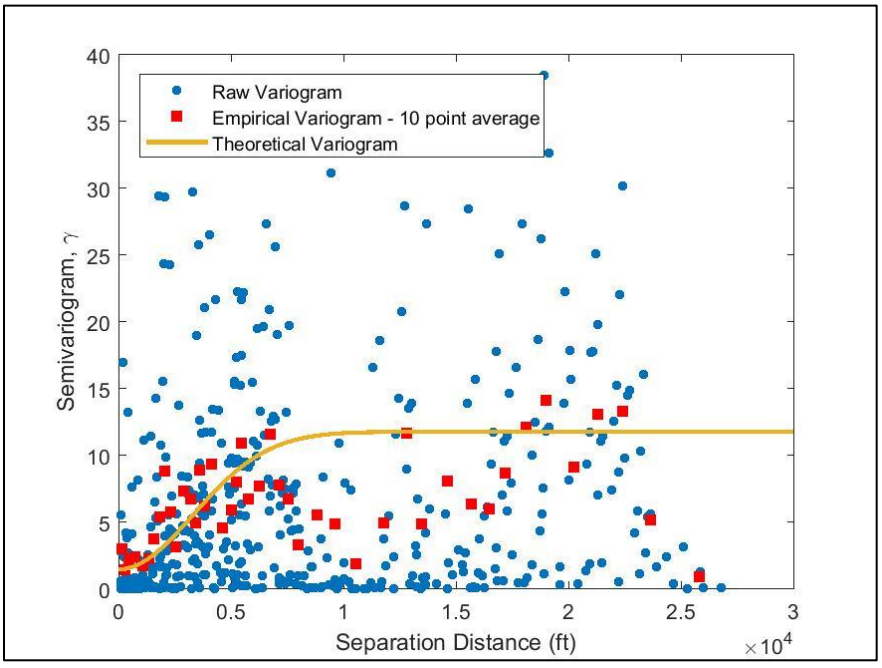

Figure 4.56: Variogram of potential vertical rise using data from only the Houston Black borings to a depth of 6 ft

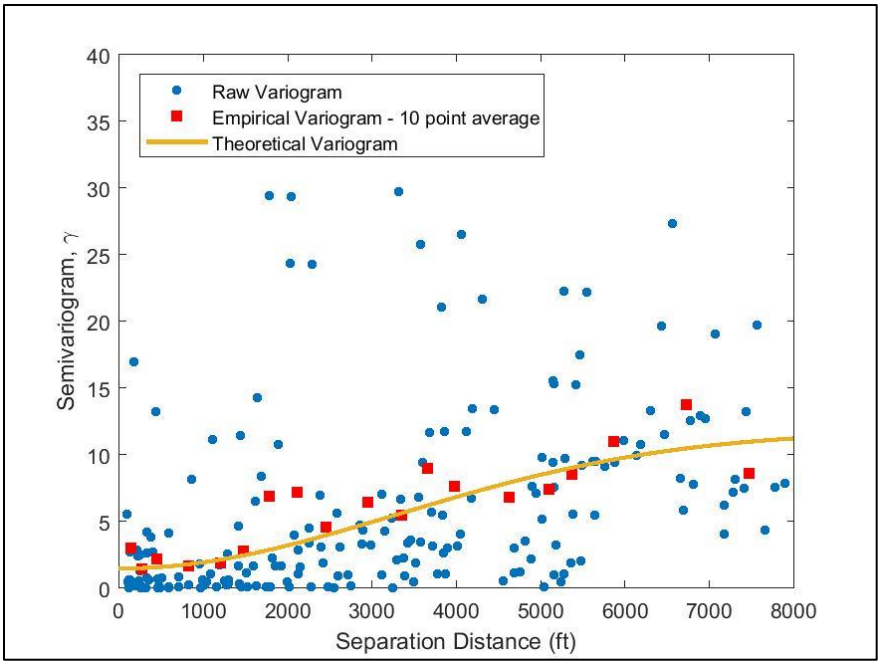

Figure 4.57: Variogram of potential vertical rise using data from the Houston Black clay from B-8 to B-46 to a depth of 6 ft

In general, the range from the variograms tends to increase with a more finely refined data set (i.e. the range using all of the borings is approximately 5,000 ft. whereas the range using only borings from the Houston Black clay is between 7,000 to 9,000 ft). The most specific data set, using results from the heavily sampled region from between B-8 and B-46 in the Houston Black clay, indicated that the range can be upwards of 8,000 ft. This increase in the range can be expected, as specimens within the same soil series or geographic region are expected to be more similar. However, this distance to reach the sill may not capture the variability in the potential vertical rise due to the relatively high semivariance. Therefore, further analysis is required to determine the necessary spacing between borings to capture the variability of the potential vertical rise.

In order to further assess the distance between borings, the maximum and minimum error between the calculated and estimated potential vertical rise was analyzed.

The maximum section error, in terms of an absolute value, was calculated based on the distribution of the residuals from the estimated potential vertical rise. These errors are shown in Figure 4.58 for the case of using all the borings to a depth of 6 ft, Figure 4.59 for using all the borings between B-8 and B-46 to a depth of 6 ft, and Figure 4.60 for using only the Houston Black borings to a depth of 6 ft.

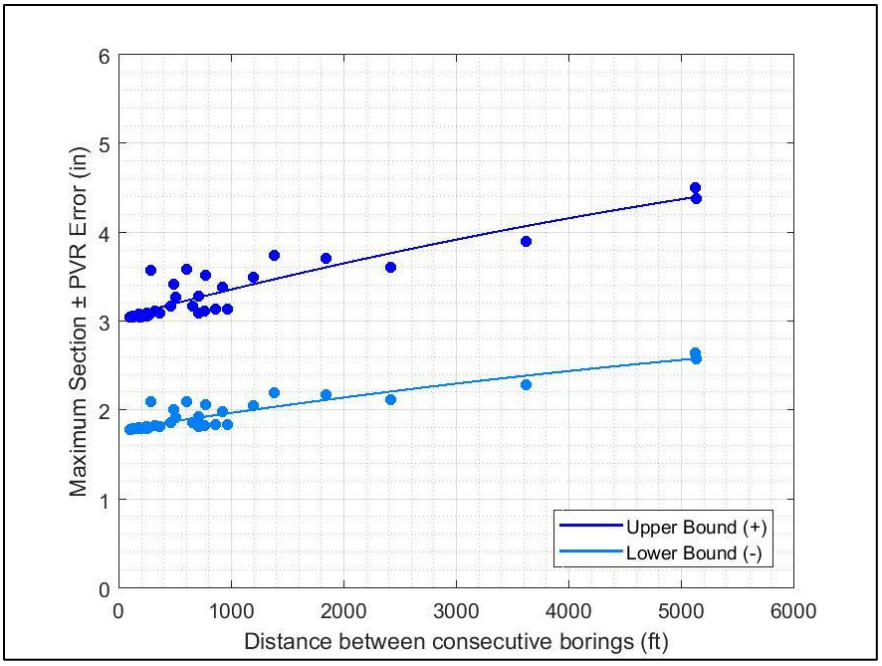

Figure 4.58: Maximum section potential vertical rise error using data from the boring data from all borings to a depth of 6 ft

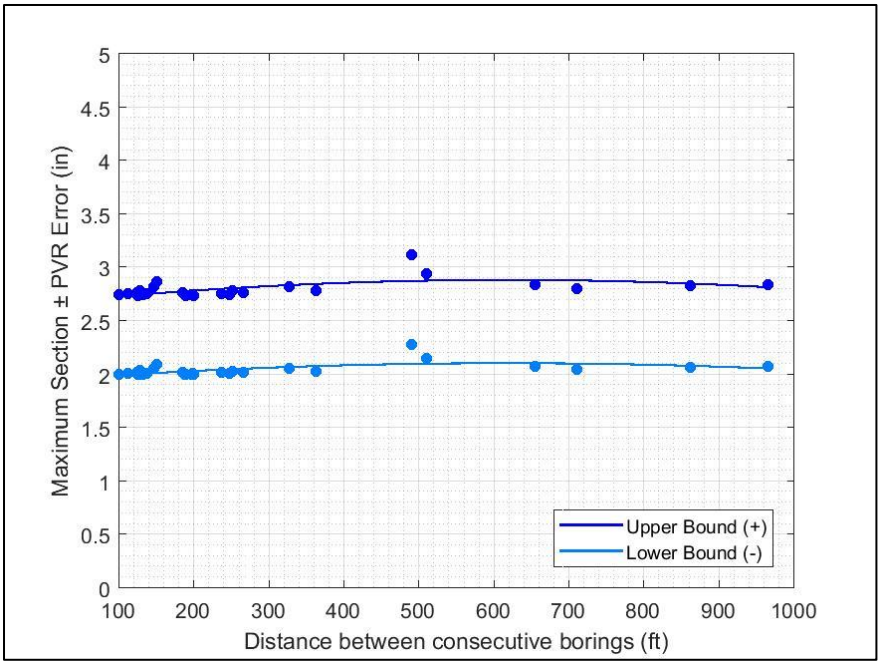

Figure 4.59: Maximum section potential vertical rise error using data from the boring data from B-8 to B-46 to a depth of 6 ft

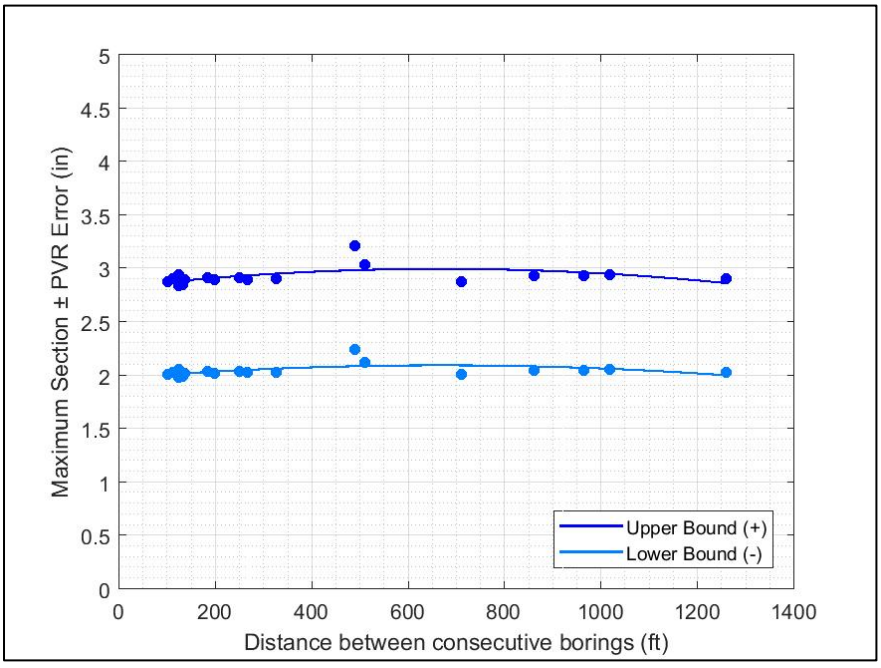

Figure 4.60: Maximum section potential vertical rise error using data from the boring data from only the Houston Black clay from B-8 to B-46 to a depth of 6 ft

Using the data from all of the evaluated borings along the roadway, the maximum error increased linearly with increasing distance between borings. The error tended to flatten with a higher refinement of the data set, indicating that natural heterogeneity in the subgrade affected the prediction of the potential vertical rise. However, the error from these refined data sets was relatively high at between 2 and 3 in. This high error was observed when using data from all of the borings, regardless of soil series, and when using data from only the borings in the Houston Black series. This similarity is consistent with the results from the analysis of the semivariograms and indicates that that geographic region significantly affects the potential vertical rise of the subgrade, even between borings in different clayey soil series. Due to the high potential error between borings, the spacing between borings the MEPDG, 500 to 1500 ft, is recommended instead of the range from the kriging analysis.

4.5 Comparison of Regional versus Local Variability in Taylor-Navarro Groups

The results from Sections 4.3 and 4.4 were analyzed to evaluate the variability of soil deposits at a regional scale (Section 4.3) and at a local scale (Section 4.4). Results from only the Houston Black series were used for this evaluation due to comparatively high amount of data. In total, results from the 13 locations in Section 4.3 were used to analyze the variability at a regional scale, and results from 118 soil subsections in 30 borings from Section 4.3 were used to analyze the variability at a local scale. In the following figures, the results from the regional scale are identified as “Central Texas” results, and the results from the local scale are identified as “I-10” results. The soil properties and swelling characterization were compared between the two scales. To simplify the comparison between the two scales, a normal distribution of test results was assumed for this analysis.

The variability of the Liquid Limit was analyzed between the two scales. The experimental method to determine the Liquid Limit differed between the two scales. The Liquid Limits for the soils in the regional scale were fully characterized by using multiple data points and a semi-log-linear regression. The Liquid Limits for the soils in the local scale were estimated by using the single point method from ASTM D4318 Method B. The difference in the methodology to determine the Liquid Limit of a soil may affect the variability between the two scales. The probability density functions and histograms are shown in Figure 4.61. The empirical and theoretical cumulative density functions are shown in Figure 4.62.

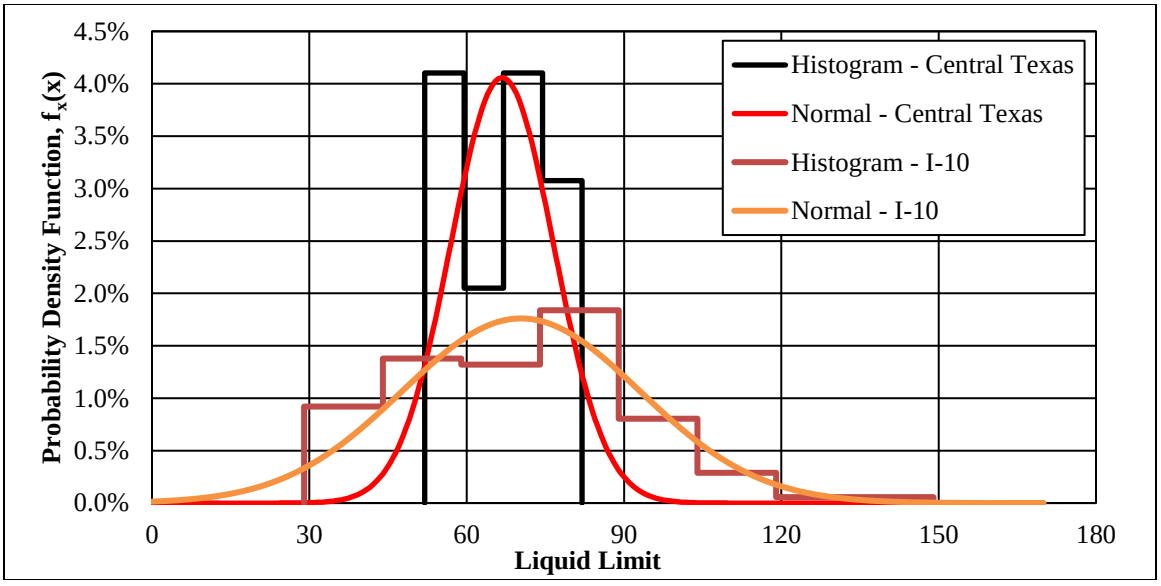

Figure 4.61: Probability density functions and histograms for Liquid Limit of Houston Black clay at two scales

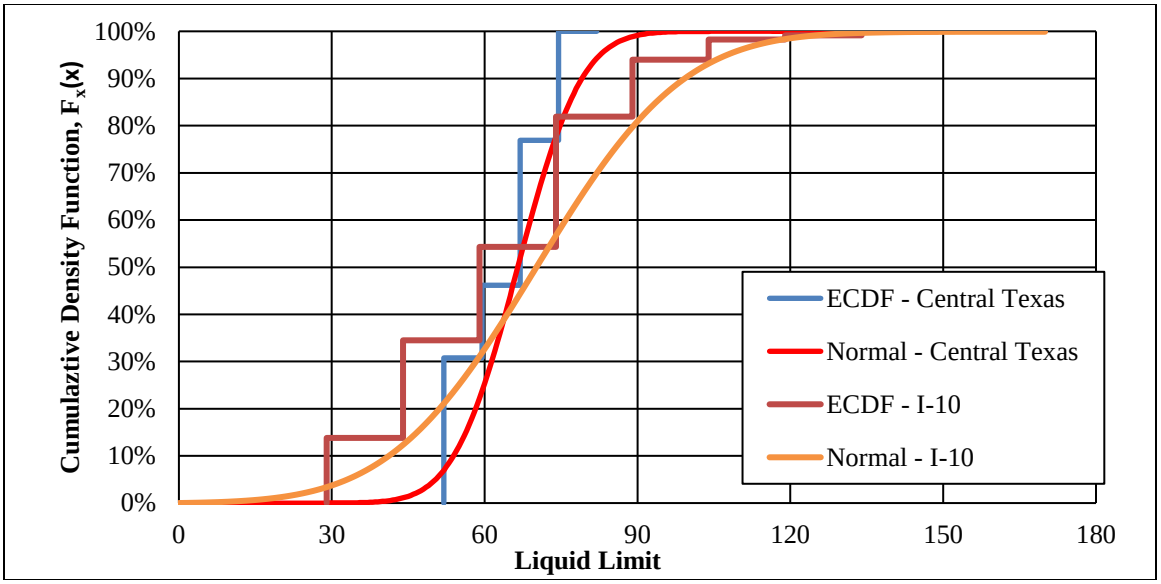

Figure 4.62: Cumulative density functions for Liquid Limit of Houston Black clay sampled at two scales

The median values for both scales were similar. However, the tails of the distribution was longer for the local scale analysis than those from the regional analysis. This difference between the scales were analyzed at both the upper and lower tails of the distribution of the local scale. At the lower tail, results from the local scale were assumed to be affected more from the presence of local creeks that would increase the amount of non-plastic material in the soil deposits. The bulk sampling of soils used in the regional scale reduced the effect of non-plastic materials as the sampling locations were selected away from creek beds or inclines. At the upper tail, soil sampled at depth using the Shelby tube sampler were assumed to be portions of the Houston Black clay for the local scale analysis. This assumption may not be valid for portions of the borings that with parent material at depth.

The variability of the Plasticity Index was analyzed between the two scales. The experimental method to determine the Plasticity Index differed between the two scales.

The Plasticity Index for the regional scale analysis were calculated using the Plastic Limit determined from ASTM D4318. The Plasticity Index for the local scale analysis estimated Plastic Limits based on test results from a previous geotechnical consultant for several locations. As previously discussed, there was additionally a difference in the method to determine the Liquid Limit for the different scale analyses. The probability density functions and histograms are shown in Figure 4.63. The empirical and theoretical cumulative density functions are shown in Figure 4.64.

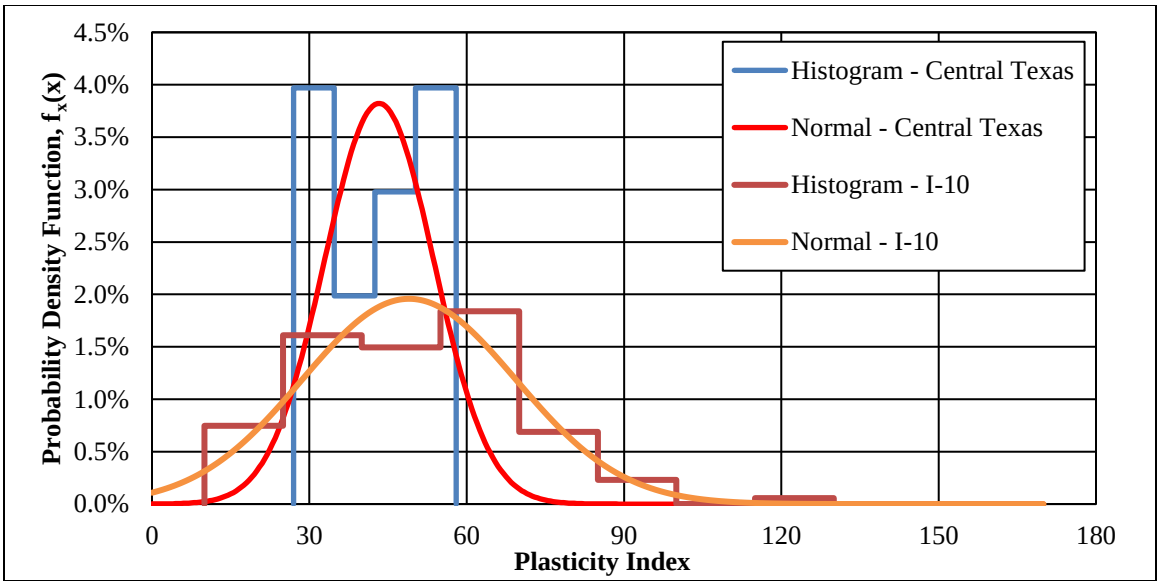

Figure 4.63: Probability density functions and histograms for Plasticity Index of Houston Black clay at two scales

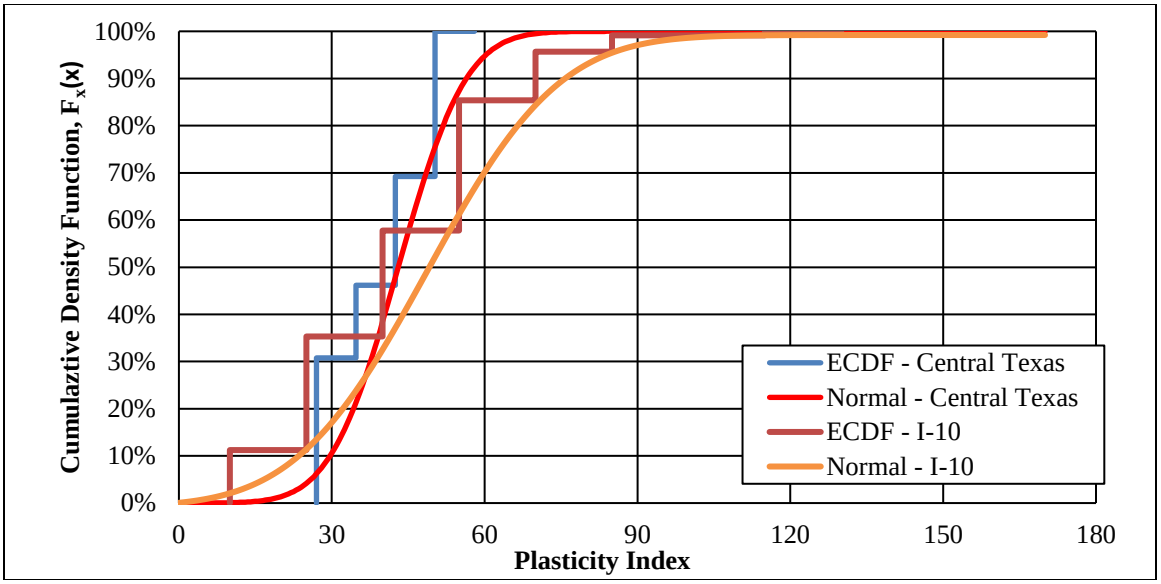

Figure 4.64: Cumulative density functions for Plasticity Index of Houston Black clays at two scales

The trends from the analysis of the Plasticity Index slightly differed from the those from the analysis of the Liquid Limit. The results from local scale tends to have a higher Plasticity Index than the results from the regional scale. This difference affected both the mean value of the Plasticity Index and the tails of the normal distributions. This behavior for the local scale analysis was attributed to the estimation of the Plastic Limit for some specimens and the inclusion of soil specimens sampled at depth. However, in general, the distribution of the Plasticity Index was relatively similar between the two scales.

The variability potential vertical rise, using the results to a depth of 6 ft, were analyzed between the two scales. For the bulk sampled soils from the regional scale analysis, a semi-log-linear stress-swell curve was assumed between the estimated maximum and minimum stresses in the deposit. The stress-swell curves were determined from swelling test results, and a semi-log-linear curve was used to simplify the analysis. The stresses used for the analysis were estimated by averaging the maximum and

minimum stresses from the borings tested in Section 4.4. The logarithmic average of maximum and minimum stresses was determined for each 6 ft deposit, and the strain at this stress was used to estimate the potential vertical rise for the bulk sampled soil. This method is similar to the IV method used to estimate the effective specimen stress from Zornberg et al. (2014). The potential vertical rise for the local scale analysis was determined from the cumulative potential vertical rise of borings in the Houston Black clay from Section 4.4. The probability density functions are shown in Figure 4.65. The empirical cumulative density functions are shown in Figure 4.66. A normal distribution was not used for this analysis, and only the empirical data is shown.

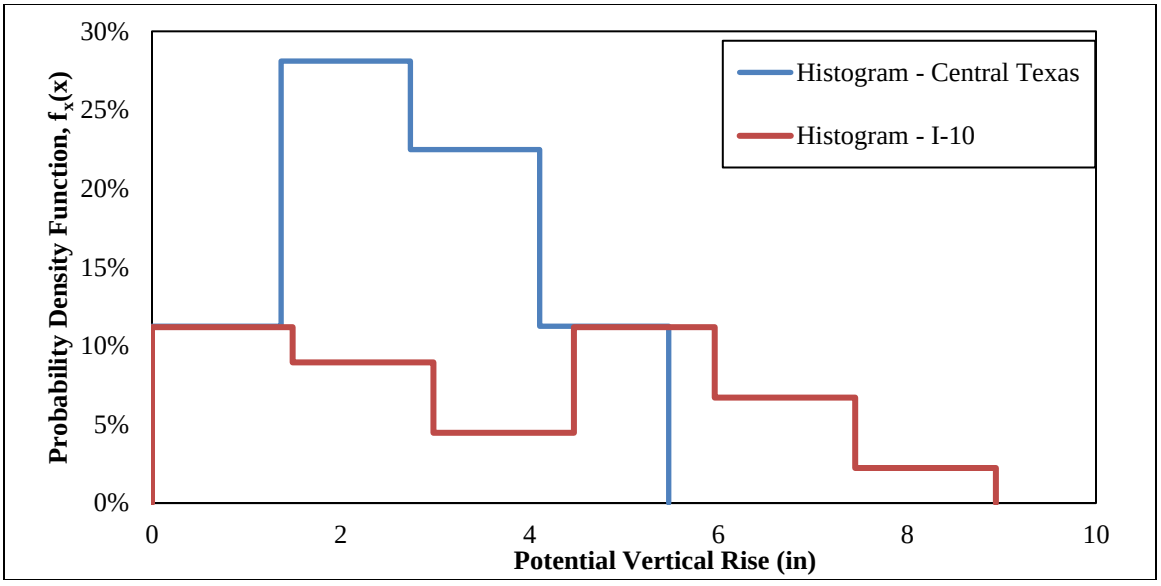

Figure 4.65: Probability density functions and histograms for potential vertical rise to a depth of 6 ft of Houston Black clays at two scales

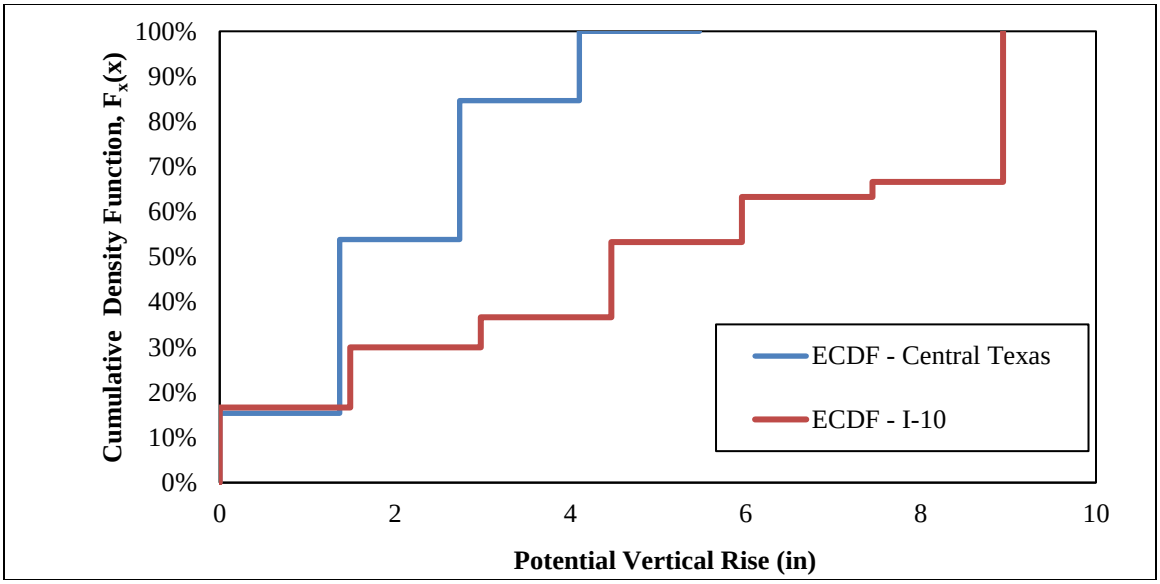

Figure 4.66: Empirical cumulative density functions for potential vertical rise to a depth of 6 ft of Houston Black clays at two scales

Unlike the variability of the Atterberg Limits, there was a significant difference in the distribution of the potential vertical rise between the two scales. The potential vertical rise from the local scale analysis tends to be significantly higher than the potential vertical rise from the regional scale analysis. This difference was attributed to the difference in the sampling methodology. The bulk sampled soils were collected from the upper region of the soil, rarely exceeding the upper 2 ft of the deposit. As such, the soil near the surface tends to undergo more of the cyclic wetting and drying than the specimens at depth. With the increased amount of wetting and drying, the soil near the surface is expected to undergo a significant amount of leaching and intermixing with granular material near the surface that can reduce the percentage of clay minerals in the sampled soils. These changes are expected to affect the swelling of the soils. To validate this assumption, the empirical probability density functions of the Liquid Limits from Section 4.4, grouped based on the depth of the subsection, is shown in Figure 4.67

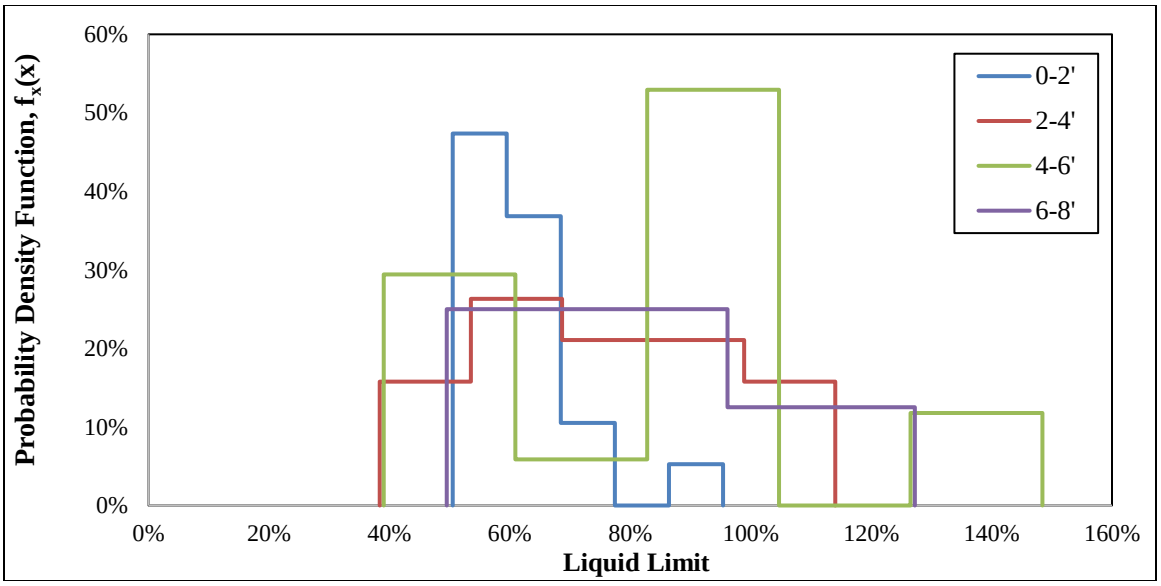

Figure 4.67: Empirical probability density functions for Liquid Limit of Houston Black clay sampled along the IH-10 Project with depth

The Liquid Limit tends to increase with increasing depth. Further, the distribution of the Liquid Limit in the upper 2 ft. is skewed towards lower values. At depth, the distribution of the Liquid Limit is more similar to a normal distribution. These trends are consistent with the assumption that soils near the surface tended to have a lower Liquid Limit due to impact of more cyclic wetting and drying.

Additionally, the distribution of the in-situ gravimetric moisture content at the time of sampling was analyzed. This analysis was conducted in order to identify differences in the in-situ gravimetric moisture content with depth. Only results from the local scale analysis were used as the soils from the regional scale analysis were intermixed during sampling. The empirical probability density functions are shown in Figure 4.68. The empirical cumulative density functions are shown in Figure 4.69.

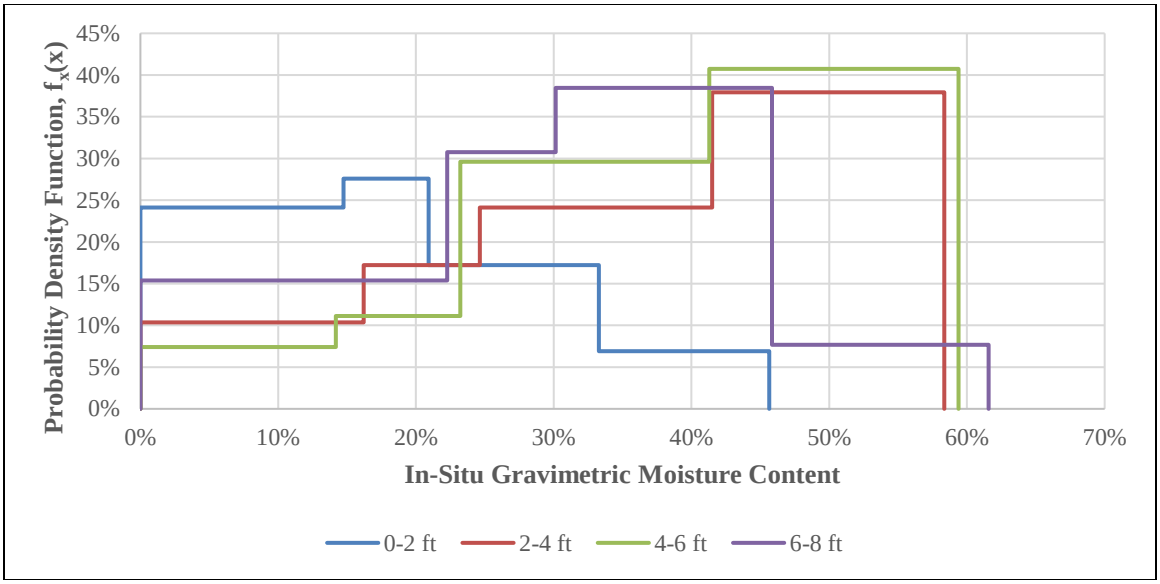

Figure 4.68: Empirical probability density functions for in-situ gravimetric moisture content of soils sampled along the IH-10 Project with depth

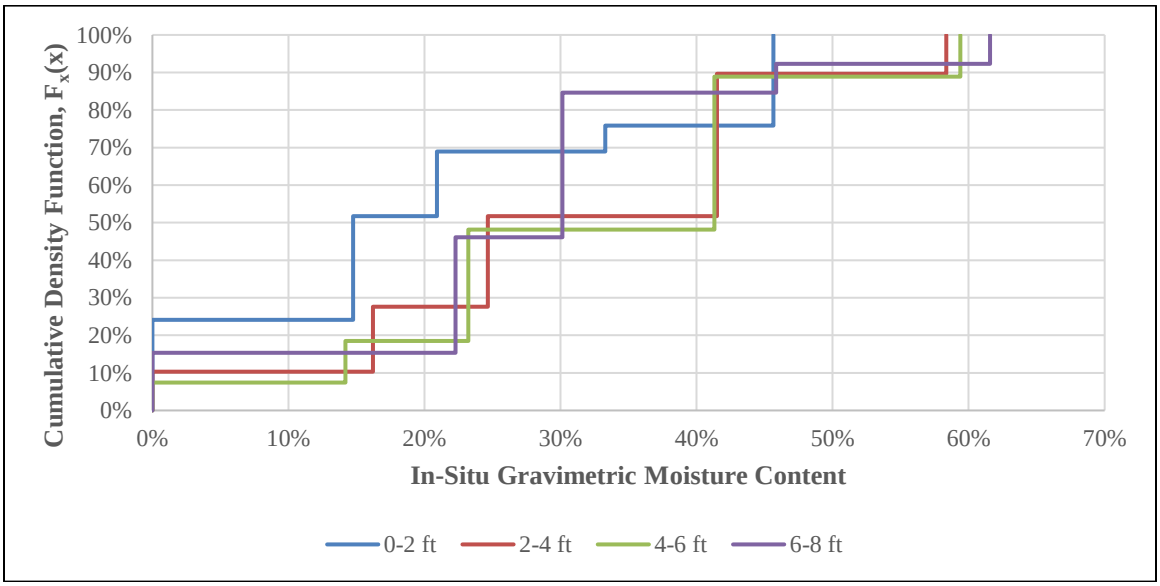

Figure 4.69: Empirical cumulative density functions for in-situ gravimetric moisture content of soils sampled along the IH-10 Project with depth

Both the empirical probability and cumulative distribution functions indicate that the soil sampled near the surface tended to have a lower gravimetric moisture content than soil

sampled at depth. The in-situ gravimetric moisture content tends to skew to higher moisture contents with increasing depth. These trends are consistent with soil near the surface undergoing more significant moisture fluctuations than soils at depth.

The variability in soil properties and the potential vertical rise was analyzed and compared at a regional scale and at a local scale. The variability of both the Liquid Limit and Plasticity Index did not vary significantly, with a similar median value between the two scales and slightly more significant tails for the local scale analysis. The higher variability for the local scale was attributed to the inclusion of specimens at deeper depths than those from the regional scale and differences in the methods to measure the Atterberg Limits between the two analyses. Additionally, the variability of the Liquid Limit was analyzed with depth for the local scale analysis. The Liquid Limit tends to increase with increasing depth. Additionally, the Liquid Limit tends to skew to lower measurements for soils closer to the ground surface. These trends are consistent with the variability of the in-situ gravimetric moisture content from the local scale analysis, which increases with increasing depth. However, there was a significant difference in the variability of the potential vertical rise. The results from the local scale analysis tend to be significantly higher than the results from the regional scale analysis. This difference can be attributed to differences in the Liquid Limit with depth and the reduced amount of clay minerals closer to the ground surface due to cyclic wetting and drying.

4.6 CONCLUSIONS

An analysis of the soil properties and unsaturated soil behavior in the Taylor-Navarro groups was performed to understand the variability of soil deposits in Central Texas. The analysis consisted of two research components. The first component evaluated the variability of the soil properties and unsaturated soil behavior on a regional

scale, and the second component evaluated the variability of these properties and behavior on a local scale. The regional-scale study analyzed differences between the Branyon and Houston Black clays, both prominent soil series in the Taylor-Navarro groups, that were sampled at various locations in Central Texas. These soils were evaluated for their differences in soil properties, soil-water retention curves, and stress-swell curves. The local-scale analysis evaluated a more heavily sampled portion of a highway on the Taylor-Navarro groups for the variability of the potential vertical rise and Atterberg Limits. Geospatial estimators were additionally used to estimate the potential vertical rise between borings for this analysis. The results from the regional-scale and local-scale analyses were compared to evaluate the differences in the variability of the potential vertical rise and Atterberg Limits between the two scales.

For the regional-scale analysis, several expansive soil deposits across Central Texas were sampled in bulk and characterized for their geotechnical and swelling properties. The soil deposits all derived from the Taylor-Navarro groups and were identified as either Houston Black or Branyon clay. In total, 13 deposits of the Houston Black clay and 6 deposits of the Branyon clay were sampled. The test results from the sampled soils were analyzed for the variability of their soil and swelling properties. Based on the results from this analysis, the following conclusions can be made:

- The Houston Black clay tends to have a higher Liquid Limit and Plasticity Index than the Branyon clay.
- The Houston Black clay also tends to have a higher percentage of fines and clay particles than the Branyon clay.
- These trends are consistent with the difference in the depositional environment and parent materials. The Houston Black clay is residuum derived from Cretaceous shale, whereas the Branyon clay derives from the

erosion of a younger mudstone. Based on these differences, the Branyon clay can be expected to have a lower percentage of fines and lower Atterberg Limits.

- The optimum compactions condition, according to Standard Proctor compaction energy, were found to not vary significantly between the two soil series. This trend indicates that the optimum compaction conditions may be reasonably independent of soil series.
- The soil-water retention curves did not vary significantly between the two soil series. This trend is consistent when using either the degree of saturation or volumetric moisture content as a dependent variable to define the curves.
- The total suction at the same volumetric moisture content or degree of saturation tends to be slightly higher for soils with a higher Liquid Limit.
- The Houston Black clay tends to swell more than the Branyon clay at the same effective stress. This difference is attributed to the difference in parent material and soil properties of the two soil series.
- Primary swelling tends to increase with increasing Liquid Limit for both soil series.

For the local-scale analysis, 43 locations were sampled using Shelby tubes along a future roadway expansion east of San Antonio, TX. The borings were grouped into 2 ft subsections based on Tex-124-E, and each subsection was tested for its Atterberg Limits and swelling characteristics. The results from swelling tests in each subsection of the borings were used to generate stress-swell curves and calculate the potential vertical rise for each boring. Geospatial estimators were used to predict the potential vertical rise

between boring locations. Based on the results from the analysis, the following conclusions can be made:

- The traditional methodology used to predict the potential vertical rise in field sites, Tex-124-E, was found to significantly under predict the magnitude of the potential vertical rise at the IH-10 borings.
- The deepest subsection of each boring can significantly affect the prediction of the potential vertical rise. These portions of the borings were assumed to not be part of the active zone.
- The Liquid Limit, Plasticity Index, and in-situ gravimetric moisture content tended to increase with increasing depth at the location of this project. These results indicate that the soil at depth may not be a part of the active zone.
- The kriging method was found to be useful to predict the potential vertical rise between borings. However, the method tends to smooth the predictions to the mean and is heavily affected by the high potential vertical rise of the deepest subsections.
- Due to a high potential error of the estimated potential vertical rise between borings, the boring spacing for future projects should use the recommendations from the MEPDG (500 to 1,000 ft).

The results from the regional-scale and local-scale analyses were compared to evaluate the differences in the variability of soils derived from the Taylor-Navarro groups at different scales. Based on the results of this analysis, the following conclusions can be made.

- The variability of the Liquid Limit and Plasticity Index are similar at both scales. The mean values of the Atterberg Limits were found to be similar at the two scales.
- The tails from the analysis of the Atterberg Limits were slightly longer for the local scale analysis due to the inclusion of specimens at increasing depths.
- From the local scale analysis, the Liquid Limit, Plasticity Index, and in-situ gravimetric moisture content tends to increase with increasing depth. These results indicate that the lowest portion of the deposits may not be as significantly affected by seasonal moisture fluctuations.
- The potential vertical rise from the local scale analysis tended to be significantly higher than that from the regional scale analysis.
- This difference in the potential vertical rise can be attributed to differences in the sampling methodology between the two scales. The soil specimens for the regional scale only included laboratory-reconstituted portions of the surficial soil deposit. The soil specimens for the local scale included undisturbed specimens with field soil fabric. This soil fabric from the local scale specimens may increase the swelling based on the presence of peds and clusters, as previously discussed in Chapter 3.

Chapter 5: Hydraulic Monitoring of a Subgrade in a Roadway Founded on Expansive Soils

ABSTRACT

The subgrade of a roadway founded on expansive soils was instrumented using volumetric moisture content and matric suction sensors. The sensors were placed beneath the shoulder of a newly built roadway to examine the moisture migration patterns. The site was monitored during two distinct periods, one in which the surface of the roadway involved only a temporary flexible base surface and the other in which a final asphaltic surface had been added. The two time periods showed markedly different behavior in relation to moisture infiltration fronts, with the flexible base surface having more rapid moisture infiltration than the final asphaltic surface. The expansive deposit tended to dry to a lower moisture content beneath the asphaltic surface than the flexible base surface. Additionally, results from the suction and moisture content sensors were filtered and fitted to define field-generated soil-water retention curves. Results collected during the two time periods indicate that the soil-water retention curve did not vary significantly over the two time periods for the locations where sensors provided reliable readings. However, the field-generated soil-water retention curves differed from those obtained in the laboratory. This difference was attributed to the difference in soil fabric. Finally, the surficial pavement deflections were measured during periodic field visits. The pavement tended to settle during the summer and heave after rainfall events. Overall, the field site indicated that expansive soil deposits can be monitored using current technology.

5.1 INTRODUCTION

Expansive soil subgrades have been shown to be particularly problematic for the long-term performance of flexible pavements as seasonal moisture fluctuations can cause significant longitudinal cracking due to heave and settlement of the pavement edges.

These subgrades are of major concern along the IH-35 corridor, between Dallas and San Antonio, due to the abundance of expansive soil deposits. Pavement design in Texas has conventionally relied on an index, the Potential Vertical Rise (PVR) as outlined in McDowell (1966) and Tex-124-E, which estimates the maximum vertical heave based on subgrade soil's Atterberg Limits. More recent guidelines from the Mechanistic-Empirical Pavement Design Guide (MEPDG) call for the use of water-flow analyses to account for changes in mechanical behavior of the subgrade with corresponding changes in moisture content. However, these analyses require proper understanding of seasonal variations in moisture content and matric suction, and limited studies have examined these seasonal fluctuations. One field study involved continuous monitoring of gravimetric moisture content fluctuations and periodic monitoring of matric suction fluctuations close to the shoulder of a roadway near Houston, TX (Puppala et al., 2011). Climatic conditions, particularly surface evaporation and average monthly rainfall during the summer months, are particularly different in Houston and in Central Texas. Therefore, a field assessment of moisture content and suction fluctuations in Central Texas sites is needed to further understand the impact of expansive subgrade behavior in relation to pavement design. Additionally, the readings from the moisture and suction sensors can be used to define field soil-water retention curves. These field-generated, in-situ curves can be compared to soil-water retention curves from laboratory methods to evaluate differences between in-situ and laboratory-reconstituted soils.

The hydraulic properties of the upper pavement layer of a roadway are an important input for modeling of moisture flow in the underlying subgrade (Hansson et al. 2005). Asphalt surfaces are assumed to be often impermeable without the presence of cracks. However, flexible base surfaces with an applied prime coat, which are used for temporary pavement surfaces, have not been extensively studied. Consequently, an

examination of each surface's impact on seasonal moisture fluctuations would be particularly beneficial. Due to the construction schedule at the field site, moisture fluctuations were monitored during a time period with a temporary flexible base surface sealed with a prime coat and during a time period with the final asphalt surface. Results from these time periods were compared for variations in seasonal moisture fluctuations.

The impact of moisture fluctuations on roadway performance has rarely been documented in field studies. One method involves the use of a non-prism total station to periodically measure the profile of a roadway (Roodi et al., 2016). With this technology, a visual representation of the heave and settlement of the pavement edges can be obtained during regular field visits. However, this study did not examine how moisture fluctuations in the subgrade affected the surface of the roadway, as sensors were not installed at the field sites evaluated. The study presented herein provides correlation between the performance and profile of a pavement structure with moisture fluctuations in the subgrade material.

5.2 Background Information for Monitoring of Expansive Subgrades

The literature review presented herein includes four sections. The first section evaluates the sensors used in this research component to monitor moisture content and matric suction fluctuations and the results from previous studies that used these sensors in expansive soils. The second section reviews previous studies on the moisture monitoring of field expansive soil deposits. The third section summarizes a previous study on the use of surveying techniques to monitor surficial pavement deflections. The final section examines previous studies on the deformation of flexible pavements over expansive subgrades.

5.2.1 Moisture and Suction Sensors in Soil Deposits

Various volumetric moisture content (VMC) sensors have been developed to monitor moisture fluctuations in soil deposits. For this project, the Decagon 5TE sensors were used. The sensors record the VMC, electrical conductivity, and temperature of the surrounding soil matrix by measuring the bulk electrical conductivity of the surrounding medium. These sensors are typically referred to as capacitance moisture content sensors. The dielectric permittivity of the soil is measured using oscillators in the sensors, and the sensor predicts the VMC using Topp's equation (Decagon, 2016). The sensors have an accuracy of ±0.03 m^3/m^3 for the VMC of the soil and are shown in Figure 5.1.

Figure 5.1: Decagon 5TE moisture content sensors (Decagon, 2016)

The moisture content sensors were initially selected over other moisture content sensors (such as time-domain reflectometers, or TDRs) due to previous field studies indicating inconsistent readings from TDRs used in an expansive soil deposit (Brown, 2013). Previous research indicated that expansive soils can be problematic for TDRs due to the attenuation and interpretation of the wave forms (Dellinger, 2011). The 5TE sensors were selected over another capacitance moisture content sensors, the EC-5, because the EC-5 sensors did not have the required accuracy to differentiate the flow of moisture for clayey soils (Plaisted, 2014). Additionally, the EC-5 sensors have previously shown poor survivability in expansive soil deposits beneath pavement structures (Azevedo, 2016).

The data from the 5TE sensors require corrections based on the environmental conditions. Garcia (2015) found that the moisture content readings were influenced by the temperature of the surrounding soil medium. Kocarek and Kodesova (2012) generated corrections for the moisture content readings from capacitance sensors based on the difference in the surrounding soil temperature and a reference temperature as follows:

$$\theta_{ref} = \theta_m - 0.002 * (t_m - t_{ref}) \quad (5.1)$$

Where t_m is the measured soil temperature in degrees Celsius, θ_m is the measured volumetric moisture content, and t_{ref} is a reference temperature of 20°C. This correction was originally generated for single frequency sensors that were the predecessor for the 5TE sensor.

Previous research studies indicated that the 5TE sensors can be problematic for moisture monitoring in expansive soils. Rosenbaum et al. (2010) found that the variability of the readings between sensors were higher than the expected maximum error. This variability indicated that sensor specific calibrations were needed. An issue with this calibration is that the correction is applied to the apparent permittivity of the soil. The readings from the 5TE sensor does not provide the apparent permittivity. Thus, the apparent permittivity must be back analyzed from Topp's equation. An additional study by Rosenbaum et al. (2011) indicated that the effects of the soil temperature and electrical conductivity on the moisture content reading were significant. A correction that incorporates these effects requires a third-order polynomial function applied to the apparent permittivity. In order to determine how well these corrections worked, a comparison of the corrections from Rosenbaum et al. (2011), from Kocarek and Kodaseva (2012), and comparative data from a TDR sensor in an expansive soil is shown

in Figure 5.2. This data for this analysis was taken an instrumented expansive soil in Central Texas.

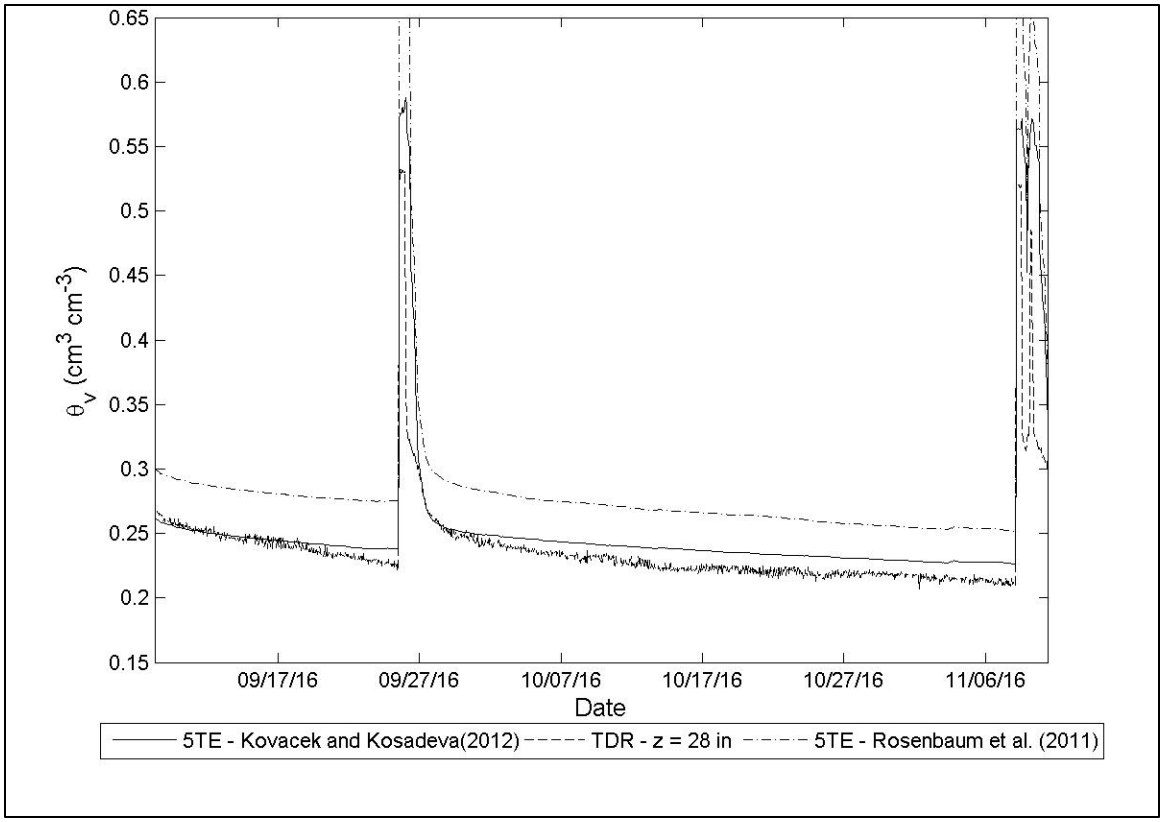

Figure 5.2: Comparison of corrections of data from capacitance moisture content sensors against results from a TDR sensor from the Taylor research site

Figure 5.2 indicates that the correction used by Kocarek and Kodaseva (2012) is relatively consistent with the more rigorous correction from Rosenbaum et al. (2011). The methods from Kocarek and Kodaseva (2012) and Rosenbaum et al. (2011) to correct the moisture content based on the difference in the soil and reference temperature resulted in similar corrections. However, the correction based on the bulk electrical conductivity from Rosenbaum et al. (2011) increases the amount of error between the

5TE reading and the TDR data. Due to these trends and the relative ease of application, the field data for this research component was corrected using the method from Kocarek and Kodaseva (2012). Additional studies that used the 5TE moisture content sensors indicate that the sensors are suitable for soils with an apparent electrical conductivity less than 1.7 dS m^{-1} (Visconti et al., 2013). Overall, the capacitance sensors are suitable for use in field, expansive soil deposits if the readings are corrected for the effect of the temperature of the surrounding soil.

In order to determine the matric suction fluctuations in the active zone, suction sensors were placed in the expansive subgrade. Decagon MPS-2 sensors were selected for use in the field project. The sensors utilize the capacitance of a calibrated ceramic disk to measure the volumetric moisture content of the disk. The soil-water retention curve of the ceramic disk is calibrated by the manufacturer. Since the volumetric moisture content and soil-water retention curve are known, the matric suction of the ceramic disk can be calculated and used to measure the matric suction of the surrounding soil assuming thermodynamic equilibrium between the disk and soil. These sensors were chosen instead of tensiometers due to the ease of installation and the lack of a water reservoir. The sensors have an accuracy of ±25% of the reading plus an additional 2 kPa for the readings from a range of -9 to -100 kPa. The expected range of suction is expected to be within a range of -9 kPa to 50 kPa, meaning the potential error is limited to a range of 4 kPa to 14 kPa. Therefore, these sensors may have a significant range of errors. A view of a MPS-2 sensor is shown in Figure 5.3.

Figure 5.3: Decagon MPS-2 matric suction sensor (Decagon, 2016)

5.2.2 Lessons Learned from Previous Field Sites

A few studies have been conducted to evaluate moisture fluctuations in expansive soil deposits beneath low overburden infrastructure. Puppala et al. (2012) instrumented subgrades beneath roadways in Fort Worth, San Antonio, and Paris, TX with moisture content sensors and matric suction sensors. The sensors were used to determine the moisture content fluctuations that corresponds to incipience of longitudinal cracking. The monitoring of the subgrade, as shown in Figure 5.4, indicated that the longitude cracking occurs primarily in periods of drying. Due to this result, the researchers concluded that settlement is what led to the onset of longitudinal cracking. Continuous suction sensor readings were not recorded due to limitations with the data acquisition system and sensors. In general, the study indicated that an expansive subgrade could be monitored for fluctuations in volumetric moisture contents and matric suctions.

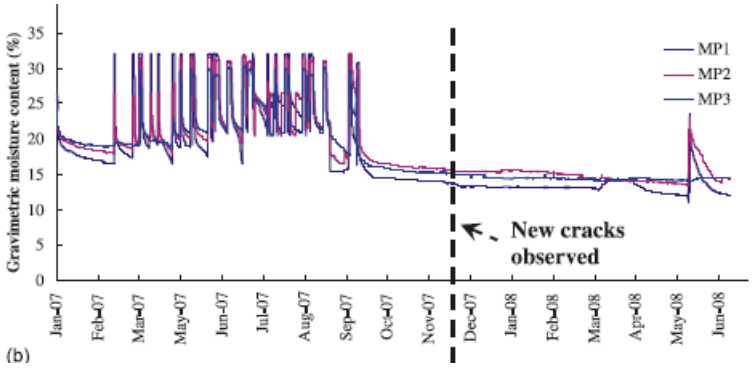

Figure 5.4: Volumetric moisture content with time in an expansive deposit in San Antonio (Puppala et al. 2012)

A study by Dinka et al. (2012) was performed at a site in Central Texas to analyze the behavior of swelling across a deposit. The soil deposit included portions of the Houston Black and Heiden clay. Results from their study indicated that the presence of carbonates (i.e. portions of limestone in the soil) were negatively correlated to the swelling potential of soils. Additionally, the shrinkage from the loss of water was less than the 1:3 ratio of change in height to water loss that is typically used. The study also indicated that the highest variability of swelling was from the surficial deposits and not the underlying, presumably unweathered, clays that were not exposed to the leaching of carbonates.

5.2.3 Monitoring of Surficial Pavement Deflections

A methodology that uses a prism-less total station system to monitor the profile of the roadway was developed by Zornberg et al. (2016) and Roodi et al. (2016). A prism-less total station system is used to measure the relative position of various points along a cross-section of a roadway. The prism-less system allows for the measurements of points without the needed for a worker to stand on the roadway. Measurement are taken at 1-ft

intervals along the cross-section, which is marked with a white line and evenly spaced orange points. An example of a marked roadway is shown in Figure 5.5.

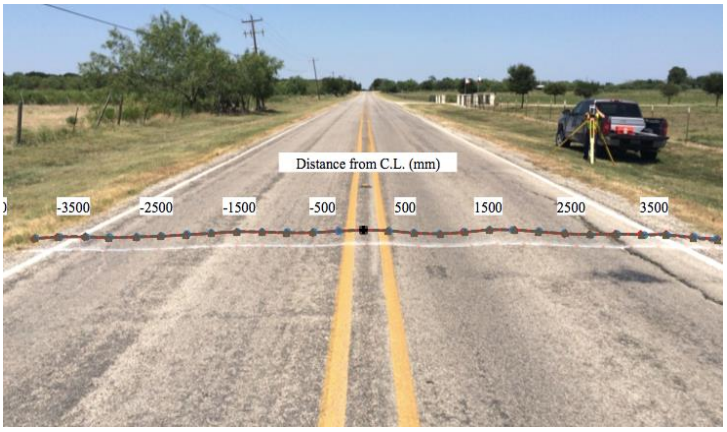

Figure 5.5: Marking for total-station monitoring of pavement profile (Zornberg et al., 2016)

Measurements are converted in relative displacements by geometry and assuming that the centerline does not vary between visits to the site. These assumptions are used to plot the surficial pavement deflections. Representative results from a roadway that was monitored using this methodology are shown in Table 5.1 and Figure 5.6.

Table 5.1: Representative results from total station monitoring (Zornberg et al., 2016)

FM 1979-Westbound Readings-Section#8-Visit #1							FM 1979-Eastbound Readings-Section#8-Visit #1						
Total Station Coordinate Reading Relative to center line				Modified coordination for cross section of the road			Total Station Coordinate Reading Relative to center line				Modified coordination for cross section of the road		
	Z	X	Y	Z	X	Y		Z	X	Y	Z	X	Y
Pt.	m	m	m	mm	mm	mm	Pt.	m	m	m	mm	mm	mm
1	0	0	0	0	0	0	1	0	0	0	0	0	0
2	-0.00762	0.217932	0.224028	-7.62	313	0	2	-0.0061	-0.19812	-0.22403	-6.096	299	0
3	-0.01981	0.428244	0.44196	-19.812	615	0	3	-0.02286	-0.39472	-0.4511	-22.86	599	0
4	-0.02134	0.641604	0.673608	-21.336	930	0	4	-0.02896	-0.61265	-0.67208	-28.956	909	0
5	-0.01524	0.839724	0.897636	-15.24	1229	0	5	-0.01829	-0.80467	-0.89002	-18.288	1200	0
6	-0.01372	1.042416	1.124712	-13.716	1533	0	6	0.001524	-1.03327	-1.11404	1.524	1519	0
7	-0.02591	1.260348	1.344168	-25.908	1843	0	7	0	-1.23292	-1.33807	0	1819	0
8	-0.03658	1.444752	1.56972	-36.576	2133	0	8	-0.01372	-1.43256	-1.54991	-13.716	2111	0
9	-0.04877	1.674876	1.7907	-48.768	2452	0	9	-0.02743	-1.6322	-1.7907	-27.432	2423	0
10	-0.05334	1.868424	2.013204	-53.34	2747	0	10	-0.03505	-1.83032	-2.01168	-35.052	2720	0
11	-0.05944	2.112264	2.25552	-59.436	3090	0	11	-0.03048	-2.04673	-2.24028	-30.48	3034	0
12	-0.05334	2.289048	2.465832	-53.34	3365	0	12	-0.03505	-2.2479	-2.4704	-35.052	3340	0
13	-0.05486	2.526792	2.692908	-54.864	3693	0	13	-0.03505	-2.45212	-2.68834	-35.052	3639	0
14	-0.06706	2.706624	2.912364	-67.056	3976	0	14	-0.05486	-2.67919	-2.91084	-54.864	3956	0
15	2.717292	-12.7559	3.003804	2717.292	13105	0	15	-0.0701	-2.87426	-3.14554	-70.104	4261	0

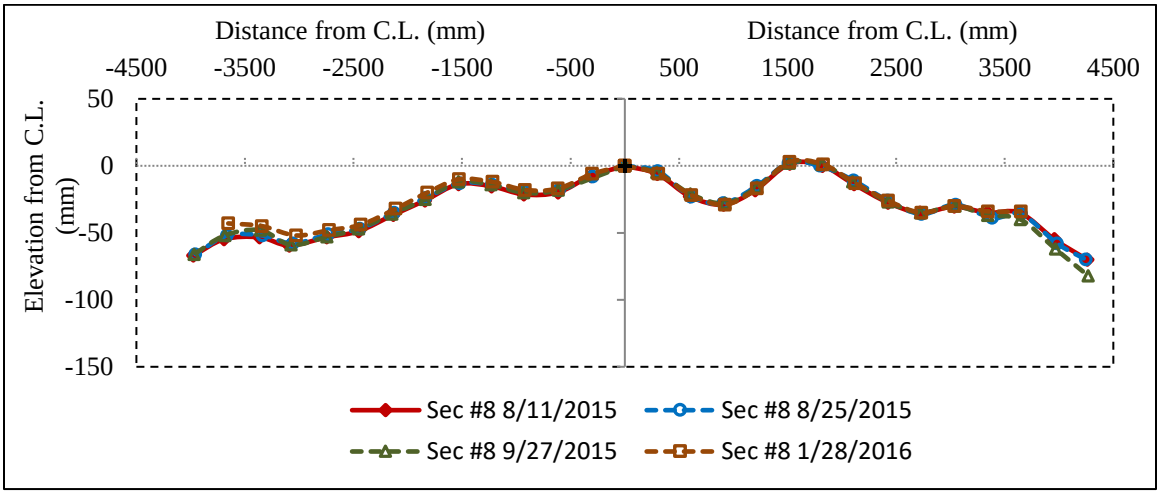

Figure 5.6: Representative pavement profile from total station monitoring (Zornberg et al., 2016)

5.2.4 Deformation of Flexible Pavements Structures over Expansive Clay Subgrades

Pavements founded on an expansive subgrade can undergo significant environmental cracking caused by the heave and settlement of the subgrade at the pavement edges. During the rainy season, the expansive subgrade tends to wet and can cause tensile stresses that may result in cracking on the edge of the pavement due to uplift

of the base and asphalt material as shown in Figure 5.7 (Zornberg et al., 2010). During the dry season, the expansive soil tends to dry and can cause additional tensile stresses that may result in cracking on the edge of the pavement due to settlement of the base and asphalt material.

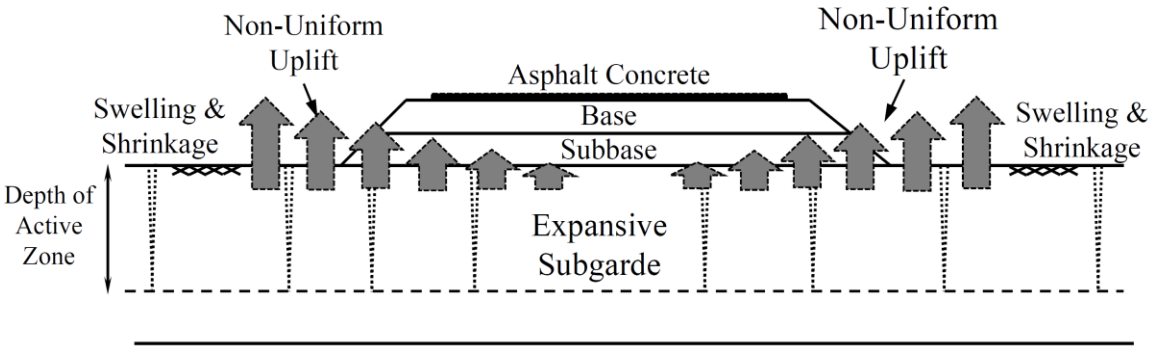

Figure 5.7: Effect of expansive soils on the performance of flexible pavements (Zornberg et al., 2010)

Numerous remediation techniques have been developed to minimize volume changes caused by expansive soils. The most common methodologies to treat the expansive subgrade involve in removal of the surficial expansive soil layer or mixing of lime or cement in the expansive soil for stabilization (National Highway Institute, 2006). Additional additives to stabilize the expansive soils include fly ash and other industrial by-products. These additives stabilize the expansive soil by flocculating the clay minerals with the substation of the monovalent ions on the clay surface with Ca^{2+} ions (Seco et al., 2010). Other remediation methods include the use of geogrid reinforcement in the base material to minimize the tensile stresses on the asphalt material (Zornberg and Gupta, 2009). Azevedo (2016) indicated that a geosynthetic can be used to separate the base course and subgrade in order to reduce cracking. Certain geosynthetics also incorporate wicking material to redistribute moisture across the subgrade to a more uniform condition

Expansive subgrades can also be modeled in order to determine the extent and magnitude of moisture fluctuations. The hydraulic properties of a roadway's upper pavement layer are an important input for modeling moisture flow beneath pavements (Hansson et al., 2005). Using a simulated roadway design with a base, subbase, and gravel shoulders, a roadway was modeled using HYDRUS 2-D to evaluate the moisture fluctuations beneath the pavement with or without cracking in the upper layer. The researchers found that cracking affected the infiltration of moisture. Apul et al. (2007) indicated that the velocity field and pressure head is greatest on the corresponding embankment next to the pavement shoulder and that the presence of cracking accelerates the infiltration of moisture into the subgrade. Additionally, the evaporation of moisture from the subgrade depends heavily upon the type of surficial pavement material (Brown and Borst, 2015).

5.3 Overview of the Monitored Site

The research component presented in this section covers the instrumentation and characterization of an expansive subgrade beneath a pavement structure. The results and analysis from the site selection and geotechnical investigation were grouped into two sections. The first section examines the location and selection of the field site. The second section summarizes the characterization of the subgrade for the geotechnical properties and unsaturated soil behavior.

5.3.1 Site Location and Instrumentation Layout

The field site, shown in Figure 5.8, is located on a Farm-to-Market road, FM 685. The site is approximately 25 miles northeast of Austin, Texas. The roadway was undergoing a widening from a two-lane road to a four-lane road. As part of the widening of the roadway, driveways into various farming operations and subdivisions were

additionally constructed. The subgrade at the northern portion of the project is a known expansive soil in Central Texas, the Branyon clay. A driveway was selected for monitoring due to a lack of geosynthetic reinforcement, a relatively thin layer of asphalt, and a sporadic and small amount of vehicular traffic. These conditions were expected to result in a significant amount of surficial pavement deflections and cracking that could be attributed primarily to the expansive soil subgrade.

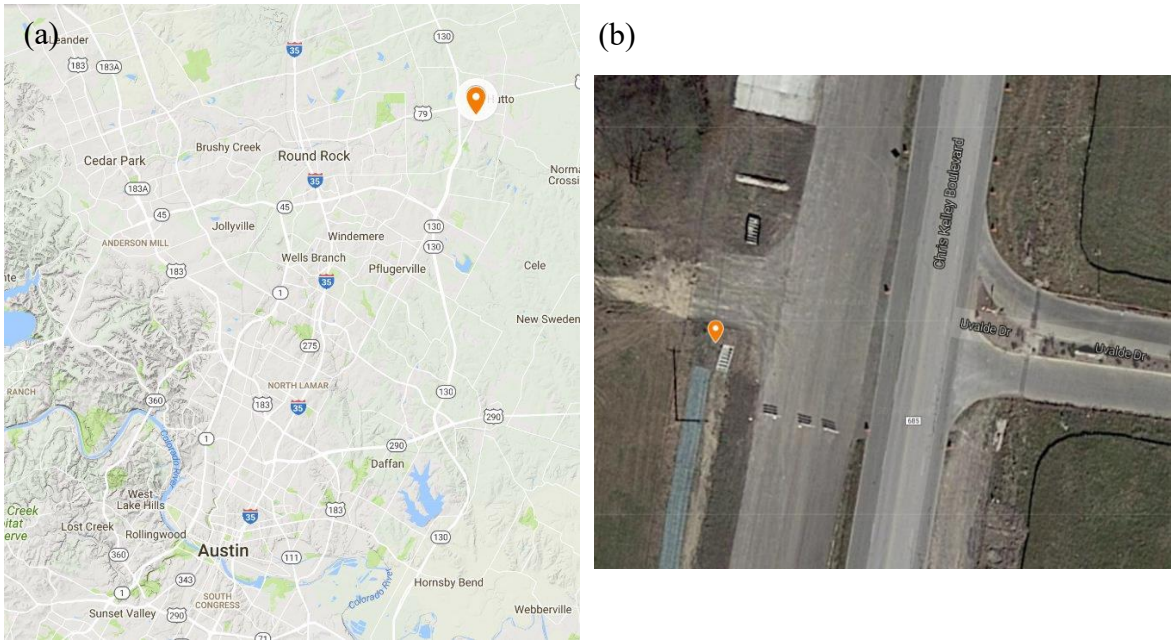

Figure 5.8: Location of FM685 site (a) and aerial view of instrumented location (b) (Google, 2016)

The construction of the driveway was involved two time periods with differing surficial pavement conditions. A flexible base surface with a prime coat, a temporary surface used during construction, was the first surface condition. This time period is referred to as the flexible base time period. The prime coat is a sprayed asphaltic emulsion that is applied to the top surface of unbound material in order to reduce the

infiltration of moisture, stabilize fines in the base material, and improve bonding for the final asphaltic layer. A year after the flexible base was placed, the final asphaltic surface, Type C hot mix, was paved on top of the flexible base surface. This time period is referred to as the asphalt time period. These different surficial conditions allow for a comparison of the subgrade moisture fluctuations and corresponding surficial pavement deflections.

The final cross-section of the driveway consisted of 2 in. (5.1 cm) of asphalt underlain by 5 in. (12.7 cm) of flexible base. The subgrade at the driveway consisted of 5 ft of an expansive soil, the Branyon clay as identified from soil surveys, underlain by a non-expansive tan clay. The flexible base surface with the prime coat is shown in Figure 5.9a. A cross-section of the instrumented roadway during the flexible base time period is shown in Figure 5.9b. The final asphalt surface is shown in Figure 5.9c. A cross-section of the instrumented roadway during the asphalt time period is shown in Figure 5.9d. The sensors were installed at the approximate edge of the asphalt surface in order to monitor moisture fluctuations at the expected location of longitudinal cracks. The slope of the soil from the edge of the pavement to the drainage ditch was approximately 3H:1V. The stratigraphy of the subgrade where the sensors were installed and the delineation between the Branyon clay and the underlying tan clay is shown in Figure 5.10.

Sensors were instrumented at four depths in the subgrade. All instrumented depths included both 5TE and MPS-2 sensors in order to evaluate the moisture and suction fluctuations. The sensors were installed at the approximate edge of the final asphalt surface. The first set of sensors were installed 0.5 ft (0.15 m) below the base-subgrade interface in the Branyon clay. The second set of sensors were installed 1.5 ft (0.45 m) below the base-subgrade interface in the Branyon clay. The third set of sensors were installed 4 ft (1.22 m) below the base-subgrade interface in the Branyon clay. The final

set of sensors were installed 5.5 ft (1.52 m) below the base-subgrade interface and 0.5 ft (0.15 m) below the Branyon clay-tan clay interface in the tan clay. Each set of sensors were installed approximately at 1 ft (0.30 m) horizontal spacing from the box culvert shown in Figure 5.8.

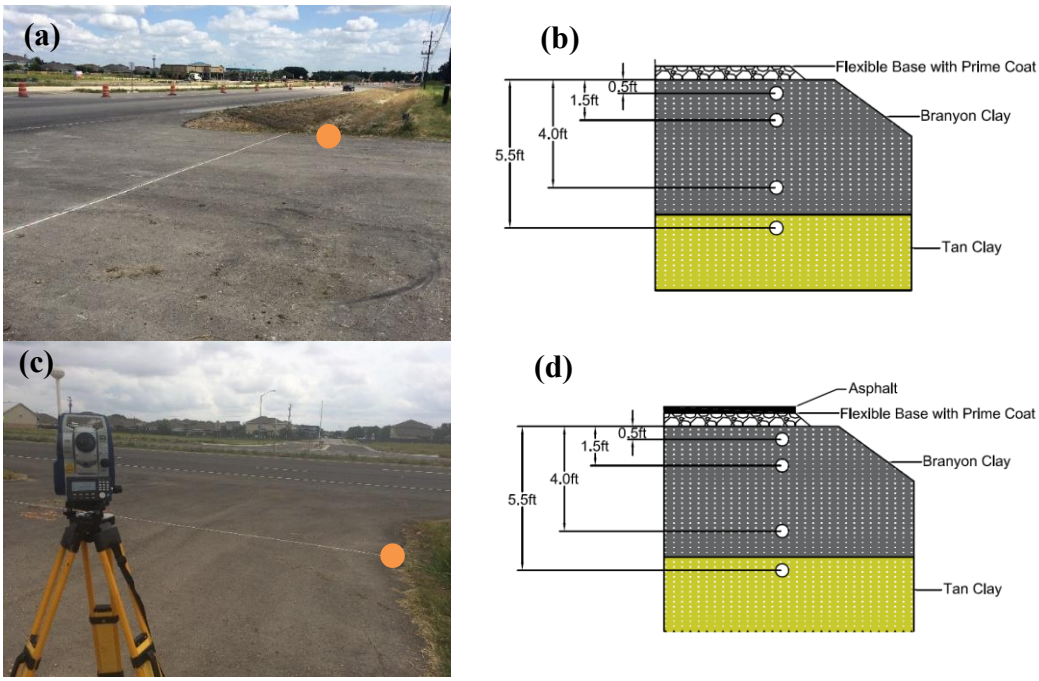

Figure 5.9*:* FM 685 site: (a) Pavement with flexible base surface, (b) Site layout for flexible base surface, (c) Pavement after asphalt placement, (d) Site layout for asphalt surface

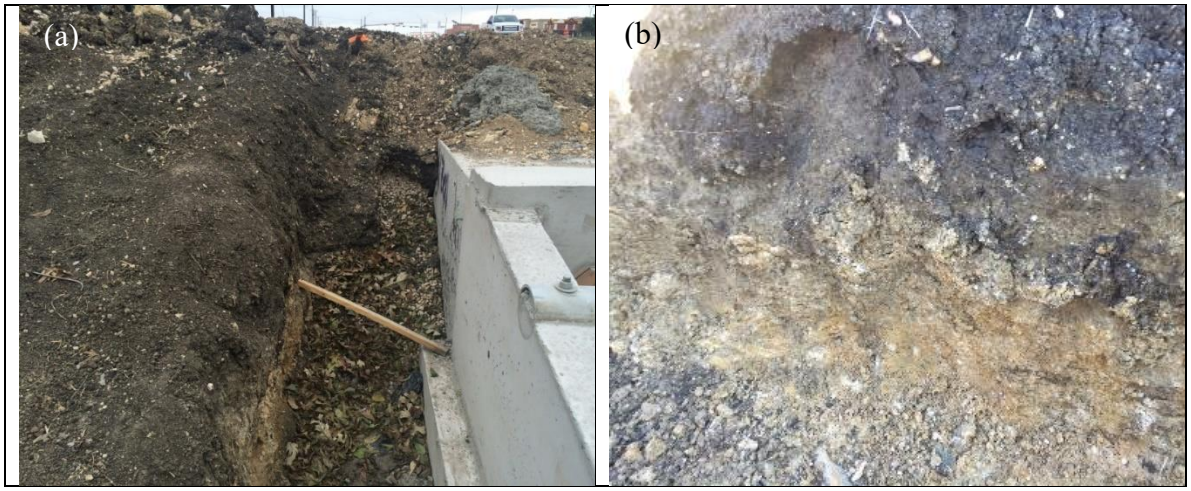

Figure 5.10: Stratigraphy at instrumented location (a) and delineation between Branyon clay and tan clay (b)

The sensors were installed in November 2015. A vertical cut of the subgrade was excavated to install the sensors beneath the edge of the proposed roadway. Openings were excavated from the vertical cut to install sensors. These openings were excavated approximately 3 to 4 in. (7.6 to 10.2 cm) within the vertical cut of the subgrade. The moisture content sensors were pressed into the subgrade in the openings. The matric suction sensors were covered with trimmings from the openings and placed inside the openings for installation. After the sensors were placed, the openings were recompacted with the trimmings from the installation process. An instrumented opening prior to recompaction and the vertical cut of the subgrade after instrumentation is shown in Figure 5.11.

Figure 5.11*:* Installation of sensors (a) and the site after sensor installation (b)

However, the installation and placement of the sensors may affect the moisture fluctuations into the deposit. The instrumented portions of the subgrade were located next to a concrete box culvert, which may result in a different subsurface flow regime than at the edge of the shoulder of the main roadway. There may be discontinuities between the drainage structure and expansive subgrade during the dry seasons, which could increase moisture infiltration into the deposit. However, the construction of the driveway did include vibratory compaction of the soil next to the drainage structure. This vibratory compaction was expected to reduce the discontinuities between the soil and the box culvert. Additionally, the non-expansive tan clay was exposed to the moisture fluctuations in the drainage ditch next to the instrumented site, which may provide an additional infiltration path for moisture. Finally, the recompaction of the holes with the excavated soil may have created a discontinuity in the installed locations due to low relative compaction from hand compaction.

5.3.2 Geotechnical Characterization of the Site

Both the Branyon and tan clay were collected in bulk from exposed portions of the subgrade. The bulk samples of each soil were intermixed and air-dried at a temperature of approximately 23°C. The air-dried soil was passed through a rock crusher until the majority of the soil passed the No. 10 sieve. The soils were then tested to obtain their Atterberg Limits according to ASTM D4318. The Branyon clay was classified as a high plasticity clay (CH), and the tan clay was classified as a low plasticity clay (CL), according to the United Soil Classification System (USCS) from ASTM D2487. The soils were additionally tested for their fines content from wet sieving of the processed soil (ASTM D422), and clay content from hydrometer analysis of soil that passed the No. 200 sieve (ASTM D422). The total suction at varying volumetric moisture contents was determined from chilled mirror hygrometer measurements (ASTM D6836). The characterized soil properties are provided in Table 5.2.

Table 5.2: Geotechnical characterization of soils collected from FM685

Property	Branyon Clay	Tan Clay
Liquid Limit	65	36
Plasticity Index	34	17
Fines Content	93	94
Clay Content	55	52

Centrifuge-based inundation tests, outlined by Zornberg et al. (2017), were conducted to define stress-swell curves for both soils. Swelling tests were conducted on soil specimens prepared at a dry condition, three percentage points dry of the optimum moisture content and at the maximum dry unit weight from compaction curves using Standard Proctor compaction energy. The moisture content and maximum dry unit weight corresponding to optimum compaction conditions were estimated using correlations (Equations 3.1 and 3.2) from the U.S. Navy Design Manual, NAVFAC (1962). Results

from centrifuge swelling tests on both soils and the fitted swell-stress curve for the Branyon clay are shown in Figure 5.12. The vertical strains were taken at the end of primary swelling to be consistent with ASTM D4546.

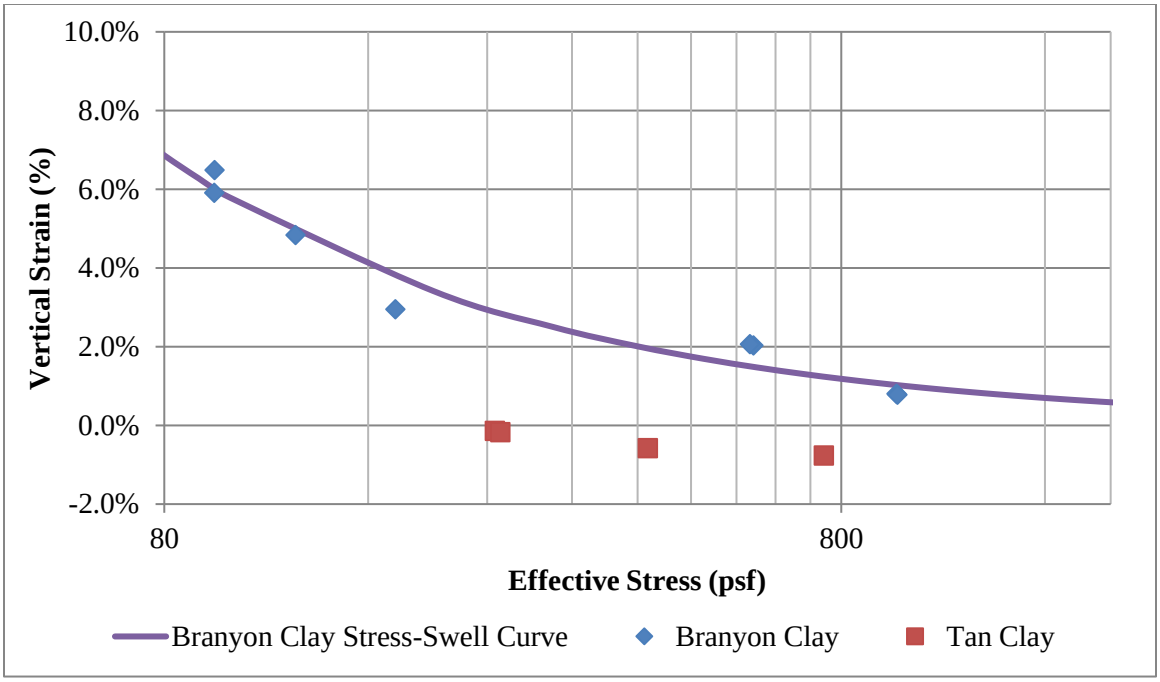

Figure 5.12: Results from swelling tests on FM685 soils and fitted stress-swell curve for the Branyon clay

Results from the centrifuge swelling tests indicate that the tan clay is non-expansive and that the Branyon clay is moderately expansive. The potential vertical rise of the subgrade can be determined by integrating the Branyon clay stress-swell curve from the stress corresponding to the stresses at the top and bottom of the expansive soil subgrade. Based on this integration, the potential vertical rise of the deposit was calculated as 1.76 in. (4.47 cm). Based on this predicted potential vertical rise, environmental cracking was expected at the driveway based on TxDOT design standards. Since the driveway was primarily used for a hay-bailing operation with only a minimal

amount of traffic, the primary source of distresses in the driveway was expected to be longitudinal cracking from the seasonal movement of the subgrade.

The total suction at varying volumetric moisture contents was determined for each soil by a chilled mirror hygrometer (the WP4C, from Decagon). Soil specimens were prepared at the maximum dry unit weight from the NAVFAC correlations (Equation 3.2) using different initial gravimetric moisture contents. The measured total suctions were used to fit soil-water retention curves. The soil-water retention curves were fitted using the van Genuchten model (1990). The solver in Excel was used to vary the van Genuchten parameters in order to reduce the root-mean-squared error to a minimum based on the GRG Non-linear method. A more detailed outline of this fitting technique is presented in Section 2.3. The total suction measured from chilled mirror hygrometer tests and the fitted soil-water retention curves are shown in Figure 5.13.

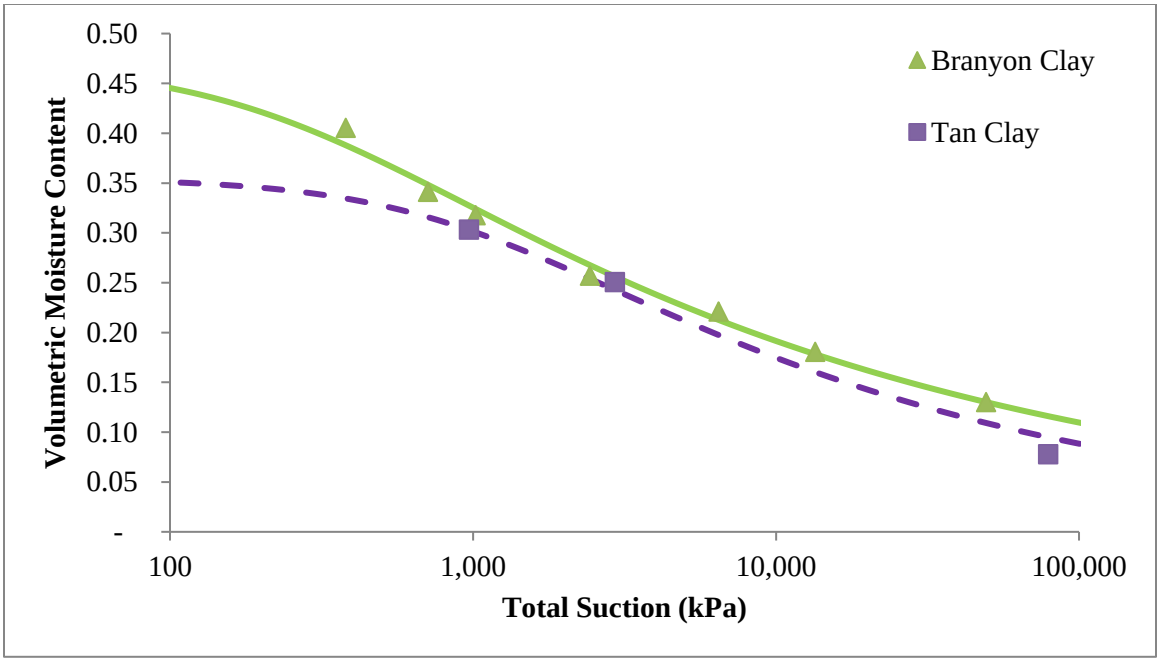

Figure 5.13: Chilled mirror hygrometer measurements of FM685 soil specimens and fitted soil-water retention curves

The measurements from the chilled mirror hygrometer indicate that both soils have a similar total suction at the same volumetric moisture content beyond a total suction of 1,000 kPa. These laboratory-generated soil-water retention curves were later compared to soil-water retention curves generated from the field monitoring of the volumetric moisture content and matric suction.

5.4 Field Data Description and Evaluation

The research component presented in this section covers the monitoring and evaluation of an expansive subgrade beneath a pavement structure. The results and analysis from the monitoring of moisture, suction, and surficial deflections were grouped into three sections. The first section analyzes the results the results from the moisture and suction monitoring of the site. The second section examines the generation of in-situ soil-water retention curves from the monitoring of moisture and suction fluctuations. The final section analyzes the pavement performance and its relationship to moisture fluctuations.

5.4.1 Hydraulic Monitoring of FM 685 Subgrade

The hydraulic monitoring of the subgrade at the FM 685 involved the monitoring of volumetric moisture content and matric suction fluctuations. Decagon 5TE sensors were used to monitor moisture content fluctuations, and Decagon MPS-2 sensors were used to monitor matric suction fluctuations. Data was recorded by the sensors every thirty minutes. The time of monitoring was grouped into two time periods. The first time period began in January 2016 after a flexible base surface with a prime coat was placed over the subgrade. This time period is referred to as the flexible base time period. The second time period began in December 2016 after the final asphaltic surface was placed over the flexible base layer. This time period is referred to as the asphalt time period. Based on

previous field sites, the subgrade was expected to undergo more frequent moisture fluctuations closer to the base-subgrade interface due to the shorter distance for moisture to travel. However, this assumption relies on a one-dimensional analysis of the subgrade and does not incorporate the distance from the slope. Due to this simplification, this assumption will later be evaluated.

Results from the volumetric moisture content monitoring during both time periods are shown in Figure 5.14. The daily precipitation at the site is shown in Figure 5.15. The vertical black line indicates the delineation between the flexible base and asphalt time periods.

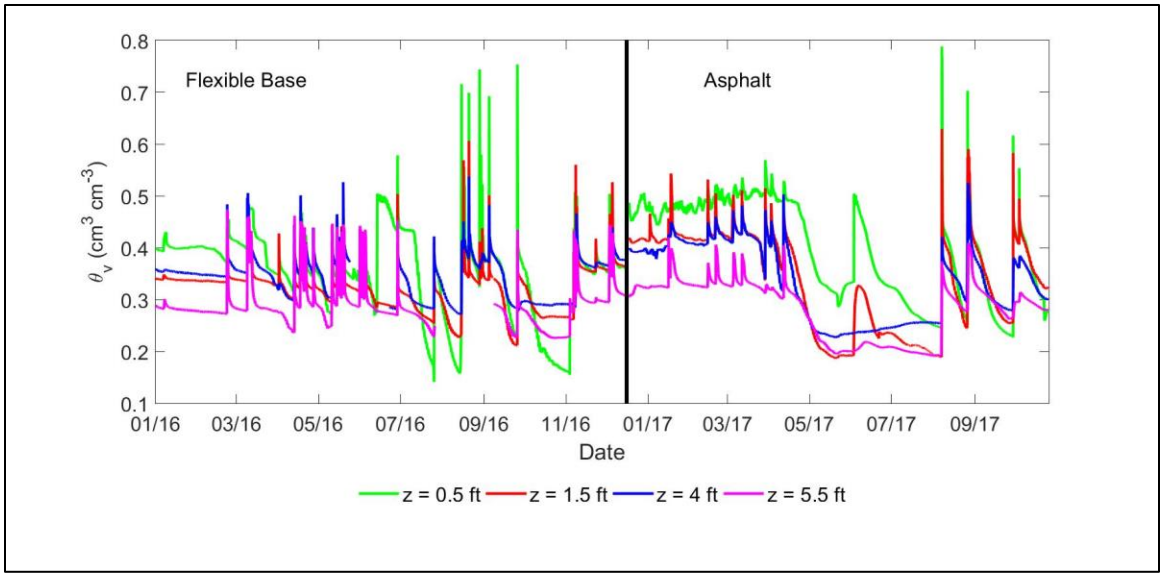

Figure 5.14: Volumetric moisture content time history at the FM685 site

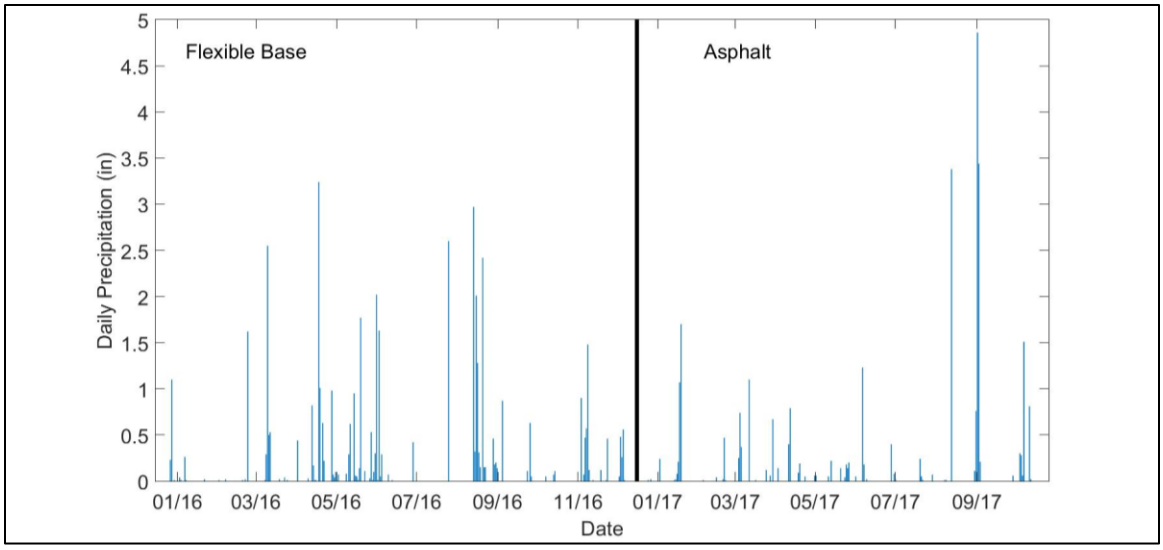

Figure 5.15: Precipitation data during the monitoring time period at the FM 685 site

The volumetric moisture content sensors were able to record volumetric moisture contents during both time periods. The readings from the sensors are consistent with the predicted behavior of an expansive deposit beneath a pavement structure (i.e. the subgrade tends to dry during periods without rainfall and tends to wet during periods with rainfall). These trends indicate that the 5TE capacitance sensors are suitable for use in expansive soils. In general, the sensors in Branyon clay near the base-subgrade interface underwent more frequent wetting and drying cycles than the Branyon clay closer to the Branyon clay-tan clay interface. After rainfall events, the sensor at a depth of 0.5 ft tends to have the highest volumetric moisture content, and the sensor at a depth of 4 ft below the base-subgrade interface tends to have the lowest volumetric moisture content in the Branyon clay. During the drying of the deposit, discontinuities or jumps in moisture content data were not observed, indicating that the sensors did not lose contact with the soil. However, the sensor in the tan clay underwent more frequent wetting and drying cycles than the sensor at a depth of 4 ft in the Branyon clay. The difference in moisture

fluctuations can be attributed to the tan clay being exposed in the drainage ditch, reducing the distance for moisture to infiltrate. Additionally, since the tan clay was classified as a low plasticity clay, the hydraulic conductivity is assumed to be significantly higher than the Branyon clay. This assumed higher hydraulic conductivity would decrease the time for moisture to infiltrate and dry from the tan clay.

While the sensors generally monitored moisture fluctuations continuously, there were several periods with poor or no moisture measurements. Some sensors were accidently disconnected during field visits, leading to gaps in moisture content data during the summer of 2016 for sensors at depths of 4 ft and 5.5 ft below the base-subgrade interface. Additionally, an increase in the moisture content from the sensor at a depth of 0.5 ft without a rainfall event was observed in June 2016. This increase in moisture content was attributed to maintenance activities associated with the widening of the roadway. Instability in the moisture content in the sensor at a depth of 0.5 ft was observed after the placement of the final asphaltic surface. This instability was attributed to the change in the boundary conditions after the placement of the asphalt surface, requiring for the top portion of the Branyon clay to come into a new moisture equilibrium. The final discrepancy in the data dealt with maximum volumetric moisture content in the sensor at a depth of 0.5 ft. Readings were high for this sensor, with very maximum moisture content values exceeding 0.60. These high values can be attributed to the potential formation of macro-void during the installation of the sensor.

An additional research objective was to validate the dry condition targeted for soil specimens tested using the centrifuge-based inundation tests. The dry condition from the NAVFAC correlations corresponds to an initial volumetric moisture content of 0.310. From the monitoring of the subgrade during both time periods, this volumetric moisture condition is higher than the minimum volumetric moisture contents recorded during

summer months. This trend is consistent for all depths in the Branyon clay. Therefore, laboratory-reconstituted soil specimens should be drier than the dry conditions estimated from NAVFAC in order to represent the driest field moisture condition.

To further analyze the data, the degree of saturation was used to normalize the moisture content fluctuations in the Branyon clay. The degree of saturation can be estimated as follows:

$$S = \frac{\theta}{\theta_{max,i}} \tag{5.2}$$

Where S is the degree of saturation, θ is the volumetric moisture content reading, and $\theta_{max,i}$ is the maximum measured volumetric moisture content for a given depth. The maximum volumetric moisture content for each depth was measured using the capacitance sensors. This moisture content was used to estimate the degree of saturation instead of the porosity of the soil as the field site was not sampled using Shelby tubes to calculate the in-situ dry unit weight or porosity. Additionally, this estimation of the porosity does not consider changes in porosity with swelling of the expansive subgrade. With these caveats, the degree of saturation fluctuations at depth is shown in Figure 5.16.

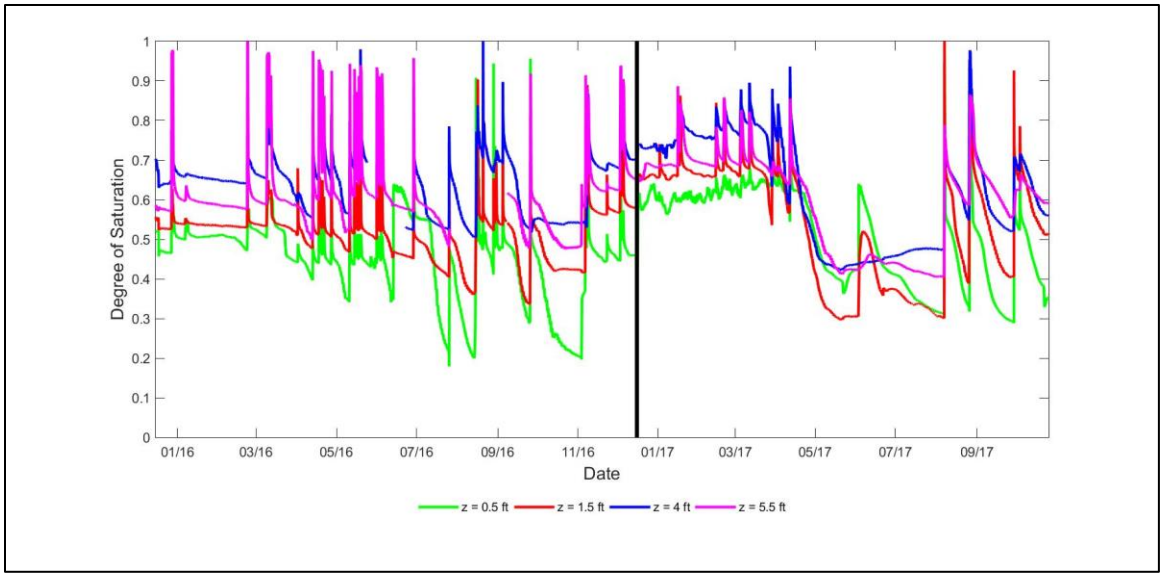

Figure 5.16*:* Degree of saturation time history at the FM 685 site

In general, the degree of saturation tends to increase with depth in the Branyon clay. This trend is consistent with the assumption that soils closer to the surface will undergo more significant moisture fluctuations due to influence of climatic and atmospheric conditions. Seasonally, the moisture content sensors were more wet during the winter months and drier during the summer months. This trend is consistent with the fluctuations in temperature and relative humidity in the region. Between the two surface conditions, less frequent wetting fronts were observed for the sensors at depth during the summer and fall for the asphalt time period. The tan clay tends to have a lower degree of saturation than the sensor at a depth of 4 ft in the Branyon clay. This trend can be attributed to the tan clay being exposed at the base of the drainage ditch near the instrumented driveway. Due to this exposed portion of the tan clay, a more complex, three-dimensional wetting and drying fronts can be assumed to affect moisture fluctuations in the tan clay. However, the trends from the degree of saturation fluctuations are more clear than the trends from the volumetric moisture content fluctuations. As such, the degree of saturation is generally

used for further analyses. Analyses that use the volumetric moisture content are presented in Appendix C.

Each depth was instrumented to monitor both volumetric moisture content and matric suction fluctuations. These fluctuations were compared at each depth for both time periods. Trends from Figure 5.16 indicate that rainfall was able to wet the subgrade during the flexible base time period in a shorter time frame than the asphalt time period. Additionally, the subgrade tends to dry in a shorter time frame beneath the flexible base surface. The subgrade appears to dry more significantly in the summer of 2017, during the asphalt time period, than the summer of 2016, during the flexible base time period. To compare the time periods, the degree of saturation and matric suction fluctuations for the second sensor at a depth of 1.5 ft below the base-subgrade interface is shown in Figure 5.17 for the flexible base time period and in Figure 5.18 for the asphalt time period. The precipitation at the site is also included in both figures. The readings from the sensors indicate that there was generally a larger increase in degree of saturation response for similar rainfall intensities for flexible base time period. An example of these responses is seen in the rainfall at the end of September 2016 for the flexible base time period and at the beginning of June 2017 for the asphalt time period. Additionally, the subgrade tends to dry over a shorter time frame for the flexible base time period. However, the subgrade during the asphalt time period tends to reach a lower degree of saturation during the summer months. This difference may be attributed to a higher amount of rainfall during the summer of 2016 than the summer of 2017.

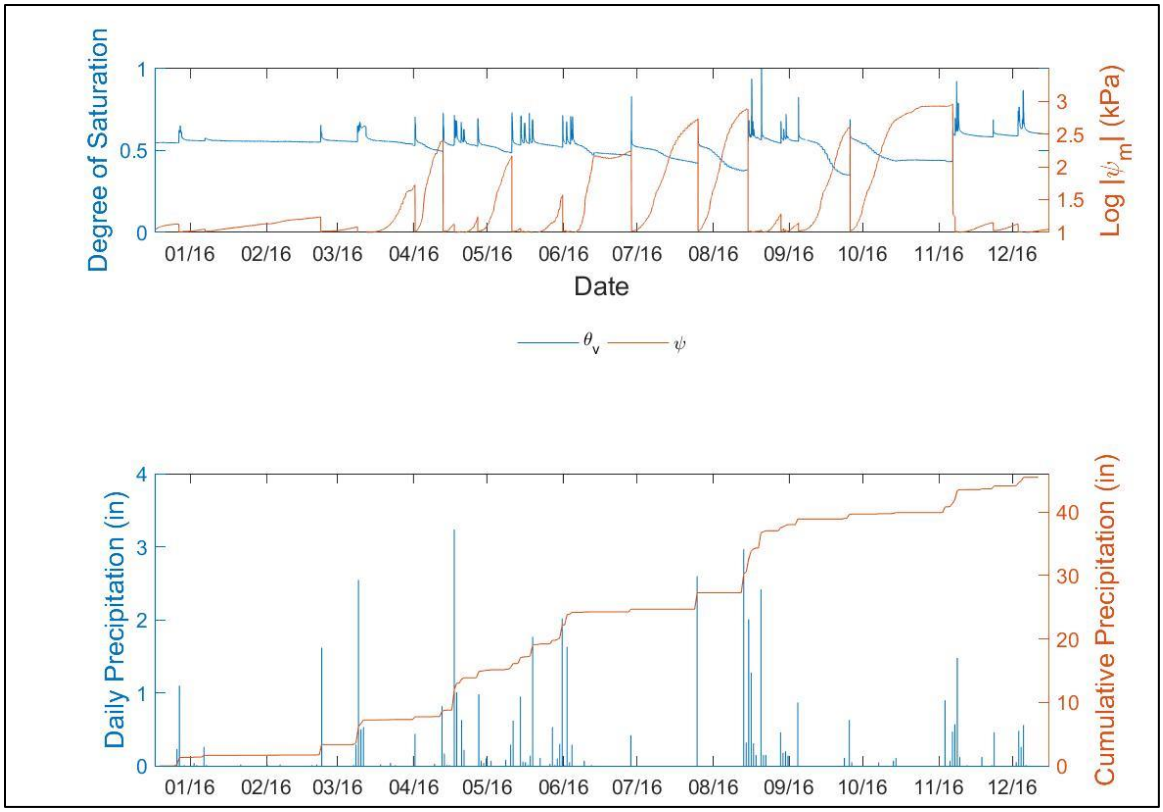

Figure 5.17*:* Hydraulic time history and precipitation data for the sensor pairing at a depth of 1.5 ft below the base-subgrade interface for the flexible base time period

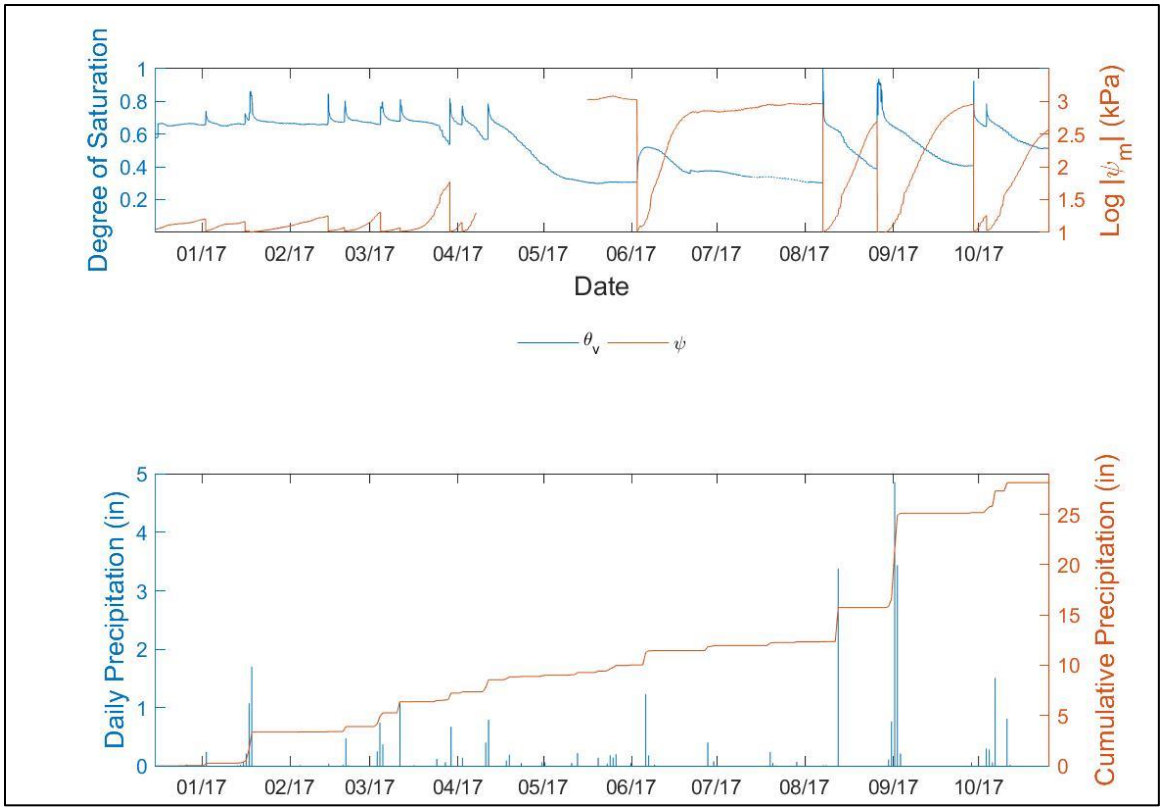

Figure 5.18: Hydraulic time history and precipitation data for the sensor pairing at a depth of 1.5 ft below the base-subgrade interface for the asphalt time period

In addition to the comparison in the seasonal moisture fluctuations, individual rainfall events with similar conditions were compared between the two surficial conditions. Rainfall events with similar durations and rainfall intensities and similar environmental conditions during drying (i.e. temperature and relative humidity) were selected for each pavement. Moisture fluctuations recorded during these events beneath the flexible base surface and asphalt pavement surface are shown in Figure 5.19. The cumulative and maximum precipitation rates, as taken from a nearby weather station, were 0.83 in. (2.10 cm) and 0.65 in./hr. (1.65 cm/hr.) for the flexible base time period and 1.23 in. (3.12 cm) and 0.71 in./hr. (1.80 cm/hr.) for the asphalt time period. Rainfall

lasted approximately an hour for the rainfall during the flexible base time period and two hours for the rainfall during the asphalt time period.

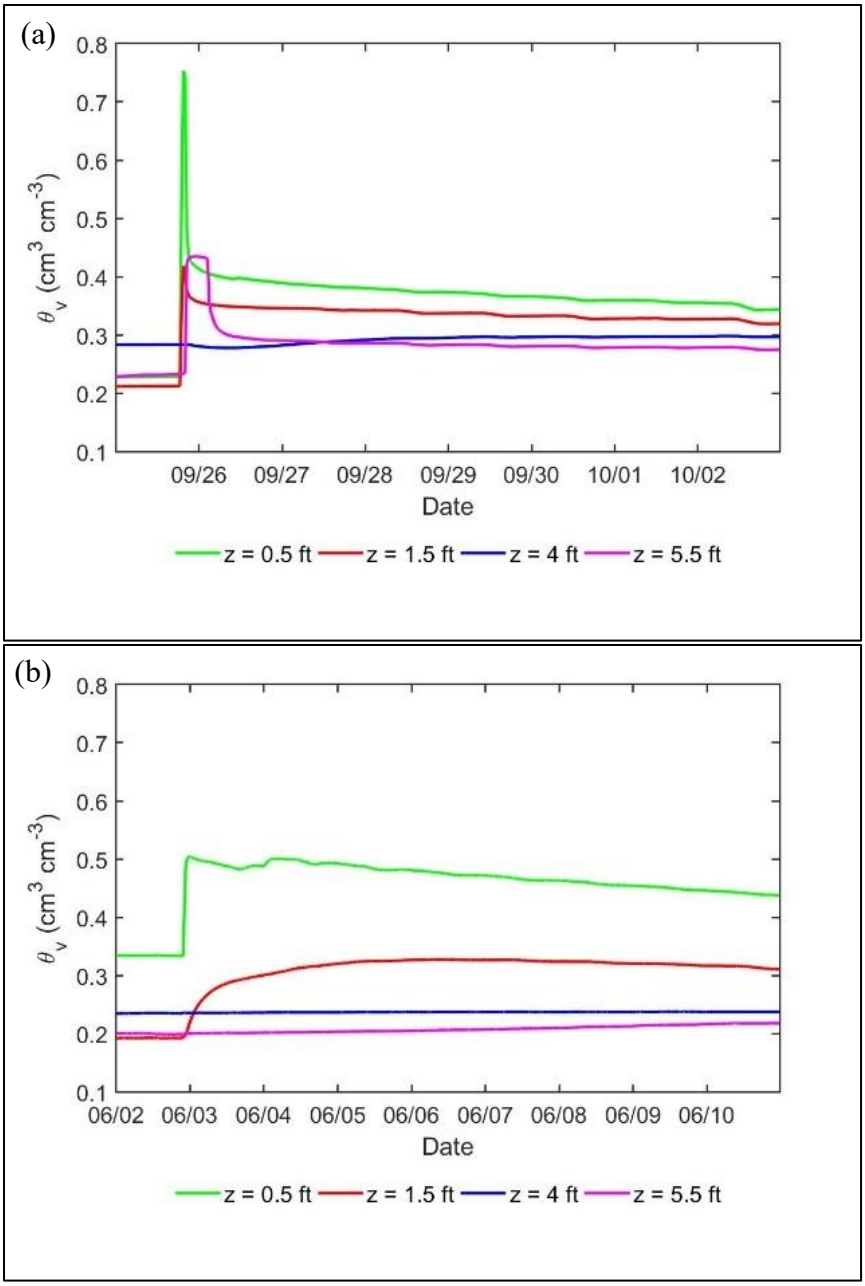

Figure 5.19*:* Subgrade moisture time histories during a rainfall event for a flexible base surface (a) and asphalt surface (b)

The moisture front reached the upper sensor in the deposit soon after the beginning of rainfall for both rainfall events. However, the moisture infiltration during the flexible base time period was able to permeate the Branyon clay to the sensor at a depth of 1.5 ft. in a shorter time frame. Additionally, the sensor in the tan clay was also wetted in a short time frame for the flexible base time period. This wetting of the tan clay may be due to the complex geometry of the site next to the culvert structure and the exposure of the tan clay in the drainage ditch. The bottom Branyon clay sensor was not wetted significantly for the flexible base time period. For the rainfall during the asphalt time period, the moisture front advanced through the subgrade over a longer time frame. Additionally, the rainfall during the asphalt time period did not wet the deposit as significantly as the rainfall during the flexible base time period, with the sensor at a depth of 1.5 ft. undergoing only a slight increase in moisture content, and the sensor at a depth of 4.5 ft not indicating an increase in moisture content. The difference in the moisture response between the two time periods can be attributed to the asphalt surface acting as a semi-impervious barrier with more runoff occurring at the surface.

In order to further evaluate the difference in the moisture response between the two time periods for the rainfall event, the moisture content fluctuations at depth are shown in Figure 5.20. The month and day for each moisture content profile is indicated by the color bar. The initial profiles are indicated by the red lines. These moisture content profiles are consistent with the trends from Figure 5.19. The Branyon clay tends to wet during a rainfall and dry after a rainfall more rapidly during the flexible base time period. The profiles of the moisture content from the asphalt time period after 11 days (i.e. the yellow lines in Figure 5.20b) were at higher moisture contents than the profiles from the flexible base time period after 8 days (i.e. the yellows lines in Figure 5.20a). Therefore, the surface condition affected the wetting and drying of the subgrade after a rainfall.

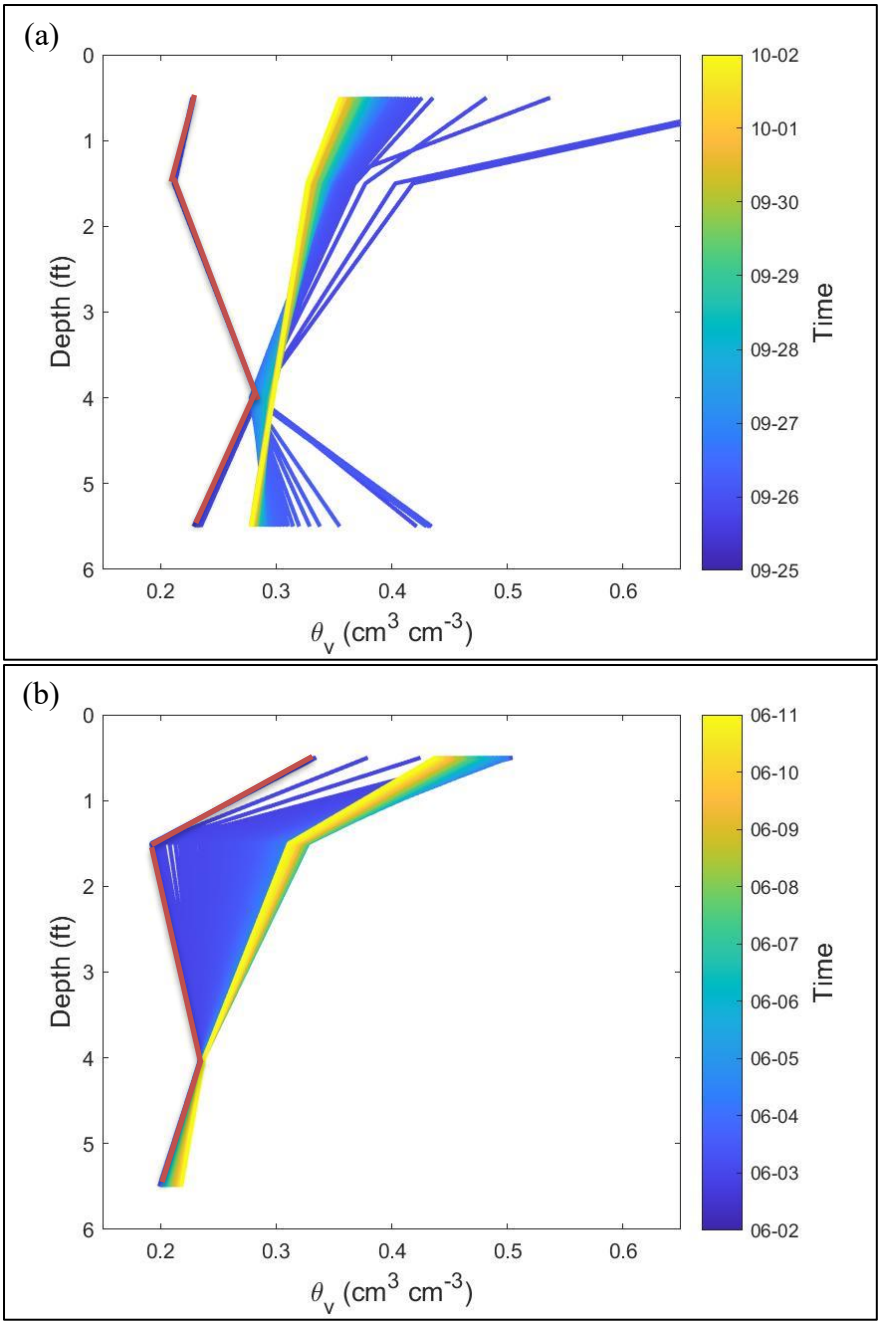

Figure 5.20*:* Moisture time histories with depth during a rainfall event for a flexible base surface (a) and asphalt surface (b)

The trends from the previous comparison were evaluated with an additional rainfall event. The rainfall events that caused the maximum volumetric moisture content in the subgrade during both time periods are compared in Figure 5.21. The cumulative precipitations, as taken from a nearby weather station, were 9.76 in. (24.79 cm) over the course of a week for the flexible base time period and 9.38 in. (23.83 cm) over the course of five days for the asphalt time period. The last significant rainfall fell on August 27th, 2017 for the asphalt time period. The moisture front reached the sensor at a depth of 0.5 ft in a short time frame for both rainfall events. Unlike the previous rainfall events from Figure 5.19, the entire Branyon clay deposit was thoroughly wetted as seen by the increase in the moisture content from the sensor at a depth of 4 ft and the sensor in the tan clay. The time for the infiltrating moisture front to reach the moisture sensor at a depth of 4 ft was similar between the two time periods. However, the drying of the subgrade differed significant between the two time periods. For the flexible base time period, the deposit dried rapidly after the moisture front had advanced through the deposit. The sensors at a depth of 0.5 and 1.5 ft in the Branyon clay both underwent significant drying in a short duration after reaching the peak volumetric moisture content from the rainfall event. For the asphalt time period, the drying of the Branyon clay occurred over a longer time frame. The sensors at a depth of 1.5 ft and 4 ft did not reach a volumetric moisture content of 0.4, the volumetric moisture content that the subgrade dried to between rainfall events during the flexible base time period, even after three days without rainfall for the asphalt time period.

In order to further evaluate the difference in the moisture response between the two time periods for the rainfall event, the moisture content fluctuations at depth are shown in Figure 5.22. The month and day for each moisture content profile is indicated by the color bar. The initial moisture content profile is indicated by the red lines.

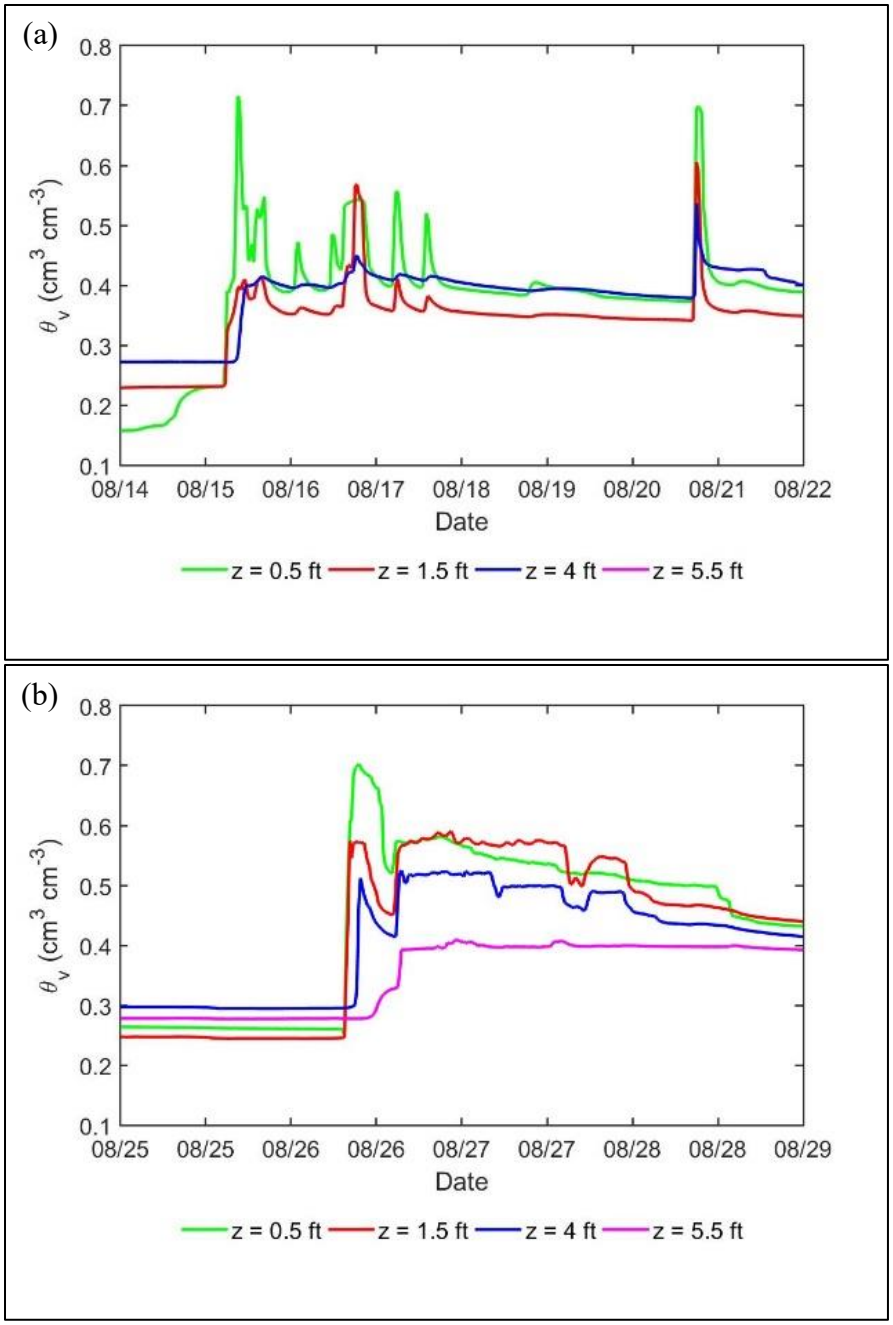

Figure 5.21*:* Subgrade moisture time histories during the maximum rainfall event for a flexible base surface (a) and asphalt surface (b)

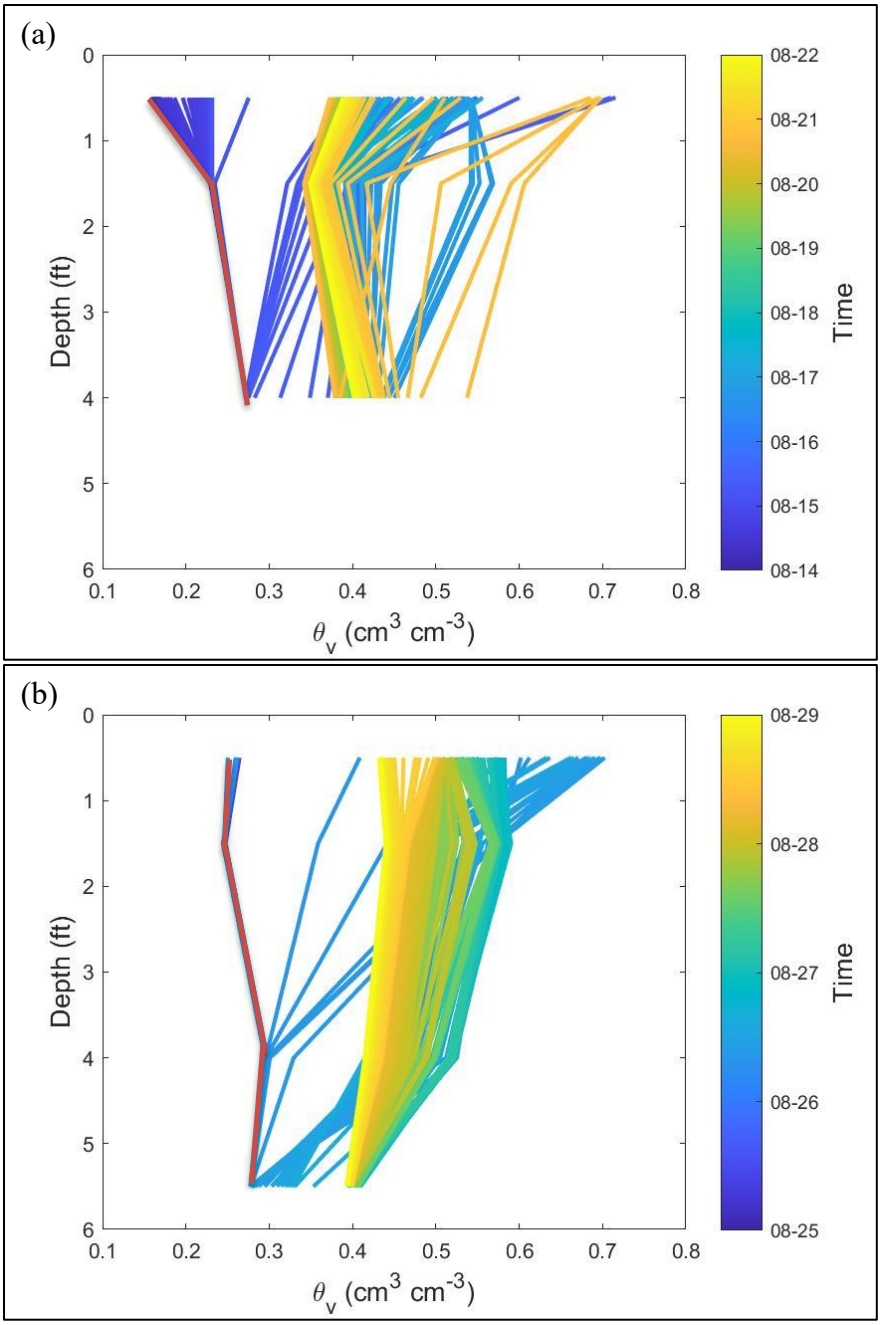

Figure 5.22*:* Moisture time histories with depth during the maximum rainfall event for a flexible base surface (a) and asphalt surface (b)

The moisture content profiles indicate that the subgrade dries more significantly over a shorter time frame for the flexible base time period. Additionally, the drying tends to be

more uniform across the Branyon clay for the asphalt time period. These trends are consistent with the results from Figure 5.21 and the lower rainfall intensity analysis. Therefore, based on the analyses over the overall moisture content fluctuations and individual rainfall events, the surface condition affected the infiltration of moisture and drying of the subgrade.

The difference in the moisture fluctuations of the subgrade beneath the different surfaces can be attributed to the difference in the upper boundary conditions. A prime coat was added to the upper surface of the flexible pavement to reduce the infiltration of moisture into the flexible base and subgrade material. However, the moisture fluctuations from the sensors indicate that the prime coat does not act as a significant barrier for the infiltration of moisture. Since the flexible base does not act as a significant hydraulic barrier, the upper boundary condition allows for moisture to flow into and out of the subgrade more easily than the final asphalt surface. During rainfall events, moisture can infiltrate through the upper boundary condition, and, during drying, moisture can be removed through the upper boundary condition. After the placement of the asphalt surface, the upper boundary condition behaves as a semi-impermeable barrier that significantly reduces the infiltration and removal of moisture through the upper boundary condition. Instead, moisture infiltrates primarily through the unpaved portion of the road and the side slope.

The difference in the moisture fluctuations of the subgrade beneath the different surfaces can also be attributed to a two-dimensional infiltration of moisture. In order to visualize this infiltration of moisture, an expected flow regime for the two time periods is shown in Figure 5.23. This expected flow regime assumes that moisture is falling only on one side of the roadway and that the roadway is relatively flat. Figure 5.23a indicates the expected flow regime for the flexible base time period, and Figure 5.23b indicates the

expected flow regime for the asphalt time period. The flexible base surface with a prime coat is the upper surface in Figure 5.23a, and the asphalt surface over the flexible base is the upper surface in Figure 5.23b. The Branyon clay is represented by the dark gray color, and the tan clay is represented by the tan color. The side slope is approximately 3H:1V and extends about 15 ft to the drainage ditch. The sensors were installed at the approximate edge of the asphalt pavement as indicated by the red circles. Initially, moisture infiltration was assumed to infiltrate one-dimensionally. Based on the results from monitoring, the infiltration and removal of moisture into the Branyon clay can be grouped into three components that are shown in Figure 5.23. The primary component comes from the unpaved portion of the roadway, the side-slope, and the base of the drainage ditch, as indicated by the large blue arrows in Figure 5.23. A secondary component comes from the upper boundary condition, which was assumed to differ between the flexible base and asphalt time periods. This component for the flexible base time period, as indicated by the arrows at the top of the pavement surface in Figure 5.23a, was assumed to allow moisture to infiltrate more significantly than asphalt time period. The asphalt surface was assumed to significantly reduce the infiltration and removal of moisture based on the results from monitoring. The final component of the infiltration and removal of moisture was assumed to come from the tan clay. The sensor in tan clay indicated that wetting and drying cycles were more frequent than the sensor at a depth of 4 ft below the base-subgrade interface in the Branyon clay. However, this component was not as significant as the infiltration of moisture from the unpaved sections and the upper boundary condition based on the monitoring of moisture fluctuations. Based on these three components, the expected moisture fronts are represented by the white lines in the deposit.

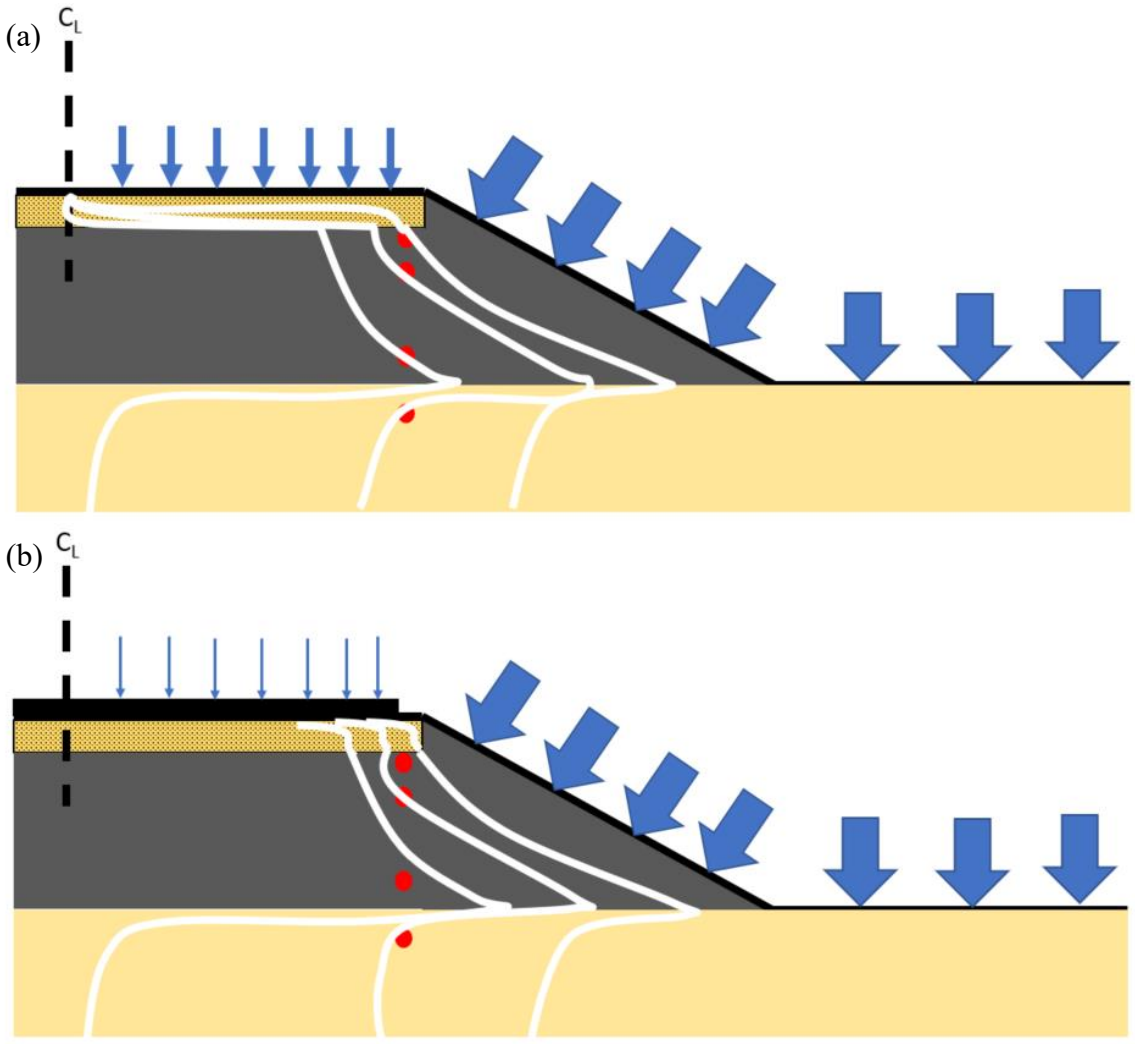

Figure 5.23*:* Boundary conditions between the flexible base surface (a) and asphaltic surface (b)

The moisture fronts for the flexible base time period are expected to be influenced by moisture infiltrating at the upper boundary condition, resulting in moisture infiltration and drying over a short time frame. The estimated moisture fronts therefore can reach deeper portions of the deposit in a similar timeframe. Due to the reduction in the moisture infiltration from the upper surface, the moisture fronts for the asphalt time period are expected to more significantly depend on the distance from the side slope. With moisture

significantly reduced through the upper boundary condition, the subgrade can be expected to dry out over a longer time frame. The moisture fronts for the asphalt time period were assumed to be more affected by infiltration from the side slope due to the change in the upper boundary condition. One additional aspect is the groundwater table. While the groundwater table was not recorded at the site, fluctuations in the sensor in the tan clay indicate that the groundwater table does not affect moisture fluctuations in the Branyon and tan clays.

The moisture fluctuations for the two surficial conditions were analyzed by evaluating the monthly mean, minimum, and maximum of the volumetric moisture content, matric suction and degree of saturation readings. This statistical approach was used to evaluate differences in the hydraulic behavior between the two surficial conditions. In addition to these statistical values, the monthly cumulative precipitation is also presented. The cumulative precipitation is used to compare the intensity of rainfall for each month.

The fluctuations of mean monthly volumetric moisture content were analyzed for each instrumented depth as shown in Figure 5.24. The delineation between the flexible base and asphalt time periods is indicated by the solid black line in December 2016.

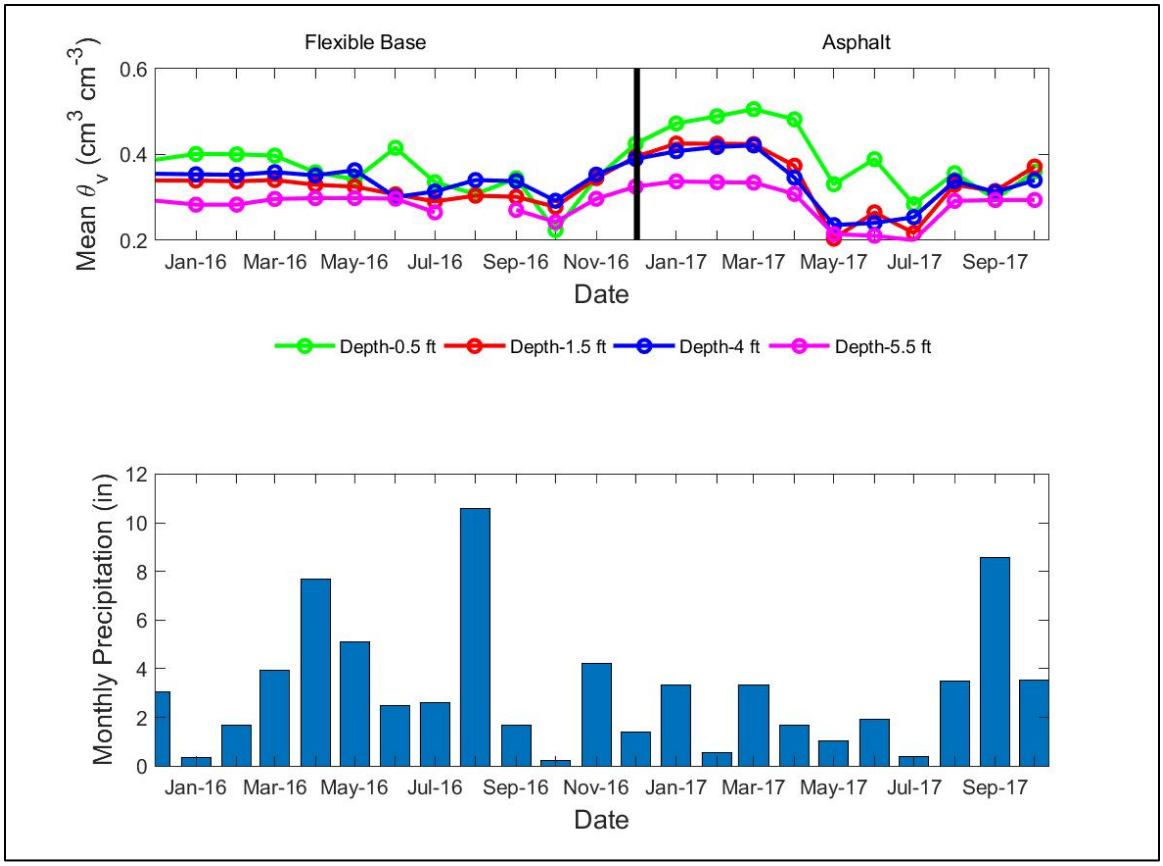

Figure 5.24*:* Mean monthly volumetric moisture content at the FM685 site

In general, the mean monthly volumetric moisture content decreases with depth for both time periods. This decrease can be attributed to the reduced number of wetting and drying cycles and an increased duration for the soil to dry at depth. Several differences in the mean volumetric moisture content were observed between the two time periods. The subgrade during the winter months was more wet for the asphalt time period. This difference in the volumetric moisture content occurred under similar amounts of precipitation for both surficial conditions. Additionally, the subgrade during the summer months was more dry for the asphalt time period. However, this difference may be attributed to the higher amount of precipitation in the summer 2016 for the flexible base

time period. For similarly dry conditions in October 2016, during the flexible base time period, and July 2017, during the asphalt time period, the mean moisture content was similar for each of depth.

The fluctuations of the mean monthly degree of saturation at each depth is shown in Figure 5.25. The degree of saturation was estimated using Equation 5.2. The maximum volumetric moisture content used to estimate the degree of saturation differed slightly between the two time periods.

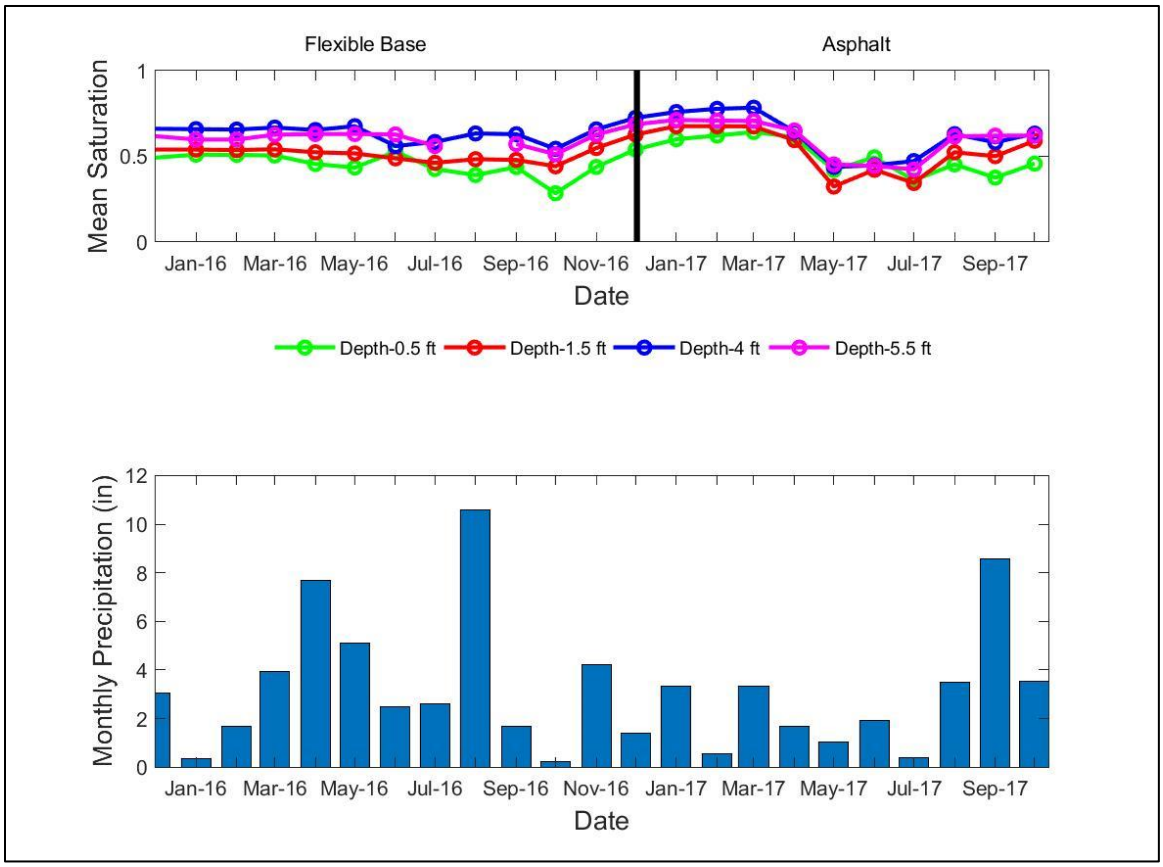

Figure 5.25: Mean monthly degree of saturation at the FM685 site

The trends from this analysis are consistent with the trends from Figure 5.24. The degree of saturation increases with depth due to the lower maximum volumetric moisture content. The degree of saturation during the winter months was higher for the asphalt time period. This difference can be attributed to the reduced drying of the subgrade with the asphalt surface performing as a semi-impervious barrier. The degree of saturation during the summer months were lower for the asphalt time period. This difference was again attributed to the difference in the cumulative precipitation in the summer of 2016 compared to the summer of 2017. When comparing months with a similarly dry time period (i.e. October 2016 and June 2017), the degree of saturation was slightly lower for the sensor at a depth of 0.5 ft below the base-subgrade interface for the flexible base time period. Again, this result indicates that the drying rate was higher during the flexible base time period as the prime coat at the surface did not create a significant hydraulic barrier. At deeper depths, difference in the degree of saturations between the two time periods was not observed.

In order to further analyze the difference in the drying of the subgrade beneath the two surficial conditions, the monthly minimum degree of saturation is shown in Figure 5.26. This statistical evaluation was analyzed in order to evaluate how the subgrade dried between rainfall events.

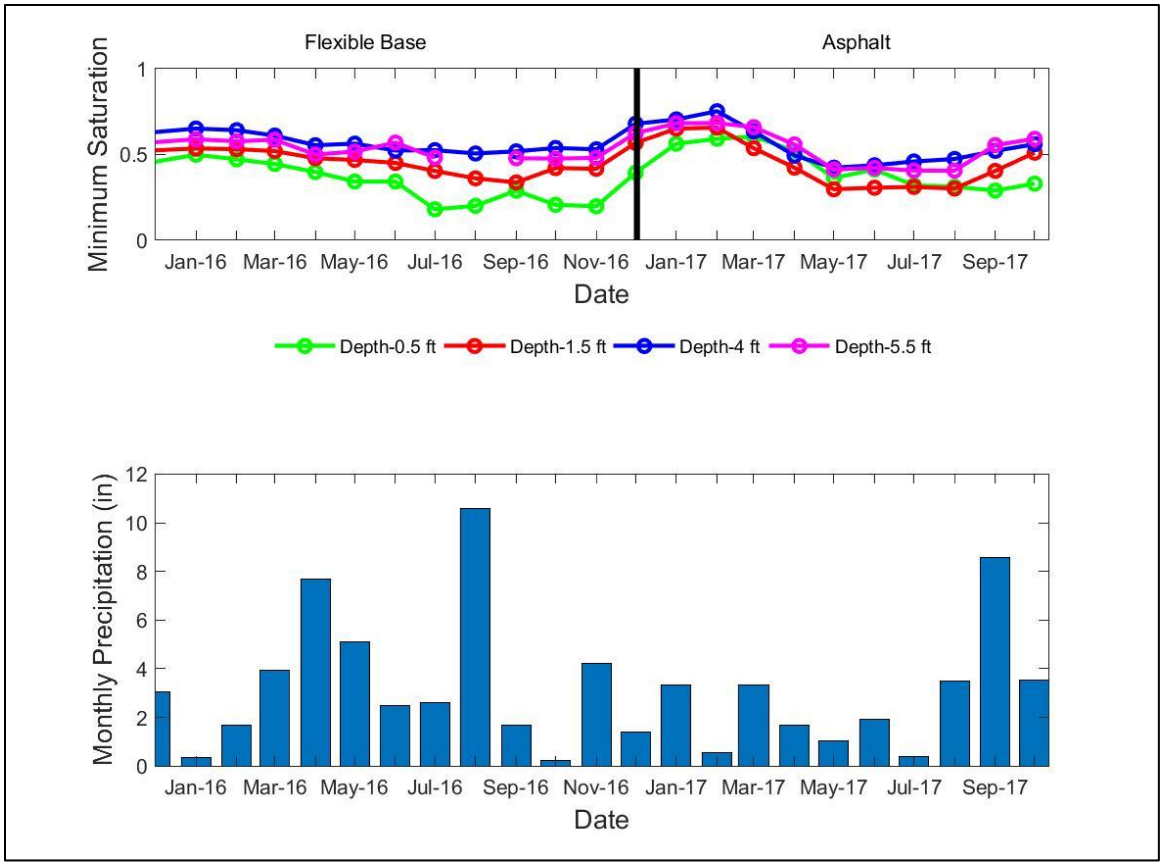

Figure 5.26*:* Monthly minimum degree of saturation at the FM685 site

In general, the trends from the monthly minimum degree of saturation were consistent with the trends from the monthly mean degree of saturation. The minimum degree of saturation during the winter months was higher, particularly at depth, for the asphalt time period. The minimum degree of saturation was significantly lower during the summer months for the asphalt time period. Comparing the driest months for both surficial conditions, the minimum degree of saturation was lower during June 2017, during the asphalt time period, than during October 2016, during the flexible base time period. Further, the minimum monthly degree of saturation varies more significantly during the asphalt time period. These trends are consistent with the hypothesis that the asphalt

pavement performs as a semi-impermeable hydraulic barrier, reducing the moisture infiltration into the subgrade.

The last analysis examined the monthly maximum degree of saturation for each depth, as shown in Figure 5.27. This analysis evaluated the extent to which rainfall events wetted the subgrade between seasons.

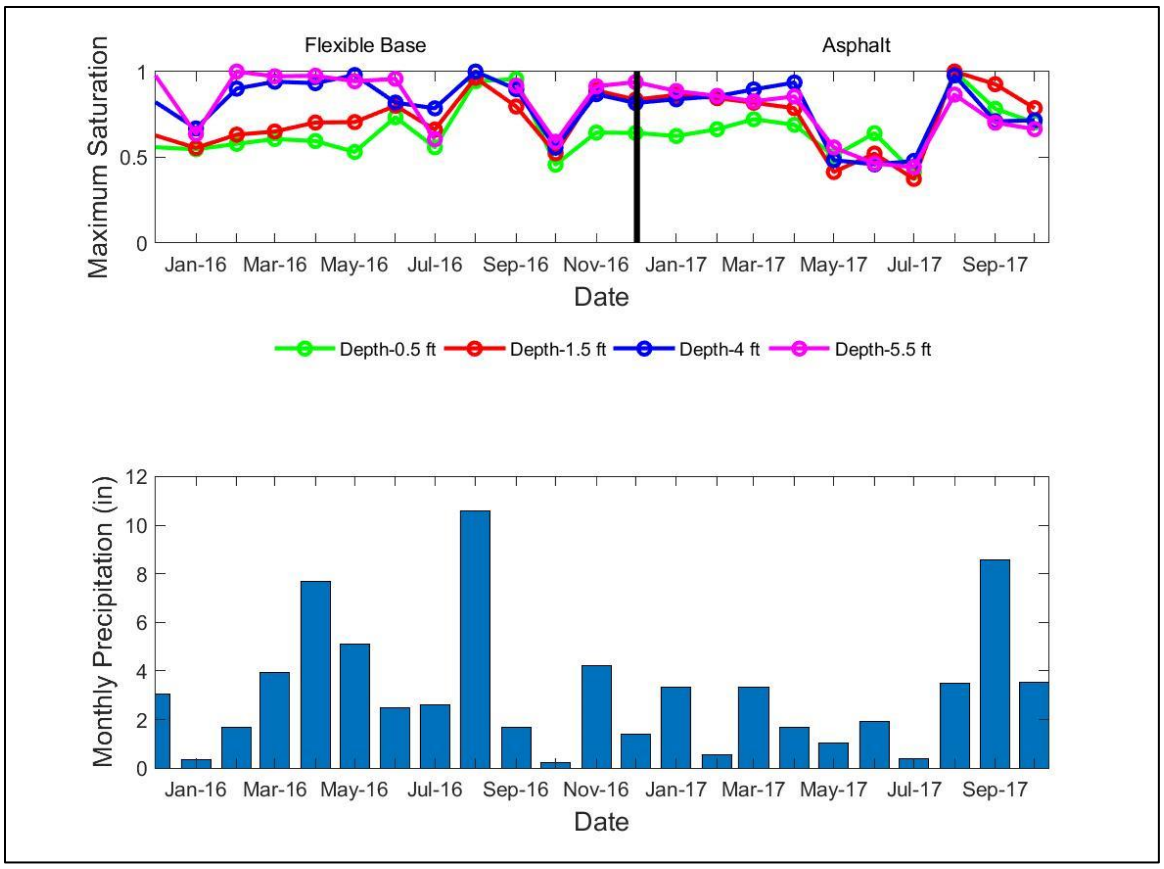

Figure 5.27*:* Monthly maximum degree of saturation at the FM685 site

In general, the maximum degree of saturation in the subgrade was slightly during the flexible base time period. While differences in the spring of 2016 and spring of 2017 were attributed to the difference in the cumulative precipitation, the subgrade behaved

differently between months of similar rainfall (i.e. April 2016 and September 2017). Again, the difference in the subgrade behavior can be again attributed to the asphalt surface performing as a semi-impermeable hydraulic barrier. More significant rainfall events were needed to fully wet the deposit as compared to the flexible base surface with the prime coat.

An additional research objective was to compare the saturated volumetric moisture content from the field versus the final volumetric moisture content from the end of centrifuge-based inundation tests. This objective evaluated whether the end of testing laboratory conditions were similar to the moisture content conditions after significant rainfall events. For laboratory tests, the maximum volumetric moisture content was estimated by using the porosity at the end of the test and assuming that the specimen was fully saturated at the end of testing. The porosity was estimated using the method from Chapter 2 of this dissertation. The volumetric moisture content at the end of testing versus the effective specimen stress is shown in Figure 5.28 for both the Branyon clay and tan clay. For the field results, the monthly maximum volumetric moisture content is shown in Figure 5.29.

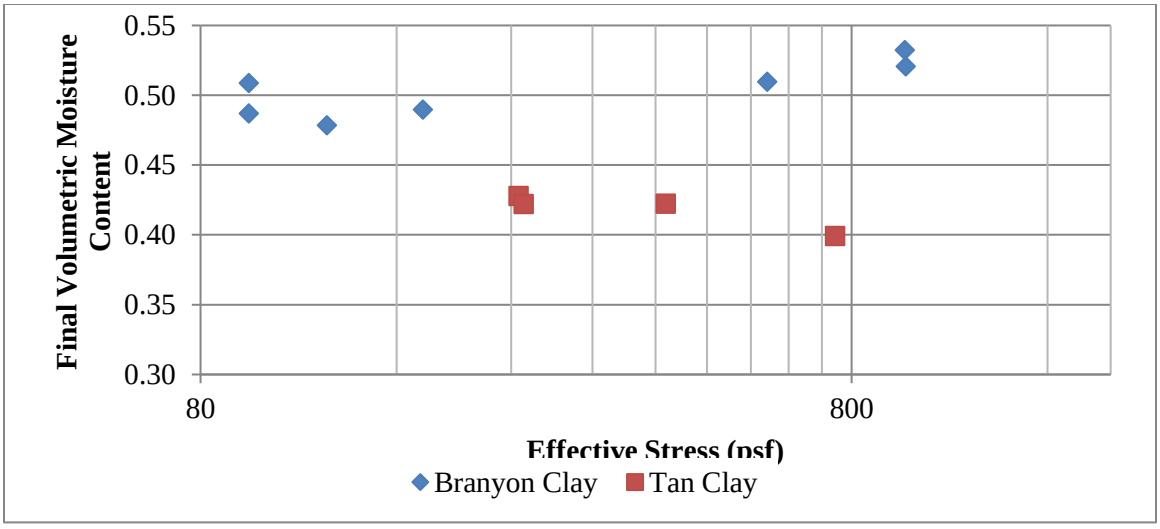

Figure 5.28: Final volumetric moisture content versus effective specimen stress for soils sampled at FM685

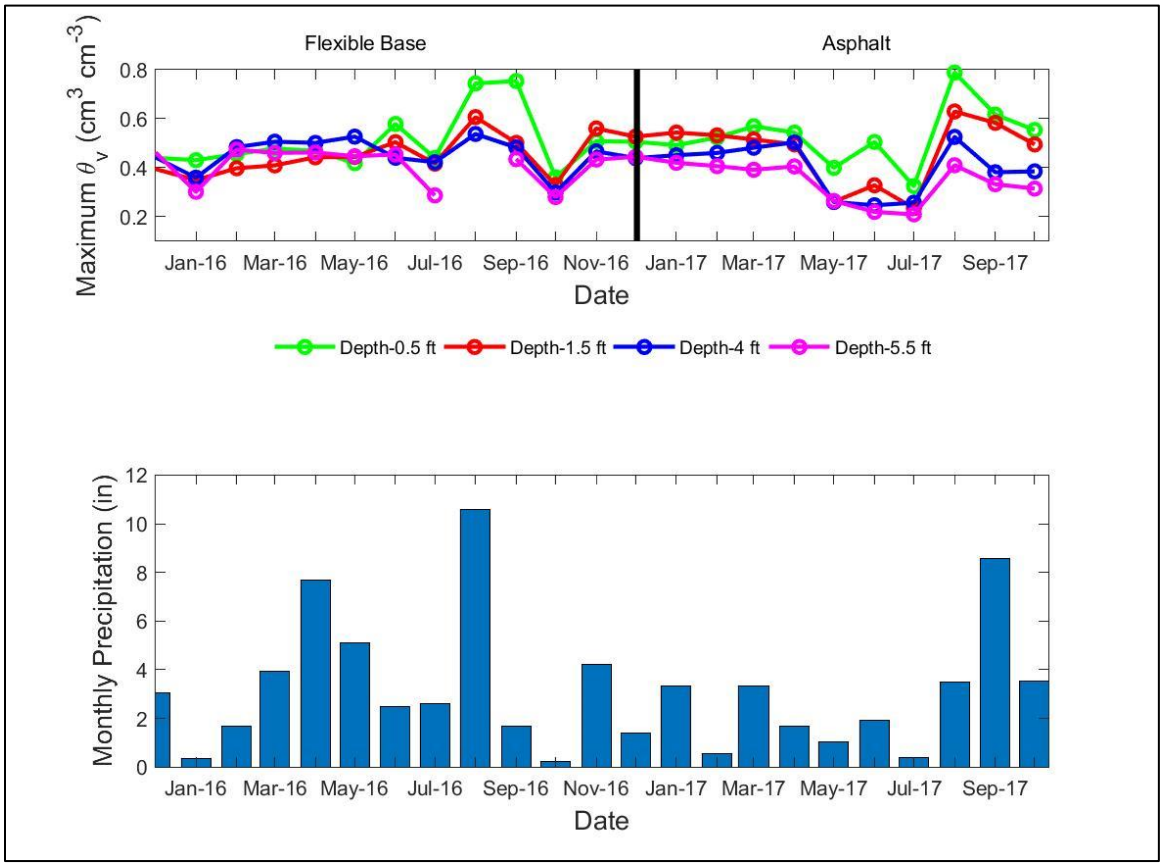

Figure 5.29: Monthly maximum volumetric moisture content at FM685 site

The volumetric moisture content at the end of laboratory testing was approximately 0.50 for the Branyon clay and 0.42 for the tan clay over the range of effective stresses tested. From the field monitoring, the monthly maximum volumetric moisture content exceeded the end of testing moisture content for the Branyon clay at all depths. The maximum field volumetric moisture content was approximately 0.10 higher for the sensor at a depth of 1.5 ft and 0.05 higher for the sensor at a depth of 4 ft than the laboratory end of testing moisture content. The sensor at a depth of 0.5 ft was not evaluated due to the inconsistent readings. However, for the tan clay, the maximum field volumetric moisture content was similar to the laboratory end of testing moisture content. The differences in the laboratory tested and field measured moisture contents can be attributed to the difference in the initial volumetric moisture contents prior to wetting. The initial volumetric moisture content of the field Branyon clay prior to significant rainfall events was lower than the initial volumetric moisture content of the laboratory-reconstituted soil specimens. From Chapter 2 of this dissertation, a lower volumetric moisture content, assumed to be caused by a lower gravimetric moisture content, will increase the porosity at the end of swelling.

In addition to the volumetric moisture content monitoring, the matric suction fluctuations were monitored at depth. Results from this matric suction monitoring is shown in Figure 5.30 for both time periods.

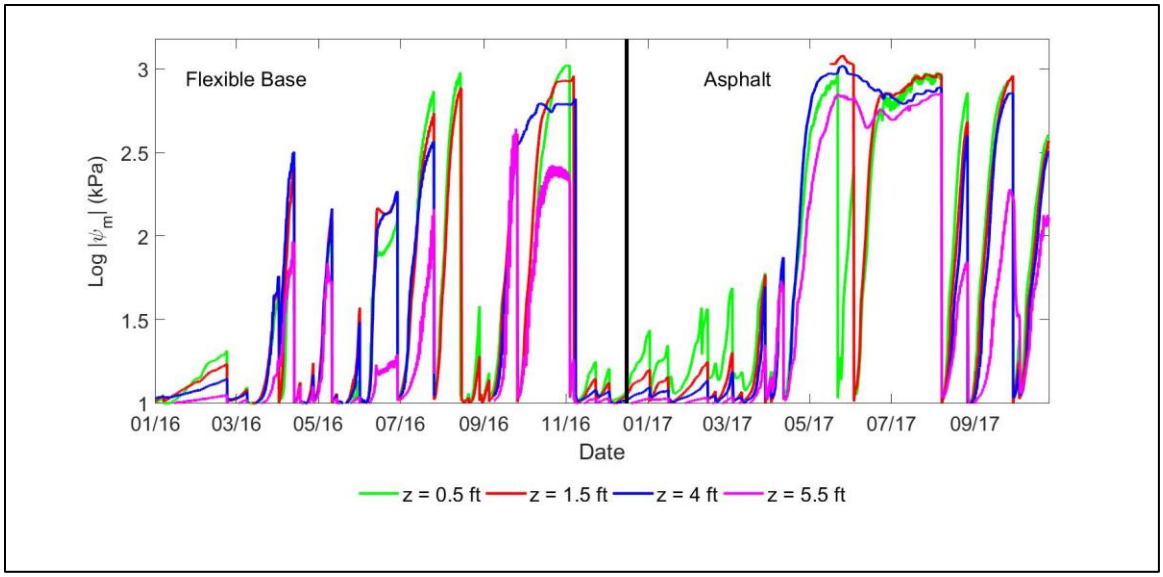

Figure 5.30: Matric suction time history at the FM685 site

Matric suction fluctuations, did not show as significant of a difference between the two time periods. The matric suction sensors worked well during the drying of the soil. However, the readings from the sensors were affected by the time required for hydraulic equilibrium with the surrounding medium. As with the moisture content fluctuations, the matric suction tends to drop uniformly with the advancing moisture front during the flexible base period. However, there were periods where the deposit was only partially wetted (e.g. October 2016 and June 2017) which caused periods of instability in the matric suction readings. The increase in the matric suction differed between seasons, with drier seasons (i.e. the summer) showing more significant increases in matric suction than the wetter seasons (i.e. the winter). The drying rate was slightly higher for the asphalt time period during the winter months than during the flexible base time period, but this difference was attributed to climatic conditions and a reduced amount of precipitation events.

5.4.2 In-Situ Soil-Water Retention Curves

Each of depths monitored were instrumented with volumetric moisture content and matric suction sensors. By using the data from these two sensors, an in-situ, field generated soil-water retention curve can be fitted to the field data. The field data required filtering prior to fitting a soil-water retention curves due to the accuracy in the wet region of the matric suction sensors. The readings from the matric suction sensors were relatively inaccurate in the wet end of the data. The manufacturer provides an accuracy of 25% of the reading plus 2 kPa for a range of matric suction values from -9 to -100 kPa. A visual representation of this error is shown in Figure 5.31. The fitted data was taken from one of the field-generate soil-water retention curves as an example.

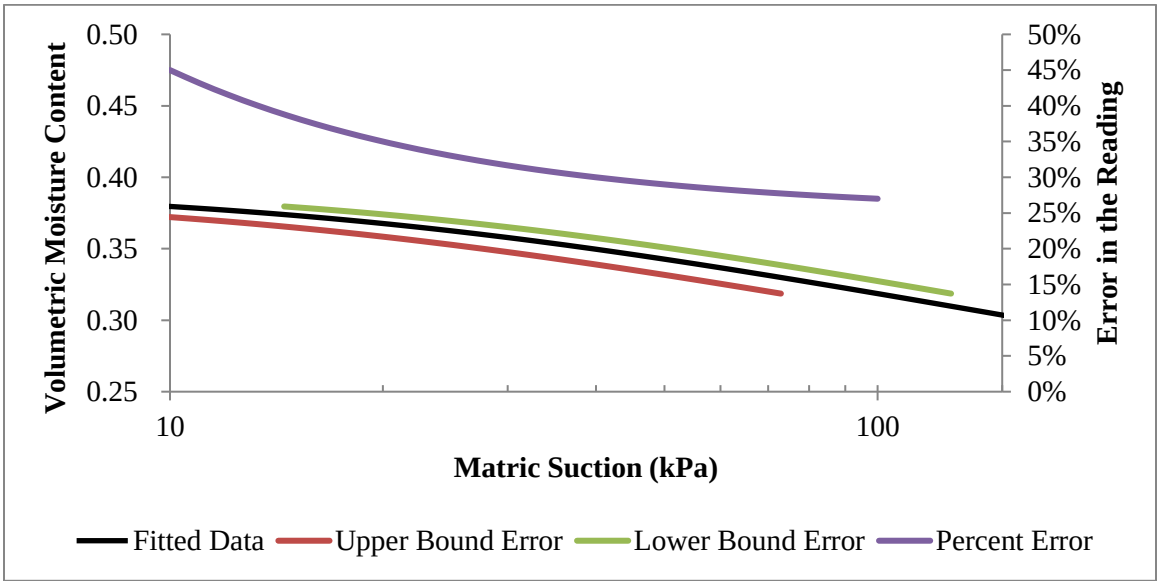

Figure 5.31: Potential error in the soil-water retention curves from matric suction sensors

The potential error from the matric suction sensors can shift the soil-water retention curve significantly. Due to this potential error from the matric suction sensors, all field data with matric suction readings below 100 kPa was removed. Additionally, due to issues

with the equilibrium between the ceramic disk and surrounding soil, all field data with volumetric moisture content measurements greater than 0.45 was removed. Data from the dry end of the matric suction readings were expected to provide more reliable data as the equilibrium between the soil and ceramic disk would improve with less rapidly changing soil conditions. For the dry end of the matric suction readings, previous studies have indicated that the sensor can measure matric suction values up to 4,500 kPa (Decagon, 2016). Therefore, the filtering of the data primarily focused on the wet-end of the soil-water retention curves.

The curve fitting processed involved fitting the van Genuchten (1990) equation, presented in Section 2.3, to the filtered data. To validate the curve fitting process, two curve fitting methods were used; a non-linear least squares curve fitting from MATLAB and the shuffle complex evolution developed by Duan (1993). Both curve fitting techniques were evaluated in MATLAB with the shuffle complex evolution using a code developed by Duan (2004). The shuffle complex evolution method works by generating various sample points in a given range that are ranked based on a criterion condition, in this case the minimization of the root-mean-square error. Each of the points are then grouped into complexes. These complexes are analyzed by ranking the sample population. These new rankings are then checked for convergence in order to verify whether a global maximum has been reached. The method is complex but results a global maxima or minima as opposed to only a local maxima or minima. The least-squares method involves reducing residuals between the recorded data and fitted curves. This method may have issues with finding only a local minimum instead of a global minimum due to the initial search conditions.

These methods were used to fit the data from each of the instrumented depths. A comparison in these fits is shown for the fitting of the field data from the sensors at a

depth of 0.5 ft below the base-subgrade interface for both the flexible base and asphalt time periods in Figure 5.32. A color bar is used to indicate the date, in terms of the month and year, that the field data was recorded.

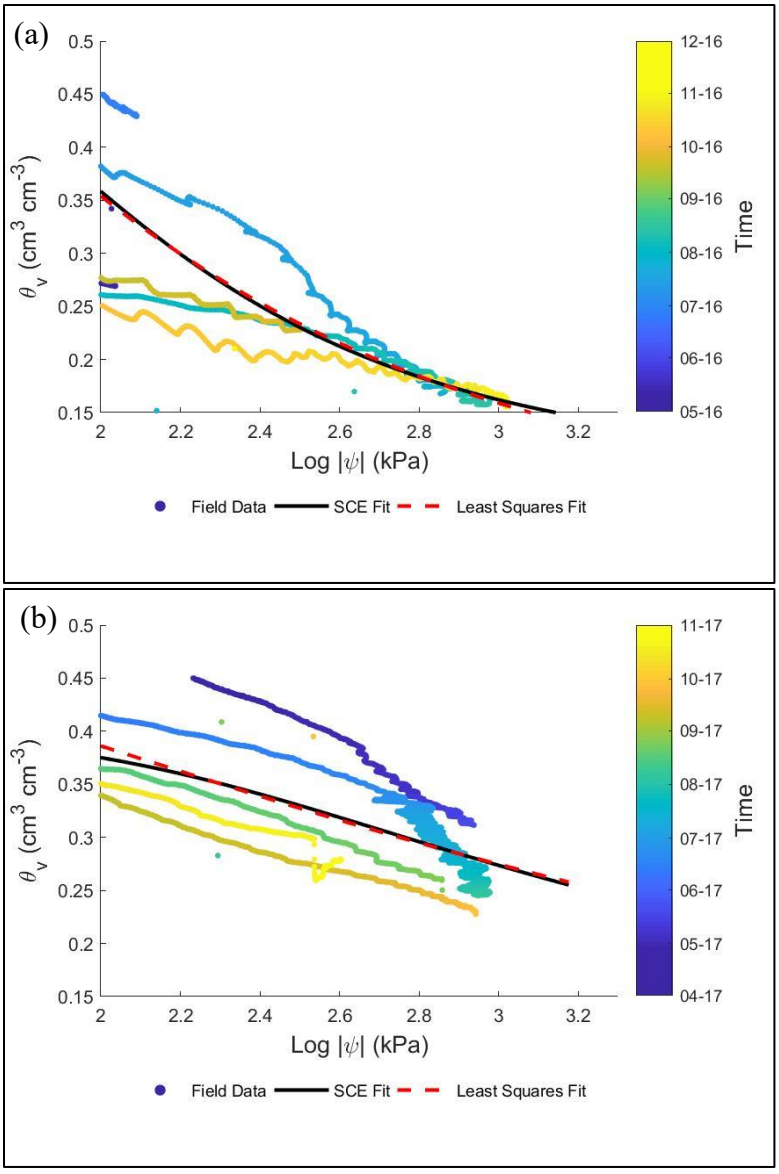

Figure 5.32*:* Comparison of the curve-fitting techniques for soil-water retention curves using field data from sensors at a depth of 0.5 ft below the base-subgrade interface for the flexible base time period (a) and asphalt time period (b)

The fitted curve using the least-squares method is the similar as the curve fit from the shuffle complex evolution for the flexible base surface. However, the two methods generate slightly different curves for the field data from the asphalt surface time period. This difference in the fit was attributed to the instability of the volumetric moisture content data from this time period, as previously shown in Figure 5.14 and discussed in Section 5.4.1. This difference slightly affected the data from the more wet portion of the soil-water retention curve. Additionally, differences between the fitted soil-water retention curves from each method were observed for the field data from the sensors at a depth of 1.5 ft below the base-subgrade interface, as shown in Figure 5.33. A color bar is used to indicate the date, in terms of the month and year, that the field data was recorded.

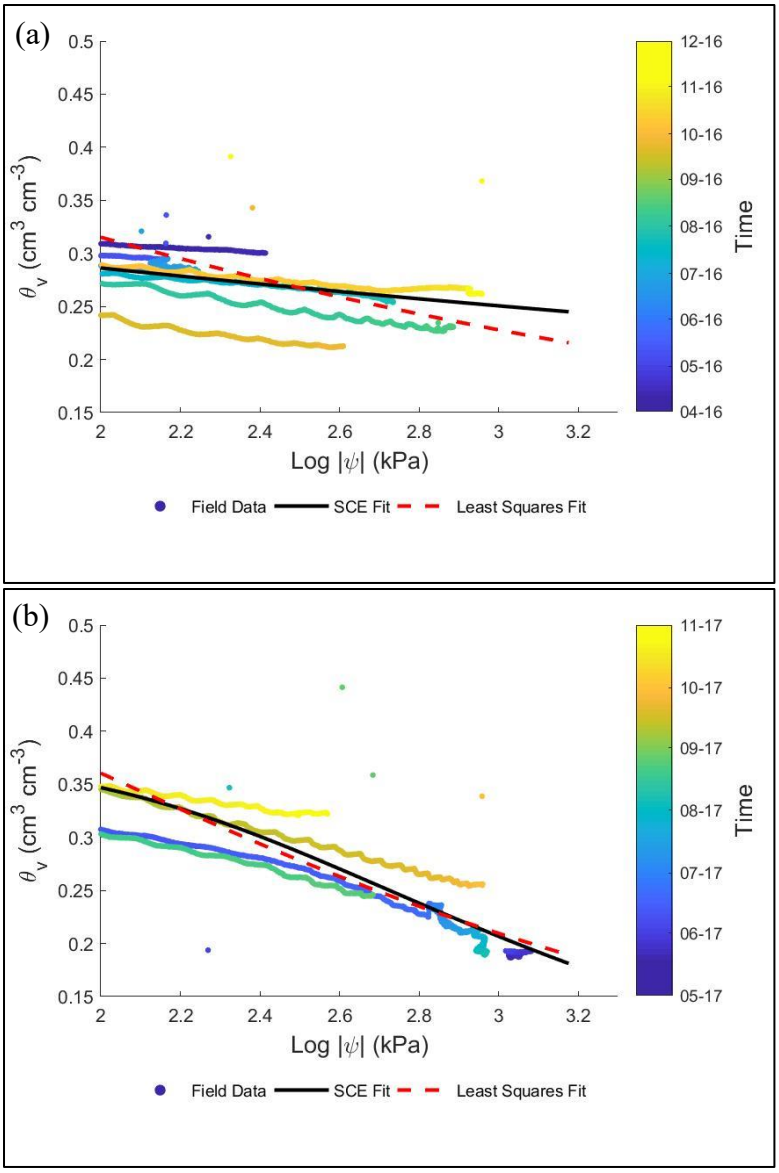

Figure 5.33: Comparison of the curve-fitting techniques for soil-water retention curves using field data from sensors at a depth of 1.5 ft below the base-subgrade interface for the flexible base time period (a) and asphalt time period (b)

The shuffle complex evolution method, while robust, can be influenced significantly by portions of the data that are away from the mean, as seen by the lower matric suction values in Figure 5.33a. This data that biased the fitting of the soil-water retention curve

was taken from the period of a partial wetting front. Removal of this data improved the fitted soil-water retention curves, with similar fitted curves from both methods. Therefore, for the majority of data, the least-square fitting method generated similar soil-water retention curves as the more complex shuffle complex evolution. Due to the similarity in the results between the methods and the computational time required for the shuffle-complex evolution fitting, the least-square fitting method was used for the remaining fitted curves.

Field-generated soil-water retention curves were generated for several conditions. The first analysis evaluated the soil-water retention curve using the field data from all of the sensor in the Branyon clay. Further analyses evaluated the soil-water retention curves using field data from each depth to evaluate the variability of the curves with depth. These analyses additionally analyzed whether the soil-water retention curves varied for the two time periods. Finally, the soil-water retention curves from the tan clay were evaluated for the two time periods. The field-generated soil-water retention curves were compared to the curves generated from total suction measurements from chilled mirror hygrometer tests, as previously shown in Section 5.32 and Figure 5.13. The laboratory-generated soil-water retention curves were expected to provide an upper bound for the field-generated curves as the matric suction should not exceed the total suction.

A soil-water retention curve was first generated using the filtered data from the sensors in the Branyon clay. The data from the sensors at a depth of 0.5 ft, 1.5 ft, and 4 ft below the base-subgrade interface were grouped into the flexible base surface time period and asphalt surface time period, filtered to remove data near the wet end of the matric suctions sensors, and fitted to a soil-water retention curve using the least-squares method, as shown in Figure 5.34. The suction differed between the field data and curves and the

laboratory curves. The field data and curves were generated from matric suction measurements, and the laboratory curve was generated from total suction measurements.

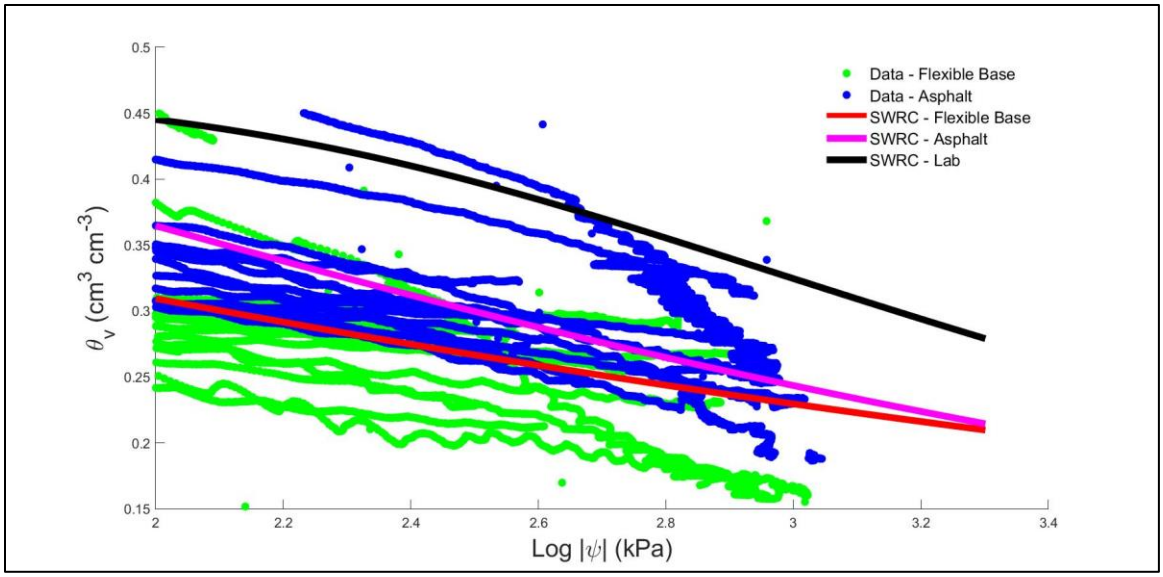

Figure 5.34: Soil-water retention curves using field data from the Branyon clay for the two time periods

The fitted soil-water retention curves differed between the two time periods. The difference in the curves can be attributed to a portion of the filtered data from the asphalt time period that was an outlier from the majority of the data. In this portion of the data, the volumetric moisture content and matric suction exceeds the laboratory-generated soil-water retention curve. This behavior indicates these readings may be erroneous. These discrepancies will later be evaluated for the data taken from each sensor pairing. For the remaining filtered data, the two time periods show similar trends with more variability in the field data encountered at lower matric suction values. This increased variability was attributed to the potential error in the suction measurements, as previously shown in Figure 5.31.

Since the maximum volumetric moisture content varied at depth, degree of saturation measurements were estimated from the field volumetric moisture content data using Equation 5.2. The degree of saturation allows for a normalization of the moisture content at each depth. Additionally, the soil-water retention curves can be converted from the volumetric moisture content space to the degree of saturation space. The field data and fitted curves are shown in Figure 5.35. The degree of saturation for the laboratory measurements were estimated with the curve-fitted saturated volumetric moisture content.

.

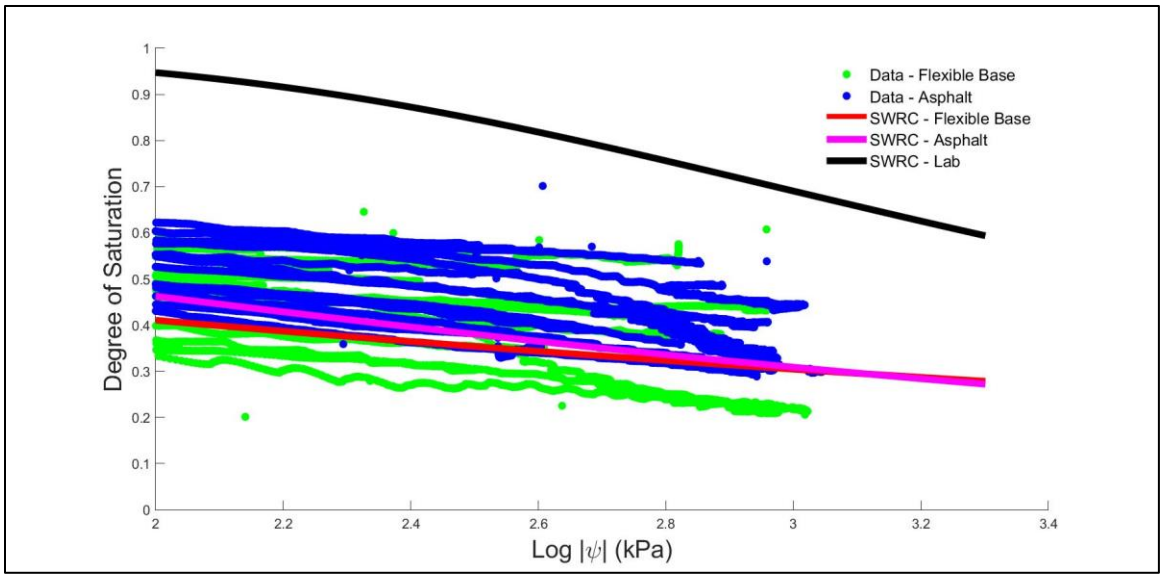

Figure 5.35: Soil-water retention curves using field estimate degree of saturations from the Branyon clay for the two time periods

The filtered data and fitted soil-water retention curves are more similar when using the degree of saturation. The filtered data did not vary as significantly as the data from Figure 5.34 with the data not exceeding the laboratory-generated soil-water retention curves. Due to this better consistency in the results, the filtered data and soil-water retention

curves were plotted using the degree of saturation. The degree of saturation was higher for the laboratory-generated soil-water retention curve than the field data. This increased degree of saturation can be attributed to the lower volumetric moisture content used to estimate the degree of saturation the maximum volumetric moisture contents from the field data.

The filtered data was analyzed at each depth to determine whether the soil-water retention curve varied with depth. The filtered data was plotted using a color bar to indicate the time of each data point. Data from the sensors at a depth of 0.5 ft below the base-subgrade interface was analyzed first. There was some instability in the volumetric moisture content readings after the placement of the final asphalt surface as previously shown in Section 5.4.1. This instability of the moisture content readings affected the fitting of the soil-water retention curves. The filtered data and fitted soil-water retention curves are shown in Figure 5.36 for the two time periods. Soil-water retention curves fitted using the laboratory measurements and fitted using field data from all sensors in the Branyon clay deposits are additionally plotted. The maximum volumetric moisture content used for the degree of saturation calculation differed slightly between the two time periods.

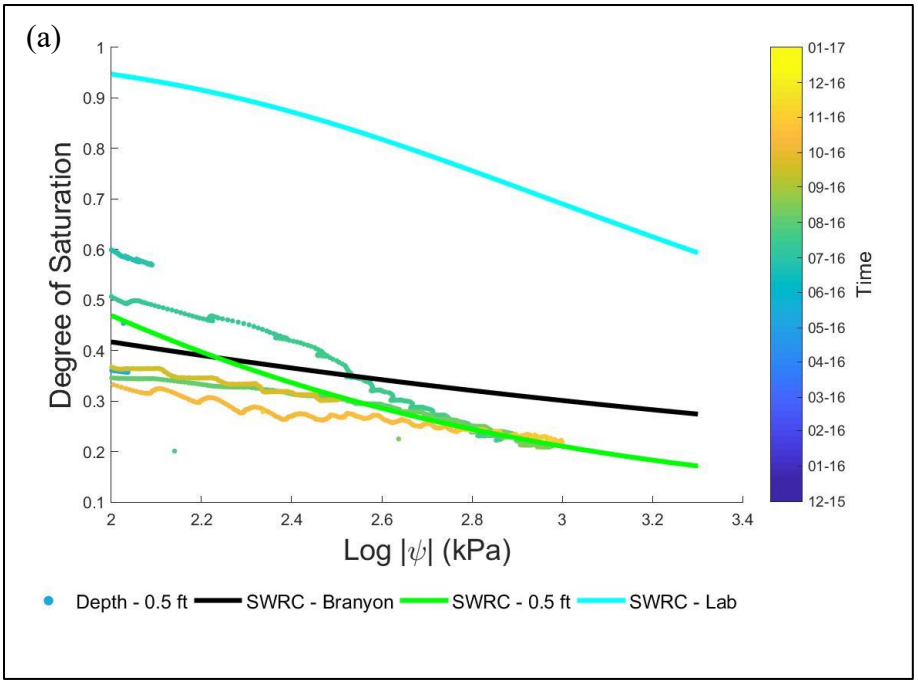

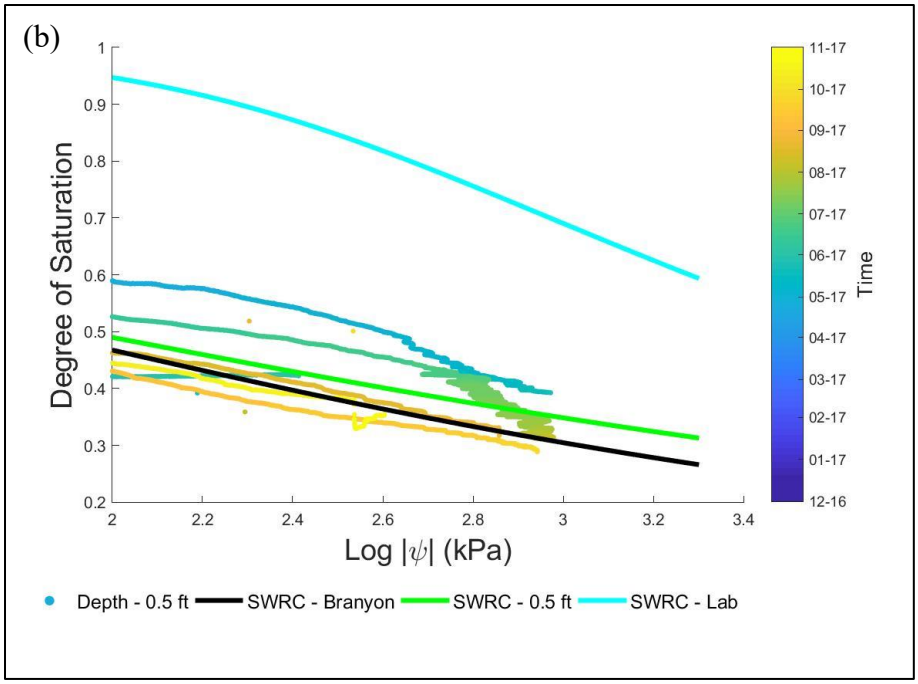

Figure 5.36: Field data and fitted soil-water retention curves for the Branyon clay at a depth of 0.5 ft below the base-subgrade interface for the flexible base time period (a) and asphalt time period (b)

The fitted soil-water retention curves differed slightly between the two time periods. These differences can be attributed to the high amount of scatter in the field data during both time periods, and the instability in the volumetric moisture content readings after the placement of the asphalt surface. The instability of the volumetric moisture content measurements following the placement of the asphalt (i.e. in January and February of 2017) affected the fit of the soil-water retention curve. This instability was assumed to be caused by the upper portion of the Branyon clay coming into moisture equilibrium after the change in the upper boundary condition. These volumetric moisture content at the same matric suction for these data points was higher than data from the summer of 2017 and the data from the flexible base time period. An additional issue is the amount of data points used for the curve fitting of the soil-water retention curves. Due to the filtering of the data below a matric suction of 100 kPa, the amount of field data used for curve-fitting of the soil-water retention curves is significantly less than the total amount of field data recorded.

Field data from sensors at a depth of 1.5 ft below the base-subgrade interface in the Branyon clay was also analyzed. These sensors did not experience the instability in the volumetric moisture content readings after the placement of the asphalt surface. The filtered data and fitted soil-water retention curves are shown in Figure 5.37 for the two time periods.

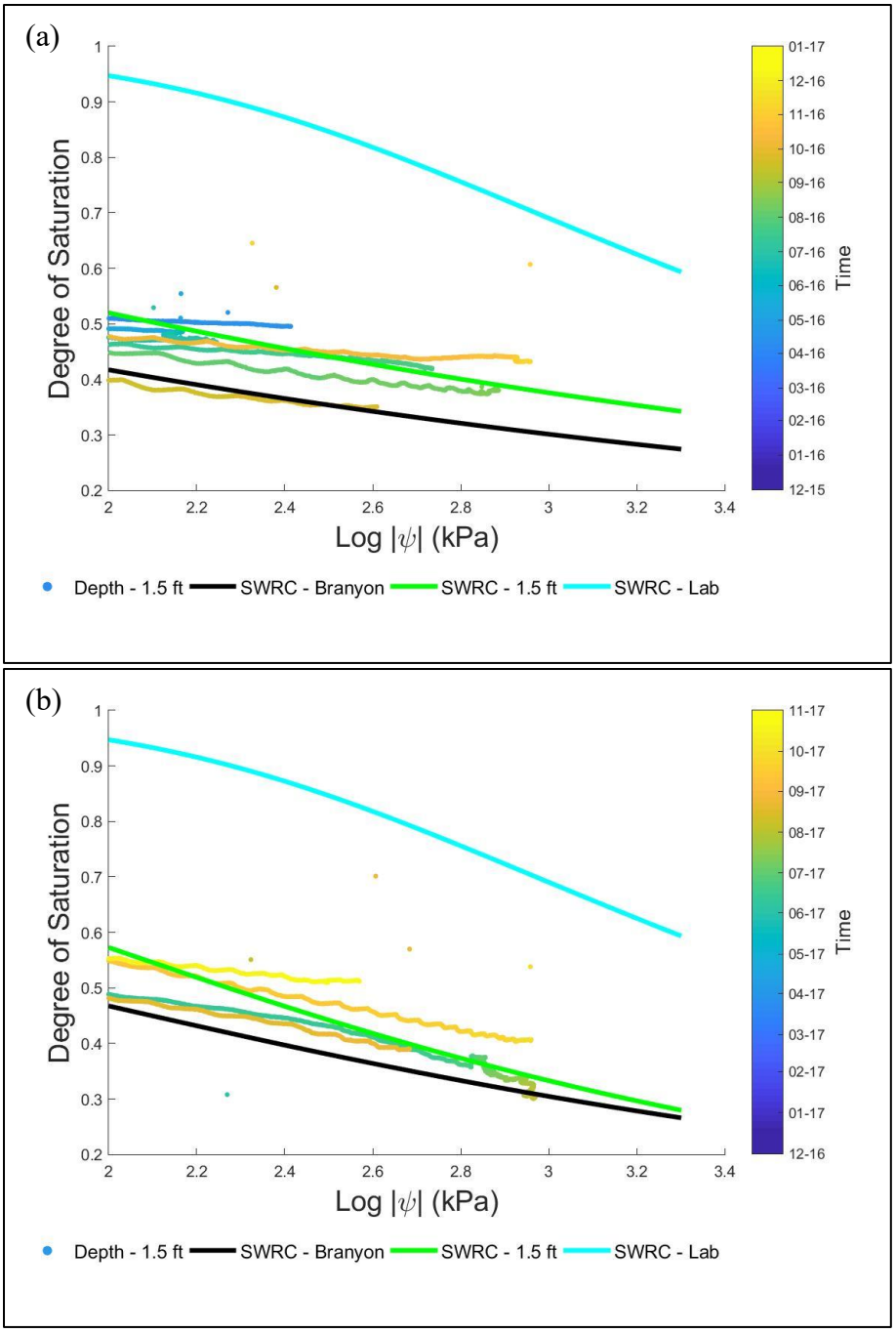

Figure 5.37*:* Field data and fitted soil-water retention curves for the Branyon clay at a depth of 1.5 ft below the base-subgrade interface for the flexible base time period (a) and asphalt time period (b)

While the fitted soil-water retention curves were more similar than the curves from Figure 5.36, there were some discrepancies in the filtered data. The filtered data from the flexible base surface time period was more flat and at a lower degree of saturation than the data from the asphalt surface time period. Additionally, the filtered data does not exceed the total suction measured from the WP4C sensor and show a similar decreasing trend. However, this similar decreasing trend is over orders of magnitude, indicating that the osmotic suction was not constant. This difference can be assumed to be caused by the difference in the soil fabric. From Chapter 3, the soil fabric differs significantly between field-sampled and processed, laboratory-reconstituted specimens. These differences can be assumed to affect the micro-voids based on the differences in the microstructure and soil fabric observed using electron microscopy in Chapter 3.

The more flat portions of the filtered data from Figure 5.37 occurred during the winter months for both time periods. Based on the moisture monitoring, more low intensity rainfall events that only partially wet the deposit were observed during the winter months. During these low intensity rainfall events, the matric suction readings went through a period of inconsistent readings. The matric suction sensors require a time period for the ceramic disk to come into equilibrium with the surrounding soil. Due to this partial wetting of the deposit, this equilibrium is assumed to not have taken place. However, the filtered data during the summer months, where drying of the soil is expected to be most significant, were similar between the two time periods. This consistency indicates that the matric suction sensors provide reliable data during periods of significant drying when the soil is more likely to come into thermodynamic equilibrium with the matric suction sensors.

Field data from sensors at a depth of 4.5 ft below the base-subgrade interface in the Branyon clay was additionally analyzed. Field data from this depth was expected to more affected by the partial wetting of the soil deposit. The filtered data and fitted soil-water retention curves are shown in Figure 5.38 for the two time periods. The fitted soil-water retention curves were more consistent at this depth for the two time periods. More flat portions of the filtered data occurred during both time periods in the winter months. These portions of the curves are attributed to partial wetting fronts as previously discussed. Additionally, the number of data points is smaller than the other instrumented depths as this portion of the soil deposit was typically more wet. However, the slope between the soil-water retention curves fitted from the field data and the laboratory measurements are similar beyond a suction of 300 kPa. Additionally, the slope of the total suction and matric suction soil-water retention curves are similar in the field beyond a suction of 300 kPa. This similarity indicates that laboratory-generated soil-water retention curves from chilled mirror hygrometer tests can be used to estimate the difference in suction between soils at different degree of saturations.

To determine whether the soil-water retention curves are consistent with depth in the same soil deposit, the filtered data at each depth, the fitted soil-water retention curves from each depth is shown for the two time periods is shown in Figure 5.39 using the degree of saturation.

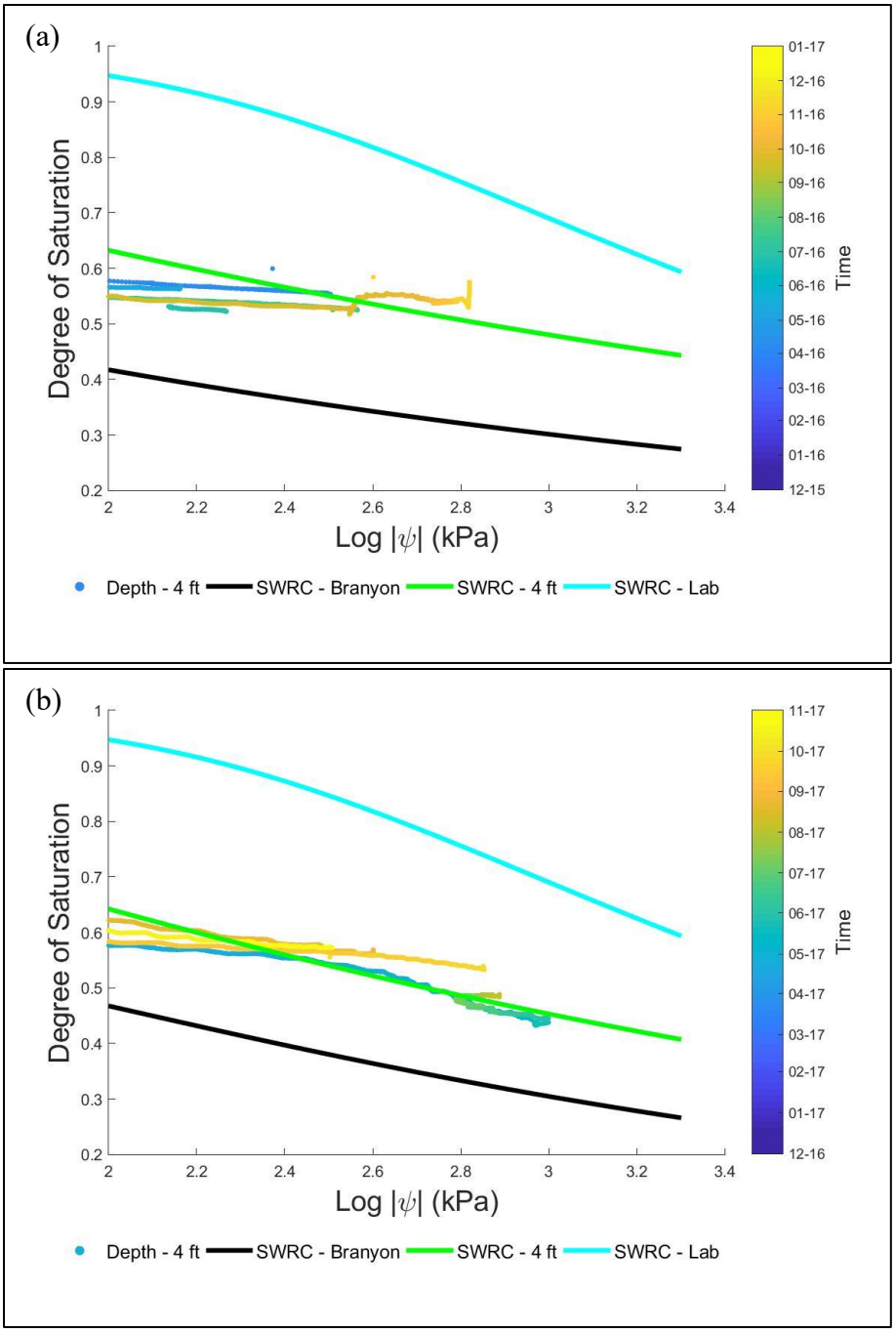

Figure 5.38: Field data and fitted soil-water retention curves for the Branyon clay at a depth of 4.5 ft below the base-subgrade interface for the flexible base time period (a) and asphalt time period (b)

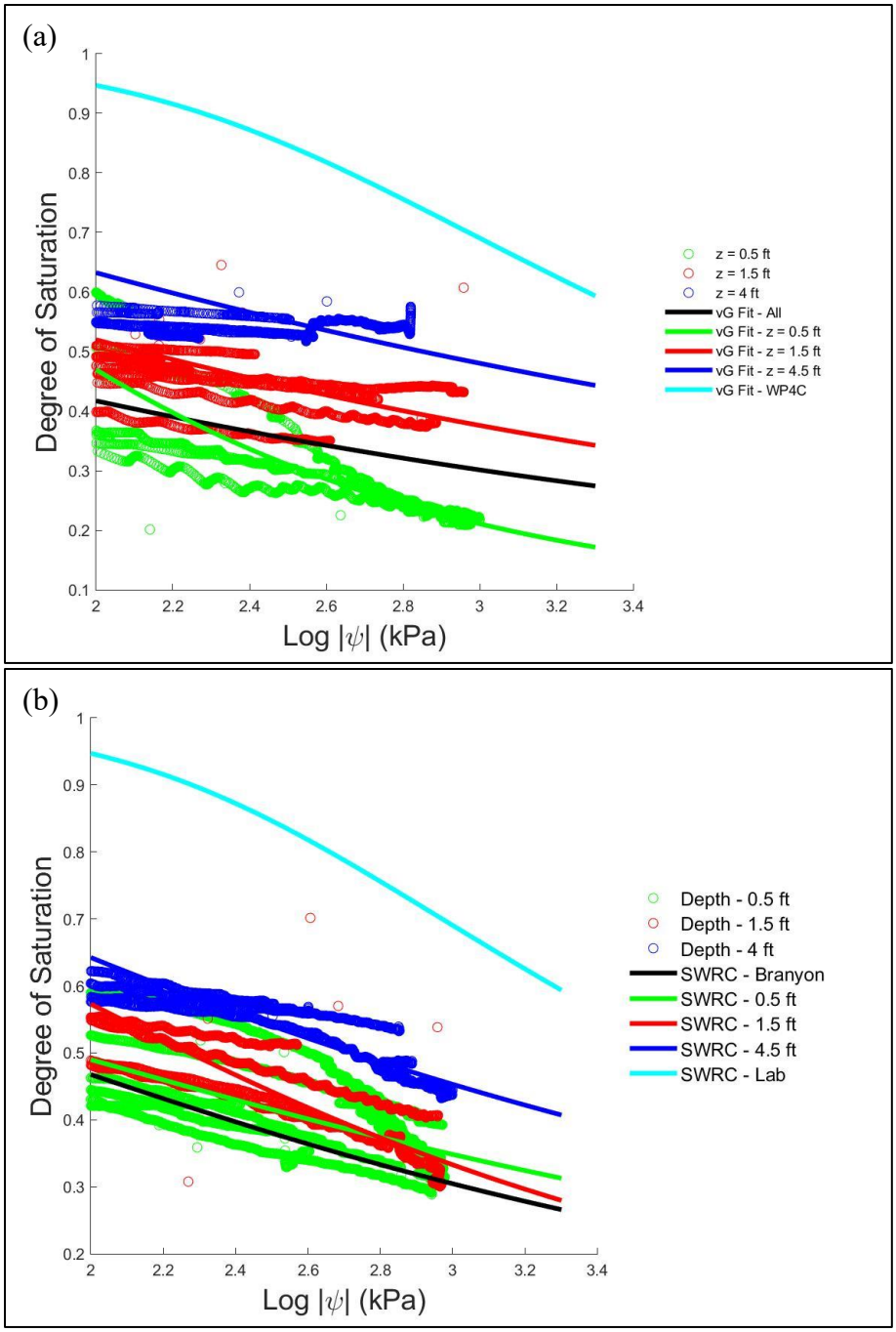

Figure 5.39*:* Filtered field data and fitted soil-water retention curves for various depths in the Branyon clay for the flexible base time period (a) and asphalt time period (b)

As with the analysis of the individual sensors, there was some variability between the filtered data at each depth. This variability can be attributed to the instability of the sensors at a depth of 0.5 ft after the placement of the asphalt surface and partial wetting fronts for the sensors at depths of 1.5 and 4.5 ft. Since the asphalt time underwent a drier period of monitoring with a semi-impermeable upper boundary condition that reduced the number of wetting fronts, the results from the asphalt surface time period were expected to provide more consistent results. The soil-water retention curves did not vary significantly between the sensors at a depth of 0.5 ft and 1.5 ft from Figure 5.39. The majority of the filtered data were consistent between these instrumented depths. To evaluate the differences between the sensors at a depth of 4.5 ft and the shallower sensors, the filtered data and fitted soil-water retention curves using the volumetric moisture content are shown in Figure 5.40 for the asphalt surface time period.

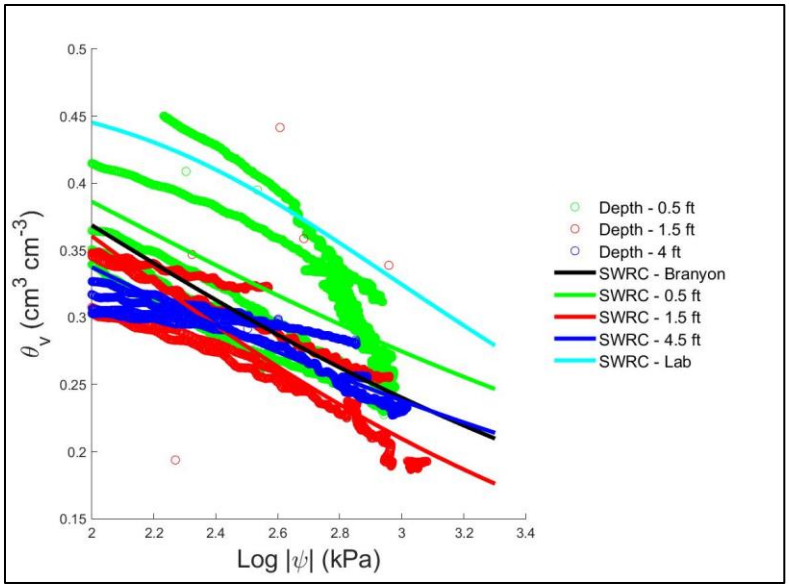

Figure 5.40: Filtered field data and fitted soil-water retention curves for various depths in the Branyon clay

The filtered data are more consistent using the volumetric moisture contents instead of the degree of saturation. As the sensors at a depth of 4.5 ft had the lowest maximum volumetric moisture content, data from this region was significantly affected by the normalization of the data. From Figure 5.40, the variation in the soil-water retention curves was primarily driven by differences in the curves from partial wetting front. Without these unstable values, the soil-water retention curve and filtered data did not vary significantly with depth.

Soil-water retention curves were generated using a wider range of filtered data points in order to verify the trends. Data points with matric suction measurements below 50 kPa were filtered instead of 100 kPa threshold previously used. This condition was selected as the potential percent error of matric suction measurements is similar between 50 and 100 kPa, as seen in Figure 5.31. Additionally, the maximum volumetric moisture content from the sensors at a depth of 1.5 ft were used to estimate the degree of saturation for laboratory-generated soil-water retention curve. This change was to reduce the difference between the laboratory-generated soil-water retention curve and the field data. The filtered data and fitted soil-water retention curves for each time period are shown in Figure 5.41. The soil-water retention curves were generated using both the volumetric moisture content and degree of saturation.

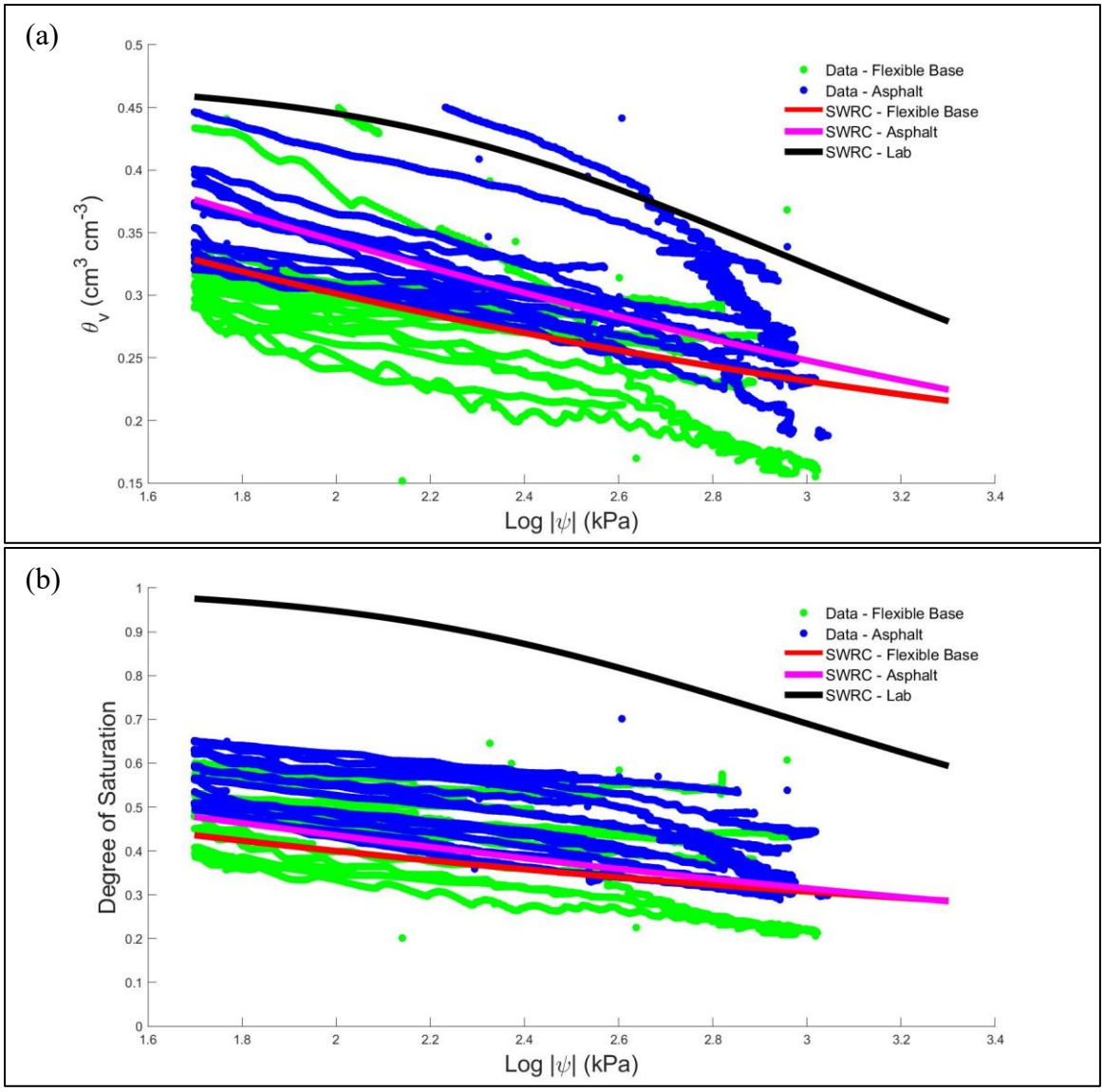

Figure 5.41: Filtered field data and fitted soil-water retention curves for the Branyon clay at all depths in terms of the volumetric moisture content (a) and degree of saturation (b)

The trends using a less restrictive threshold is consistent with previous trends. There is a higher amount of variability when using the volumetric moisture content than when using the degree of saturation. The measurements with matric suctions less than 100 kPa were similar to previous trends. Additionally, the change in the laboratory-generated maximum

volumetric moisture content did not affect the difference between the field data and laboratory curve. The field data did not exceed the total suction from the fitted soil-water retention curves at the same degree of saturation values.

The filtered data from the sensors in the tan clay were used to generate a soil-water retention curve. Again, the WP4C chilled mirror hygrometer tests were used to verify that the matric suction measurements from the field did not exceed the laboratory-measured total suction. The filtered data and fitted soil-water retention curves are shown in Figure 5.42. Unlike the curves from the Branyon clay, the soil-water retention curves varied significantly between the two time periods for the tan clay. Field data from the flexible base time period did not see significant increases in the degree of saturation with increasing matric suction when compared to field data from the asphalt time period. This difference indicates that the deposit was drier at the same matric suction for the asphalt time period. The difference between these time periods was attributed to the surrounding environment during construction. During the flexible base time period, the drainage ditch was consistently mowed, allowing for moisture to more freely infiltrate at the base of the deposit due to the reduction in the active root zone. Due to the reduction in vegetation, moisture was more freely able to infiltrate and dry in the tan clay. After the placement of the final asphalt surface, the root zone was more stable, preventing rapid infiltration of moisture during rainfall. Due to the presence of the roots and the assumed reduction in the infiltration of moisture, the results from the asphalt surface time period were expected to be more representative of the in-situ behavior of the tan clay. The soil-water retention curve from the asphalt surface time period had similar trends to the laboratory-generated soil-water retention curve beyond a suction of 300 kPa. This trend indicates that laboratory-generated curves can be used to estimate differences in suction between different initial field conditions.

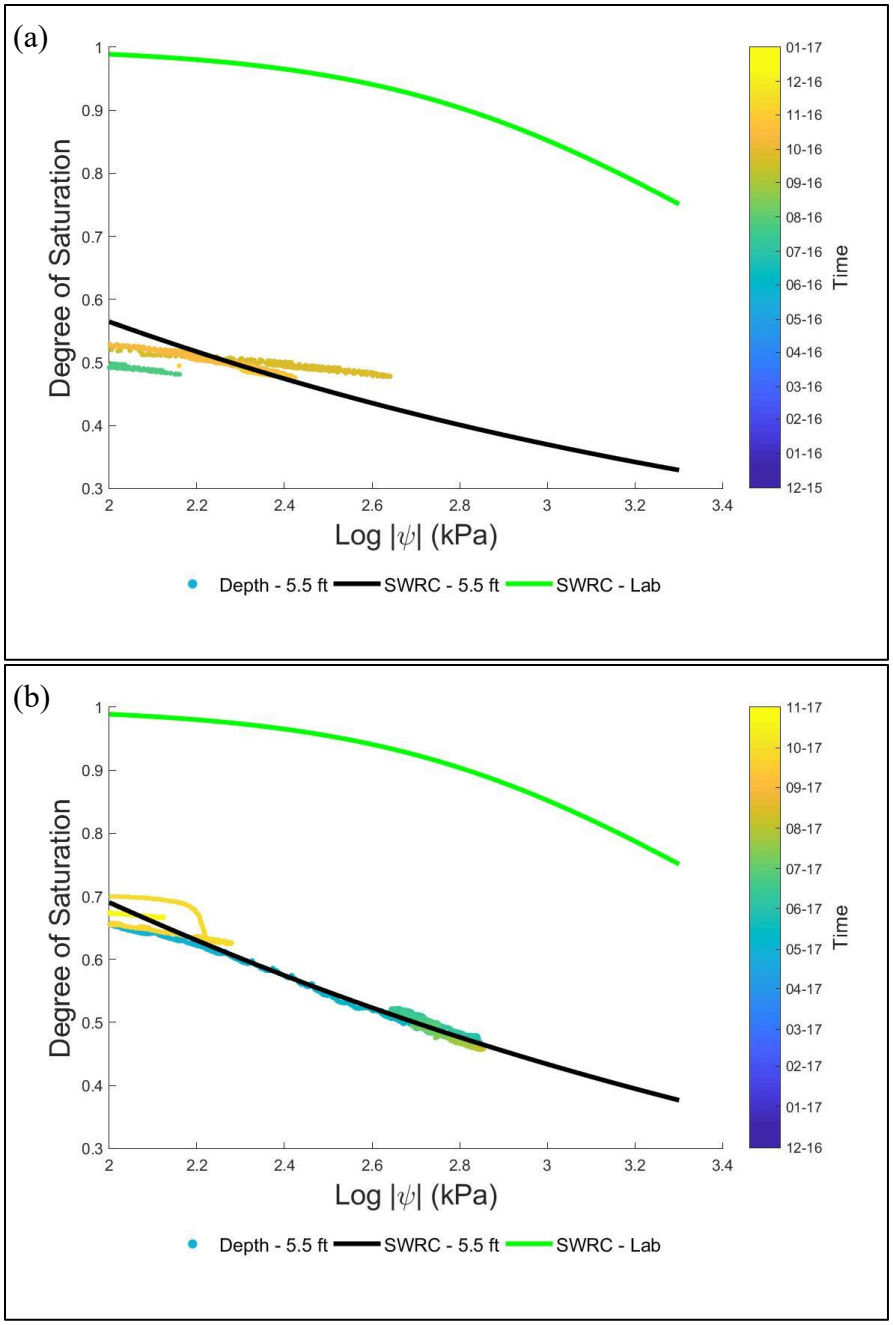

Figure 5.42: Field data and fitted soil-water retention curves for the tan clay at a depth of 5.5 ft below the base-subgrade interface for the flexible base time period (a) and asphalt time period (b)

The remaining results for the volumetric moisture content, saturation and matric suction fluctuations and the remaining data from the curve fitting of the soil-water retention curve can be found in Appendix C. Additionally, the fitting parameters for the van Genuchten soil-water retention curves are presented in Appendix C for the two time periods. Monitoring of moisture content and matric suction fluctuations was used to generate field soil-water retention curves. The fitting of these soil-water retention curves was determined based on a non-linear, least-squares regression. In general, the soil-water retention curves did not vary significantly with depth in the same soil deposit. However, the field data was significantly affected by partial wetting fronts.

5.4.3 Monitoring of Pavement Deflections

The roadway surface was monitored using a total station and a technique outlined in Section 5.2.4 and Roodi et al. (2016). The roadway surface was monitored in order to evaluate the performance of the roadway with moisture fluctuations. A line was painted on the roadway to monitor pavement, including the approximate location of the sensors. Targets were painted on the line at a horizontal spacing of 1 ft. (0.30 m) near the edges of the roadway and at a spacing of 2 ft. (0.61 m) in the middle of the roadway. A non-prism total station was used to measure deflections at each target in the roadway during regular site visits. The total station system recorded the distance from the total station to the targets in three-dimensions coordinates (i.e. x, y, and z). As the location and height of the total station varied between site visits, these coordinates were normalized to the change in elevation from the centerline. The centerline was assumed to remain at a constant elevation. In total, the flexible base surface was monitored during three site visits, and the asphalt surface was monitored during four additional visits.

The flexible base surface was monitored between June 2016 and December 2016 with three site visits. The roadway profile for each of the visits is shown in Figure 5.43, and the corresponding volumetric moisture contents at the time of each visit are shown in Figure 5.44. The roadway is instrumented on the right side of Figure 5.43. The approximate location of the sensors is indicated by the black vertical line.

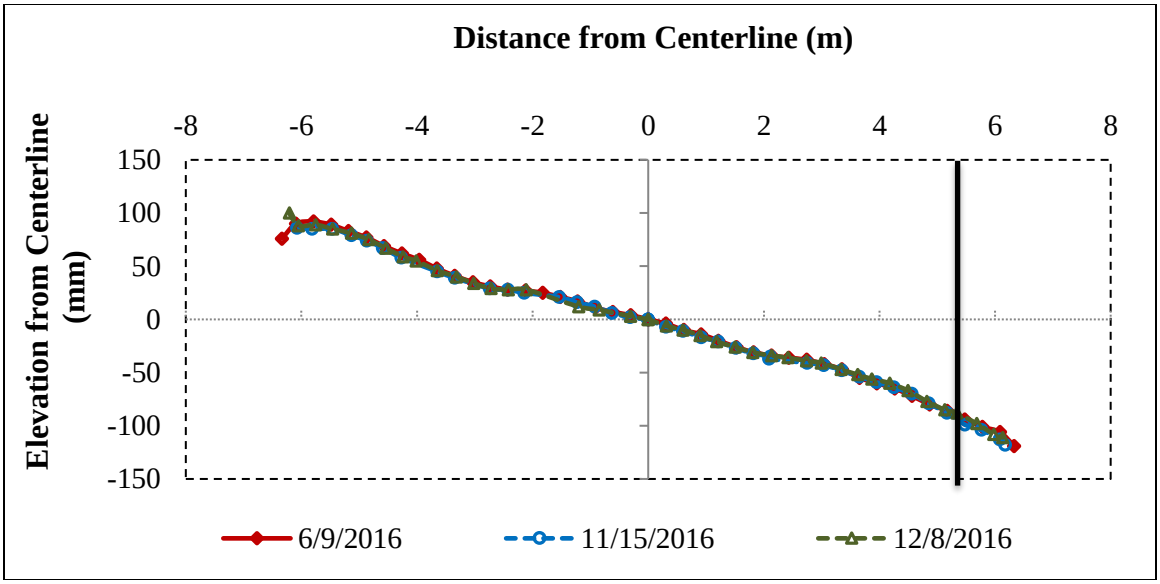

Figure 5.43: Overall pavement profiles during monitoring of flexible base surface with an applied prime coat

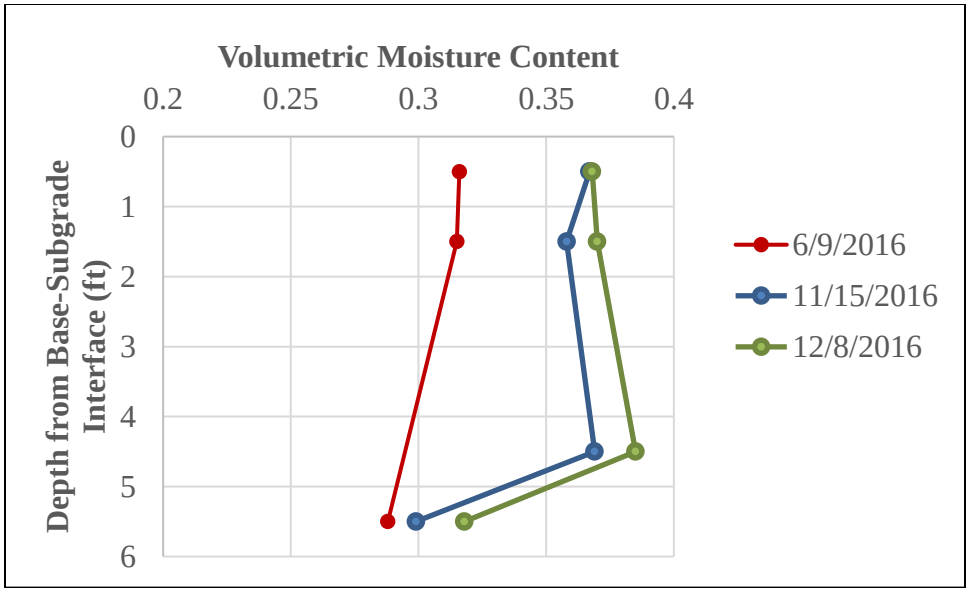

Figure 5.44: Volumetric moisture content during site visits for flexible base surface

The general profile of the roadway was consistent between the summer and winter months despite the increase in the volumetric moisture content. The overall consistency of the pavement profile indicates that there is not a significant variation in the elevation of the centerline. However, there does appear to be a heave of approximately 25 mm during the December reading on the north (left) side of the roadway. However, this heave was attributed to an incorrect data point based on the results from the instrumented portion of the roadway. In order to analyze the heave at the edge of the instrumented roadway, the profile of the pavement over the instrumented section is shown in Figure 5.45. The vertical scale of the figure was reduced to evaluate the deflections above the sensors. The approximate location of the sensors is indicated by the black vertical line.

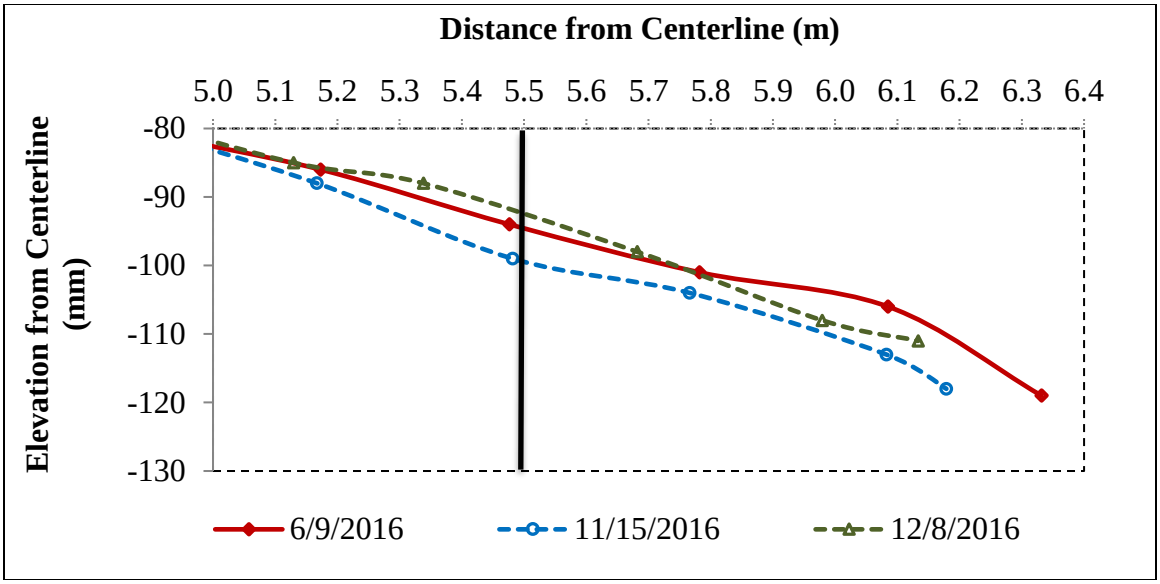

Figure 5.45: Instrumented section of pavement profiles during monitoring of flexible base surface

The edge of the roadway settled approximately 10 mm between the summer of 2016 to the winter of 2016. This settlement occurred despite a higher volumetric moisture content. In order to analyze the cause for the settlement of the pavement, the moisture content fluctuations for the monitored time period is shown in Figure 5.46.

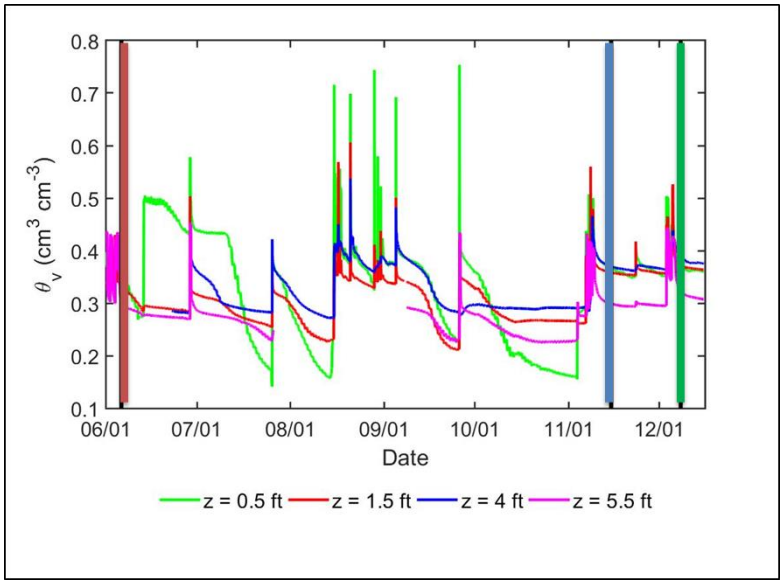

Figure 5.46: Moisture content time history during monitoring of pavement profile for flexible base surface

The site visits during November and December 2016 occurred after rainfall events had taken place. Due to the flexible base surface allowing for a more rapid drying of the subgrade, the subgrade was drying during these site visits. The visit during November 2016 occurred approximately a week after a significant rainfall event, and the visit during December 2016 occurred approximately 12 hours after a significant rainfall event. Thus, the history of the volumetric moisture fluctuations may be more important than the absolute value of the volumetric moisture content.

Although heave was not observed from the monitoring of the pavement surface, longitudinal cracking occurred in the flexible base surface, as shown in Figure 5.47.

Figure 5.47: Longitudinal cracking at the FM 685 site in December 2016

The crack was approximately 5 mm wide. This cracking occurred within a year of the application of the prime coat, indicating that significant environment cracking can occur on these pavement structures. While vegetation built up on the edges of the roadway, the root zone of this vegetation was found to be relatively shallow. Even with this shallow root structure, the vegetation may increase the drying in the subgrade and accelerating the formation of longitudinal cracks.

Monitoring of the roadway profile after the asphalt pavement differed from the flexible base performance. More frequent visits to the site occurred in order to analyze the surface of the pavement. Monitoring of the pavement profile began during the drier, summer months and lasted until a significant rainfall event at the end of August 2017. In total, four site visits were conducted. During this time frame, the profile of the roadway was measured during three visits. The first visit occurred at the end of spring in May 2017 during which the soil was drying out. The second visit took place approximately two weeks after the rainfall event shown in Figure 5.19. The third visit took place in July

2017 during the drying of deposit. The final visit took place at the end of August 2017 following a period of five days with a cumulative precipitation of 9.38 in. (23.83 cm). The overall profile of the roadway is shown in Figure 5.48,and the moisture contents for these visits is shown in Figure 5.49. The approximate location of the sensors is indicated by the black vertical line.

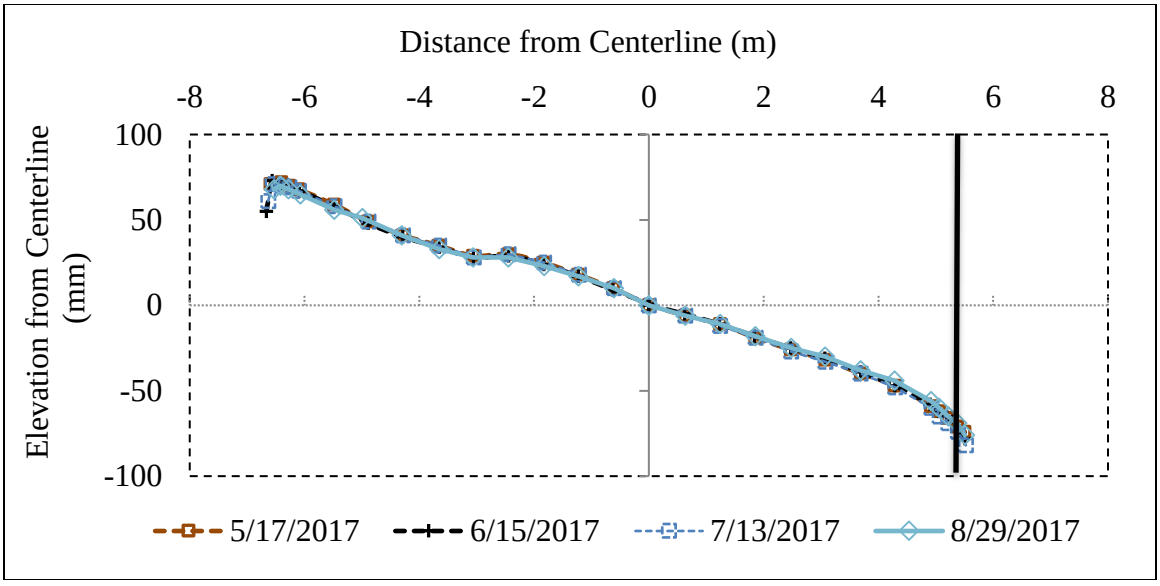

Figure 5.48: Overall pavement profiles during monitoring of asphalt surface

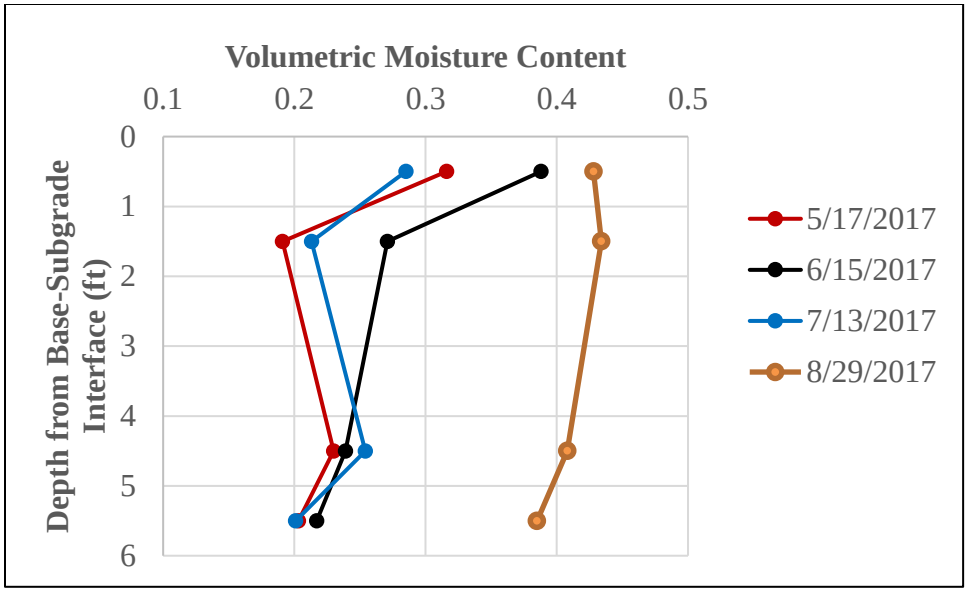

Figure 5.49: Volumetric moisture content during site visits for asphalt surface

As with the overall pavement profile from the flexible base surface monitoring, the overall roadway profile did not vary significantly during the summer months. This trend indicates that the centerline elevation did not vary significantly between seasons. Additionally, the wetted deposit (i.e. the results from August 29th) had a much higher moisture content profile for the asphalt surface than for the flexible base surface (i.e. the results from December 8th). To better understand the moisture history of the site, the moisture content fluctuations during the monitoring of the deflections of the asphalt surface is shown in Figure 5.50.

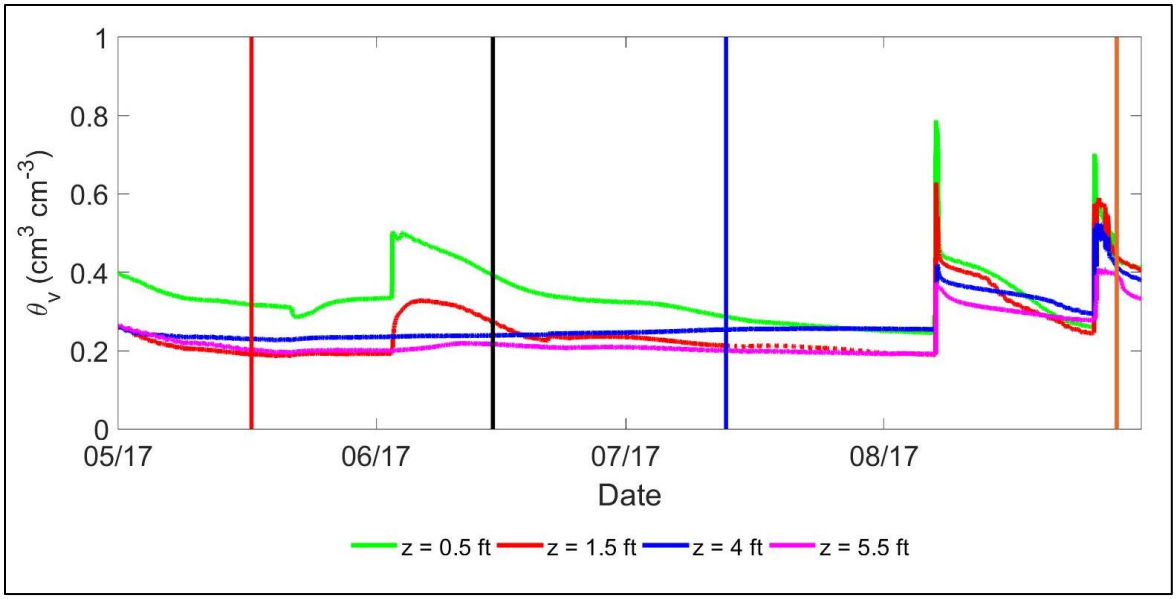

Figure 5.50: Moisture content time history during monitoring of pavement profile for asphalt surface

The subgrade underwent significant drying during the summer of 2017. There was a significant rainfall event in June 2017 and the early portion of August 2017, but in general, there were not as significant of moisture content fluctuations as during the flexible base time period from Figure 5.46.

Under the instrumented portion of the roadway, differential movement of the roadway was observed during the drying of the subgrade and after the significant rainfall event. The drying period extended from May 2017 until July 2017. At the end of August 2017, there was a significant rainfall event during which 9 in of rainfall was recorded at a nearby weather station. The profile of the pavement was monitored during the drying period for three visits, and 8 hours after the end of the significant rainfall at the end of August 2017. The profile of the pavement over the instrumented section is shown in Figure 5.51. The approximate location of the sensors is indicated by the black vertical line.

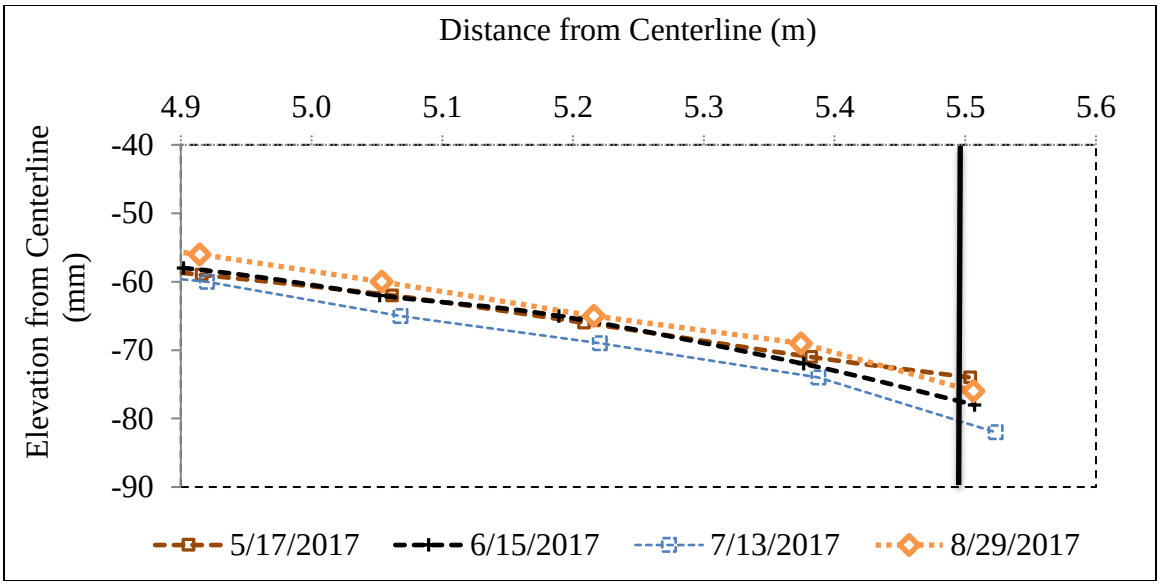

Figure 5.51: Instrumented section of pavement profiles during monitoring of asphalt surface

A settlement of approximately 10 mm was measured from May 2017 to July 2017. While the deeper sensors were slightly more wet in July 2017, the upper portion of the deposit was considerably drier, as seen in Figure 5.49. This upper portion of the deposit dominates the potential volumetric changes due to the lower overburden stress. Furthermore, while the June 2017 profile was more wet than that of May 2017, rainfall had occurred at the site approximately 13 days before the profile was taken in June. This time frame in which drying had occurred, shown in Figure 5.50, explains the settlement at the edges in June as compared to the May profile. This behavior again indicates that the history of moisture fluctuations had a more significant effect on pavement deflections than the absolute value of the moisture content.

In addition to this drying period, August 2017 also had two significant rainfall events that wetted the deposit, a major thunderstorm in the early portion of the month and

Hurricane Harvey at the end of the month. After Hurricane Harvey, monitoring was performed, and the change in the pavement profile from the last field visit in July 2017 during the drying period to the end of August with the wetting of the deposit is shown in Figure 5.52. The approximate location of the sensors is indicated by the black vertical line.

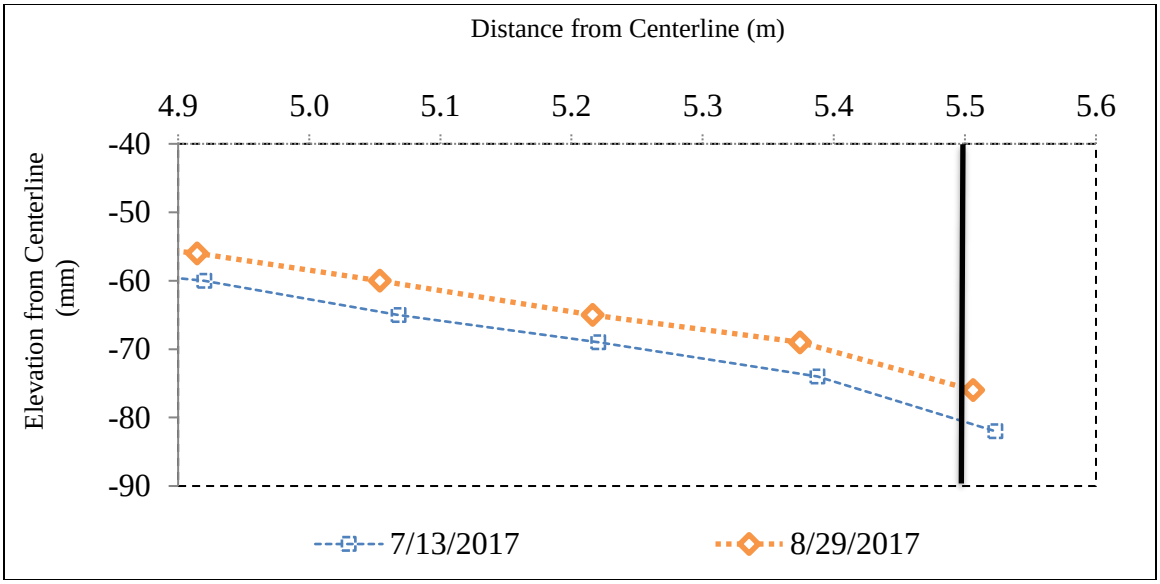

Figure 5.52: Instrumented section of pavement profiles before and after significant wetting of subgrade beneath the asphalt surface

Due to the rainfall event, a heave of 10 mm was encountered on the edge of the roadway. Despite a similar time frame after the end of the rainfall event, the drying of the subgrade beneath the asphalt surface was less significant than the flexible base surface. The heave, while significant, was lower than the laboratory-predicted potential vertical rise in Section 5.3. This difference can be attributed to volumetric strains in the subgrades. Further analysis of the differences in the field-measured and the laboratory-predicted

heave will later be presented in Chapter 7 of this dissertation. However, the total station monitoring was able to capture the heave from a rainfall event on a dry soil deposit.

Results from the total station monitoring of the pavement profile were consistent with the results from the hydraulic monitoring. For the flexible base time period, the roadway settled a small amount during the rainy, winter months. This behavior was attributed to the flexible base surface allowing for the subgrade to dry more rapidly. Additionally, this monitoring indicated that the history of the moisture fluctuations is more important for the pavement profile instead of the absolute value of the volumetric moisture content. For the asphalt time period, a clear settling and heaving of the shoulder of the pavement was observed during a more rigorous monitoring program. This difference amounted to approximately 10 mm during the driest portion of the summer to a significant rainfall event. These results indicate that the total station technology is a valuable tool in the monitoring of a pavement founded on an expansive soil subgrade.

5.5 CONCLUSIONS

To understand the impact of moisture fluctuations on pavement structures found over expansive subgrades, a site in Central Texas was instrumented using moisture content and matric suction sensors. Monitoring was grouped into two time periods during the construction process; one occurred while the subgrade was beneath a temporary flexible base, and the other occurred while the subgrade was beneath the final asphalt pavement. The analysis of the data collected at the field site aimed at three research objectives. The first objective was to compare the moisture and suction fluctuations beneath the two time periods. The second objective was to generate in-situ soil-water retention curves using the field data and to compare them to curves generated using

laboratory data. The final objective was to correlate the moisture time history with the performance time-history of the roadway deflections.

Monitoring of volumetric moisture content and matric suction fluctuations for the two time periods led to the following conclusions:

- Capacitance moisture content sensors are suitable for use in expansive soils.
- The expansive soil subgrade was able to wet rapidly and dry significantly during seasonal fluctuations for both time periods.
- Expansive soil in the field can dry out to a lower volumetric moisture content than the "dry condition" tested in laboratory tests.
- The different surface conditions affected the moisture fluctuations in the deposit.
- The subgrade beneath the flexible base surface was wetted more significantly under low intensity rainfall events than the subgrade beneath the asphalt surface.
- Drying occurred over a longer timeframe for the subgrade beneath the asphalt surface than for the subgrade beneath the flexible base surface.
- The difference in the behavior was attributed to the asphalt surface performing as a semi-impermeable hydraulic barrier, whereas the prime coat on the flexible base surface allowed for more moisture to infiltrate through the upper surface.

Field generated soil-water retention curves were generated by curve fitting field data from the moisture and suction sensors. The data from these sensors were filtered in order to remove data near the wet end of the soil-water retention curve. Based on the generation of these soil-water retention curves, the following conclusions were made:

- The non-linear least squares method was suitable to find global minima for the curve fitting data. A more rigorous shuffle complex evolution was used to validate the curve fitting for the expansive subgrade.
- The fitted soil-water retention curve did not vary significantly with depth in the expansive soil deposit.
- Fitting of the soil-water retention curves was affected by low-intensity rainfall events that partially wetted the deposit.
- The laboratory-generated and field-generated soil-water retention curves had similar slopes beyond a suction of 300 kPa. This difference indicates that laboratory-generated soil-water retention curves can be used to estimate differences in suction between different initial field conditions.

The surficial pavement deflections were monitored during regular field visits using a non-prism total station surveying equipment. Based on the results of total station monitoring, the following conclusions were made:

- The settlement and heave of the pavement profile depends on the moisture history and not the absolute value of the volumetric moisture content.
- The magnitude of the heave after a significant rainfall event was less than the laboratory-predicted vertical rise from centrifuge-based inundation tests.

Chapter 6: Validation of Centrifuge-Based Swelling Predictions using Large Column Infiltration Test

ABSTRACT

A large soil column was instrumented in order to evaluate predictions of heave using centrifuge swelling test results. Soil collected from a field site was compacted to a dry moisture condition into a latex membrane within an acrylic soil column to replicate an expansive soil deposit. The column was instrumented with moisture content sensors to monitor moisture fluctuations. Results from this monitoring indicated that the moisture front advanced at a slower rate than field moisture infiltration from the site presented in Chapter 5. However, the rate of moisture infiltration was higher than rate expected for a highly plastic clay based its expected saturated hydraulic conductivity. A grid printed on the latex membrane surrounding the compacted soil was evaluated using image analysis techniques. Results from this analysis indicated that heave in the column was similar to the vertical rise predicted using centrifuge test results. Additionally, different methods to determine the suction of the soil, the filter paper and chilled mirror hygrometer tests, were compared using the soil collected from the field site. Soil-water retention curves fitted using measurements from each methodology were similar beyond a suction of 1,000 kPa. The osmotic suction tends to be relatively constant for soils sampled at deeper depths. However, the osmotic suction varied with decreasing volumetric moisture content for soils sampled closer to the ground surface.

6.1 INTRODUCTION

The centrifuge-based inundation test was originally developed in order to measure the swelling of expansive soils in a reasonable timeframe. The relevance of experimental determination of soil volume changes was emphasized in order to characterize the swelling in field expansive soil deposits. Use of direct measurement of volume changes

provides a significant advance in the station of practice, which currently relies on correlation to predict the swelling behavior Results from the centrifuge-based tests, namely the magnitude of primary swelling, have previously been shown to be consistent with the swelling results obtained using the traditional methodology, ASTM D4546 (Plaisted, 2009; Zornberg et al., 2013, 2014; Armstrong, 2014). However, the swelling results from the centrifuge-based tests have not previously been compared to swelling of soils on a large-scale, either at a field site or in large laboratory tests.

Two sites were selected for the large-scale evaluation, one an expansive soil deposit beneath a pavement structure, as outlined in Chapter 5, and the other a large column test that is presented in this chapter. The column was comprised of laboratory-reconstituted soil collected from an expansive soil deposit. Bulk samples of the field expansive soil were collected at various depths in order to prepare a laboratory column that recreated the stratigraphy of a soil deposit. The main objective for this large-column test is to compare the predicted heave from the centrifuge-based inundation tests to the heave from a large-scale column test that represents field conditions. The heave in the large column was monitored using image analysis techniques and were compared with corresponding moisture fluctuations. A secondary objective for this research involved comparing soil-water retention curves generated from the filter paper tests and curves generated from chilled mirror hygrometer measurements.

This research component was grouped into three sections. The first section focuses on the background information from previous studies that have evaluated the swelling behavior of expansive soil deposits. The second section focuses on the geotechnical characterization of the soil sampled from the field site, including the characterization of the soil-water retention curves. The final section focuses on the instrumentation, testing, and analysis of results from the large column test.

6.2 BACKGROUND INFORMATION FOR MONITORING OF EXPANSIVE CLAYS

In order to better understand the studies previously performed on field projects and large-scale tests with expansive soils, a literature review was performed. Section 5.2 presents the background on instrumentation in expansive soil deposits and expansive soils beneath pavement structures. This literature review is complemented with that presented in this section which provides: (1) previous studies on bare expansive soil deposits and (2) previous large-scale laboratory tests involving expansive soils.

6.2.1 Previous Studies Involving Field Monitoring of Expansive Soil Deposits

Several studies have examined expansive soil behavior through field monitoring. Zhan et al. (2006) examined an unsaturated expansive slope using thetaprobes, tensiometers, thermal conductivity sensors to measure moisture and suction fluctuations, using tipping buckets, flow meter and evaporimeter to measure the environmental conditions at the site. In addition, they used pressure cells, inclinometers and movement points to measure the stresses and strains on the slope. The researchers prevented water flow into the small cracks around the installation holes for the sensors by the use of sample coverings. The instrumentation recorded the moisture fluctuations and corresponding changes in the stresses and strains in the slope over a two month period within a reasonable range of values.

Hu and Vu (2011) instrumented the interior of a pipe and the surrounding expansive soil. The instrumentation captured the seasonal changes of moisture infiltration and frost heave on the deformation in the pipe and moisture fluctuations in the surrounding deposit. The water content reflectometers in the expansive soil deposit provided results that were consistent with seasonal changes in moistures. Monitoring took place along several locations between the ground surface and base of the trench over the course of three years. Monitoring results indicated that moisture content fluctuations

occurred mainly near the ground surface. Changes in the soil's temperature and moisture content lagged behind the changes near the surface due to the presence of frost in the soil. Additionally, the researchers found that cracking in the native soil affected the rate of moisture infiltration into the deposit.

A retaining wall with an expansive soil backfill was instrumented and monitored for lateral deflections under wetting by Brown (2013) and Dellinger (2011). The project used time-domain reflectometers to measure moisture content fluctuations in an expansive soil deposit behind a retaining wall. The moisture front was able to quickly enter the expansive soil deposit from the clay fissures. However, the natural moisture fluctuations did not create a scenario in which the capacity of the retaining wall was exceeded by the lateral expansion of the deposit. An inundation test behind the wall also indicated that the infiltration of moisture into the deposit was rapid. However, moisture content fluctuations from the time-domain reflectometers were affected by attenuation of the wave-forms in the expansive soil deposit (Dellinger, 2011). The conventional methods to analyze the wave-forms did not work for the expansive soil deposit due to the attenuation of the signal in the highly conductive soil. Additionally, the moisture content sensors tended to separate from the soil during desiccation. The researchers recommended that future studies be wary of the debonding of the soil from the moisture content sensors during the drying cycle.

Dinka et al. (2013) also conducted a large field test on a portion of a vertisol in Central Texas. Portions of both the Heiden and Houston Black clays were instrumented using steel rods that were anchored into the deposit. Moisture content readings were collected using a neutron moisture meter, and moisture fluctuations were compared to the volumetric changes at various points along a hill. Shrink-swell potential was shown to decrease with an increase in the inorganic carbon content from the carbonates of the

parent material. This result is consistent with the mixing of additives, such as lime, to reduce the shrink-swell potential of expansive soils. Cracks were shown to store much of the infiltrating moisture content after periods of drying. Additionally, the majority of the rainfall at the site was found to be runoff instead of infiltration into the deposit.

6.2.2 Previous Large-Scale Experiments using Expansive Soils

Several studies have examined the swelling characteristics and unsaturated properties of clays using large-scale laboratory experiments. Cui et al. (2010) compacted a soil layer in a 1 m x 0.8 m x 0.95 m box with expansive soil to determine its hydro-mechanical behavior. The soil was instrumented with thetaprobes to measure the moisture content and relative humidity and psychrometer sensors to measure the suction within the soil. LVDTs were instrumented at the top portion of the deposit to measure the change in height during the test. An artificial rainfall was imposed on the expansive soil layer for 48 days. After the rainfall ended, a constant head of water was held on the surface of the expansive soil layers. The soil reached moisture equilibrium after 25 days and was inundated for approximately 300 days. The researchers indicated that the soil-water retention curve varied at depth based on the amount of volumetric change during swelling. Additionally, the researchers were able to estimate the unsaturated and saturated hydraulic conductivity of the soil based on the instantaneous profile method.

At the University of Texas, large column tests have frequently been used to measure unsaturated properties of geotechnical material. Lima et al. (2015) examined the difference between moisture profiles of the two columns, approximately 120 cm each, with a non-woven geotextile placed at depth in one of the columns to examine the change in the water retention of a soil. The column with the non-woven geotextile was shown to have a higher water retention capacity based on infiltration tests. Azevedo (2016)

constructed a 110 cm tall soil column with moisture content and suction sensors to examine the formation of capillary barriers above a geotextile that provided cross plane drainage. Results from the column showed that the development of the capillary barrier significantly affected the time for moisture to pass through the geotextile and transport laterally across the geotextile. Both of these researches showed that the flow of moisture through a clay in a large-column provided valuable insight into the expected field behavior of clay deposits.

6.3 CHARACTERIZATION OF SAMPLED FIELD SITE

In addition to the site detailed in Chapter 5, a large soil column was prepared and instrumented to evaluate the moisture and heave fluctuations. This large column was prepared to represent a bare expansive soil deposit. In order to construct the large-column, a field expansive soil deposit was investigated to identify its geotechnical properties. Soil samples were collected in bulk at various depths at the deposit, and the sampled soil was characterized for its geotechnical properties and to define soil-water retention curves.

6.3.1 Location of Expansive Soil Deposit

An expansive soil deposit was sampled at a TxDOT maintenance facility located in Taylor, TX (Figure 6.1).

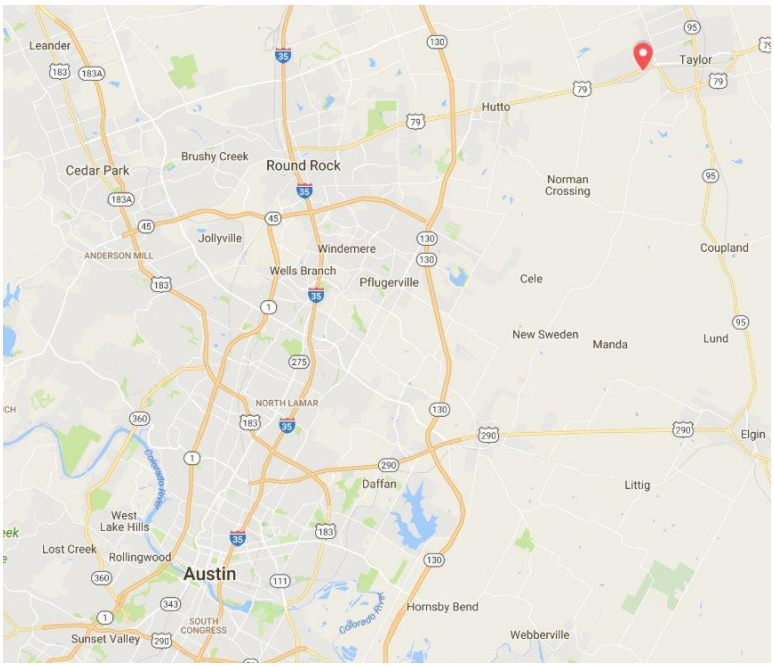

Figure 6.1: Location of the expansive soil deposit (Google, 2016)

The soil deposit is approximately 40 miles northeast of Austin, TX and 10 miles east of the field site described in Chapter 5. The soil deposit was determined to be the Houston Black clay based on USDA soil series. A Houston Black clay deposit was selected as it derives from the Taylor-Navarro group, an important geologic formation in Central Texas, and is an abundant soil series east of the IH-35 corridor. Additionally, the soil deposit is in a similar geologic and geographic region as the field site evaluated in Chapter 5.

To verify that the soil on site was expansive, a geologic investigation was completed prior to the collection of samples. The geologic map of the region near Taylor, TX is shown in Figure 6.2 with the border of the maintenance facility outlined in black. The USDA soil survey is shown in Figure 6.3 with the distribution of the soil in the region shown in Table 6.1. The soil survey of the region places the maintenance yard on

the Houston Black clay (HuC2) with portions of the Algota or Heiden clay possible at depth due to the topography of the region.

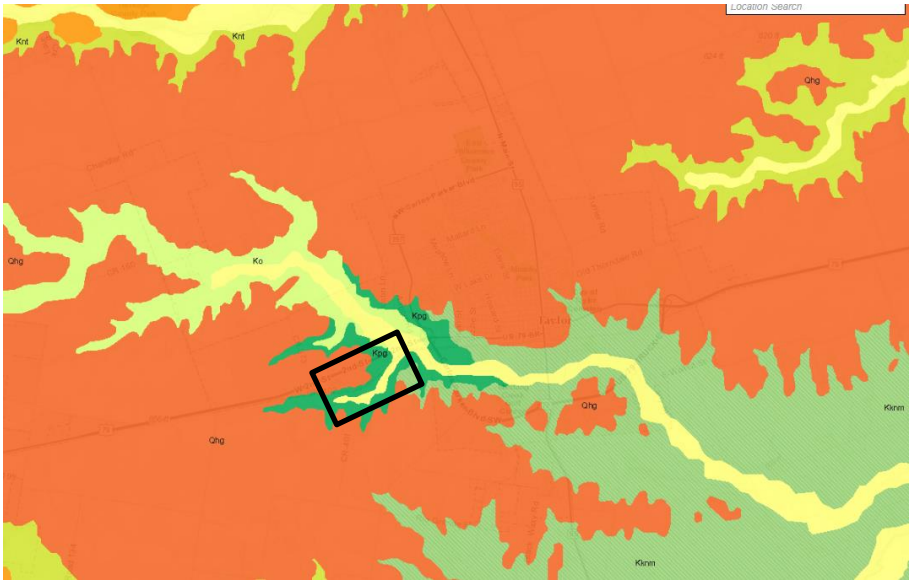

Figure 6.2: Geologic map of Taylor Field Site (USGS, 2017)

Figure 6.3: Soil survey of Taylor Maintenance Office (USDA, 2015)

Table 6.1: Soil series located near the Taylor Maintenance Office (National Resources Conservation Resource, 2015)

Williamson County, Texas (TX491)			
Map Unit Symbol	Map Unit Name	Acres in AOI	Percent of AOI
AgC2	Altoga silty clay loam, 3 to 5 percent slopes, eroded	11.7	12.8%
AgD2	Altoga silty clay loam, 5 to 8 percent slopes, eroded	3.1	3.4%
FhE	Ferris-Heiden complex, 5 to 20 percent slopes, severely eroded	12.2	13.4%
HeD2	Heiden clay, 5 to 8 percent slopes, eroded	12.5	13.7%
HuB	Houston Black clay, 1 to 3 percent slopes	5.4	5.9%
HuC2	Houston Black clay, 3 to 5 percent slopes, moderately eroded	28.9	31.6%
KsB	Krum silty clay, 1 to 3 percent slopes	6.3	6.9%
Tn	Tinn clay, frequently flooded	11.3	12.4%
Totals for Area of Interest		**91.4**	**100.0%**

From Figure 6.2, the location predominantly sits on portion of the Pecan Gap change (Kpg – dark green) with some portion of the Ozan formation (Ko – light yellow) lying on the eastern portion of the maintenance office. Both of these geologic formations are from the Cretaceous period when the Central Texas region was underwater. Formations formed during this time period have previously been identified to be the parent material for several expansive soil series. A large amount of Quaternary alluvial deposits (Qhg - red) are seen in the surrounding region, which indicates that residuum material may be present as opposed to the parent material. The region is typical of those sitting on the Taylor-Navarro group east of IH-35.

The samples of the deposit were collected twice at this site. The first soil sampling campaign was conducted in 2014. The sampling collected bulk portions of the surficial soil to a depth of approximately 0.5 ft. The sampled soil was homogenized and tested for its geotechnical properties and using the centrifuge-based inundation tests to measure its swelling potential. The surficial soil was determined to be moderately

expansive and selected to be a location for a more extensive soil sampling campaign. A second soil sampling campaign was conducted in the summer of 2016 using a truck-mounted auger. Samples were collected from the upper 6 ft with additional drilling conducted to examine the stratigraphy at the site. The deposit consisted of approximately 4 ft of gray to dark brown expansive soil, presumed to be a portion of the Houston Black clay. The Houston Black clay extended to a depth of approximately 4 ft until a light brown to tan clay was encountered. Since the light brown to tan soil does not appear to be weathered as it was relatively chalky, this portion of the deposit was not considered to be a part of the active zone.

6.3.2 Geotechnical Characterization of Sampled Soils

The soils from both the 2014 and 2016 soil sampling campaigns were characterized for their geotechnical properties. The bulk soil was air-dried at approximately 23°C for approximately two weeks. The air-dried soil was then passed through a rock-crusher twice in order to break up the clay clods. The processed soil was tested for its Atterberg Limits, fines content using wet-sieve testing, and clay content using hydrometer test on portions of the processed soil that passed the No. 200 sieve. The soil from the 2014 soil sampling campaign is referred to as the "Original Sampling." The soil from the 2016 soil sampling campaign is referred to be the depth that it was collected from (i.e. "Depth: 0 – 2 ft" represents the soil collected from depths ranging from 0 to 2 ft below the ground surface during the 2016 soil sampling campaign). A summary of the characterization is listed in Table 6.2. The results from the wet sieve and hydrometer tests were combined to generate gradation curves that are presented in Figure 6.4.

Table 6.2: Summary of geotechnical properties of soils sampled at the Taylor Maintenance Office

Sample	Liquid Limit	Plastic Limit	Plasticity Index	Fines Content	Clay Content
Original Sampling	55	23	32	92%	65%
Depth: 0 - 2 ft	67	22	45	94%	52%
Depth: 2 - 3 ft	70	20	50	95%	59%
Depth: 3 - 4 ft	57	18	39	90%	54%
Depth: 4 - 5.5 ft	43	19	28	90%	42%

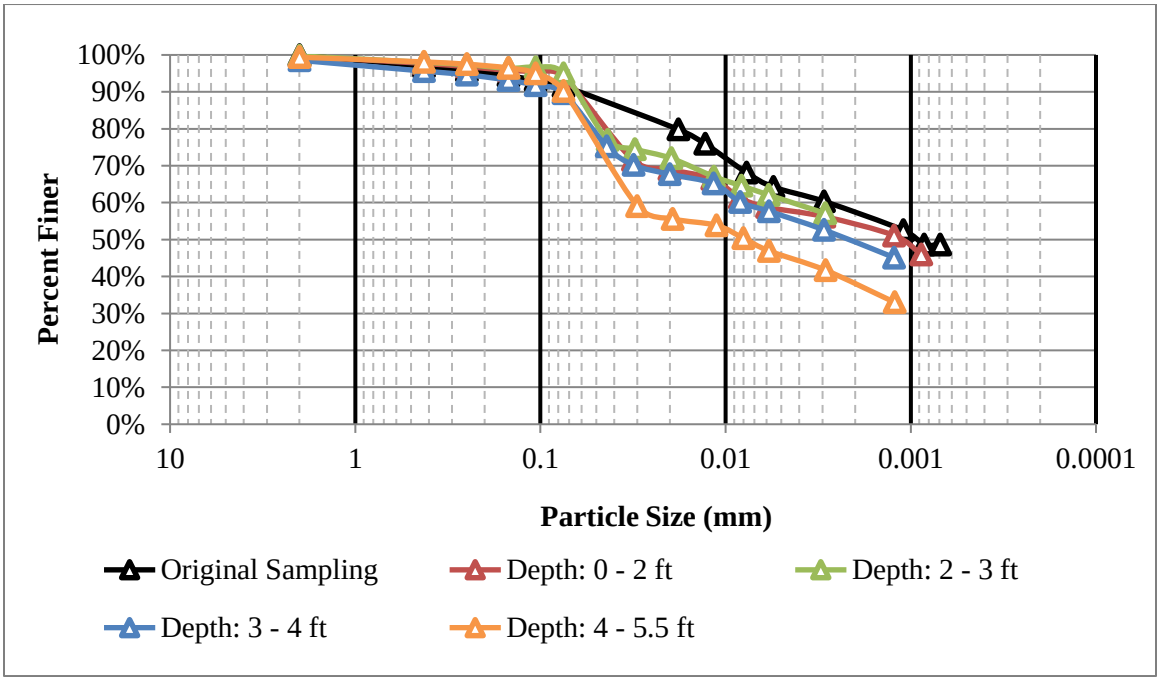

Figure 6.4: Gradation curves for sampled soils

The sampled soils tend to be less plastic with depth. Additionally, the fines content and clay content tend to decrease with depth. These trends are consistent with the geology of the site as neither the Heiden clay or Altoga loam are expected to have a high percentage of fines.

As a reference, optimum density and moisture content (in relation to those determined from compaction curves defined using Standard Proctor compaction energy) were estimated for each soil using correlations from NAVFAC DM-2 (1962). This estimation was used as the method has previously been shown to correlate well to experimental results from soils in Central Texas (Snyder, 2015). A "dry" condition adopted as that corresponding to three percentage points dry of the optimum gravimetric moisture condition at the maximum dry unit weight. This condition was predicted for each of the sampled soil deposits and used as the target compaction conditions for the soil samples used in centrifuge swelling tests. The optimum conditions and volumetric moisture contents at the dry condition for centrifuge tests are listed in Table 6.3.

Table 6.3: Estimated optimum compaction conditions and initial volumetric moisture content for centrifuge-based swelling tests

Sample	ω_{opt}	$p_{d,max}$ (g/cm^3)	θ_i
Original Sampling	23.7%	1.51	0.313
Depth: 0 - 2 ft	23.2%	1.42	0.286
Depth: 2 - 3 ft	23.3%	1.41	0.285
Depth: 3 - 4 ft	20.0%	1.52	0.259
Depth: 4 - 5.5 ft	16.4%	1.65	0.221

In order to determine the swelling potential of the deposit, the centrifuge-based swelling test was used to define the swelling characteristics of the sampled soils. Centrifuge swelling tests were conducted at various effective stresses to determine the stress-swell curve for each sampled soil. The vertical strain at the end of primary swelling from the centrifuge swelling tests and fitted stress-swell curves are shown in Figure 6.5 for each of the sampled soils.

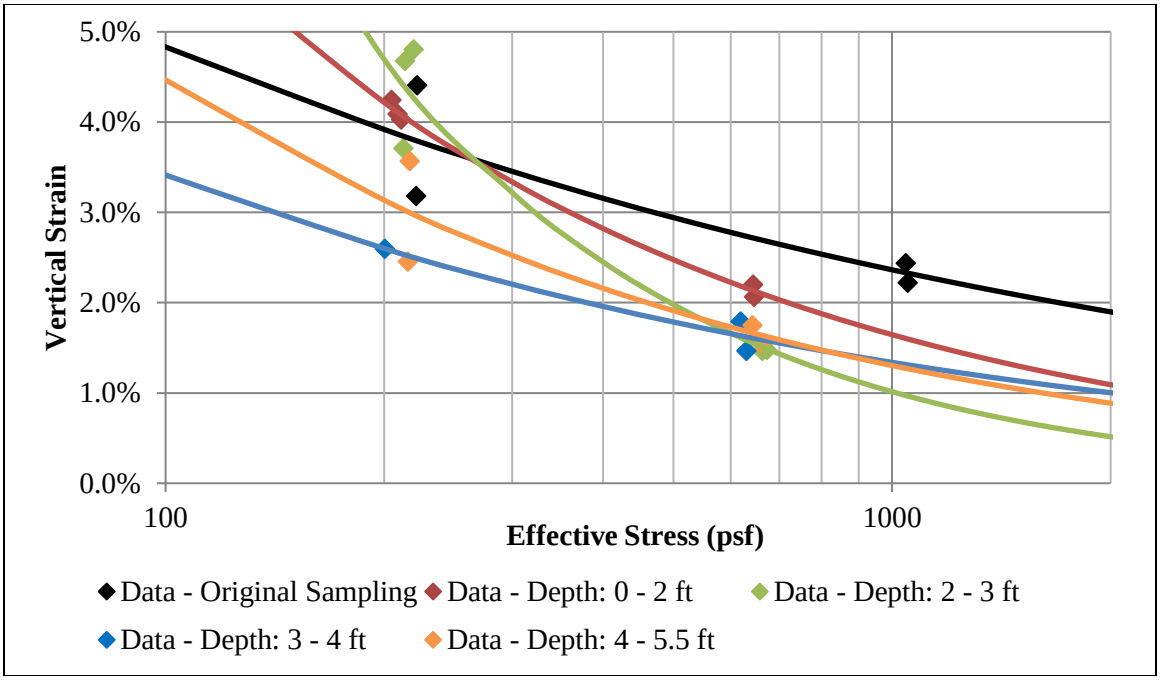

Figure 6.5: Stress-swell curves for soils sampled at the Taylor Maintenance Office (tests conducted using a "dry" condition)

Overall, the soil deposit was found to be moderately expansive. The swelling potential decreases with depth, which is consistent with the results from the geotechnical characterization. The decreased swelling was primarily observed at low overburden stresses, which are typical in the active zone. A potential vertical rise can be calculated based on the method outlined in Zornberg et al. (2017). The potential vertical rise at this site was predicted to be 2.1 in (5.28 cm) using the fitted stress-swell curves shown in Figure 6.5.

6.3.3 Unsaturated Behavior of Sampled Soils

To understand the unsaturated behavior of the soils sampled, the total and matric suction values were measured at various volumetric moisture contents. The processed soils were re-hydrated at varying initial gravimetric moisture contents and compacted at

the maximum dry density from Table 6.2. Total and matric suction values were measured using filter paper tests run according to ASTM D5298. The filter papers for testing were weighed approximately three weeks after compaction to allow for hydraulic equilibrium. Total suction values were additionally measured using a chilled mirror hygrometer. The chilled mirror hygrometer system measures the relative humidity above a soil specimen in an enclosed system by measuring the dew that forms on a mirror using an optical sensor. Vapor equilibrium is achieved by using a fan to circulate air in the chamber, and the total suction can be measured using the dew point and soil temperature. Mantri and Bulut (2014) indicated that soils with high osmotic suction may have inaccurate total suction measurements. Due to this potential error, the results from filter paper tests were additionally used to verify that the osmotic component of the suction was not significant.

The compaction methods between the filter paper and chilled mirror hygrometer methods differed. The specimens for the filter paper testing were compacted using static compaction in a 7 cm diameter compaction mold to a 2.5 cm height. The specimens for the chilled mirror hygrometer tests were compacted using kneading compaction to a total volume of approximately 7 mL. The different methods for compaction may affect the comparison of the suction measurements based on the findings from Attom et al. (2001).

Suction measurements were used to fit soil-water retention curves to the data. The van Genuchten model (1980), defined in Equation 2.2, was used for curve fitting. The fitted parameters include the θ_s (saturated volumetric moisture content), θ_r (residual volumetric moisture content), α, m and n. The residual volumetric moisture content was assumed to be zero. Parameter m was estimated using Equation 2.3. The curves were fit using the data solver in Excel to minimize the sum of root-mean-square error for the data points. A more extensive overview of the curve fitting method is found in Section 2.3.

Filter paper tests were conducted on the sampled soil at the various depths. Three soils specimens were compacted at different targeted volumetric moisture contents. The compaction conditions varied the initial gravimetric moisture content with a constant initial targeted dry density. The data from the filter paper tests and fitted soil-water retention curves are shown in Figure 6.6 in terms of the matric suction and in Figure 6.7 in terms of the total suction.

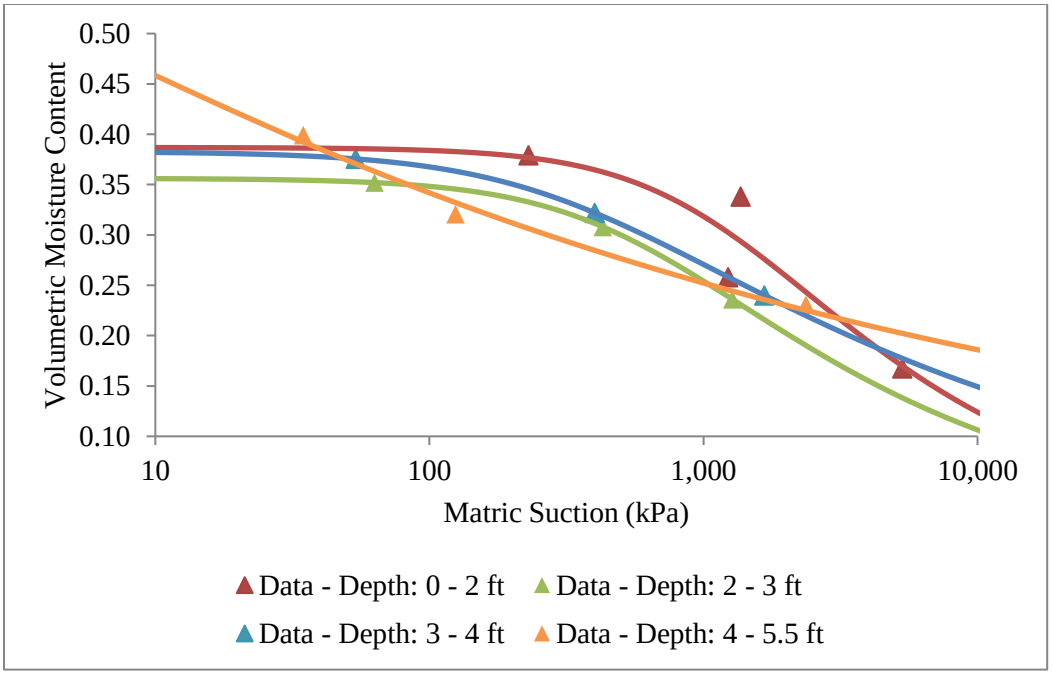

Figure 6.6: Soil-water retention curves for matric suction using filter paper measurements for soils sampled from Taylor Maintenance Office

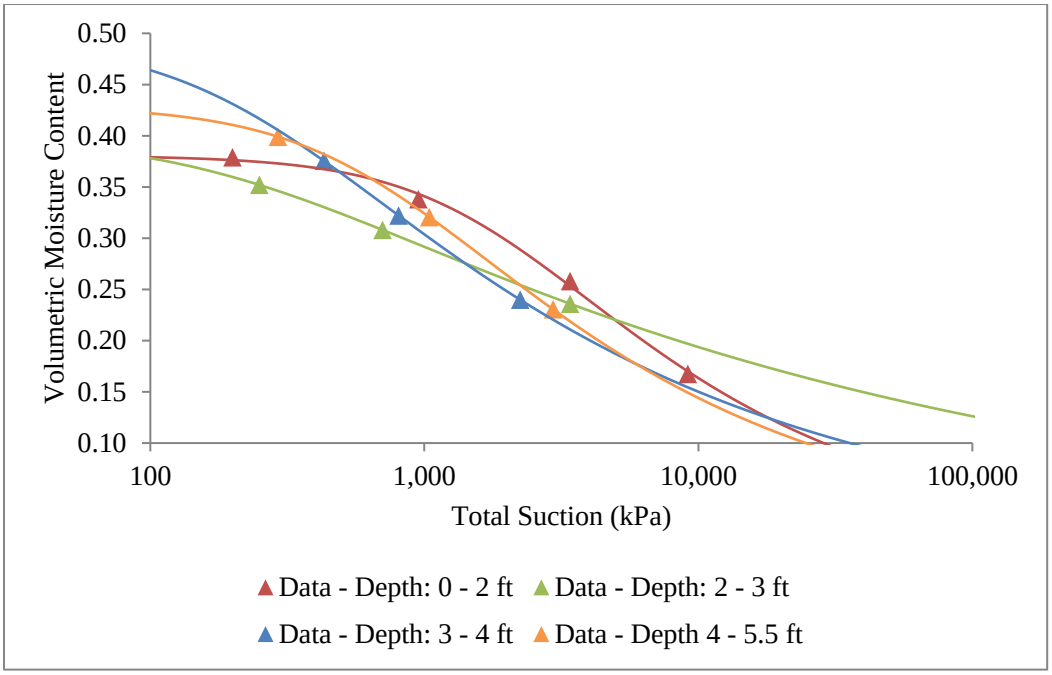

Figure 6.7: Soil-water retention curves for total suction using filter paper measurements for sampled soils

The soil sampled from the upper 2 ft of the deposit tends to have a higher matric suction value at the same volumetric moisture content than the soils sampled at deeper depths. Overall, the soil specimens sampled from the upper 4 ft of the deposit have similar soil-water retention curves defined using matric suction. The soil specimens sampled from depths ranging from 4 to 5.5 ft have similar total suction values to the rest of the deposit but differ for the matric suction measurements. For the soil-water retention curves defined using total suction, the curves are similar throughout the soil deposit.

Total suction values were measured using the chilled mirror hygrometer, which gages the relative humidity above a specimen at equilibrium to determine the suction in the specimen. Again, specimens were compacted at varying initial gravimetric moisture contents with a constant initial dry density. The benefit of the chilled mirror hygrometer tests is the duration of testing is comparatively shorter than the filter paper test. For the

chilled mirror hygrometer tests, the total suction for a soil specimen is measured in approximately 30 minutes to an hour. For the filter paper tests, the total suction for a soil specimen is measured in approximately 7 to 14 days. The total suction measurements from the chilled mirror hygrometer and fitted soil-water retention curves are shown in Figure 6.8 for each of the sampled soils. The last measurement for the soil sampled from depths ranging from 0 to 2 ft was not used for curve fitting.

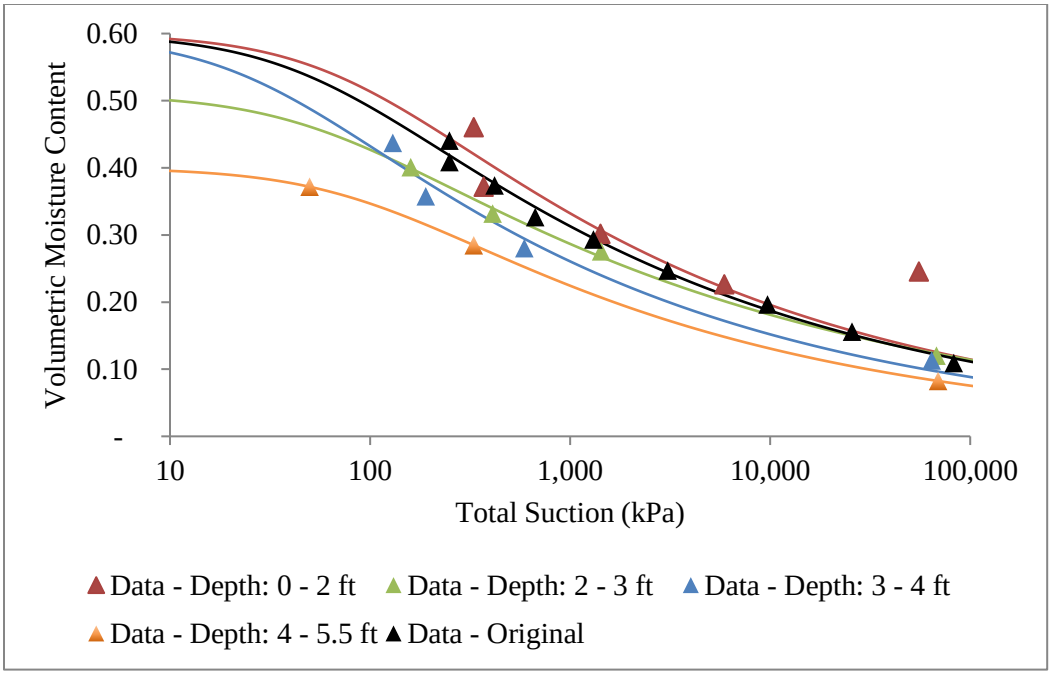

Figure 6.8: Soil-water retention curves using results from chilled mirror hygrometer measurements for sampled soils

Results from the chilled mirror hygrometer testing indicate that soils at depth tend to have a lower total suction at the same initial volumetric moisture content than soils closer to the ground surface. The trend can be observed for the soil sampled between depths ranging from 4 to 5.5 ft at a total suction less than 1,000 kPa. Additionally, the soils tend to come to a similar total suction near the air-dried residual gravimetric moisture content.

The soil sampled in the 2014 soil sampling campaign behaves similarly to the specimens from the upper 2 ft of the deposit. Since the location of sampling differed between the first and second sampling of the site, the assumption that the site is relatively homogenous is validated.

The results from the chilled mirror hygrometer and filter paper tests were compared in order to analyze the consistency of the results obtained using these two methods. The soil-water retention curves were obtained using both total and matric suction measurements from the filter paper tests and only total suction measurement from the chilled mirror hygrometer. These soil-water retention curves from each method were compared in order to evaluate the consistencies of the fitted curves. A comparison between the total suction soil-water retention curves generated using filter paper tests and chilled mirror hygrometer measurements are shown in Figure 6.9 for soils sampled at depths ranging from 0 to 2 ft, in Figure 6.10 for soils sampled at depths ranging from 2 to 3 ft, in Figure 6.11 for soils sampled at depths ranging from 3 to 4 ft, and in Figure 6.12 for soils sampled at depths ranging from 4 to 5.5 ft.

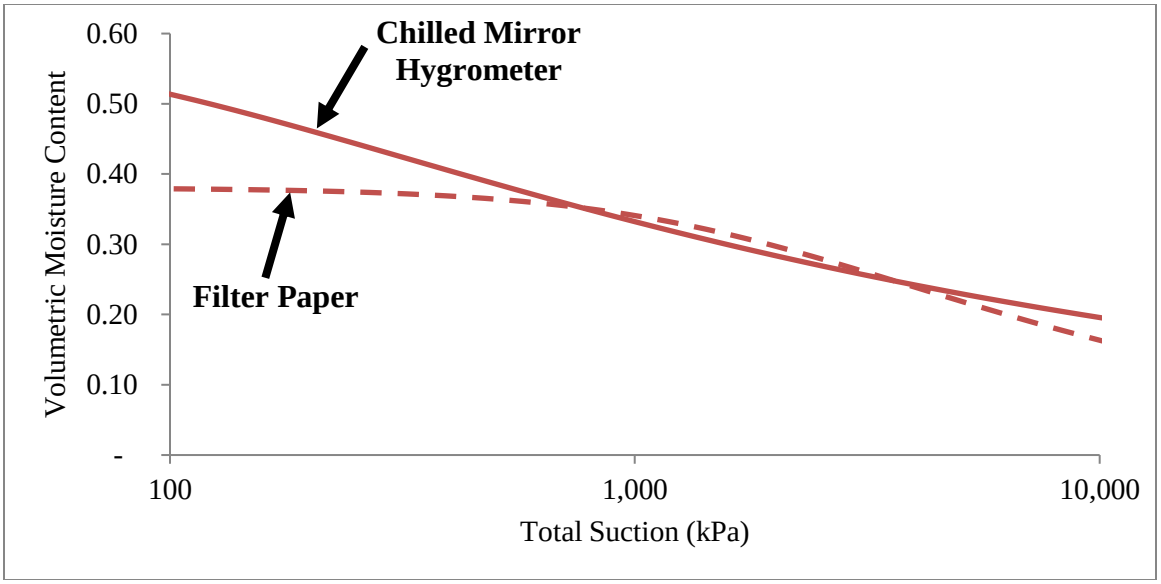

Figure 6.9: Comparison of soil-water retention curves defined using chilled mirror hygrometer or filter paper total suction measurements for soils sampled from a depth of 0 to 2 ft at the Taylor Maintenance Office

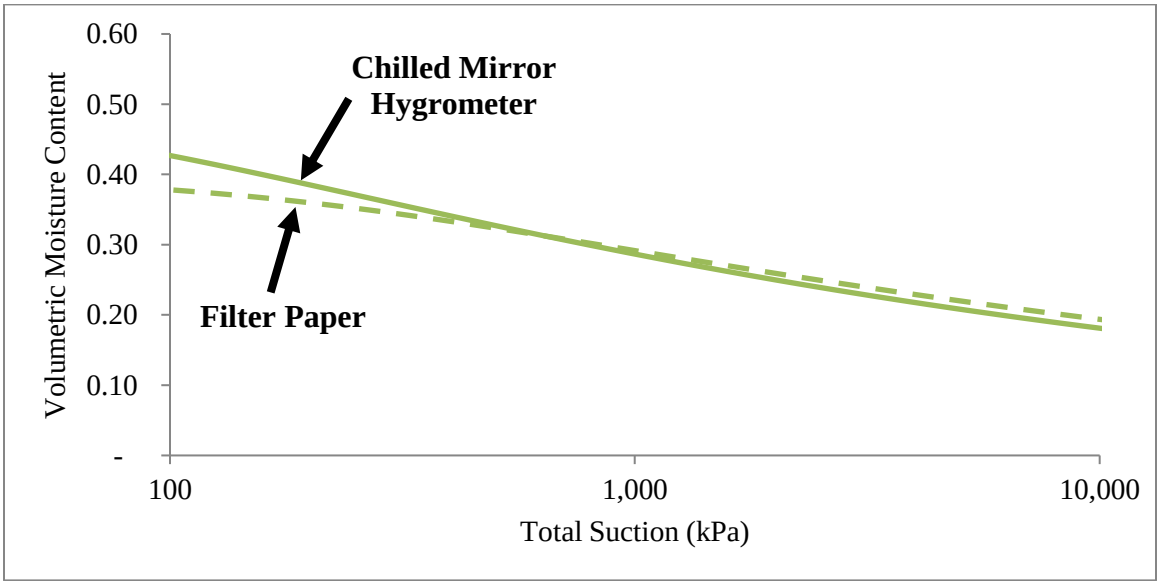

Figure 6.10: Comparison of soil-water retention curves defined using chilled mirror hygrometer or filter paper total suction measurements for soils sampled from a depth of 2 to 3 ft at the Taylor Maintenance Office

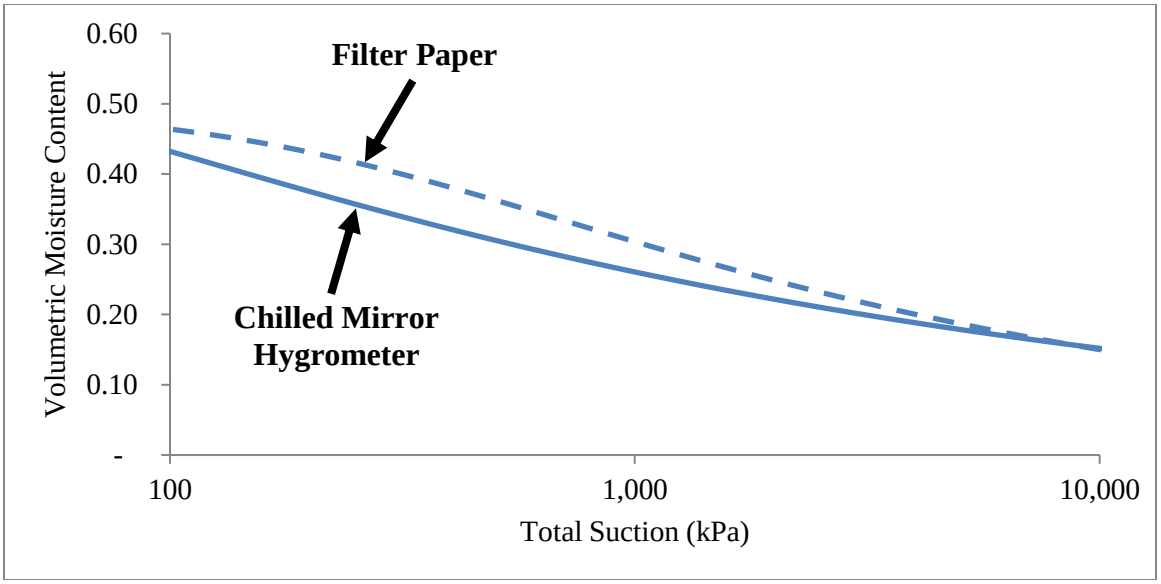

Figure 6.11: Comparison of soil-water retention curves defined using chilled mirror hygrometer or filter paper total suction measurements for soils sampled from a depth of 3 to 4 ft at the Taylor Maintenance Office

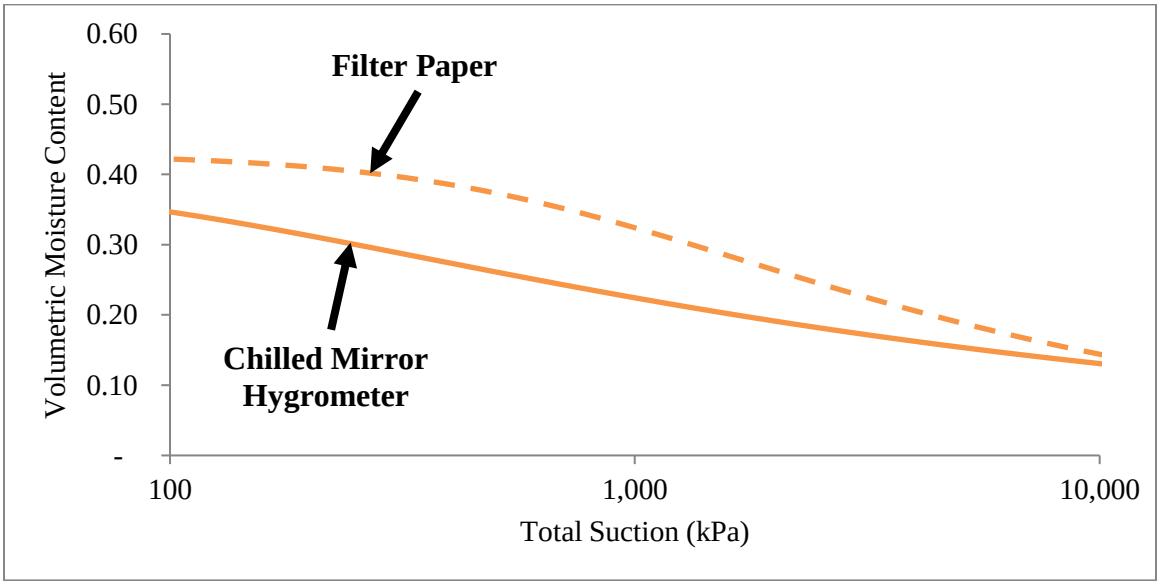

Figure 6.12: Comparison of soil-water retention curves defined using chilled mirror hygrometer or filter paper total suction measurements for soils sampled from depths ranging from 4 to 5.5 ft at the Taylor Maintenance Office

There are several differences between the soil-water retention curves generated from each methodology. Below a total suction of 1,000 kPa, the soil-water retention curves only show a fair agreement. Also, the air-entry pressures differed between the curves generated by the two tests. Beyond 1,000 kPa, the soil-water retention curves compared well for soils sampled near the ground surface (Figure 6.9 and Figure 6.10) but show some discrepancies for the soils sampled at depth (Figure 6.11 and Figure 6.12). Due to the similarity of the curves for shallower soils in the active zone, the chilled mirror hygrometer test is preferred due to the shorter time of testing.

The comparison between the matric suction soil-water retention curves from the filter paper tests and the total suction soil-water retention curves from the chilled mirror hygrometer are shown in Figure 6.13 for soils sampled at depths ranging from 0 to 2 ft, Figure 6.14 for soils sampled at depths ranging from 2 to 3 ft, Figure 6.15 for soils sampled at depths ranging from 3 to 4 ft, and Figure 6.16 for soils sampled depths ranging from 4 to 5.5 ft. This comparison was conducted in order to evaluate whether the soil-water retention curves defined using matric suction measurements showed similar trends to those of curves defined using total suction measurements from the chilled mirror hygrometer. If these curves followed similar trends, the chilled mirror hygrometer method could be used in evaluations that only require the slope of the soil-water retention curve (e.g. to evaluate differences between soil specimens at differing compaction conditions).

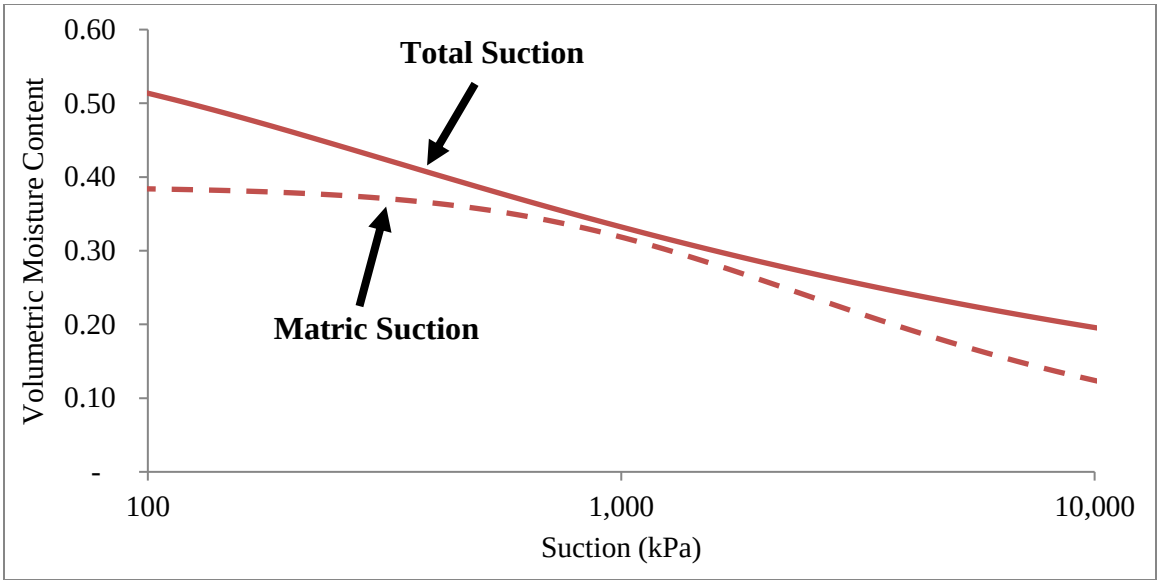

Figure 6.13: Soil-water retention curves defined using chilled mirror hygrometer total suction measurements or filter paper matric suction measurements for soils sampled from depths ranging from 0 to 2 ft at the Taylor Maintenance Office

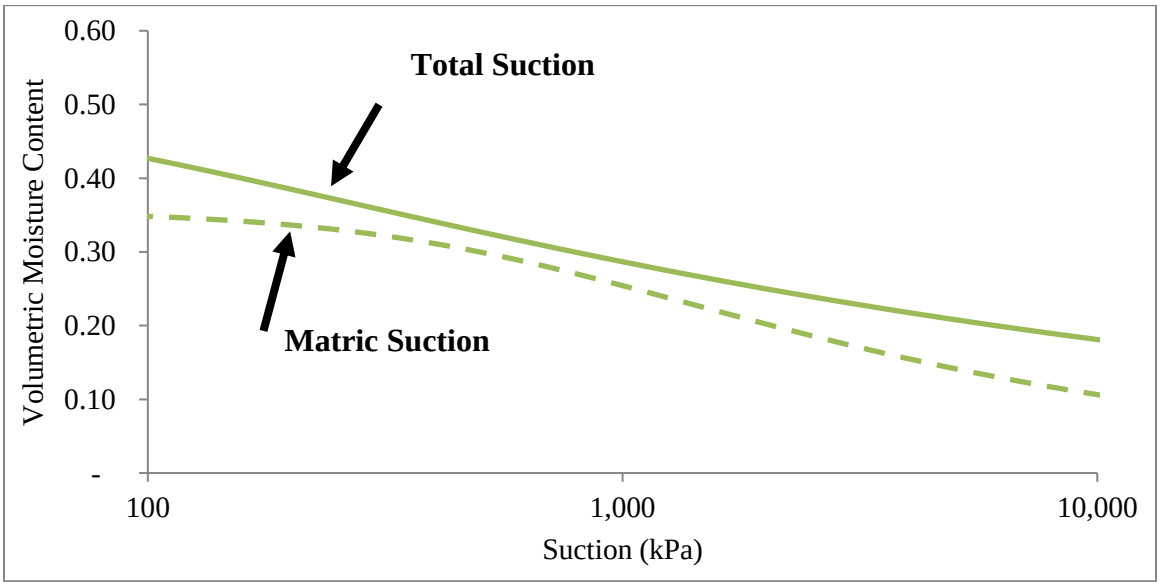

Figure 6.14: Soil-water retention curves defined using chilled mirror hygrometer total suction measurements or filter paper matric suction measurements for soils sampled from depths ranging from 2 to 3 ft at the Taylor Maintenance Office

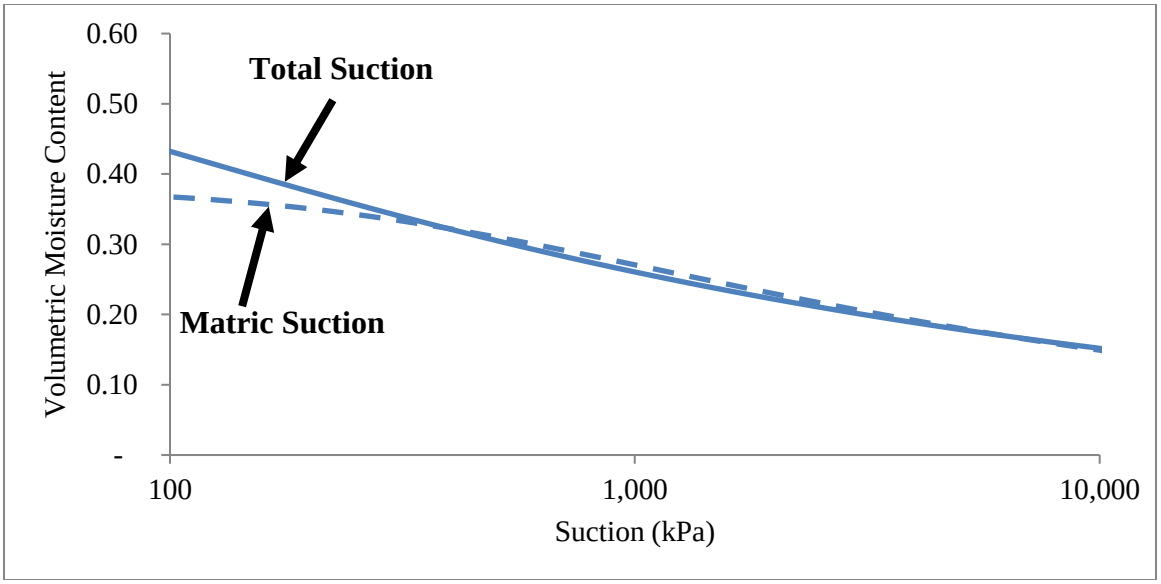

Figure 6.15: Soil-water retention curves defined using chilled mirror hygrometer total suction measurements or filter paper matric suction measurements for soils sampled from depths ranging from 3 to 4 ft at the Taylor Maintenance Office

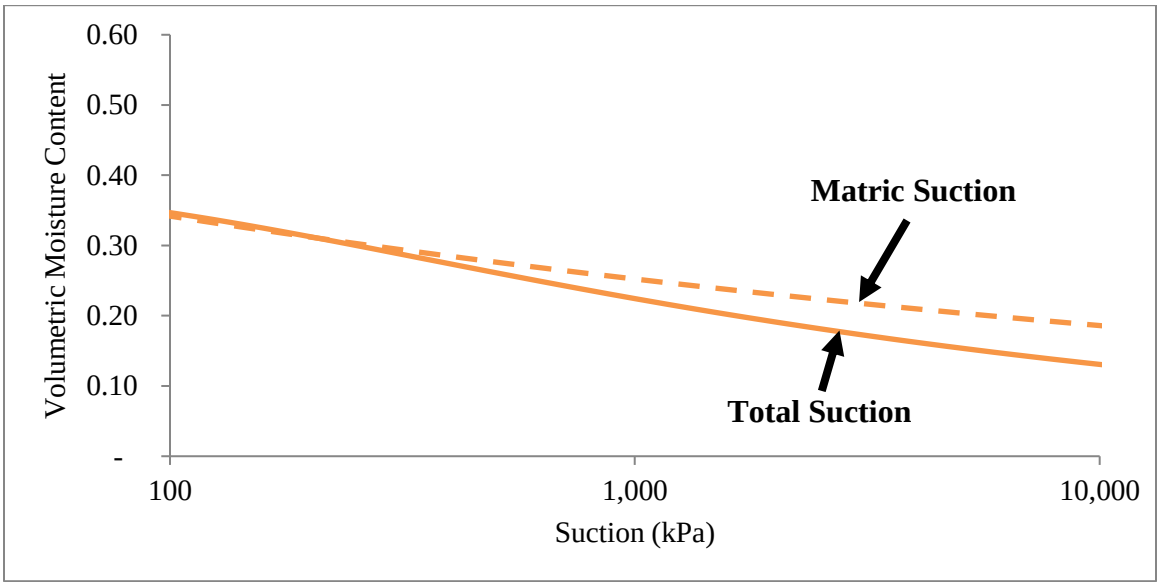

Figure 6.16: Soil-water retention curves defined using chilled mirror hygrometer total suction measurements or filter paper matric suction measurements for soils sampled from depths ranging from 4 to 5.5 ft at the Taylor Maintenance Office

In general, the soil-water retention curves defined using total suction measurements from the chilled mirror hygrometer test exceeds curves defined using matric suction measurements from the filter paper tests. The exception is the curves defined for the sampled soil at depths ranging from 4 to 5.5 ft in Figure 6.16 where the soil-water retention curve defined using matric suction measurements exceeds the curve defined using total suction measurements. This difference can be attributed to the relative lack of total suction measurements using the chilled mirror hygrometer at higher total suctions, with only one measurement above a total suction of 350 kPa (Figure 6.8). Additionally, below the air-entry pressure for the matric suction defined curves, the soil-water retention curves differed significantly. Beyond the air-entry pressures from the matric suction filter paper tests, the slopes of the soil-water retention curves were similar, with only some differences observed for the soils sampled at depths ranging from 0 to 2 ft and 4 to 5.5 ft. In general, the soil-water retention curves defined using chilled mirror hygrometer methods can be used to estimate the matric suction trends for initial soil conditions at suctions higher than the air-entry pressure.

Since both the matric and total suction were measured, the osmotic suction of the soil can be calculated. The osmotic suction, π, can be calculated as follows:

$$\pi = \psi - (u_a - u_w) \tag{6.1}$$

Where ψ is the total suction, and $(u_a - u_w)$ is the matric suction (Fredlund and Rahardjo, 1993). The osmotic suction can be defined using the total suction measured either from the chilled mirror hygrometer test or the filter paper test. The osmotic suction defined using the total suction measured the chilled mirror hygrometer is shown in Figure 6.17. The osmotic suction defined using the total suction measured the filter paper test is shown in Figure 6.18.

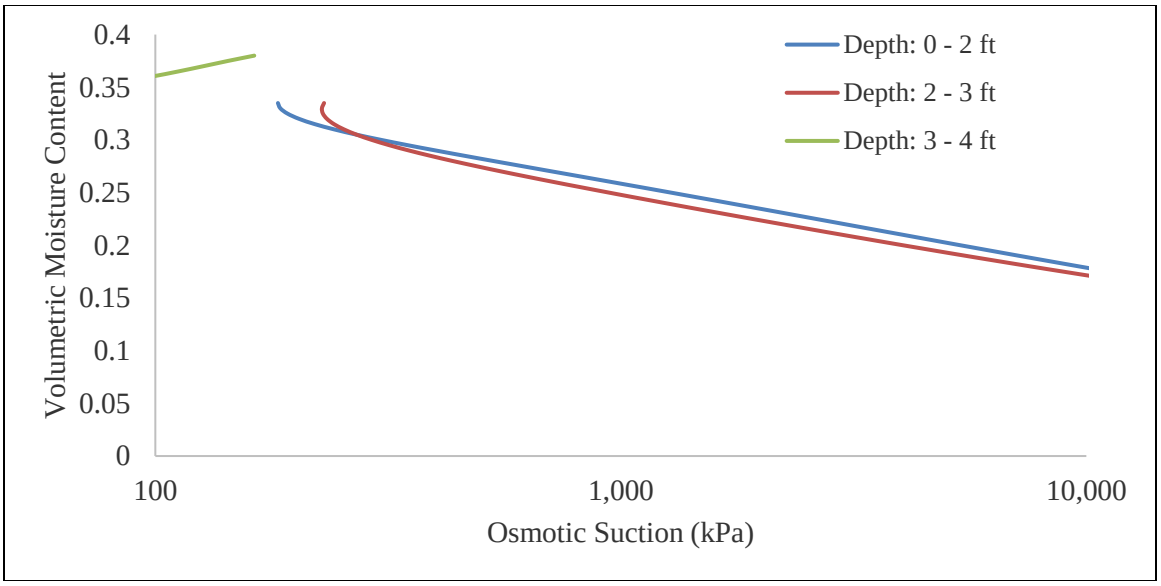

Figure 6.17: Osmotic suction for soils sampled at depth using chilled mirror hygrometer total suction measurements

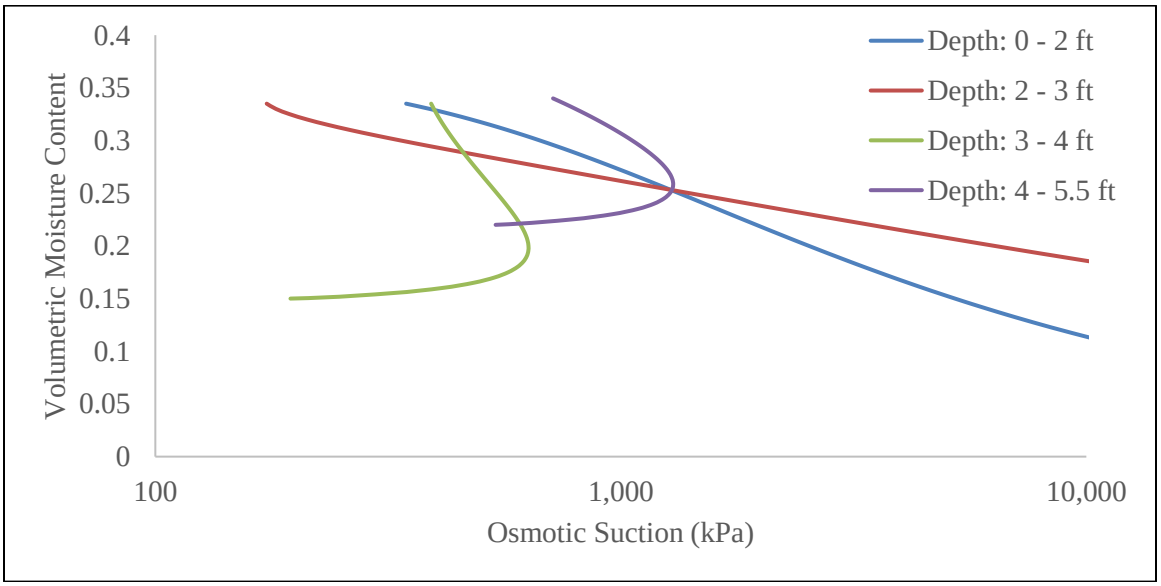

Figure 6.18: Osmotic suction for soils sampled at depth using filter paper total suction measurements

The osmotic suction tends to increase with decreasing volumetric moisture content for soils sampled at depths ranging from 0 to 2 ft and 2 to 3 ft for both methodologies. However, the osmotic suction behavior differs between the two methodologies for the soils sampled at deeper depths. The osmotic suction defined using chilled mirror hygrometer measurements remains relatively constant. The osmotic suction defined using chilled mirror hygrometer measurements was not measured for soils sampled at depths ranging from 4 to 5.5 ft due to the matric suction exceeding the total suction at the same volumetric moisture content as previously shown in Figure 6.16. The osmotic suctions defined using filter paper total suction measurements are relatively constant for soils sampled at depths ranging from 3 to 4 ft and 4 to 5.5 ft. From the previous geotechnical characterization, the soils sampled at depths ranging from 3 to 4 ft and 4 to 5.5 ft tend to be less plastic with a lower percentage of clay minerals than the soils sampled closer to the ground surface (Table 6.2). These soils can be assumed to have a constant osmotic suction, which for the soils evaluated in this study was approximately 800 kPa and 1,000 kPa for soils sampled at depths ranging from 3 to 4 ft and 4 to 5.5 ft, respectively. However, for the more plastic clays closer to the ground surface, a constant osmotic suction may not be a valid assumption.

6.4 LARGE COLUMN TESTING

A large column test was conducted in order to evaluate expansive soil behavior. The large column test was prepared in order to replicate a field deposit that was thoroughly sampled. The main objective for the study was to the accuracy of the centrifuge-based inundation tests used to predict heave in expansive soil deposits. The assembly and preparation of the large column is outlined in Section 6.4.1. Section 6.4.2

analyzes the moisture time history during an infiltration test. Section 6.4.3 determines the vertical displacements during the infiltration test using image analysis techniques.

6.4.1 Assembly of Large Column Test

The laboratory soil column was compacted in an acrylic tube based on soil preparation approaches followed by Lima et al. (2015) and Azevedo (2016). The acrylic tube had a height of 122.5 cm and an inner diameter of 19.4 cm. Bulk soil samples for the large column test were collected using a 10 in. auger to a depth of 5.5 ft from an expansive soil deposit. The sampled soils were grouped into five layers and characterized for their geotechnical properties. A summary of these geotechnical properties is provided in Table 6.2.

The large soil column was grouped into five layers listed in Table 6.4. Each soil layer was defined by the soil used for compaction. The first layer was compacted using the soil sampled during the 2014 soil sampling campaign. The remaining soil layers were compacted using the sampled soil from the 2016 soil sampling campaign. The second layer was compacted using the soil sampled during the 2016 soil sampling campaign at depths ranging from 0 to 2 ft from the field site. The third layer was compacted using the soil sampled at depths ranging from 2 to 3 ft from the field site. The fourth layer was compacted using the soil sampled at depths ranging from 3 to 4 ft from the field site. The fifth layer was compacted using the soil sampled at depths ranging from 4 to 5.5 ft from the field site. The soil sampled during the 2014 soil sampling campaign was placed in order to increase the total height of the soil column. This soil was considered suitable for use based on the consistency in soil properties, stress-swell curves, and soil-water retention curves with the sampled soil at depths ranging from 0 to 2 ft from the 2016 soil sampling campaign (Section 6.3).

Each soil layer was 24 cm tall and compacted in 4 cm lifts. A drop-hammer was used to compact each lift to the specified height. Each soil layer was instrumented with 5TE sensors to monitor the volumetric moisture content fluctuations. Additionally, three soil layers, 1, 3, and 5, were instrumented with MPS-2 matric suction sensors. A summary of the compaction conditions of the large soil column is provided in Table 6.4. The table includes the initial volumetric moisture content (θ_i) calculated using the initial gravimetric moisture content (ω_i) and dry unit weight ($\gamma_{d,i}$). The mass of soil prepared for the large soil column is also provided in the table.

Table 6.4: Overview of targeted initial soil conditions for large column test

Layer	Soil	ω_i (%)	$\gamma_{d,i}$ (kN/m^3)	θ_i	Soil Mass (g)
1	Taylor-Original	22.1%	11.17	0.252	13,220
2	Taylor-1	22.0%	11.17	0.250	11,030
3	Taylor-2	21.9%	11.05	0.247	10,000
4	Taylor-3	20.0%	11.98	0.244	10,730
5	Taylor-4	15.6%	13.00	0.207	11,500

The compaction conditions were selected to target the “dry” moisture condition from the centrifuge swelling test. This “dry” condition corresponds to a gravimetric moisture content that is three percentage points dry of the optimum moisture content estimated from NAVFAC (1962) correlations. A relative compaction of 80% was targeted, as higher degrees of compaction would not be able to be reached due to limitations of the compaction hammer. The soil was compacted within a latex membrane with a printed grid in order to measure the vertical displacement during the infiltration test with image analysis techniques. However, the latex membrane was in direct contact with the acrylic tube as talc powder was found to obscure the printed grid. Since the latex was in direct contact with the acrylic tube, friction may have developed between the two surfaces that reduced the magnitude of heave in the soil column. The potential effect of this side

friction is evaluated in Section 6.4.3. A view of the column during compaction is shown in Figure 6.19.

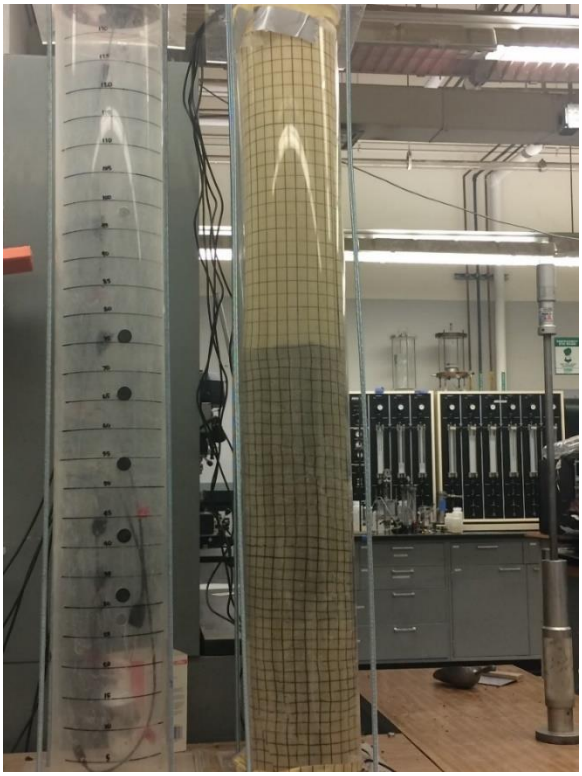

Figure 6.19: View of large soil column during compaction

In order to improve the prediction of the potential vertical rise using test results from the centrifuge-based swelling test, the stress-swell curves were corrected due to the lower dry unit weight and slight differences in the initial gravimetric moisture content. The relative compaction of each lift is shown in Figure 6.20. Additionally, the weighted average relative compaction used for the correction of the stress-swell curves is indicated by the red line in each soil layer in Figure 6.20. The average relative compaction of the soil layers ranged from 74 and 81% in the soil column. In general, the relative compaction was lower at depth due to limitations with the compaction hammer.

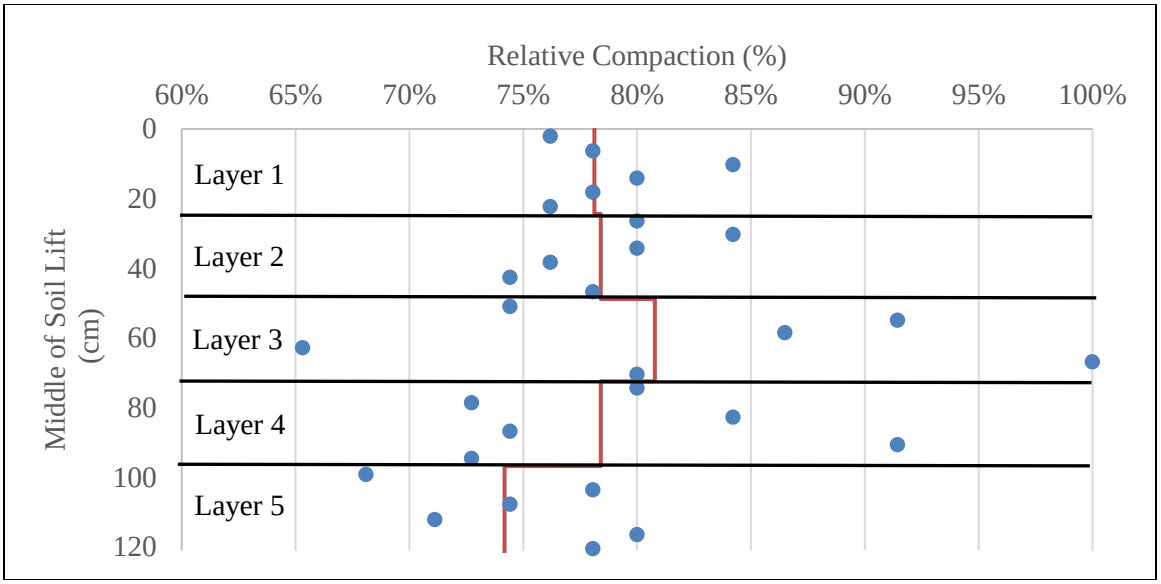

Figure 6.20: Calculated relative compaction for each soil lift in large column

The correction for the different initial conditions was determined using the results from Section 2.3.3. Results from the Branyon clay were used to generate the correction as the soil was collected from a similar geographic region and derives from similar parent material as soil from the Taylor Maintenance Office. Details on the method to adjust the potential vertical rise is presented in Section 7.3.2. The potential vertical rise that accounts for the lower dry unit weight was determined to be 0.74 mm compared to the 5.28 cm using the centrifuge results. Therefore, the lower dry unit weight was expected to significantly affect the heave in the large column.

6.4.2 Analysis of Moisture Time Histories during Infiltration Test

After compaction, the soil was covered for three weeks in order to reach moisture equilibrium among the soil layers. The upper surface of the soil column was sealed from the environment using the latex membrane. The volumetric moisture content did not vary significantly during this time frame. Additionally, a change in the vertical displacements at the surface of the soil column was not observed. However, the matric suction sensors

came into thermodynamic equilibrium with the surrounding soil mass during this time period. The initial matric suction was determined in order to later evaluate the initial conditions of the soil column prior to the infiltration test. The change in matric suction prior to and during the infiltration test is shown in Figure 6.21.

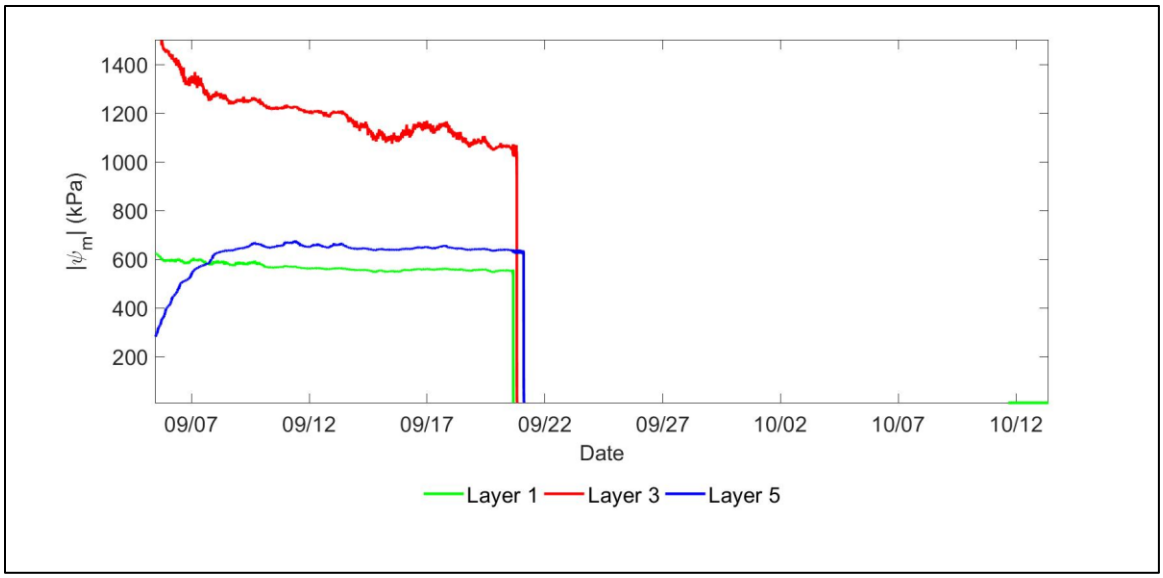

Figure 6.21: Matric suction time histories during compaction and infiltration test of large soil column

The matric suction sensors came into equilibrium with the surrounding soil, with good agreement overserved between the sensor closest to the surface (i.e. Layer 1) and the sensor at the base of deposit (i.e. Layer 5). The matric suction in these soil layers are relatively similar, consistent with the results from Section 6.3.3. However, the matric suction readings were not as stable in Layer 3. This instability in the readings was attributed to the poor soldering of the wires connected to the MPS-2 sensor prior to the soil column test. After moisture was applied to the column, the matric suction decreased

to the lower bound of the sensors range. The matric suction did not increase after the application of moisture.

Moisture was applied to the column by ponding approximately 4 cm of water at the top surface of the soil in the large column. Tap water was used for the infiltration to prevent geochemical changes in the soil pores. In order to continuously apply water to the column, a low-flow water pump was used to apply a constant supply of water. However, the maximum applied flow rate was not able to provide a volume of water that would allow for ponding on the surface of the soil column due to the high flow rate. Water was re-applied when the 4 cm head of water was depleted. There was a period during the overnight portion of the test where water was not re-applied to the column. This discrepancy was caused by the higher than expected flow rate of water through the soil column.

The volumetric moisture content fluctuations were monitored by capacitance sensors placed at the middle of each soil layer. The volumetric moisture content time histories during the infiltration test are shown in Figure 6.22.

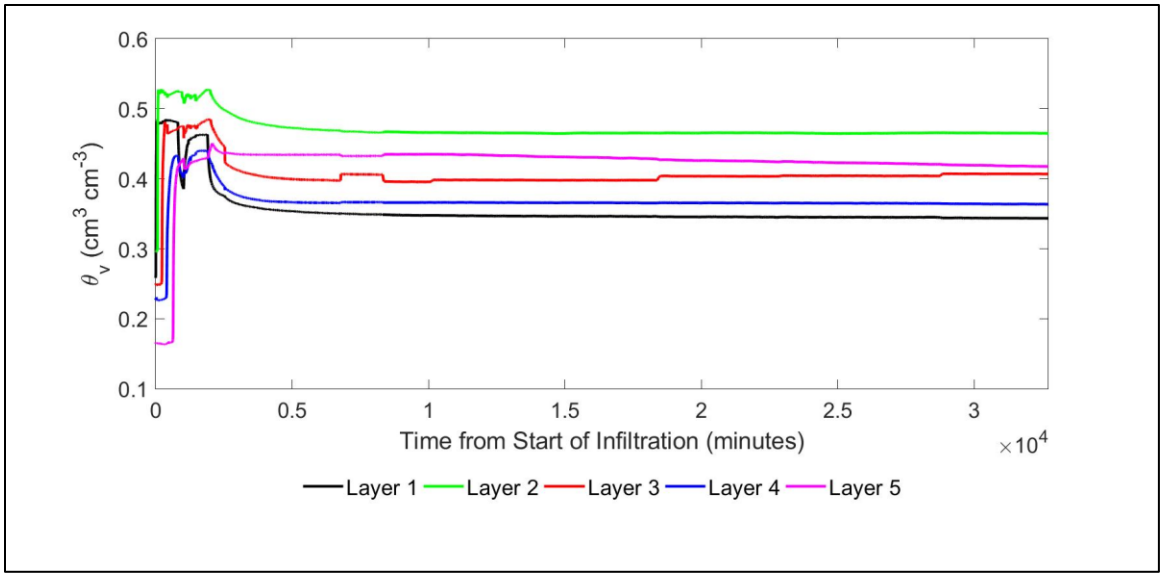

Figure 6.22: Volumetric moisture content time histories versus duration of infiltration for the large column test

The moisture content time histories indicate that the initial moisture front permeated the soil column within approximately 700 minutes. This time frame is longer than the time for moisture to infiltrate the field soil deposit in Chapter 5 (Section 5.4.1). The difference in these time frames can be assumed to be caused to the drying of the soil deposit in the field. Cracks in the expansive soil will occur during the drying of the field soil deposit. These cracks can form interconnect macro-voids that can significantly increase the infiltration of moisture into the deposit. For the large column test, these interconnected macro-voids were not assumed to be as significant due to compaction and a lack of a drying cycle prior to the infiltration test. However, the time frame for moisture to permeate through the column was significantly shorter than the expected time frame based on the saturated hydraulic conductivity of the soils. The difference between the actual and expected time frame to permeate the column can be assumed to be caused by

the low relative compaction and a high hydraulic gradient due to the initial matric suction.

In order to further analyze the initial moisture front, volumetric moisture content time histories were evaluated using the readings from only the first day (Figure 6.23).

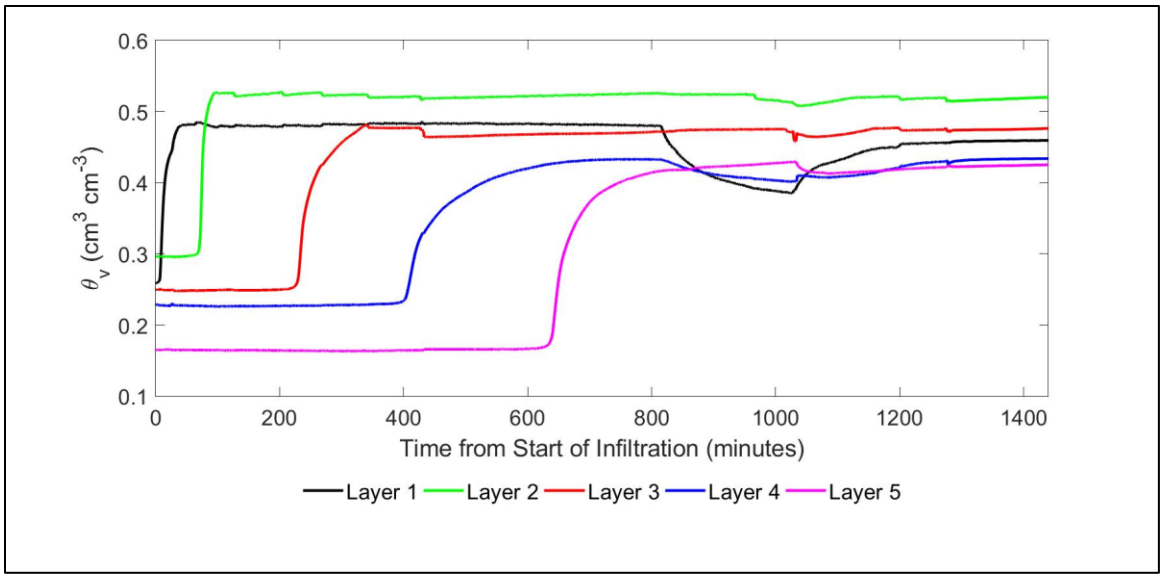

Figure 6.23: Volumetric moisture content time histories versus duration of infiltration during column test for the first day

Results from only the first day indicate that moisture front advanced over a longer time frame for the soil layers at depth. This increased time frame was attributed to a reduced flow rate due to less interconnected macro-voids at depth. In general, the time history of the moisture front was similar to the time history of the field site during a low intensity rainfall events, as shown in Section 5.4.1.

The degree of saturation was additionally used to analyze the data. The porosity of the soil layer was calculated based on compaction of the soil lifts within the volume of soil that the moisture content sensors measure. The calculated porosity at each of the

sensor locations is listed in Table 6.5. Using this porosity and Equation 5.2, the corresponding degree of saturation time histories were determined and are shown in Figure 6.24.

Table 6.5: Calculated porosity of soil layers for large column test

Soil Layer	$\gamma_{d,m}$ (kN/m^3)	Relative Compaction	Void Ratio	Porosity
1	10.91	78%	1.428	0.588
2	11.06	79%	1.394	0.582
3	11.13	81%	1.380	0.580
4	12.38	83%	1.140	0.533
5	11.93	73%	1.220	0.550

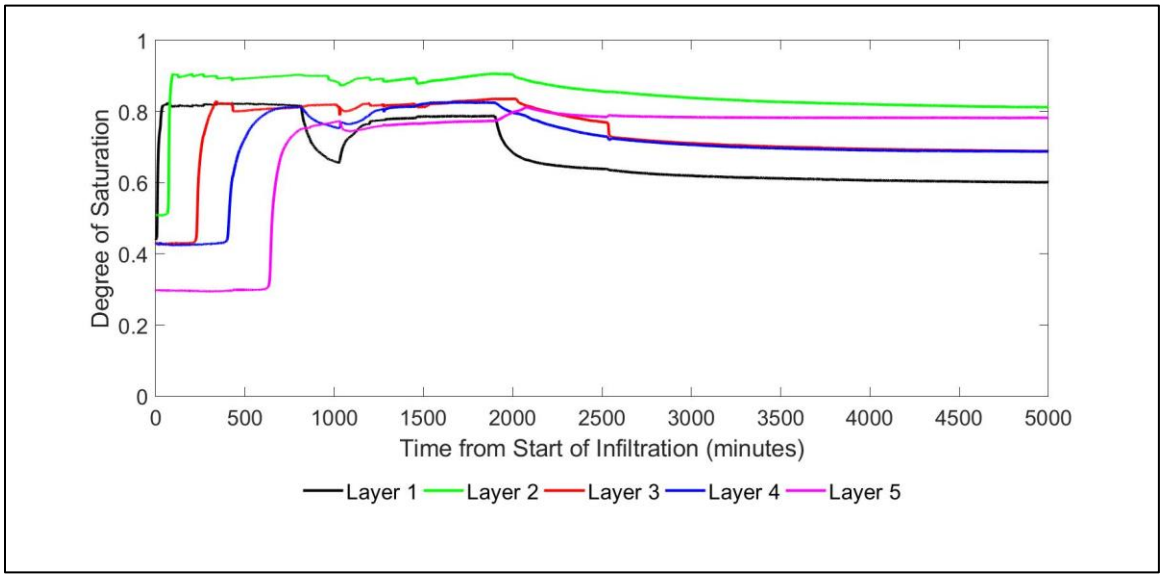

Figure 6.24: Degree of saturation time histories versus time of infiltration during large column test

The trends from the degree of saturation time histories are similar to the trends from the moisture content time histories. The degree of saturation increases in each progressive soil layer, with this increase in the degree of saturation occurring over a longer time

frame for the soil layers at depth. Unlike the estimated degree of saturation time histories from the field site in Chapter 5, the soil layers in the large column did not reach full saturation. This result was attributed to the assumptions used for to calculate the field degree of saturation (i.e. that the maximum volumetric moisture content can be used to estimate the porosity of the soil) not being valid.

In terms of the flow through the soil column, the cumulative outflow of moisture at the base of the column was measured using a tipping bucket. The calculated outflow rate in cm/s and the cumulative volume of water collected at the base of the soil column versus the time of testing are shown in Figure 6.25.

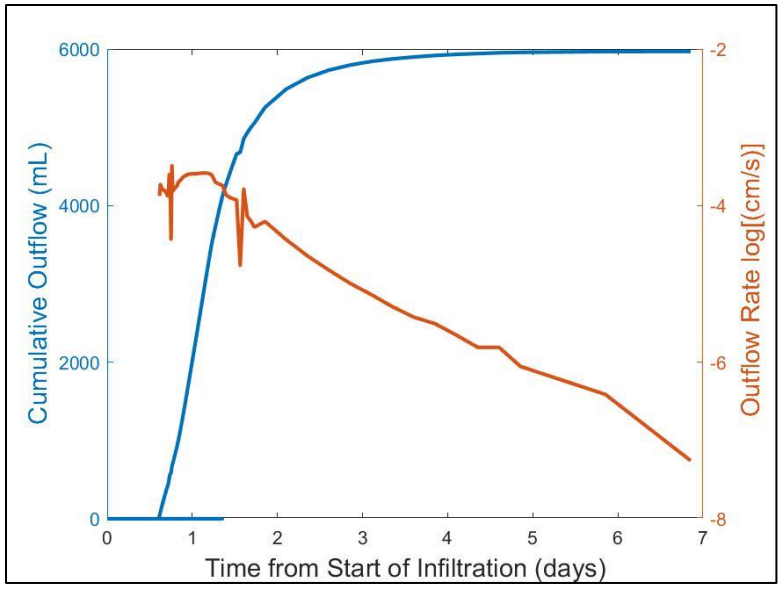

Figure 6.25: Outflow of water at base during large column test

The outflow rate during the test was approximately two orders of magnitude higher than the typical saturated hydraulic conductivity for expansive soils, which is estimated to range from 10^{-6} to 10^{-8} cm/s. The higher flow rate in the large column test can be attributed to dual-porosity system in the expansive soil. The infiltration of moisture is

assumed to advance through the macro-voids in the expansive soil more rapidly than the infiltration of moisture into the micro-voids and peds. Due to the low relative compaction of the large column, these macro-voids were assumed to be significant and increase the flow of water through the expansive soil layers. The head of water imposed above the soil column was removed after approximately 2,000 minutes due to the high flow rate of water through the soil column. After the removal of the head of water, the flow rate at the bottom of the soil column decreased significantly until the last measurement from the tipping bucket approximately seven days after the beginning of the test. The flow of moisture after the removal of water was assumed to be caused by the flow of moisture in the macro-voids due to the gravitational gradient.

The drying behavior of the laboratory soil column was also analyzed. This behavior was evaluated to compare difference in the drying of the large soil column and the drying of the subgrade in Section 5.4.1. The volumetric moisture content time histories during the first week of monitoring is shown in Figure 6.26. The first week of monitoring was evaluated as this time frame was typical for the drying of the field expansive soil deposit.

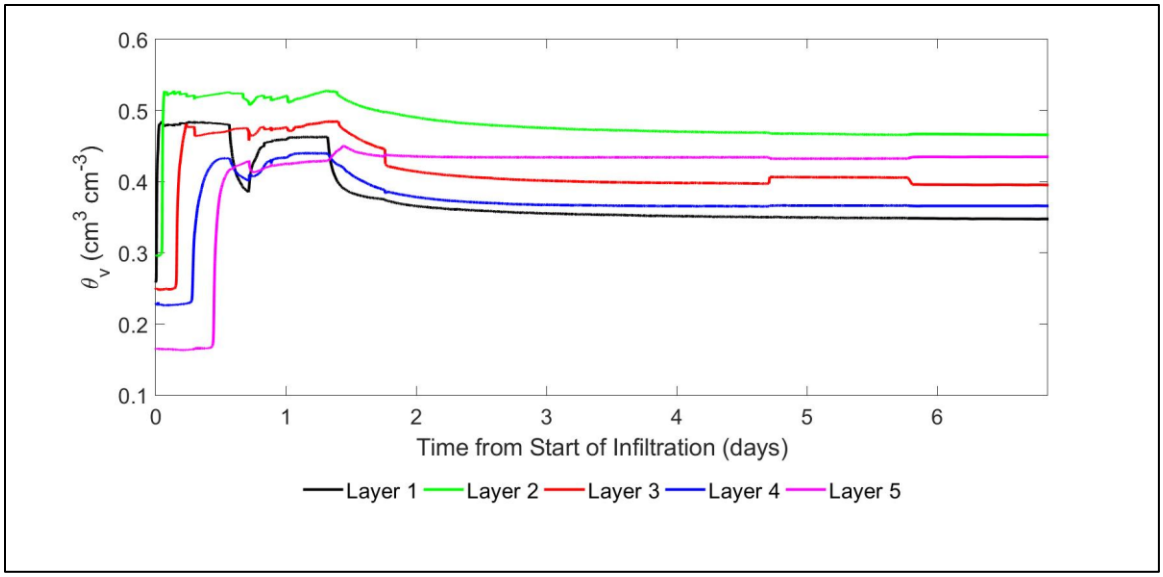

Figure 6.26: Volumetric moisture content time histories versus duration of infiltration during first week of large column test

The volumetric moisture content of the soil layers decreased shortly after the removal of water at 2,000 minutes (1.4 days). As the drying temperature can affect the swelling behavior of the soil, a drying lamp was not used to dry the large soil column (Basma et al., 1994). The drying of the large column occurred over a longer time frame than the drying of the field soil deposit. This increased time frame was attributed to the lack of radiative energy and wind increases the drying rate. The rapid decrease in moisture content was also observed in Layer 1 during the first night of testing. After a reapplication of water, the volumetric moisture content increased again but to a smaller volumetric moisture content. The decrease in the wetted volumetric moisture content was attributed to the macro-voids sealing during the infiltration of moisture.

6.4.3 Image Analysis of Vertical Displacements

An additional aspect of the large column was the use of image analysis techniques to track the vertical displacement of the soil column. A 2 cm by 2 cm square grid was

drawn on the outside of the membrane in order to track the deformation of the drawn grid. The grid itself was slightly deformed during compaction, thus the printed grid was not completely horizontal during testing. Two cameras were used to monitor the deformation at the top of the column and throughout the entire column. The higher resolution camera was used for the analysis of the full soil column. An example of both of the images taken during testing is shown in Figure 6.27.

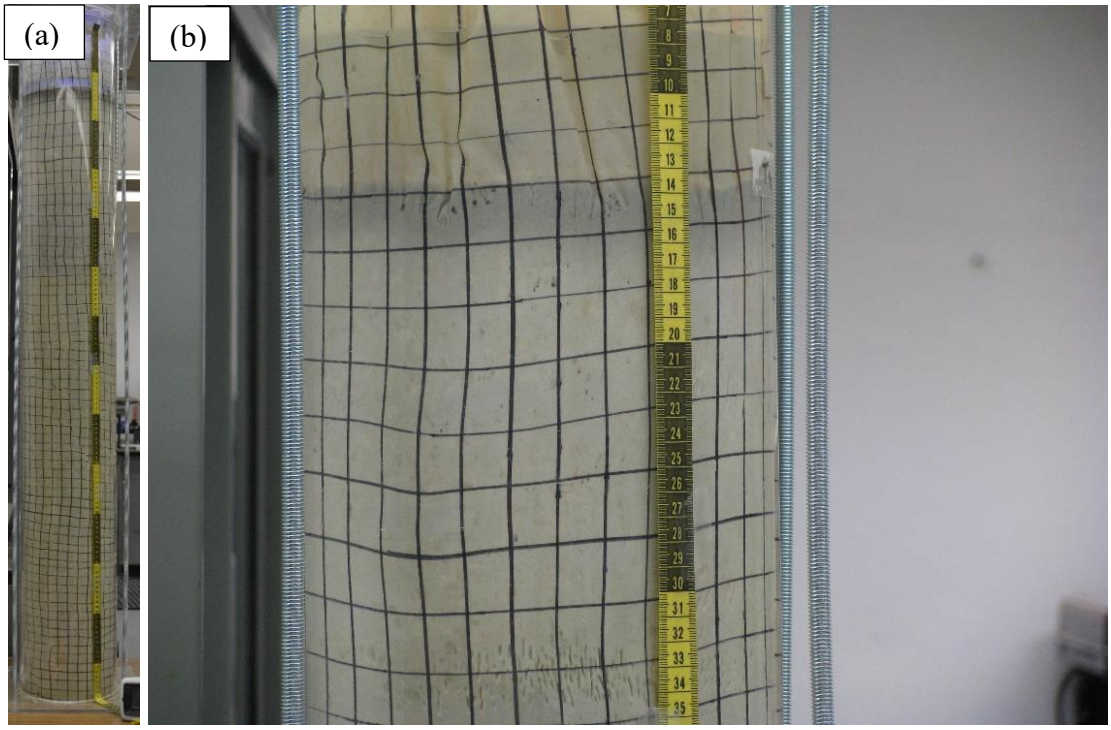

Figure 6.27: Example of images used for image tracking during large column test for (a) full column and (b) top of the column

Images of the full column were taken at a higher resolution than images of the top of the column. Approximately 40 pixels comprised 1 cm for the images of the full column, and approximately 84 pixels comprised 1 cm for the images of the top of the column. Tracking of the horizonal lines from the grid that were located 4 cm away from the

measuring tape was performed on both sets of images. Tracking was performed using a MATLAB code developed at the University of Texas and outlined in Quaglia (2017). The method tracks the movement of a rigid edge, in this case the horizontal grid that was isolated, and assumed to only displace vertically. Images were collected for approximately a week after the beginning of infiltration.

The vertical displacements from image analysis and the monitoring of the volumetric moisture contents were combined to evaluate the change in displacements with moisture fluctuations. The vertical displacements were measured by analyzing images of the full column. This combined analysis is shown in Figure 6.28 for the sensor located in the upper soil layer, Layer 1. This soil layer consisted of soil sampled from the 2014 soil sampling campaign. The depth of the grid used for the vertical displacements analysis is approximately 8 cm from the initial soil column surface.

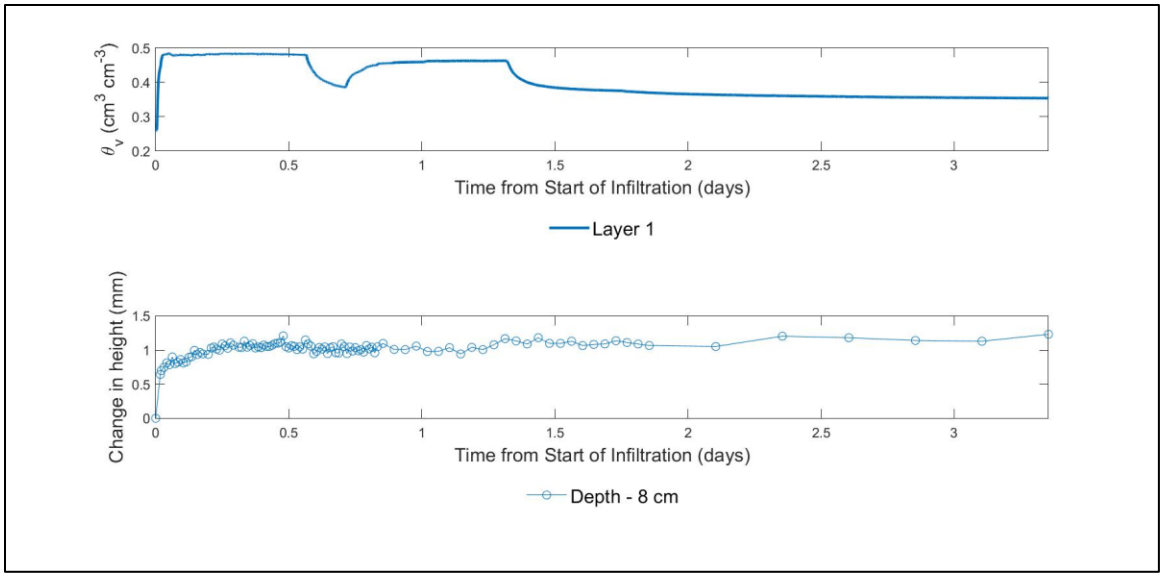

Figure 6.28: Change in volumetric moisture content and height in Layer 1 during the large column test

The vertical displacements increase over a similar time frame as the time to the end of primary swelling from centrifuge tests. Additionally, the vertical displacements indicate that there is secondary swelling that occurs after the initial moisture front. This behavior was attributed to soil behaving as a dual porosity system. In this system, moisture infiltrates into the micro-voids of the soil after the macro-voids are filled from the initial wetting front. Additionally, the vertical displacements did not decrease significantly during the decrease in moisture content during the first night of testing. This result indicates that the assumed infiltration of moisture into the micro-voids affects the vertical displacements more than infiltration of moisture into the macro-voids.

The vertical displacements with the moisture content time history was also evaluated for Layer 2, as shown in Figure 6.29. This soil layer consisted of soil sampled at depths ranging from 0 to 2 ft at the Taylor Maintenance Office. Two portions of the horizontal grid were evaluated using the image analysis techniques in this section of the laboratory column at approximate depths of 24 and 32 cm from the initial soil column surface.

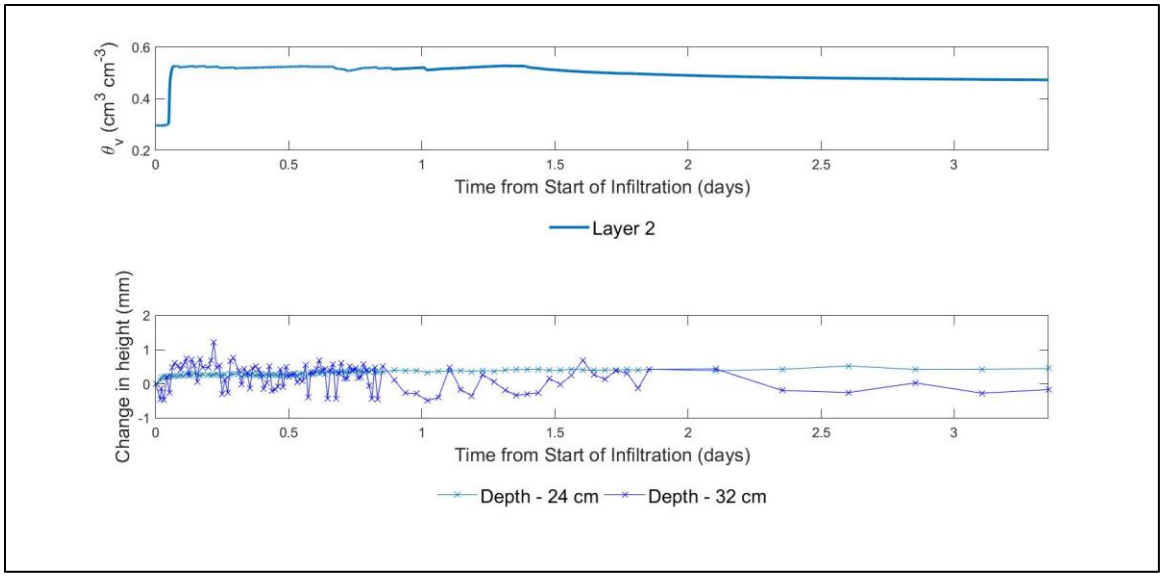

Figure 6.29: Change in volumetric moisture content and height in Layer 2 during the large column test

Significant scatter was observed for the image analysis of the horizontal grid at a depth of 32 cm. The results from the image analysis on the horizontal grid indicate vertical displacements in Layer 2 were smaller than the vertical displacements from Layer 1. These lower vertical displacements were attributed to the compression of the lower soil layers in the large column with the addition of water. However, the trends were consistent with those from Layer 1. This soil layer experienced swelling beyond the advancement of the initial moisture front. Secondary swelling occurred even after the removal of water at the top surface of the large column, again indicating that the assumed infiltration of moisture into the micro-voids affects the vertical displacements more than infiltration of moisture into the macro-voids.

The bottom soil layer, Layer 5, was evaluated as this layer was expected to compress upon the addition of moisture. The vertical displacements with the moisture content time history are shown in Figure 6.30 for the sensor in this soil layer. This soil

layer consisted of soil sampled at depths ranging from 4 to 5.5 ft at the Taylor Maintenance Office. Two portions of the horizontal grid were evaluated using the image analysis techniques in this section of the laboratory column at approximate depths of 95 and 105 cm from the initial soil column surface.

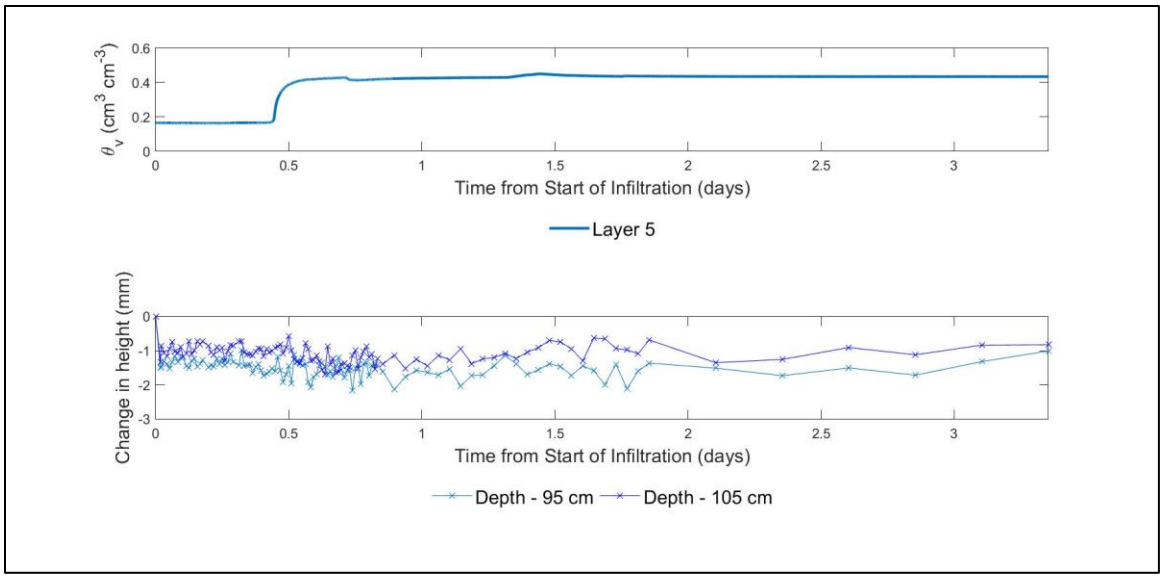

Figure 6.30: Change in volumetric moisture content and height in Layer 5 during the large column test

The vertical displacements indicated that the soil layer compressed prior to the moisture front reaching the soil layer. While some scatter was observed for the vertical displacements, the compression of this soil layer was attributed to the additional stresses from the wetting of the surface layers closer to the ground surface. After the moisture front advanced to this soil layer, the vertical displacements did not decrease significantly.

The results from Layers 3 and 4 are presented in Figure 6.31 and Figure 6.32, respectively.

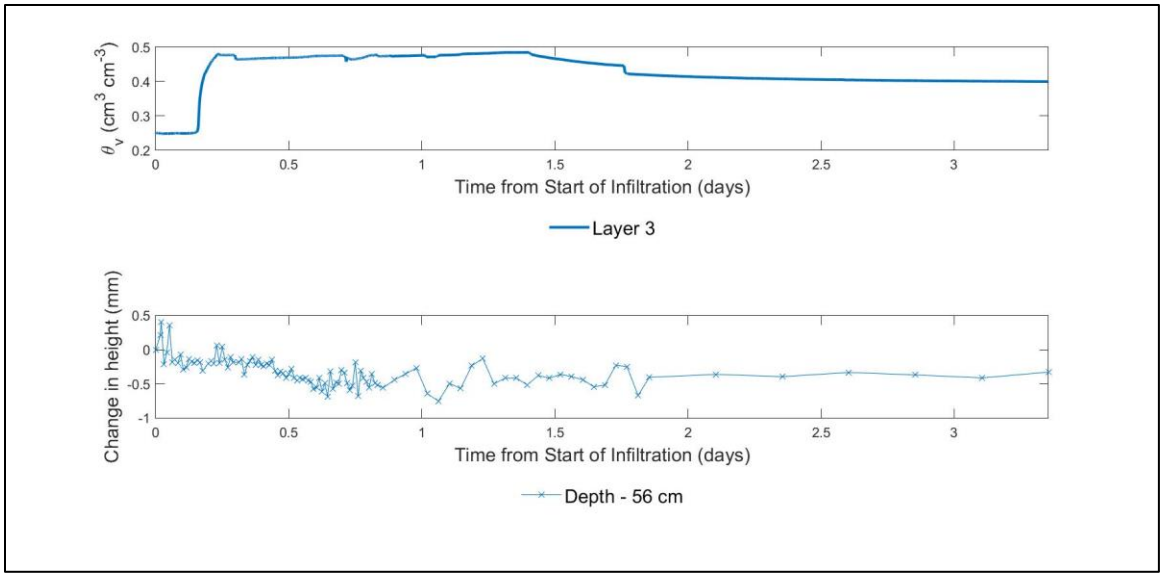

Figure 6.31: Change in volumetric moisture content and height in Layer 3 during the large column test

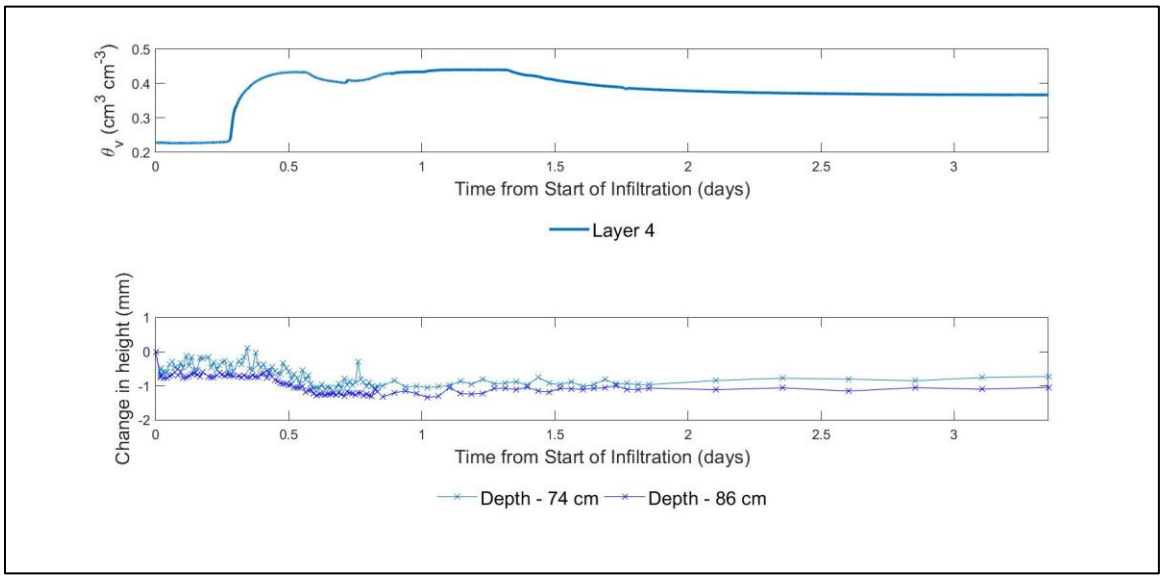

Figure 6.32: Change in volumetric moisture content and height in Layer 4 during the large column test

Results from these coupled analyses indicate that there is compression in both soil layers. Layer 3 compressed slightly after the moisture front reached the sensor, and Layer 4

compressed immediately after the addition of water at the large column surface. Additionally, the compression was higher for Layer 4 than Layer 3, indicating that the vertical displacements decreases with depth.

Results from the analysis of the full column images differed from those from the analysis of the top of the column images. The vertical displacement determined from the full column images are shown in Figure 6.33. These results were determined from the horizontal grid lines tracked using the image analysis techniques. Results from additional horizontal grid lines were deemed to have a significant scatter and were not used in the analysis.

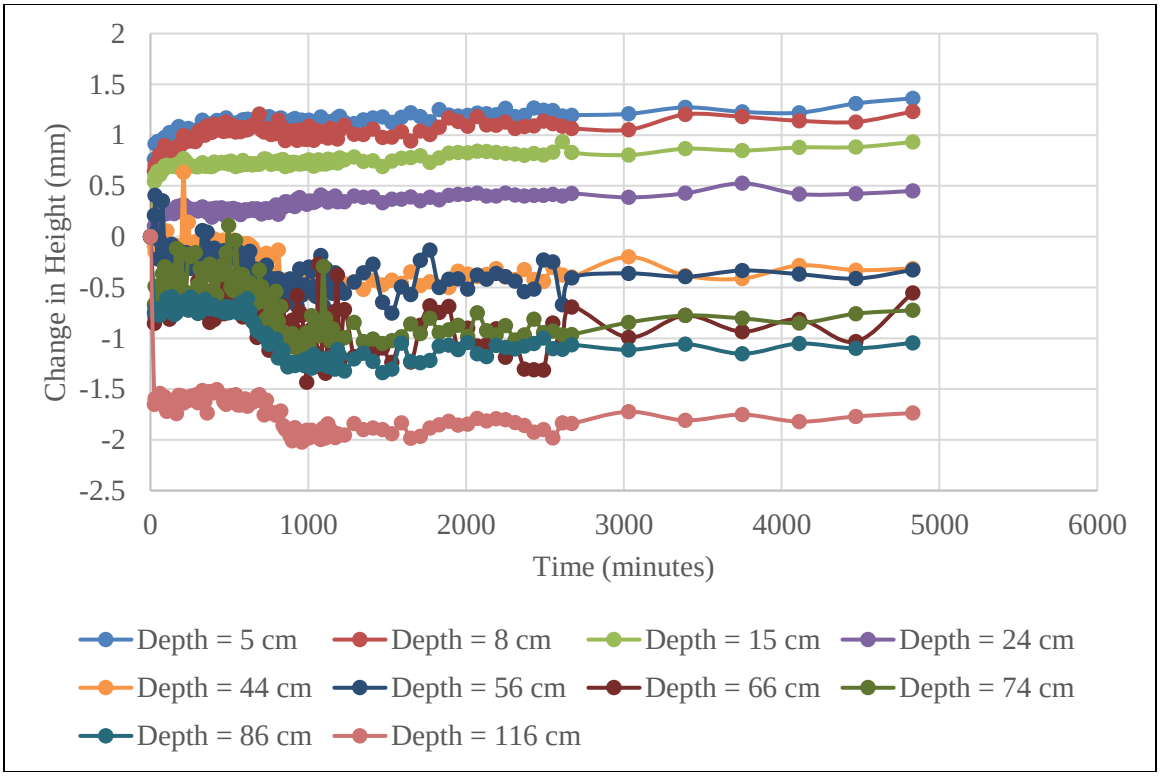

Figure 6.33: Change in heights from the image analysis using the full column images

The results indicate that the soil column heaved up to a depth of approximately 34 cm. Below this depth, the soil column compressed. The magnitude of vertical displacements at the surface of the soil column was smaller than the potential vertical rise from the centrifuge-test results. However, the heave at the surface of the column is similar to the predicted potential vertical rise that incorporates the effect of the lower initial dry unit weight. A more extensive analysis of these strains is presented in Section 7.3.2.

Vertical displacements were also determined using the images of the top of the column. The vertical displacement time history of the surface of the column using these images is shown in Figure 6.34.

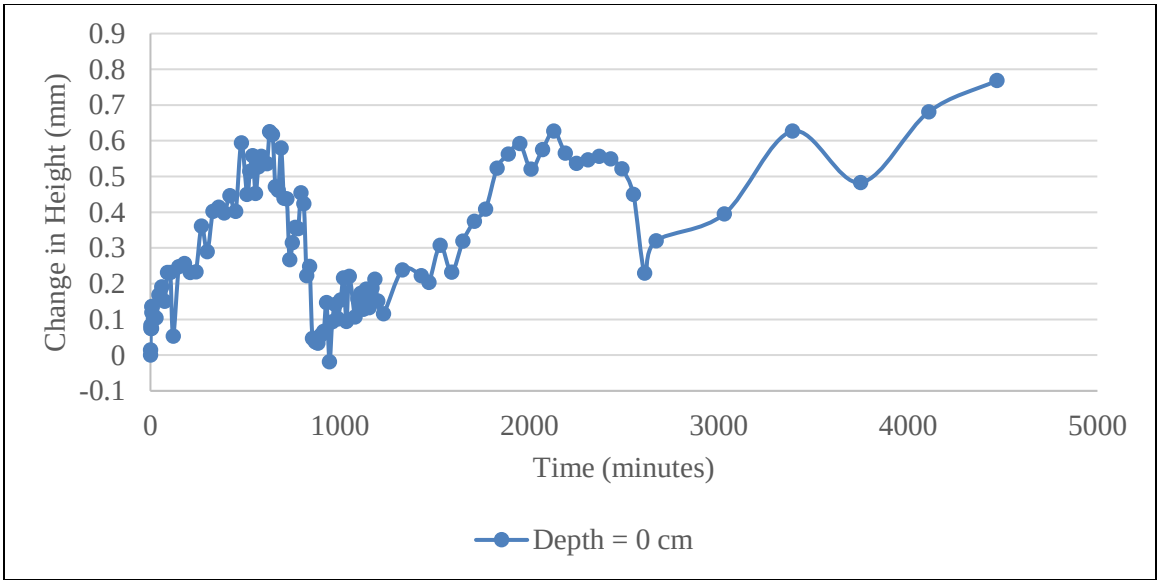

Figure 6.34: Change in surficial height from the image analysis using at top of the column images

The heave from the analysis of the top of the column images was lower than the heave from the analysis of the full column images. Additionally, the heave from the top of the column images were inconsistent, as indicated by a decrease in the height starting at a

time of approximately 700 minutes after the start of infiltration. Analysis of the top of the column images also indicate that the column heaved after the removal of water at approximately 2,000 minutes. To evaluate the consistency of the trends, the results using all of the horizontal grid lines in the top of the column images is shown in Figure 6.35.

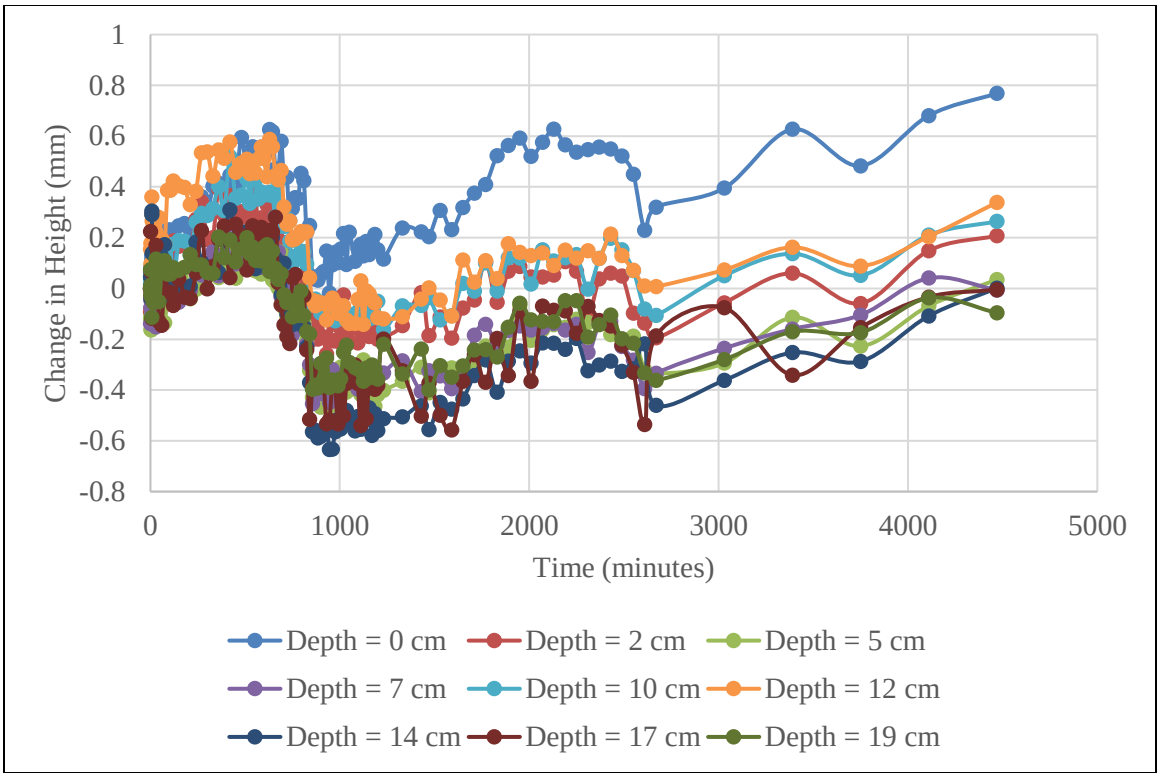

Figure 6.35: Change in heights from the image analysis using all of the top of the column images

The trends from the remaining grid lines are consistent with those from the top gridline. These trends indicate that the analysis of these images is not consistent with the behavior of the large column and may have been affected by the lower resolution of the camera or potential movement of the camera stand.

The moisture profile of the soil column was analyzed at various times during the initial wetting front. These times were determined by the approximate arrival of the wetting front at each volumetric moisture content sensors. The volumetric moisture content profiles at each time are shown in Figure 6.36. The times in the analysis correspond to the time at which the wetting front reached each of the moisture content sensors (i.e. the first time corresponds to the time to reach the first sensor, the second time corresponds to the time to reach the second sensor, etc.). Additionally, the change in height profile of the soil column were determined using the analysis of the full column images. The change in height profiles at these times are shown in Figure 6.37.

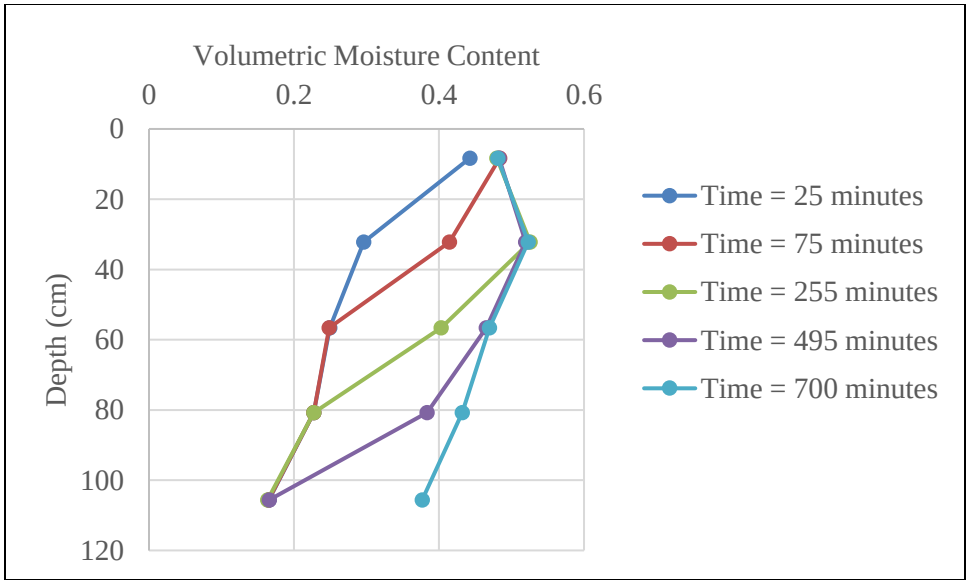

Figure 6.36: Volumetric moisture content profile at various times during large column test

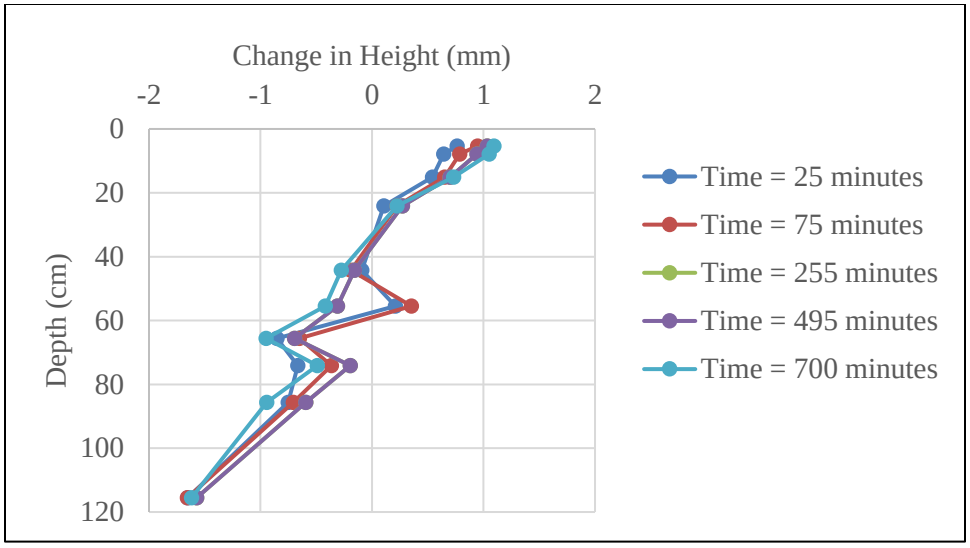

Figure 6.37: Change in height profile at various times during large column test

The volumetric moisture content profiles indicate that the increase in moisture content upon the advancement of the wetting front was relatively consistent in each of the layers. After the wetting front reached each sensor, the volumetric moisture content increased to approximately 0.40 for the corresponding soil layer. However, the volumetric moisture content did not increase significantly after the wetting front had advanced past each soil section (i.e. after the wetting front reached the sensor in the second soil layer, the sensor in the first soil layer was not observed to significantly increase in moisture content). This result indicates that moisture was flowing through the soil layers at the top surface instead of increasing the water content in these layers.

The results from the change in vertical height indicate that the upper two soil layers experienced swelling while the lower three soil layers experienced compression during the advancement of the moisture front. The upper portion of the soil was observed to continuously heave during the initial wetting front. This consistently increasing heave indicates that secondary swelling occurred in the upper soil layers. This secondary

swelling typically occurred without an increase in the volumetric moisture content. The behavior of the soil column is assumed to perform as a dual porosity system. This model assumes that moisture will first fill the macro-voids and then the micro-voids of each soil layer. Based on this assumption and the results from the moisture time histories, the secondary swelling can be attributed to wetting of the micro-voids in the specimen without a significant increase in moisture content. Additionally, the compression of the lowest soil layer during the infiltration test occurred immediately and remained relatively constant during the infiltration of the wetting front. This increase in settlement can be attributed to the increase in stress from the wetting of the deposit. However, in the third and fourth soil layer, there was an increase in settlement during the advancement of the wetting front. This increase in settlement can be attributed to the reduction in the soil stiffness. The behavior of the soil layers is generally consistent with the trends from the potential vertical rise predicted using a lower dry unit weight that is presented in Section 7.3.2. The difference in the predicted and measured heave was significantly lower than the difference from the field site in Chapter 5, indicating that centrifuge test results can be used to predict the heave in a large-scale test that represents a field expansive soil deposit.

The side friction was evaluated between the latex membrane and the acrylic. This evaluation was performed to determine the potential reduction in the potential vertical rise predictions based on the effect of the side friction. In order to calculate the at-rest earth pressures, an effective friction angle of 22° was assumed for all soil layers, and the following equation was used (Jaky, 1948):

$$K_o = 1 - sin\phi' \tag{6.2}$$

Where K_o is the at-rest earth pressure coefficient, and ϕ' is the effective friction angle. The horizontal soil stresses were estimated as follows:

$$\sigma_h = K_o * \gamma * z \tag{6.3}$$

Where σ_h is the horizontal soil stresses, γ is the bulk unit weight of the soil, and z is the depth. The lateral shear stresses can be calculated as follows:

$$\tau = \sigma_h * tan\delta \tag{6.4}$$

Where τ is the lateral shear stress, and δ is the interface friction angle. This lateral shear force exerted on a differential area of height, *dz*, can be estimated as follows:

$$dF_f = \tau * \pi * d * dz \tag{6.5}$$

Where dF_f is the lateral shear force, and d is the inner diameter of the column. The lateral shear force on the entire column can be calculated as follows:

$$F_f = \int_0^z dF_f * dz = (K_o * tan\delta * \pi * d) * \sum \gamma_i * \frac{1}{2} * (z_i - z_{i-1})^2 \tag{6.5}$$

Where the bulk unit weight and height vary for each soil layer *i.* This force is converted into a pressure by dividing by the area of the soil column and latex membrane interface for each soil layer. Using this pressure, the vertical stress used to calculate the potential vertical rise was calculated as the effective vertical stress from the soil plus the lateral interface friction. The lateral interface friction was only calculated at the top and bottom of each soil layer and did not consider the friction between the latex membrane and the soil. The interface friction angle, δ, was varied from 0° to 20°. The effect of the interface friction angle on the potential vertical rise calculated from the stress-swell curves is shown in Table 6.6.

Table 6.6: Effect of interface friction of acrylic and latex membrane on the predicted potential vertical rise

δ (°)	PVR (mm)
0	0.74
5	0.51
10	0.28
20	-0.16

The result indicates that the interface friction affects the magnitude of the potential vertical rise, but this effect is relatively small on the overall magnitude of swelling. The lower dry unit weight of the compacted soils in the column affected the magnitude of swelling significantly more than the estimated effect of the interface friction.

As the distance between the horizontal grid lines were known, a strain can be calculated for the strain between horizontal lines at each time. The strain was calculated as follows:

$$\varepsilon_{v,i} = \frac{d_i(t) - d_{i+1}(t)}{d_i(t_o) - d_{i+1}(t_o)} \tag{6.6}$$

Where $\varepsilon_{v,i}$ is the strain for a grid line at a specific depth i, d_i is the vertical displacement for a grid line at a specific depth i, d_{i+1} is the vertical displacement for a grid line that is deeper than depth i, t is at a given time, and t_o is the initial time. The strain profiles at each of the times are shown in Figure 6.38.

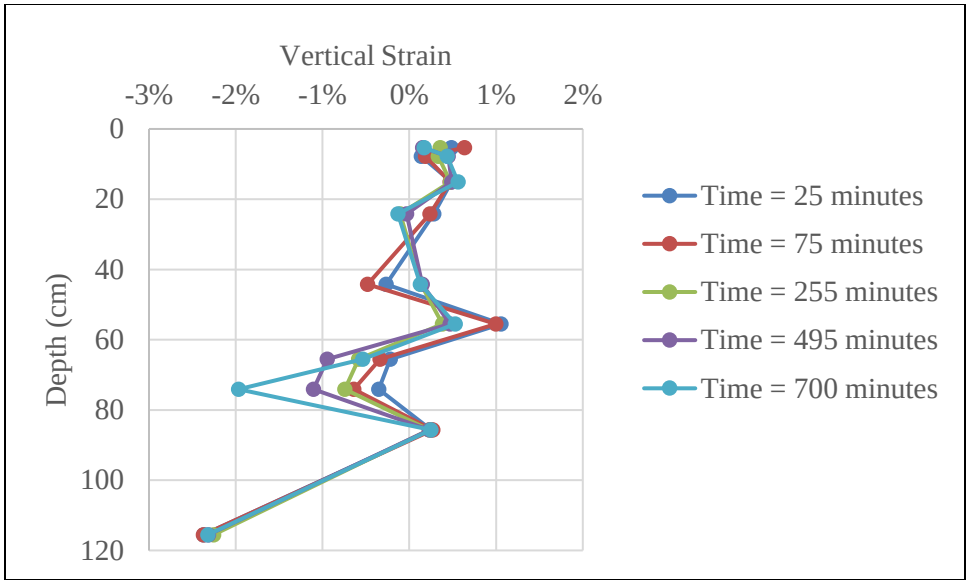

Figure 6.38: Strain profile at various times during large column test

The strain profiles indicate that the upper three soil layers experienced swelling during the advancement of the initial wetting front. This trend is consistent with the behavior from the predicted vertical rise in each of the soil sections presented in Chapter 7. However, there was a significant scatter in Layer 4 (i.e. at a depth of 80 cm) which was attributed to the scatter in the image analysis results. In general, when accounting for the displacements of the lower soil layers, the displacements in each soil layer followed similar trends to the predicted behavior based on centrifuge tests.

Analysis of the large column experiment provided insight into the behavior of a loosely compacted expansive soil in a latex membrane. The results from the large column were compared to the field site from Chapter 5. The large column and field site experienced a rapid influx of moisture at a flow rate that was higher than saturated hydraulic conductivity. The rapid infiltration of moisture for the large column test was attributed to the low relative compaction, which allowed for moisture to more rapidly permeate the deposit via the macro-voids in the soil. However, the time for the moisture

front to advance through the laboratory column was longer than the advancement of wetting fronts at the field site from Chapter 5. The difference in these time frames was attributed to the presence of desiccation cracks at the field site which can not be easily replicated in a laboratory environment. The magnitude of the maximum volumetric moisture content was lower in the large column test than at the field site. This difference was again attributed to a lack of desiccation cracks for the large column test. The drying rate in the laboratory soil column was slower than the rate at the field site. This difference was attributed to the reduced removal of moisture from the large soil column due to a lack of radiative energy from the sun and wind that increases the drying rate. Image analysis techniques were used to compare the change in height from the large column test and the prediction of heave using stress-swell curves from centrifuge test results that were corrected based on the different initial dry unit weights. The behavior of the soil in large column was consistent with the results from the corrected potential vertical rise. The soil near the surface experienced heave while the soil at depth experienced compression. However, the magnitude of heave was lower in the large soil column than from the predicted vertical rise. This difference was attributed to the lower dry unit weight for the soil layers in the column, volumetric strains in the soil layers, and the side friction between the latex membrane and the acrylic column.

6.5 CONCLUSIONS

A large soil column was instrumented in the laboratory to evaluate predictions of heave using centrifuge swelling test results. Soil retrieved from a field site was compacted into a latex membrane within an acrylic soil column. Volumetric moisture content sensors were placed at the middle section of each soil layer, and the column was given access to moisture. A grid drawn on the outside of the latex membrane allowed for

image analysis of changes in the soil column during the infiltration of moisture. The stress-swell curves from the centrifuge swelling tests were adjusted based on the results from Chapter 2 and the lower initial dry unit weight. Results from the large column test were additionally compared to the trends from the field site in Chapter 5. Based on the results from the large soil column, the following conclusions can be made:

- Soil-water retention curves generated using filter paper measurements were similar to those generated using chilled mirror hygrometer measurements for suctions greater than 1,000 kPa.
- The osmotic suction was found to be relatively constant for soils sampled deeper than 3 ft below the ground surface. However, the osmotic suction was found to vary with moisture content for soils sampled near the ground surface.
- The moisture front advanced over a longer time frame in the large column than at the field site from Chapter 5. This difference was attributed to desiccation cracking at the field site that are not easily replicable in a laboratory environment.
- The vertical displacement of soil layers followed similar trends to the predicted potential vertical rise from centrifuge swelling tests. The upper soil layers of the large column experienced swelling while the lower soil layers experienced compression.

Chapter 7: Prediction of Potential Heave in Expansive Soil Deposits

The five research components presented in Chapters 2, 3, 4, 5, and 6 analyzed interrelated aspects of expansive soil behavior using laboratory experimental methods and monitoring of a field soil deposit. However, the results from these research components can be used to improve the methodology currently used to predict the potential vertical rise of field sites. Currently, the potential vertical rise in the field is predicted either by using correlations based on geotechnical properties or by integrating the swell-stress curves generated from centrifuge swelling test results. Chapters 2, 3, and 4 evaluated aspects that affect the generation of stress-swell curves, including the initial testing and soil conditions, soil fabric, and variability of expansive soil deposits. Chapters 5 and 6 examined aspects related to the large-scale behavior of expansive soils, including monitoring of moisture fluctuations and surficial deflections of an instrumented field site and a large-scale laboratory soil column. Findings from each of these research components can be synthesized to improve the prediction of the potential heave in field expansive soil deposits by adjusting the laboratory-generated stress-swell curves and accounting for differences between the laboratory-predicted and field-measured heave.

The application of the results from this dissertation to improvement the prediction of the potential vertical rise is grouped into two separate sections. The first section focuses on the prediction and correction of the laboratory-generated stress-swell curves. The second section evaluates differences between the laboratory-predicted and field-measured heave from the field site and the large-column test. Previous studies and the results from a large column test were additionally used to improve these predictions. The improved predictive approach is then applied to results from the field site and the large-scale laboratory tests to evaluate the effectiveness of the corrections.

7.1 PREDICTION OF STRESS-SWELL CURVES

Methods that predict the vertical heave of field deposits that were developed in previous studies are detailed in Section 2.2 of this dissertation. These methods typically predict the vertical rise based on geotechnical properties (e.g. the Atterberg Limits) and the expected overburden stress in the soil deposit. However, these predictive methods typically do not incorporate a one-dimensional stress-swell curve. Due to a lack of stress-swell curves, these methods were not further evaluated.

For the predictive technique outlined in this chapter, a semi-log-linear fit of the vertical strains at the end of primary swelling and vertical effective stress can be used to define stress-swell curves. This semi-log-linear fit is defined as follows:

$$\varepsilon\ (\%) = A * \log(\sigma') + B \tag{7.1}$$

Where ε is the vertical strain at the end of primary swelling, A and B are fitting parameters, and σ′ is the vertical effective stress. Fitting parameters A and B depend on the units of the effective stress. For this study, pounds per square foot were used. Parameter A represents the slope of the curve in the swelling versus logarithm of effective stress space, and Parameter B represents the swelling at 1 psf. In order to incorporate the effect of the initial and testing conditions from this dissertation, Parameter A and B can be corrected to adjust the stress-swell curves.

The correction of the stress-swell curves is based on the effect of the initial conditions (i.e. the gravimetric moisture content, dry unit weight, suction, and soil fabric) presented in Chapters 2 and 3 of this dissertation. Specifically, the change in the void ratio at the end of primary swelling can be adjusted based on differences of the initial gravimetric moisture content and dry unit weight between laboratory soil specimens and field conditions. Results from Chapter 2 (Figures 2.27 and 2.34) indicate the vertical strains at the end of primary swelling tend to linearly decrease with increasing initial

gravimetric moisture content and decreasing initial dry unit weight. Due to these relationships, the test results used to fit the stress-swell curves can be easily adjusted. However, the use of these linear relationships is recommended only for soils from a similar soil series defined by National Resources Conservation Service (NRCS) soil survey maps.

The change in the void ratio (Δe_{ps}), from the end of the compression phase to the end of primary swelling, was corrected based on difference in the initial soil condition. This test result was used instead of the vertical strains at the end of primary swelling as the vertical strains are dependent upon the initial conditions. The initial conditions, particularly the initial dry unit weight, significantly affect the initial void ratio, which is used to calculate the vertical strains based on Equation 2.5. Using the results from Chapter 2, the change in void ratio at the end of primary swelling versus the initial gravimetric moisture content is shown in Figure 7.1. For this figure, the initial dry unit weight is constant for the soil specimens. The change in void ratio at the end of primary swelling versus the initial dry unit weight is shown in Figure 7.2. For this figure, the initial gravimetric moisture content is constant for the soil specimens. The slope of the linear relationships between the change in void ratio and initial gravimetric moisture content (i.e. C_{ω}) is shown for the Branyon clay in Figure 7.1. The slope of the linear relationship between the change in the void ratio and initial dry unit weight (i.e. $C_{\gamma d}$) is shown for the Branyon clay in Figure 7.2.

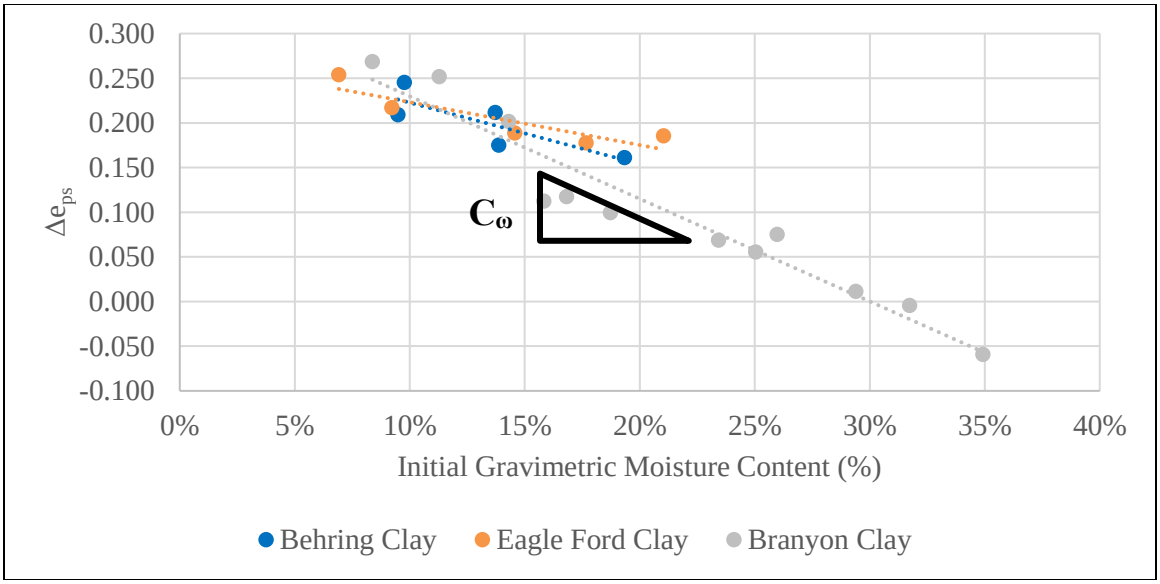

Figure 7.1: Effect of initial gravimetric moisture content on the change in void ratio at the end of primary swelling for the three soils, tested at a constant initial dry unit weight

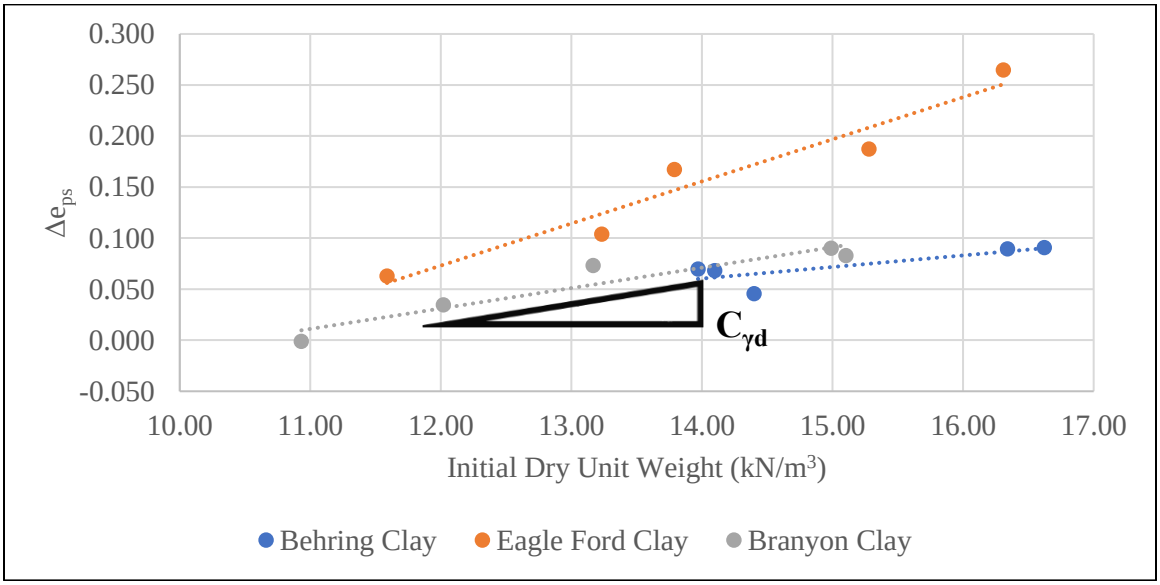

Figure 7.2: Effect of initial dry unit weight on the change in void ratio at the end of primary swelling for the three soils, tested at a constant initial gravimetric moisture content

The test results indicate that there is a linear relationship between the change in void ratio at the end of primary swelling and both the initial dry unit weight and gravimetric moisture content. These linear relationships are consistent with previous studies (Komine and Ogata, 1992; Kong and Guo, 2011). The slope of these linear relationships can be determined in order to correct the test data used to fit stress-swell curves. A correction factor for the change in the void ratio at the end of primary swelling can be calculated as follows:

$$\Delta e_{cor} = \mathrm{C}_{\omega} * \left(\omega_{i,c} - \omega_{i,i}\right) + \mathrm{C}_{\gamma_d} * \left(\gamma_{d,c} - \gamma_{d,i}\right) \tag{7.2}$$

Where C_{ω} and $C_{\gamma d}$ are the linear slopes from Figures 7.1 and 7.2, $\omega_{i,i}$ is the initial gravimetric moisture content from the test data, $\omega_{i,c}$ is the gravimetric moisture content that the test is corrected to, $\gamma_{d,i}$ is the initial dry unit weight from the test data, and $\gamma_{d,c}$ is the dry unit weight that the test is corrected to. After the correction for the change in void ratio is calculated, the corrected magnitude of vertical strain can be calculated as follows:

$$\varepsilon_c = \frac{\Delta e_{ps} + \Delta e_{cor}}{1 + e_{o,c}} \tag{7.3}$$

Where ε_c is the corrected vertical strain at the end of primary swelling, Δe_{ps} is the initial magnitude in the change in void ratio from the end of the compression phase to the end of primary swelling, and $e_{o,c}$ is the void ratio at the end of compression phase that has been corrected for the initial dry unit weight. This corrected void ratio can be calculated as follows:

$$e_{o,c} = \frac{G_s * \gamma_w}{\gamma_{d,c}} - 1 \tag{7.4}$$

Where G_s is the specific gravity of the soil, typically assumed to be 2.7 for analysis of centrifuge testing results, γ_w is the unit weight of water, and $\gamma_{d,c}$ is the dry unit weight of the soil at the corrected initial dry unit weight.

After the data is corrected for the differences in the initial soil conditions, the stress-swell curves can be adjusted, and a corrected potential vertical rise can be calculated. The corrections based on differences in initial conditions can be used to re-plot the data. An example of the adjustment of the stress-swell curves is shown in Figure 7.3.

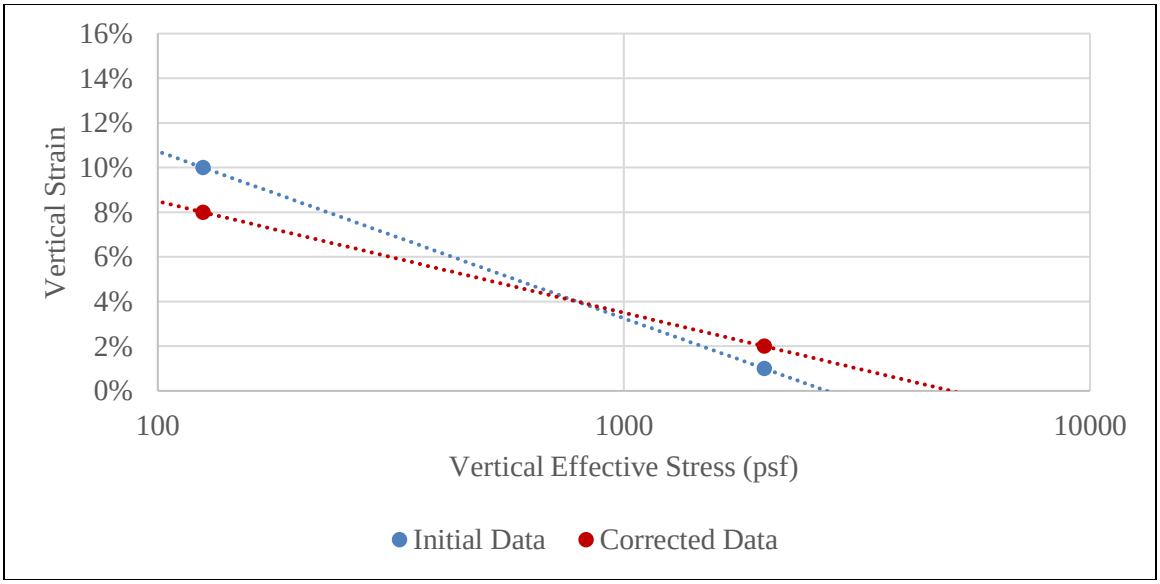

Figure 7.3: Correction of stress-swell curves for potential vertical rise

The correction of the data described in the preceding methodology can vary and either raise or lower the vertical strains based on the initial conditions. Using the adjusted stress-swell curve, a potential vertical rise can be calculated based on the method outlined in Zornberg et al. (2017). This method integrates the stress-swell curve by subdividing the area below the curve for the range of effective stresses expected in the field. Each of the subdivided stresses can be assigned to a thickness of soil, based upon the saturated unit weight of the soil. Each of these soil layers have a strain from the stress-swell curve

and corresponding heave which can be summed to estimate the potential vertical rise of the expansive soil deposit.

Other initial conditions that have been reported to affect the vertical strain are the initial suction and the soil fabric. Suction has previously been used to estimate the heave of expansive soils by Lin and Cerato (2012), Farid and Mosaid (2014), and Erzin and Erol (2007). Lin and Cerato (2012) indicated that the matric suction can predict the magnitude of swelling for four soils taken from Oklahoma and North Texas, as shown in Figure 7.4.

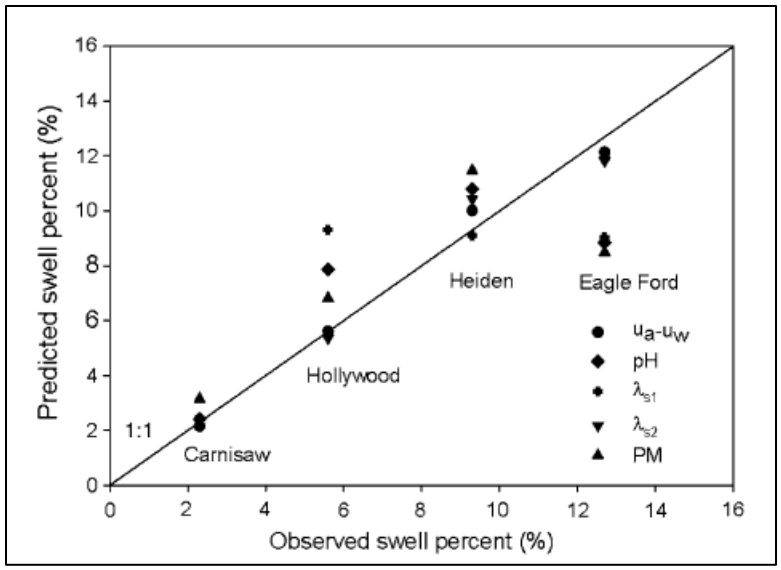

Figure 7.4: Comparison between observed and predictive swelling using various microscale properties (Lin and Cerato, 2012)

Test results from Chapter 2 indicated that an increase in total suction results in a higher primary swelling for soil specimens with differing initial gravimetric moisture content but constant initial dry unit weights. However, test results from soils specimens with differing initial dry unit weights and a constant gravimetric moisture content did not

show a similar trend. Thus, correction of swelling data based on differences in the initial suction should also incorporate the effect of other initial soil conditions.

The fabric was shown to affect the magnitude of swelling for soil specimens that were either field-sampled or laboratory-reconstituted in Chapter 3. Additionally, the results presented in Chapter 4 indicated that there was a difference in the potential vertical rise between soil deposits that were sampled using different methodologies. However, further analyses are needed to quantify these effects.

7.2 Prediction of Field Heave

The potential vertical rise calculated from the corrected stress-swell curves can be used to predict the maximum heave at field sites. To predict heave in the field, the expansive soil deposit is assumed to begin at a comparatively dry condition, which are subsequently wetted to near saturation. This assumption is made to correlate the field results to swelling test in the laboratory, where near saturation conditions are typical at the end of testing. However, to reach a comparatively dry condition, a significant amount of desiccation cracks may have occurred. These desiccation cracks can change the swelling behavior in an expansive soil deposit as the soil will first swell laterally to seal cracks and macro-voids prior to heaving vertically. Additionally, based on stresses in the field, a significant portion of the volumetric strains may occur laterally. Thus, the laboratory-predicted one-dimensional heave must be corrected to account for these volumetric strains. This correction of the one-dimensional swelling test results to volumetric strains has been studied previously. Additionally, findings from Chapters 5 and 6 of this dissertation can be used to quantify the differences between the laboratory-predicted and field-measured heave from the field site.

The differences between one dimensional and volumetric strains for expansive soils have been evaluated previously. Seed et al. (1962) observed that the swelling pressure from a one-dimensional swelling test was not reached if the expansive soil specimen was allowed to swell laterally. This reduction in the swelling pressure was attributed to volumetric strains reducing the one-dimensional heave of the soil specimens. This trend was attributed to the strains being volumetric, as opposed to vertical, and the sealing of the crack structure within the soil specimen. Al-Shamrani and Al-Mhaidib (1999) compared the axial strain from triaxial swelling tests versus vertical strains from oedometer tests as shown in Figure 7.5.

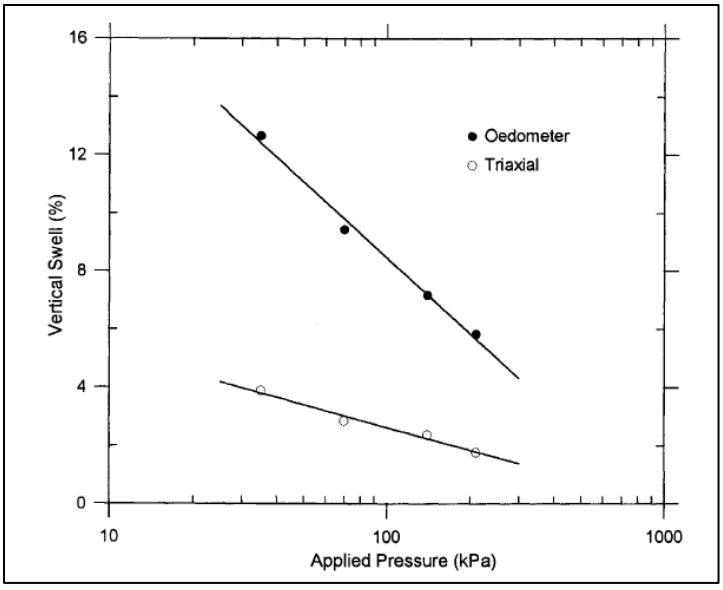

Figure 7.5: Stress-axial strain curves for triaxial and oedometer swelling tests (Al-Shamrani and Al-Mhaidib, 1999)

The axial strains from triaxial swelling tests were approximately a third of the vertical strains from oedometer swelling tests. This reduction was attributed differences in the lateral restrictions of the test. The soil specimens in the triaxial tests were allowed to

undergo volumetric strains, whereas the soil specimens in the oedometer tests were allowed to undergo solely vertical strains due to the rigid lateral confinement from the testing set-up. The researchers also evaluated the differences between the heave measured at a field site versus the heave predicted from laboratory triaxial and oedometer tests as shown in Figure 7.6.

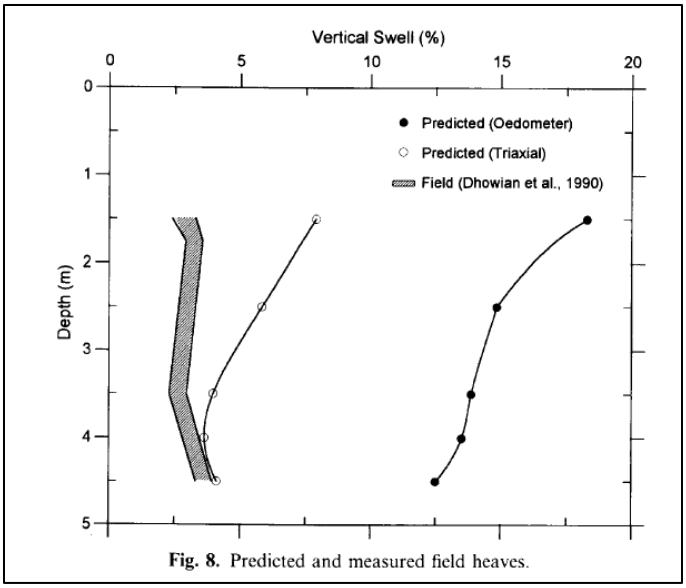

Figure 7.6: Predicted versus field heave for an expansive shale (Al-Shamrani and Al-Mhaidib, 1999)

The field-measured heave has been reported to be approximately a fourth to a seventh of the predicted heave from the oedometer tests and approximately a third of the predicted heave from the triaxial tests (Al-Shamrani and Al-Mhaidib, 1999). This reduction in the field-measured heave indicate that the lateral expansion and sealing of cracks significantly reduces the vertical rise in the field. However, these results also indicate that there is potential for a correction of laboratory-predicted heave to match the field-measured heave.

Since the centrifuge-based swelling test used in this dissertation has a similar lateral restraint as the oedometer swelling test, the laboratory-predicted heave was expected to exceed the field-measured heave. Results from Chapter 5 of this dissertation, which evaluated the field-measured heave from field site, are consistent with this assumption and previous studies. From the expansive subgrade beneath a pavement structure in Chapter 5, the maximum field-measured heave was approximately 10 mm from the driest portion of the summer to after a significant rainfall event. However, the heave at this site may be higher due to a delay in the measurement of the pavement surface after the end of rainfall. Using the centrifuge-based swelling tests, the laboratory-predicted potential vertical rise was 44.7 mm. Differences in the laboratory-predicted versus field-measured vertical rise were attributed to lateral restraint of the soil specimens during laboratory tests and desiccation cracks in the field. Using the results from this site, the field-measured heave is approximately a fourth to a fifth of the laboratory-predicted heave. However, the laboratory-predicted heaves were based upon a dry condition estimated for laboratory testing instead of the conditions encountered in the field.

7.3 Correction of Predicted Heave from Research Components

Sections 7.1 and 7.2 outlined the method to correct laboratory-generated stress-swell curves and the differences between laboratory-predicted versus field-measured vertical rise. In order to analyze the effectiveness of these corrections, results from Chapters 5 and 6 of this dissertation were reanalyzed. This section covers the correction of the data, the influence of the initial conditions on the corrections, and the methodology and rationale behind the estimation of variables needed for this reanalysis. The laboratory-generated stress-swell curves were corrected based on the difference between the dry moisture condition used for the centrifuge-based inundation tests and the field-

measured initial conditions prior to wetting. The corrected stress-swell curves were then used to determine a corrected potential vertical rise and compared it against the field-measured heave at the sites. The sites that were corrected included the FM685 site during the rainfall event at the end of August 2017 and the large soil column test that used the soils from the Taylor Maintenance Office.

7.3.1 Correction of Predictions for FM 685 Site

The FM685 site was analyzed for the large rainfall event from Hurricane Harvey in August 2017. The site sits on approximately 5 ft of expansive soil, the Branyon clay. The rainfall event occurred near the end of monitoring of the site when only the moisture content sensors at depths of 1.5 ft and 4.5 ft below the base-subgrade interface were working properly. Due to this, the sensor at a depth of 1.5 ft was used to estimate the variables for the upper 2.5 ft of the deposit, and the sensor at a depth of 4.5 ft was used to estimate the variables for the lower 2.5 ft of the deposit. The rainfall event consisted of approximately 9.76 in. of rain that fell over the course of a week. The moisture content fluctuations for this rainfall event were previously shown in Figure 5.21.

In order to correct the stress-swell curves, an estimation of the in-situ dry unit weight is needed. To obtain the estimated in-situ dry unit weight, an estimated porosity was determined. Since the rainfall event was significant and over long duration, the maximum volumetric moisture content from this rainfall event was used to estimate the porosity of the soil deposit. This estimated porosity assumes that the pores reached saturation during the rainfall event and that the dry unit weight did not vary significantly between the condition prior to the rainfall and during the rainfall. Previous studies, including Quaglia (2017), have shown that the soil can be assumed to be near saturation at the end of primary swelling and that the volumetric moisture content does not increase

significantly beyond the end of primary swelling, as shown in Figure 7.7. These previous studies indicate that, for a significant rainfall event, the voids in an expansive soil may be near saturation.

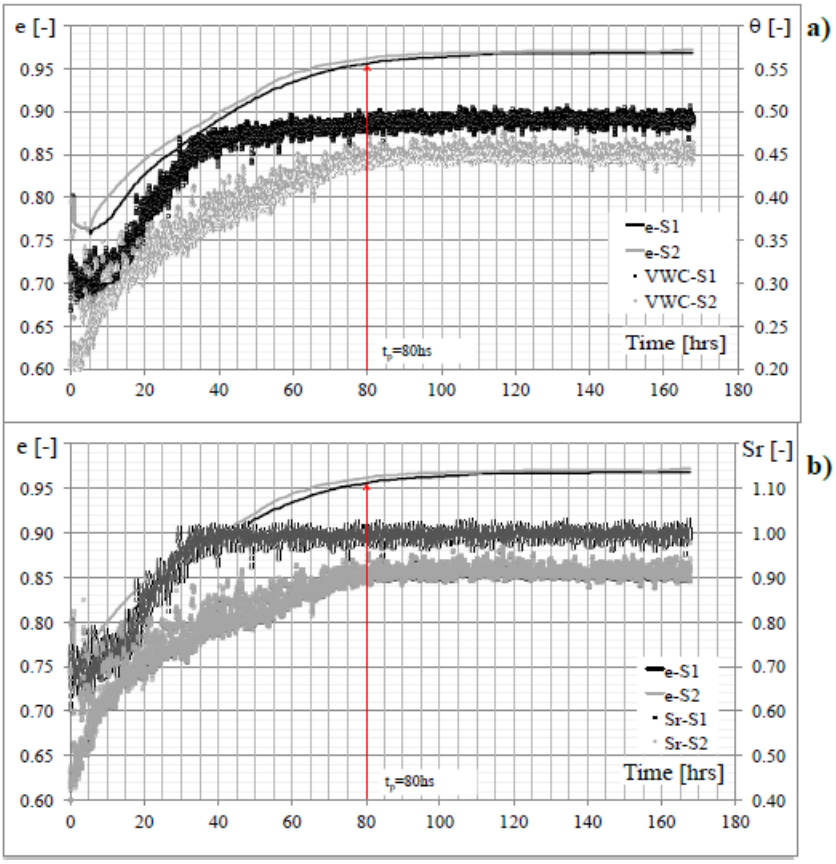

Figure 7.7: Swelling curves using the void ratio for: a) volumetric moisture content: b) degree of saturation (Quaglia, 2017)

However, the dry unit weight will vary significantly from the dry condition to the end of swelling condition based on the magnitude of volumetric strains. Despite this issue, this approximation was assumed for the field site in order to estimate the porosity due to a lack of data about the in-situ dry unit weight. Results from the large column test are later analyzed to evaluate the validity of this assumption.

After estimating the porosity, the estimated void ratio can be calculated as follows:

$$e_{est} = \frac{\emptyset_{est}}{1 - \emptyset_{est}} \tag{7.5}$$

Where ϕ_{est} is the estimated porosity of the soil and e_{est} is the estimated void ratio. After the void ratio is estimated, the estimated initial dry unit weight can be calculated as follows:

$$\gamma_{d,est} = \frac{G_s * \gamma_w}{e_{est} + 1} \tag{7.6}$$

Where G_s is the specific gravity and assumed to be 2.7, $\gamma_{d,est}$ is the estimated initial dry unit weight of the soil, and γ_w is the unit weight of water. The other soil condition needed to correct the stress-swell curves, the initial gravimetric moisture content, can additionally be estimated using the field data. The measured initial volumetric moisture content and the estimated initial dry unit weight can be used to estimate the initial gravimetric moisture content as follows:

$$\omega_{i,est} = \frac{\theta_i}{\gamma_{d,est}/\gamma_w} \tag{7.7}$$

Where $\omega_{i,est}$ is the estimated initial gravimetric moisture content, and θ_i is the initial volumetric moisture content. The final variable needed to determine the potential vertical rise, the saturated unit weight, was estimated using the final volumetric moisture content. This estimation assumes that the dry unit weight of the soil does not change significantly from the dry unit weight calculated by Equation 7.6. Using the preceding methodology, the estimated initial gravimetric moisture content and dry unit weight, porosity, relative compaction, void ratio, and saturated unit weight are shown in Table 7.1. The dry unit weight for the bottom layer was assumed for the top layer as the estimated dry unit weight was unreasonably low.

Table 7.1: Estimated porosity and corresponding initial field conditions for FM685 site

Depth (ft)	θ_i	$\theta_{max, sensor}$	ϕ_{est}	$e_{i,est}$	$\gamma_{d, est}$ (pcf)	R.C.est	$\omega_{i, est}$	$\gamma_{sat, est}$ (pcf)
1.5	0.245	0.590	0.590	1.439	80	92%	19.1%	117
4.5	0.295	0.525	0.525	1.105	80	92%	23.0%	113

The estimated initial gravimetric moisture content and dry unit weight can be used to correct the stress-swell curves. The initial conditions for the centrifuge-based swelling tests were estimated by NAVFAC (1962) correlations. A comparison between the soil conditions estimated prior to the August 2017 rainfall and the soil conditions used for centrifuge testing is shown in Table 7.2.

Table 7.2: Initial field conditions and centrifuge testing conditions for FM 685 site

Layer	Soil Condition	Initial Field	Centrifuge
1	ω (%)	19.1%	24.6%
	γ_d (pcf)	80	87
2	ω (%)	23.0%	24.6%
	γ_d (pcf)	80	87

The relationship between the change in void ratio against both the initial gravimetric moisture content and dry unit weight were estimated from Figures 7.1 and 7.2 using the results from the Branyon clay. Using Equation 7.2, the corrected change in void ratio at the end of primary swelling was calculated, as shown in Table 7.3. The two effective specimen stresses, 125 and 1,000 psf, were selected to shift the stress-swell curves as these stresses are typical of the stresses at the top and bottom of the active zone.

Table 7.3: Correction of void ratios for swell-stress curve for FM685 site

Depth (ft)	Δe 125 psf	Δe 1000 psf	γ_d Correction	ω Correction	Δe_c 125 psf	Δe_c 1000 psf
1.5	0.201	0.042	-0.021	0.063	0.242	0.084
4.5	0.201	0.042	-0.021	0.018	0.198	0.039

These corrected changes in void ratio at the end of primary swelling were used to correct the vertical strain at the end of primary swelling at 125 and 1,000 psf based on Equation 7.3 and the estimated initial void ratio from Equation 7.5. The original and corrected vertical strain at these two stresses, along with the corrected A and B fitting parameters from Equation 7.1, are shown in Table 7.4. To visualize the effect of these corrections on the stress-swell curve, the original stress-swell curve, fitted using a semi-log-linear fit, and the corrected stress-swell curves for the two depths are shown in Figure 7.8.

Table 7.4: Corrected swell results and stress-swell curve for FM685 site

Depth (ft)	ε_v 125 psf	ε_v 1000 psf	$\varepsilon_{v,c}$ 125 psf	$\varepsilon_{v,c}$ 1000 psf	A_c	B_c
1.5	10.3%	2.2%	9.9%	3.4%	-3.8E-02	13.8%
4.5	10.3%	2.2%	9.4%	1.8%	-4.4E-02	13.8%

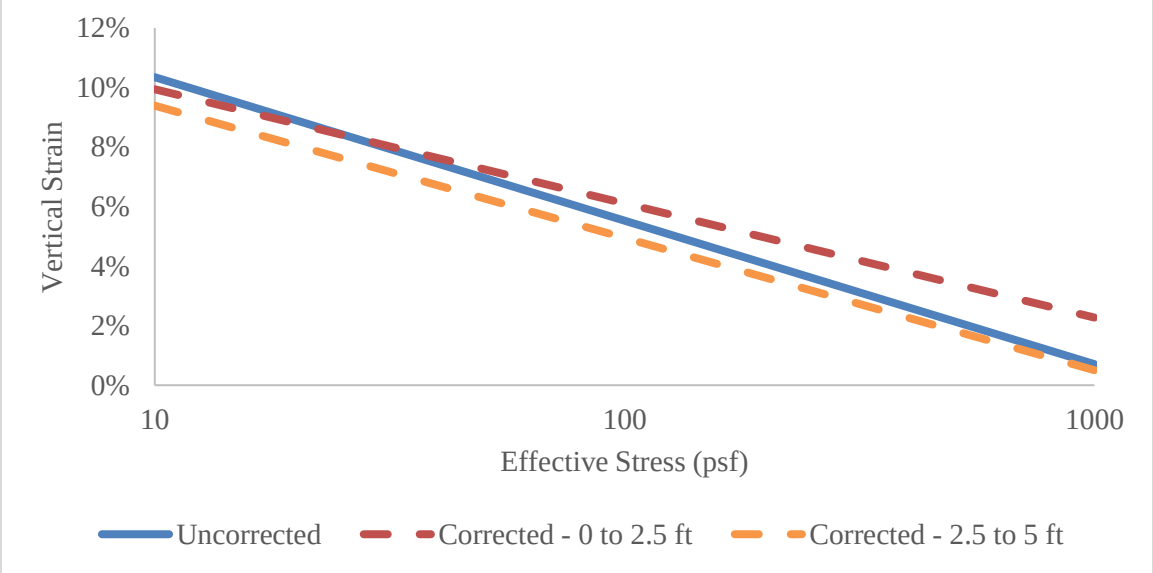

Figure 7.8: Original and corrected stress-swell curves for FM685 site

The effect of the initial conditions is observed in the stress-swell curves for both depths. This effect was larger for the portion of the deposit closer to the base-subgrade interface. This region of the deposit typically affected the calculated potential vertical rise more significantly. However, this correction of the stress-swell curves is not solely a shift of the vertical strains as the correction of the initial dry unit weight additionally affects the initial void ratio.

With the corrected stress-swell curves, a corrected potential vertical rise can be calculated. The effective overburden stress at the top and the bottom of each of the two layers was calculated, and the logarithmic mean of the stresses was calculated. The vertical strain at this logarithmic mean was determined using the corrected fitting parameters from Table 7.4 and Equation 7.1. Using this average vertical strain, the potential vertical rise was calculated by multiplying each strain by the thickness of the layer. Results from this analysis are shown in Table 7.5.

Table 7.5: Calculation of corrected potential vertical rise for FM685 site

Depth (ft)	**σ'_t (psf)**	**σ'_b (psf)**	**σ'_{avg} (psf)**	**$\varepsilon_{v,average}$**	**PVR (mm)**
1.5	81	217	133	5.6%	42.94
4.5	217	343	273	3.0%	22.93

Using the corrected stress-swell curves and accounting for a lower initial dry unit weight and lower initial gravimetric moisture content, the potential vertical rise is 65.9 mm (2.59 in). The vertical rise was originally calculated to be 44.7 mm using the centrifuge test results at the dry condition. However, the original methodology used a more complex, non-log-linear fit for the stress-swell curves that reduced the swelling at depth in order to better fit the test results at depth. Therefore, the use of the semi-log-linear curve fit may limit the effect of these reduced strains at depth.

The vertical rise measured in the field was approximately 10 mm (Figure 5.52), which is approximately a sixth of the corrected, laboratory-predicted potential vertical rise. Again, the difference in the field-measured and laboratory-predicted vertical rise was attributed to volumetric strains and cracking in the field soil deposit as well as the measurement of surficial deflections after the rainfall event had ended. The soil deposit may have been drying during the time of measurement of the surficial heave due to limitations with the non-prism total station methodology. Additionally, the field deposit can expand laterally based on the stresses in the deposit, as shown in Section 7.2 and the centrifuge-based swelling test does not measure lateral strains due to the rigidity of the testing set-up.

7.3.2 Correction of Predictions for Large Column Test

Test results from the large column test were additionally analyzed. This test was evaluated as, unlike the analysis in Section 7.3.2, the in-situ dry unit weight, void ratio, and gravimetric moisture content were known based on the compaction conditions. The in-situ dry unit weight was determined by averaging the relative compaction of each of the soil lifts that comprised each soil layer. The initial gravimetric moisture content was measured following the method outlined in ASTM D2216. The only estimated variable for the potential vertical rise analysis was the saturated unit weight. The results from Layer 2 were used for both the sensor pairings at a depth of 10 and 34 cm due to some intermixing of the soils that comprise Layer 1 and Layer 2 during compaction of the large column. The variables used for the analysis are shown in Table 7.6.

Table 7.6: Porosity and initial field conditions for large column test

Layer	θ_i	$\theta_{max, sensor}$	ϕ_i	e_i	$\gamma_{d,i}$ (pcf)	R.C.	ω_i	$\gamma_{sat, est}$ (pcf)
1	0.255	0.485	0.588	1.428	69	67%	22.1%	100
2	0.296	0.528	0.582	1.394	70	73%	22.0%	103
3	0.250	0.485	0.580	1.380	71	81%	21.9%	101
4	0.233	0.440	0.533	1.140	75	84%	20.0%	102
5	0.166	0.451	0.550	1.220	77	81%	15.6%	105

The maximum volumetric moisture contents from the each of the sensors are plotted against the measured porosity of the surrounding soil medium in Figure 7.9. From Section 7.3.1, these maximum volumetric moisture content readings are used as the estimated porosity of the layer.

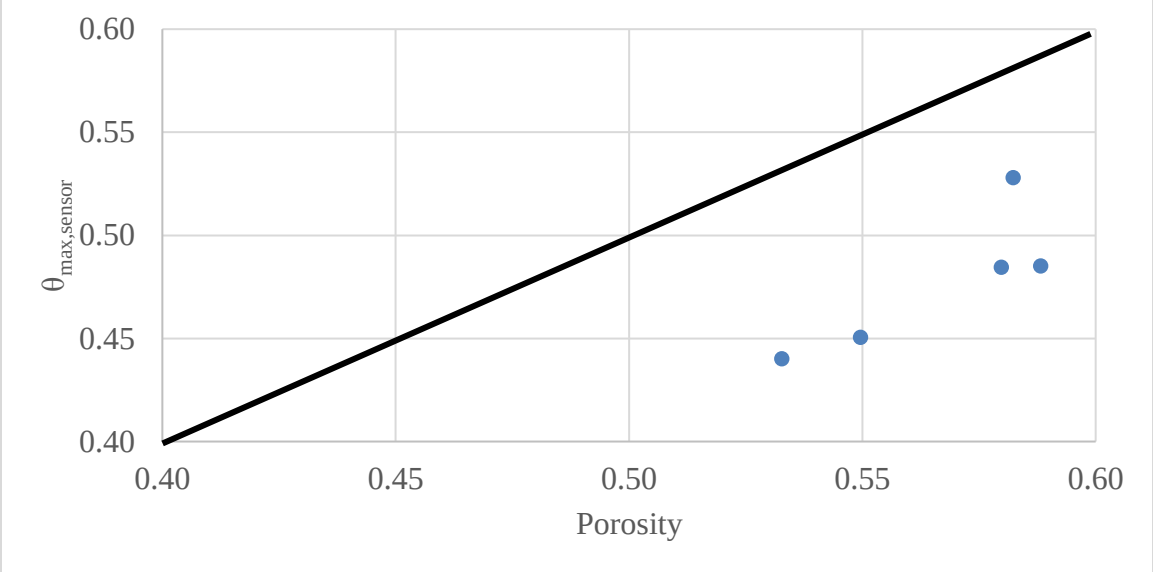

Figure 7.9: Measured porosity versus maximum volumetric moisture content from each sensor in large column test

The maximum volumetric moisture content tended to significantly underestimate the measured porosity. The porosity estimated from the moisture content sensors was

approximately 80 to 90% of the actual porosity. Therefore, the estimation of the porosity using the moisture content sensors may underestimate the actual porosity due to a lack of saturation and low resolution at higher volumetric moisture contents. Therefore, the analysis of the FM685 site in Section 7.3.1 may be significantly affected by the estimation of the porosity.

Using the initial soil conditions from the compaction of the column, corrections can be generated using the same methodology outlined in Section 7.3.1. The differences between the initial column conditions and the initial soil conditions used for centrifuge tests is shown in Table 7.7.

Table 7.7: Column soil conditions and centrifuge tests soil conditions for large column

Layer	Soil Condition	Column	Centrifuge
1	ω (%)	22.1%	20.7%
	γ_d (pcf)	69	95
2	ω (%)	22.0%	23.1%
	γ_d (pcf)	70	89
3	ω (%)	21.9%	23.4%
	γ_d (pcf)	71	88
4	ω (%)	20.0%	20.1%
	γ_d (pcf)	75	95
5	ω (%)	15.6%	16.4%
	γ_d (pcf)	77	103

In general, the initial soil conditions in the column tend to be at lower initial dry unit weights and initial gravimetric moisture contents than the initial soil conditions used for centrifuge tests. The linear trends of the Branyon clay from Figures 7.1 and 7.2 were used for the linear trends as for the large column test. The results for the Branyon clay were used as the soil used in the large column test was sampled in a similar geographic and

geologic region as the Branyon clay. Using Equation 7.2, the corrected change in void ratio at the end of primary swelling was calculated, as shown in Table 7.8.

Table 7.8: Correction of void ratios for swell-stress curve for large column

Layer	$\Delta e_{125\ psf}$	$\Delta e_{1000\ psf}$	γ_d Correction	ω Correction	$\Delta e_{c\ 125\ psf}$	$\Delta e_{c\ 1000\ psf}$
1	0.095	0.026	-0.060	0.012	0.046	-0.022
2	0.095	0.026	-0.059	0.013	0.048	-0.021
3	0.052	0.022	-0.052	0.017	0.016	-0.013
4	0.068	0.018	-0.064	0.001	0.005	-0.044
5	0.068	0.020	-0.083	0.009	-0.006	-0.054

The most significant corrections of the test results were due to the differences in the initial dry unit weight between the large column and the soil specimens used for the centrifuge-based method. The in-situ dry unit weight is an important variable for the correction and prediction of heave in expansive soil deposits and large-scale tests that should be accurately measured. Using the correction of the test data, the original and corrected vertical strain at the two stresses, along with the corrected A and B fitting parameters from Equation 7.1, are shown in Table 7.9.

Table 7.9: Corrected swell results and stress-swell curve for large column

Layer	ε_v 125 psf	ε_v 1000 psf	$\varepsilon_{v,c}$ 125 psf	$\varepsilon_{v,c}$ 1000 psf	A_c	B_c
1	9.5%	2.6%	1.9%	-0.9%	-1.7E-02	3.6%
2	9.5%	2.6%	2.0%	-0.9%	-1.7E-02	3.7%
3	5.2%	2.2%	0.7%	-0.5%	-7.3E-03	1.4%
4	6.8%	1.8%	0.3%	-2.1%	-1.4E-02	1.6%
5	6.8%	2.0%	-0.3%	-2.4%	-1.3E-02	1.0%

The vertical strains are reduced due to the correction for all layers. Based on the corrected data, the deepest two layers are expected to compress upon wetting. To visualize the

effect of these corrections on the stress-strain curves, the corrected and original stress-strain curves are shown in Figure 7.10 for Layers 1 and 2, in Figure 7.11 for Layer 3, in Figure 7.12 for Layer 4, and in Figure 7.13 Layer 5. The uncorrected stress-swell curves were generated from centrifuge test results that were previously shown in Section 6.3.2.

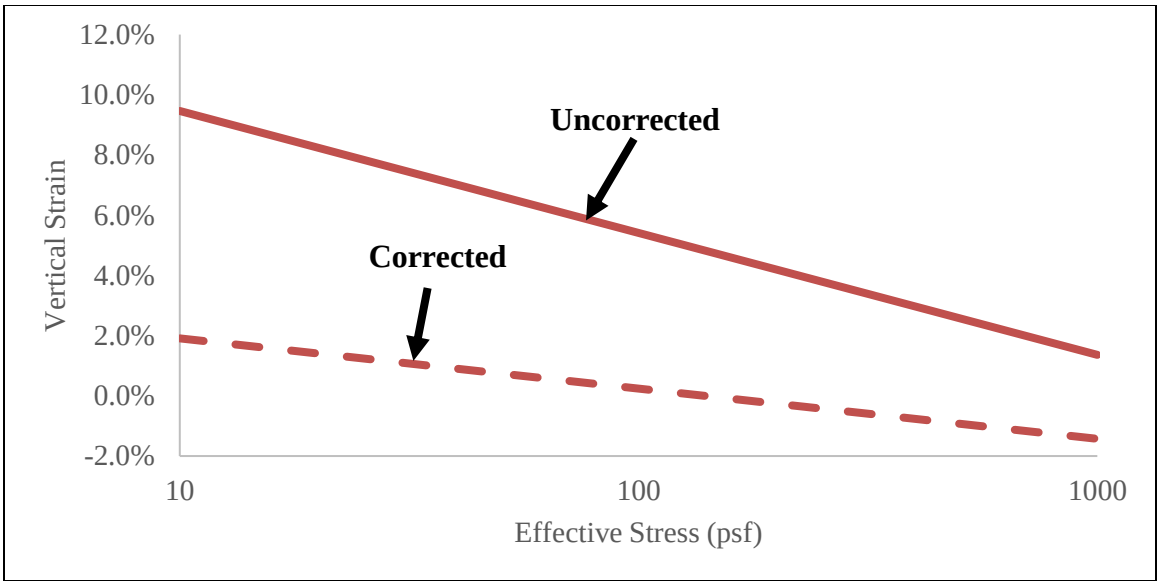

Figure 7.10: Original and corrected stress-swell curves for Layers 1 and 2 in the large column test

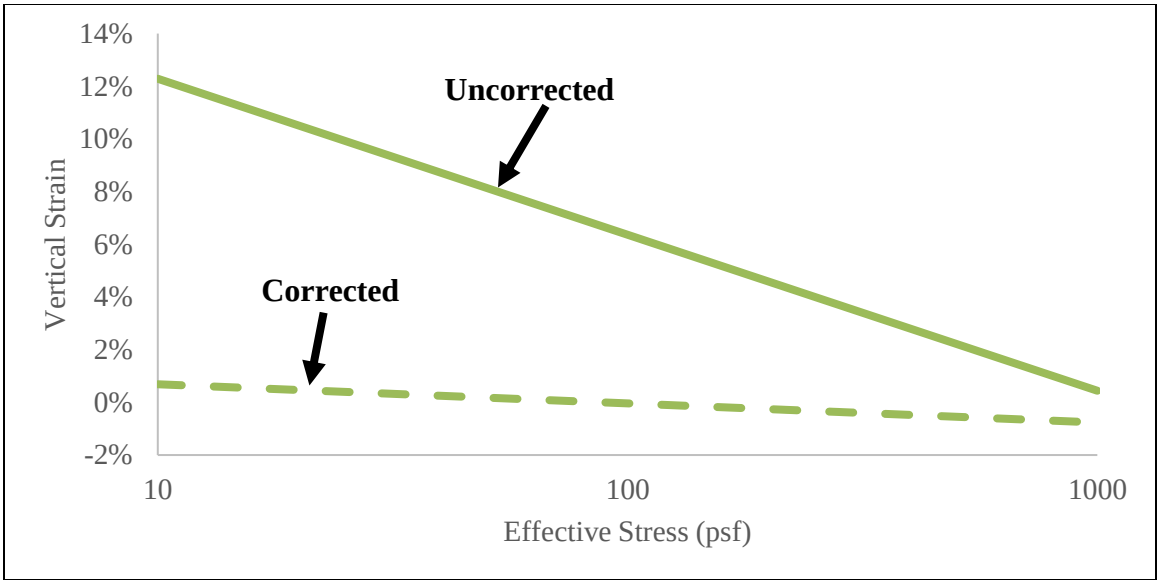

Figure 7.11: Original and corrected stress-swell curves for Layer 3 in the large column test

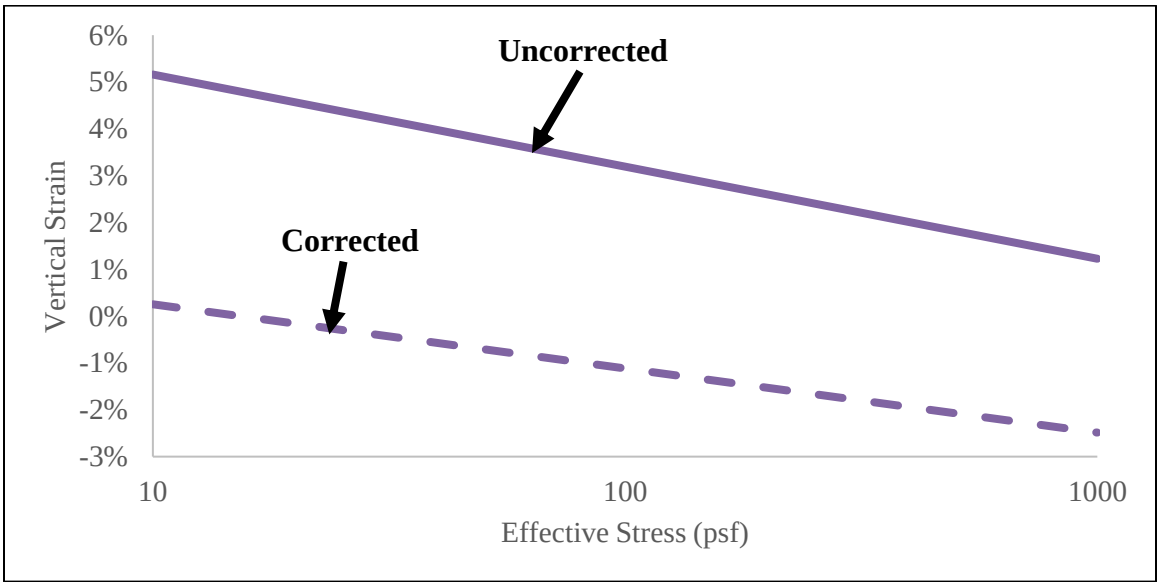

Figure 7.12: Original and corrected stress-swell curves for Layer 4 in the large column test

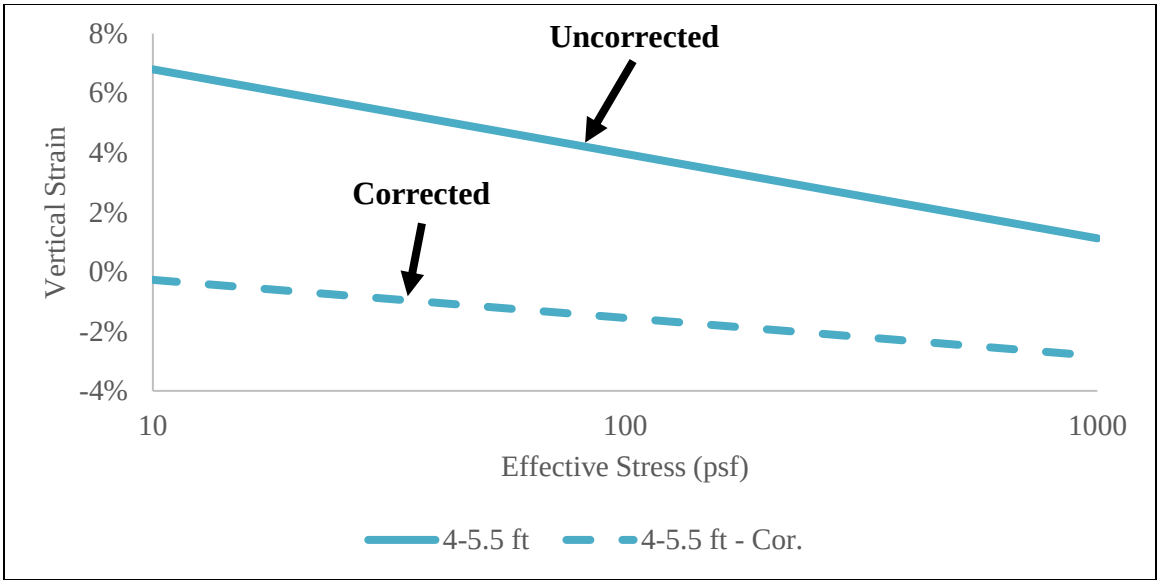

Figure 7.13: Original and corrected stress-swell curves for Layer 5 in the large column test

A potential vertical rise can be calculated for each soil layer using these corrected stress-swell curves and estimated effective stresses using the method outlined in Section 7.3.1. These stresses, corresponding vertical strains, and potential vertical rise for each layer are shown in Table 7.10.

Table 7.10: Calculation of corrected potential vertical rise for large column

Soil Layer	Depth (cm)	σ'_t (psf)	σ'_b (psf)	σ'_{avg} (psf)	$\varepsilon_{v,average}$	PVR (mm)
1	10	1	31	6	2.3%	5.69
2	34	31	63	44	0.9%	2.26
3	59	63	93	77	0.0%	0.11
4	83	93	125	108	-1.2%	-2.84
5	108	125	161	142	-1.7%	-4.48

The corrected laboratory-predicted vertical rise of the column was approximately 0.74 mm. This compares to the 1.36 mm of heave that was measured using image analysis techniques on images from the full column, 0.5 mm of heave was measured using image

analysis techniques on images from the top of the column, and the original laboratory-predicted vertical rise of 5.28 cm. This original laboratory-predicted vertical rise was calculated by using the results from centrifuge soil specimens at the centrifuge conditions in Table 7.7. Therefore, when using the actual initial soil conditions, the prediction of the vertical rise is improved.

The predicted vertical rise in each layer can additionally be compared to the vertical rise in each layer from image analysis. The vertical rise from image analysis was performed by tracking the heave at the top of each of the compacted layers and subtracting the contribution of the lower compacted soil layers. The vertical rise in each sublayer at various times during the inundation test is shown in Table 7.11.

Table 7.11: Heave (mm) of soil layers for large column test at various times

Soil Layer	Layer Mid-Depth (cm)	Heave (mm)		
		Time		
		45 minutes	255 minutes	700 minutes
1	10	0.715	0.760	0.868
2	34	0.438	0.581	0.643
3	59	0.383	0.038	0.218
4	83	0.023	-0.100	-0.005
5	108	-1.058	-0.721	-0.910

This analysis indicates that the predicted behavior from the corrected stress-swell curves (Table 7.10) were similar to actual behavior of the compacted soil layers shown (Table 7.11). Layers 4 and 5 both experienced compression while Layers 1 and 2 experienced swelling. Differences in the magnitude of the swelling were attributed to using correction factors from a different soil series and volumetric strains in the soil column due to the low relative compaction. Overall, the centrifuge method can better predict the vertical heave of a deposit with known initial conditions.

7.4 CONCLUSIONS

Results from each of the individual research components can be applied to various geotechnical problems. The potential vertical rise of an expansive soil can be predicted using a stress-curve defined using centrifuge tests. The stress-swell curves can be corrected based on differing initial conditions than the conditions that the centrifuge specimens were tested at. These corrections are based on initial soil conditions, that is, the initial gravimetric moisture content and dry unit weight. After the potential vertical rise is determined, the predicted maximum heave in the field can be estimated by accounting for volumetric strains that are not measured in centrifuge tests. Overall, results from this dissertation are suitable for used in practical engineering problems.

Chapter 8: Conclusions and Recommendations

Expansive soils are problematic for a wide range of engineering projects due to their potential to undergo significant volumetric changes upon seasonal moisture fluctuations. While a significant amount of research has been performed on laboratory-reconstituted soils specimens, additional research was necessary to examine field behavior of expansive soil deposits in Central Texas and its relationship to laboratory test results. Due to volumetric strains, desiccation cracks, and seasonal moisture fluctuations, the heave in the field can differ from the predictions using laboratory-reconstituted soil specimens. This dissertation focused on the characterization of expansive soils using laboratory techniques, in particular a centrifuge-based inundation test, and field monitoring of moisture fluctuations and corresponding changes in vertical displacements. The laboratory testing program analyzed the effects of various conditions on the swelling behavior of laboratory tested soil specimens. These effects include the effect of initial soil conditions (i.e. the initial gravimetric moisture content and dry unit weight), the effect of soil fabric, and the effect of centrifugation. Additionally, the laboratory testing program examined the spatial heterogeneity on a local and regional scale of two expansive soils located throughout Central Texas and analyzed a large column infiltration test that was prepared to represent an expansive soil deposit. The field monitoring program monitored moisture and suction fluctuations and the vertical displacements of an expansive soil deposit beneath a pavement structure. Results from monitoring were compared against predictions using laboratory test results to more accurately predict the field behavior of expansive soils.

8.1 CONCLUSIONS

This dissertation characterized expansive soil behavior using both laboratory and field techniques. The research was grouped into five self-contained research components; the effect of initial conditions on swelling characteristics of expansive soils in a centrifuge environment, the effect of soil fabric on the swelling characteristics of laboratory-reconstituted and field-sampled specimens, the spatial heterogeneity at a local and regional scale of two common expansive soils in Central Texas, the field behavior of an expansive soil deposit beneath a pavement structure undergoing seasonal moisture fluctuations, and the analysis of a large column infiltration test prepared to represent an expansive soil deposit. Conclusions from each of the self-contained studies are included at the end of each chapter. An additional chapter that synthesizes the results from the self-contained research components is included in order to better predict the heave of field deposits for future studies. A summary for the conclusions from each of the topics is presented as follows.

The effects of the initial soil conditions and centrifugation on the swelling characteristics of expansive soils were evaluated using a centrifuge-based inundation test. The evaluated variables included the initial gravimetric moisture content, initial dry unit weight, initial degree of saturation, gravitational level, and soil specimen height. Based on these tests, the following conclusions can be made:

- The vertical strain at the end of primary swelling was found to increase linearly with decreasing gravimetric moisture content and increasing dry unit weight.
- These trends are consistent with those reported by previous studies, indicating that the centrifugation methodology can be used to evaluate expansive soils.

- The effect of the degree of saturation was found to be highly non-linear. This result indicates that a single variable is not suitable to evaluate the effect of initial soil conditions on swelling characteristics.
- The vertical strain at the end of primary swelling was found to decrease with increasing gravitational level. Additionally, the time to the end of primary and final swelling was found to decrease with increasing gravitational level.
- The time to the end of primary and final swelling was found to increase with increasing specimen height. However, the vertical strains at the end of testing were not affected by increasing specimen height.

The effect of the internal clay structure, or soil fabric, on the swelling characteristics of expansive soils was evaluated with two testing series. The first testing series analyzed laboratory-reconstituted soil specimens with either a comparatively flocculated or a comparatively dispersed structure. The second testing series analyzed either laboratory-reconstituted or field-sampled soil specimens. Additionally, electron microscopy was used to visualize the soil fabric of laboratory-reconstituted and field-sampled soil specimens. Based on these tests, the following conclusions can be made:

- Soil fabric of laboratory-reconstituted soil specimens primarily affects the duration of primary swelling. The time period to reach the end of primary swelling is higher for specimens with a comparatively dispersed structure than specimens with a comparatively flocculated structure.
- The vertical strains at the end of primary swelling tends to be higher for field-sampled specimens than for laboratory-reconstituted specimens. These differing trends are attributed to the field-sampled specimens having a higher amount of micro-voids, peds, and clusters than laboratory-

reconstituted specimens based on the micrographs from electron microscopy.

- Via the use of an environmental scanning electron microscope, the soil fabric of laboratory-reconstituted soil specimens was observed to change significantly after the first wetting and drying cycle.

Over the course of a project for the Texas Department of Transportation and outlined in Zornberg et al. (2017), numerous roadways in Central Texas that had potentially expansive subgrades were sampled in bulk and characterized for their soil properties and swelling characteristics. Additionally, a six mile stretch along a highway in Central Texas was heavily sampled using Shelby tube samples and characterized for its soil properties and swelling characteristics. Soils were grouped into either the Branyon clay or the Houston Black clay based on NRCS soil surveys. Based on the soil properties, soil-water retention curves generated from suction measurements, and stress-swell curves defined using results from centrifuge-based swelling tests of each site, the following conclusions can be made:

- The Houston Black clay tends to have a higher Plasticity Index and a higher percentage of fines than the Branyon clay.
- For unsaturated characteristics, the Houston Black clay tends to swell more than the Branyon clay. However, the soil-water retention curves are similar between the two soils.
- The potential vertical rise of the expansive subgrades determined from the centrifuge swelling tests is higher than the potential vertical rise from traditional methodologies (i.e. Tex-124-E).
- The variability of the Atterberg Limits of clays from the same soil series is similar at a regional and local scale.

- However, the variability of the potential vertical rise differed between the bulk sampled soils and the Shelby tube sampled soils, with the Shelby tube samples tending to have a higher magnitude of swelling. This difference was attributed to the removal of micro-void features during the preparation of laboratory-reconstituted specimens.

A field site was instrumented and monitored for moisture and suction fluctuations in an expansive soil subgrade beneath a pavement structure. The surface of the roadway was additionally monitored during periodic site visits. Monitoring was grouped into two time periods during the construction process; one occurred while the subgrade was beneath a temporary flexible base, and the other occurred while the subgrade was beneath the final asphalt pavement. Based on monitoring of the site beneath the pavement structure, the following conclusions can be made:

- The expansive soil subgrade was able to wet rapidly and dry significantly during seasonal moisture fluctuations for both time periods.
- The subgrade beneath the flexible base surface was wetted more significantly under low intensity rainfall events than the subgrade beneath the asphalt surface.
- Drying occurred over a longer timeframe for the subgrade beneath the asphalt surface than for the subgrade beneath the flexible base surface.
- Expansive soil in the field can dry out to a lower volumetric moisture content than the “dry” moisture condition tested in centrifuge-based swelling tests.
- The fitted soil-water retention curve did not vary significantly with depth in the expansive soil deposit.

- The settlement and heave of the pavement profile depends on the moisture history and not the absolute value of the volumetric moisture content.
- The magnitude of the heave after a significant rainfall event was less than the laboratory-predicted vertical rise from centrifuge-based swelling tests.

A large column test was instrumented to evaluate the large-scale swelling behavior of an expansive soil deposit in a laboratory environment. The column consisted of expansive soils collected in bulk from a field deposit in order to replicate the stratigraphy of a field site. The soil in the column was prepared at a dry moisture condition to be consistent with the centrifuge-based swelling tests. The infiltration of moisture into the column was monitored using moisture content sensors. Vertical displacements were determined using image analysis techniques. Results from the large column were compared against those from the previous field site. Additionally, two methods to measure suction, the filter paper and chilled mirror hygrometer methodologies, were compared using the soils collected for the large column test. Based on these studies, the following conclusions can be made:

- The moisture front advanced over a longer time frame in the large column than at the field site. This difference was attributed to desiccation cracking at the field site that are not easily replicable in a laboratory environment.
- The trends of the vertical displacement of soil layers were consistent with the predicted behavior of the large column from centrifuge tests. Soil layers that were predicted to heave did experience swelling in the column, and soil layers that were predicted to compress did experience compression in the column.

- Soil-water retention curves generated using filter paper measurements were similar to those generated using chilled mirror hygrometer measurements for suctions greater than 1,000 kPa.
- The osmotic suction was found to be relatively constant for soils sampled deeper than 3 ft below the ground surface. However, the osmotic suction was found to vary with moisture content for soils sampled near the ground surface.

Chapter 7 presents a synthesis of the results from the dissertation into how to apply the results and conclusions from this dissertation into practice. Correction of laboratory data based on varying initial conditions and proposed techniques to determine the actual heave in the field were presented. Additionally, the chapter presents two scenarios from this dissertation where corrected swelling results were used for the prediction of the vertical rise for the field site and large column test. The prediction of the vertical rise was more consistent with the results from the large-scale tests when the initial dry unit weight was known with remaining discrepancies being attributed to volumetric strains.

8.2 Recommendations for Future Research

This dissertation focused on methods to characterize expansive soil behavior, including both laboratory and field methods. Test results indicated that future studies are needed to further understand expansive soil behavior, particularly the magnitude of heave and settlement that occur during seasonal moisture fluctuations. These recommendations for future research can be grouped into studies either using laboratory experimental methods or field monitoring techniques.

The use of the centrifuge-based inundation method to analyze the one-dimensional swelling of expansive soils can be further expanded in order to characterize the treatment of expansive soils. Treatments of these soils, including the mixing of additives such as lime and fly ash, can be rapidly characterized using the centrifuge-based method by comparing the reduction in swelling as a function of the increase in the additive. These results can then be used in adjusted stress-swell curves and potential vertical rise analyses in order to evaluate the effectiveness of the technique. Additionally, the centrifuge-based method can be improved by adjusting the addition of moisture to soil specimens during the test. Future work should address the addition of moisture in the permeameter cups, possibly by the use of a smaller rotary joint similar to the one used in the CPUS (Kuhn, 2010) or by the use of a surrounding water reservoir and a wirelessly controlled valve. Finally, the undisturbed soil specimens from Chapters 3 and 4 were collected from Shelby tube sampled borings that were extruded in the field. A future field study is needed to evaluate the difference in the swelling characteristics between laboratory and field extruded specimens. An additional aspect of this study should examine the effect of the removal of the in-situ overburden stress from field specimens on the swelling characteristics of field deposits.

The results from Chapter 7 indicate that further work is needed to correct laboratory test results in order to improve the laboratory-predicted potential vertical rise. An analysis of how linear corrections vary with the effective specimen stress is needed for both the corrections of the initial gravimetric moisture content and dry unit weight. Additionally, the monitoring of additional field sites and large-scale laboratory experiments are needed to correct the laboratory-predicted potential vertical rise to the field behavior of expansive soil deposits. Other corrections that should be quantified include the effect of the soil fabric by evaluating additional sites with both laboratory-

reconstituted and field-sampled soil specimens, the geochemical effects based on differences in the chemistry of rainwater, and quantifying the risk and variability of soil series in a similar geographic region.

Additionally, laboratory methods that characterize soils should be more widely used in conjunction with centrifuge-based inundation tests. This dissertation utilized chilled mirror hygrometer tests to characterize the initial soil total suction comparatively faster than methods to measure the initial soil matric suction. Future testing programs should measure the initial soil total suction in order to characterize heterogeneity between laboratory-reconstituted and field-sampled soil specimens. Additionally, further work based on Quaglia (2017) and column testing should be used to evaluate changes in the volumetric moisture content with corresponding heave or compression of expansive soil specimens. Tests that are able to measure the volumetric moisture content during the swelling process should be used to predict the heave in the field for deposits that are not fully saturated during rainfall events.

Based on the results from the field site, modern sensors are suitable for monitoring of seasonal moisture content and suction fluctuations and corresponding surficial deflections. These sensors and techniques are highly recommended for future roadway projects to further evaluate moisture and suction fluctuations beneath the shoulder of pavement structures. The installation of these sensors has been shown to be relatively easy along excavated portions of the subgrade, and the resulting data is important to predict the potential vertical rises and changes in resilient moduli in clay deposits. Additionally, these sensors can be used to evaluate the depth of the active zone and its geospatial variability. Field sites beneath pavement or foundation structures should be instrumented to a suitable depth (i.e. to the groundwater table) to evaluate the depth of the active zone. Additionally, to quantify how significant drying occurs beneath

the pavement structures, a field site instrumented beneath the full width of the roadway is recommended to determine the extent of moisture fluctuations in the soil deposit. These field sites should incorporate the use of the total station methodology to monitor pavement deflections in order to correlate pavement performance with moisture fluctuations. Results from monitoring of these field sites can be used to evaluate the effectiveness of other remediation techniques, including geogrid reinforcement of base and asphalt material and vertical moisture barriers, and the effect of vegetation and trees.

Finally, the threshold potential vertical rise for pavement remediation and treatment should be further evaluated using results from the centrifuge-based inundation tests. The current guidelines use a specified threshold of the potential vertical rise to determine the remediation necessary based on evaluations using Tex-124-E. Studies are needed to analyze the pavement performance of newly constructed roads with the laboratory-predicted potential vertical rise. Monitoring of pavement performance should incorporate total station monitoring of surficial pavement deflections, condition surveys of environmental cracking at the shoulders of the roadways, and the original design and maintenance history of the instrumented roadway sections. Roadways that are founded on both expansive subgrades and moderately to non-expansive subgrades should be evaluated.

Appendices

APPENDIX A: ADDITIONAL FABRIC RESULTS FROM IH-10 TESTING

This appendix summarizes the additional results from the fabric analysis presented in Chapter 3 of this dissertation. The results include those from centrifuge-based swelling tests, which includes the swelling curves, initial soil conditions, test results, for the specimens from the IH-10 research project. These borings include those from borings B-31, B-32, B-35, and B-38. Additionally, the results used for the statistical analysis presented in Chapter 3 are presented.

A.1: Results from Boring B-31

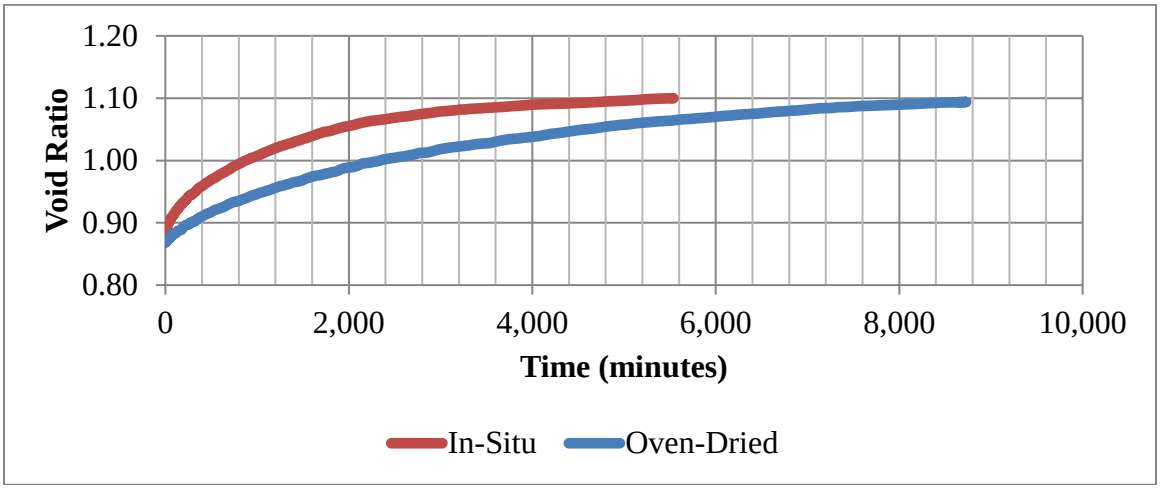

Figure A.1: Corrected swelling curves for boring B-31 from 0 to 2 ft under a gravitational level of approximately 44 g's

Table A.1: Testing conditions for samples for boring B-31 from 0 to 2 ft under a gravitational level of approximately 44 g's

		Uncorrected	Corrected
Condition	**In-Situ**	**Oven-Dried**	**Oven-Dried**
ω_i	30.9%	29.3%	29.3%
$y_{d,i}$ (kN/m^3)	14.16	14.39	14.16
Initial Sat.	0.96	0.94	0.91
e_i	0.872	0.840	0.872
e_f	1.074	1.057	1.093
e_{max}	1.100	1.058	1.094
Δe	0.203	0.216	0.221
$\varepsilon_{primary}$	10.8%	11.8%	11.8%
ε_{final}	12.2%	11.8%	11.9%
Time to ε_p	2788	8480	8480
ω_f	43.7%	43.8%	43.8%
y_f (kN/m^3)	18.35	18.52	18.19
θ_i	0.446	0.430	0.423
θ_f	0.524	0.514	0.522
Stress (psf)	391	415	415

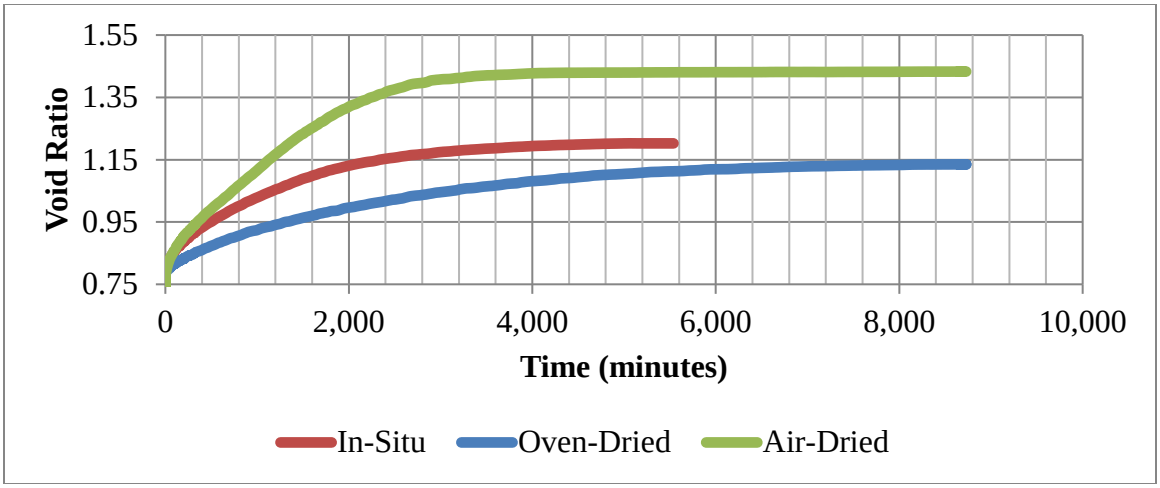

Figure A.2: Corrected swelling curves for boring B-31 from 2 to 4 ft under a gravitational level of approximately 44 g's

Table A.2: Testing conditions for samples for boring B-31 from 2 to 4 ft under a gravitational level of approximately 44 g's

		Uncorrected		Corrected	
Condition	**In-Situ**	**Air-Dried**	**Oven-Dried**	**Air-Dried**	**Oven-Dried**
ω_i	26.9%	27.4%	26.1%	27.4%	26.1%
$y_{d,i}$ (kN/m^3)	14.87	14.26	14.75	14.87	14.87
Initial Sat.	0.93	0.86	0.89	0.95	0.90
e_i	0.782	0.858	0.795	0.782	0.782
e_f	1.175	1.509	1.128	1.407	1.111
e_{max}	1.202	1.536	1.152	1.433	1.135
Δe	0.393	0.652	0.333	0.625	0.329
$\varepsilon_{primary}$	22.1%	35.1%	18.5%	35.1%	18.5%
ε_{final}	23.6%	36.5%	19.9%	36.6%	19.8%
Time to ε_p	3014	2981	5368	2981	5368
ω_f	46.4%	62.7%	47.2%	62.7%	47.2%
y_f (kN/m^3)	17.84	17.17	18.32	17.71	18.26
θ_i	0.408	0.398	0.392	0.415	0.395
θ_f	0.546	0.606	0.535	0.589	0.532
Stress (psf)	387	387	403	387	403

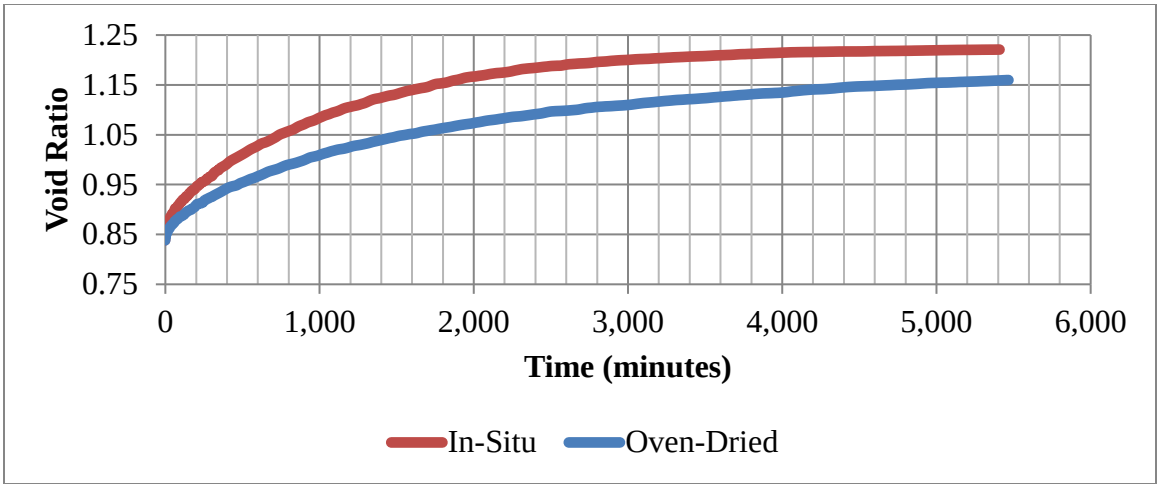

Figure A.3: Corrected swelling curves for boring B-31 from 2 to 4 ft under a gravitational level of approximately 66 g's

Table A.3: Testing conditions for samples for boring B-31 from 2 to 4 ft under a gravitational level of approximately 66 g's

		Uncorrected	Corrected
Condition	**In-Situ**	**Oven-Dried**	**Oven-Dried**
ω_i	28.6%	28.2%	28.2%
$y_{d,i}$ (kN/m^3)	14.41	14.74	14.41
Initial Sat.	0.92	0.96	0.91
e_i	0.838	0.797	0.838
e_f	1.202	1.095	1.146
e_{max}	1.221	1.108	1.160
Δe	0.364	0.299	0.308
$\varepsilon_{primary}$	19.8%	16.6%	16.7%
ε_{final}	20.8%	17.4%	17.5%
Time to ε_p	3092	4449	4449
ω_f	49.4%	46.4%	46.4%
y_f (kN/m^3)	17.98	18.50	17.95
θ_i	0.420	0.424	0.415
θ_f	0.550	0.526	0.537
Stress (psf)	583	524	524

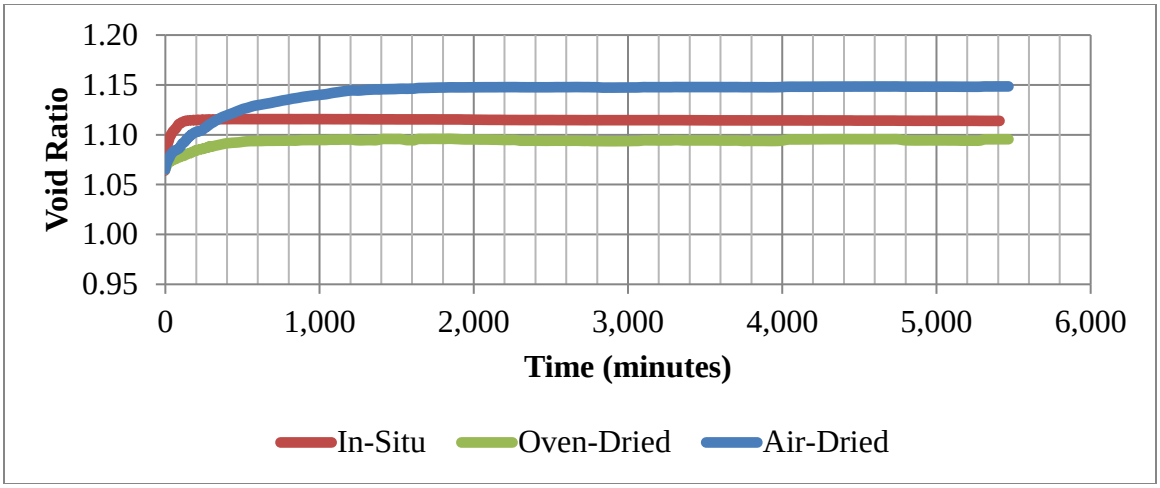

Figure A.4: Corrected swelling curves for boring B-31 from 4 to 6 ft under a gravitational level of approximately 66 g's

Table A.4: Testing conditions for samples for boring B-31 from 4 to 6 ft under a gravitational level of approximately 66 g's

		Uncorrected		Corrected	
Condition	**In-Situ**	**Air-Dried**	**Oven-Dried**	**Air-Dried**	**Oven-Dried**
ω_i	35.2%	33.2%	34.2%	33.2%	34.2%
$y_{d,i}$ (kN/m^3)	12.83	13.55	13.11	12.83	12.83
Initial Sat.	0.89	0.94	0.91	0.84	0.87
e_i	1.065	0.955	1.020	1.065	1.065
e_f	1.114	1.029	1.048	1.145	1.094
e_{max}	1.116	1.033	1.050	1.148	1.097
Δe	0.049	0.075	0.028	0.080	0.028
$\varepsilon_{primary}$	2.4%	3.8%	1.4%	3.9%	1.4%
ε_{final}	2.4%	4.0%	1.5%	4.0%	1.5%
Time to ε_p	140	1296	575	1296	575
ω_f	44.3%	42.7%	41.8%	42.7%	41.8%
y_f (kN/m^3)	18.08	18.62	18.34	17.59	17.91
θ_i	0.461	0.459	0.457	0.434	0.447
θ_f	0.527	0.508	0.512	0.535	0.523
Stress (psf)	591	520	531	520	531

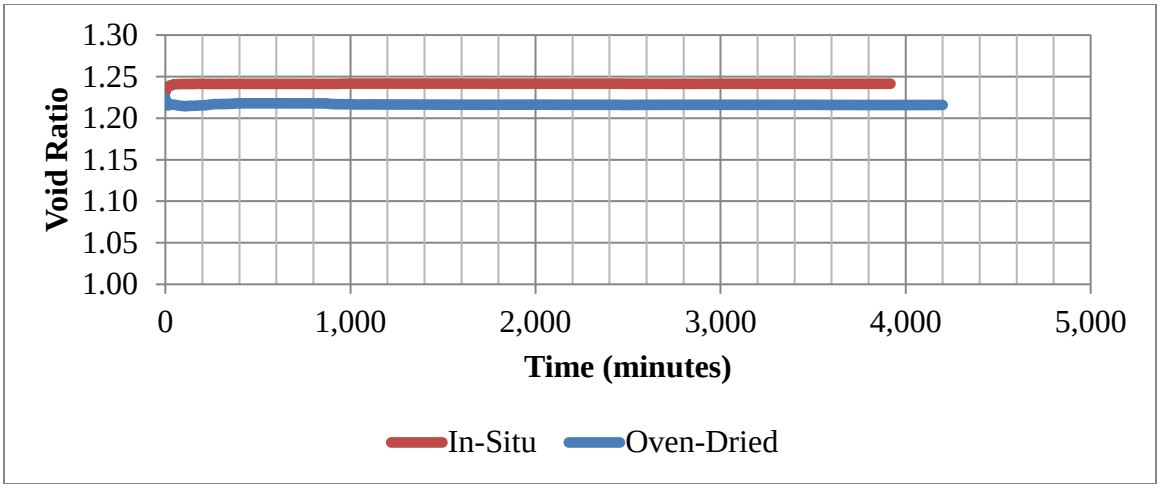

Figure A.5: Corrected swelling curves for boring B-31 from 4 to 6 ft under a gravitational level approximately 51 g's

Table A.5: Testing conditions for samples for boring B-31 from 4 to 6 ft under a gravitational level of approximately 51 g's

		Uncorrected	Corrected
Condition	**In-Situ**	**Oven-Dried**	**Oven-Dried**
ω_i	35.3%	36.4%	36.4%
$y_{d,i}$ (kN/m^3)	11.95	12.82	11.95
Initial Sat.	0.78	0.92	0.81
e_i	1.217	1.067	1.217
e_f	1.241	1.067	1.217
e_{max}	1.242	1.068	1.260
Δe	0.024	0.000	0.000
$\varepsilon_{primary}$	1.1%	0.0%	0.0%
ε_{final}	1.1%	0.1%	2.0%
Time to ε_p	52	266	266
ω_f	47.6%	41.6%	41.6%
y_f (kN/m^3)	17.45	18.15	16.59
θ_i	0.430	0.476	0.444
θ_f	0.554	0.516	0.558
Stress (psf)	825	852	852

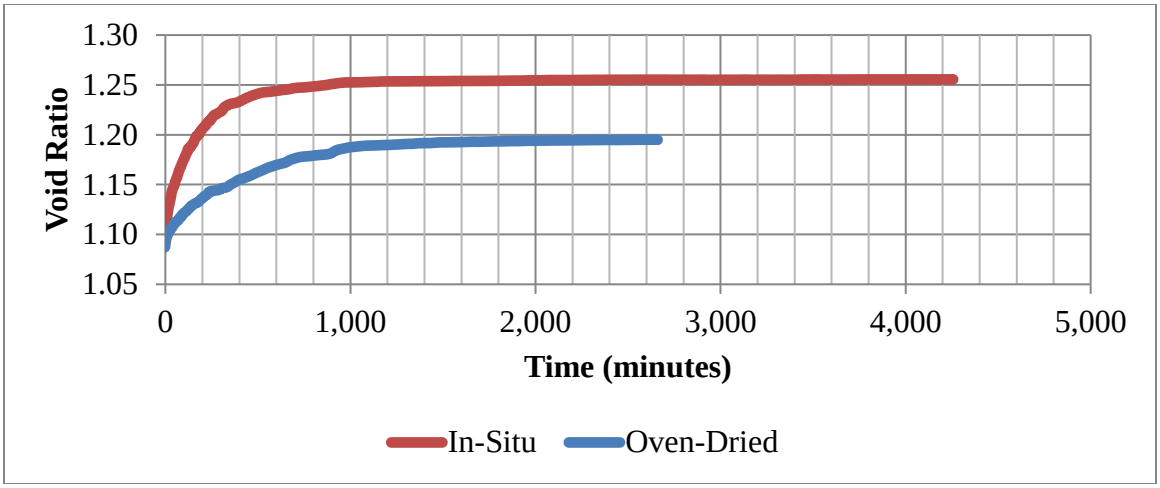

Figure A.6: Swelling curves for boring B-31 from 6 to 8 ft under a gravitational level of approximately 61 g's

Table A.6: Testing conditions for samples for boring B-31 from 6 to 8 ft under a gravitational level of approximately 61 g's

Condition	In-Situ	Oven-Dried
ω_i	30.9%	32.2%
$y_{d,i}$ (kN/m^3)	12.67	12.69
Initial Sat.	0.76	0.80
e_i	1.091	1.087
e_f	1.244	1.189
e_{max}	1.256	1.195
Δe	0.153	0.102
$\varepsilon_{primary}$	7.3%	4.9%
ε_{final}	7.9%	5.2%
Time to ε_p	591	1108
ω_f	49.4%	46.5%
y_f (kN/m^3)	17.65	17.72
θ_i	0.399	0.416
θ_f	0.557	0.544
Stress (psf)	876	892

A.2: Results from Boring B-32

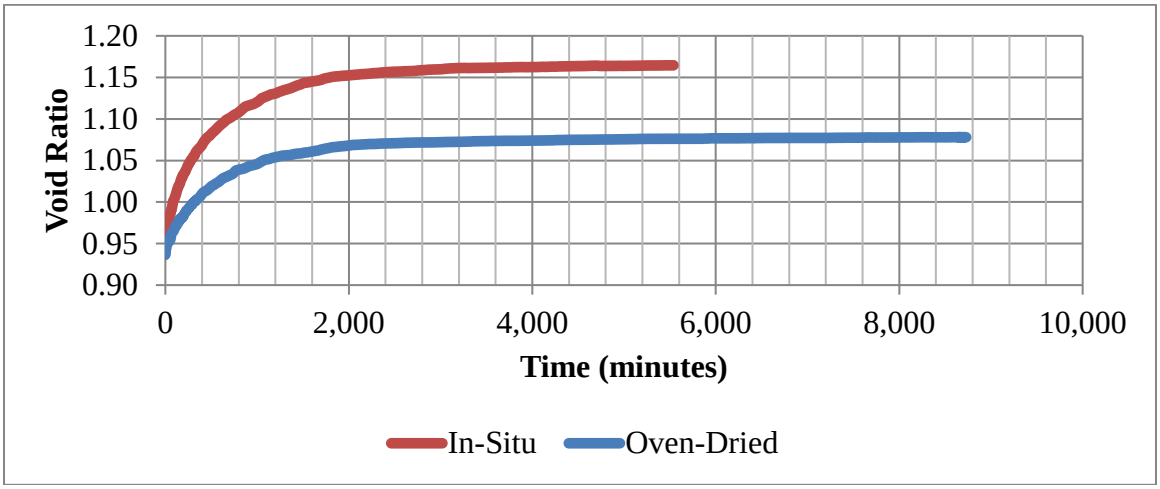

Figure A.7: Corrected swelling curves for boring B-32 from 0 to 2 ft under a gravitational level of approximately 44 g's

Table A.7: Testing conditions for samples for boring B-32 from 0 to 2 ft under a gravitational level of approximately 44 g's

		Uncorrected	Corrected
Condition	**In-Situ**	**Oven-Dried**	**Oven-Dried**
ω_i	28.4%	30.2%	30.2%
$\gamma_{d,i}$ (kN/m^3)	13.68	13.15	13.68
Initial Sat.	0.82	0.80	0.87
e_i	0.937	1.014	0.937
e_f	1.146	1.152	1.068
e_{max}	1.165	1.163	1.078
Δe	0.209	0.138	0.131
$\varepsilon_{primary}$	10.8%	6.8%	6.8%
ε_{final}	11.8%	7.4%	7.3%
Time to ε_p	1636	1989	1989
ω_f	46.1%	47.3%	47.3%
γ_f (kN/m^3)	18.04	18.13	18.77
θ_i	0.396	0.405	0.421
θ_f	0.538	0.538	0.519
Stress (psf)	380	391	391

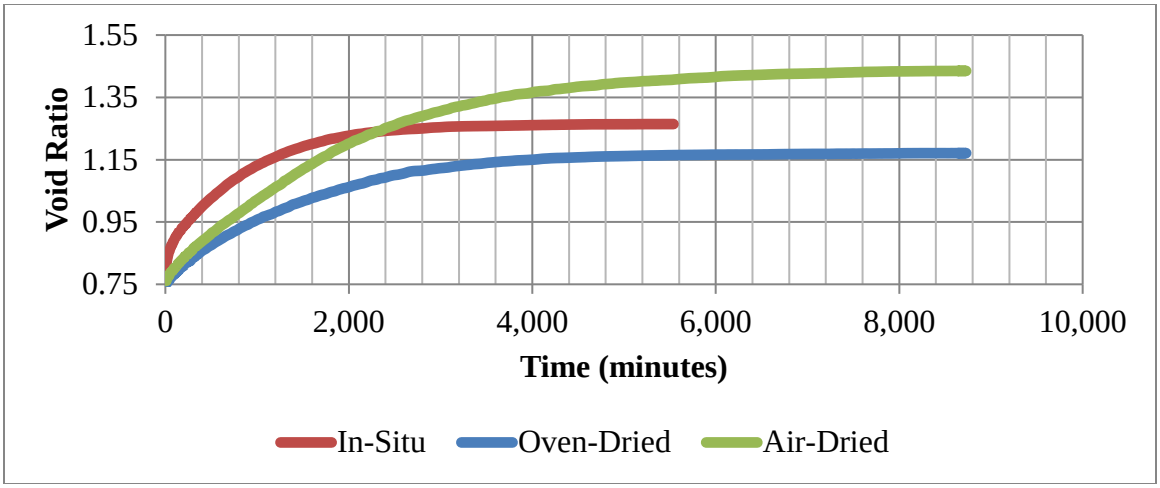

Figure A.8: Corrected swelling curves for boring B-32 from 2 to 4 ft under a gravitational level of approximately 44 g's

Table A.8: Testing conditions for samples for boring B-32 from 2 to 4 ft a gravitational level of approximately 44 g's

		Uncorrected		Corrected	
Condition	**In-Situ**	**Air-Dried**	**Oven-Dried**	**Air-Dried**	**Oven-Dried**
ω_i	24.8%	24.9%	23.4%	24.9%	23.4%
$y_{d,i}$ (kN/m^3)	14.97	14.90	15.08	14.97	14.97
Initial Sat.	0.87	0.87	0.83	0.87	0.82
e_i	0.770	0.778	0.757	0.770	0.770
e_f	1.246	1.431	1.143	1.420	1.160
e_{max}	1.264	1.446	1.154	1.435	1.171
Δe	0.476	0.653	0.387	0.650	0.390
$\varepsilon_{primary}$	26.9%	36.7%	22.0%	36.7%	22.0%
ε_{final}	27.9%	37.6%	22.6%	37.6%	22.7%
Time to ε_p	2562	6221	4747	6221	4747
ω_f	50.0%	59.7%	50.4%	59.7%	50.4%
y_f (kN/m^3)	17.69	17.41	18.59	17.38	18.35
θ_i	0.379	0.378	0.359	0.380	0.357
θ_f	0.558	0.591	0.536	0.589	0.539
Stress (psf)	377	393	406	393	406

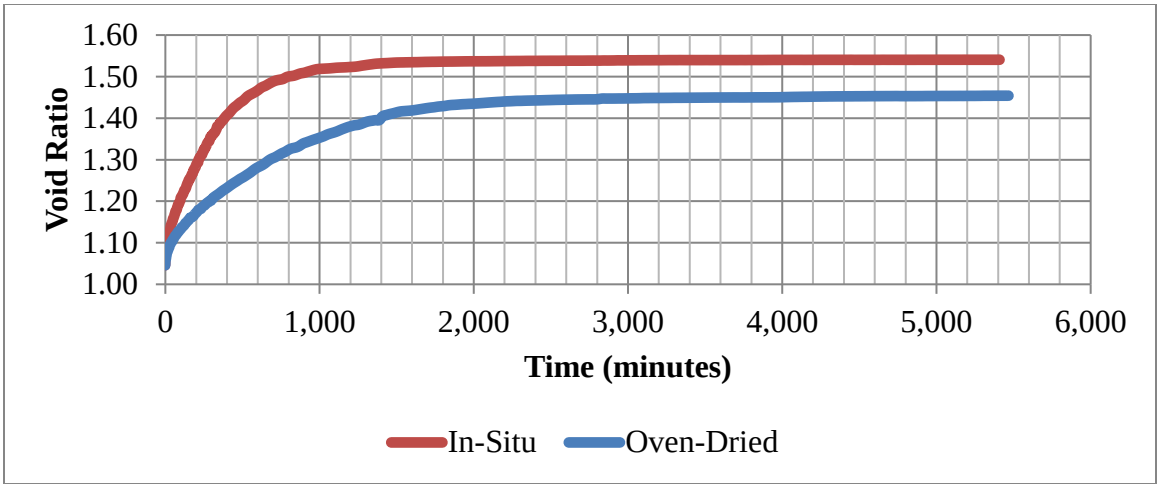

Figure A.9: Corrected swelling curves for boring B-32 from 2 to 4 ft under a gravitational level of approximately 66 g's

Table A.9: Testing conditions for samples for boring B-32 from 2 to 4 ft under a gravitational level of approximately 66 g's

		Uncorrected	Corrected
Condition	**In-Situ**	**Oven-Dried**	**Oven-Dried**
ω_i	33.7%	33.0%	33.0%
$y_{d,i}$ (kN/m^3)	12.95	12.81	12.95
Initial Sat.	0.87	0.83	0.85
e_i	1.046	1.068	1.046
e_f	1.518	1.456	1.431
e_{max}	1.541	1.480	1.454
Δe	0.472	0.389	0.385
$\varepsilon_{primary}$	23.1%	18.8%	18.8%
ε_{final}	24.2%	19.9%	20.0%
Time to ε_p	992	1834	1834
ω_f	62.3%	58.6%	58.6%
y_f (kN/m^3)	17.07	17.10	17.12
θ_i	0.445	0.431	0.435
θ_f	0.606	0.597	0.593
Stress (psf)	553	524	524

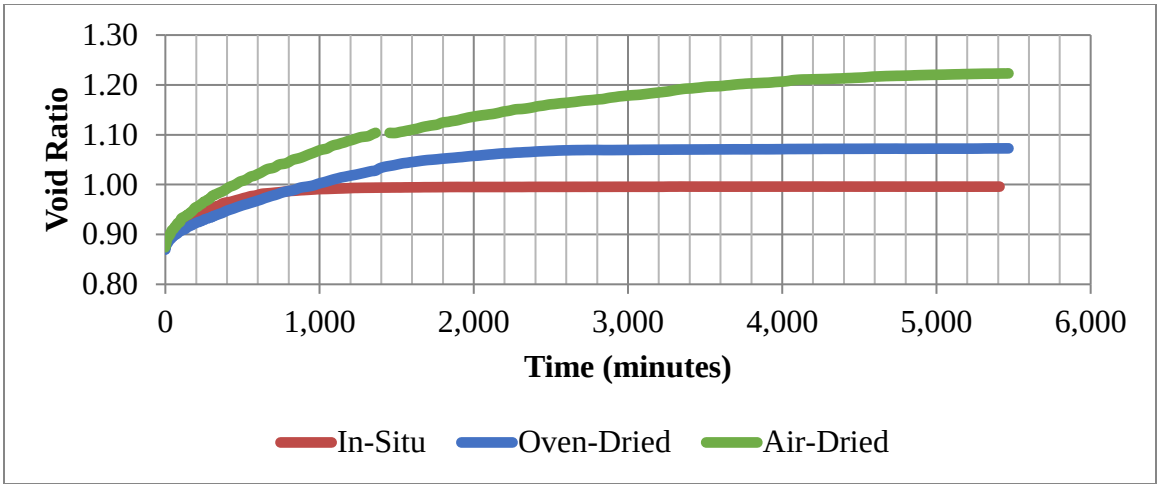

Figure A.10: Corrected swelling curves for boring B-32 from 4 to 6 ft under a gravitational level of approximately 66 g's

Table A.10: Testing conditions for samples for boring B-32 from 4 to 6 ft under a gravitational level of approximately 66 g's

		Uncorrected		Corrected	
Condition	**In-Situ**	**Air-Dried**	**Oven-Dried**	**Air-Dried**	**Oven-Dried**
ω_i	25.1%	26.4%	23.5%	26.4%	23.5%
$y_{d,i}$ (kN/m^3)	14.14	14.10	14.56	14.14	14.14
Initial Sat.	0.77	0.81	0.78	0.82	0.73
e_i	0.874	0.878	0.819	0.874	0.874
e_f	0.990	1.206	1.005	1.201	1.068
e_{max}	0.996	1.228	1.010	1.223	1.073
Δe	0.116	0.328	0.186	0.327	0.194
$\varepsilon_{primary}$	6.2%	17.4%	10.2%	17.4%	10.3%
ε_{final}	6.5%	18.6%	10.5%	18.6%	10.6%
Time to ε_p	946	3704	2519	3704	2519
ω_f	40.2%	50.3%	40.0%	50.3%	40.0%
y_f (kN/m^3)	18.67	18.05	18.49	17.90	17.89
θ_i	0.361	0.380	0.349	0.380	0.339
θ_f	0.499	0.551	0.502	0.550	0.518
Stress (psf)	595	514	530	514	530

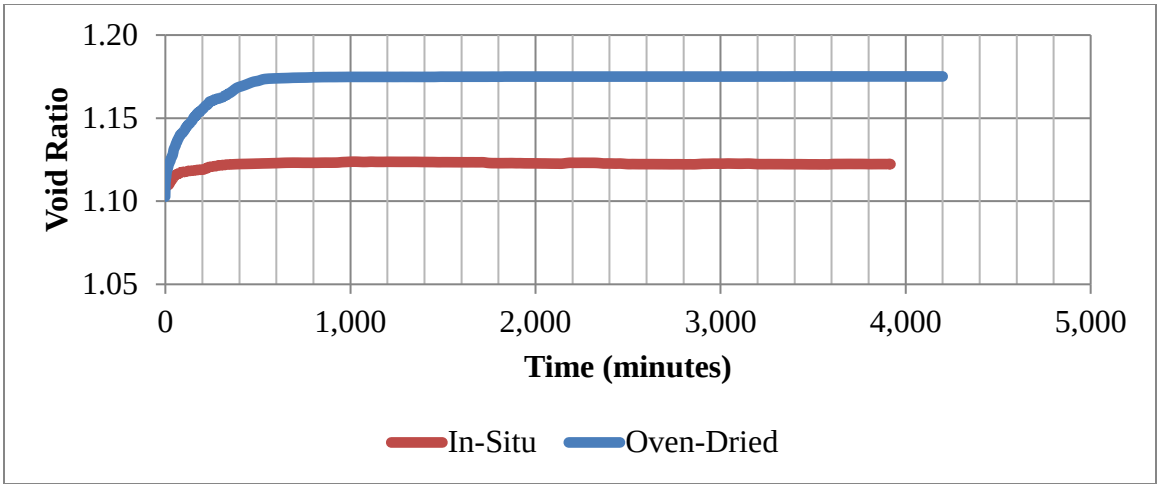

Figure A.11: Corrected swelling curves for boring B-32 from 4 to 6 ft under a gravitational level of approximately 51 g's

Table A.11: Testing conditions for samples for boring B-32 from 4 to 6 ft under a gravitational level of approximately 51 g's

		Uncorrected	Corrected
Condition	**In-Situ**	**Oven-Dried**	**Oven-Dried**
ω_i	23.7%	24.9%	24.9%
$y_{d,i}$ (kN/m^3)	12.60	12.62	12.60
Initial Sat.	0.58	0.61	0.61
e_i	1.103	1.098	1.103
e_f	1.122	1.169	1.174
e_{max}	1.124	1.171	1.175
Δe	0.019	0.071	0.071
$\varepsilon_{primary}$	0.9%	3.4%	3.4%
ε_{final}	1.0%	3.4%	3.4%
Time to ε_p	320	549	549
ω_f	41.2%	42.8%	42.8%
y_f (kN/m^3)	17.63	17.44	17.39
θ_i	0.304	0.320	0.319
θ_f	0.529	0.539	0.540
Stress (psf)	826	837	837

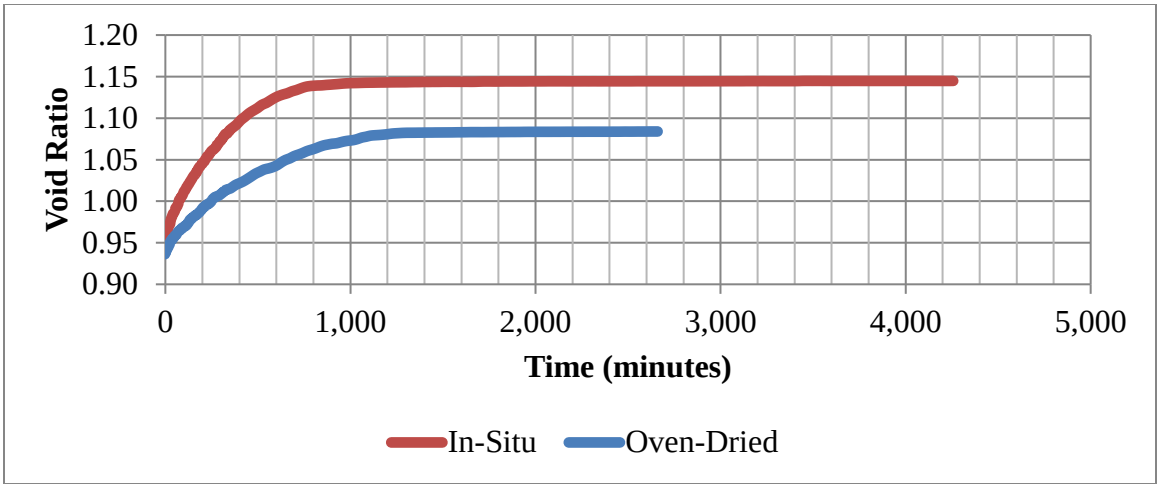

Figure A.12: Swelling curves for boring B-32 from 6 to 8 ft under a gravitational level of approximately 61 g's

Table A.12: Testing conditions for samples for boring B-32 from 6 to 8 ft under a gravitational level of approximately 61 g's

Condition	In-Situ	Oven-Dried
ω_i	22.2%	21.5%
$y_{d,i}$ (kN/m^3)	13.60	13.68
Initial Sat.	0.63	0.62
e_i	0.949	0.936
e_f	1.141	1.082
e_{max}	1.145	1.084
Δe	0.192	0.146
$\varepsilon_{primary}$	9.8%	7.5%
ε_{final}	10.1%	7.6%
Time to ε_p	914	1247
ω_f	44.3%	41.6%
y_f (kN/m^3)	17.86	18.02
θ_i	0.308	0.300
θ_f	0.534	0.520
Stress (psf)	884	894

A.3: Results from Additional Borings

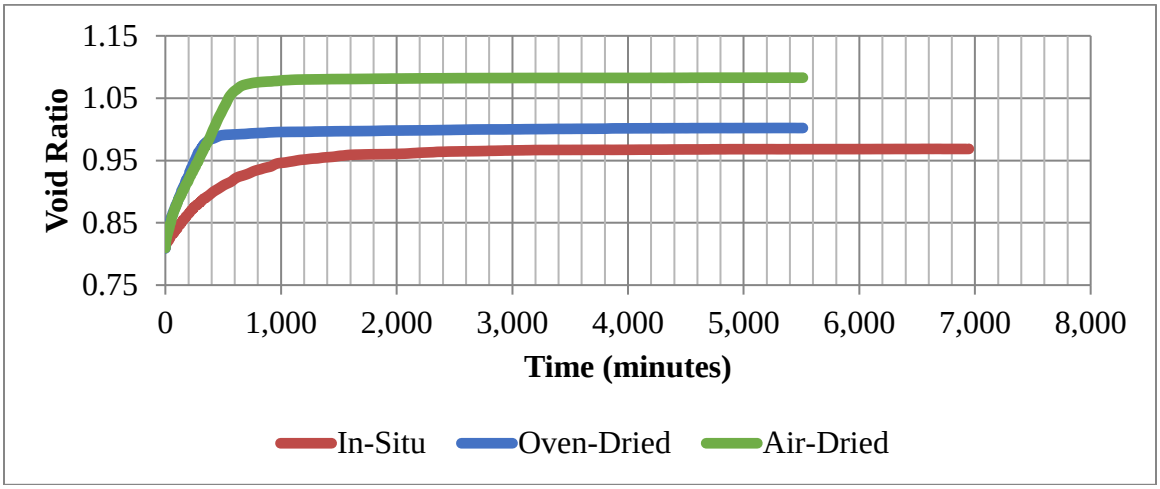

Figure A.13: Corrected swelling curves for boring B-35 from 0 to 2 ft under a gravitational level of approximately 22 g's

Table A.13: Testing conditions for samples for boring B-35 from 0 to 2 ft under a gravitational level of approximately 22 g's

		Uncorrected		Corrected	
Condition	**In-Situ**	**Air-Dried**	**Oven-Dried**	**Air-Dried**	**Oven-Dried**
ω_i	18.1%	16.6%	17.3%	16.6%	17.3%
$y_{d,i}$ (kN/m^3)	14.64	14.87	14.82	14.64	14.64
Initial Sat.	0.60	0.57	0.59	0.55	0.58
e_i	0.809	0.782	0.788	0.809	0.809
e_f	0.959	1.043	0.967	1.076	0.991
e_{max}	0.969	1.050	0.977	1.083	1.002
Δe	0.150	0.261	0.179	0.267	0.182
$\varepsilon_{primary}$	8.3%	14.7%	10.0%	14.7%	10.1%
ε_{final}	8.8%	15.0%	10.6%	15.1%	10.6%
Time to ε_p	1654	848	548	848	548
ω_f	36.0%	41.0%	37.5%	41.0%	37.5%
y_f (kN/m^3)	18.39	18.28	18.52	17.93	18.19
θ_i	0.270	0.252	0.262	0.248	0.259
θ_f	0.492	0.512	0.494	0.520	0.501
Stress (psf)	197	192	192	192	192

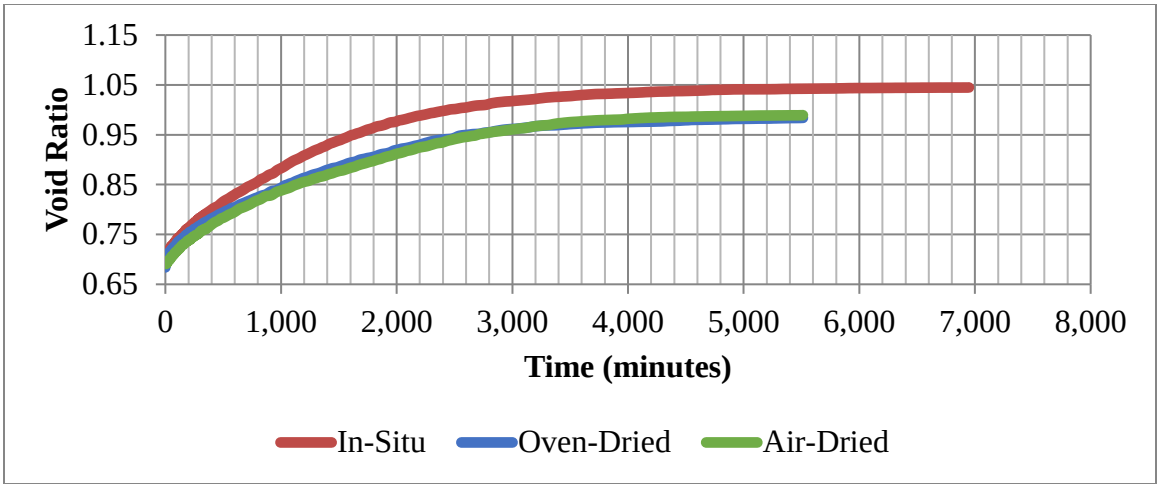

Figure A.14: Corrected swelling curves for boring B-38 from 0 to 2 ft under a gravitational level of approximately 22 g's

Table A.14: Testing conditions for samples for boring B-38 from 0 to 2 ft under a gravitational level of approximately 22 g's

		Uncorrected		Corrected
Condition	**In-Situ**	**Air-Dried**	**Oven-Dried**	**Air-Dried**
ω_i	20.8%	19.3%	20.0%	19.3%
$y_{d,i}$ (kN/m^3)	15.63	15.95	15.64	15.63
Initial Sat.	0.81	0.79	0.78	0.75
e_i	0.695	0.662	0.694	0.695
e_f	1.027	0.942	0.971	0.985
e_{max}	1.045	0.946	0.984	0.989
Δe	0.332	0.281	0.277	0.290
$\varepsilon_{primary}$	19.6%	16.9%	16.4%	17.1%
ε_{final}	20.6%	17.1%	17.1%	17.4%
Time to ε_p	3440	4289	3510	4289
ω_f	40.4%	38.4%	37.6%	38.4%
y_f (kN/m^3)	18.35	18.88	18.50	18.43
θ_i	0.332	0.314	0.318	0.308
θ_f	0.511	0.486	0.496	0.497
Stress (psf)	198	196	197	196

A.4: Comparison Between In-Situ and Reconstituted Specimens

Table A.15: Differences between field-sampled and laboratory-reconstituted specimens

				Difference between Result and In-Situ Specimen								
Boring	Depth	g's	Condition	e_p	de_p	e_{max}	de_{max}	ε_p	ε_f	Time to End of Primary (min)	θ_f	$d\theta$
B-31	0-2	22	AD	-0.223	-0.187	-0.215	-0.179	-9.7%	-9.2%	-468	-0.048	0.005
			OD	-0.146	-0.108	-0.152	-0.114	-5.4%	-5.7%	1790	-0.033	-0.003
			AD-C	-0.184	-0.184	-0.178	-0.178	-9.6%	-9.3%	-468	-0.039	-0.004
			OD-C	-0.103	-0.103	-0.110	-0.110	-5.4%	-5.8%	1790	-0.023	-0.013
		44	OD	-0.018	0.014	-0.042	-0.011	0.9%	-0.4%	5692	-0.010	-0.016
			OD-C	0.019	0.019	-0.006	-0.006	1.0%	-0.3%	5692	-0.001	-0.023
	2-4	44	AD	0.335	0.259	0.334	0.258	13.0%	12.9%	-32	0.060	-0.010
			OD	-0.047	-0.060	-0.050	-0.064	-3.5%	-3.7%	2355	-0.011	-0.015
			AD-C	0.232	0.232	0.230	0.230	13.0%	12.9%	-32	0.043	0.007
			OD-C	-0.064	-0.064	-0.067	-0.067	-3.6%	-3.8%	2355	-0.014	-0.012
		70	OD	-0.107	-0.065	-0.112	-0.071	-3.1%	-3.4%	1358	-0.024	0.004
			OD-C	-0.056	-0.056	-0.061	-0.061	-3.0%	-3.3%	1358	-0.013	-0.006
	4-6	70	AD	-0.085	0.026	-0.083	0.027	1.4%	1.5%	1156	-0.019	-0.002
			OD	-0.067	-0.021	-0.066	-0.021	-1.0%	-1.0%	435	-0.015	-0.003
			AD-C	0.031	0.031	0.033	0.033	1.5%	1.6%	1156	0.007	-0.027
			OD-C	-0.021	-0.021	-0.019	-0.019	-1.0%	-0.9%	435	-0.004	-0.014
		56	OD	-0.174	-0.024	-0.174	-0.024	-1.1%	-1.1%	214	-0.037	0.046
			OD-C	-0.024	-0.024	0.019	0.019	-1.1%	0.8%	214	0.004	0.013
	6-8	56	AD	-0.070	-0.011	-0.076	-0.017	-0.4%	-0.6%	547	-0.014	0.010
			OD	-0.011	-0.006	-0.013	-0.009	-0.3%	-0.4%	271	-0.002	-0.010
			AD-C	-0.009	-0.009	-0.014	-0.014	-0.4%	-0.6%	547	-0.003	-0.001
			OD-C	-0.006	-0.006	-0.008	-0.008	-0.3%	-0.4%	271	-0.002	-0.011
		60	OD	-0.055	-0.051	-0.061	-0.056	-2.4%	-2.7%	516	-0.012	0.017
B-32	0-2	22	AD	-0.052	-0.011	-0.053	-0.012	-0.3%	-0.3%	3463	-0.011	0.002
			OD	-0.007	-0.057	0.009	-0.042	-3.2%	-2.4%	53	0.002	-0.033
			AD-C	-0.004	-0.004	-0.016	-0.016	-0.2%	-0.8%	3463	-0.003	-0.008
			OD-C	-0.063	-0.063	-0.051	-0.051	-3.3%	-2.7%	53	-0.011	-0.022
		44	OD	0.006	-0.072	-0.002	-0.080	-4.0%	-4.4%	353	0.000	0.010
			OD-C	-0.078	-0.078	-0.087	-0.087	-4.0%	-4.5%	353	-0.019	0.026
	2-4	44	AD	0.184	0.177	0.182	0.174	9.8%	9.7%	3659	0.033	-0.001
			OD	-0.103	-0.090	-0.110	-0.097	-4.9%	-5.3%	2186	-0.023	-0.020
			AD-C	0.173	0.173	0.171	0.171	9.8%	9.6%	3659	0.031	0.001
			OD-C	-0.086	-0.086	-0.093	-0.093	-4.9%	-5.3%	2186	-0.019	-0.022
		70	OD	-0.062	-0.084	-0.061	-0.083	-4.3%	-4.2%	842	-0.010	-0.015
			OD-C	-0.087	-0.087	-0.086	-0.086	-4.3%	-4.2%	842	-0.014	-0.010
	4-6	70	AD	0.216	0.212	0.232	0.228	11.3%	12.1%	2758	0.052	0.018
			OD	0.015	0.070	0.014	0.069	4.0%	4.0%	1573	0.003	-0.012
			AD-C	0.211	0.211	0.227	0.227	11.3%	12.1%	2758	0.051	0.019
			OD-C	0.078	0.078	0.077	0.077	4.2%	4.1%	1573	0.019	-0.022
		56	OD	0.047	0.052	0.047	0.051	2.5%	2.4%	229	0.010	0.016
			OD-C	0.052	0.052	0.051	0.051	2.5%	2.4%	229	0.011	0.015
	6-8	56	AD	-0.010	-0.027	-0.011	-0.028	-1.6%	-1.6%	-53	-0.003	0.000
			OD	-0.058	-0.076	-0.064	-0.082	-4.2%	-4.5%	615	-0.016	-0.009
			AD-C	-0.029	-0.029	-0.031	-0.031	-1.6%	-1.7%	-53	-0.007	0.003
			OD-C	-0.078	-0.078	-0.084	-0.084	-4.2%	-4.6%	615	-0.021	-0.006
		60	OD	-0.059	-0.046	-0.061	-0.048	-2.3%	-2.4%	333	-0.014	-0.008
B-35	0-2	22	AD	0.084	0.111	0.081	0.109	6.4%	6.2%	-807	0.020	-0.018
			OD	0.007	0.029	0.009	0.030	1.7%	1.8%	-1106	0.002	-0.008
			AD-C	0.117	0.117	0.114	0.114	6.5%	6.3%	-807	0.028	-0.022
			OD-C	0.032	0.032	0.034	0.034	1.8%	1.9%	-1106	0.009	-0.011
B-36	0-2	22	AD	-0.097	-0.036	-0.098	-0.037	-1.7%	-1.8%	1651	-0.027	-0.001
			OD	-0.086	-0.085	-0.092	-0.091	-4.8%	-5.2%	345	-0.025	-0.001
			AD-C	-0.027	-0.027	-0.027	-0.027	-1.5%	-1.5%	1651	-0.007	-0.014
B-38	0-2	22	AD	-0.084	-0.051	-0.098	-0.065	-2.7%	-3.5%	849	-0.025	-0.018
			OD	-0.055	-0.055	-0.061	-0.060	-3.2%	-3.5%	69	-0.015	-0.014
			AD-C	-0.042	-0.042	-0.056	-0.056	-2.5%	-3.3%	849	-0.014	-0.024

APPENDIX B: CHARACTERIZATION OF IH-10 PROJECT

This appendix summarizes the additional results from the geotechnical characterization of the IH-10 research project presented in Chapters 3 and 4 of this dissertation. The first section focuses on the additional results from the commercial laboratory, and the second section focuses on the additional results from the University of Texas' research.

The first section includes the additional results from the geotechnical characterization performed by a geotechnical consultant for the Texas Department of Transportation. These results include the logging recorded during sampling, stratigraphy of the borings, the Atterberg Limits, the in-situ gravimetric moisture content, and the fines content.

The second section includes the additional results from the characterization of the swelling behavior of the subgrade using the centrifuge-based swelling test. The results from each test, fitted stress-swell curve for each soil section, fitting parameters for each swell-stress curve, and an interpolated stress-swell curve from Tex-124-E are presented for each boring that was not previously depicted. Additionally, the potential vertical rise for each boring section and the cumulative potential vertical rise for each boring, each calculated using the previous stress-swell curves, are presented.

B.1: Results from Previous Geotechnical Characterization

Table B.1: Geotechnical characterization and logging of borings P-1 to P-7

Bor.	Soil	Depth (ft)	Description of Layer	ω (%)	Liquid Limit	Plasticity Index	Fines (%)
P-1	HB	0 - 0.875	Asphalt				
P-1	HB	0.875 - 2.5	Base (GM)	5			19
P-1	HB	2.5 - 4	CH	10	53%	36	
P-1	HB	4 - 7	CH	21			
P-1	HB	7 - 8	CH				
P-2	HB	0 - 0.85	Asphalt				
P-2	HB	0.85 - 1.8	Base (GC)	29	84%	65	13
P-2	HB	1.8 - 5	CH	30	86%	65	
P-2	HB	5 - 8	CH	30			
P-3	HB	0 - 0.9	Asphalt				
P-3	HB	0.9 - 2.1	Base (Limestone)				
P-3	HB	2.1 - 5	CH	34	98%	59	80
P-3	HB	5 - 8	CH	34	86%	65	
P-4	HB	0 - 0.8	Asphalt				
P-4	HB	0.8 - 1.8	Base (Limestone)				
P-4	HB	1.8 - 2.5	CH	30	60%	42	
P-4	HB	2.5 - 5	CH	30	82%	61	
P-4	HB	5 - 8	CH	36			
P-5	HE	0 - 0.4	Asphalt				
P-5	HE	0.4 - 1.4	Base (SP-SM)				
P-5	HE	1.4 - 4	CH	33	92%	73	80
P-5	HE	4 - 7	CH	28	82%	64	63
P-5	HE	7 - 8	GM				13
P-6	HB	0 - 0.6	Asphalt				
P-6	HB	0.6 - 0.8	Concerete				
P-6	HB	0.8 - 1.6	Subbase (SP-SM)				
P-6	HB	1.6 - 2.5	CH	36	99%	80	86
P-6	HB	2.5 - 4	CH	35	84%	63	
P-6	HB	4 - 8	CH	35			
P-7	HB	0 - 0.5	Asphalt				
P-7	HB	0.5 - 1.6	Base (GC)	12	30%	13	29
P-7	HB	1.6 - 2.5	CH	27	73%	56	80
P-7	HB	2.5 - 7	CH	29	66%	47	
P-7	HB	7 - 8	CH				

Table B.2: Geotechnical characterization and logging of borings P-8 to P-15

Bor.	Soil	Depth (ft)	Description of Layer	ω (%)	Liquid Limit	Plasticity Index	Fines (%)
P-8	HE	0 - 0.4	Asphalt				
P-8	HE	0.4 - 1	Base (SC-SM)	11	24%	6	17
P-8	HE	1 - 7	CH	30	84%	65	74
P-8	HE	7 - 8	CH				
P-9	HB	0 - 0.4	Asphalt				
P-9	HB	0.4 - 1.6	Base (Limestone)				
P-9	HB	1.6 - 3	CH	25	76%	58	
P-9	HB	3 - 5	CH	24	58%	42	
P-9	HB	5 - 8	CH				
P-10	HB	0 - 0.4	Asphalt				
P-10	HB	0.4 - 0.9	Base (Limestone)				
P-10	HB	0.9 - 2.5	CH	24	76%	55	
P-10	HB	2.5 - 7	CH	29	65%	44	84
P-10	HB	7 - 8	CH	19			
P-11	HB	0 - 0.2	Asphalt				
P-11	HB	0.2 - 1.2	Base (Limestone)				
P-11	HB	1.2 - 2	CH (fill?)	28	91%	72	78
P-11	HB	2 - 5	GC				18
P-11	HB	5 - 8	CH	28			
P-12	HB	0 - 0.5	Asphalt + Base (Limestone)				
P-12	HB	0.5 - 1.5	Subbase (GC)				
P-12	HB	1.5 - 2.5	CH	22	65%	50	
P-12	HB	2.5 - 5	CH	29	67%	47	
P-12	HB	5 - 7	GC				16
P-13	HB	0 - 0.6	Asphalt + Base (Limestone)				
P-13	HB	0.6 - 1.7	Subbase (SC)				16
P-13	HB	1.7 - 2.5	CH	22	71%	54	
P-13	HB	2.5 - 5	CH	25			
P-13	HB	5 - 8	CH				
P-14	TF	0 - 1.2	Asphalt + Base (Limestone)				
P-14	TF	1.2 - 2.5	CH	23	72%	54	81
P-14	TF	2.5 - 6	CH	23	59%	43	64
P-14	TF	6 - 8	CH	34			
P-15	HB	0 - 0.6	Asphalt + Base (Limestone)				
P-15	HB	0.6 - 1.7	Subbase (Limestone)	6	32	10	15
P-15	HB	1.7 - 2.5	CH	29	82	61	
P-15	HB	2.5 - 6.5	CH	31	71	62	74

Table B.3: Geotechnical characterization and logging of borings P-16 to P-22

Bor.	Soil	Depth (ft)	Description of Layer	ω (%)	Liquid Limit	Plasticity Index	Fines (%)
P-16	HB	0 - 0.5	Asphalt + Base (Limestone)				
P-16	HB	0.5 - 1.8	Subbase (Limestone)	9	33	18	30
P-16	HB	1.8 - 2.5	CH				
P-16	HB	2.5 - 7	CH	18	37	22	83
P-16	HB	7 - 8	CH	16			
P-17	HB	0 - 0.5	Asphalt + Base (Limestone)				
P-17	HB	0.5 - 1.3	Subbase (SC)	7	30	17	39
P-17	HB	1.3 - 2.5	CH	16	52	37	
P-17	HB	2.5 - 3.5	CH	18	54	37	
P-17	HB	3.5 - 5	CH				
P-17	HB	5 - 8	CH				
P-18	HB	0 - 0.6	Asphalt + Base (Limestone)				
P-18	HB	0.6 - 1.7	Subbase (SC)	7	29	12	25
P-18	HB	1.7 - 2.5	CH (fill)	22	54	39	51
P-18	HB	2.5 - 6.5	CH	33	91	68	
P-18	HB	6.5 - 8	CH				
P-19	HB	0 - 0.6	Asphalt + Base (Limestone)				
P-19	HB	0.6 - 1.2	Subbase (SC)	4	32	12	21
P-19	HB	1.2 - 2.5	CH (fill)	20	62	47	72
P-19	HB	2.5 - 3	CH	30	74	66	
P-19	HB	3 - 8	CH				
P-20	HB	0 - 0.5	Asphalt + Base (Limestone)				
P-20	HB	0.5 - 1.5	Subbase (Limestone)				
P-20	HB	1.5 - 1.7	CH	29	77	59	
P-20	HB	1.7 - 2.5	CH	30	74	56	88
P-20	HB	2.5 - 6.5	CH				
P-20	HB	6.5 - 8	CH				
P-21	HB	0 - 0.6	Asphalt + Base (Limestone)				
P-21	HB	0.6 - 1.1	Subbase (GC)	7	32	12	17
P-21	HB	1.1 - 2.5	CH	10	66	47	
P-21	HB	2.5 - 4	CH	26			
P-21	HB	4 - 8	CH-CL	19	47	30	
P-22	TF	0 - 0.5	Asphalt + Base (Limestone)				
P-22	TF	0.5 - 1.4	Subbase (SC)	6			28
P-22	TF	1.4 - 6.5	CH	21	64%	51	
P-22	TF	6.5 - 8	GC	11			

B.2: Swelling Test Results from Additional IH-10 Borings

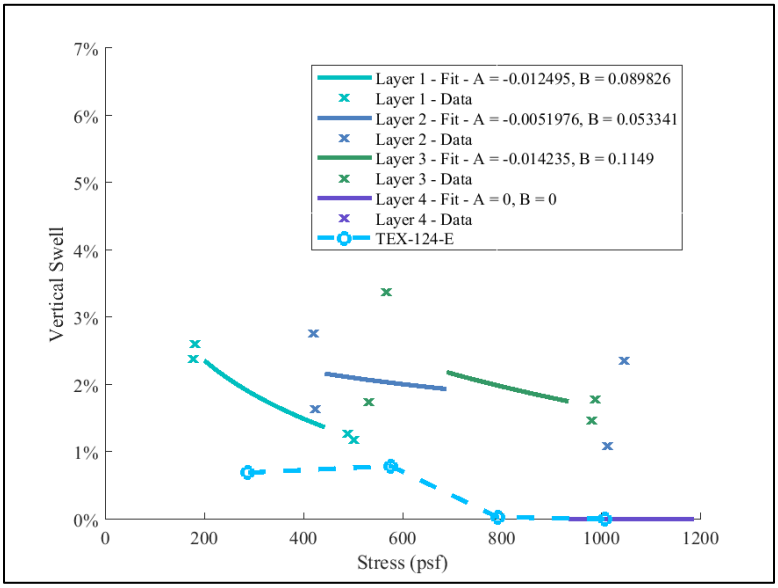

Figure B.1: Measured stress-swell curves and comparison of curves from centrifuge data to Tex-124-E for boring B-1

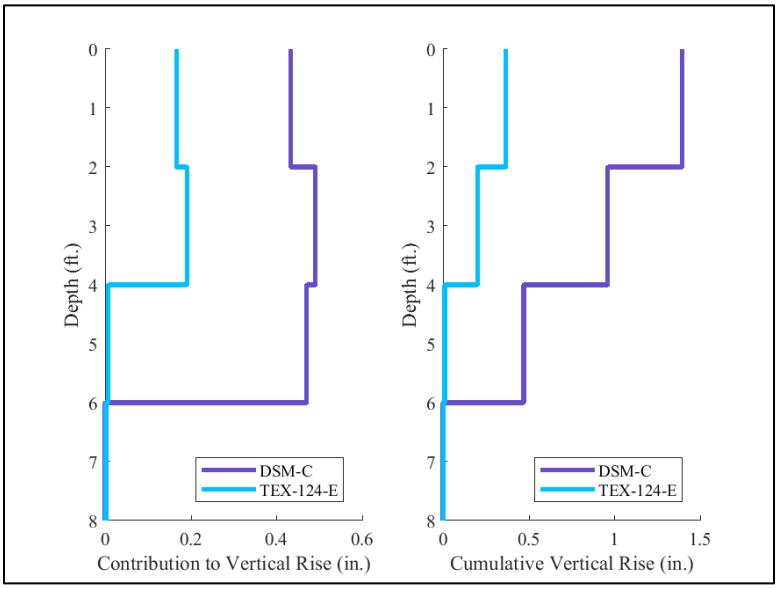

Figure B.2: Calculated vertical rise for each 2-ft section (left) and cumulative vertical rise (right) for both Centrifuge and Tex-124-E methods for boring B-1

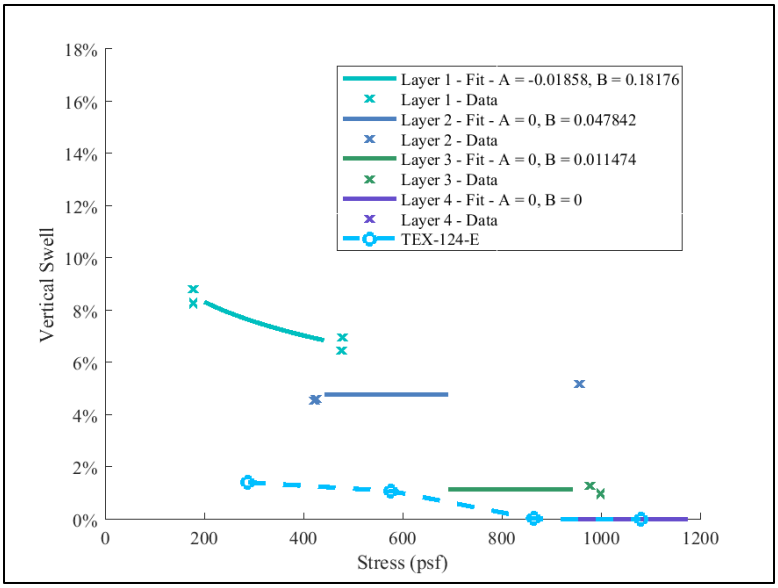

Figure B.3: Measured stress-swell curves and comparison of curves from centrifuge data to Tex-124-E for boring B-2

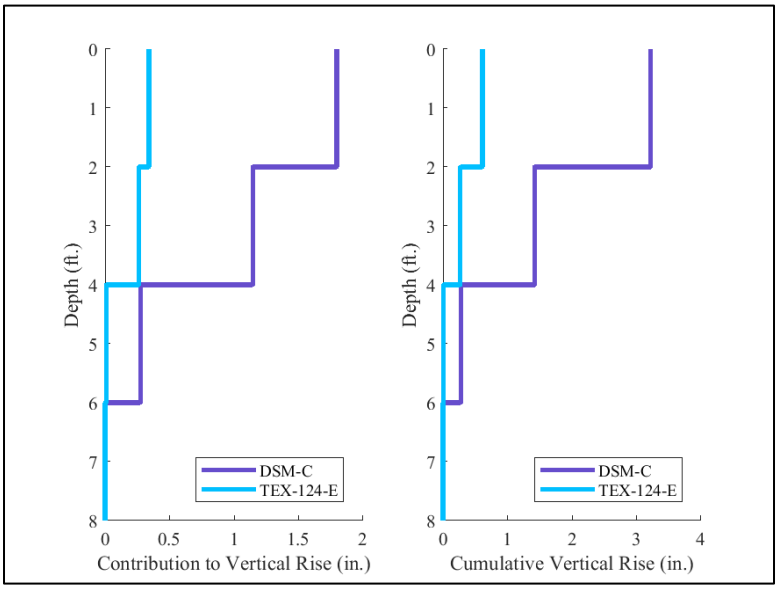

Figure B.4: Calculated vertical rise for each 2-ft section (left) and cumulative vertical rise (right) for both Centrifuge and Tex-124-E methods for boring B-2

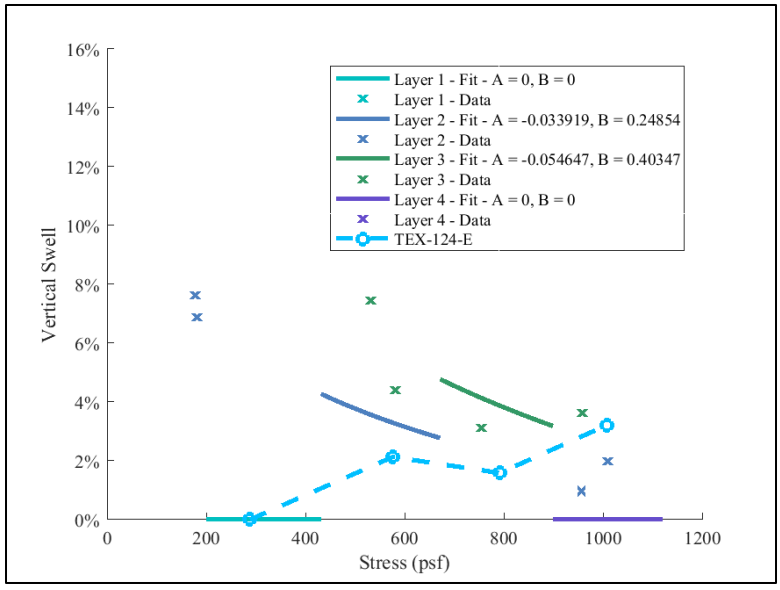

Figure B.5: Measured stress-swell curves and comparison of curves from centrifuge data to Tex-124-E for boring B-4

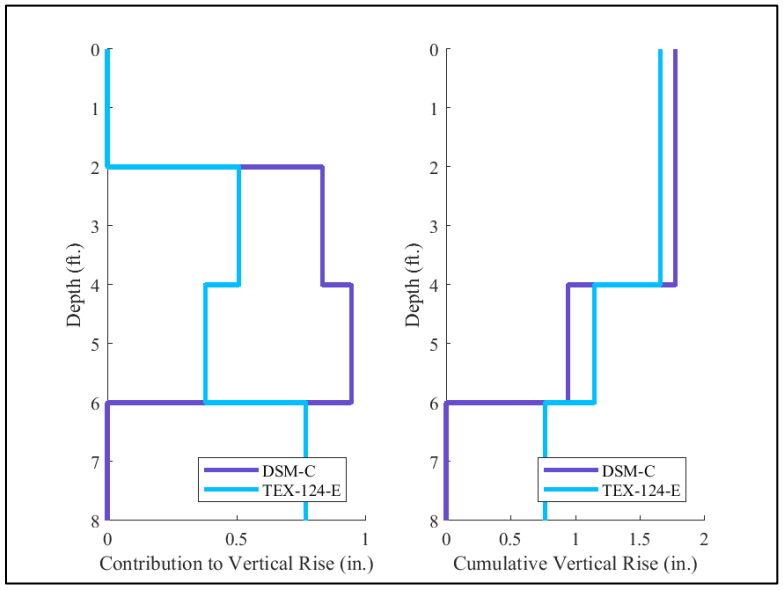

Figure B.6: Calculated vertical rise for each 2-ft section (left) and cumulative vertical rise (right) for both Centrifuge and Tex-124-E methods for boring B-4

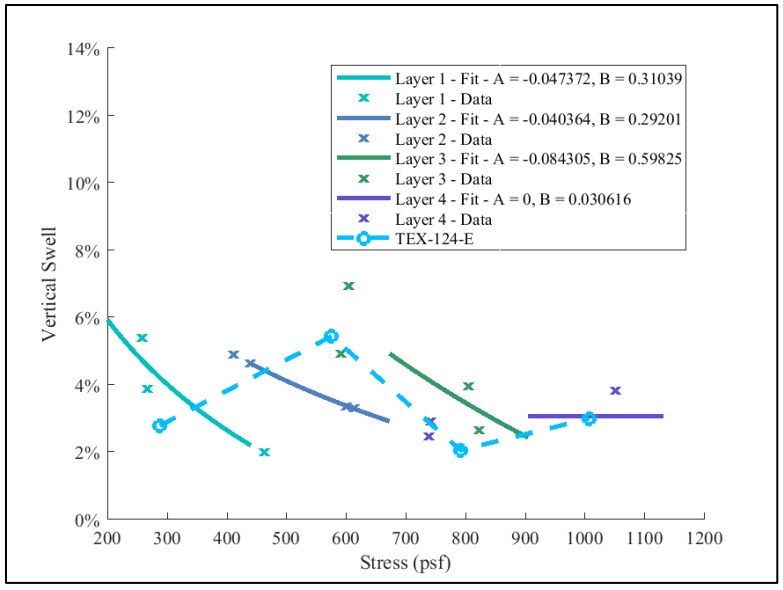

Figure B.7: Measured stress-swell curves and comparison of curves from centrifuge data to Tex-124-E for boring B-5

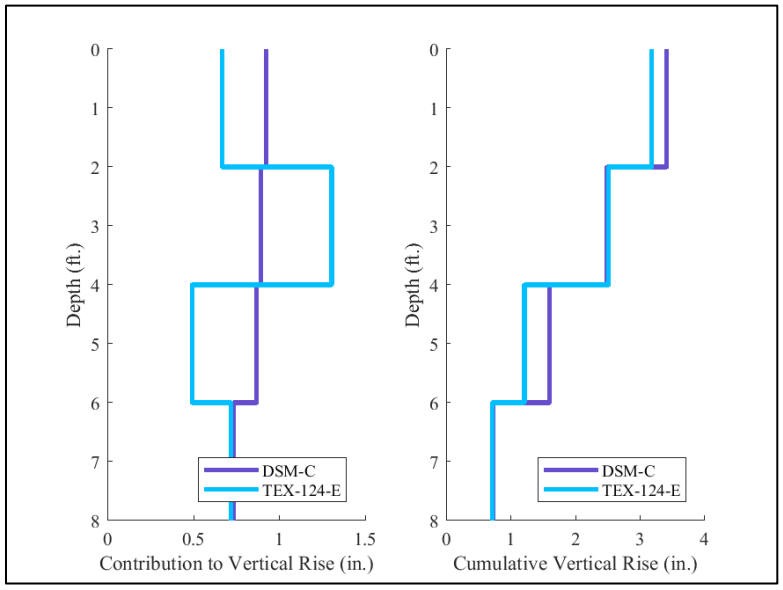

Figure B.8: Calculated vertical rise for each 2-ft section (left) and cumulative vertical rise (right) for both Centrifuge and Tex-124-E methods for boring B-5

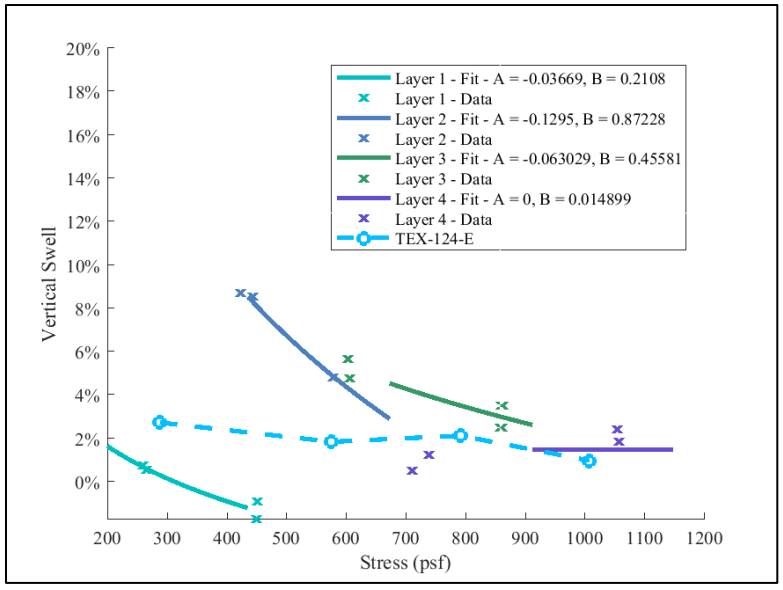

Figure B.9: Measured stress-swell curves and comparison of curves from centrifuge data to Tex-124-E for boring B-6

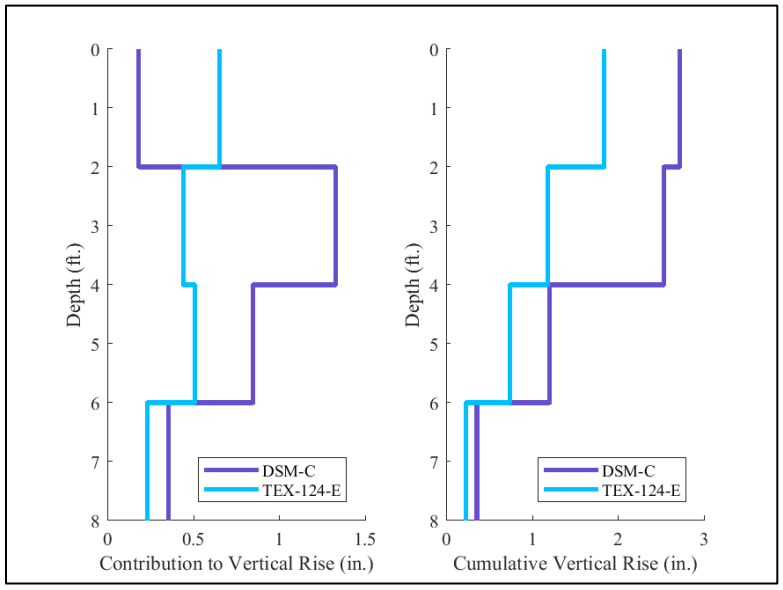

Figure B.10: Calculated vertical rise for each 2-ft section (left) and cumulative vertical rise (right) for both Centrifuge and Tex-124-E methods for boring B-6

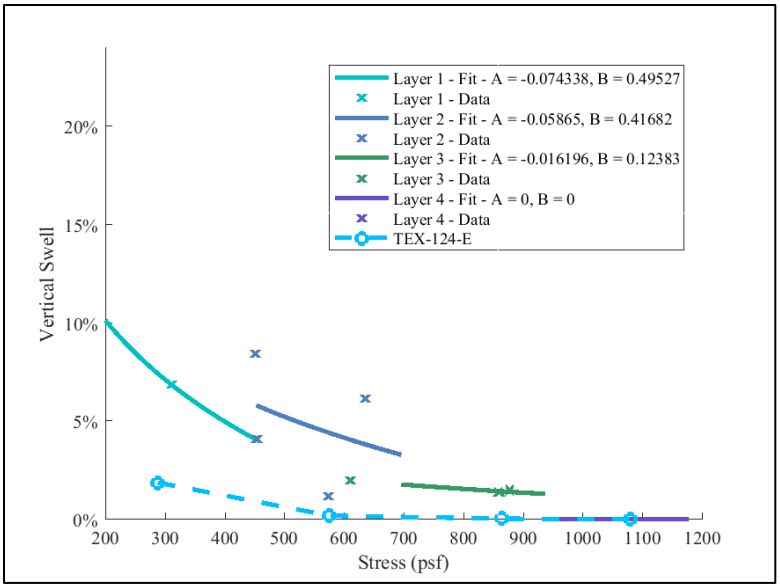

Figure B.11: Measured stress-swell curves and comparison of curves from centrifuge data to Tex-124-E for boring B-7

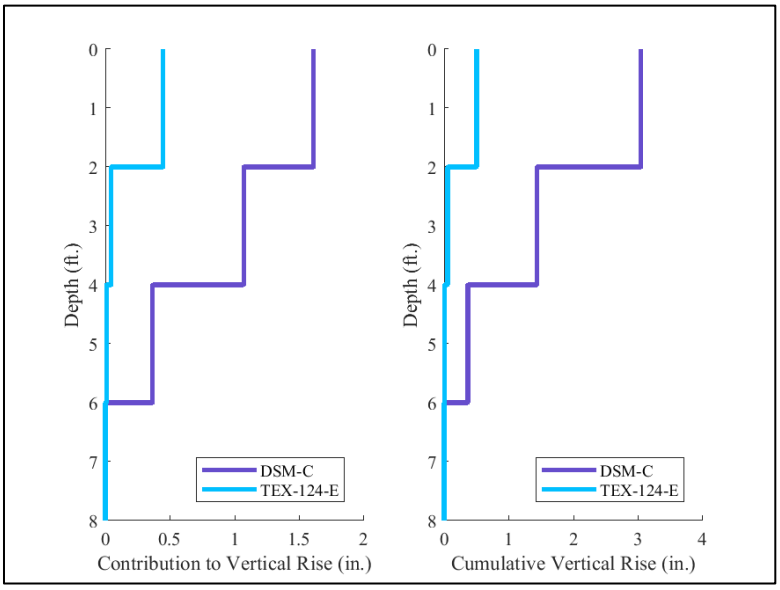

Figure B.12: Calculated vertical rise for each 2-ft section (left) and cumulative vertical rise (right) for both Centrifuge and Tex-124-E methods for boring B-7

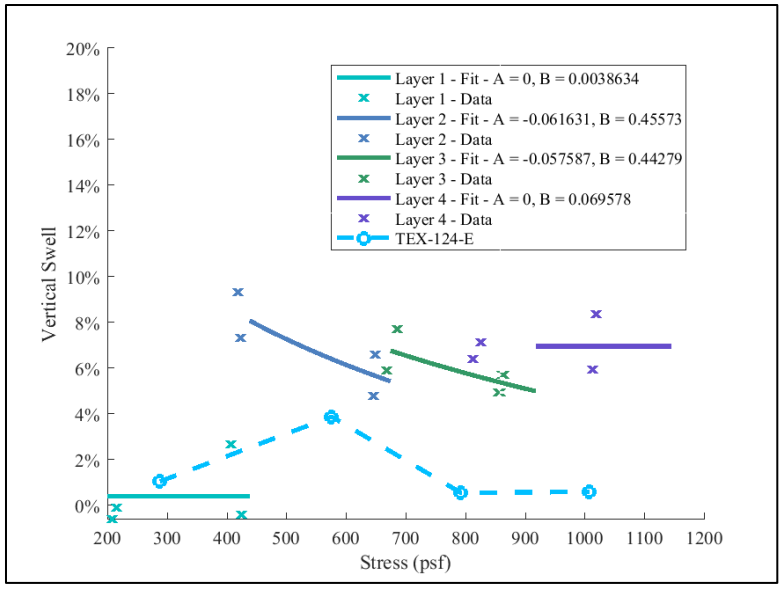

Figure B.13: Measured stress-swell curves and comparison of curves from centrifuge data to Tex-124-E for boring B-8

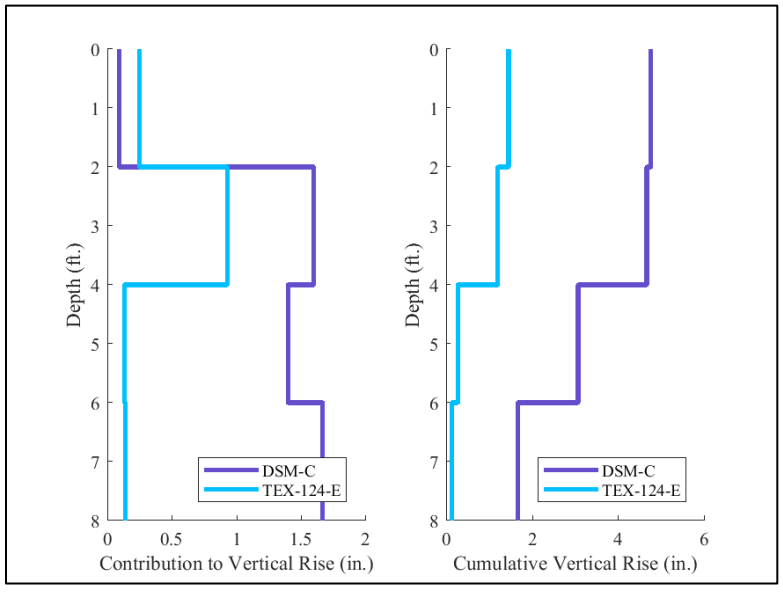

Figure B.14: Calculated vertical rise for each 2-ft section (left) and cumulative vertical rise (right) for both Centrifuge and Tex-124-E methods for boring B-8

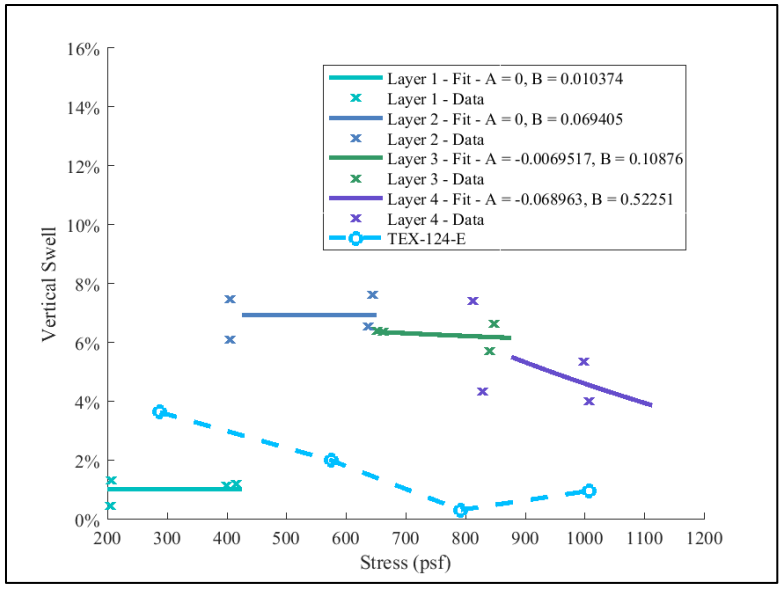

Figure B.15: Measured stress-swell curves and comparison of curves from centrifuge data to Tex-124-E for boring B-9

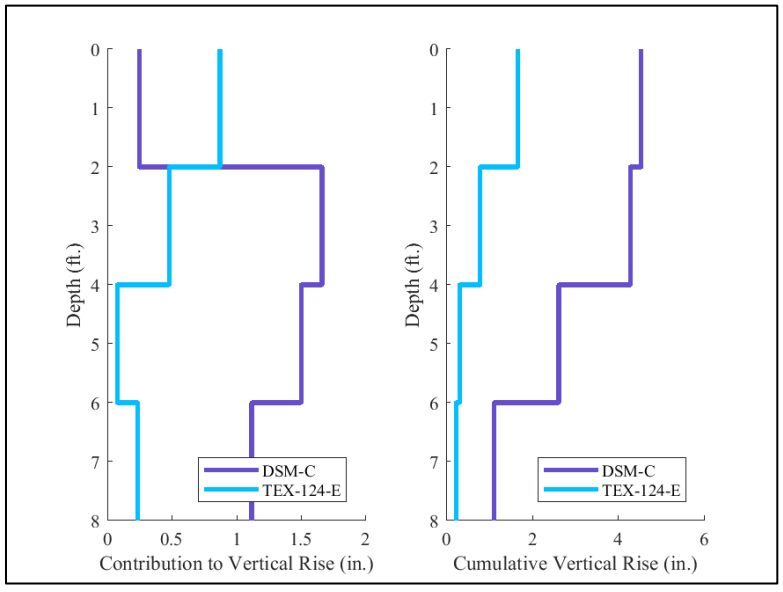

Figure B.16: Calculated vertical rise for each 2-ft section (left) and cumulative vertical rise (right) for both Centrifuge and Tex-124-E methods for boring B-9

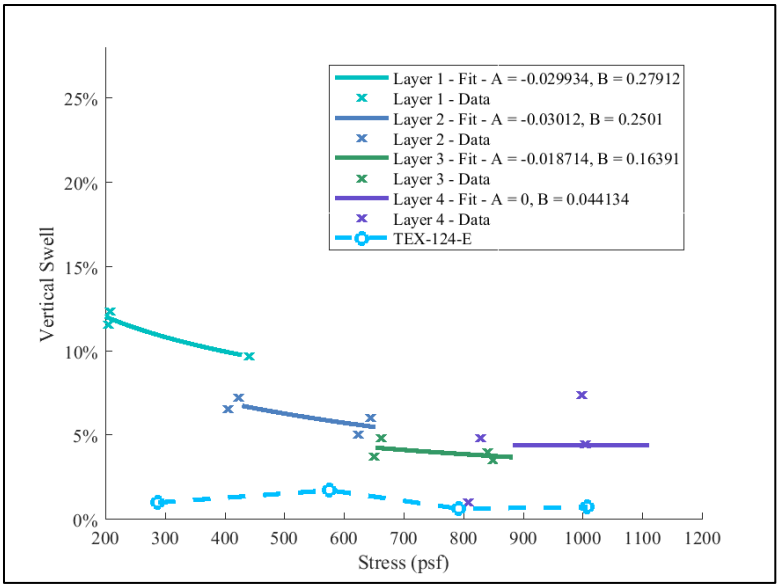

Figure B.17: Measured stress-swell curves and comparison of curves from centrifuge data to Tex-124-E for boring B-10

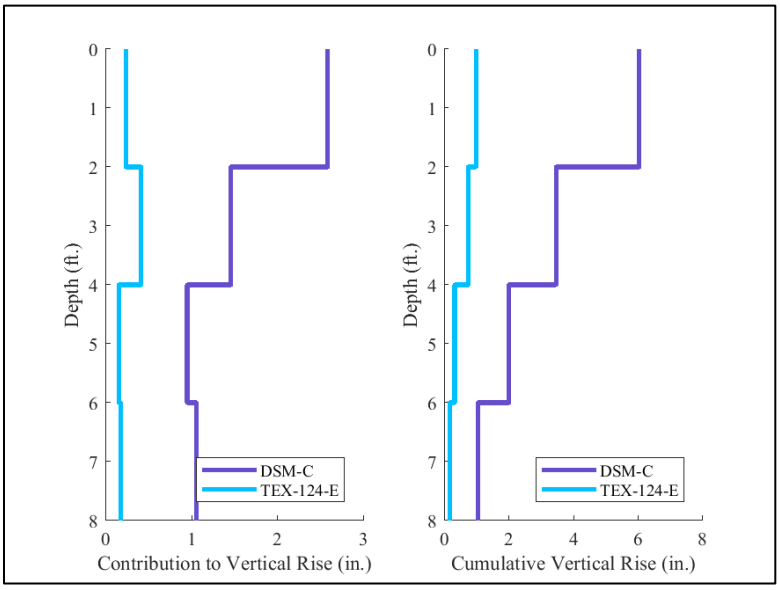

Figure B.18: Calculated vertical rise for each 2-ft section (left) and cumulative vertical rise (right) for both Centrifuge and Tex-124-E methods for boring B-10

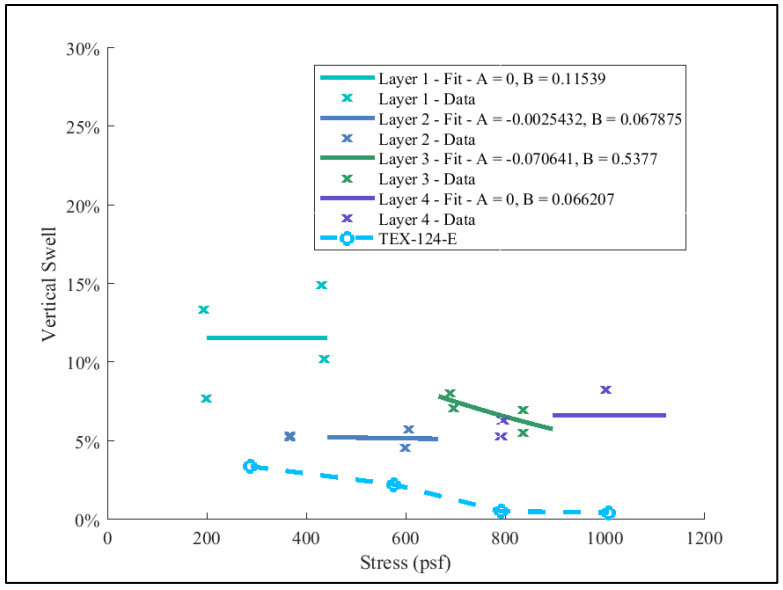

Figure B.19: Measured stress-swell curves and comparison of curves from centrifuge data to Tex-124-E for boring B-11

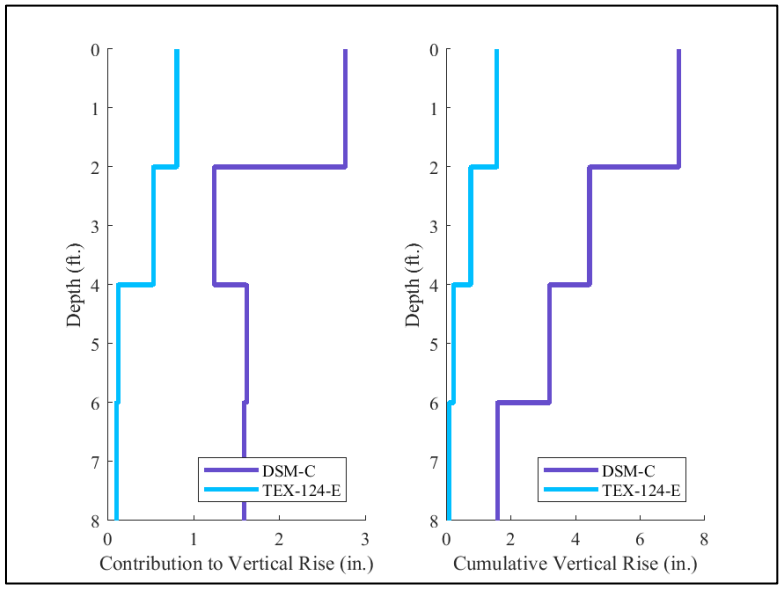

Figure B.20: Calculated vertical rise for each 2-ft section (left) and cumulative vertical rise (right) for both Centrifuge and Tex-124-E methods for boring B-11

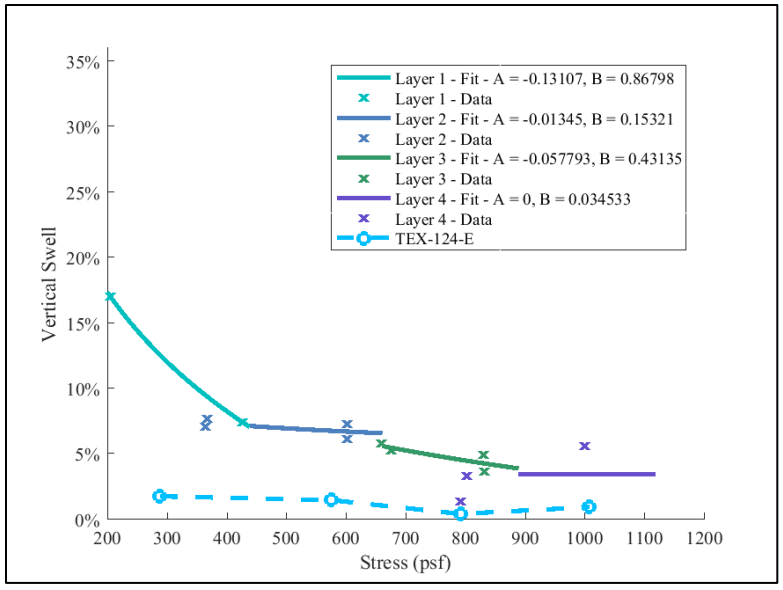

Figure B.21: Measured stress-swell curves and comparison of curves from centrifuge data to Tex-124-E for boring B-12

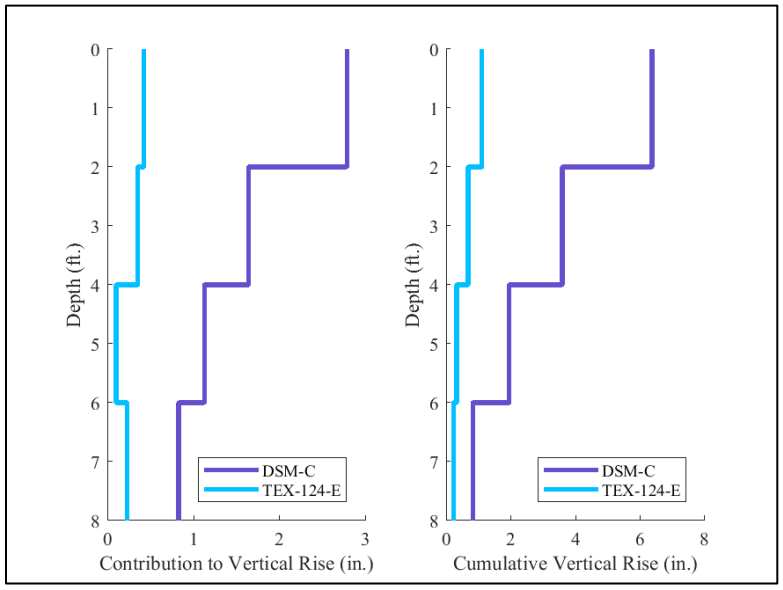

Figure B.22: Calculated vertical rise for each 2-ft section (left) and cumulative vertical rise (right) for both Centrifuge and Tex-124-E methods for boring B-12

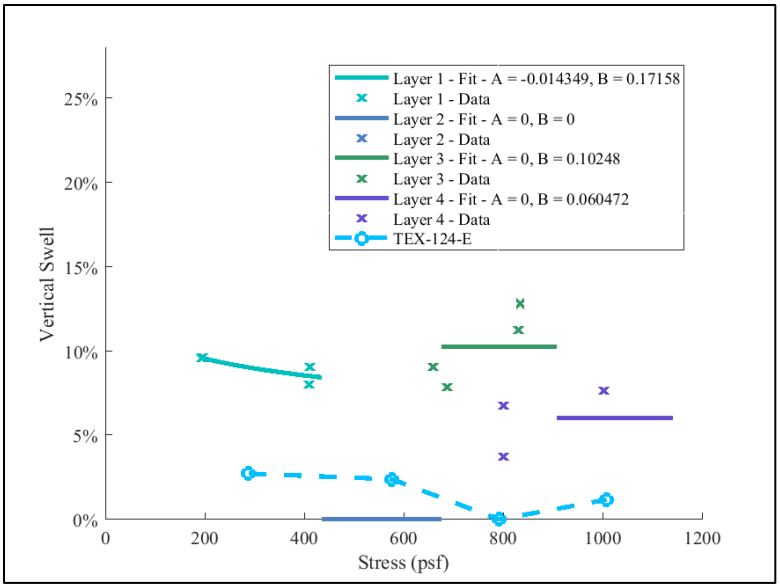

Figure B.23: Measured stress-swell curves and comparison of curves from centrifuge data to Tex-124-E for boring B-13

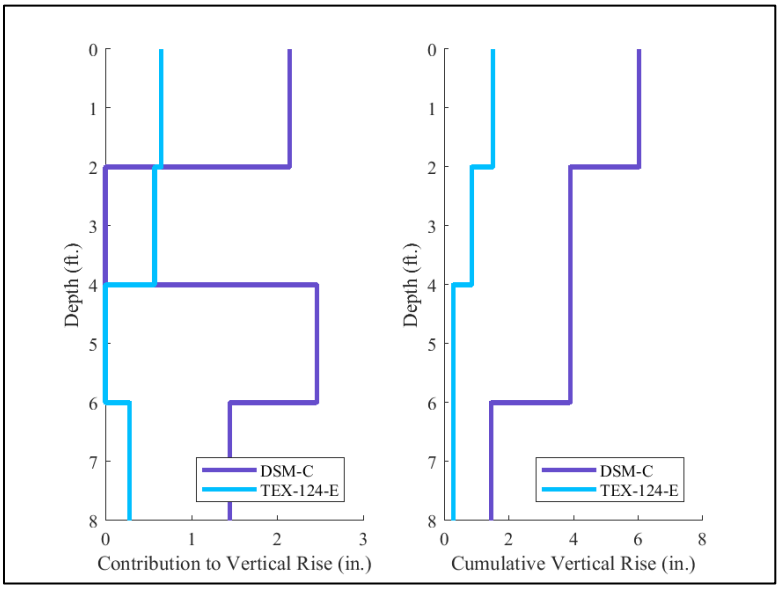

Figure B.24: Calculated vertical rise for each 2-ft section (left) and cumulative vertical rise (right) for both Centrifuge and Tex-124-E methods for boring B-13

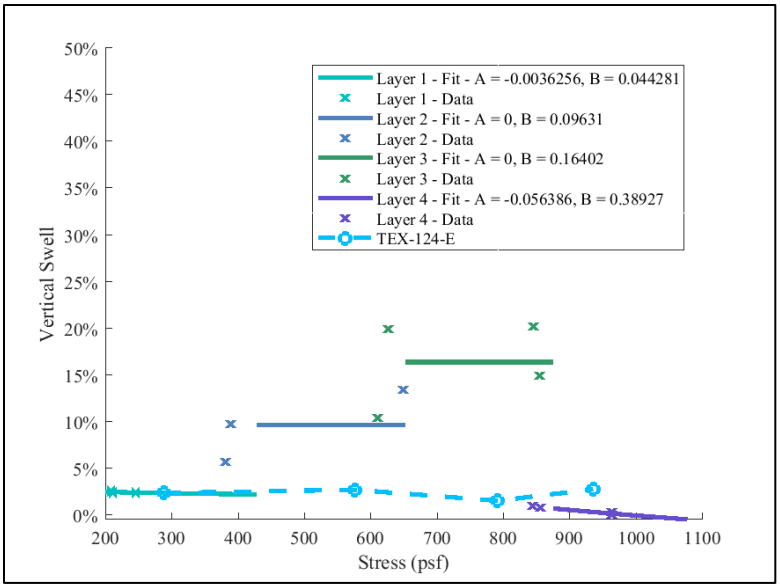

Figure B.25: Measured stress-swell curves and comparison of curves from centrifuge data to Tex-124-E for boring B-15

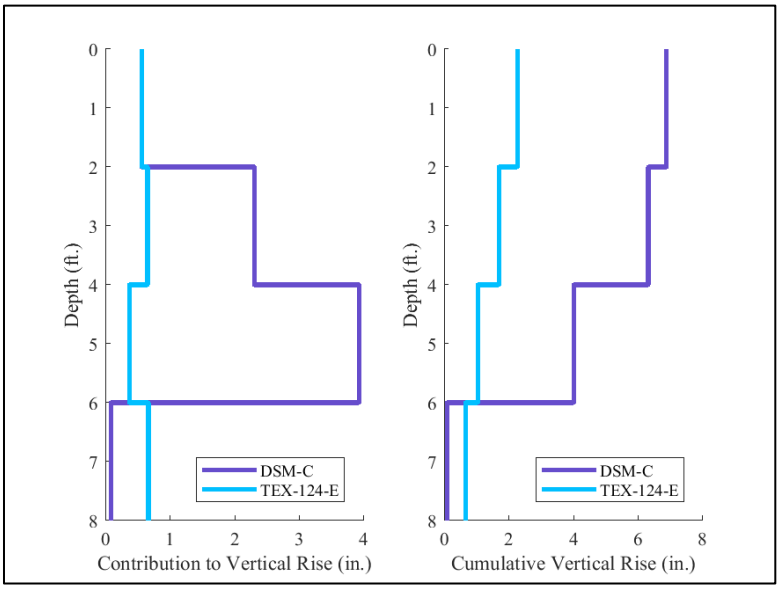

Figure B.26: Calculated vertical rise for each 2-ft section (left) and cumulative vertical rise (right) for both Centrifuge and Tex-124-E methods for boring B-15

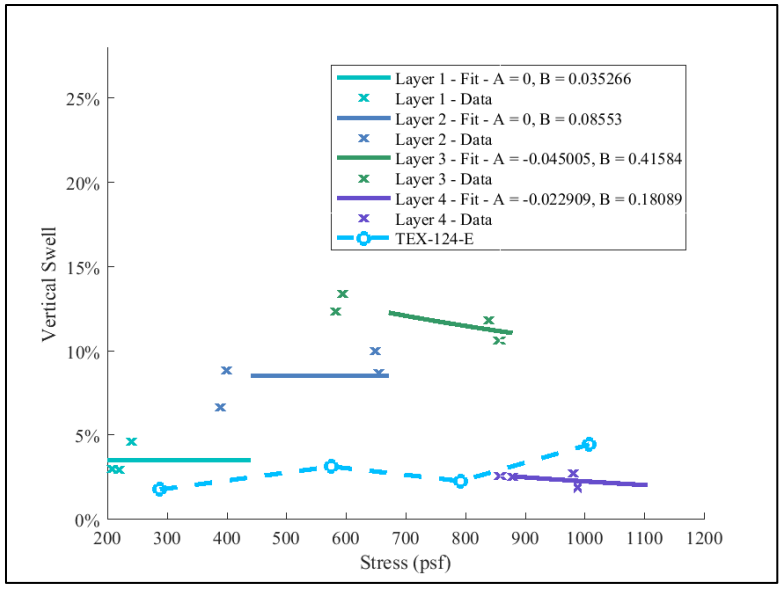

Figure B.27: Measured stress-swell curves and comparison of curves from centrifuge data to Tex-124-E for boring B-16

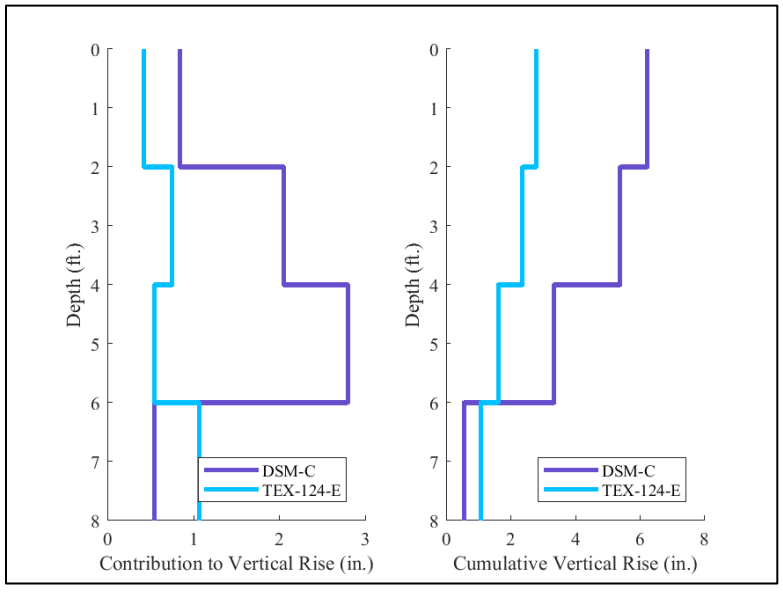

Figure B.28: Calculated vertical rise for each 2-ft section (left) and cumulative vertical rise (right) for both Centrifuge and Tex-124-E methods for boring B-16

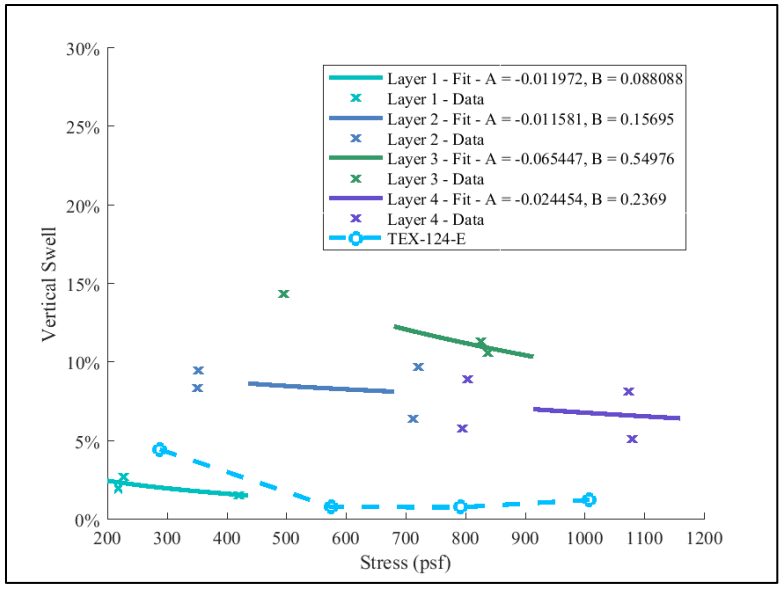

Figure B.29: Measured stress-swell curves and comparison of curves from centrifuge data to Tex-124-E for boring B-17

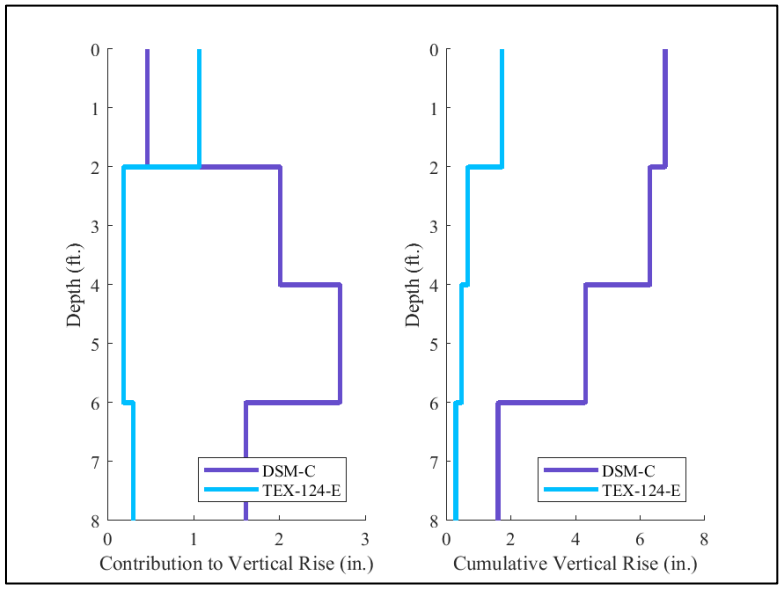

Figure B.30: Calculated vertical rise for each 2-ft section (left) and cumulative vertical rise (right) for both Centrifuge and Tex-124-E methods for boring B-17

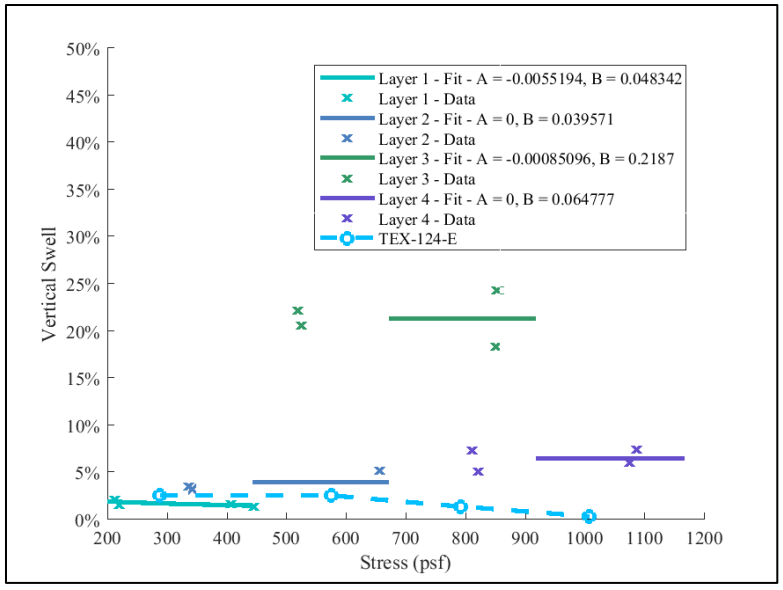

Figure B.31: Measured stress-swell curves and comparison of curves from centrifuge data to Tex-124-E for boring B-20

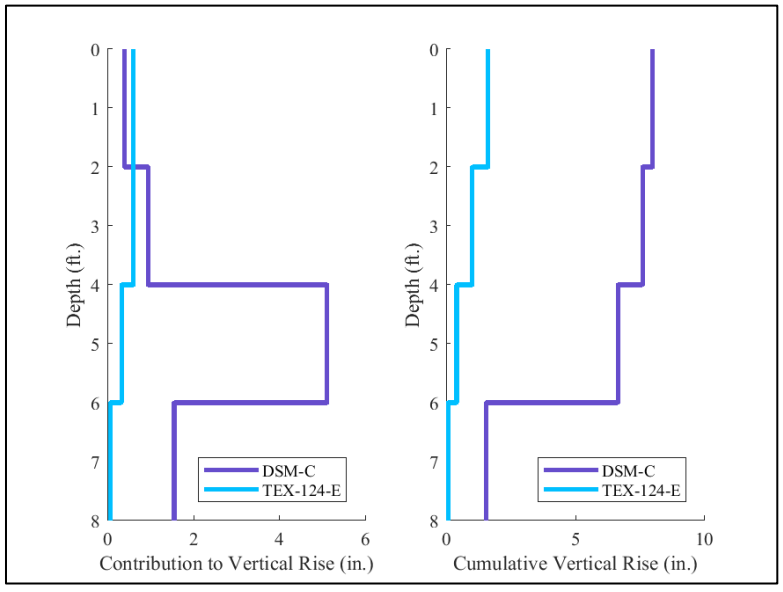

Figure B.32: Calculated vertical rise for each 2-ft section (left) and cumulative vertical rise (right) for both Centrifuge and Tex-124-E methods for boring B-20

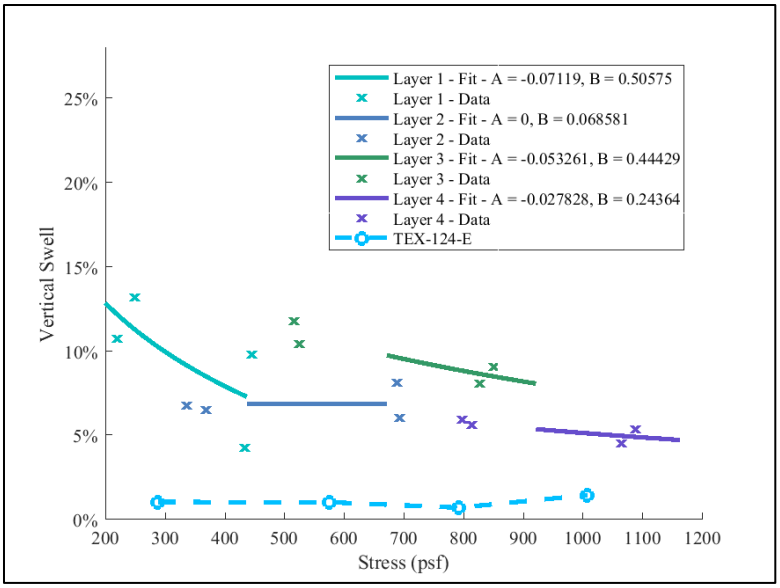

Figure B.33: Measured stress-swell curves and comparison of curves from centrifuge data to Tex-124-E for boring B-21

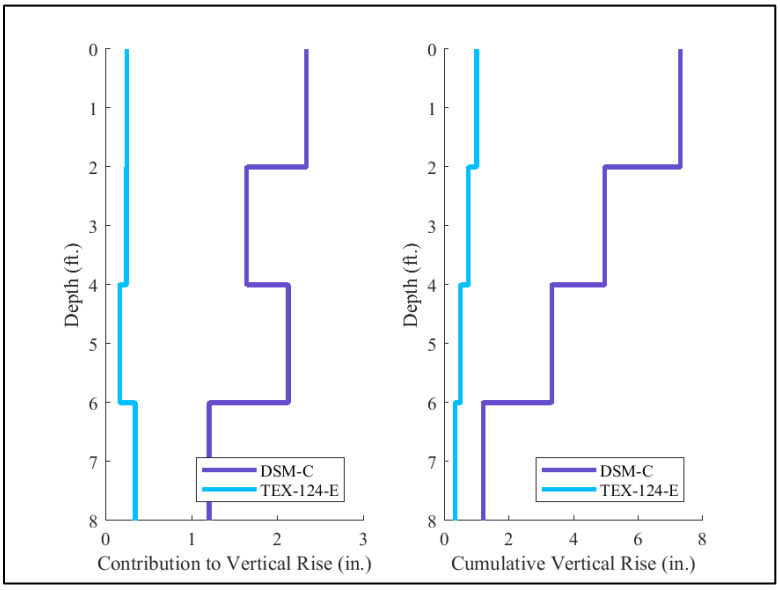

Figure B.34: Calculated vertical rise for each 2-ft section (left) and cumulative vertical rise (right) for both Centrifuge and Tex-124-E methods for boring B-21

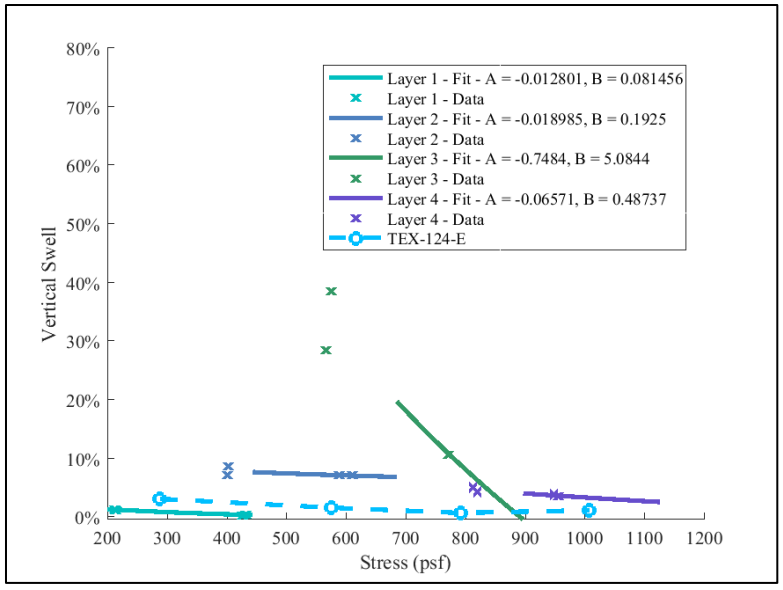

Figure B.35: Measured stress-swell curves and comparison of curves from centrifuge data to Tex-124-E for boring B-22

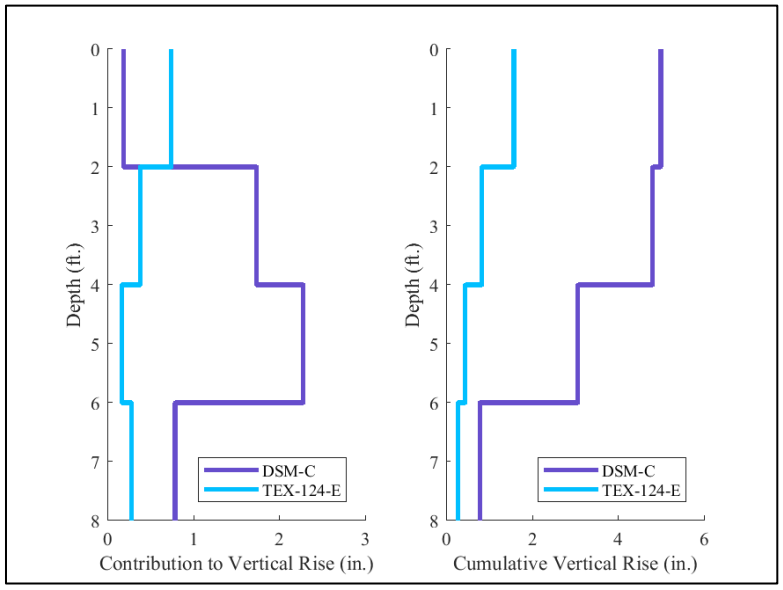

Figure B.36: Calculated vertical rise for each 2-ft section (left) and cumulative vertical rise (right) for both Centrifuge and Tex-124-E methods for boring B-22

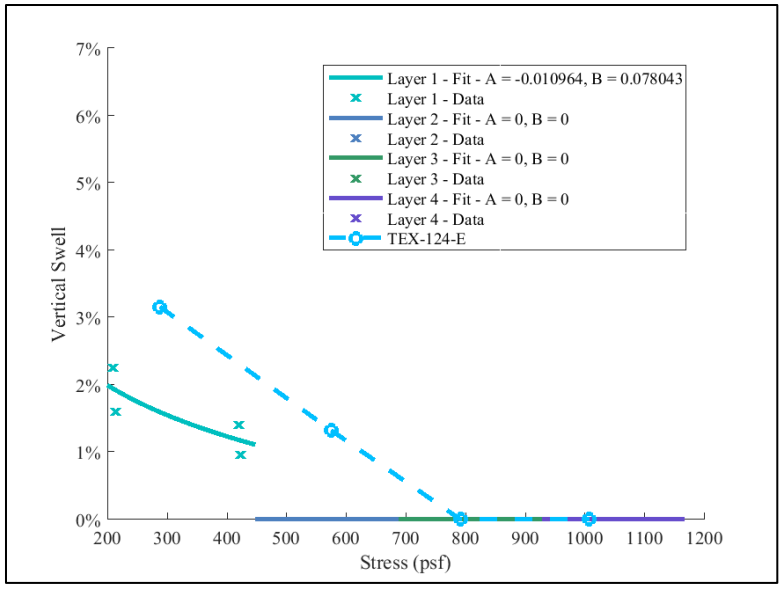

Figure B.37: Measured stress-swell curves and comparison of curves from centrifuge data to Tex-124-E for boring B-23

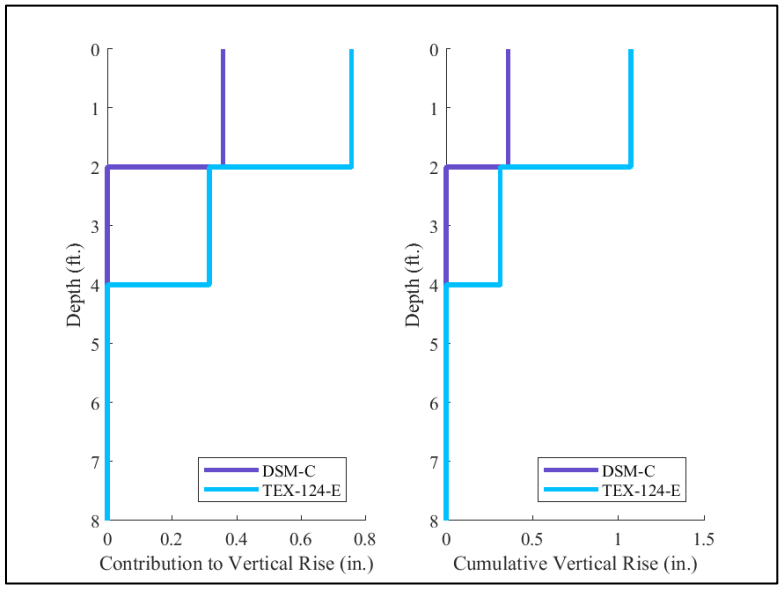

Figure B.38: Calculated vertical rise for each 2-ft section (left) and cumulative vertical rise (right) for both Centrifuge and Tex-124-E methods for boring B-23

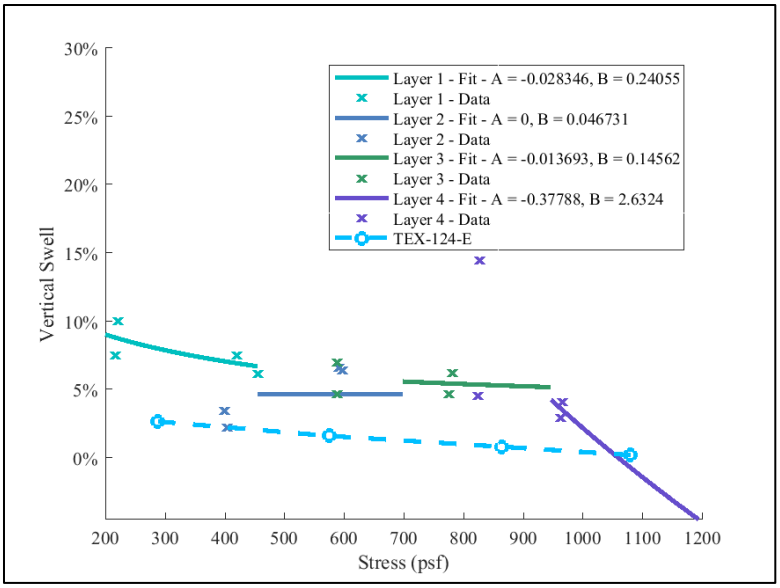

Figure B.39: Measured stress-swell curves and comparison of curves from centrifuge data to Tex-124-E for boring B-24

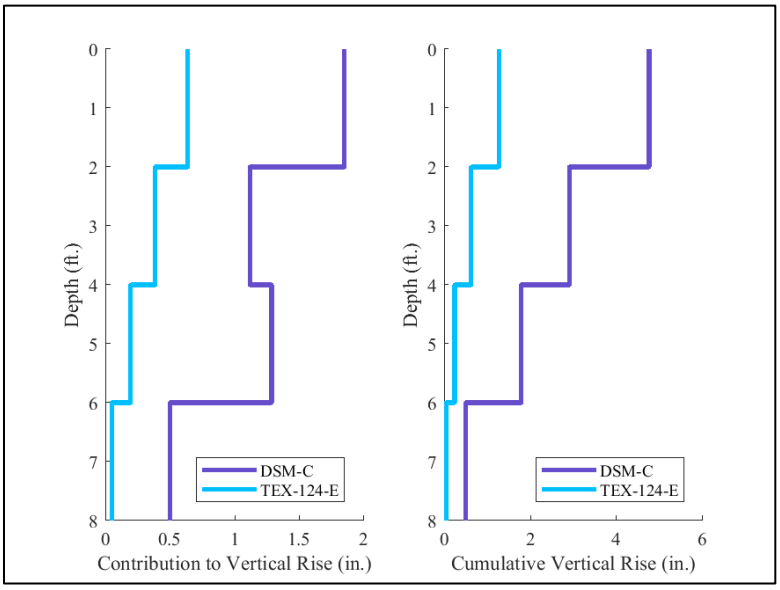

Figure B.40: Calculated vertical rise for each 2-ft section (left) and cumulative vertical rise (right) for both Centrifuge and Tex-124-E methods for boring B-24

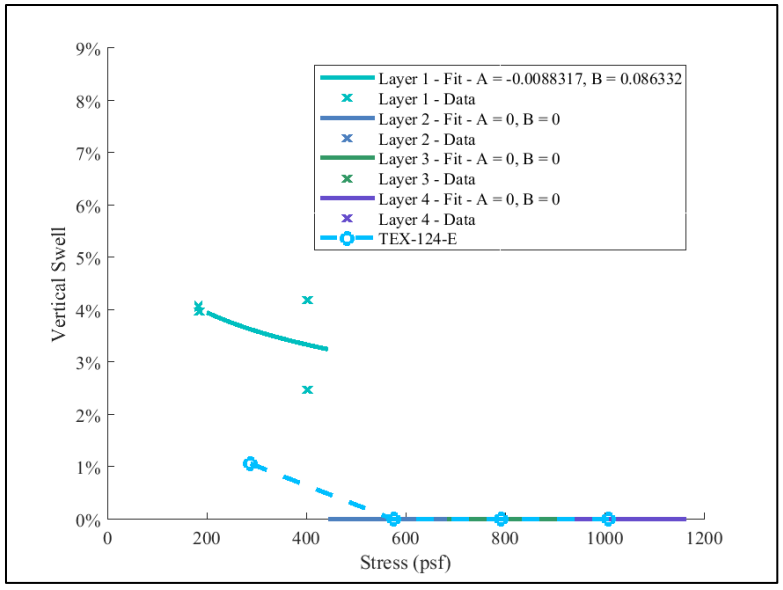

Figure B.41: Measured stress-swell curves and comparison of curves from centrifuge data to Tex-124-E for boring B-25

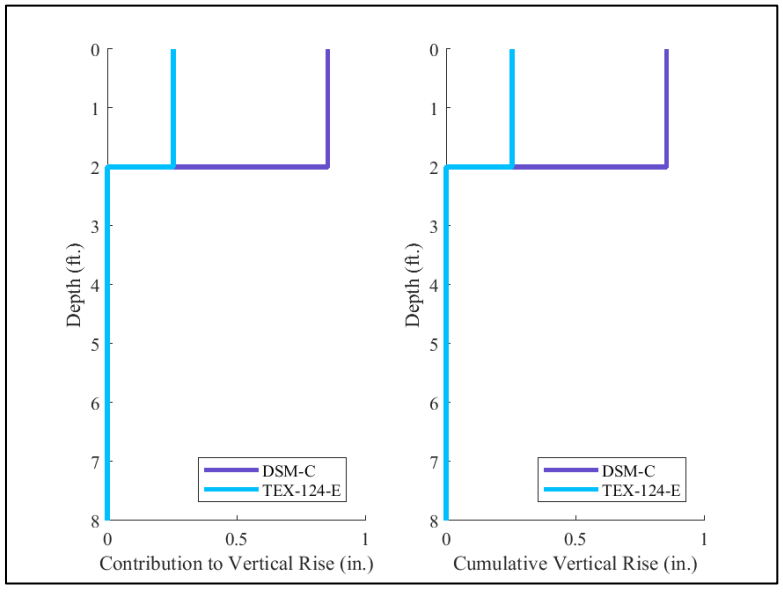

Figure B.42: Calculated vertical rise for each 2-ft section (left) and cumulative vertical rise (right) for both Centrifuge and Tex-124-E methods for boring B-25

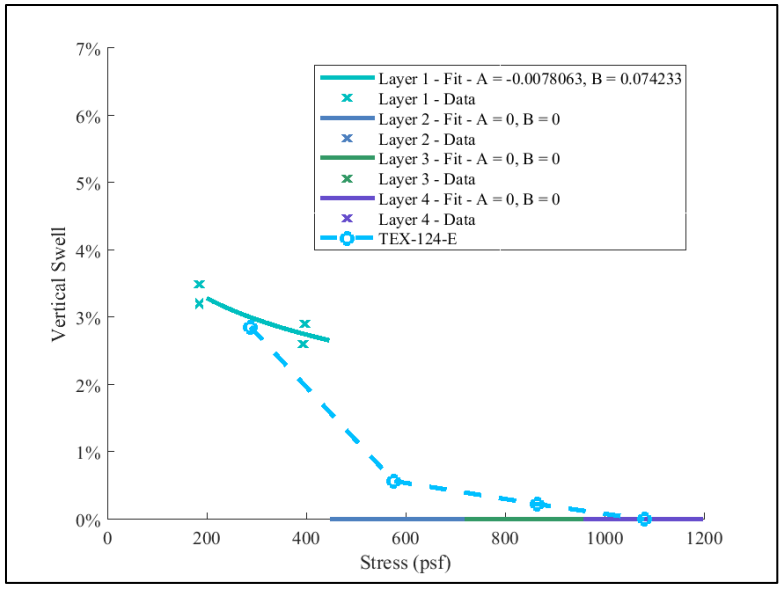

Figure B.43: Measured stress-swell curves and comparison of curves from centrifuge data to Tex-124-E for boring B-26

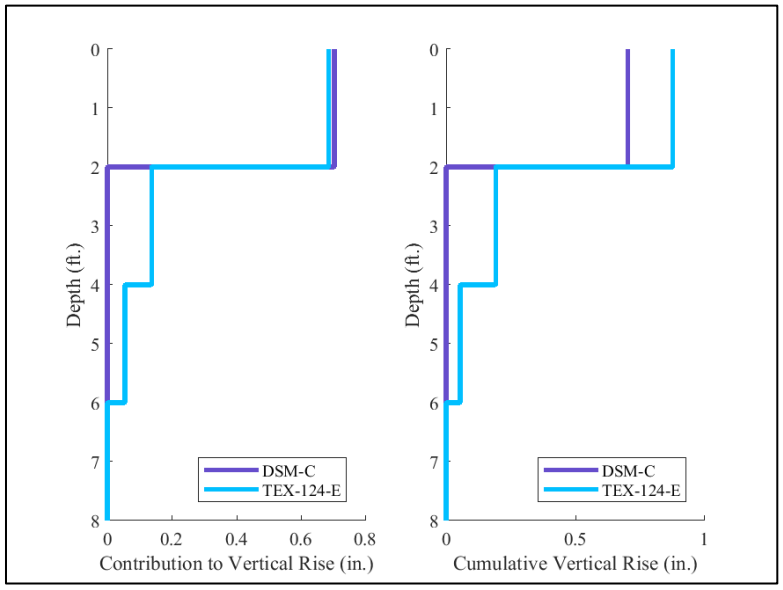

Figure B.44: Calculated vertical rise for each 2-ft section (left) and cumulative vertical rise (right) for both Centrifuge and Tex-124-E methods for boring B-26

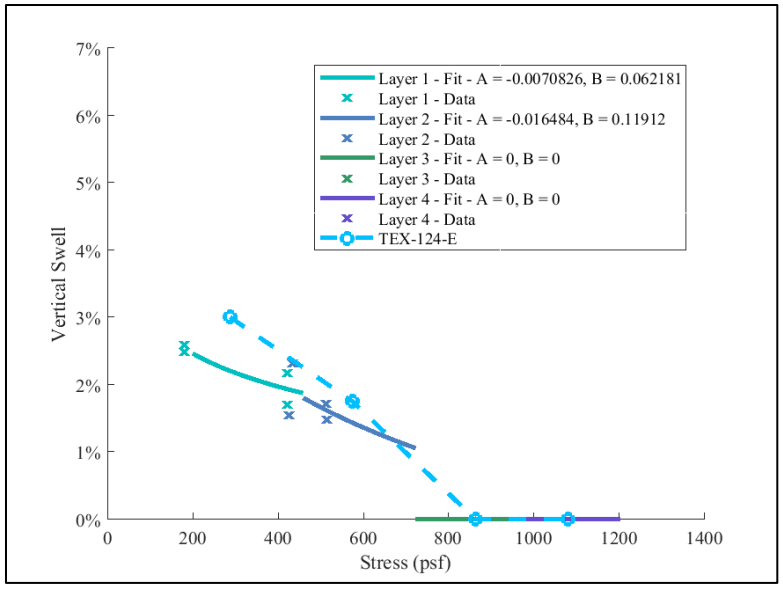

Figure B.45: Measured stress-swell curves and comparison of curves from centrifuge data to Tex-124-E for boring B-27

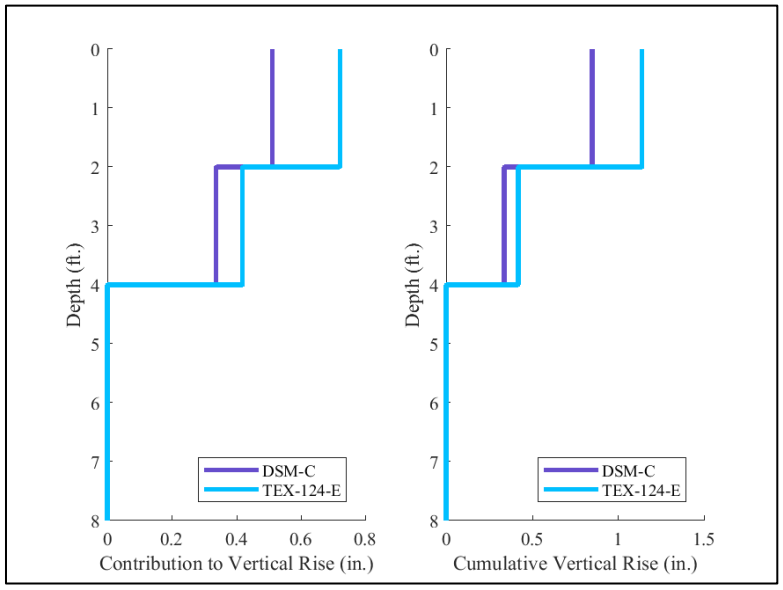

Figure B.46: Calculated vertical rise for each 2-ft section (left) and cumulative vertical rise (right) for both Centrifuge and Tex-124-E methods for boring B-27

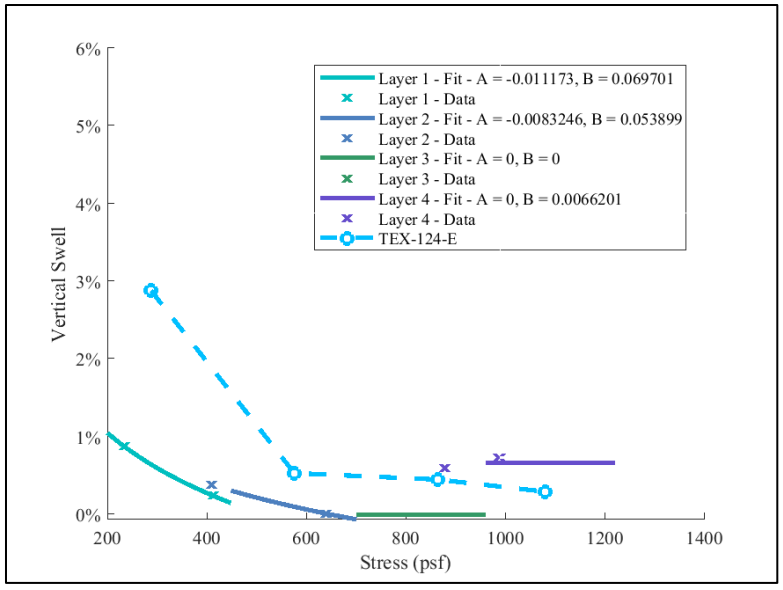

Figure B.47: Measured stress-swell curves and comparison of curves from centrifuge data to Tex-124-E for boring B-28

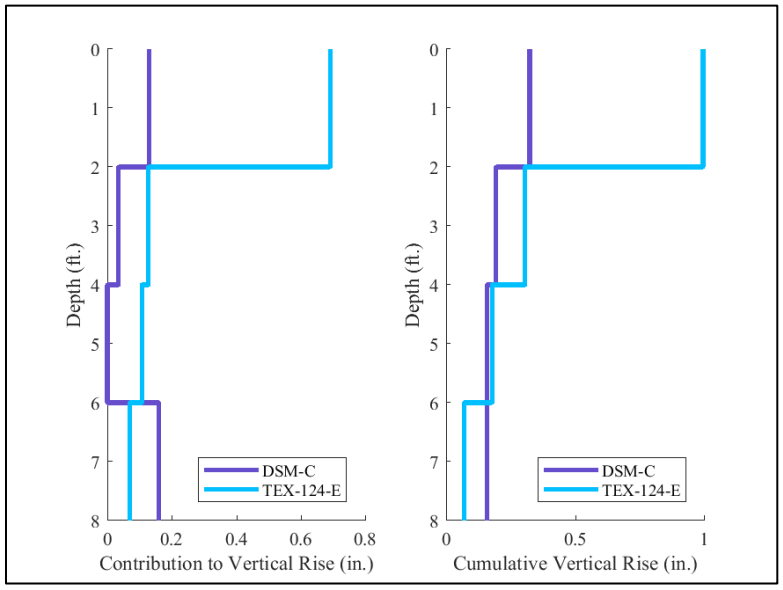

Figure B.48: Calculated vertical rise for each 2-ft section (left) and cumulative vertical rise (right) for both Centrifuge and Tex-124-E methods for boring B-28

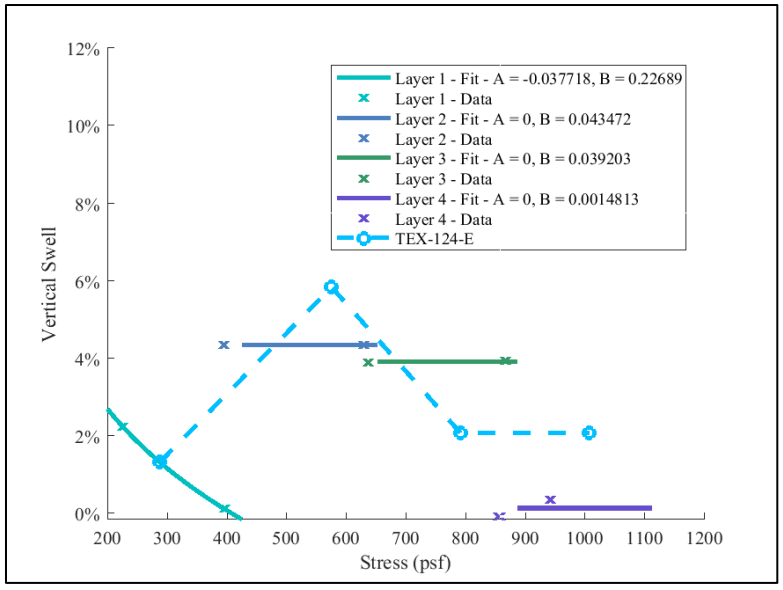

Figure B.49: Measured stress-swell curves and comparison of curves from centrifuge data to Tex-124-E for boring B-29

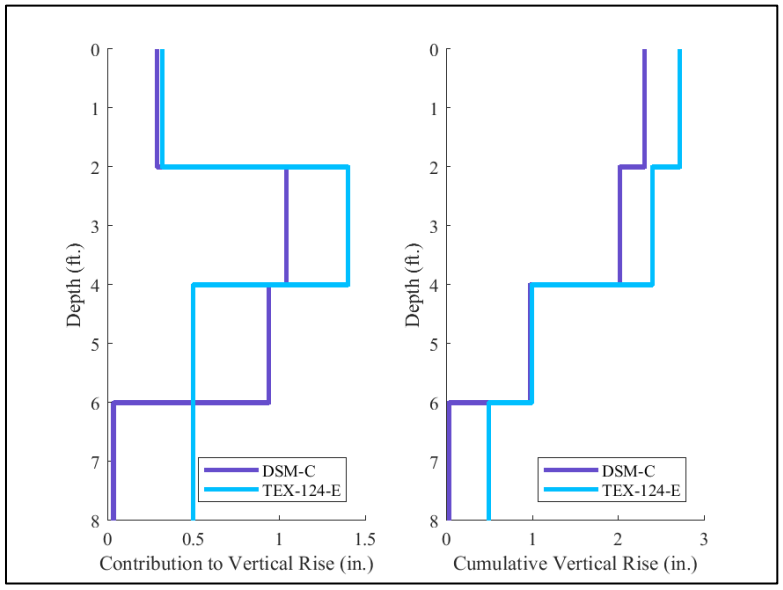

Figure B.50: Calculated vertical rise for each 2-ft section (left) and cumulative vertical rise (right) for both Centrifuge and Tex-124-E methods for boring B-29

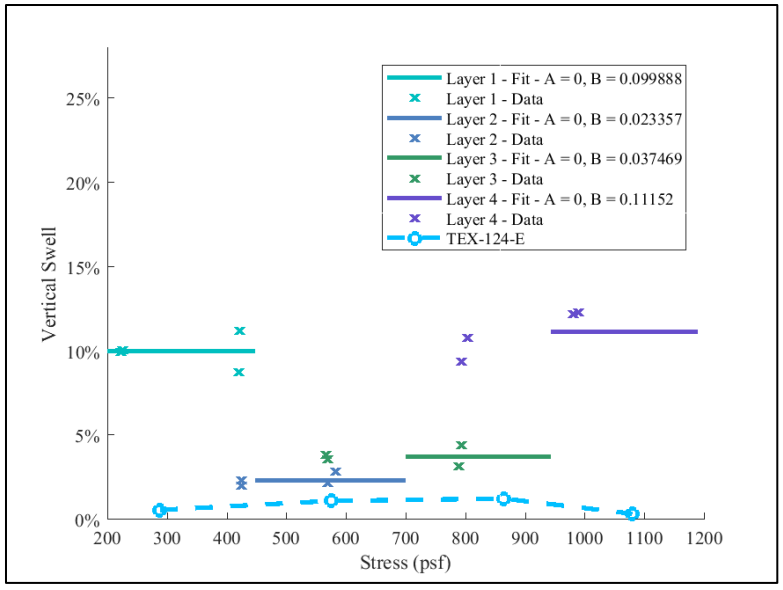

Figure B.51: Measured stress-swell curves and comparison of curves from centrifuge data to Tex-124-E for boring B-30

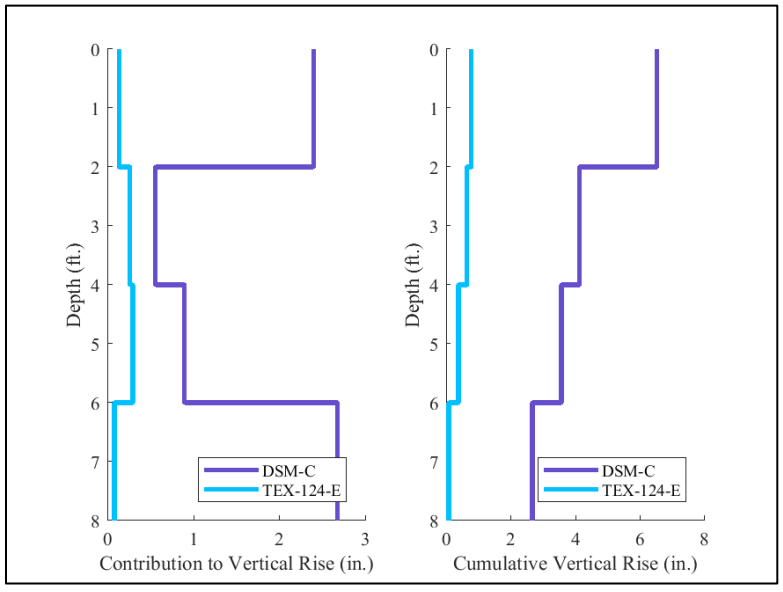

Figure B.52: Calculated vertical rise for each 2-ft section (left) and cumulative vertical rise (right) for both Centrifuge and Tex-124-E methods for boring B-30

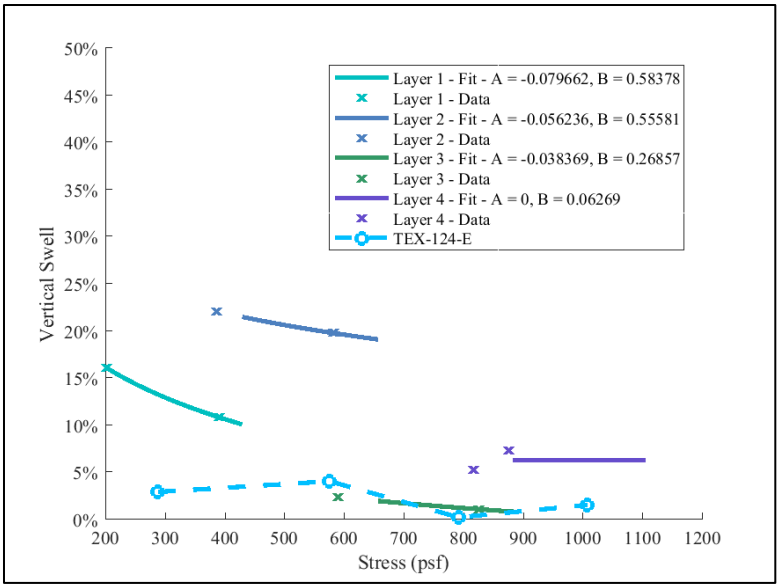

Figure B.53: Measured stress-swell curves and comparison of curves from centrifuge data to Tex-124-E for boring B-31

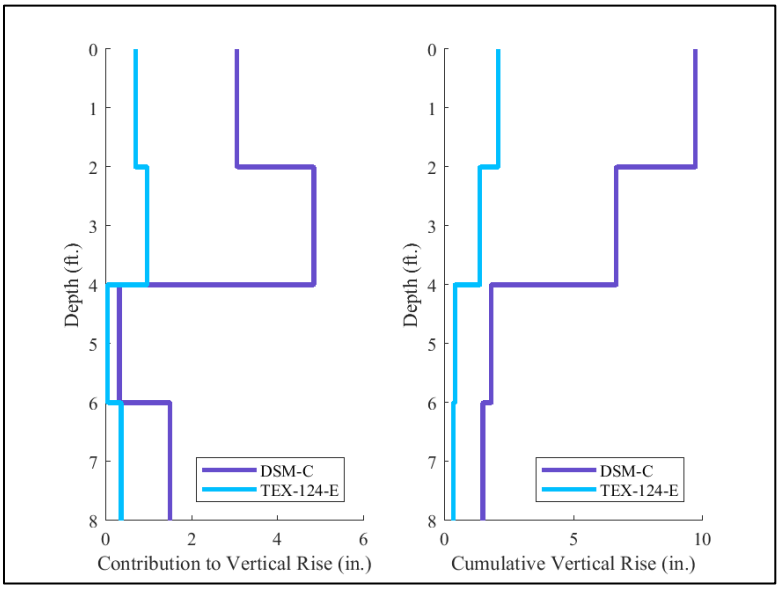

Figure B.54: Calculated vertical rise for each 2-ft section (left) and cumulative vertical rise (right) for both Centrifuge and Tex-124-E methods for boring B-31

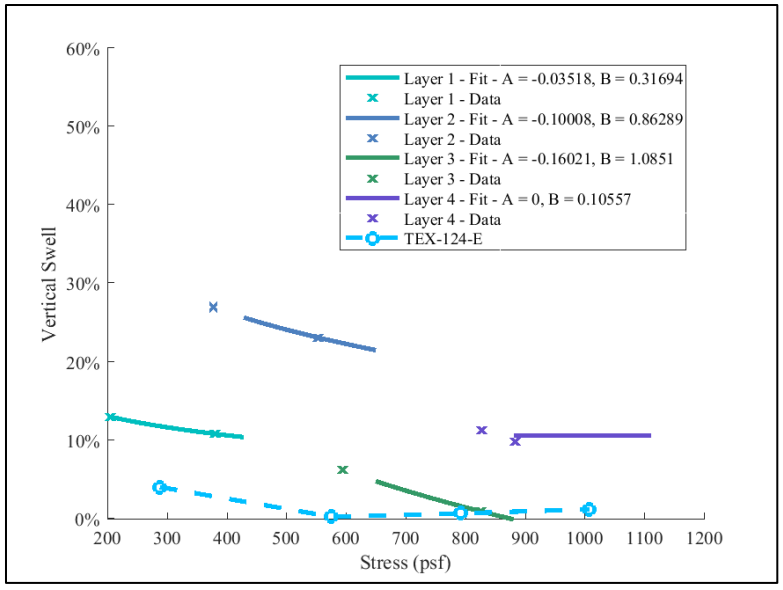

Figure B.55: Measured stress-swell curves and comparison of curves from centrifuge data to Tex-124-E for boring B-32

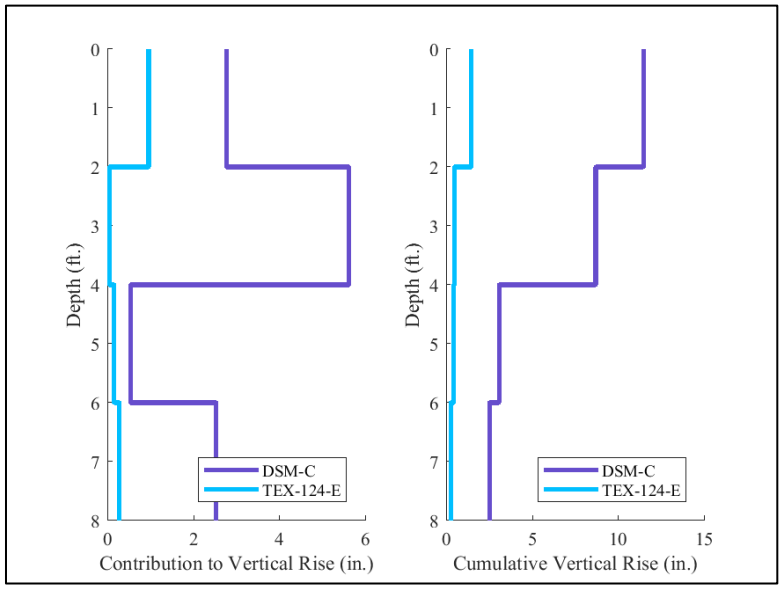

Figure B.56: Calculated vertical rise for each 2-ft section (left) and cumulative vertical rise (right) for both Centrifuge and Tex-124-E methods for boring B-32

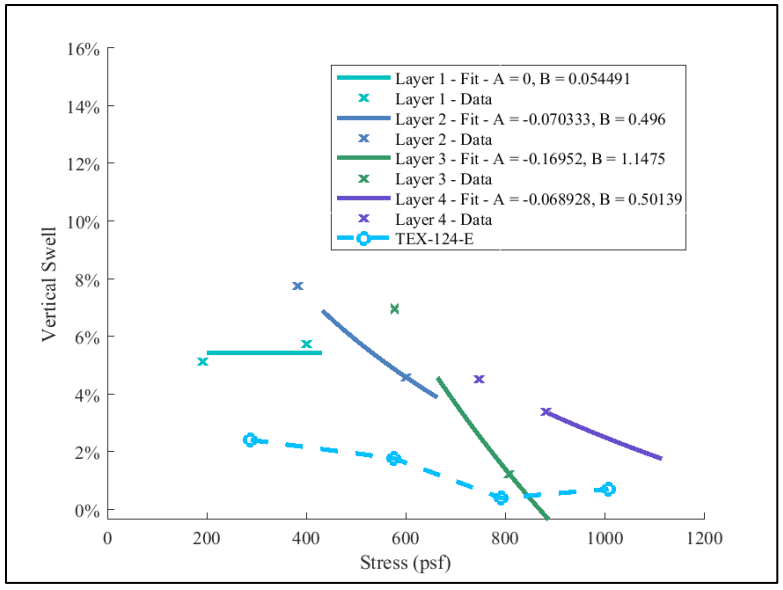

Figure B.57: Measured stress-swell curves and comparison of curves from centrifuge data to Tex-124-E for boring B-33

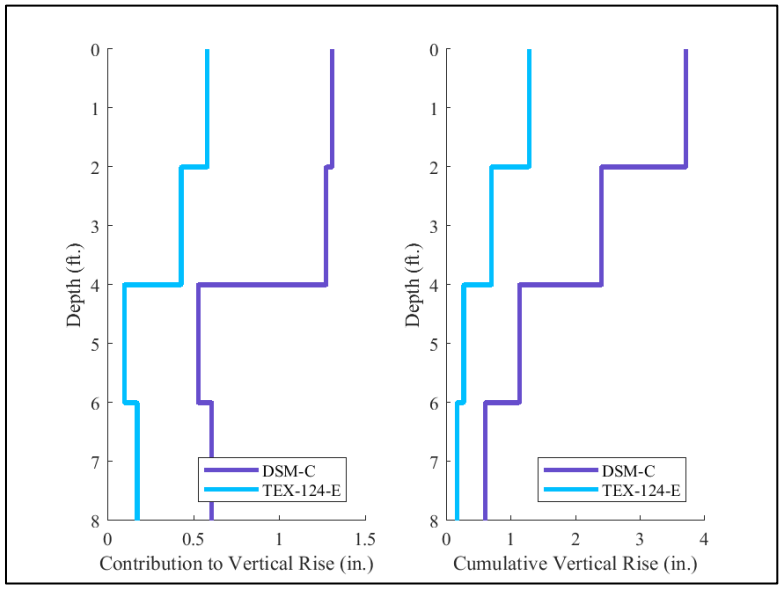

Figure B.58: Calculated vertical rise for each 2-ft section (left) and cumulative vertical rise (right) for both Centrifuge and Tex-124-E methods for boring B-33

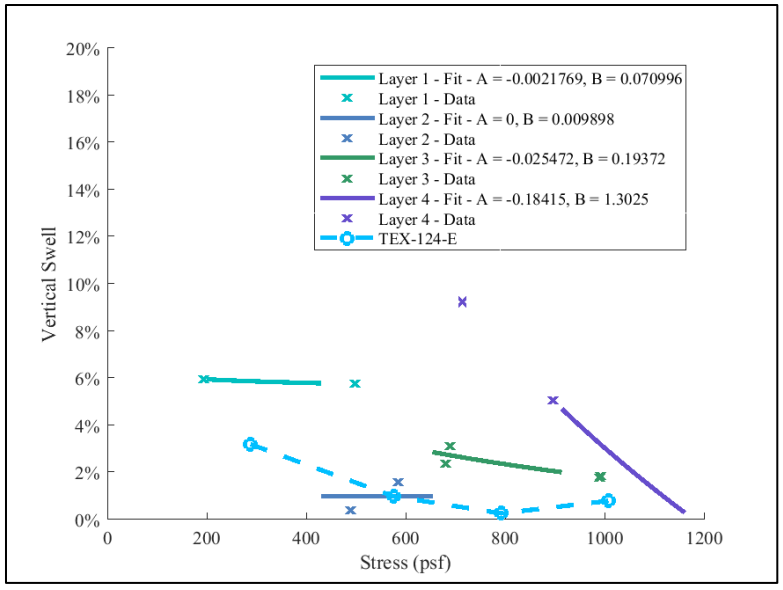

Figure B.59: Measured stress-swell curves and comparison of curves from centrifuge data to Tex-124-E for boring B-34

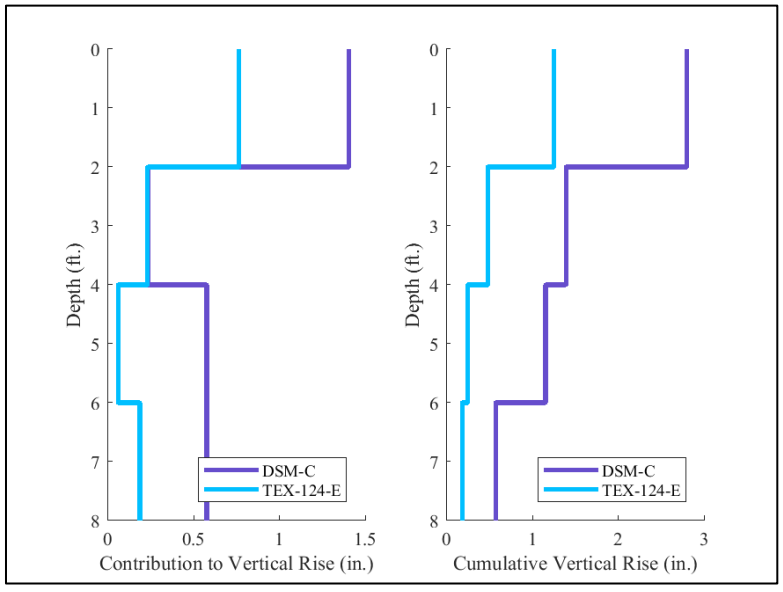

Figure B.60: Calculated vertical rise for each 2-ft section (left) and cumulative vertical rise (right) for both Centrifuge and Tex-124-E methods for boring B-34

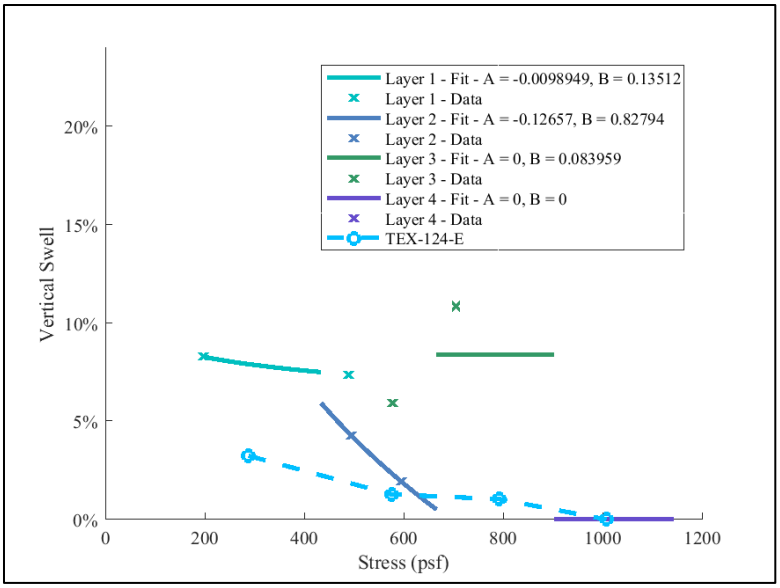

Figure B.61: Measured stress-swell curves and comparison of curves from centrifuge data to Tex-124-E for boring B-35

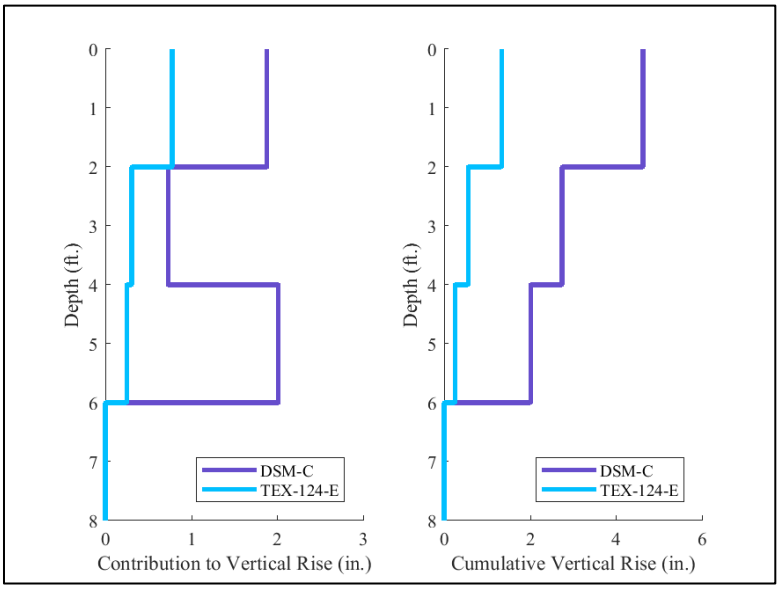

Figure B.62: Calculated vertical rise for each 2-ft section (left) and cumulative vertical rise (right) for both Centrifuge and Tex-124-E methods for boring B-35

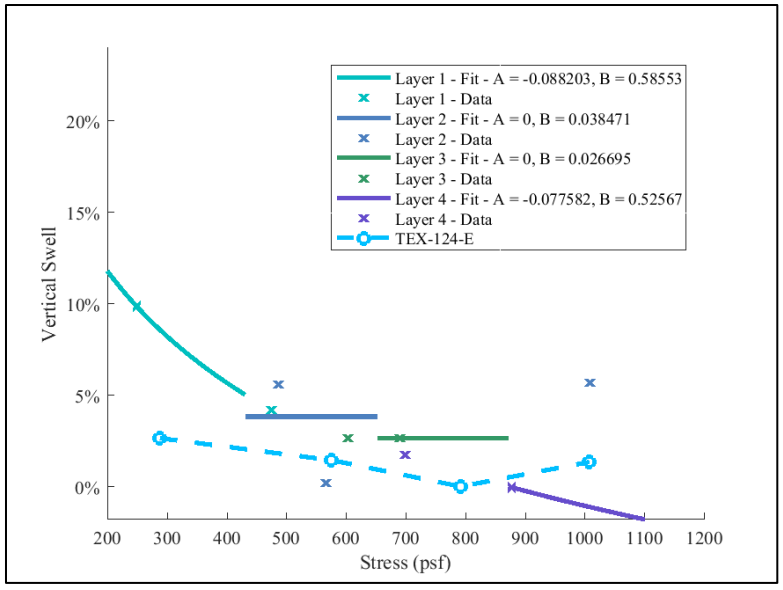

Figure B.63: Measured stress-swell curves and comparison of curves from centrifuge data to Tex-124-E for boring B-36

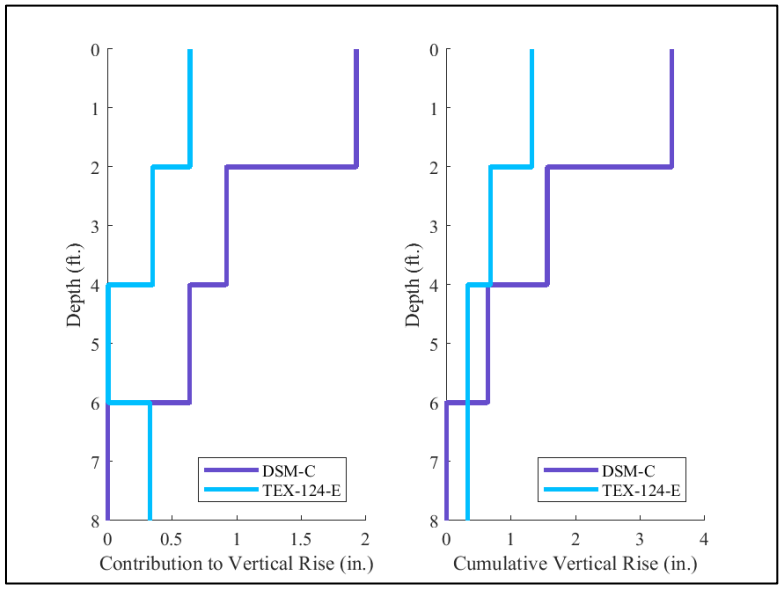

Figure B.64: Calculated vertical rise for each 2-ft section (left) and cumulative vertical rise (right) for both Centrifuge and Tex-124-E methods for boring B-36

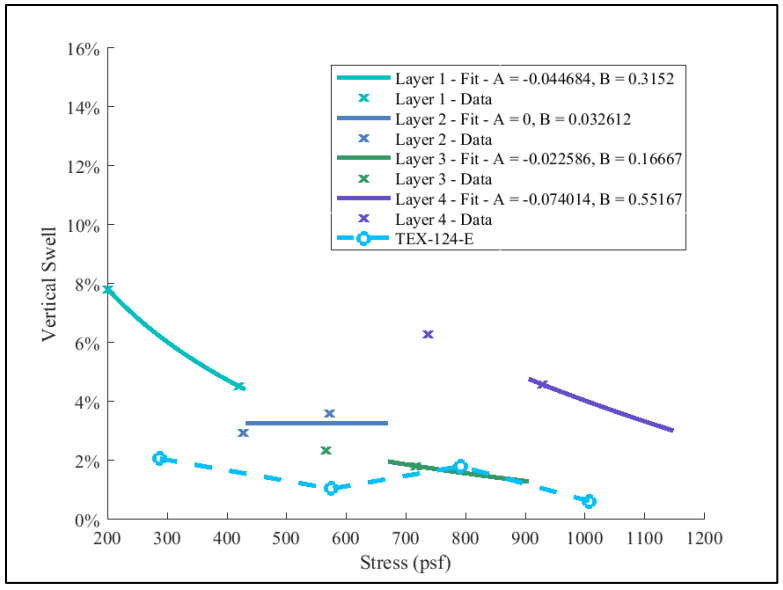

Figure B.65: Measured stress-swell curves and comparison of curves from centrifuge data to Tex-124-E for boring B-37

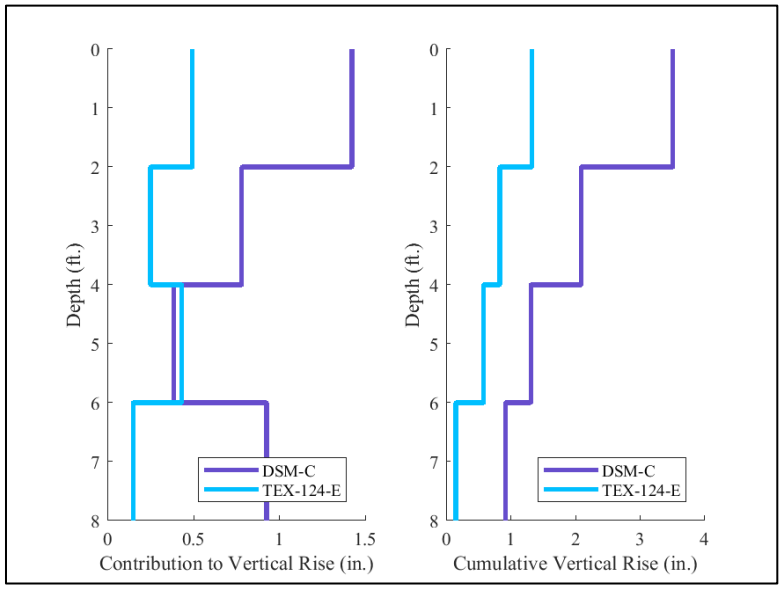

Figure B.66: Calculated vertical rise for each 2-ft section (left) and cumulative vertical rise (right) for both Centrifuge and Tex-124-E methods for boring B-37

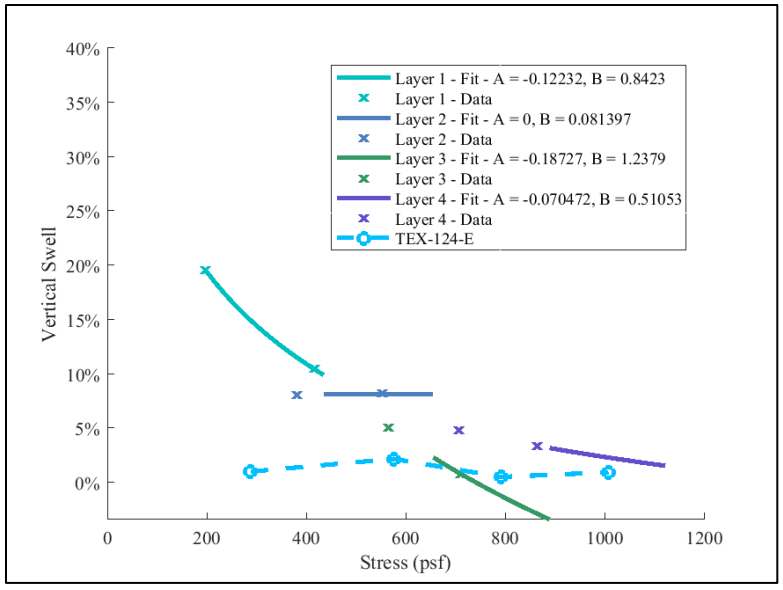

Figure B.67: Measured stress-swell curves and comparison of curves from centrifuge data to Tex-124-E for boring B-38

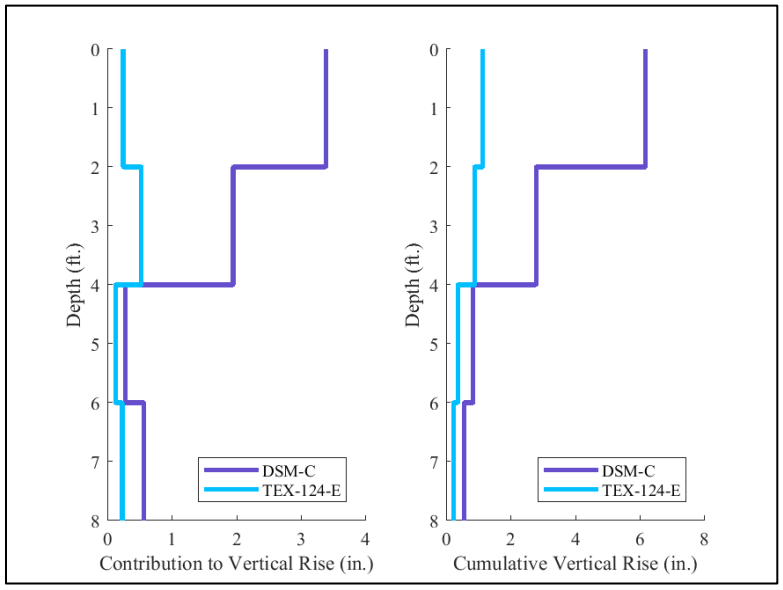

Figure B.68: Calculated vertical rise for each 2-ft section (left) and cumulative vertical rise (right) for both Centrifuge and Tex-124-E methods for boring B-38

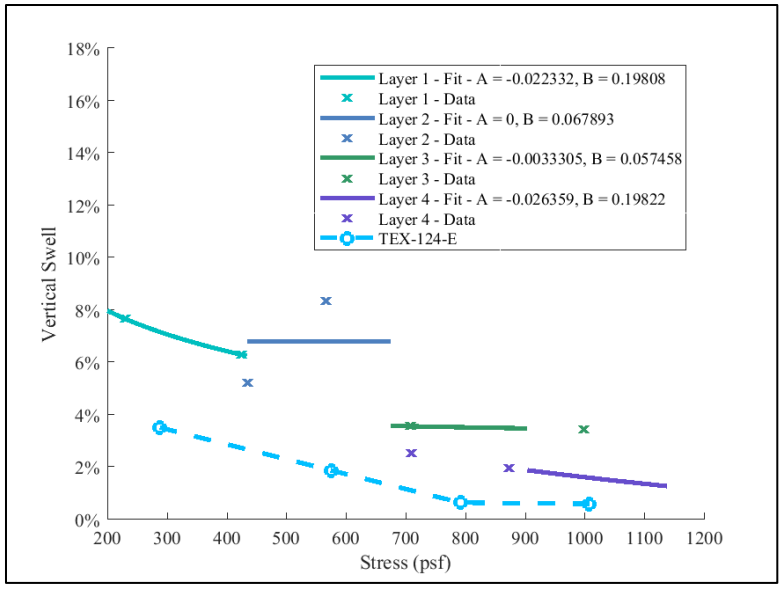

Figure B.69: Measured stress-swell curves and comparison of curves from centrifuge data to Tex-124-E for boring B-39

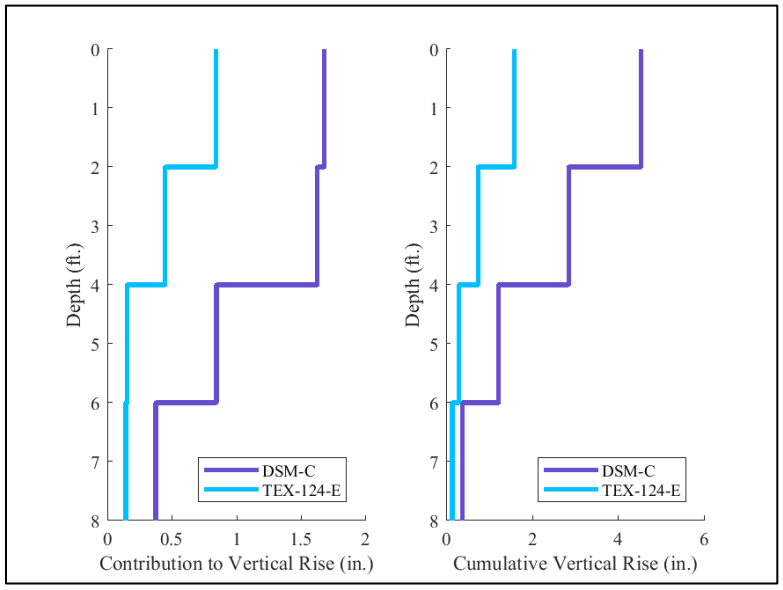

Figure B.70: Calculated vertical rise for each 2-ft section (left) and cumulative vertical rise (right) for both Centrifuge and Tex-124-E methods for boring B-39

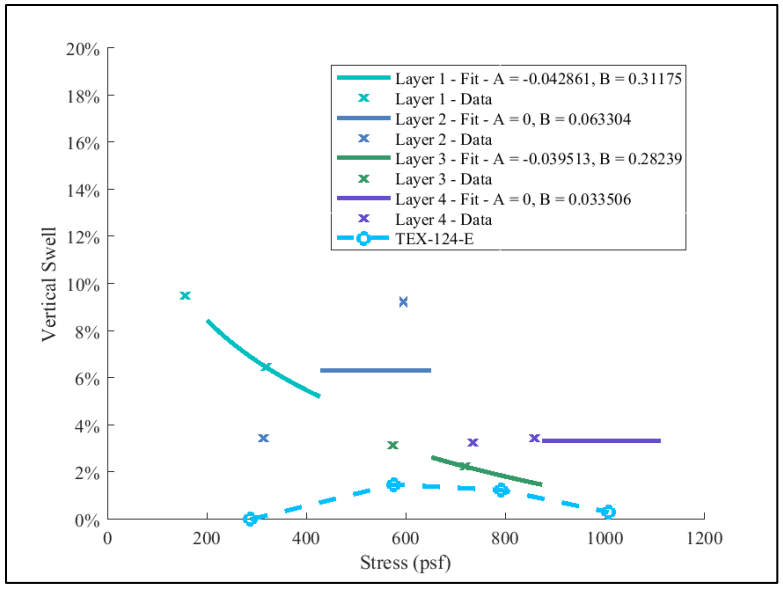

Figure B.71: Measured stress-swell curves and comparison of curves from centrifuge data to Tex-124-E for boring B-40

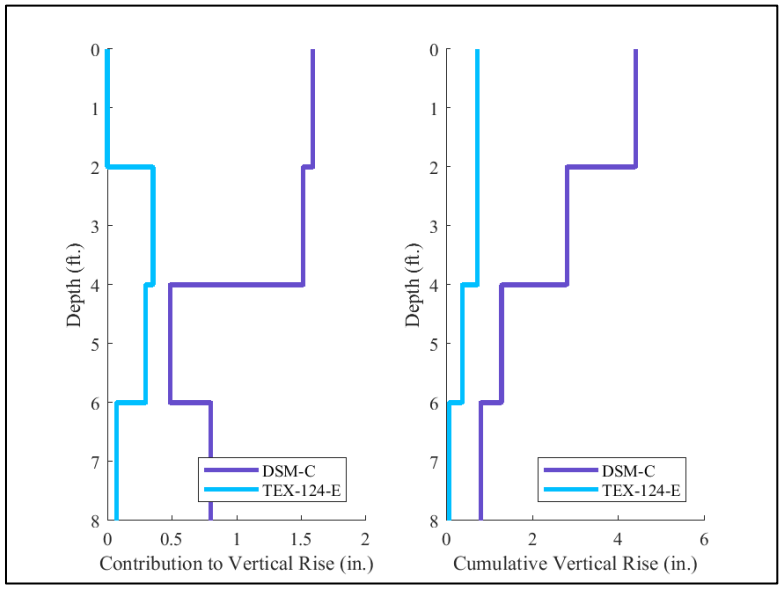

Figure B.72: Calculated vertical rise for each 2-ft section (left) and cumulative vertical rise (right) for both Centrifuge and Tex-124-E methods for boring B-40

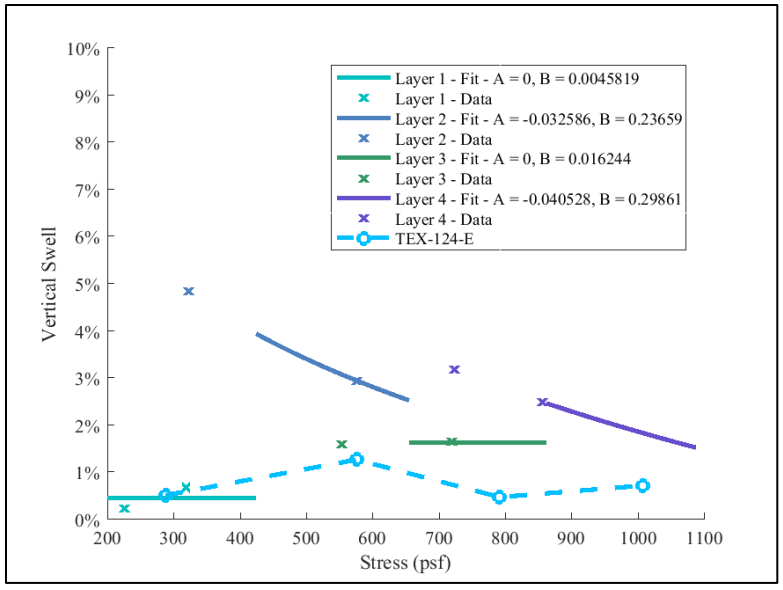

Figure B.73: Measured stress-swell curves and comparison of curves from centrifuge data to Tex-124-E for boring B-41

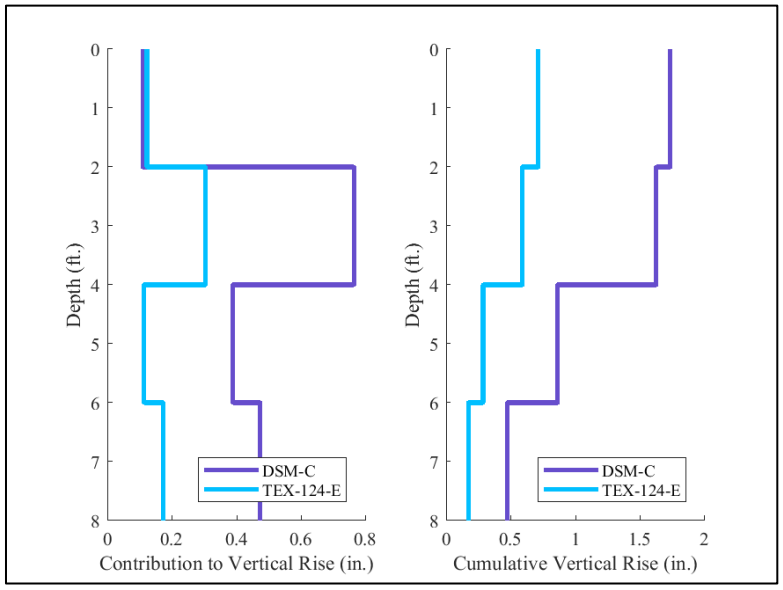

Figure B.74: Calculated vertical rise for each 2-ft section (left) and cumulative vertical rise (right) for both Centrifuge and Tex-124-E methods for boring B-41

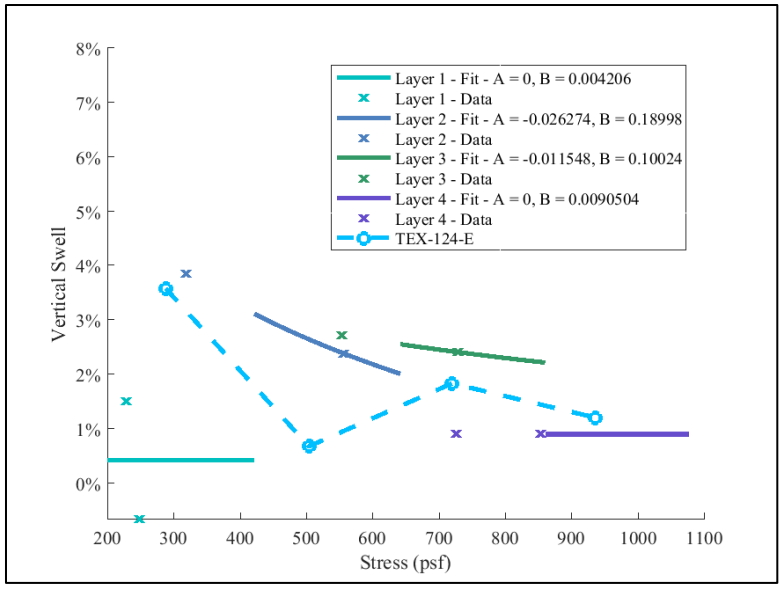

Figure B.75: Measured stress-swell curves and comparison of curves from centrifuge data to Tex-124-E for boring B-42

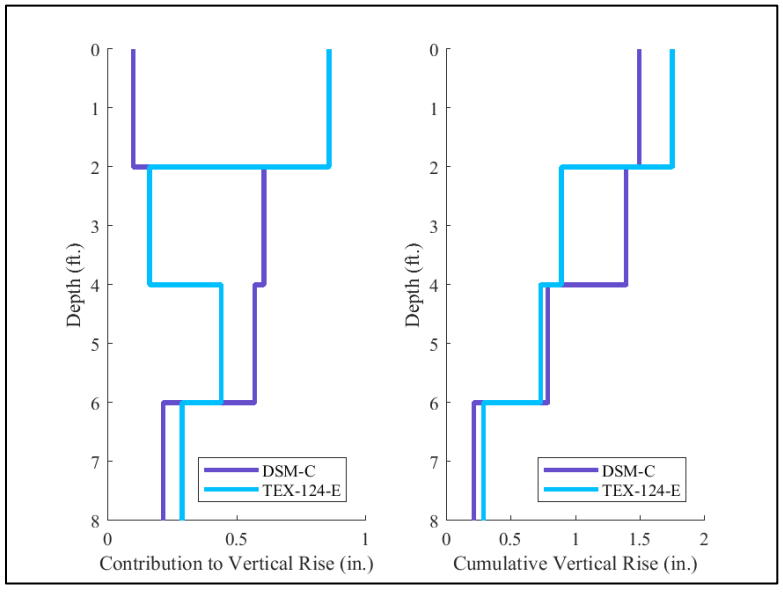

Figure B.76: Calculated vertical rise for each 2-ft section (left) and cumulative vertical rise (right) for both Centrifuge and Tex-124-E methods for boring B-42

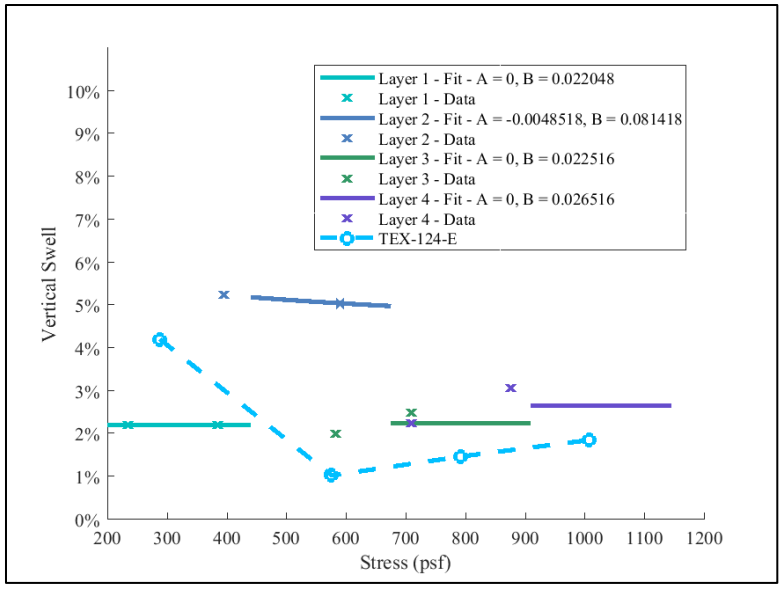

Figure B.77: Measured stress-swell curves and comparison of curves from centrifuge data to Tex-124-E for boring B-43

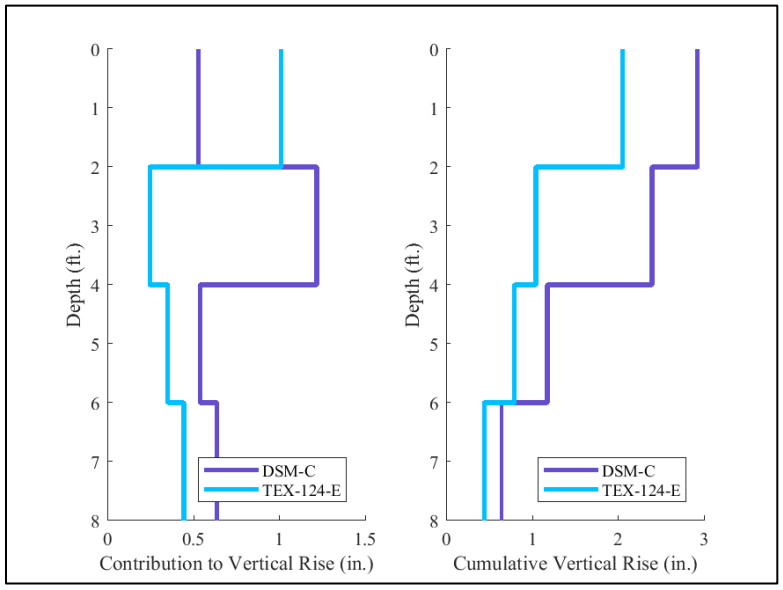

Figure B.78: Calculated vertical rise for each 2-ft section (left) and cumulative vertical rise (right) for both Centrifuge and Tex-124-E methods for boring B-43

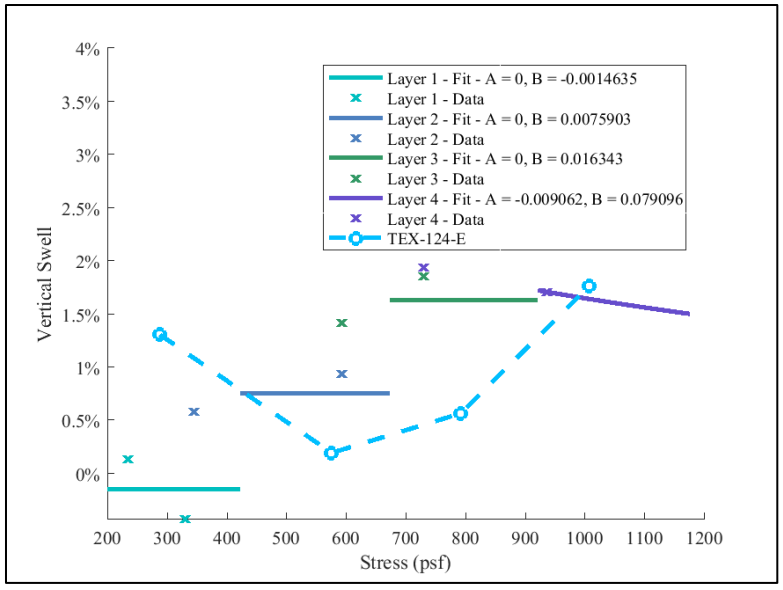

Figure B.79: Measured stress-swell curves and comparison of curves from centrifuge data to Tex-124-E for boring B-44

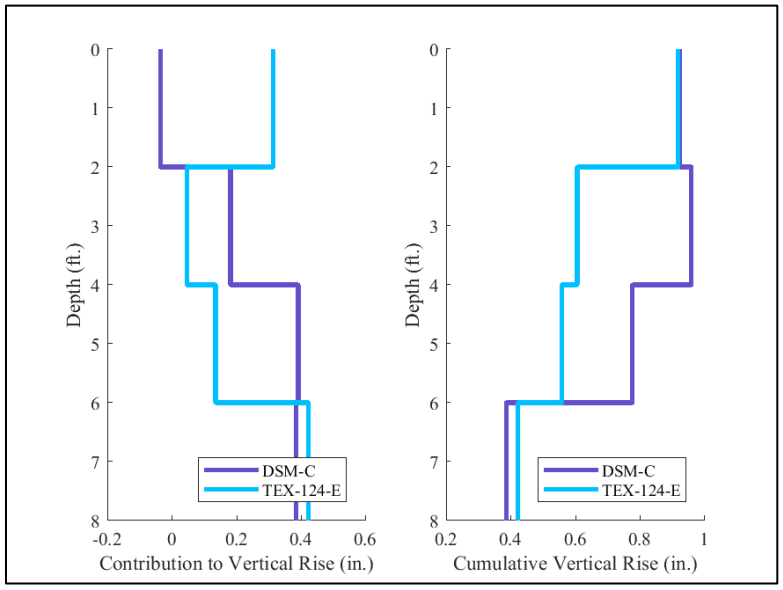

Figure B.80: Calculated vertical rise for each 2-ft section (left) and cumulative vertical rise (right) for both Centrifuge and Tex-124-E methods for boring B-44

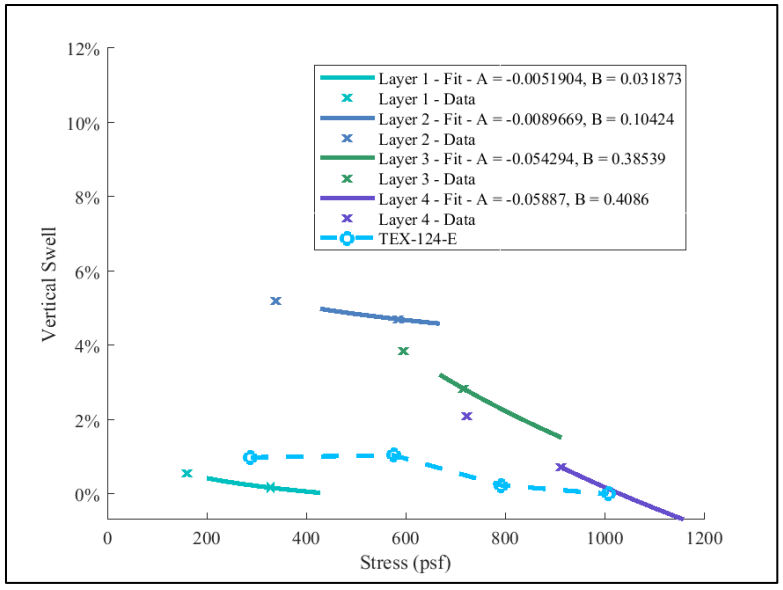

Figure B.81: Measured stress-swell curves and comparison of curves from centrifuge data to Tex-124-E for boring B-45

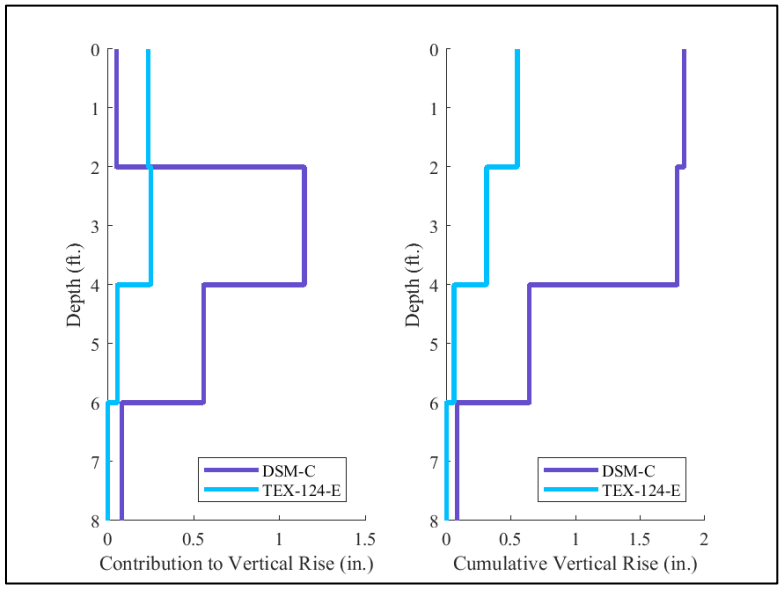

Figure B.82: Calculated vertical rise for each 2-ft section (left) and cumulative vertical rise (right) for both Centrifuge and Tex-124-E methods for boring B-45

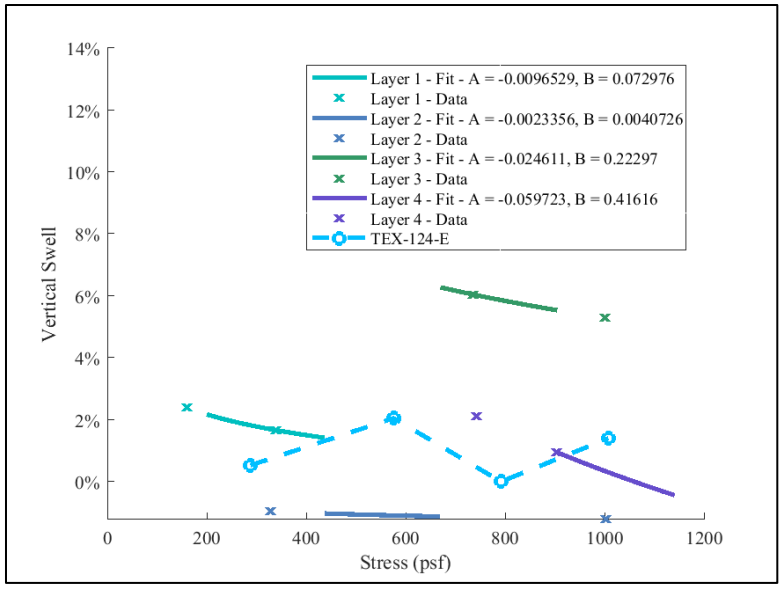

Figure B.83: Measured stress-swell curves and comparison of curves from centrifuge data to Tex-124-E for boring B-46

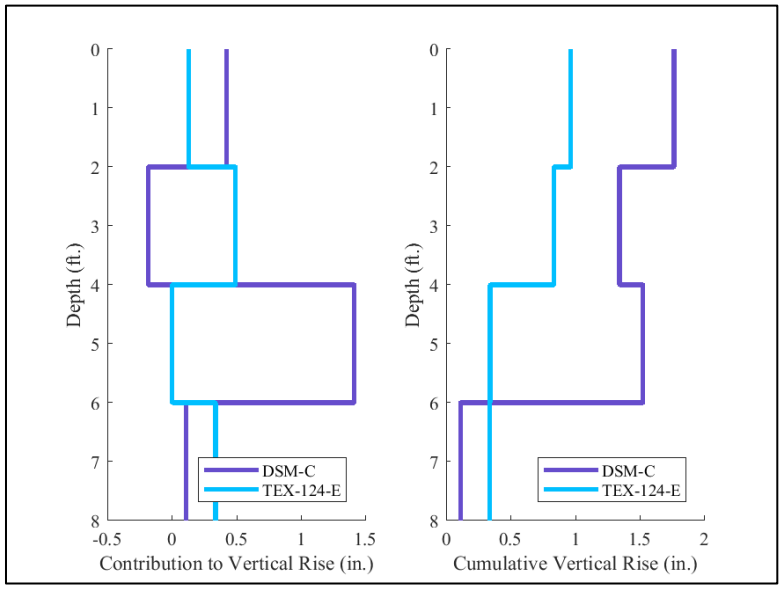

Figure B.84: Calculated vertical rise for each 2-ft section (left) and cumulative vertical rise (right) for both Centrifuge and Tex-124-E methods for boring B-46

APPENDIX C: ADDITIONAL DATA FROM MONITORING OF FM 685 SITE

This appendix summarizes the additional results from Chapter 5 of this dissertation. These results include those from monitoring of moisture time histories and the fitting of soil-water retention curves and are grouped into six sections.

The first section contains additional results from the monitoring during the flexible base time period. These results include the moisture content, matric suction, and degree of saturation time histories for sensors that were not presented previously.

The second section contains additional results from the monitoring during the asphalt time period. These results include the moisture content, matric suction, and degree of saturation time histories for sensors that were not presented previously.

The third section contains additional results from the statistical analysis of the sensor readings. These results include those from the moisture content and matric suction evaluations.

The forth section contains additional soil-water retention curves that use the volumetric moisture content readings. These results include the parameters for the fitted soil-water retention curves, additional soil-water retention curves, and comparative results using a lower matric suction threshold.

The fifth section contains additional soil-water retention curves that use the estimated degree of saturation. These results include the parameters for the fitted soil-water retention curves, additional soil-water retention curves, and comparative results using a lower matric suction threshold.

The sixth section contains additional results from the optimization of the techniques used for the fitting of the soil-water retention curves.

C.1: Moisture Monitoring of Site during Flexible Base Time Period

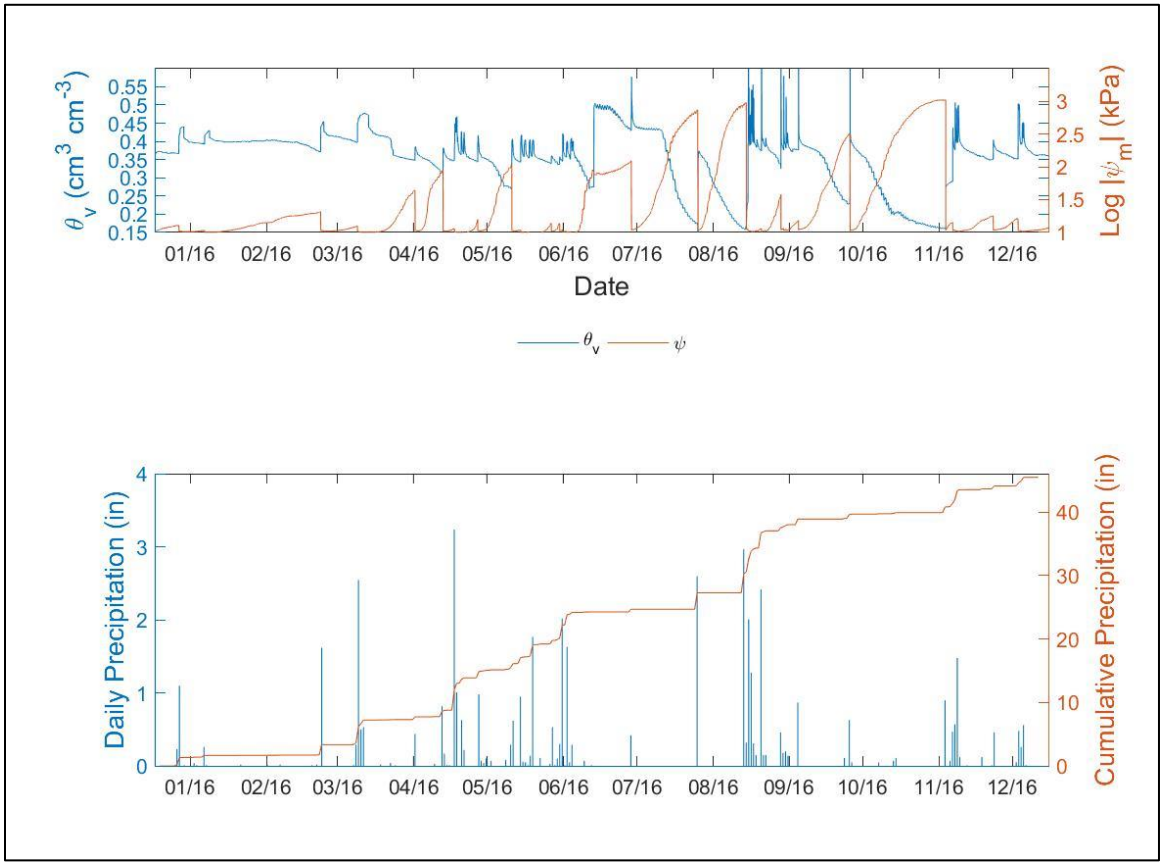

Figure C.1: Hydraulic time histories and precipitation data for the sensor pairing at a depth of 0.5 ft below the base-subgrade interface for the flexible base time period

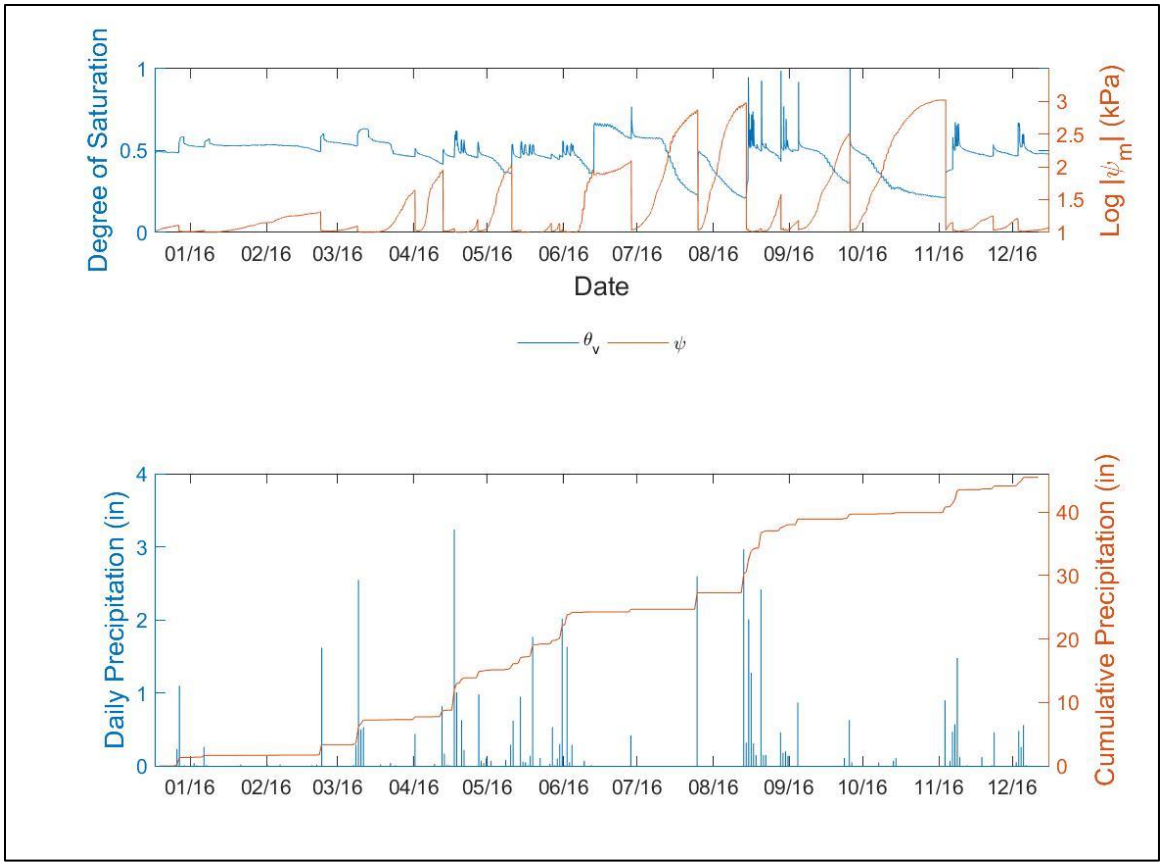

Figure C.2: Saturation and suction time histories and precipitation data for the sensor pairing at a depth of 0.5 ft below the base-subgrade interface for the flexible base time period

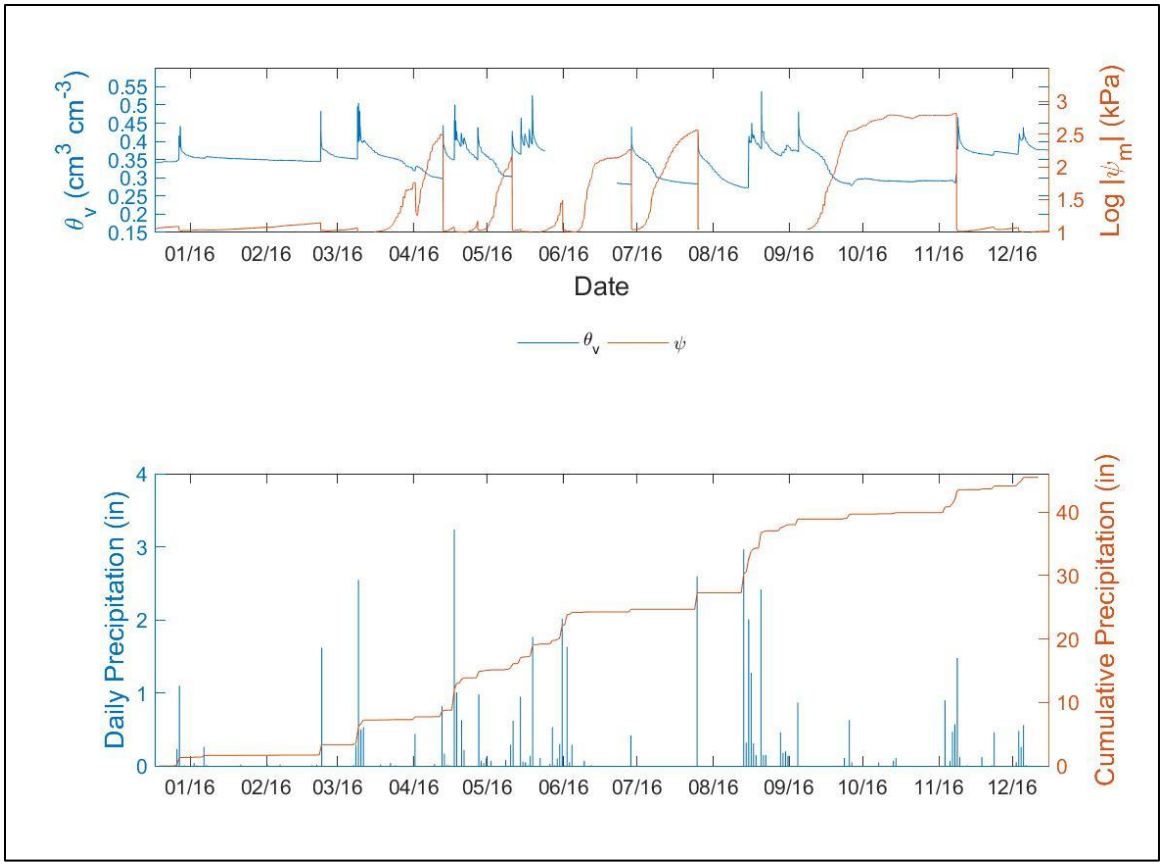

Figure C.3: Hydraulic time histories and precipitation data for the sensor pairing at a depth of 4.5 ft below the base-subgrade interface for the flexible base time period

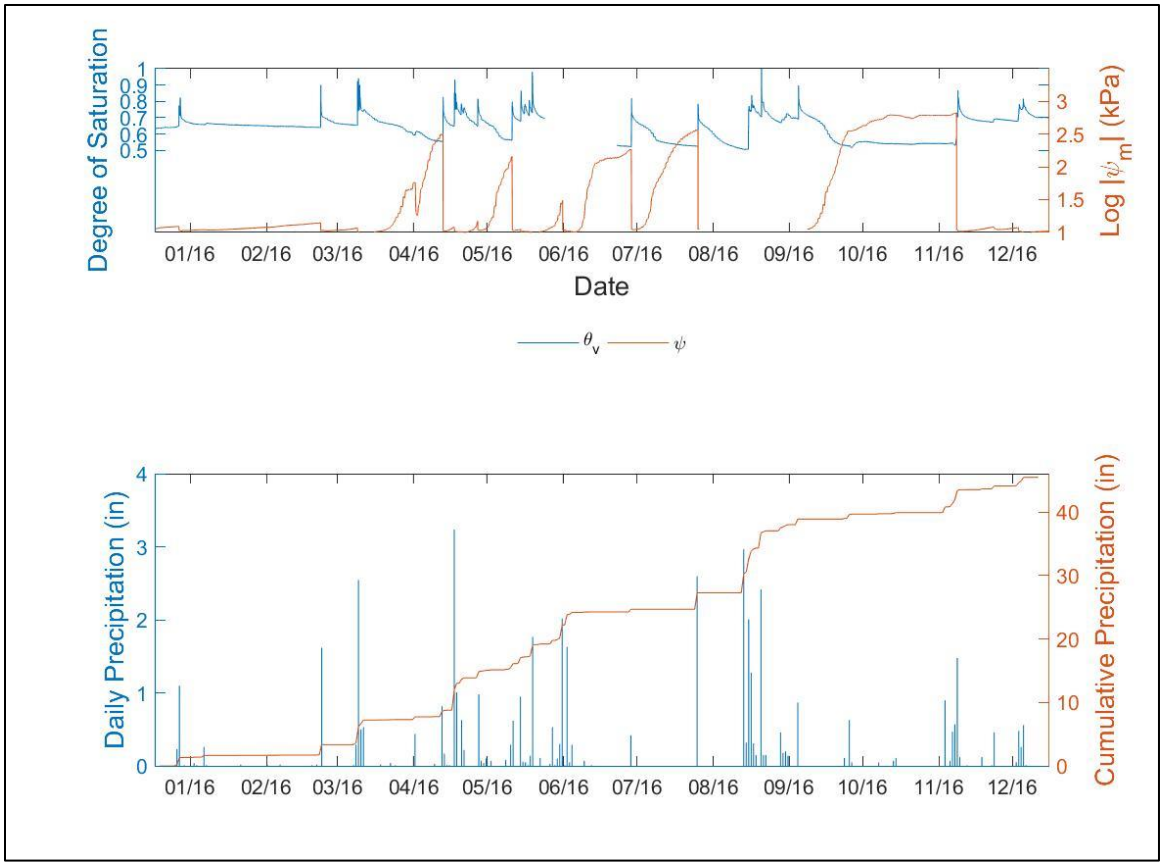

Figure C.4: Saturation and suction time histories and precipitation data for the sensor pairing at a depth of 4.5 ft below the base-subgrade interface for the flexible base time period

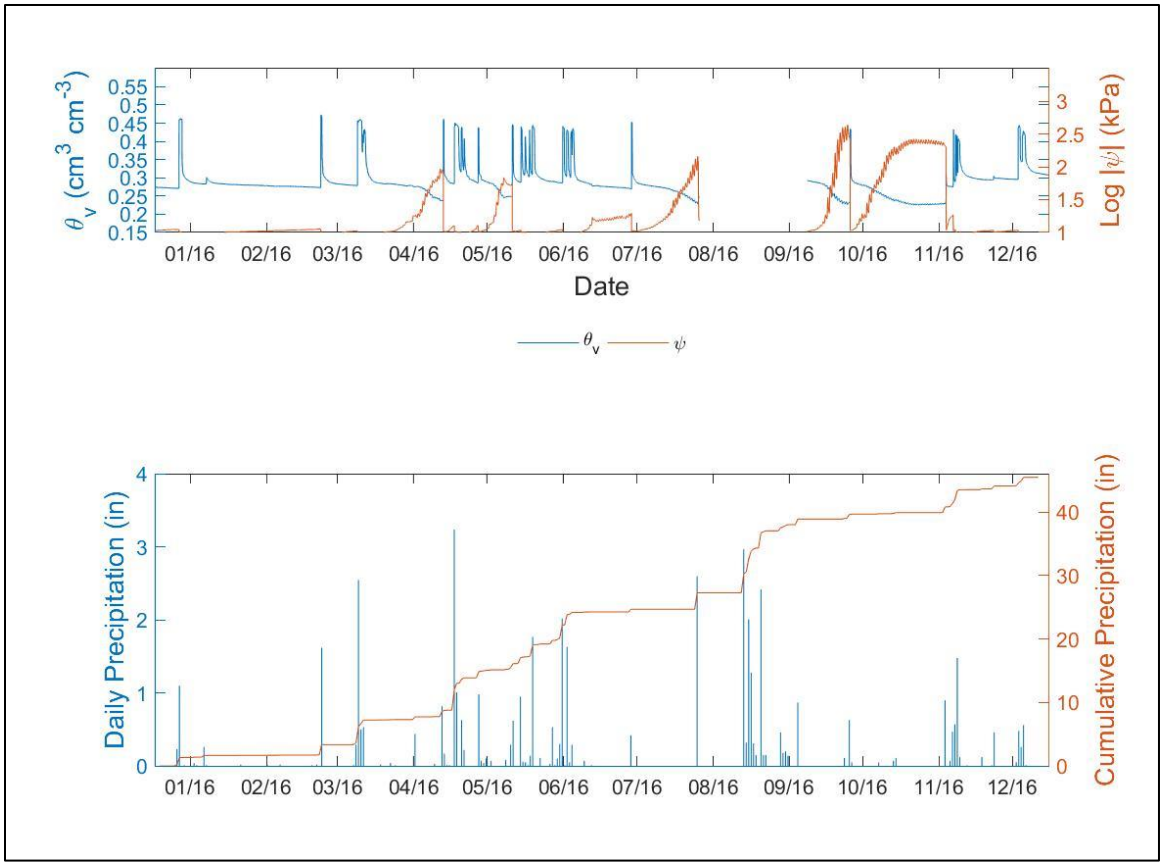

Figure C.5: Hydraulic time histories and precipitation data for the sensor pairing at a depth of 5.5 ft below the base-subgrade interface for the flexible base time period

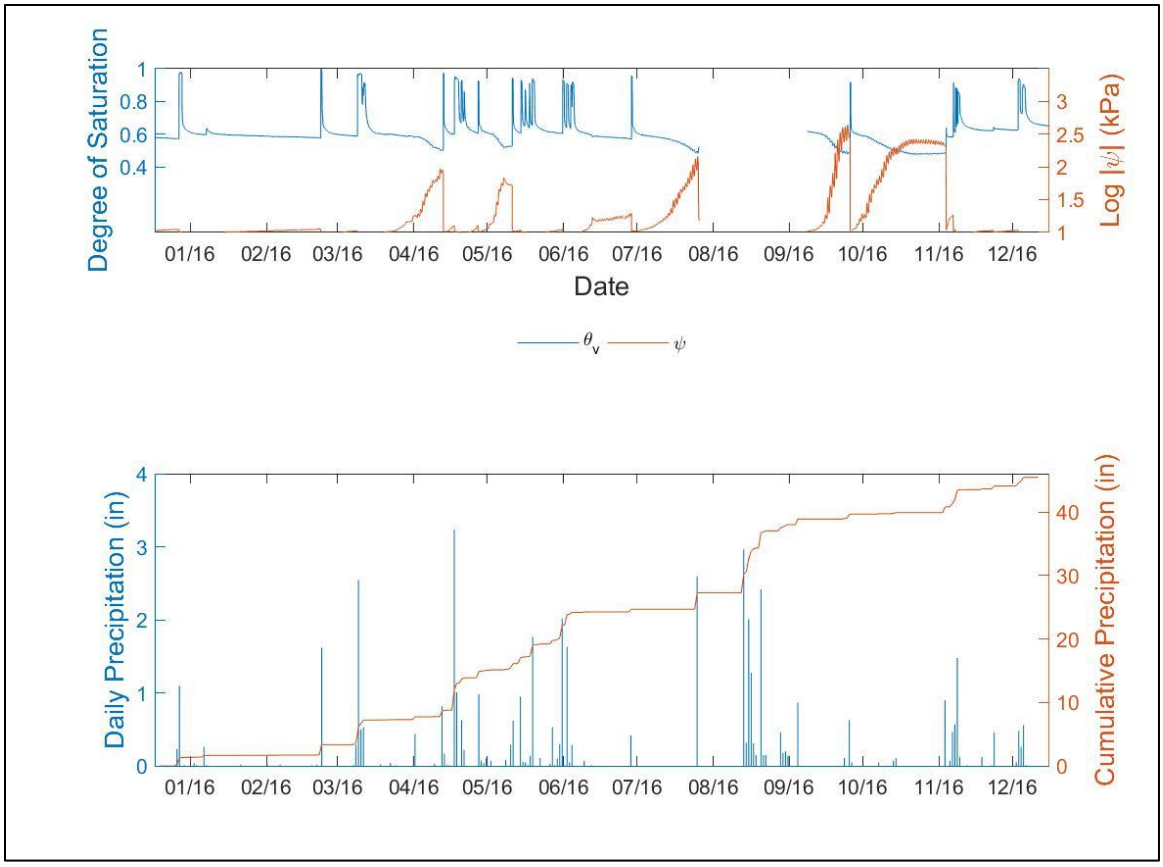

Figure C.6: Saturation and suction time histories and precipitation data for the sensor pairing at a depth of 5.5 ft below the base-subgrade interface for the flexible base time period

C.2: Moisture Monitoring of Site during Asphalt Time Period

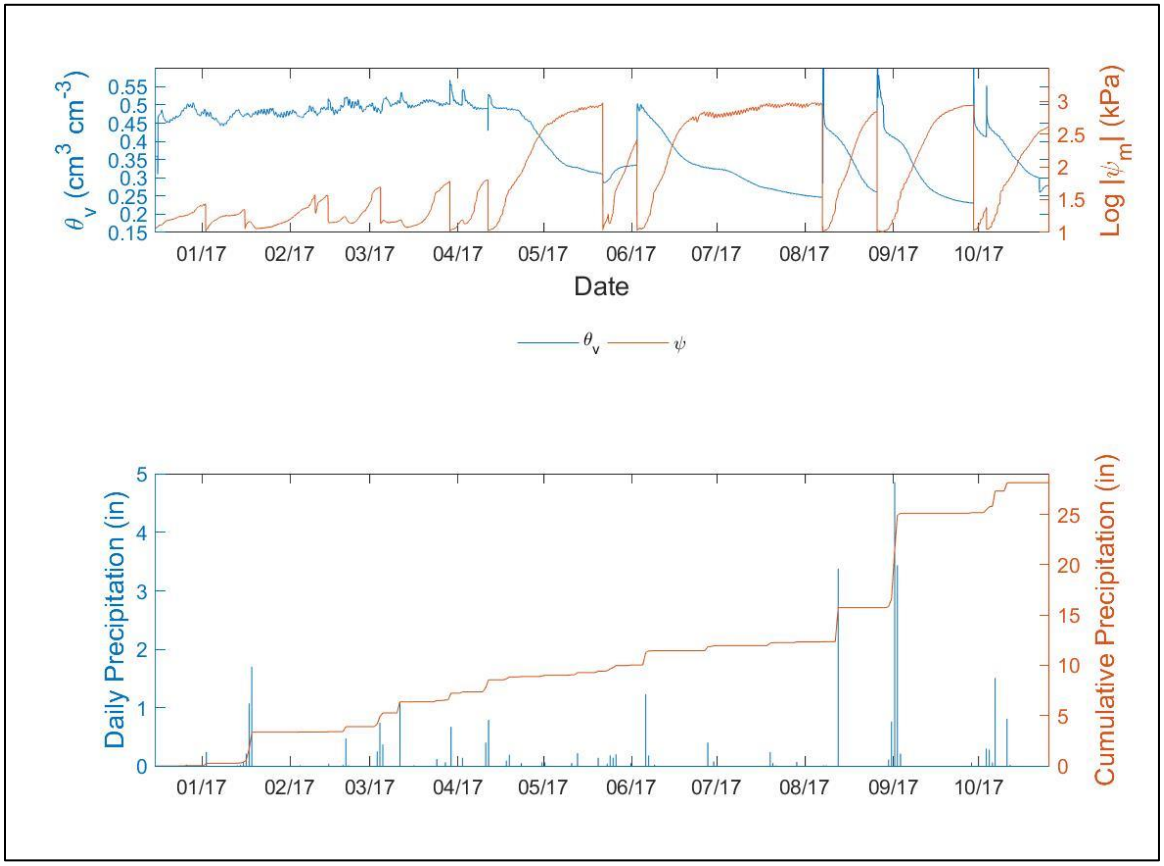

Figure C.7: Hydraulic time histories and precipitation data for the sensor pairing at a depth of 0.5 ft below the base-subgrade interface for the asphalt time period

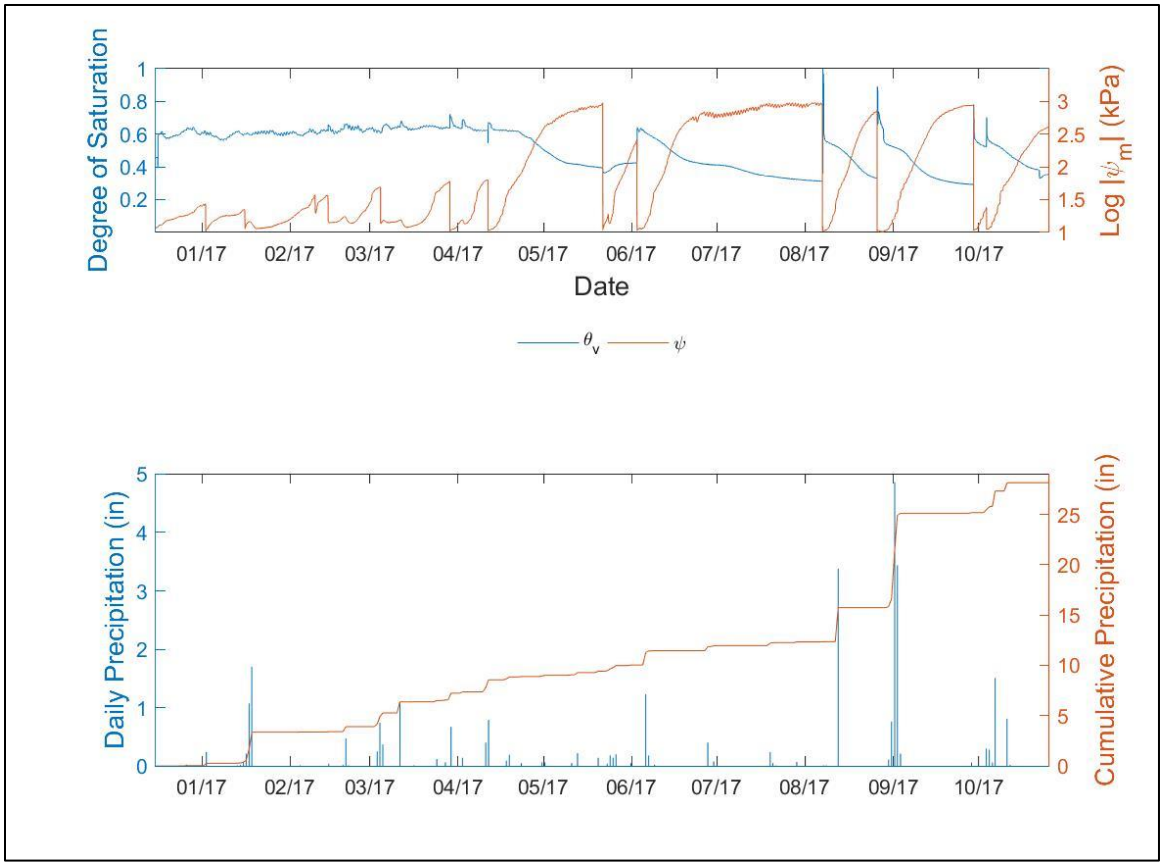

Figure C.8: Saturation and suction time histories and precipitation data for the sensor pairing at a depth of 0.5 ft below the base-subgrade for the asphalt surface time period

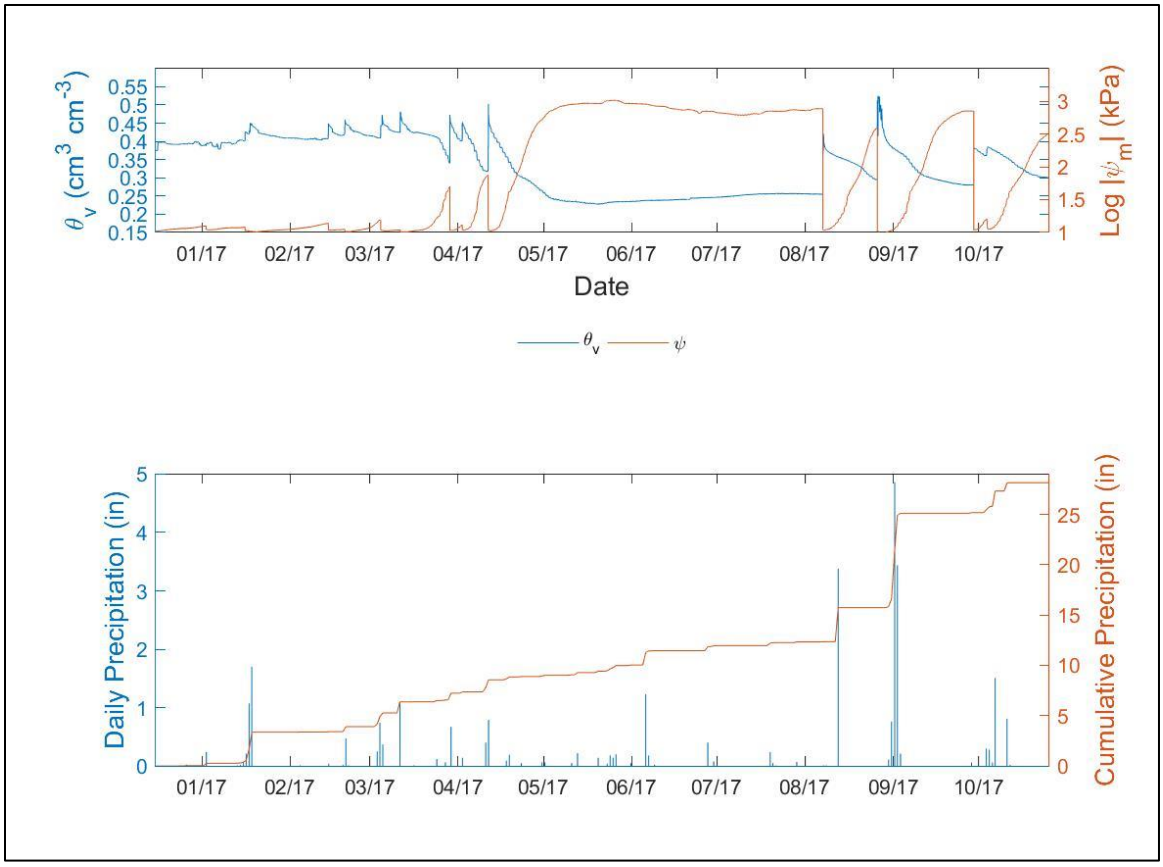

Figure C.9: Hydraulic time histories and precipitation data for the sensor pairing at a depth of 4.5 ft below the base-subgrade for asphalt surface time period

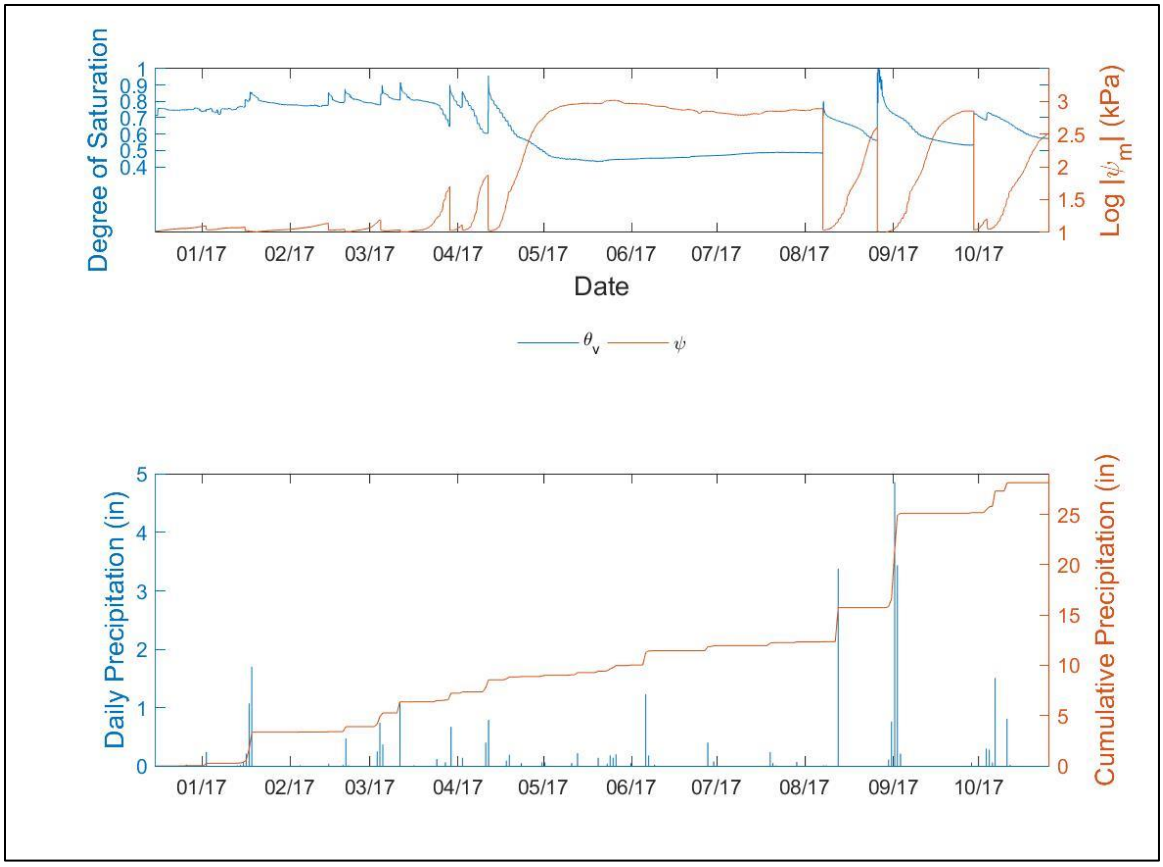

Figure C.10: Saturation and suction time histories and precipitation data for the sensor pairing at a depth of 4.5 ft below the base-subgrade interface for the asphalt time period

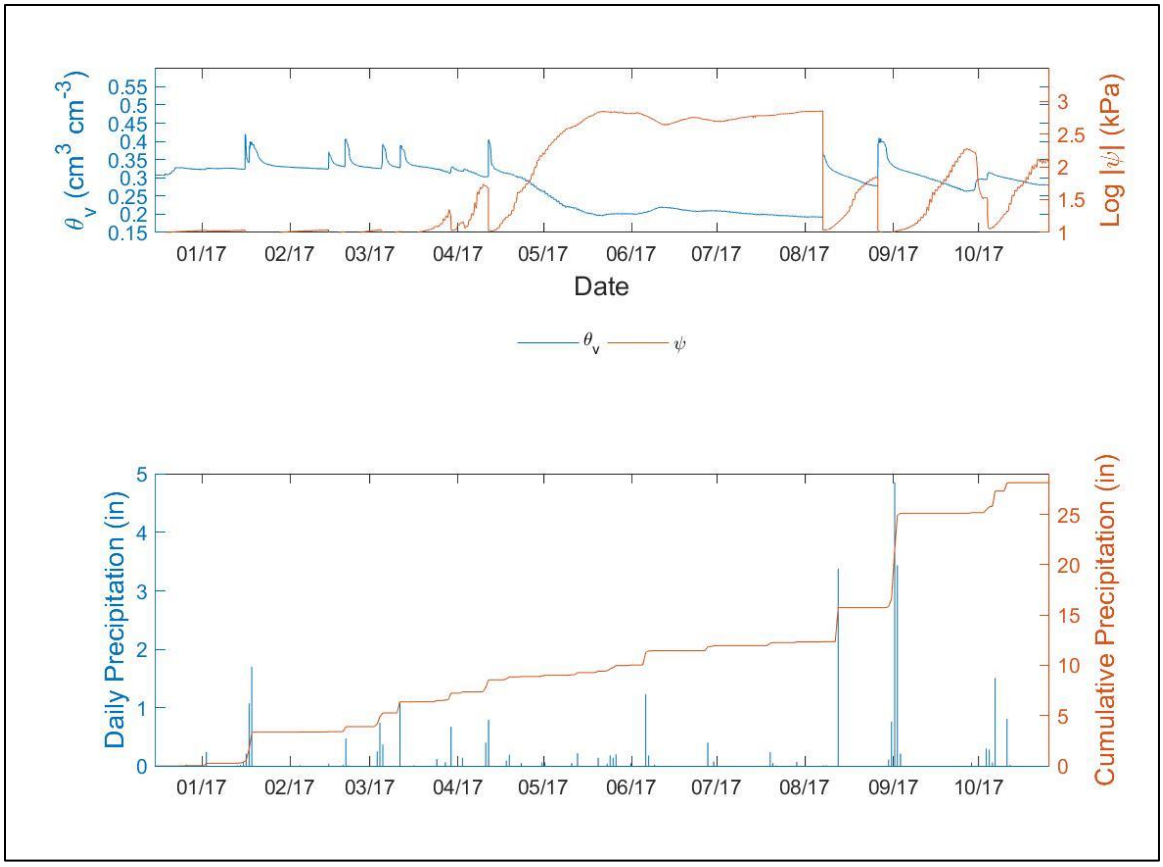

Figure C.11: Hydraulic time histories and precipitation data for the sensor pairing at a depth of 5.5 ft below the base-subgrade interface for the asphalt time period

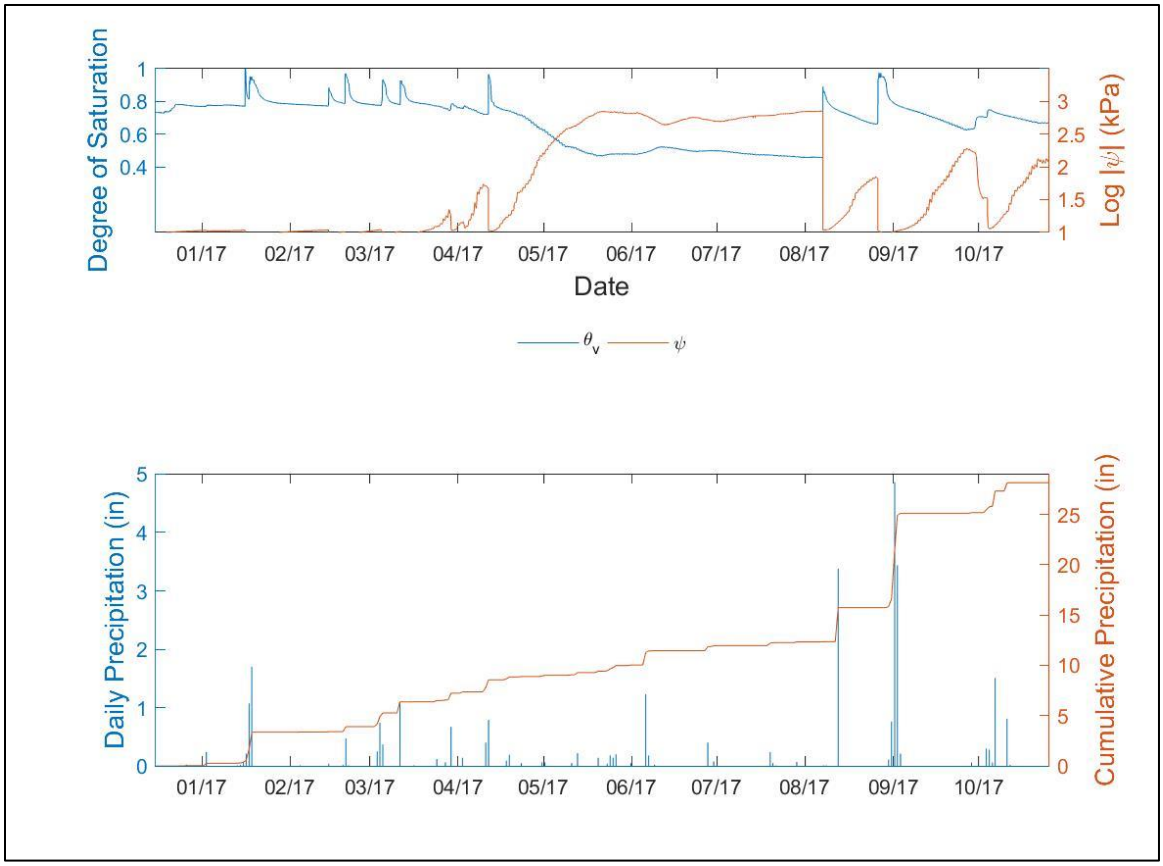

Figure C.12: Saturation and suction time histories and precipitation data for the sensor pairing at a depth of 5.5 ft below the base-subgrade interface for the asphalt time period

C.3: Additional Monthly Statistical Analysis of Hydraulic Properties

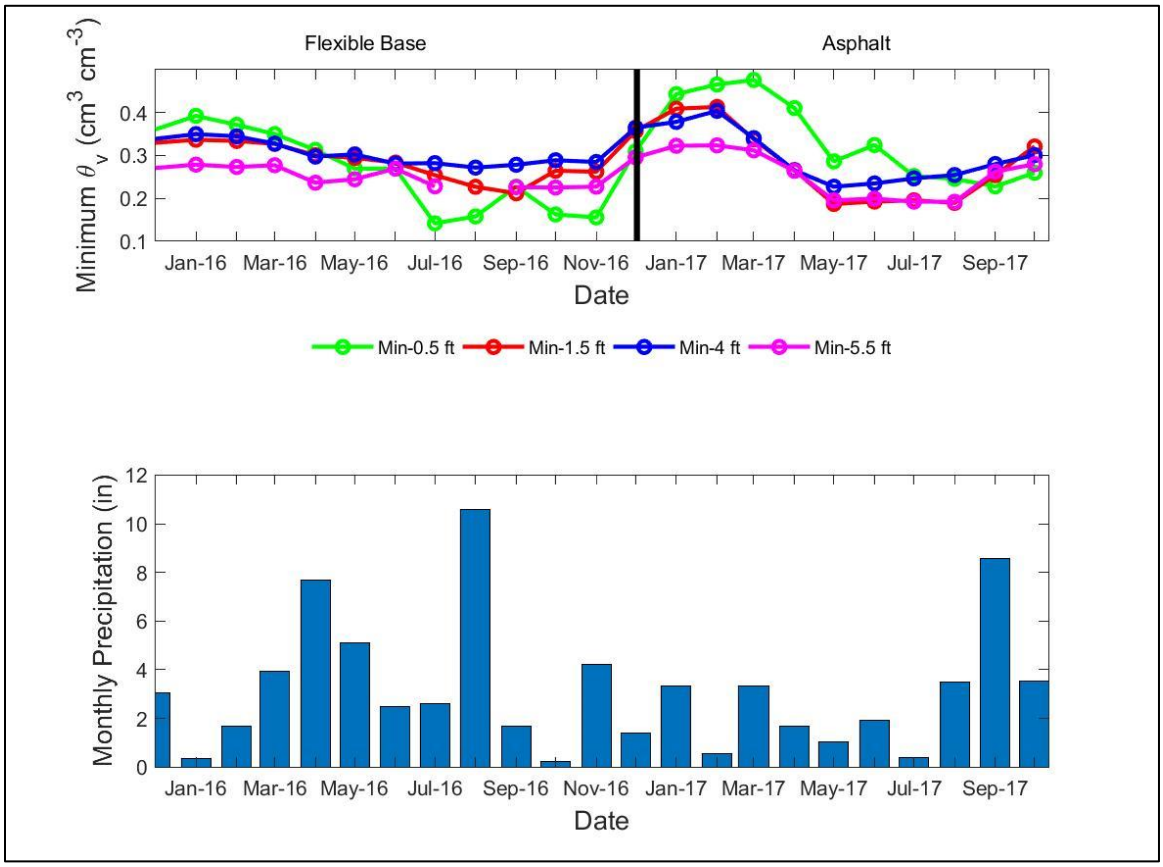

Figure C.13: Minimum monthly volumetric moisture content at FM685 site

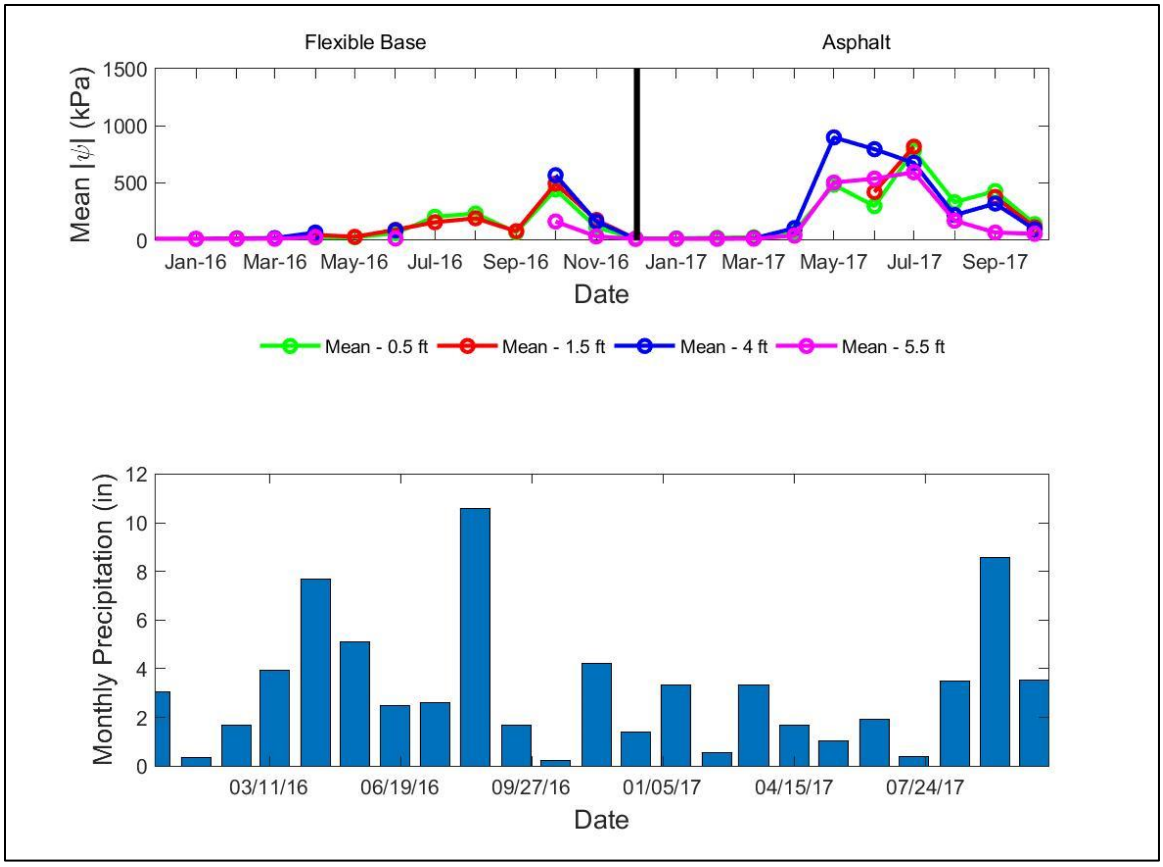

Figure C.14: Mean monthly matric suction at FM 685 site

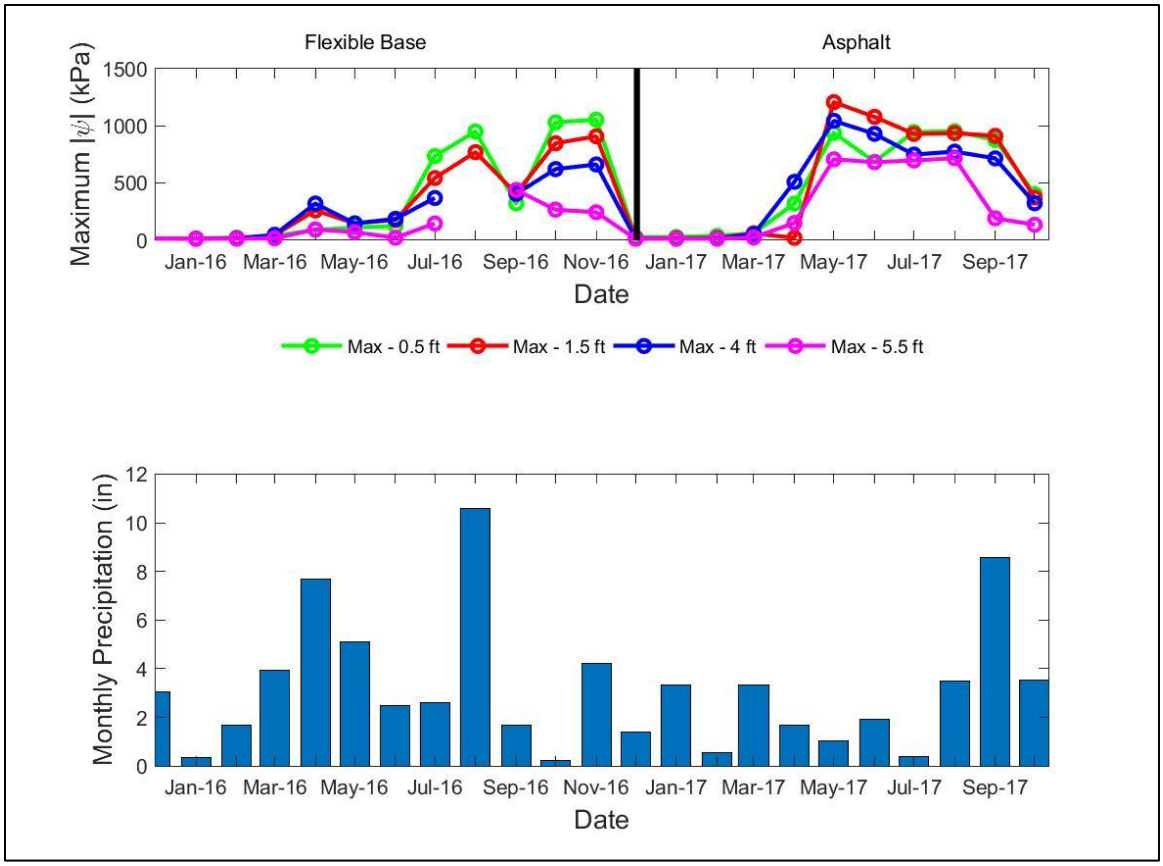

Figure C.15: Maximum monthly matric suction at FM 685 site

C.4: Additional Soil-Water Retention Curves from Volumetric Moisture Content Analyses

Table C.1: Soil-water retention curve parameters from non-linear, least-squares curve fitting using all data

Data	θ_r	θ_s	α	n	RMSE (cm^3/cm^3)
All Sensors	8.99E-08	0.328	0.0014	1.53	0.038
z = 0.5 ft	1.72E-06	0.350	0.0015	1.48	0.053
z = 1.5 ft	6.04E-07	0.327	0.0032	1.31	0.026
z = 4 ft	0.001689	0.313	0.0010	1.93	0.012
z = 5.5 ft	3.46E-10	0.300	0.0089	1.22	0.011

Table C.2: Soil-water retention curve parameters from non-linear, least-squares curve fitting using data from flexible base time period

Data	θ_r	θ_s	α	n	RMSE (cm^3/cm^3)
All Sensors	0.05	0.500	0.200	1.18	0.041
z = 0.5 ft	0.05	0.700	0.049	1.46	0.037
z = 1.5 ft	0.05	0.500	0.200	1.18	0.026
z = 4 ft	0.05	0.500	0.200	1.15	0.020
z = 5.5 ft	0.05	0.500	0.200	1.24	0.009

Table C.3: Soil-water retention curve parameters from non-linear, least-squares curve fitting using data from asphalt time period

Data	θ_r	θ_s	α	n	RMSE (cm^3/cm^3)
All Sensors	1.88E-12	0.5	0.041	1.20	0.035
z = 0.5 ft	4.15E-12	0.5	0.045	1.16	0.039
z = 1.5 ft	5.04E-14	0.5	0.030	1.25	0.021
z = 4 ft	2.29E-14	0.5	0.122	1.15	0.011
z = 5.5 ft	2.06E-12	0.5	0.140	1.20	0.004

C.4.1: Comparative Results from both Time Periods using a 100 kPa filter threshold

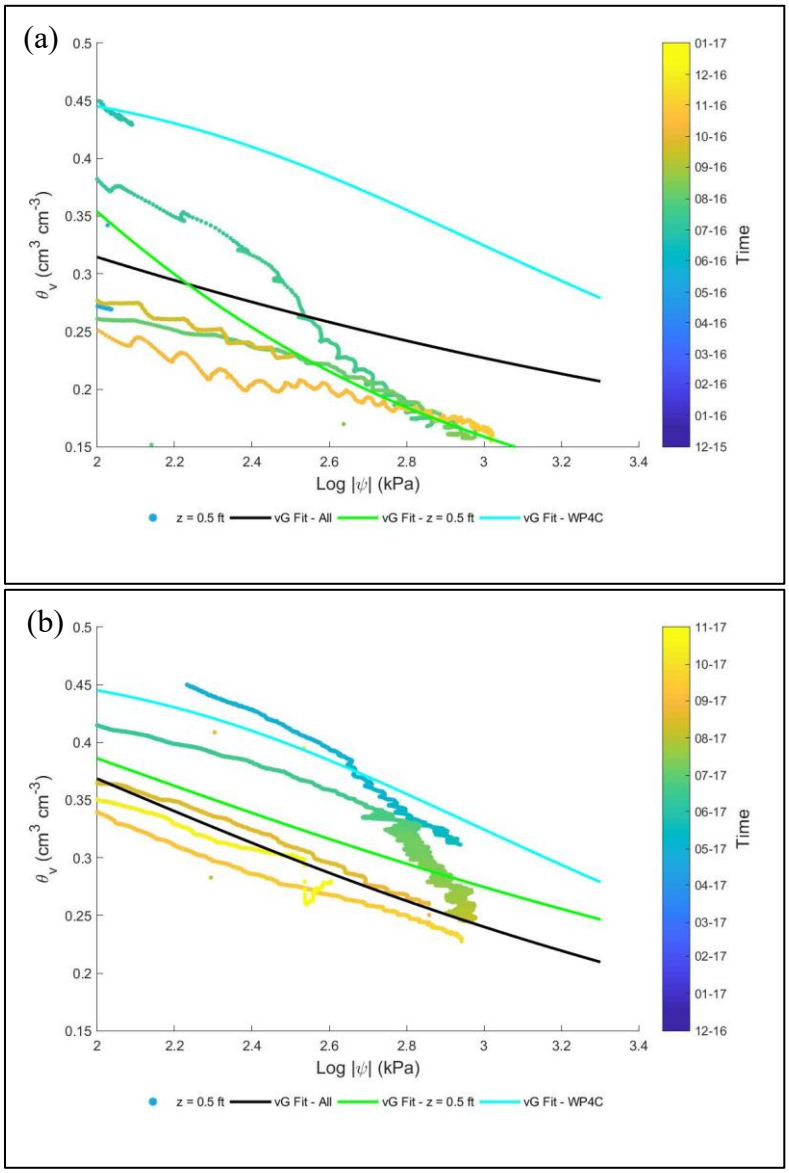

Figure C.16: Filtered unsaturated data and fitted soil-water retention curves for the Branyon clay at a depth of 0.5 ft below the base-subgrade interface for the flexible base time period (a) and asphalt time period (b)

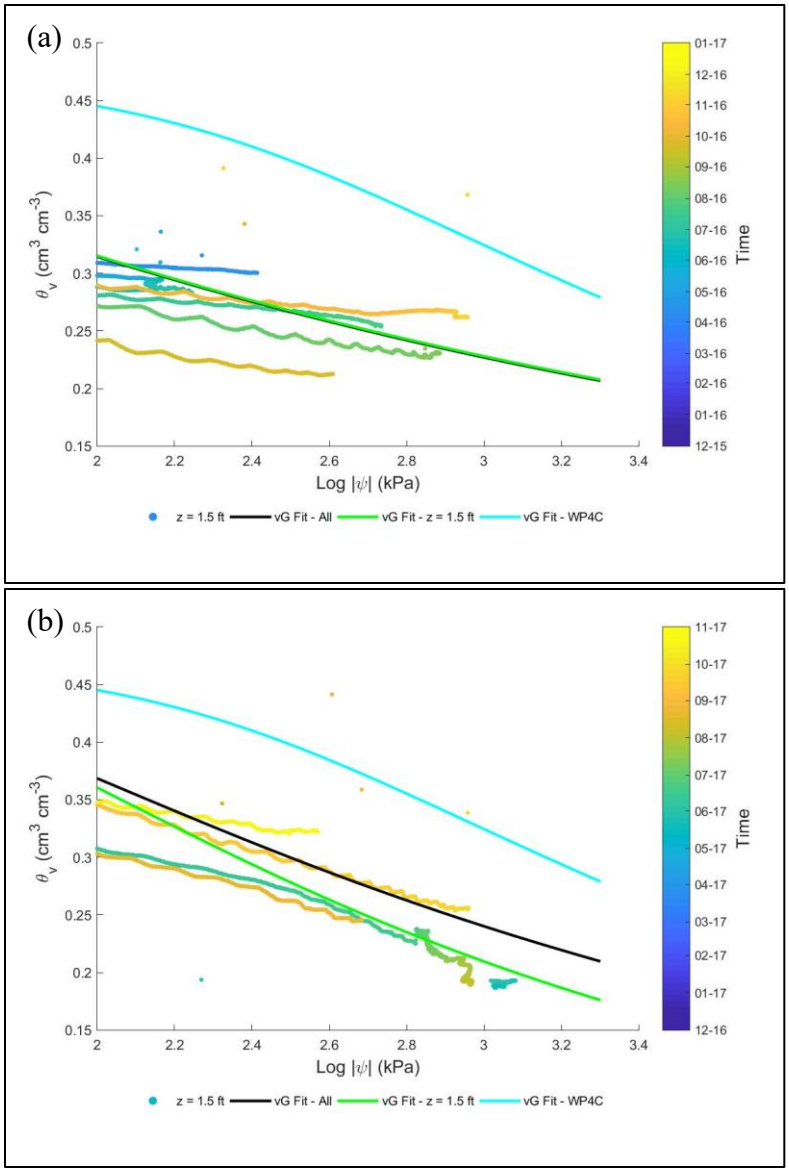

Figure C.17: Filtered unsaturated data and fitted soil-water retention curves for the Branyon clay at a depth of 1.5 ft below the base-subgrade interface for the flexible base time period (a) and asphalt time period (b)

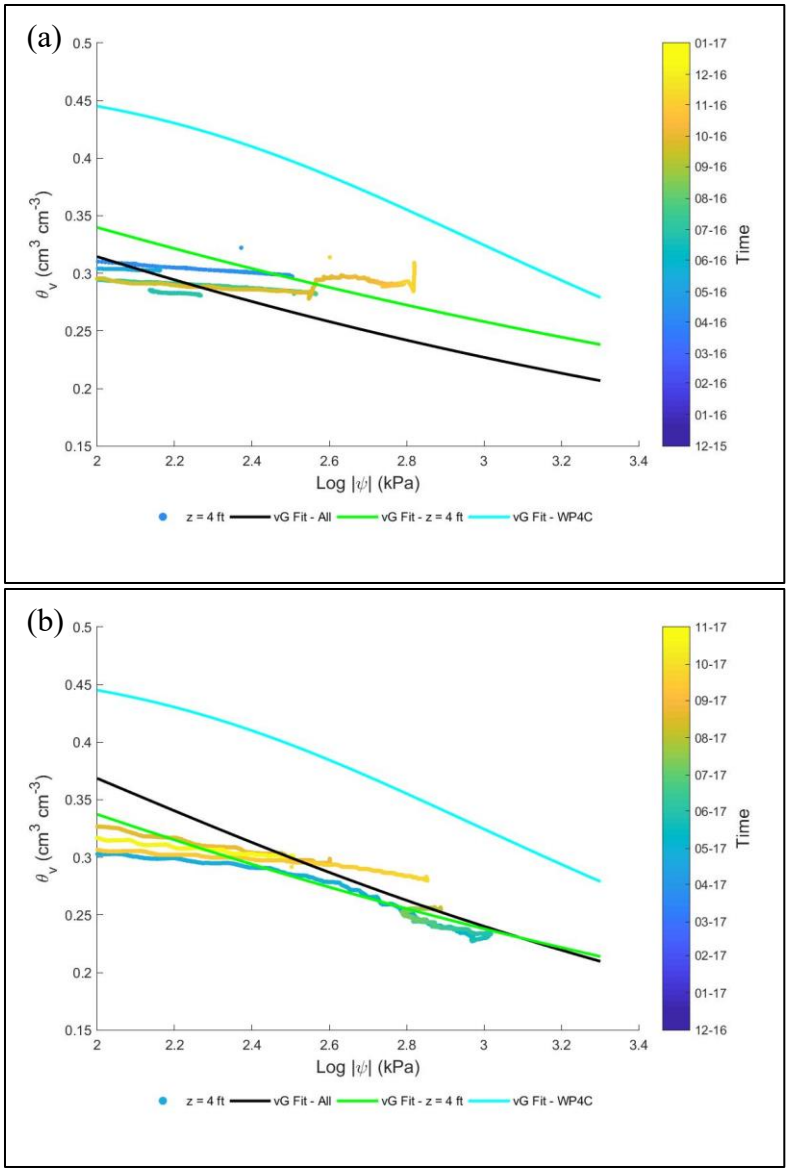

Figure C.18: Filtered unsaturated data and fitted soil-water retention curves for the Branyon clay at a depth of 4.5 ft below the base-subgrade interface for the flexible base time period (a) and asphalt time period (b)

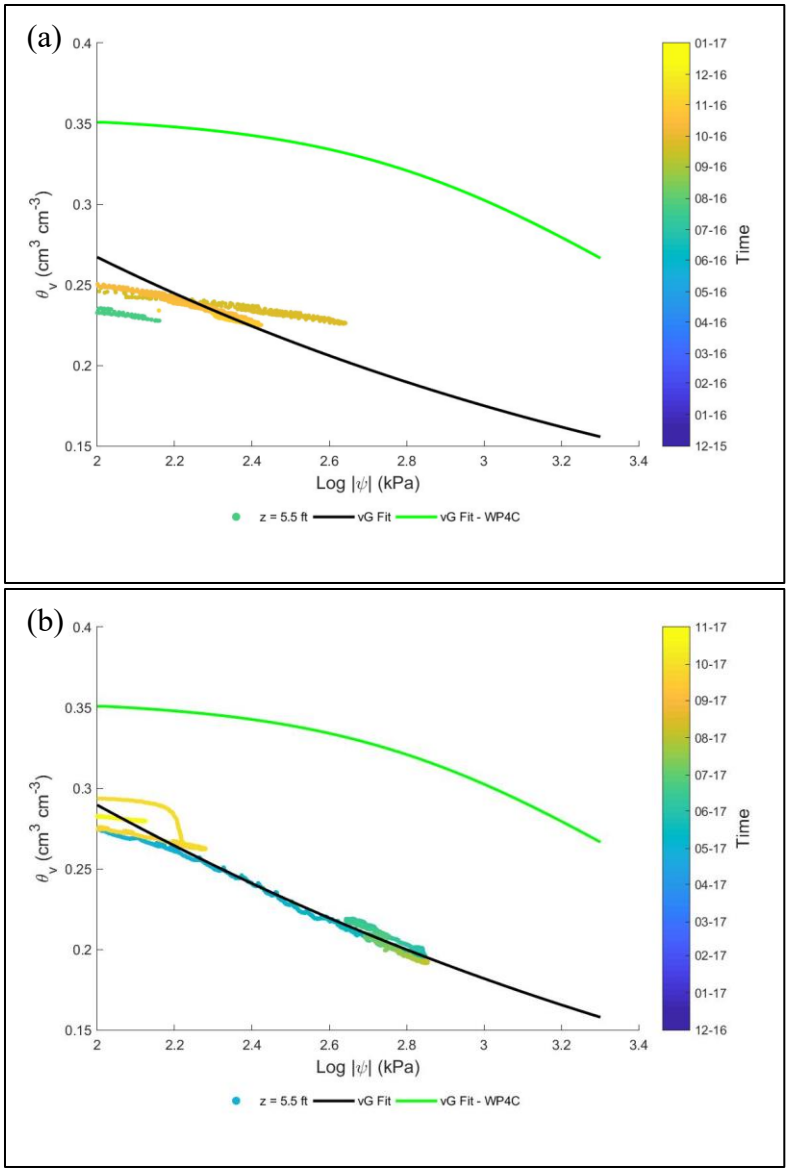

Figure C.19: Filtered unsaturated data and fitted soil-water retention curves for the Branyon clay at a depth of 5.5 ft below the base-subgrade interface for the flexible base time period (a) and asphalt time period (b)

C.4.2: Comparative Results from both Time Periods using a 50 kPa filter threshold

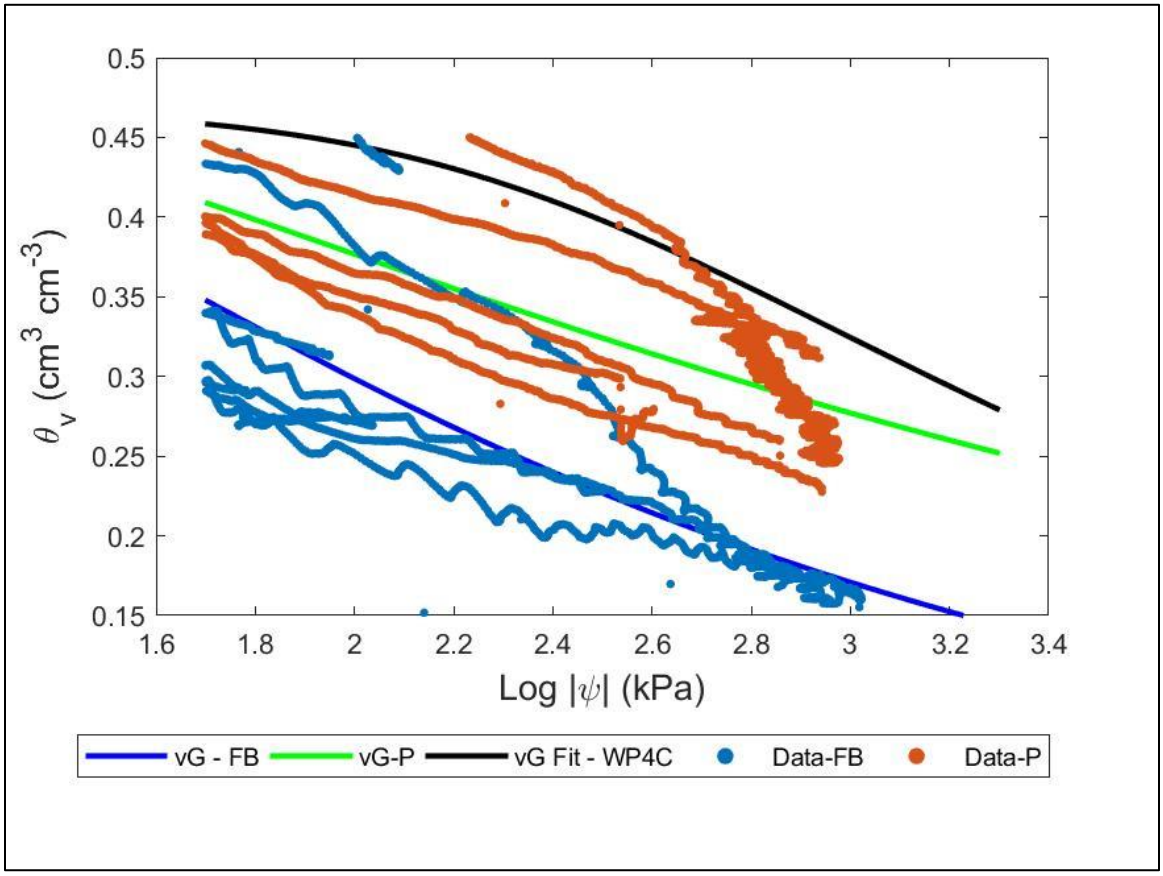

Figure C.20: Filtered data and fitted soil-water retention curves for the Branyon clay at a depth of 0.5 ft below the base-subgrade interface

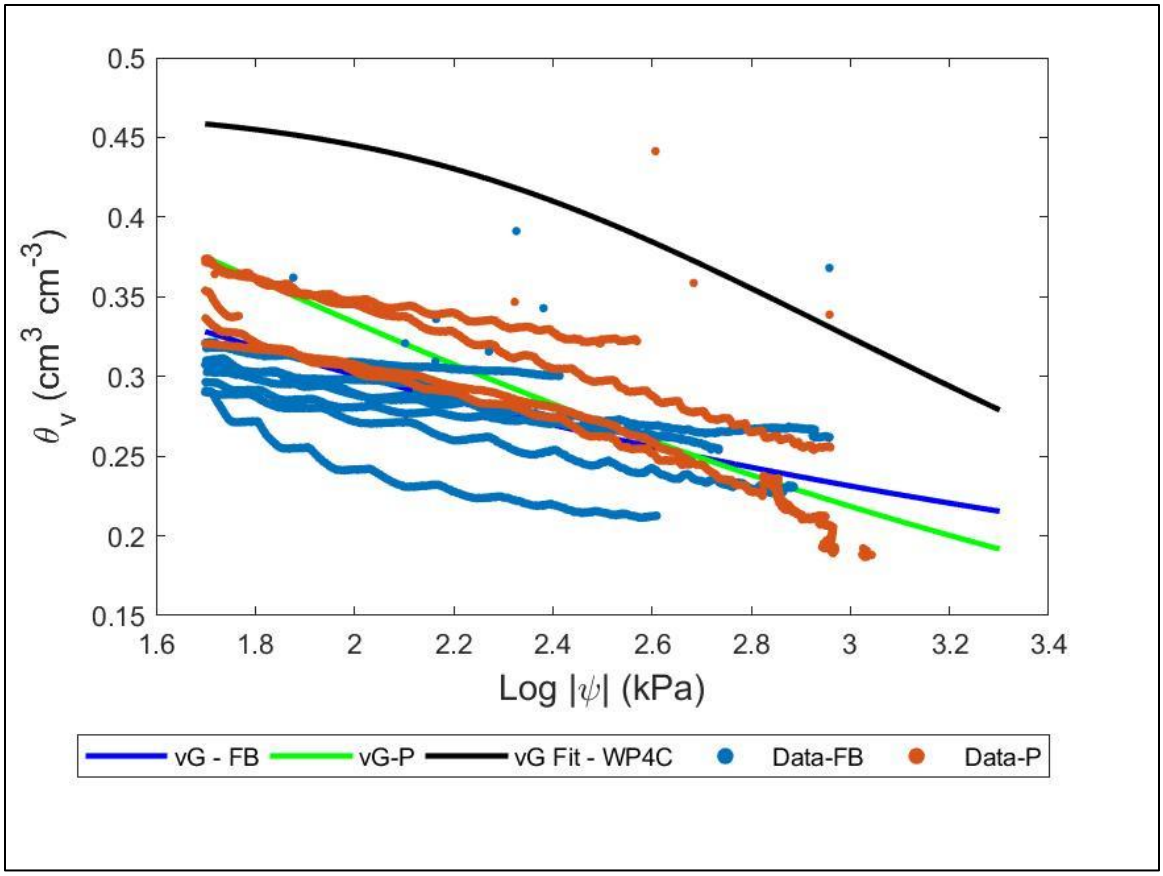

Figure C.21: Filtered data and fitted soil-water retention curves for the Branyon clay at a depth of 1.5 ft below the base-subgrade interface

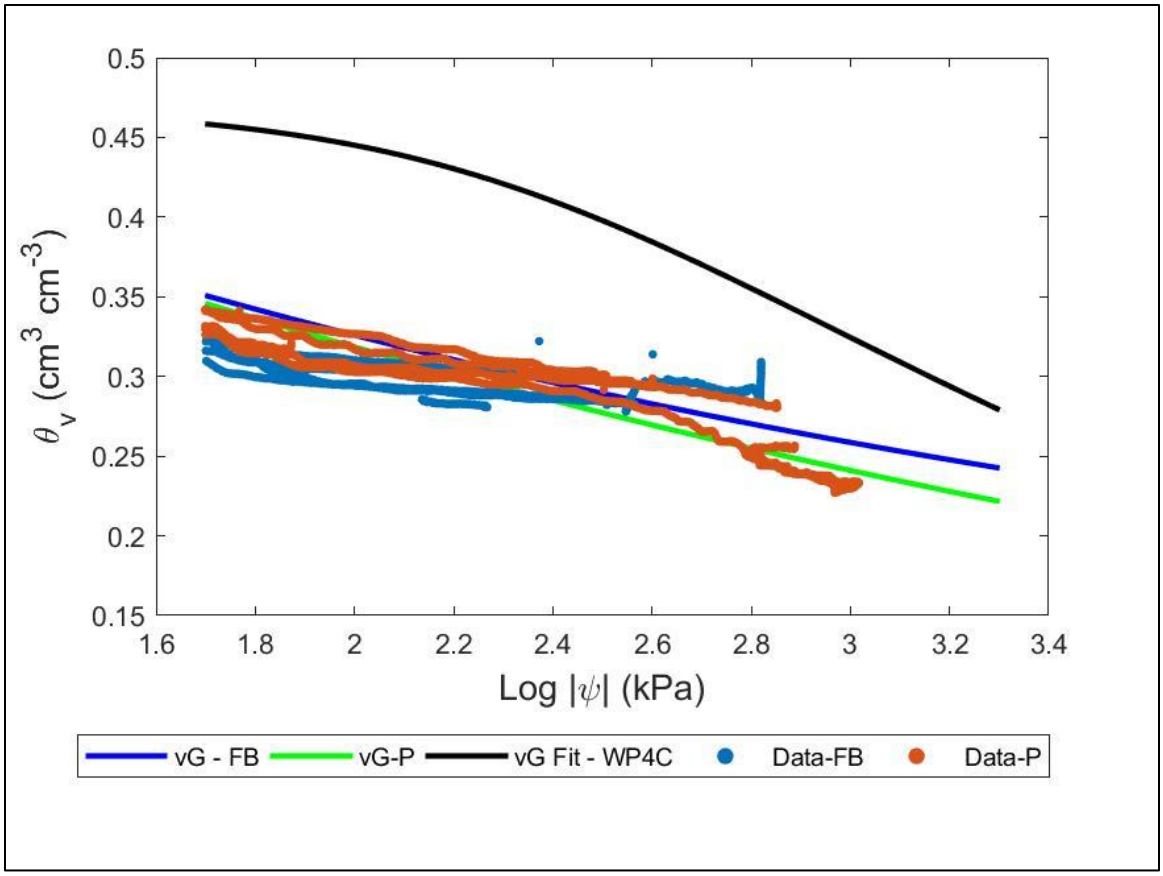

Figure C.22: Filtered data and fitted soil-water retention curves for the Branyon clay at a depth of 4.5 ft below the base-subgrade interface

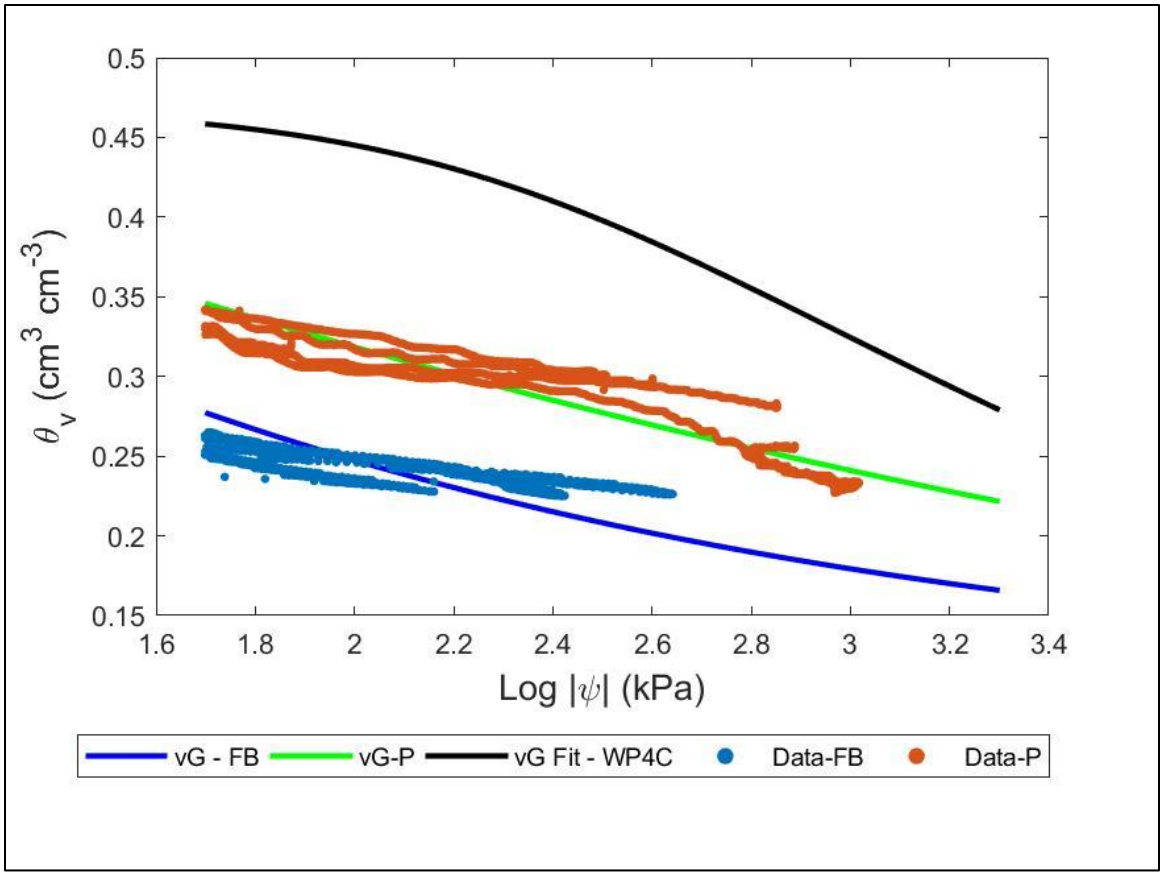

Figure C.23: Filtered data and fitted soil-water retention curves for the Branyon clay at a depth of 5.5 ft below the base-subgrade interface

C.5: Additional Degree of Saturation Soil-Water Retention Curves

C.5.1: Comparative Results from both Time Periods using a 50 kPa filter threshold

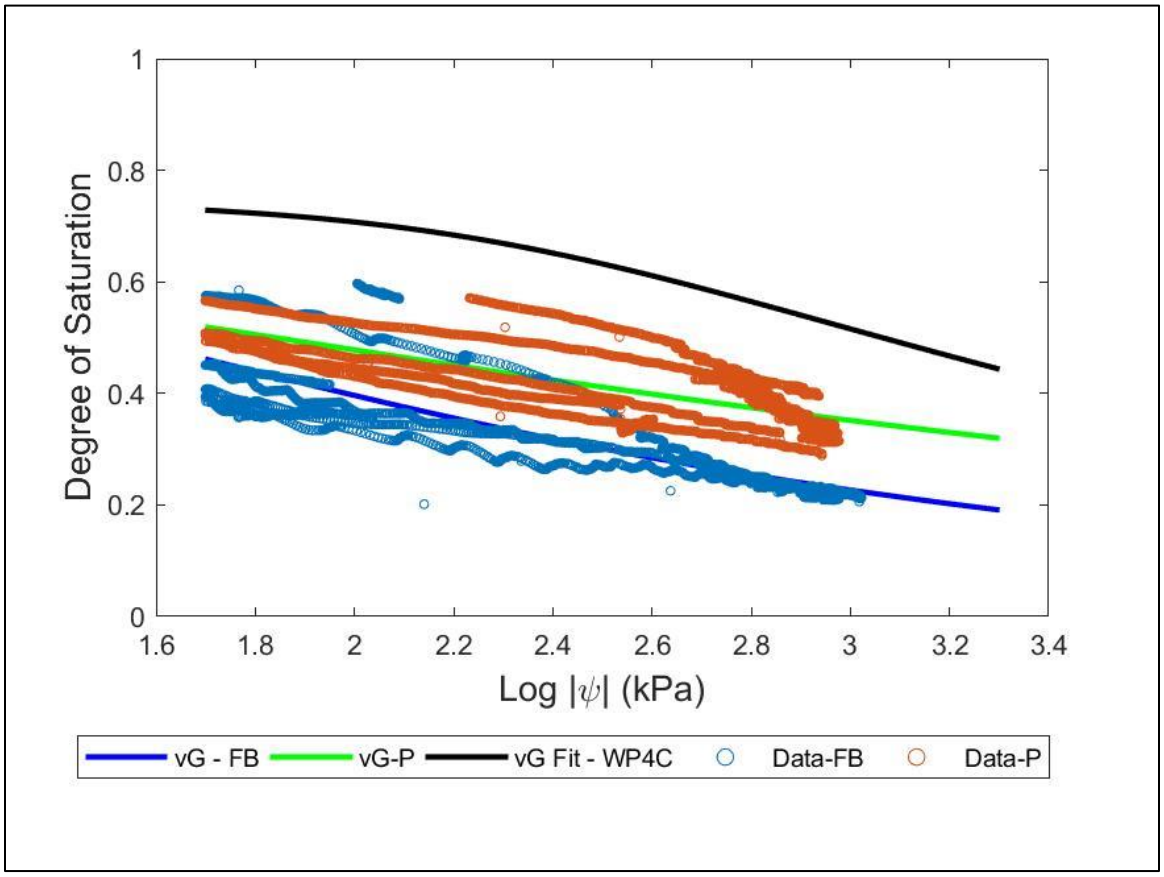

Figure C.24: Filtered data and fitted soil-water retention curves for the Branyon clay at a depth of 0.5 ft below the base-subgrade interface

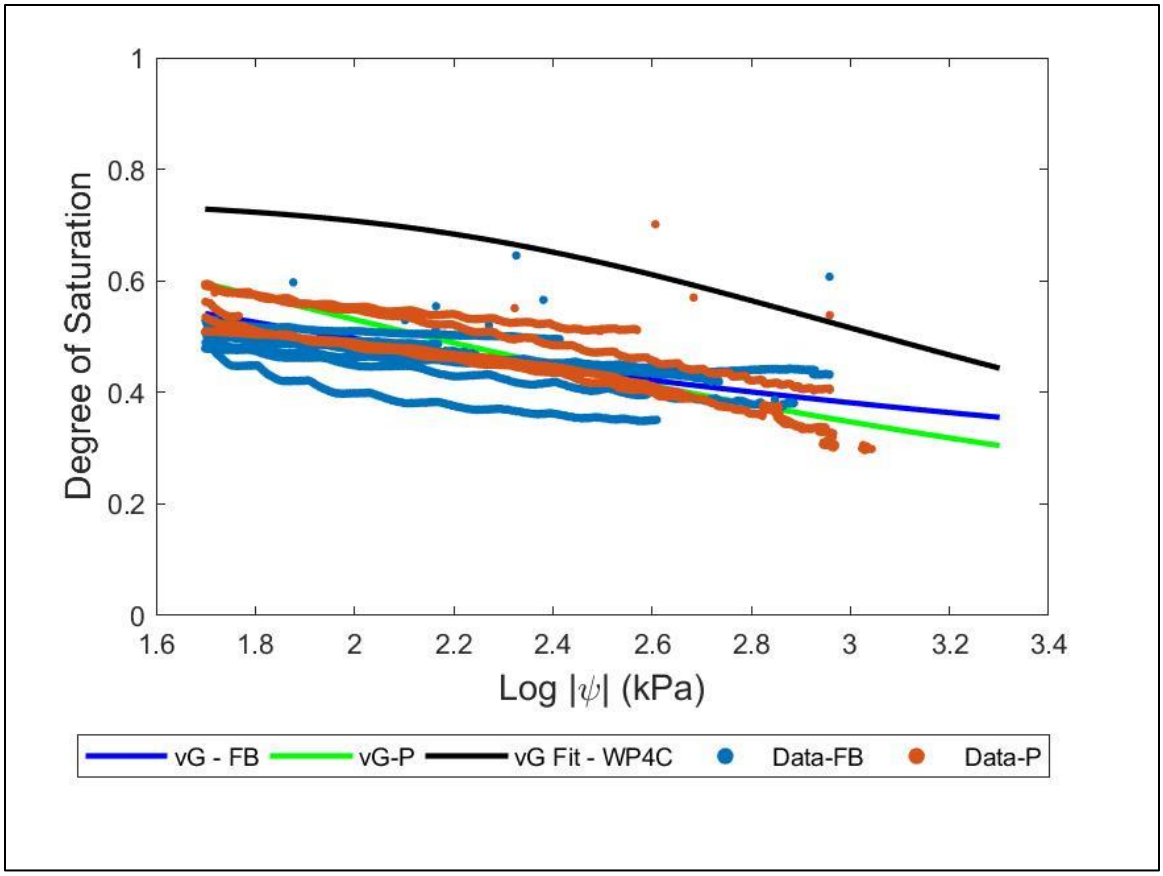

Figure C.25: Filtered data and fitted soil-water retention curves for the Branyon clay at a depth of 1.5 ft below the base-subgrade interface

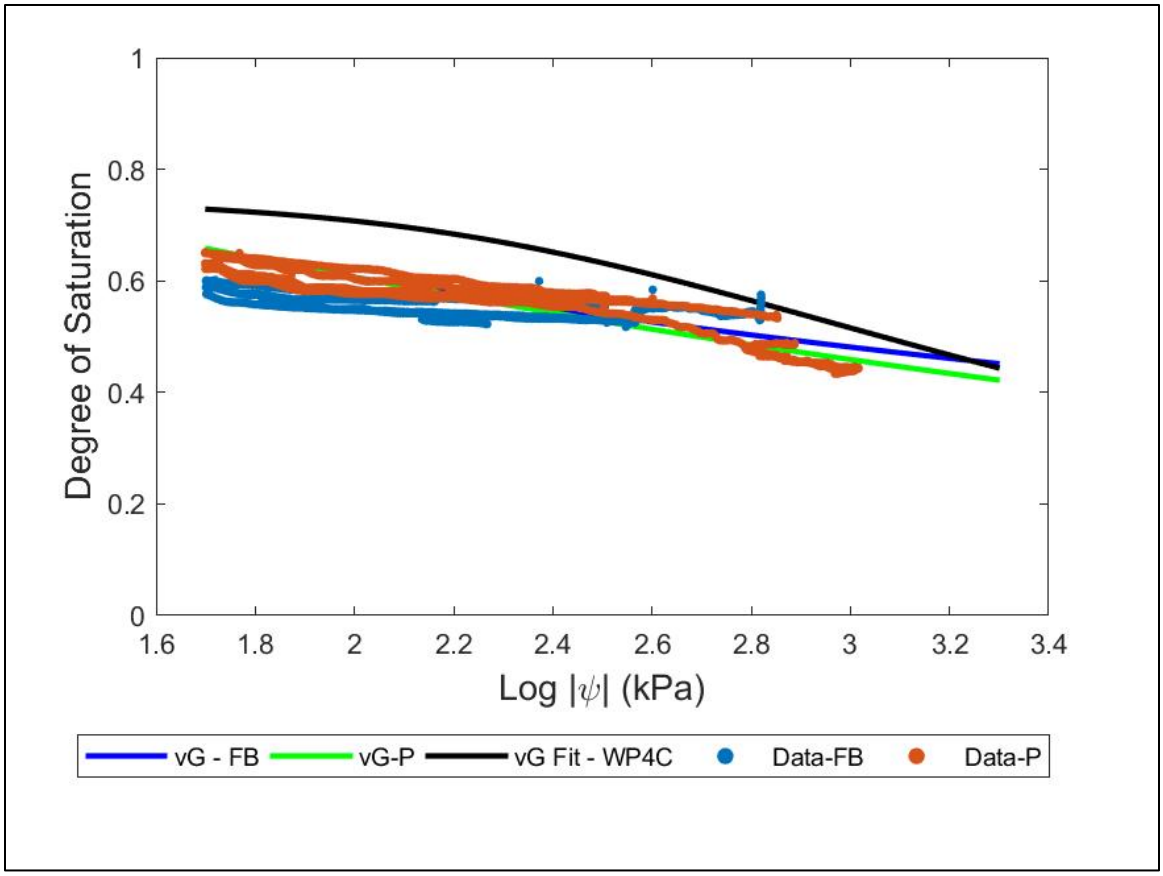

Figure C.26: Filtered data and fitted soil-water retention curves for the Branyon clay at a depth of 4.5 ft below the base-subgrade interface

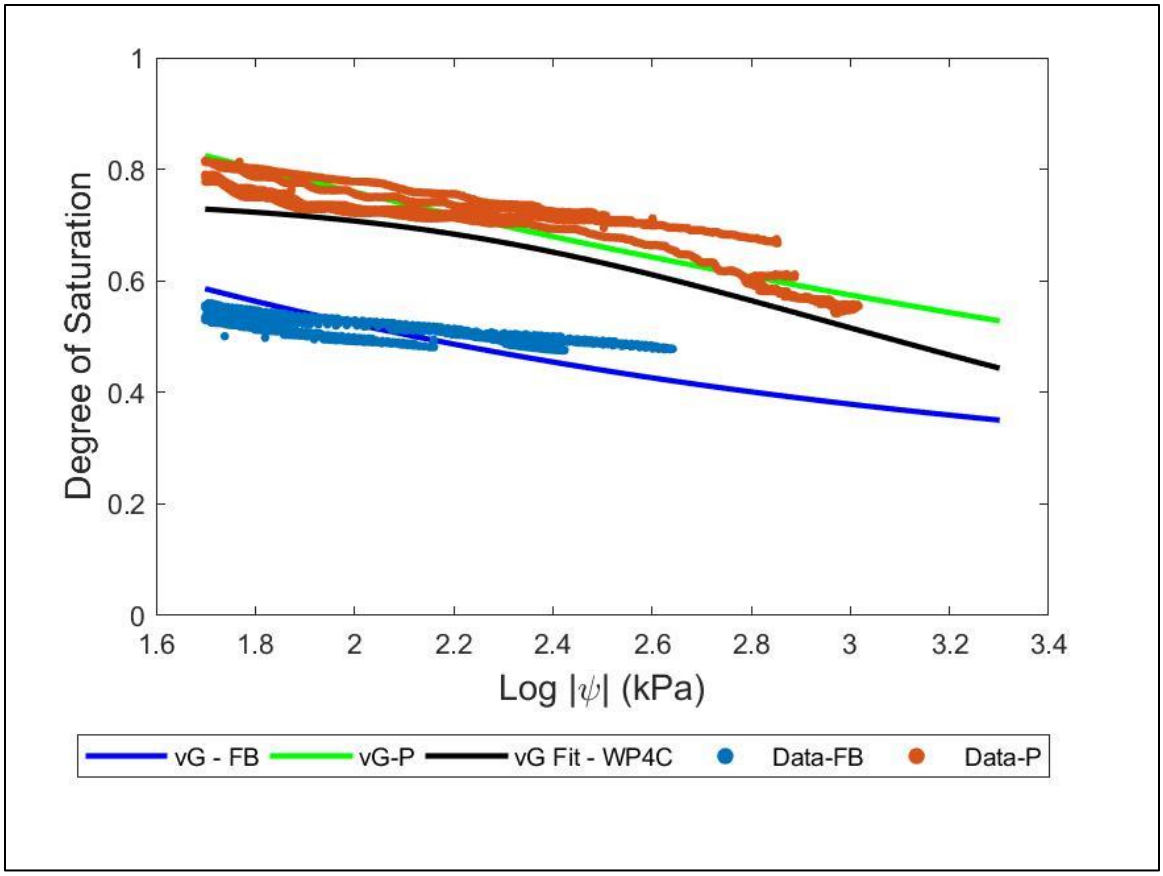

Figure C.27: Filtered data and fitted soil-water retention curves for the Branyon clay at a depth of 5.5 ft below the base-subgrade interface

C.6: Additional Results from Optimization of Soil-Water Retention Curve Fitting

Table C.4: Soil-water retention curve parameters from shuffle complex evolution curve fitting using data from flexible base time period

Data	θ_r	θ_s	α	n	RMSE (cm^3/cm^3)
All Sensors	0.017	0.402	0.065	1.14	0.041
z = 0.5 ft	0.100	0.600	0.024	1.66	0.037
z = 1.5 ft	0.100	0.345	0.182	1.09	0.020
z = 4 ft	0.098	0.300	0.200	1.01	0.006
z = 5.5 ft	0.026	0.303	0.199	1.08	0.004

Table C.5: Soil-water retention curve parameters from shuffle complex evolution curve fitting using data from asphalt time period

Data	θ_r	θ_s	α	n	RMSE (cm^3/cm^3)
All Sensors	0.022	0.325	0.001	2.50	0.032
z = 0.5 ft	0.099	0.403	0.006	1.30	0.039
z = 1.5 ft	0.000	0.380	0.0052	1.35	0.019
z = 4 ft	0.000	0.487	0.104	1.15	0.011
z = 5.5 ft	0.018	0.332	0.011	1.28	0.003

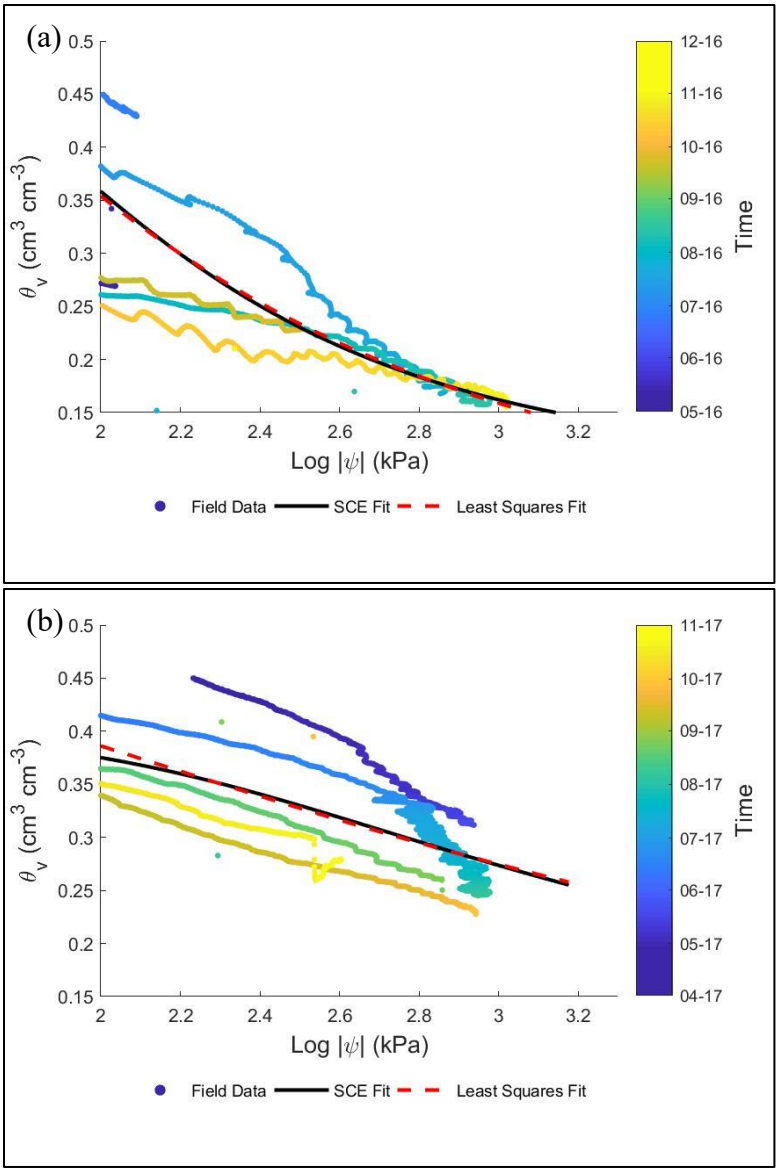

Figure C.28: Comparison of the fitting techniques for the sensors at the depth of 0.5 ft below the base-subgrade interface for the flexible base time period (a) and asphalt time period (b)

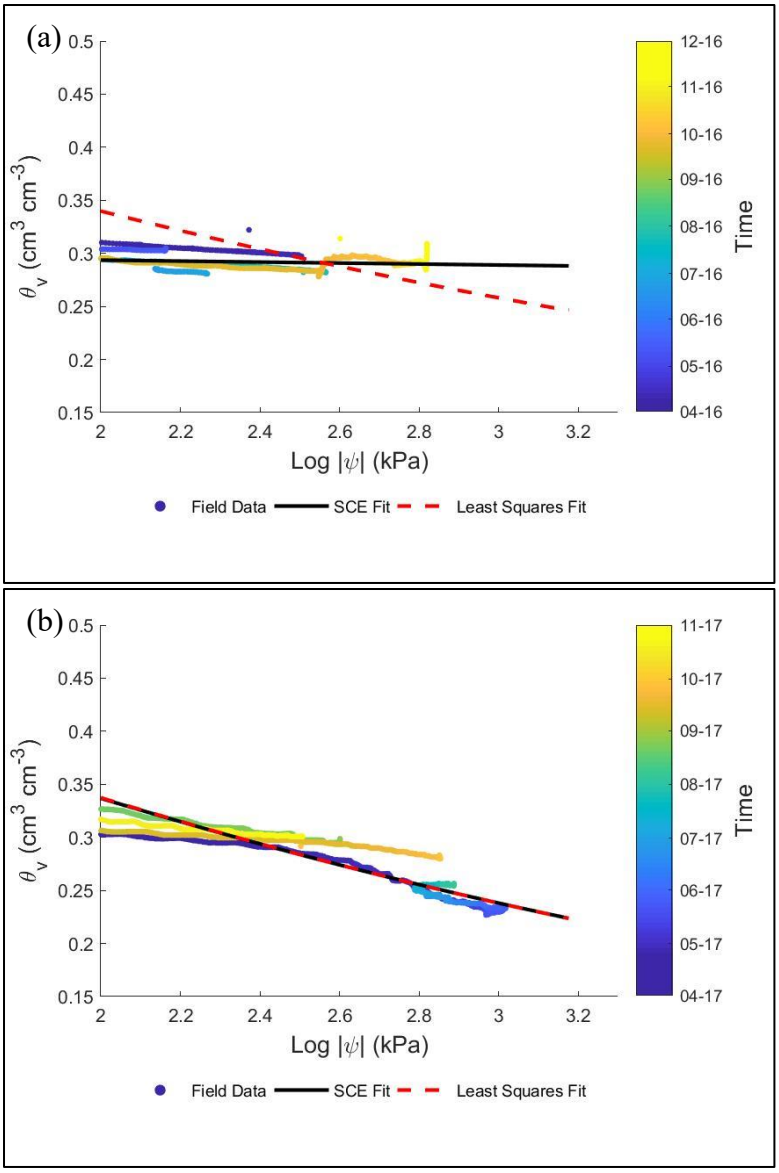

Figure C.29: Comparison of the fitting techniques for the sensors at the depth of 4 ft below the base-subgrade interface for the flexible base time period (a) and asphalt time period (b)

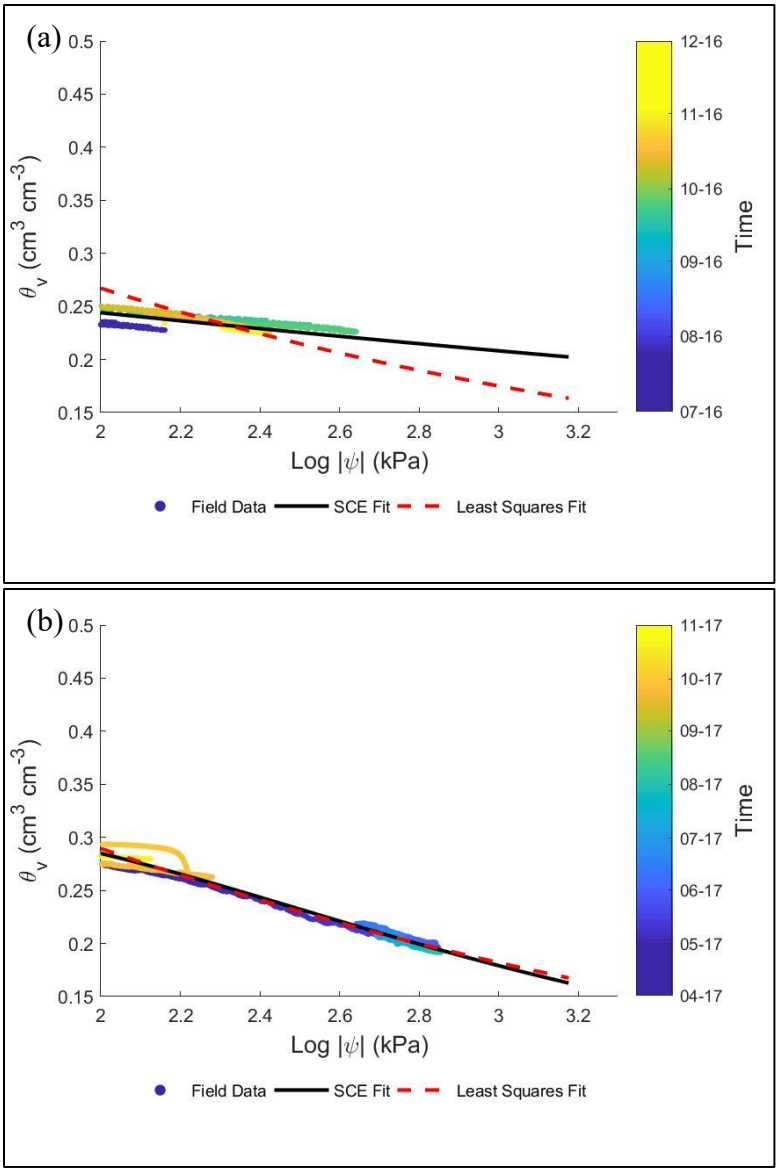

Figure C.30: Comparison of the fitting techniques for the sensors at the depth of 5.5 ft below the base-subgrade interface for the flexible base time period (a) and asphalt time period (b)

References

Acclima Inc. (2015). TDR-315 User Manual. Meridian, Idaho. Revision, July 2015.

Allen, J. and Gilbert, R. (2006). Accelerated swell-shrink test for predicting vertical movement in expansive soils. *Unsaturated Soils*, 2006.

Al-Shamrani, M. and Al-Mhaidib, A. (1999). Prediction of ptoentail vertical swell of expansive soils using a triaxial stress path cell. *Quarterly Journal of Engineering Geology*, *3*, 45-54.

Apul, D., Gardner, K., and Eighmy, T. (2007). Modeling hydrology and reactive transport in roads: The effect of cracks, the edge, and contaminant properties. *Waste Management, 27,* 1465-1475.

ARA Inc. (2004). Guide for mechanicistic-empirical design of new and rehabilitated pavement structures. Champaign, Illinois.

ArcGIS. (2017). Semivariogram and covariance functions. [Web page]. Retreieved from http://desktop.arcgis.com/en/arcmap/latest/extensions/geostatistical-analyst/semivariogram-and-covariance-functions.htm

Armstrong, C. and Zornberg, J. (2017). Effect of Fabric on the Swelling Characteristics of Highly Plastic Clays. *Proceedings of the Second Pan-American Conference on Unsaturated Soils.* Dallas, TX. 10 p.

Armstrong, C.P. (2014). *Effect of Fabric on the Swelling of Highly Plastic Clays.* Master's Thesis. The University of Texas at Austin.

ASTM D2216. (2010). *Standard Test Method for Laboratory Determination of Water (Moisture) Content of Soil and Rock by Mass*. West Conshohocken, PA: American Society of Testing Materials.

ASTM D2435. (2011). *Standard Test Method for One-Dimensional Consolidation Properites of Soils Using Incremental Loading*. West Conshohocken, PA: American Society of Testing Materials.

ASTM D2487. (2011). *Standard Practice for Classification of Soils for Engineering Purposes (Unified Soil Classification System)*. West Conshohocken, PA: American Soceity of Testing Materials.

ASTM D422-63. (2007). *Standard Test Method for Particle-Size Analysis of Soils*. West Conshohocken, PA: American Society of Testing Materials.

ASTM D4318. (2010). *Standard Test Method for Liquid Limit, Plastic Limit, and Plasticity Indecies of Soils*. West Conshohocken, PA: American Society of Testing Materials.

ASTM D4546. (2008). *Standard Test Methods for One-Dimensional Swell or Collapse of Cohesive Soils*. West Conshohocken, PA: American Society of Testing Materials.

ASTM D6836-16. (2008). *Standard Test Methods for Determination of the Soil Water Characteristic Curve for Desorption Using Hanging Column, Pressure Extractor, Chilled Mirror Hygrometer, or Centrifuge*. West Conshohocken, PA: American Society of Testing Materials.

ASTM D854-02. (2010). *Standard Test Method for Specific Gravity of Soil Solids by Water Pycnometer*. West Conshohocken, PA: American Society of Testing Materials.

Attom, M., Abu-Zreig, M., and Obaidat, M. (2001). Changes in clay swelling and shear strength properties with different sample preparation techniques. *Geotechnical Testing Journal*, *23*, 157-163.

Azevedo, M. (2016). *Performance of Geotextiles with Enhanced Drainge.* PhD Dissertation. The University of Texas at Austin.

Barnes, V.E. (1981). Geologic Atlas of Texas, Austin Sheet, digitized from Barnes 1981 map: Texas Water Development Board, scale 1:250,000.

Basma, A., Al-Homoud, A., and Al-Tabari, E. (1994). Effects of methods of drying on the engineering behavior of clays. *Applied Clay Science, 9,* 151-164.

Beal, A. O. (1964). Stratigraphy of the Taylor Formation (Upper Cretaceous), East-Central Texas. Baylor Geological Studies Bulletin No. 6, Baylor University.

Brown, R. and Borst, M. (2014). Quantifying evaporation in a permeable pavement system. *Hydrological Processes, 29*, 2100-2111.

Chen, F.H. (1988). Foundations on Expansive Soils. Amsterdam: Elsevier.

Christopher, B.R., Schwartz, C., and Boudreau, R. (2006). Geotechnical Aspects of Pavements. Federal Highway Administration (FHWA), Product No. FHWA NHI-05-037. Washington D.C., p. 598.

Covar, A. and Lytton, R. (2001). Estimating Soil Swelling Behavior using Soil Classification Properities. *Expansive Clay Soils and Vegetive Influences on Shallow Foundations, ASCE Geotechnical Publications. 44.*

Cui, Y., Ta, A., Tang, A., and Lu, Y. (2010). Investigation of the hydro-mechanical behaviour of compacted expansive clay. *Frontiers of Architecture and Civil Engineering in China, 4*(2), 154-164.

Decagon Devices. (2015). MPS-2 & MPS-6: Dielectirc Water Potential Sensors. Pullman, Washington. Revision, May 2015.

Decagon Devices. (2016). 5TE: Water Content, EC, and Temperature Sensor. Pullman, Washington. Revision, March 2016.

Dellinger, G. (2011). *The Use of Time Domain Reflectometry Probes for the Moisture Monitoring of a Drilled Shaft Retaining Wall in Expansive Clay.* Master's Thesis. The University of Texas at Austin.

Diamond, S. (1971). Microstructure and Pore Structure of Impact-Compacted Clays. *Clay and Clay Minerals, 19,* 239-249.

Dif, A. and Bluemel, W. (1991). Expansive Soils under Cyclic Drying and Wetting. *Geotechnical Testing Journal, 14,* 96-102.

Dinka, T., Morgan, C., McInnes, K., Kishne, A. and Harmel, R. (2013). Shrink-swell behavior of soil across a Vertisol catena. *Journal of Hydrology, 476,* 352-359.

Driese, S., Jacobs, J., and Nordt, L. (2003). Comparison of modern and ancient Vertisols developed on limestone in terms of their geochemistry and parent material. *Sedimentary Geology, 157,* 49-69.

Driese, S., Mora, C., Stiles, C., Joeckel, R., and Nordt, L. (2000). Mass-balance reconstruction of a modern vertisol: implications for interpreting the geochemistry and burial alteration of paleo-Vertisols. *Geoderma, 95,* 179-204.

Duan, Q., Sorooshian, S., and Gupta, V. (1992). Effective and efficient global optimization for conceptual rainfall-runoff models. *Water Resources Research, 28*(4), 1015-1031.

Duan, Q., Sorooshian, S., and Gupta, V. (1994). Optimal use of the SCE-UA global obtimization methed for calibrating watershed models. *Journal of Hydrology, 158,* 265-284.

Erzin, Y. and Erol, O. (2007). Swell pressure prediction by suction methods. *Engineering Geology, 92,* 133-145.

Ewing, T.E. (1994). The Cook Mountain problem: stratigraphic reality and semantic confusion. *Gulf Coast Association of Geological Societies Transactions, 44,* 225–232.

Farid, A. and Mosaid, M. (2014). Swelling Potential Predicition of Expansive Soils using Blue Metheylene Value. *Soul Behavior and Geomechanics, 236,* 25-33.

Ferber, V., Auriol, J.C., Cui, Y.J., and Magnan, J.P. (2009). On the Swelling Potential of Compacted High Plasticity Clays. *Engineering Geology, 104,* 200-210.

Fityus, S. and Buzzi, O. The Place of Expansive Clays in the Framework of Unsaturated Soil Mechanics. *Applied Clay Science, 43,* 150-155.

Foley, D. and Woodruff, C.M. (1986). The Balcones Escarpment: Geothermal Resources of Bexar County. *Geological Society of America*. 145-152.

Fredlund, D. and Rahardjo, H. (1993). Soil Mechanics for Unsaturated Soils. John Wiley& Sons: New York.

Frydman, S. and Weisberg, E. (1991). A Study of Centrifuge Modeling of Swelling Clay. In *Centrifuge 91*. 113-120.

Gadre, A.D. and Chandrasekaran, V.S. (1994). Swelling of Black Cotton Soil using Centrifuge Modeling. *Journal of Geotechnical Engineering, 120,* 914-919.

Garcia Delgado, I.E., (2015). *Use of Geotextiles with Enhanced Lateral Drainage in roads over expansive clays.* Master's Thesis. The University of Texas at Austin.

Geokon Inc. (2013). Instruction Manual Model 4650: VW Settlement Sensor. Lebanon, NH. Revision, June 2013.

Godfrey, C.L., Carter, C.R., and McKee, G.S. (1968). Resource areas of Texas: Land. Texas A&M University.

Google Earth. (2017). *Map of IH-10 east of San Antonio*. Viewed August 2017. http://www.google.com/earth/index.html.

Goovaerts, P. (1999). Geostatistics in soil science: state-of-the-art and perspectives. *Geoderma, 89,* 1-45.

Hansson, K., Lundin, L.C., and Simunek, J. (2005). Modeling Water Flow Patterns in Flexible Pavements. *Journal of Transportation Research Board, 1936,* 133-141.

Hitachi High-Technologies Corporation. (2008). Let's Familiarize Ourselves with the SEM. Tokyo, Japan.

Hu, Y. and Vu, H. (2011). Analysis of soil conditions and pipe behavior at a field site. *Canadian Geotechnical Journal, 48,* 847-866.

Huang, S.L., Speck, R.C., and Wang, Z. (1995). The Temperature Effect on Swelling of Shales Under Cyclic Wetting and Drying. *International Journal of Rock Mechanics and Mining Sciences, 32*(3), 227-236.

Ito, M. and Azam, S. (2013). Engineering properties of a vertisolic expansive soil deposit. *Bulletin of Engineering Geology, the Environment, 152,* 10-16.

Izenman, A. (1991). Recent developments in nonparametric density estimation. *Journal of the American Statistical Association, 86*(413), 205-224.

Jaky, J. (1948). Pressures in Silos. *Proceedings of the 2nd International Conference on Soil Mechanics and Foundation Engineering,* Balkema, Rotterdam, 103-107.

Kocarek, M. and Kodesova, R. (2012). Influence of temperature on soil water content measured by ECH$_2$O-TE sensors. *International Agrophysics, 26*, 259-269.

Komine, H. and Ogata, N. (1992). "Swelling Characteristics of Compacted Bentonite." *Proceedings of the 7th International Conference on Expansive Soils,* Dallas, TX, 216-221.

Kong, L. and Guo, A. (2011). Bearing Strength and Swelling Behavior of Jingmen Expansive Soil. *Road Materals and Pavement Design, 12*(2), 441-450.

Kuhn, J. (2010). *Characterization of the Swelling Potential of Expansive Clays using Centrifuge Technology.* PhD Dissertation. The University of Texas at Austin.

Lambe, T. (1958). The Engineering Behavior of Compacted Clays. *Journal of the Soil Mechanics and Foundation Division*, *84,* 1655-1 to 1655-35.

Lambe, T.W. (1958). The Structure of Compacted Clay. *Journal of the Soil Mechanics and Foundation Division*, *84,* 1654-1 to 1654-35.

Lambe, T.W. (1964). "How dry is a soil?" Highway Research Board, 491-496.

Lima, M., Palmeira, E., Zornberg, J, and Castro, C. (2015). Evaluation of the Efficiency of Geotextiles in an Evapotranspirative Cover System to Mitigate Acid Mine Drainage in Coal Mining Disposal Sites. *Proceedings of the VII Brazilian Congress on Geosynthetics*, Brasilia, Brazil.

Lin, B. and Cerato, A. (2012). Prediction of expansive soil swelling based on four micro-scale properties. *Bulletin of Engineering Geology, the Environment, 71,* 71-78.

Lin, B. and Cerato, A. (2013). Hysteretic Soil Water Characteristics and Cyclic Swell-Shrink Paths of Compacted Expansive Soils. *Bulletin of Engineering Geology, the Environment, 72,* 61-70.

Lin, B. and Cerato, A. (2014). Applications of SEM and ESEM in Microstructural Investigation of Shale-Weathered Expansive Soils along Swelling-Shrinkage Cycles. *Bulletin of Engineering Geology, the Environment, 177,* 66-74.

Lytton, R., Aubeny, C., and Bulut, R. (2006). Design Procedures for Pavements on Expansive Soils: Volume 1. Technical Report 0-4518-1, Texas Transporatation Institute.

Mantri, S. and Bulut, R. (2014). Evaluating Performance of a Chilled Mirror Device for Soil Total Suction Measurements. *Advances in Tranportation Geotechnics and Materials for Sustainable Infrastructure.* 56-64.

McCartney, J. (2007). *Determination of the Hydraulic Characteristics of Unsaturated Soils using a Centrifuge Permeameter.* PhD Dissertation. The University of Texas at Austin.

McDowell, C. (1959). The Reation of Laboratory Testing to Design for Pavements and Structures on Expansive Soils. *Quarterly of the Colorado School of Mines, 54,* 129-153.

Messier, P. and Vitale, T. (1993). Cracking in Albumen Photographs: An ESEM Investigation. *Microscopy Research and Technique, 25*(5), 374-383.

Michel, L., Driese, S., Nordrt, L., O'Breecker, D., Labotka, D., and Dworkin, S. (2013). Stable-isotope geochemistry of vertisols formed on marine limestone and implications for deep-time paleoenvironmental reconstructions. *Journal of Sedimentary Research*, *83*, 300-308.

Mitchell, J., Hooper, D., and Campanella, R. (1966). Permeability of compacted clay. *Institute of Transportation and Traffic Engineering*, 152.

National Highway Institute. (2006). Geotechnical Aspects of Pavements. NHI Course No. 132040.

Nayak, N. and Christenesen, R. (1974). Swelling Characteristics of Compacted Expansive Soils. *Clays and Clay Minerals, 19*, 251-261.

Nelson, J. and Miller, D. (1992). Expansive Soils: Problems and Practice in Foundation and Pavement Engineering. New York: John Wiley & Sons, Inc.

Norwine, J., Giardino, J., Krishnamurthy, S., and Sayavedra, L. (2005). Water for Texas. College Station: Texas A&M University Press.

Olive, W., Chleborad, A., Frahme, C., Schlocker, Julius, Schneider, R., et al. (1998). *U.S. Geological Survey Swelling Clays Map of Counterminous U.S. Soil Map of Texas and Oklahoma.* Retrieved from http://www.surevoid.com/soil_maps/tx.php.

Oliver, M. and Webster, R. (2014). A tutorial guide to geostatistics: Computing and modelling variograms and kriging. *Catena*. Vol. 113. 56-69.

Olson, R. E. (2009). Expansive clay course notes.

Plaisted, M. (2009). *Centrifuge Testing of an Expansive Clay.* Master's Thesis. The University of Texas at Austin.

Plaisted, M. (2014). *Characterization of Soil Unsaturated Flow Properties Using Steady State Centrifuge Methods.* PhD Dissertation. The University of Texas at Austin.

Prashant, A. and Penumadu, D. (2007). Effect of Microfabric on Mechanicl Behavior of Kaolin Clay Using Cubical True Triaxial Testing. *Journal of Geotechnical and Geoenvironmental Engineering, 133*(4)*,* 433-444.

Puppala, A., Manosuthkij, T., Nazarian, S., Hoyos, L., and Chittoori, B. (2012). In situ matric suction and moisture content measurements in expansive clay during seasonal fluctuations. *Geotechnical Testing Journal, 35.*

Puppala, A., Manosuthkij,T., Nazarian, S., and Hoyos, L. (2011). Threshold moisture content and matric suction potentials in expansive clays prior to initiation of cracking in pavements. *Canadian Geotechnical Journal, 48,* 519-531.

Quaglia, G. (2017). *Hydro-mechanical characterization of unsaturated expansive clays.* PhD Dissertation. The University of Texas at Austin.

Rao, A., Phanikumar, B., and Sharma, R. (2004). Prediction of Swelling Characteristics of Remoulded and Compacted Expansive Soils using Free Swell Index. *Quarterly Journal of Engineering Geology and Hydrogeology, 37,* 217-226.

Rao., S., Sridharan, A., and Chandrakaran. S. (1989). Influence of drying on the liquid limit behavior of a marine clay. *Geotechnique*, *39*(4), 715-719.

Roodi, G.H., Phillips, J.R., and Zornberg, J.G. (2016). Evaluation of Vertical Deflections in Geosynthetic Reinforced Pavementes Constructured on Expansive Subgrades. *Proceedings of the 3rd Pan-American Conference on Geosynthetics*.

Rosenbaum, U., Huisman, J.A., Vrba, J., Vereecken, H., and Bogena, H.R. (2011). Correction of Temperature and Electical Conducitivty Effects on Dielectric

Permittivity Measurements with ECH_2O Sensors. *Vadose Zone Journal, 10,* 582-593.

Rosenbaum, U., Huisman, J.A., Weuthen, A., Vereecken, H., and Bogena, H.R. (2010). Sensor-to-Sensor Variability of the ECH_2O EC-5, TE, and 5TE Sensors in Dielectric Liquids. *Vadose Zone Journal, 9*(1), 181-186.

Schwartz, R.C., Evett, S.R., Anderson, S.K., and Anderson, D.J. (2016). Evaluation of a Direct-Coupled Time-Domain Reflectometry for Determination of Soil Water Content and Bulk Electrical Conductivity. *Vadose Zone Journal*, *15*(1).

Seco, A., Ramirez, F., Miqueleiz, L, and Garcia, B. (2011). Stabilization of expansive soils for use in construction. *Applied Clay Science, 51,* 348-352.

Seed, H. and Chan, C. (1959). Structure and Strength Characteristics of Compacted Clays. *Journal of the Soil Mechanics and Foundations Division, 84,* 87-128.

Seed, H., Woodward, R., and Lundgren, R. (1962). Prediction of swelling potential for compacted clays. *Journal of the Soil Mechanics and Foundation Division*, *88*(3), 53-87.

Skempton, A. (1953). The Colloidal Activity of Clays. *Preceedings of 3rd Onternational Conference on Soil Mechnics and Foundation Engineering*, *1,* 57-61.

Snyder, L. (2015). *Determination of the Potential Vertical Rise in Expansive Soils Using Centrifuge Technology.* Master's Thesis. The University of Texas at Austin.

Tex-124-E. (1999). *Determing Potential Vertical Rise.* Austin, TX: Texas Department of Transportation. Revision, August 1999.

Thyagaraj, T. and Rao, S. M. (2013). Osmotic Swelling and Osmotic Consolidation Behaviour of Compacted Expansive Clay. *Geotechnical and Geological Engineering*, *31,* 435-445.

Tripathy, S. and Rao, K. (2009). Cyclic Swell-Shrink Behaviour of a Compacted Expansive Soil. *Geotechnical and Geologic Engineering*, *27,* 89-103.

Tripathy, S., Rao, K., and Fedlund, S. (2002). Water content-void ratio swell-shrink paths of compacted expansive soils. *Candian Geotechnical Journal, 39*, 938-959.

United States Department of Agriculture. (1974). Soil Survey of Travis County, Texas. Washington, D.C. 117.

United States Department of Agriculture. (1983). Soil Survey of Williamson County, Texas. Washington, D.C. 163.

United States Department of Agriculture. (2017). *Web Soil Survey.* [Web page]. https://websoilsurvey.sc.egov.usda.gov/. Accessed Summer 2017.

United States Department of Commerce. (2012). *Texas:2010 Population and Housing Unit Counts.* [PDF Document]. Retrieved from https://www.census.gov/prod/cen2010/cph-2-45.pdf.

United States Geological Society. (2013). *Unsaturated Flow Basics* [Web page]. Retrevied from http://wwwrcamnl.wr.usgs.gov/uzf/unsatflow/unsatflow.html

United States Geological Society. (2017). *Geologic maps of US states* [Web page]. Retrevied from https://mrdata.usgs.gov/geology/state/

van Genuchten, M. (1980). A Closed-form Equation for Predicting the Hydraulic Conductivity of Unsaturated Soils. *Soil Sciences Society of America, 44*(5), 892-898.

Vaysse, K., Heuvelink, G., and Lagacherie, P. (2017). Spatial aggregation of soil property predictions in support of local land management. *Soil Use and Management, 33,* 299-310.

Vijayavergiya, V. and Ghazzaly, O. (1973). Prediction of Swelling Potential for Natural Clays. In *Proceedings of the 3rd International Conference on Expansive Soils.* Haifa, Israel*, 1*, 227-236.

Visconti, F., de Paz, J., Martinez, D., and Molina, M. (2014). Laboratory and field assessment of the capacitance sensors Decagon 10HS and 5TE for estimating the water content of irrigated soils. *Agricultural Water Management, 132,* 111-119.

Walker, T. (2012). *Quantification using Centrifuge of Variables Governing the Swelling of Clays.* Master's Thesis. The University of Texas at Austin.

Webster, R. and Oliver, M. (1993). How large a sample is needed to estimat the regional variogram adequately? *Geostatistics Troia*. 155-166.

Williams, H. (2009). Gis-based analysis of foundation repairs and soil conditions in the Dallas-Fort Worth region, Texas. *Environemtnal Geology, 58,* 919-928.

Wong, L. and Guo, A. (2011). Bearing Strength and Swelling Behavior of Jingmen Expansive Soil. *Road Materials and Pavement Design, 12*(2), 441-450.

Wright, S., Zornberg, J., and Ageuttant, J. (2007). The Fully Softened Shear Strength of Highy Plasticity Clays. Center for Transportation Research (CTR), Product Report No. 0-5202-3, Austin, Texas, February, 132 p.

Zemenu, G., Martine, A., and Roger, C. (2009). Analysis of the Behavior of a Natural Expansive Soil under Cyclic Drying and Wetting. *Bulletin of Engineering Geology, the Environment.* Vol. 68. 421-436.

Zhan, T, Ng, C., and Fredlund, D. (2006). Instrumentation of an Unsaturated Expansive Soil Slope. *Geotechnical Testing Journal, 30*(2).

Zornberg, J.G. (2012). Properties of Compacted Clay in Geoenvironmental Engineering course notes.

Zornberg, J.G. and Gupta, R. (2009). Reinforcement of pavements over expansive clay subgrades. *Proceedings of the 17th International Conference on Soil Mechnics and Geotechnical Engineering*. 765-768.

Zornberg, J.G., Armstrong, C.P., and Potkay, A. (2017). Implementation of Centrifuge Testing of Expansive Soils for Pavement Design. Technical Report 5-6048-03, Center for Transportation Research.

Zornberg, J.G., Armstrong, C.P., Plaisted, M.D., and Walker, T.M. (2013). Swelling of Highly Plastic Clays under Centrifuge Loading. Technical Report 5-6048-01, Center for Transportation Research.

Zornberg, J.G., Gupta, R., and Ferreira, J.A.Z. (2010). Field performance of geosynthetic reinforced pavements over expansive clay subgrades. *Proceedings of the 9th International Conference on Geosynthetics.* 1481-1484.

Vita

Christian Armstrong was born in El Paso, TX to his parents, Dale and Ofelia Armstrong. He attended Carroll Senior High School in Southlake, Texas, where he focused on academics and football, and graduated in May 2008. He graduated in January 2011 with a Bachelor of Science in Civil Engineering with Honors from the University of Texas at Austin. He received his Master of Science in Engineering in May 2014 from the University of Texas at Austin.

Permanent address (or email): christian.armstrong@utexas.edu

This dissertation was typed by Christian Philip Armstrong.